



**HAL**  
open science

# Modélisation, conception, fabrication et caractérisation de diode électroluminescente organique avec une microcavité à contre réaction répartie en régime d'excitation électrique impulsionnel

Amani Ouirimi

► **To cite this version:**

Amani Ouirimi. Modélisation, conception, fabrication et caractérisation de diode électroluminescente organique avec une microcavité à contre réaction répartie en régime d'excitation électrique impulsionnel. Physics [physics]. Université Paris-Nord - Paris XIII, 2022. English. NNT : 2022PA131044 . tel-04718307

**HAL Id: tel-04718307**

**<https://theses.hal.science/tel-04718307v1>**

Submitted on 2 Oct 2024

**HAL** is a multi-disciplinary open access archive for the deposit and dissemination of scientific research documents, whether they are published or not. The documents may come from teaching and research institutions in France or abroad, or from public or private research centers.

L'archive ouverte pluridisciplinaire **HAL**, est destinée au dépôt et à la diffusion de documents scientifiques de niveau recherche, publiés ou non, émanant des établissements d'enseignement et de recherche français ou étrangers, des laboratoires publics ou privés.

Thèse de Doctorat  
de l'UNIVERSITÉ SORBONNE PARIS NORD

Spécialité : Physique

réalisée au  
Laboratoire de Physique des Lasers UMR CNRS 7538

présentée par  
**Madame Amani OUIRIMI**

pour obtenir le grade de:  
DOCTEUR DE L'UNIVERSITÉ SORBONNE PARIS NORD

Sujet

**Modeling, design, fabrication and characterization of organic light emitting diodes with distributed feedback micro-cavity under ultra-short electrical pulsed regime**

soutenance le 28 Septembre 2022

Jury

Peter Bobbert	Pr.	Technische Universiteit Eindhoven	Rapporteur
Isabelle Sagnes	DR CNRS	Université Paris Saclay, C2N	Rapporteuse
Isabelle Seguy	CR CNRS	Université de Toulouse LAAS	Examinatrice
Abbas Mamatimin	CR CNRS	Université de Bordeaux, IMS	Examineur
Nathalie Lidgi-Guigui	MCF (HDR)	Université Sorbonne Paris Nord	Examinatrice
Daan Lenstra	Pr. Emerite	Technische Universiteit Eindhoven	Invité
Alex Chime	CC	Université de Dschang Cameroun	Encadrant
Alexis Fischer	Pr.	Université Sorbonne Paris Nord	Directeur de thèse

*À la mémoire de mes grands parents ;  
Hajj Kilani, Omi Chouikha et Hajj Abdallah  
A ma grande mère Zohra*

# Remerciement

*Le travail présenté dans ce manuscrit a été réalisé au sein de l'équipe Photonique Organique et Nanostructure du Laboratoire de Physique des Lasers de l'Université Sorbonne Paris Nord. Toute la partie expérimentale a été menée au sein de la Centrale de Proximité en Nanotechnologie de Paris Nord.*

*Tout d'abord, j'adresse mes remerciements à Madame Anne Amy Klein, Professeur à l'Université Sorbonne Paris Nord et Directrice du Laboratoire de Physique des Lasers pour m'avoir accueilli dans son laboratoire.*

*Je remercie sincèrement les membres du jury qui m'ont fait l'honneur d'examiner et d'évaluer la qualité de ce travail. Que Monsieur Peter Bobbert professeur à la Technische Universiteit Eindhoven et Madame Isabelle Sagnes, directrice de recherche au CNRS à Saclay trouvent ici toute ma reconnaissance pour avoir accepté de rapporter mon mémoire de thèse. J'adresse ma reconnaissance à Madame Isabelle Seguy, Monsieur Mamatimin Abbas et Madame Nathalie Lidgi-Guigui d'avoir accepté de faire partie des membres du jury.*

*Je remercie infiniment Monsieur Alexis Fischer, Professeur à l'Université Sorbonne Paris Nord et mon directeur de thèse pour m'avoir proposé et dirigé ce travail. Je le remercie également pour l'agréable environnement de travail qu'il a su mettre à disposition. Merci de m'avoir fait confiance, de m'aider à m'accrocher à ce sujet et de m'encourager chaque jour pour atteindre mon objectif. Je le remercie pour tout son investissement, son soutien, son écoute, et sa très grande disponibilité pendant toutes ces années de thèse. Infiniment merci.*

*Je remercie très chaleureusement Monsieur Alex Chime pour son encadrement et sa participation à la réalisation de ce travail, pour ses conseils et son appui aussi bien pour l'automatisation des banc de mesure que pour l'interprétation des résultats et pour ses nombreuses relectures.*

*Je remercie également Monsieur Frédéric Du Burck Professeur à l'Université Sorbonne Paris Nord d'avoir accepté être mon tuteur pendant ces années de thèse et Madame Hélène Perrin directrice adjointe du laboratoire physique des laser de sa participation pour diriger les comités de suivies de ce travail.*

*Je voudrais également adresser mes remerciements aux membres de l'équipe Photoniques Organiques et Nanostructures, en commençant par Monsieur Azzedine Boudrioua, directeur de l'équipe, pour ses conseils dans la pédagogie du travail d'équipe. Je tiens à remercier aussi Monsieur Mahmoud Chakaroun, maître de conférence pour son aide pour la calibration du banc optique ainsi que pour les discussions enrichissantes sur l'analyse des résultats.*

*Je remercie notamment Madame Jeanne Solard, responsable adjoint de la salle blanche, pour son aide et ses conseils à l'utilisation des outils de la salle blanche en particulier le MEB. Merci à Monsieur Dejan Kocic, technicien salle blanche pour sa grande disponibilité, sa réactivité et son bienveillance. Merci aussi Monsieur Min Lee, Monsieur Quentin Guimard pour leurs soutiens et encouragements.*

*J'aimerais également remercier Monsieur Albert Kaladjian, responsable de l'atelier mécanique du laboratoire et Monsieur Thierry Billeton, responsable de l'atelier optique du laboratoire, pour leur*



soutiens techniques sur la réalisation des systèmes expérimentaux dédiés à la caractérisation ainsi que sur la fabrication des échantillons.

Je remercie sincèrement Monsieur Chii-Chang Chen de la National Central University à Taiwan, de son appui pour la modélisation et simulation par Rsoft. Je remercie Monsieur Souheil Bensmida de University of Bristol qui a partagé avec moi son expérience en mesure RF.

Je remercie également Monsieur Daan Lenstra pour ses conseils technique dans le calcul et simulation de la dynamique des lasers ainsi que pour ses nombreux encouragements. Merci d'avoir accepté notre invitation.

Je tiens à remercier tout particulièrement, Madame Yamina Amzal, chef de département RT, de sa bienveillance et de ses encouragements qui m'ont motivée à chaque fois.

J'aimerais remercier l'équipe administrative du laboratoire, Madame Maryse Medina, Madame Carole Grangier pour leurs aides et conseils administratifs tout au long de ma thèse.

Je voudrais remercier également mes amis doctorants : Dr Amadou Thierno Diallo, Dr Sarrah Hamdad, Dr Safia Mohand-Oussaid et futur Dr Yara Droubi pour les agréables moments passés ensemble aussi bien dans le cadre professionnel que le cadre personnel.

J'exprime ma grande reconnaissance et mon affection à Nixson Loganathan, ingénieur salle blanche. Mon binôme et mon collègue depuis l'année 2016 je le remercie pour son attention, sa disponibilité sans pareil et son encouragement. Ensemble, nous avons pu surmonter bien des problèmes aussi bien professionnels que privés. Je ne saurais assez le remercier d'être pour moi plus qu'un ami, un membre de la famille. மிக்க நன்றி

Je dédie ce travail à mes très chers parents ; à mon symbole de patience, d'amour et de tendresse ma mère « Saida Ghedhoui » et à mon pilier et protecteur mon papa « Habib Ouirimi ». Je les remercie d'avoir dû supporter mes très longues périodes d'absence. J'espère qu'ils trouveront dans ce travail le fruit des sacrifices consentis.

Je remercie chaleureusement ma perle rare ma deuxième mère « Tata Ouassila » et mon oncle « Tonton Mongi » pour leurs soutiens, encouragements et conseils afin de réussir mes projets professionnels et personnels

A mes chers frères « Zied » et « Walid » pour leurs soutiens indéfectibles. A mes sœurs « Rafika », « Afrah », « Naziha » et « Asma » pour m'avoir accompagné et vécu cette expérience à mes côtés. Merci à mes oncles et mes cousins de m'aider à surmonter plusieurs challenges. Merci à « Hatem » d'avoir pris soin de moi, à m'encourager et d'avoir supporté mon absence et mes crises de stress

Merci à toutes les personnes avec lesquelles j'ai pu échanger, partager et qui ont contribué à la réalisation de ce travail de thèse.



# Résumé

Ce travail à dominante expérimentale vise la conception, la micro-nano-fabrication et la caractérisation d'un composant combinant une diode électroluminescente organique (OLED) et une cavité à contre-réaction répartie (DFB) pour aller vers la diode laser organique.

Si l'essor de l'électronique organique a donné naissance à de nombreux composants optoélectroniques la démonstration de la diode laser organique reste encore un défi majeur malgré une publication très récente par l'équipe japonaise d'Adachi. Parmi les verrous scientifiques qui freinent la réalisation de la diode laser organique, on peut noter premièrement la faible densité de courant que peut accepter les semi-conducteurs organiques ( $100\text{-}1000\text{mA/cm}^2$  en courant continu) alors que le seuil laser est estimé au-delà de plusieurs  $\text{kA/cm}^2$ . Deuxièmement, les pertes par annihilation dues à l'accumulation des états triplets qui apparaissent au-delà de la dizaine de nanosecondes et qui renchérisent le seuil laser. A défaut de disposer de matériaux particuliers à faible taux d'annihilation, l'effet laser peut être observé dans une autre configuration correspondant à une fenêtre temporelle inférieure à 10ns et à des impulsions électriques de l'ordre du  $\text{kA/cm}^2$  dans le cas le plus favorable pour des OLEDs placées dans des cavités à très haut facteur de qualité offrant un seuil laser parmi les plus bas.

Cette thèse, étudie les aspects électriques, optiques et matériaux des trois constituants d'une diode laser organique, à savoir, une cavité, un milieu à gain, et une source d'excitation.

Le premier chapitre, permet grâce à une étude bibliographique d'identifier les enjeux et faire une première série de choix pour orienter la suite des travaux.

Le deuxième chapitre de ces travaux est consacré à des conceptions et modélisations. Un modèle électrique amélioré par rapport à l'état de l'art est proposé qui permet de concevoir des OLEDs plus rapides avec des constantes de temps de l'ordre de 100ps. Ce modèle électrique permet de dimensionner et fabriquer des composants capables de répondre aux exigences de densité de courant élevée pour atteindre les seuils laser visés. Un modèle laser dynamique qui prend en compte l'excitation électrique et la dynamique des émissions spontanée et stimulées est ensuite proposé. Ce modèle de diode laser organique, qui constitue une avancée par rapport à l'état de l'art permet de prédire la dynamique laser comme le seuil laser à partir des paramètres clés et des propriétés du matériau. Le troisième point étudié est la cavité laser. Une étude théorique basée sur la modélisation 1D et 2D a été réalisée afin de dimensionner le type de cavité à fabriquer.

Le troisième chapitre, met en œuvre les conclusions du chapitre précédent pour fabriquer les électrodes par photolithographie, les cavité de type DFB combinant un premier et un deuxième ordre par lithographie électronique, et les OLEDs par évaporation sous vide.

Le chapitre quatre présente des mesures électriques et optiques résolues en temps des constituants élémentaires de la diode laser organique conçus selon les résultats des chapitres précédents. La rapidité des OLEDs à l'échelle de quelques centaines de ps, ainsi que des densités de courant dépassant des dizaines de  $\text{kA/cm}^2$  sont ainsi démontrées. Sous pompage optique, les cavités de type DFB présentent des facteurs de qualité de l'ordre de plusieurs milliers validant ainsi la conception et la fabrication. Finalement, une série de composants combinant une OLED ultra-rapide, une cavité DFB faite d'un premier ordre et d'un deuxième ordre sont caractérisés. Des premiers résultats montrent une réponse optique 2.9 plus intense lorsque l'OLED est combinée avec une microcavité DFB que l'OLED de référence sans cavité. A l'aide du modèle dynamique laser, nous montrons que le seuil de transparence a été franchi.

# Abstract

This work is mainly experimental and aims at the design, the micro-nano-fabrication and the characterization of a device that combines an organic light-emitting diode (OLED) and a distributed feedback (DFB) cavity to progress towards the organic laser diode.

If the development of organic electronics has given rise to many optoelectronic devices, the demonstration of organic laser diode remains a major issue despite a very recent publication by the Adachi's Japanese team. Several scientific challenges still need to be overcome for the realization of the organic laser diode. Firstly the organic semiconductors known as a low conductive materials, can only sustain low current density ( $100\text{-}1000\text{mA}/\text{cm}^2$  in DC) while the laser threshold is estimated beyond several  $\text{kA}/\text{cm}^2$ . Secondly, the annihilation losses due to the accumulation of triplet states appear beyond ten nanoseconds and further increase the laser threshold. Without specific materials offering low annihilation rates, lasing can be achieved in another configuration corresponding to a time window shorter than 10ns and to pulsed current density of the order of  $\text{kA}/\text{cm}^2$  achievable in the most favorable case with an OLED combined with a very high quality factor optical cavity, in a configuration corresponding.

This thesis studies the electrical, optical and material aspects of the three basic components of an organic laser diode namely a cavity, a gain medium, and an excitation source.

Based on a bibliographic study, the first chapter identifies issues leading to make first series of choices guiding the rest of the work.

The second chapter of this work is devoted to design and modeling. An electrical model improved compared to the state of the art is proposed and allows to design faster OLEDs with time constants of the order of 100ps. This electrical model allows to design and fabricate devices that can meet the high current density requirements to reach the targeted laser thresholds. A dynamic laser model that takes into account the electrical excitation and the dynamics of spontaneous and stimulated emissions is then proposed. This organic laser diode model allows to predict the laser dynamics such as the laser threshold from key material parameters. The third point studied, in this chapter, is the laser cavity. A theoretical study based on 1D and 2D modeling has been carried out to define the type and the geometrical parameters of cavity to be manufactured.

The third chapter, implements the conclusions of the previous chapter to fabricate the electrodes by photolithography, the DFB-type-cavity combining a first and a second order by electronic lithography, and the OLEDs by vacuum evaporation.

Chapter four presents time-resolved electrical and optical measurements of the different components of the organic laser diode designed according to the previous chapters. From the OLED characterizations, high-speed response in a time scale of a few hundred ps, as well as current densities exceeding tens of  $\text{kA}/\text{cm}^2$  have been observed. Under optical pumping, the DFB cavities show quality factors of the order of several thousandss, which validates its design and fabrication. Finally, a series of devices combining an ultrafast OLED, a DFB cavity with first and second order grating are characterized. Preliminary results show an optical response 2.9 times more intense when the OLED is combined with a DFB microcavity than the reference OLED without cavity. Using the upgraded laser dynamics model, we show that the transparency threshold has been reached.

# Contents

<b>Introduction.....</b>	<b>1</b>
References.....	4
<b>Chapter I : Basic Concepts.....</b>	<b>6</b>
I. Basic Concepts.....	7
I.1. Introduction.....	7
I.2. Organic optoelectronics.....	8
I.2.1 Organic semiconductors.....	8
I.2.2 Organic Light Emitting Diode.....	10
I.2.2.1 Injection of charges.....	10
I.2.2.2 Charge transport.....	12
I.2.2.3 Exciton formation and energy transfer.....	14
I.2.2.4 Light emission and non-radiative exciton de-excitation.....	16
I.2.2.4.1 Emission of photons.....	16
I.2.2.4.2 Exciton annihilations.....	17
I.3. Electrical Concepts.....	18
I.3.1 Pulsed OLED.....	18
I.3.2 Electrical modeling.....	20
I.3.3 Spatial distribution of charge.....	22
I.3.4 Microwave electrodes.....	22
I.4. Basic laser concepts and state of the art of organic lasers.....	24
I.4.1 Laser principle.....	24
I.4.1.1 Absorption, spontaneous and stimulated emissions.....	24
I.4.1.1.1 Laser structure.....	26
I.4.1.1.1.1 Gain medium.....	26
I.4.1.1.1.2 Cavities.....	28
I.4.1.2 Excitation sources.....	31
I.4.2 State of the art of organic lasers.....	32
I.5. Challenges towards the organic laser diode.....	40
I.5.1 Gain media.....	40
I.5.2 Laser cavities.....	40
I.5.3 Electrical excitation of organic materials.....	42
I.6. Conclusion.....	44
References.....	45
<b>Chapter II: Model, Design and Simulation.....</b>	<b>52</b>
II. Model, Design and Simulation.....	53
II.1. Introduction.....	53
II.2. Electrical modeling.....	54
II.2.1. Improved equivalent electrical model.....	54
II.2.2. Numerical estimation of the time constant.....	58
II.2.2.1. Numerical estimation of the maximum current-density.....	60

II.2.3. Design of coplanar waveguided electrodes (CPW).....	62
II.2.3.1. CPW structure.....	62
II.2.3.2. Design of the measurement resistance geometry.....	64
II.2.3.3. Estimation of the parasitic serial resistances.....	64
II.2.3.4. Estimation of the parasitic capacitance.....	68
II.2.3.5. Estimation of the time constant with the CPW geometry.....	68
II.3. An Organic Laser diode model.....	70
II.3.1. Introduction.....	70
II.3.2. The model.....	71
II.3.2.1. The polaron differential equation.....	73
II.3.2.2. The host singlet-exciton equation.....	73
II.3.2.3. The host triplet-exciton equation.....	74
II.3.2.4. The dopant singlet-exciton equation.....	74
II.3.2.5. The dopant triplet-exciton equation.....	74
II.3.2.6. The photonic equation.....	75
II.3.2.7. The optical gain.....	75
II.3.2.8. More about the W-factor.....	75
II.3.2.9. Relation between the quality factor and cavity lifetime $T_{cav} = 1/kCAV$ .....	76
II.3.3. Dynamical response to pulsed electrical excitation.....	77
II.3.3.1. Threshold estimation.....	82
II.3.4. Conclusion on the model.....	84
II.4. Optical design.....	86
II.4.1. Objectives.....	86
II.4.2. Laser gain material.....	87
II.4.2.1. Laser gain coefficient of different organic compounds.....	87
II.4.2.2. Residual absorption.....	90
II.4.2.2.1. Objectives and method.....	90
II.4.2.2.2. Theory of the residual absorption and intrinsic residual absorption.....	90
II.4.2.2.3. Absorbance and electroluminescence spectra.....	94
II.4.2.2.4. Residual absorption calculation.....	100
II.4.2.2.5. The effective gain.....	102
II.4.3. OLED structure from the optical waveguide point of view.....	105
II.4.3.1. Objectives and method.....	105
II.4.3.2. Considered stack.....	105
II.4.3.3. Confinement factor.....	106
II.4.3.3.1. Role of the ITO thickness on the confinement factor.....	106
II.4.3.3.2. Role of the Organic layer thickness on the confinement factor.....	108
II.4.3.3.3. Conclusion on the optimal layer thicknesses from the confinement factor.....	110
II.4.4. Laser cavity design.....	112
II.4.4.1. Objectives and method.....	112
II.4.4.2. Study of the effective index.....	112
II.4.4.2.1. High effective index.....	114
II.4.4.2.2. Low effective index.....	116
II.4.4.2.3. Effective index contrast and conclusion.....	116
II.4.5. Design of the distributed feedback cavity.....	120
II.4.5.1. Objectives and methods.....	120
II.4.5.2. Single multilayered (DFB) mirror.....	120
II.4.5.3. Cavities consisting of DFB mirrors and defects in between.....	124
II.4.5.4. Quality factor of DFB cavities.....	126
II.4.5.5. Finite-difference time domain analysis and confirmation.....	128
II.4.5.5.1. FDTD method.....	128
II.4.5.6. Presentation of structure and parameters.....	130
II.4.5.6.1. Geometric parameters.....	130

II.4.5.6.2. Numerical parameters.....	132
II.4.5.7. 2D studies.....	134
II.5. Conclusions on the electrical, material and optical designs.....	136
<b>References.....</b>	<b>142</b>
<b>Chapter III: Fabrication.....</b>	<b>146</b>
III. Fabrication.....	147
III.1. Introduction.....	147
III.2. Substrates dimensions, properties and samples.....	150
III.3. Mask Design.....	152
III.3.1 Etching mask.....	152
III.3.2 Metalization mask.....	154
III.3.3 Thinning mask.....	156
III.3.4 Hollow masks.....	158
III.3.4.1 Hollow masks for organic materials.....	158
III.3.4.2 Hollow masks for aluminum cathode.....	160
III.4. Electrodes patterning.....	162
III.4.1 Cleaning.....	162
III.4.2 Photolithography.....	162
III.4.3 Etching.....	164
III.4.4 Metalization.....	166
III.4.5 Validation.....	168
III.4.5.1 Optical inspection and validation.....	168
III.4.5.2 Electrical validation.....	168
III.5. $\mu$ -cavity patterning.....	172
III.5.1 Scanning electronic lithography :.....	173
III.5.1.1 Principle of Scanning electron lithography:.....	173
III.5.1.2 Fabrication parameters.....	174
III.5.2 Preliminary observation and validation.....	182
III.5.2.1 Structure observation.....	182
III.5.2.2 Indication of second order diffraction.....	184
III.6. Organic hetero-structure deposition.....	186
III.6.1 Small-molecule organic stack.....	186
III.6.2 Vacuum evaporation.....	186
III.6.3 macro-molecule stack.....	187
III.7. Conclusion.....	190
<b>References.....</b>	<b>192</b>
<b>Chapter I : Experimental results and analysis.....</b>	<b>193</b>
<b>IV. Experimental results and analysis.....</b>	<b>194</b>
IV.1. Introduction.....	194
IV.2. Characterization setup.....	194

IV.2.1. DC characterization setup.....	194
IV.2.2. Time-resolved characterization setup.....	196
IV.2.2.1 Probe station.....	196
IV.2.2.2 Pulsed electrical excitation.....	196
IV.2.2.3 Optical setup.....	196
IV.3. Measurements of OLED without cavity.....	198
IV.3.1. DC measurement (JVL) and spectral.....	198
IV.3.2. Optical and Electrical pulsed measurements.....	200
IV.3.2.1 Experimental Validation of the proposed laser model.....	202
IV.3.2.1.1 Comparison between calculated response and experimental results.....	202
IV.3.3. Ultra-short response under electrical excitation.....	206
IV.3.3.1 Objectives of the experiments.....	206
IV.3.3.2 Results.....	206
IV.3.3.3 Analysis.....	210
IV.3.3.3.1 Electrical level.....	210
IV.3.3.3.2 Optical level.....	212
IV.4. Devices with DFB cavities.....	214
IV.4.1. Laser properties of DFB patterns under optical pumping.....	214
IV.4.1.1 Samples.....	214
IV.4.1.2 Experimental setup.....	215
IV.4.1.3 Experimental results.....	215
IV.4.2. OLED with DFB micro-cavity under high current density.....	222
IV.4.2.1 Sample description.....	222
IV.4.2.2 Measurements.....	222
IV.4.2.3 Analysis.....	224
IV.4.2.3.1 Simulations with the current model.....	224
IV.4.2.3.2 Improved model.....	226
Identifying the intermediate situation: the transparency Threshold.....	226
Upgrade the OLD model: Taking into account polaronic and triplet losses.....	227
Simulation with the upgraded model.....	227
IV.4.2.4 Conclusion.....	230
<b>References.....</b>	<b>232</b>
<b>General conclusion.....</b>	<b>234</b>





# **Introduction**



# Introduction

## Context

With relatively simple, economic, and environmentally friendly production processes, virtually unlimited availability of amorphous organic semiconductors, organic optoelectronic has become a large research field on various devices type such as organic photovoltaic cells (OPV), organic field effect transistors (OFETs) and biosensor [1,2,3,4,5].

In past decades, organic light emitting diode (OLED) field has made huge steps forward reaching the market stage. These progresses result from intense efforts that began in 1953, with Bernanose reporting electroluminescence of an orange acridine crystal under 100V bias voltage[6,7]. Ten years later, Pope demonstrated electroluminescence of an organic anthracene monocrystal[8]. In 1965, Helfrich and Schneider produced a double injection of electrons and holes in an anthracene monocrystal leading to recombination and electroluminescence. In 1977, a huge step forward was obtained by Heeger with the discovery of the conductive properties of doped polyacetylene[9]. This discovery won him the 2000 Nobel prize in chemistry. The emergence of “plastic conductivity” has not only paved a new way in the world of electronics, but also brought the organic semiconductor technology to take a step forward. Since this demonstration, researchers have sought to prove that inorganic semiconductor components can be replaced by organic semiconductors like light-emitting diode. The first “efficient” organic light-emitting diode has been demonstrated by Tang and Van Slyke in 1987. It is a small molecules based bilayer device with a film thickness around 135nm requiring forward voltage as low as few Volts [10]. In 1990, the first polymer OLED was presented by Burroughs[11].

Nowadays, OLEDs dominate displays and lighting technologies such as for TV screens and mobile phones.

Recently, Stephen Forrest questioned the future of organic electronics with “What’s beyond OLED displays?”[12]. This question has arisen probably because by reaching the market stage with efficient OLEDs, the conditions for funding academic research on the OLED topic have greatly reduced.

In the field of organic optoelectronics, the only organic light sources not demonstrated at the beginning of this thesis are the organic laser diode.

## Motivation

There are two ways to answer the question asked by Forrest “what’s beyond displays?”, firstly the organic laser diode, secondly, the high-speed properties of OLEDs.

Until 2019, solid-state organic lasers have been demonstrated under optical pumping exclusively. Only in 2019, in the middle of this thesis, the Adachi’s group published a paper entitled “Indication of current-injection lasing from an organic semiconductor” [13]. These encouraging results

discovered when our experiments were under conduct, generated more questions than answers. What's the quality factor of the laser cavity? What are the most important materials properties to achieve lasing? Do other materials offer similar properties...? How come the laser threshold is as low as  $500\text{A}/\text{cm}^2$

Regarding the second way, until recently, OLEDs used in displays (and in a less extent in lighting), have been considered as slow devices with turn-on time constants in the order of a few milliseconds, just fast enough for fluidity of screen images. However, recent results by Chime demonstrated that OLED dynamics is in the nanosecond range as fast as inorganic LEDs<sup>[14]</sup>. Moreover, a great advantage of OLEDs compared to GaN LEDs is the simplicity of the fabrication process. Indeed, high-speed micro-OLEDs are fabricated in tens of steps whereas micro-LED requires more than hundreds of steps. In global context of energy saving and climate change, the optoelectronic solution with potential high-speed organic optoelectronic platform could offer opportunities for a less complex, more resilient and sustainable microelectronic industry. For example, high-speed OLED could be used to transmit data allowing high-speed organic optoelectronic to offer a bright future for OLEDs thus answering Forrest question<sup>[15]</sup>.

## **Challenges**

Since the early times of laser, with the first solid-state organic laser under optical pumping demonstrated in 1967, organic materials (dyes) are known to offer good laser gain however the realization of organic laser diode under electrical excitation is still a major scientific and technological challenge, despite recent advances <sup>[13,16]</sup>. This is due to several physical issues at the material and the device levels from both the electrical and optical point of view:

- At the materials level, low charge mobilities of  $\pi$ -conjugated organic semiconductors are the main limitation to reach electrical current densities high enough to achieve the laser threshold.
- In addition, organic materials suffer from optical losses and from different types of annihilation although they offer relatively large laser gain coefficient <sup>[17, 18]</sup>. Zeng intuited that because of some annihilation mechanisms, lasing is possible only during a narrow time window of about ten ns <sup>[19]</sup>. Devices with fast dynamic are required to fit in this narrow time window.
- At the device level, an organic heterostructure allowing current density high enough to reach the laser threshold is to be combine with high-Q laser cavity compatible with planar integration in an OLED

## **Objectives**

The main objective of this thesis is to progress towards the organic laser diode from the experimental point of view. Therefore, the secondary objectives are firstly, the design and the fabrication of distributed feedback micro-cavity compatible with OLEDs and secondly, the integration of such a microcavity on coplanar waveguide electrodes. These microwave electrodes are based on recent advances obtained by Chime allowing ultra-intense pulsed electrical excitation of OLEDs.

From a more fundamental point of view, we would like to investigate the dynamical behaviors of OLEDs at the nanosecond time scale. Also we would like to investigate, what difference electrical excitation induces in terms of physical processes leading to laser operation compared to optical pumping.

## **Scientific approach**

The scientific approach is mainly experimental with micro and nano-fabrication of devices and their characterization. However, the theoretical development and modeling remain essential to restrict the design choices and thus reduces the time spent in clean room for fabrication which is known to be time consuming.

Indeed, a pure trial-and-error approach would very quickly be confronted with the significant time required to fabricate several micro and nano-devices which would limit the number of possible iterations.

Our scientific approach takes place in 4 stages; first, a literature review will lead us to identify more precisely the issues and to narrow the number of solutions. In a second stage, we will model and design as precisely as possible one or more devices that will be manufactured in a third stage. Finally, they will be characterized and their electrical and optical responses measured before possible iterations

## **Outline**

This manuscript is organized in four parts as follows ;

Chapter I recalls basic concept on organic semiconductors and organic light emitting diode (OLED), electrical concepts on pulsed OLED before presenting laser concepts, the history and the state of art of organic lasers. The main goal of this chapter is to identify challenges towards the organic laser diode and to propose a first level of solutions for the three keys elements of lasers namely gain medium, cavity and excitation source.

The second chapter builds up on the initial choices decided in the preceding chapter to model and design more precisely a device combining an OLED and a microcavity. Modeling and design apply at the electrical, optical and material level to identify the essential parameters of a high-performance laser micro-cavity compatible with OLED structure, the best gain medium and the optimal electrical excitation source. The final choices must lead to a ready-to-be fabricated design.

The third chapter is dedicated to the fabrication of the final device according to the design identified in the previous chapter. It takes into account fabrication difficulties and issues to establish reproducible processes. The procedures of fabrication of OLED, electrodes and microcavities will be included

Chapter IV is focused on the characterization and measurement of the different devices fabricated as describe in the third chapter. Dedicated measurement setups, will be described before being used. OLED with and without microcavities will be measured and compared to investigate the microcavity effects hoping to observe a laser manifestation.

## References

- [1] C. W. Tang, «*Two-layer organic photovoltaic cell*», Applied Physics Letters, vol. 48, 1985, DOI: [10.1063/1.96937](https://doi.org/10.1063/1.96937)
- [2] N. S. Sariciftci, «*Photoinduced Electron Transfer from a Conducting Polymer to Buckminsterfullerene*», Science, vol. 258, 1992, DOI: [10.1126/science.258.5087.1474](https://doi.org/10.1126/science.258.5087.1474)
- [3] Tsumura, A.; Koezuka, H.; Ando, Tsuneya, "Macromolecular electronic device: Field-effect transistor with a polythiophene thin film", Applied Physics Letters, 49, 1986, DOI: [10.1063/1.97417](https://doi.org/10.1063/1.97417)
- [4] Koezuka, H.; Tsumura, A.; Ando, Tsuneya, "Field-effect transistor with polythiophene thin film", Synthetic Metals, 1987, DOI: [10.1016/0379-6779\(87\)90964-7](https://doi.org/10.1016/0379-6779(87)90964-7)
- [5] V. Podzorov, S. E. Sysoev, E. Loginova, V. M. Pudalov, and M. E. Gershenson, «Single-crystal organic field effect transistors with the hole mobility 8 cm<sup>2</sup>/Vs», Applied Physics Letters 83, 2003, DOI: [10.1063/1.1622799](https://doi.org/10.1063/1.1622799).
- [6] A. Bernanose, M. Comte, P. Vouaux, «Sur un nouveau mode d'émission lumineuse chez certains composés organiques», J. Chim. Phys. 50, 64, 1953, DOI: [10.1051/jcp/1953500064](https://doi.org/10.1051/jcp/1953500064)
- [7] A. Bernanose, P. Vouaux, «Électroluminescence organique : étude du mode d'émission», J. Chim. Phys. 50, 1953, DOI: [10.1051/jcp/1953500261](https://doi.org/10.1051/jcp/1953500261)
- [8] M. Pope, H. P. Kallmann, and P. Magnante, «Electroluminescence in Organic Crystals», J. Chim. Phys. 38, 1963, DOI: [10.1063/1.1733929](https://doi.org/10.1063/1.1733929)
- [9] C. K. Chiang, C. R. Fincher, Jr., Y. W. Park, A. J. Heeger, H. Shirakawa, E. J. Louis, S. C. Gau, and Alan G. MacDiarmid, «Electrical conductivity in doped polyacetylene», Phys. Rev. Lett. 39, 1098, 1977, DOI: [10.1103/PhysRevLett.39.1098](https://doi.org/10.1103/PhysRevLett.39.1098)
- [10] C. W. Tang and S. A. VanSlyke, "Organic Electroluminescent Diodes," Applied Physics Letters, Vol. 51, No. 12, 1987, DOI: [10.1063/1.98799](https://doi.org/10.1063/1.98799)
- [11] Burroughes, J. H., Bradley, D. D. C., Brown, A. R., Marks, R. N., Mackay, K., Friend, R. H., Burn, P. L., and Holmes, A. B., «Light-emitting diodes based on conjugated polymers», Nature, 347(6293)539-541, 1990, DOI: [10.1038/347539a0](https://doi.org/10.1038/347539a0)
- [12] S. R. Forrest, «Waiting for Act 2: what lies beyond organic light emitting diode (OLED) displays for organic electronic?», Nanophotonics, V. 10, no. 1, pp. 31-40, Aug. 2020, doi: [10.1515/nanoph-2020-0322](https://doi.org/10.1515/nanoph-2020-0322)
- [13] A. S. D. Sandanayaka et al., "Indication of current-injection lasing from an organic semiconductor," Appl. Phys. Express, vol. 12, no. 6, p. 061010, May 2019, doi: [10.7567/1882-0786/ab1b90](https://doi.org/10.7567/1882-0786/ab1b90).
- [14] A. C. Chime, S. Bensmida, M. Chakaroun, M. W. Lee, H. Nkwawo, and A. P. A. Fischer, "Electrical modelling and design of ultra-fast micro-OLED with coplanar wave-guided electrodes in ON-OFF regime," Organic Electronics, vol. 56, pp. 284-290, May 2018, doi: [10.1016/j.orgel.2017.12.026](https://doi.org/10.1016/j.orgel.2017.12.026).

## References

- [15] K. Yoshida et al., “245 MHz bandwidth organic light-emitting diodes used in a gigabit optical wireless data link,” *Nat Commun*, vol. 11, no. 1, p. 1171, Dec. 2020, doi: [10.1038/s41467-020-14880-2](https://doi.org/10.1038/s41467-020-14880-2).
- [16] H. Soffer and B. B. McFarland, “CONTINUOUSLY TUNABLE, NARROW-BAND ORGANIC DYE LASERS,” *Applied physics letters*, vol. 10, p. 266, 1967.
- [17] S. V. Frolov, Z. V. Vardeny, K. Yoshino, A. Zakhidov, and R. H. Baughman, “Stimulated emission in high-gain organic media,” *Physical Review B*, vol. 59, no. 8, p. R5284, 1999.
- [18] C. Gärtner, C. Karnutsch, U. Lemmer, and C. Pflumm, “The influence of annihilation processes on the threshold current density of organic laser diodes,” *Journal of Applied Physics*, vol. 101, no. 2, p. 023107, Jan. 2007, DOI:[10.1063/1.2425003](https://doi.org/10.1063/1.2425003).
- [19] Lei ZENG, “Étude théorique et expérimentale de  $\mu$ -OLED en régime impulsionnel à très haute densité de courant”, Thesis from the Université Paris 13, 2016





# **Chapter I – Basic Concepts**



# I. Basic Concepts

## I.1. Introduction

This first chapter is an opening to the subject of this thesis. It recalls some results of the previous thesis and presents the basic concepts necessary to found the research strategy on the pursuit of electrically-driven organic semiconductor lasers. First of all it is necessary to understand what organic semiconductors are, and how they are used to make OLEDs. Section.I.2 presents the physics of organic semiconductors (section. I.2.1 ) and the organic light emitting diodes (OLED) operation principles (section. I.2.2 ) as the most relevant organic solid-state electrically-driven basic building blocks to start with. Because we aimed at designing and fabricating electrically driven organic lasers, the results of previous Ph.D works mainly dealing with high current density in OLEDs will be recapped; More precisely, to achieve high excitation level above  $\text{kA/cm}^2$  necessary to reach the laser thresholds while preventing thermal destruction, model for pulsed electrical excitation of OLEDs in the nanosecond range will be recalled (section. I.3.2 ). This is the subject of section.I.3 that will gather some basic electrical concepts including a bibliographic study on pulsed OLED (section. I.3.1 ), and some microwaves basics (section. I.3.4 ). Because we aim at building a laser, section.I.4 recall basic optical concepts including laser principles (section. I.4.1 ). Also, the laser history being rich with many experiments and results on dye lasers, we will explore existing solutions on gain medium, laser cavity types and sources of excitation so as to identify the most adapted solutions for our objectives (section. I.4.2 ). From there, our scientific approach to progress towards the organic laser diode will be refined (section I.5).

## I.2. Organic optoelectronics

We recall basic concepts on organic semiconductors as a prerequisite to organic optoelectronic devices.

### I.2.1 Organic semiconductors

In this section, we gather basic concepts on organic materials to understand how their molecular structures affect the electrical and optical properties. Organic compounds are molecules containing mainly hydrogen and carbon atoms. Among them, organic semiconductors exhibit specific physical properties related to the electronic structure of carbon atoms. More precisely, the way carbon atoms are bound to each other is key to explain the electrical conduction in organic semiconductors. Three types of carbon-carbon bonds called hybridation ( $sp^1$ ,  $sp^2$ ,  $sp^3$ ) exist. They result from the combination of  $2s$  and  $2p$  orbitals (fig.I.1.a). In the  $sp^2$  hybridation, two carbon atoms are bound with  $\sigma$  and  $\pi$ -bonds. The electrons involved in this  $\pi$ -bond are delocalized and can pass freely from one carbon atom to another. A typical example is the ethylene molecule shown in fig.I.1.c where the  $\pi$ -bonds are displayed in yellow. A more complex molecule with several carbon atoms alternatively bounded with simple and double bonds is called  $\pi$ -conjugated molecule.  $\pi$ -electrons can then participate in the motion of charges within the  $\pi$ -conjugated molecule passing from one carbon atom to another and thus giving rise to the conduction properties. Depending on the length of the molecular chain, one can distinguish polymers with typical molecular weight  $>1000$  or small molecules. These electrical properties exist although the organic materials are amorphous.

The  $\pi^-$  and  $\pi^+$  energy levels corresponding to the double bonds of a small molecule like ethylene have a low energy difference (fig.I.2.a). Pauli's principle states that only the bounded orbital should be occupied at equilibrium, while the anti-bounded orbital remains unoccupied [1]. By increasing the number of carbon atoms, and therefore the length of delocalization, the  $\pi^-$  and  $\pi^+$  molecular orbitals change from discrete energy levels to two quasi-continuous energy bands called  $\pi^-$  bands or highest occupied molecular orbital (HOMO) and  $\pi^+$  bands or lowest unoccupied molecular orbital (LUMO) (fig.I.2.b).

The Jablonsky diagram shown in fig.I.3 summarizes the changes in energy levels due to several photo-physical processes occurring in organic materials. At equilibrium and in the vibrational ground state  $\nu=0$ , the energy level of the molecule is the fundamental state  $S_0$ . Depending of the wavelength (blue and purple arrows) absorption (Abs) of photon increases the energy level to higher states (singlet states  $S_1$ ,  $S_2$ , ...) and different vibrational levels ( $\nu=1,2,3,\dots$ ). This transition occurs at the attosecond time scale. Under vibration relaxation (VR), the molecule relaxes to lower vibrational level on a 1-100 ps timescale (stripped blue arrows). The internal conversion (IC) is a non-radiative transition between the fundamental level of a higher electronic state and vibrational levels of the lower singlet state (0.01-1 ns). The fluorescence (Flu) is a radiative transition from the  $S_1$  singlet state to vibrational levels of the ground state  $S_0$ . The energy decay is accompanied by the emission of photons (green wavy arrows). The decay time also named singlet lifetime is in the 0.1-100 ns timescale. Note that the energy gaps of the fluorescence are smaller than the energy gaps of absorption because of the vibrational relaxation which spectrally translates in a difference between the spectral position of the maximum of the absorption band and the maximum of the fluorescence emission called the Stokes shift [2,3]. Nevertheless, an overlap between the absorption and emission spectra exists which may induce re-absorption.

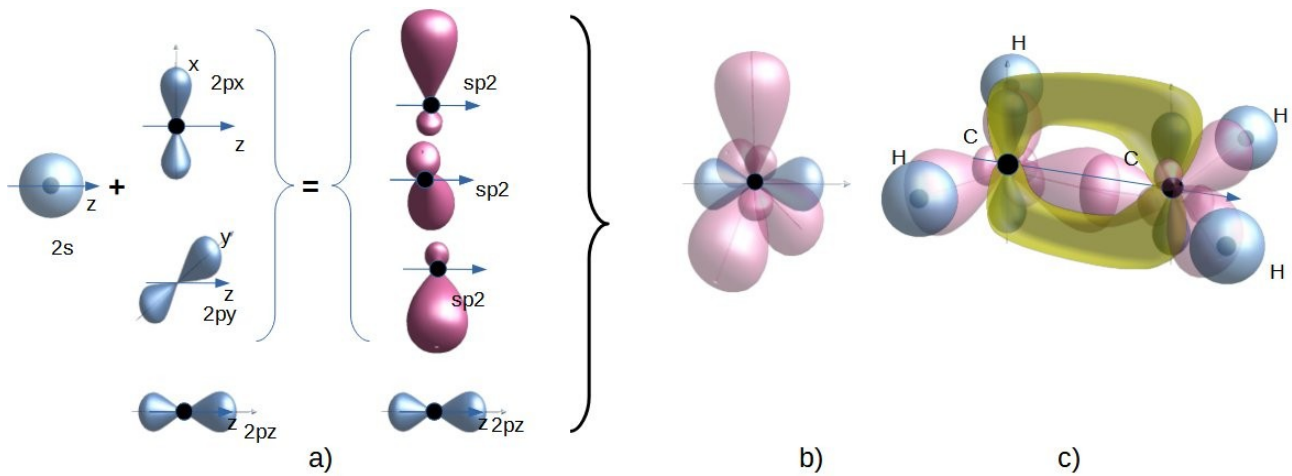


Figure I.1:  $sp^2$  hybridization of carbon

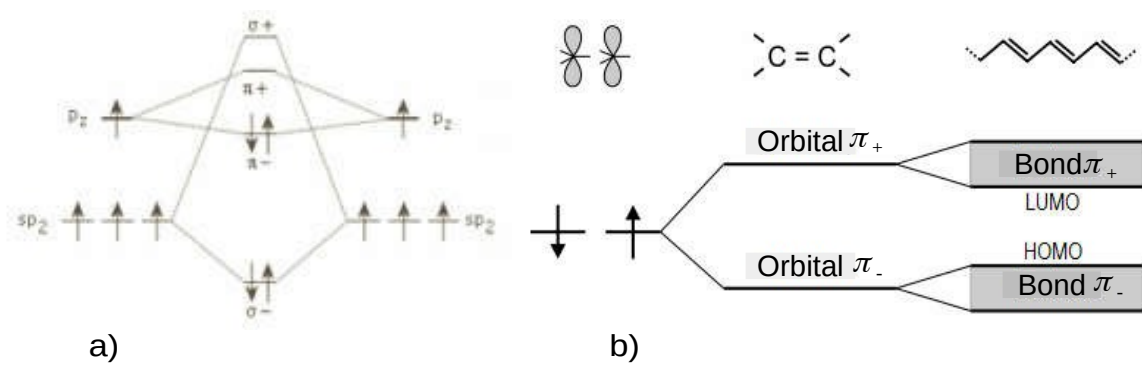


Figure I.2: energy diagram

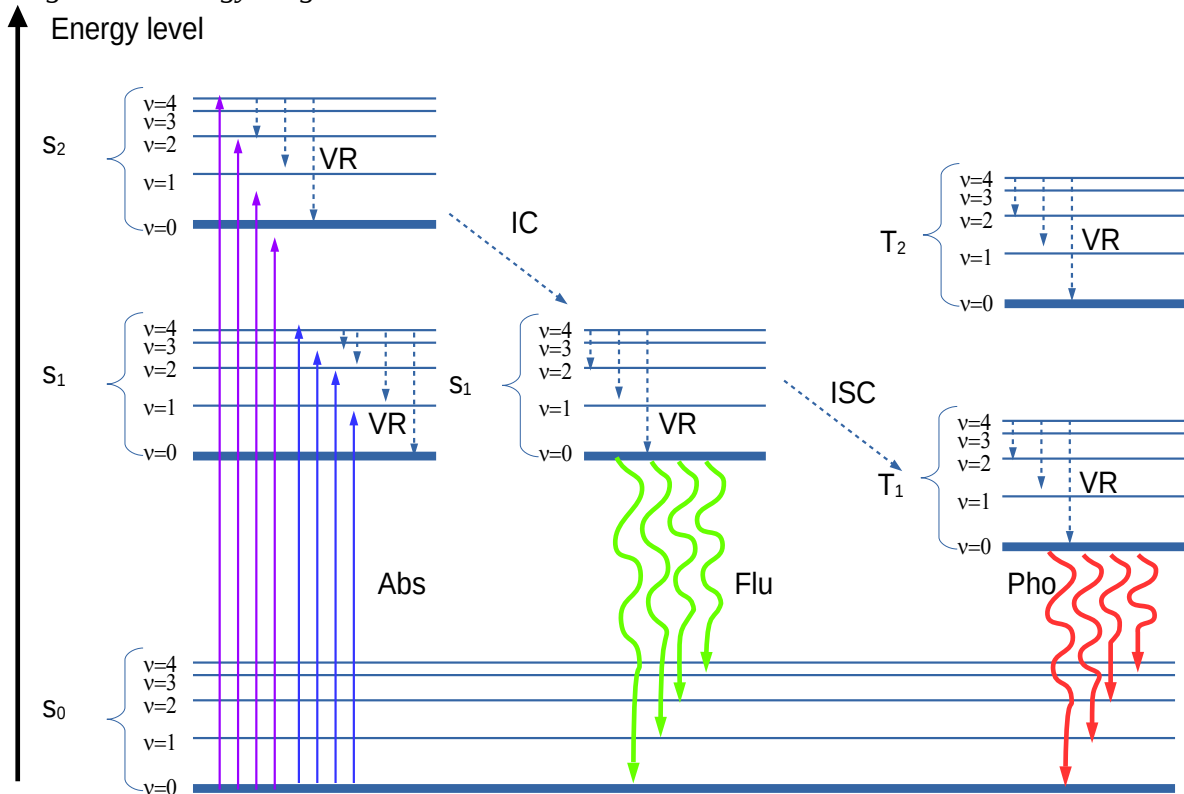


Figure I.3: Jablonsky diagram

The interSystem crossing (ISC) transition is a non-radiative transition from the  $S_1$  singlet state to  $T_1$  triplet state. It requires a flip of the spin angular momentum which is Pauli forbidden but weakly allowed and for this reason it occurs on a long timescale in 0.1 ns-1  $\mu$ s range. Transition from the  $T_1$  triplet state to the  $S_0$  state occurs non-radiatively unless spin-orbit coupling occurs allowing weak radiative transition again normally Pauli forbidden. In that case, the radiative transition between triplet and singlet states is called phosphorescence (red arrows) and therefore occurs on a much longer timescale 1 $\mu$ s-10s range [4,5].

## **I.2.2 Organic Light Emitting Diode**

Two major classes of OLEDs exist; polymer OLED and small molecule OLED. An OLED is a stack of organic layers in between an anode and a cathode that emits light when submitted to a current. In a bottom emission small molecule OLED, the anode is a transparent and conductive layer usually made of indium tin oxide (ITO). On top of anode a first organic layer plays the role of hole injection layer (HIL). It is covered with a hole transporting layer (HTL) that facilitates hole transport into the device. It is followed with an emissive layer (EL), an electron transporting layer (ETL), eventually a hole blocking layer (HBL) and an electron injection layer (EIL). The stack is ended by a metallic cathode such as (Mg/Ag or LiF/Al).

The OLED stack is engineered in different manners so as to optimize the device efficiency by playing with the thickness of each layers and with the choice of organic compounds that impacts intrinsic material properties like HOMO, LUMO levels and the charge carriers mobility. The operating principle of such device relies on four physical processes; injection of charges ( I.2.2.1 ), charge transport ( I.2.2.2 ), exciton formation ( I.2.2.3 ) and light emission ( I.2.2.4 ) as presented in fig.I.5.a.

### **I.2.2.1 Injection of charges**

The first process to be considered in the electroluminescence is the injection of charge from one layer to another and more specifically from electrodes to organic layers. To favor the hole injection, the work function of the anode should be as close as possible to the HOMO level of the adjacent organic layer (HIL). Similarly, electron injection is optimized when the work function of the cathode is closed to the LUMO level of the electron injection layer (EIL) (Fig.I.6).

Depending on the difference in the energy levels between electrodes and the adjacent organic layers, two types of injection have been identified; thermoionic injection when the energy difference is small, and tunnel effect when the energy difference is large [6,7].

These energy level difference affect the threshold voltage of OLED and hence its efficiencies. The same is true with the energy level difference between the organic layers and for this reason organic materials should be properly chosen to minimize the energy level difference between the HIL and HTL on the one hand, and between the EIL and ETL on the other hand. The hole blocking layer (HBL) is based on this principle; a layer with a material chosen for its large HOMO difference with the emitting layer is introduced to block the injection of hole-like polarons in the ETL (Fig.I.6)

Once injected in the organic layers, the carriers are present as polarons; polarons appear in two types, positively charged hole-like polarons present mainly in the HIL and HTL, and negatively charged electron-like polarons present mainly in the EIL and ETL. Solid ions are a good image for polarons.

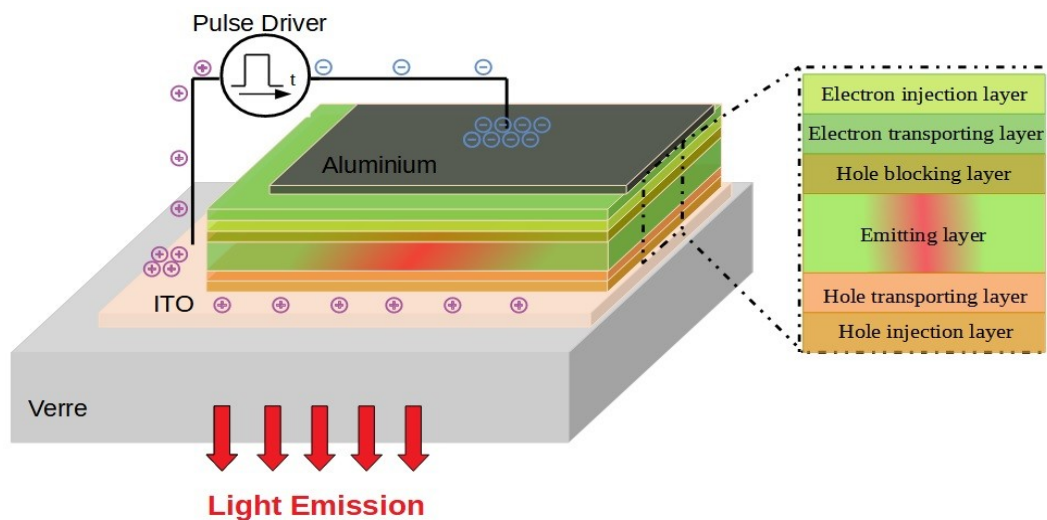


Figure I.4: OLED structure

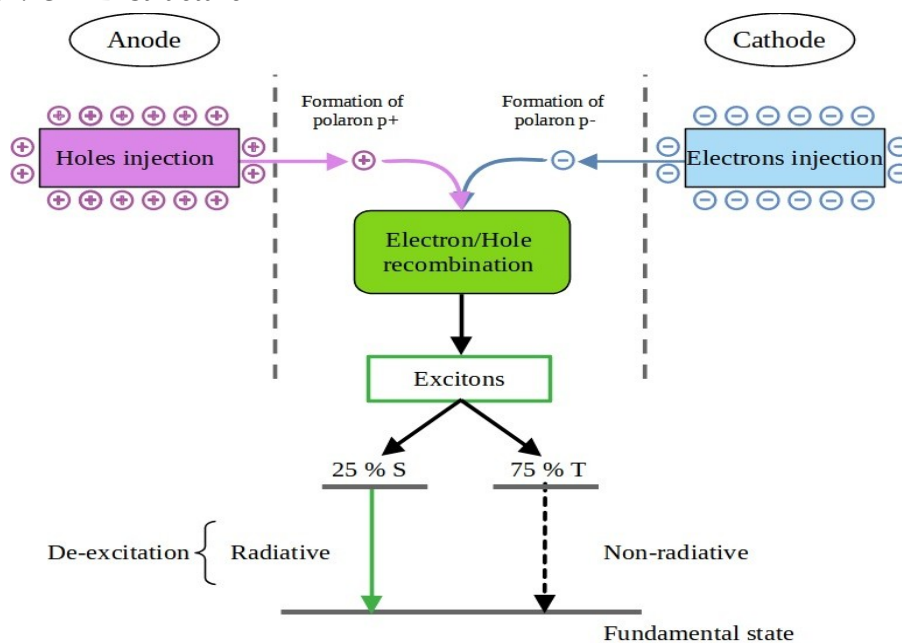


Figure I.5: Physical mechanisms participating to the OLED electroluminescence

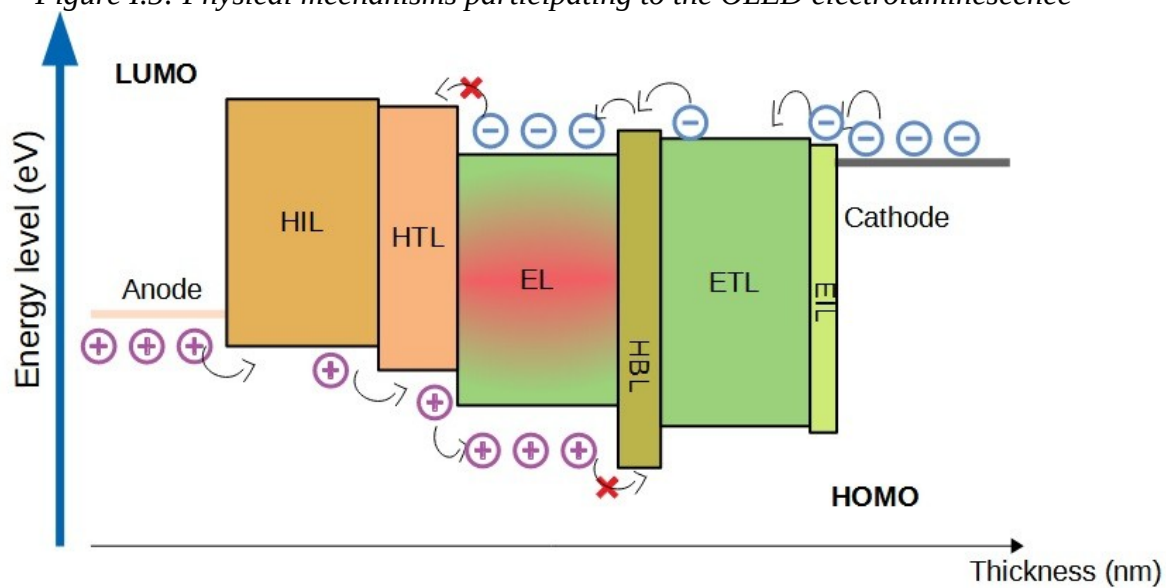


Figure I.6: Energy level of an OLED stack



### I.2.2.2 Charge transport

In each organic layers, the polarons as quasi particles move under the effect of the electrical field due to the combination of two transport mechanisms; the intra-molecular conduction related to the  $\pi$ -conjugation of the molecule (section I.2.1 ), and the inter-molecular conduction which is obtained by hopping between discrete molecular sites. The overall physical process can be modeled in different manners, among which the Poole Frenkel model is the most common.

According to the Poole-Frenkel law, the mobility  $\mu$  for one material and one type of polaron varies with the exponential of the electrical field [8]:

$$\mu = \mu_0 \exp\left(-\frac{\Delta}{k_B T}\right) \exp(\beta \sqrt{E}) \quad \text{Eq.(I.1), where } \mu_0 \text{ is the zero field mobility; } K_B \text{ is the}$$

Boltzman constant,  $T$  is the temperature,  $\Delta$  is the activation energy,  $E$  is the electrical field. From figure.I.7, it is obvious that the mobility of organic semiconductors is some orders of magnitude lower than in silicon ( $\mu_e = 1400 \text{ cm}^2 \text{ V}^{-1} \text{ s}^{-1}$ ).

A first model for the charge transport in the whole device is the Space Charge Limited Current (SCLC) introduced by Mott and Gurney [9], and Rose [10] known as a Child's law, states that the current density is a quadratic function of the applied voltage:

$$J_{SCLC} = \frac{9}{8} \epsilon \mu \frac{V^2}{d^3} \quad \text{Eq.(I.2)}$$

$\epsilon$  is the dielectric constant,  $\mu$  is the charge mobility,  $d$  is the thickness of the organic materials, and  $V$  is the applied voltage.

This simple model assumes that the charge injection from electrodes to organic layers is efficient with an ohmic contact (small an energy level difference). A more sophisticated model takes into account trap states distributed exponentially between the HOMO and LUMO levels. This Trap Charge Limited Current (TCLC) reads:

$$J = \alpha V^{m+1} \quad \text{Eq.(I.3) , where } \alpha = q \mu N_c \left( \frac{\epsilon_r \epsilon_0 m}{q N_{LUMO}} \right)^m \frac{(2m+1)^{m+1}}{(m+1)^{2m+1}} \frac{V^{m+1}}{d^{2m+1}} \text{ , with } m = T_{trap}/T \text{ , } T \text{ is}$$

the temperature,  $T_{trapp}$  is a trap distribution temperature,  $q$  is the electron charge,  $N_{LUMO}$  is the trap density at the LUMO energy,  $N_c$  is the density of state at the LUMO energy.  $m$  has been experimentally validated for a large selection of organic materials estimated in the range of 6-13 [11,12, 13]. According to Yamamoto et al., when the Joule effect increases the temperature of the devices, the number of trapped charges decreases, and the J-V characteristic changes from TCLC to SCLC. Further they add that: "*it is probable that the trapped charge carriers build up an additional external electrical field that enhances carrier mobility. Therefore the smaller device size leads to the accumulation of a larger number of charge carriers, in turn leading to higher carrier mobility*" [12]. The larger the cathode size, the larger the Joule effect, and the lower the current density for which this transition from TCLC to SCLC occurs at low current density. We believe, the size of the OLED active area might be of importance for achieving high current density.

Interestingly, Lampert stated that the current density-voltage (J-V) curves of an organic layer in between electrodes are confined within a "triangle" in the logJ—logV plane bounded by three limiting laws: Ohm's law, Child's law for solids ( $J \sim V^2$ ) and a TCLC as shown in fig.I.8 [14].

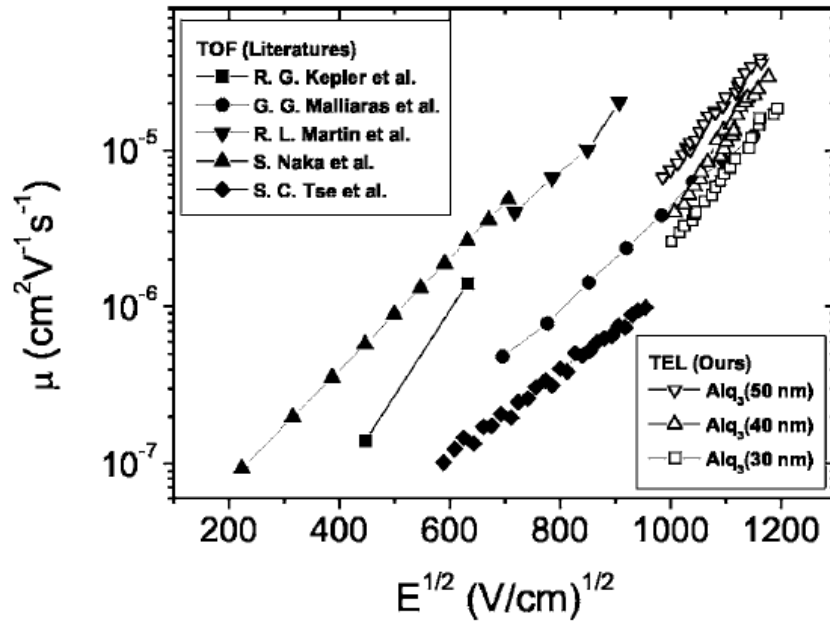


Figure I.7: Transient electroluminescence (TEL) compared of time of flight (TOF) of Alq3

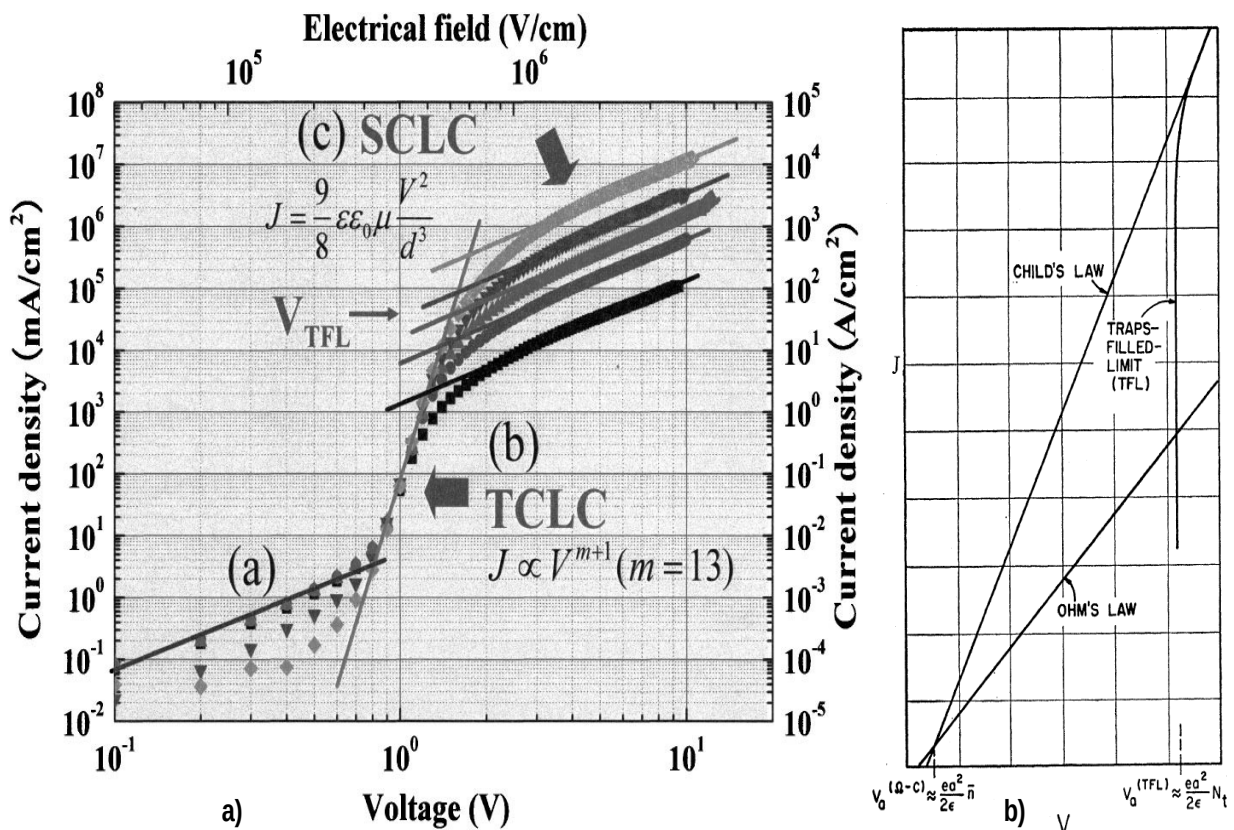


Figure I.8: **a)** Cathode size dependence of steady state current density–voltage ( $J$ – $V$ ) characteristics in an ITO (110 nm) /CuPc (25 nm) / MgAg (100 nm)/Ag (10 nm) device with fitting of the space charge limited current (SCLC) and the trapped charge limited current (TCLC) models (cathode radius; diamond:  $r=25$  mm, triangle down= $50$  mm, triangle up:  $r=100$  mm, circle:  $r=200$  mm, and square:  $r=500$  mm) [12], **b)** The current density–voltage ( $J$ – $V$ ) triangle (shaded) formed by three charge transport mechanisms in organics: Ohm's law, space charge limited current (SCLC), and trapped charge limited current (TCLC) [13,14]

### I.2.2.3 Exciton formation and energy transfer

Submitted to the electrical field, hole-like polaron and electron-like polaron are attracted to each other by Coulombian forces forming a neutral and excited bound state in process called recombination. This new neutral and excited state is called an exciton. Two types of exciton exist; The FRENKEL exciton, where the electron-like polaron and the hole-like polaron are strongly bounded with binding energy of 1eV and a radius of 1nm which is typical of organic materials. By comparison, the WANNIER-MOTT excitons typical of inorganic semiconductors exhibit a lower binding energy around 10meV and a large radius of 10nm[15].

Because the mobility of polarons in organic semiconductors is several orders of magnitudes lower than in inorganic semiconductors, a pair of polarons that the Coulombian forces have brought at the distance smaller than the binding radius, are almost irreversibly linked. The density of exciton is given by the Langevin formula [16]:

$$R_L = \gamma np \quad \text{Eq.(I.4)}$$

where  $\gamma = \frac{q}{\epsilon} [\mu_e(E, T) + \mu_h(E, T)]$  is the Langevin recombination rate,  $\mu_e$  and  $\mu_h$  are the electron and hole mobilities,  $E$  the electric field,  $T$  the temperature of the device,  $n$  and  $p$  are the densities of electron-like polaron and hole-like polaron.

Under current excitation, the charge injection occurs with random spin orientation and the recombination leads to a random oriented excitons either with spin momentum "0" called singlet exciton or with spin momentum "1" called triplet exciton. The spin statistic impose 25% of the excitons are singlet and 75% of the excitons are triplet as illustrated in fig.I.5.

The energy of an exciton can be transferred from one molecule called donor D\*, to another molecule called acceptor A. This energy transfer mechanism occurs more likely when the donor emission spectrum covers partially the acceptor absorption spectrum as illustrated in fig.I.9. Two types of energy transfer process have been propose by Förster and Dexter (fig.I.10[17]).

The Förster mechanism also called Fluorescence Resonance Energy Transfer (FRET) explains the energy transfer by long distance (>1nm) dipole-dipole interaction [18]. This mechanism that does not induce electron exchange or photon emission-absorption. Instead, when the donor molecule in its excited state (D\*) returns to the fundamental state (D), it induces an oscillation of its dipole while the dipole of the acceptor molecule (A) enters into resonance, allowing the acceptor molecule to reach an excited state (A\*) [19]. The Förster transfer rate is given by

$$\Gamma_{\text{Förster}} = \frac{1}{\tau_D} \left( \frac{R_0}{R_{DA}} \right)^6 \quad \text{Eq.(I.5) where, } \tau_D \text{ is the life time of the donor in the}$$

excited state,  $R_0$  the effective distance between the donor and the acceptor is up to 10nm [18,20],

$R_{DA}$  is the distance between two molecules. This mechanism is also known as guest: host system where the guest is the acceptor and the host is the donor. The most frequent guest:host system in the OLED literature is the Alq3 doped with DCM (fig. I.11).

The Dexter transfer mechanism involves the exchange of two electrons between the molecular donor and the acceptor. Contrary to the Förster mechanism, the HOMO LUMO orbitals of both molecules need to overlap which require them to be close to each other. As presented in fig.I.9.b, an excited electron is transferred from the donor excited energy level D\* to the acceptor excited energy level A\* while an electron is transferred from the fundamental state of the acceptor A to the fundamental state of the donor D [21].

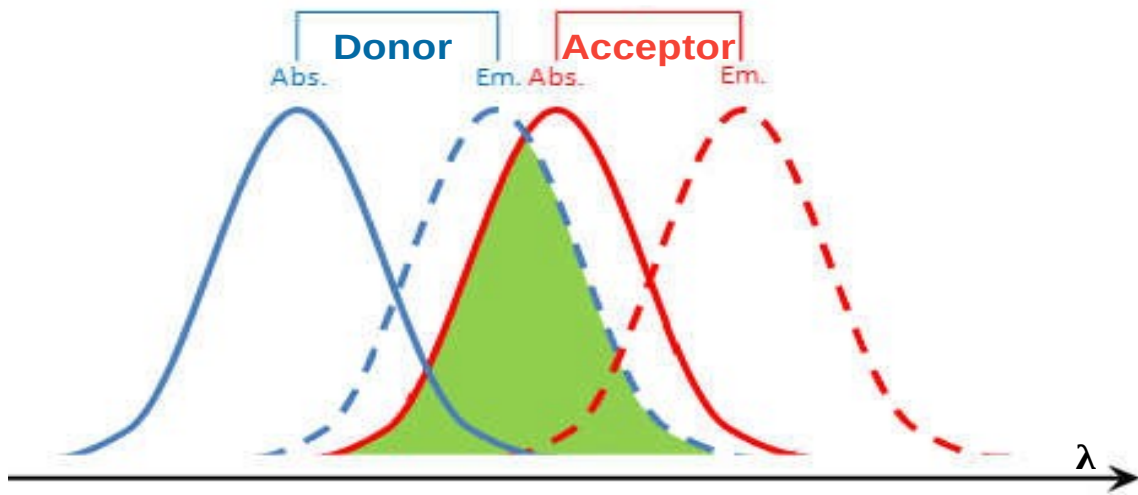


Figure I.9: Förster energy transfer

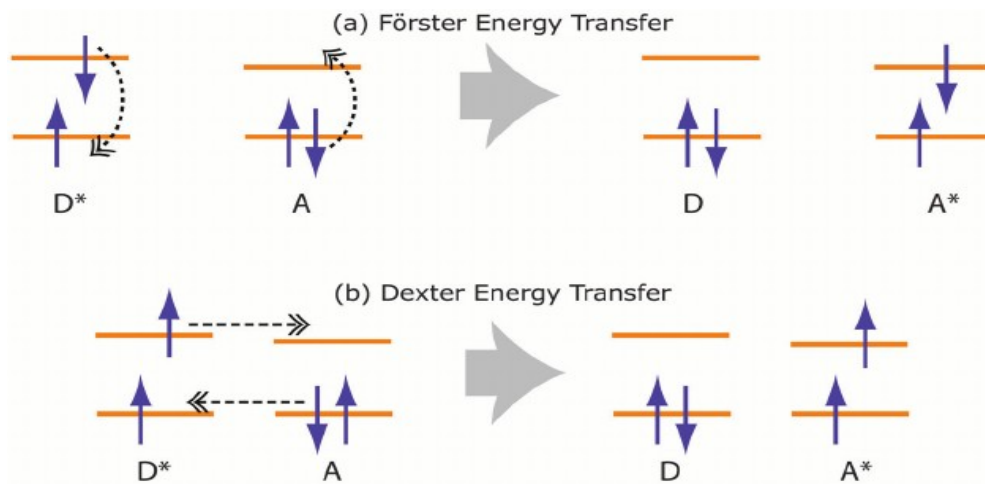


Figure I.10: Förster and Dexter energy transfer mechanisms from [17]

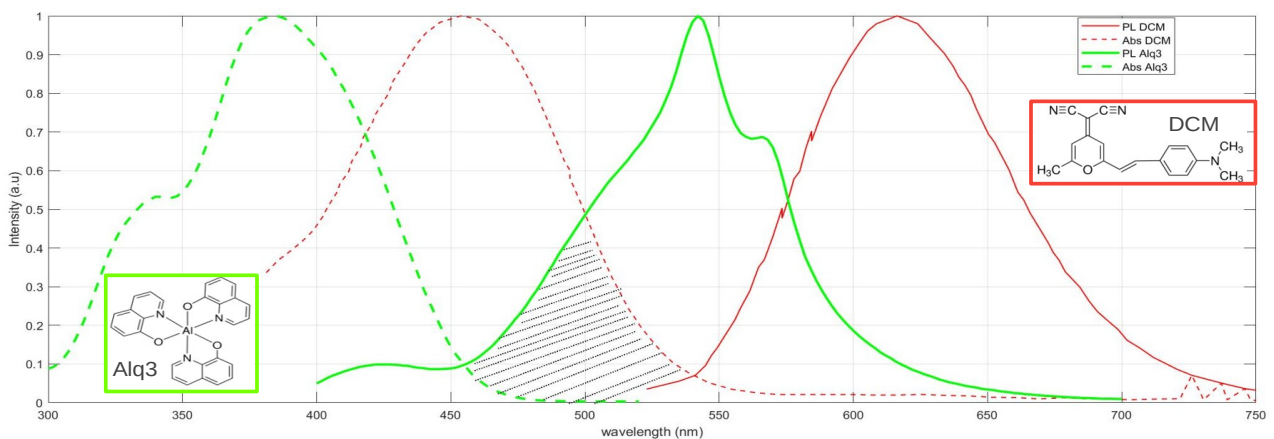


Figure I.11: Forster energy transfer for a Host:Guest system: Alq3 as a host media (green line) and DCM as guest media (red line), spilled line presents the absorption of media and continue line present the photoluminescence of media

## I.2.2.4 Light emission and non-radiative exciton de-excitation

### I.2.2.4.1 Emission of photons

Once formed, the exciton, is deactivated either radiatively or non-radiatively depending on whether the exciton is a singlet or a triplet. The relative weight of both these processes determines the final efficiency of the OLED. In fluorescent organic materials, only the singlet decay radiatively and therefore the theoretical quantum efficiency is limited to 25%. The emission wavelength  $\lambda$  is related to the energy gap  $E$  between the LUMO and HOMO levels of the organic material with  $E=hc/\lambda$ . With an almost unlimited library of organic materials covering the entire visible spectrum, there are plenty of choice for choosing a specific emission wavelength of OLEDs.

The radiation deactivation of a singlet gives rise to the phenomenon of fluorescence, with a theoretical efficiency of up to 100%. As for a triplet excitons, they deactivate non radiatively except in special cases where radiative deactivation gives rise to phosphorescence with however an almost zero yield for fluorescent materials. For organic compounds containing a heavy atom like platinum strong spin-orbit coupling occurs in the molecules leading to the fast intersystem crossing (ISC) and efficient phosphorescence from the triplet states even at room temperature [22]. Therefore, the maximum internal quantum efficiency of devices based on fluorescent materials is theoretically limited to 25% given by the ratio of singlet excitons generation.

The dynamics of singlet density  $N_s$  submitted to an optical excitation  $S_0(t)$  reads [23]

$$\frac{dN_s}{dt} = S_0(t) - (\kappa_r + \kappa_{nr})N_s \quad \text{Eq.(I.6)}$$

where  $S_0$  is a source term,  $\kappa_r$  is the rate of radiative process and  $\kappa_{nr}$  is the rate of non-radiative process. After the system has reached equilibrium, if the source abruptly stops and becomes null, the solution is  $N_s(t) = N_{s0} \exp\left(\frac{-t}{\kappa_r + \kappa_{nr}}\right)$  Eq.(I.7)

where  $N_{s0}$  is the exciton density at equilibrium.

The fluorescence life-time  $\tau$  is a measure of the time required for an exciton to interact with its environment either by radiative and non-radiative transitions. Experimentally, it can be determined by measuring the decrease in fluorescence intensity. Numerically, the life time is based on the assumption that the fluorescence decay follows the first order as presented in Eq.(I.17) and it reads [23]:

$$\tau = \frac{1}{\kappa_r + \kappa_{nr}} \quad \text{Eq.(I.8)}$$

The quantum efficiency of fluorescence  $\eta$  is the ration between the number of photons emitted during the excited state life-time and the number of the absorbed photons. It is defined by

$$\eta = \frac{\kappa_r}{\kappa_r + \kappa_{nr}} = \frac{1}{1 + \frac{\tau_r}{\tau_{nr}}} \quad \text{Eq.(I.9)}$$

where  $\tau_r = \frac{1}{\kappa_r}$  and  $\tau_{nr} = \frac{1}{\kappa_{nr}}$  are the radiative and no-radiative life-time.

#### I.2.2.4.2 Exciton annihilations

As a quasi-particles, excitons interact with other excitons and also with polarons which often result in exciton annihilation. The understanding of these annihilations are crucial for the laser operation because it constitutes potential losses. It is a difficult topic still under investigation although an important input was brought by Kasemann et al.[24]. The different types of exciton interactions [25, 26, 27] in organics include singlet-polaron annihilation (SPA) [27], triplet-polaron annihilation (TPA) [28, 29], singlet-triplet annihilation (STA) [30, 31], triplet-triplet annihilation (TTA) [28, 32]. Kaseman et al, describe different types of annihilation as follows [24]:

Singlet excitons can be quenched by the same type of excitons. It produces a singlet  $S_1$  and a de-excited state  $S_0$ . This interaction is called singlet-singlet annihilation (SSA) with  $\kappa_{SS}$  as a rate coefficient for this annihilation which is given by:

$S_1 + S_1 \xrightarrow{\kappa_{SS}} S_1 + S_0$  Eq.(I.10), where  $S_1$  is a singlet exciton and  $S_0$  is a de-excited electron in the molecular ground state.

A polaron (electrons or hole) can interact with a singlet excitons leading to a de-excitation (quenching). This interaction is known as singlet-polarons annihilation (SPA), characterized by  $\kappa_{SP}$  as a rate coefficient and written as

$S_1 + n \xrightarrow{\kappa_{SP}} S_0 + n$  Eq.(I.11), where  $n$  is polaron.

When a triplet exciton interacts with a polaron, triplet-polaron annihilation (TPA) happens and quenches triplets. It is given by:

$T_1 + n \xrightarrow{\kappa_{TP}} S_0 + n$  Eq.(I.12), where  $\kappa_{TP}$  is the rate coefficient for TPA,  $T_1$  is a triplet.

Singlet quenches by interaction with triplets in a process known as singlet-triplet annihilation (STA) expressed by:

$S_1 + T_1 \xrightarrow{\kappa_{ST}} T_1 + S_0$  Eq.(I.13), where  $\kappa_{ST}$  is the rate coefficient for STA.

The triplet-triplet annihilation (TTA) occurs through energy transfer between two excitons leading to one of them is being excited to a higher state. This exciton subsequently relaxes down to either a singlet  $S_1$  or a triplet state  $T_1$ . Based on the spin statistics, there are 25% of singlets and 75%% of triplets. The TTA is expressed by:

$T_1 + T_1 \xrightarrow{3/4\kappa_{TT}} T_1 + S_0$  Eq.(I.14)

$T_1 + T_1 \xrightarrow{1/4\kappa_{TT}} S_1 + S_0$  Eq.(I.15), where  $\kappa_{TT}$  is the rate coefficient for TTA,

Injection of charges, transport of polarons, excitons formation, radiative and non-radiative de-excitation of excitons, energy transfer, and excitons annihilation are relatively known under DC electrical excitation. Next section focus on dynamical behaviors of OLEDs among other under electrical pulsed excitation.

## I.3. Electrical Concepts

The challenge of electrical excitation is twofold; firstly, achieving ultra-short pulses in the ns time scale, and secondly, large pulse amplitude. Electrical excitation at the nanosecond time scale requires not only materials with short fluorescence life-time but also small electrical time constant. Also, special care should be applied at the device level and at the electrical excitation circuit level; Section I.3.1 . aims at investigating how high current density can be achieved in OLEDs under pulsed electrical excitation in the literature. Section I.3.3 reports spatial distribution of charge at the OLED interfaces at pulse turn-on. Section I.3.4 deals with microwave techniques useful for impedance matching of the device with the excitation circuit helping to deliver the electrical energy contained in pulses to the organic opto-electronic components and to avoid pulse reflection.

### I.3.1 Pulsed OLED

In 1992, Heeger et al. Reported transient electroluminescence from polymer light emitting diode mounted on a microstrip transmission line. They observed fall and rise time of 50ns and current values up to 10A/cm<sup>2</sup>. It is to be noted that the idea to combine microwave techniques with OLEDs has been proposed by the winner of the 2000 Nobel prize for chemistry 30 years ago. Interestingly, they observed that temporal response is limited by the electrode geometry and not by the material properties [33]. In 2000, the group of Forrest investigating structures for organic diode laser reported organic semiconductors under intense electrical excitation up to 35 A/cm<sup>2</sup> with a pulse duration of 10  $\mu$ s [34]. [35]. In 2002, Heeger reported turn-on response time of 12ns with electrical pulse duration of 200ns. They proposed a simple equivalent circuit model with the polymer OLED replaced by a fixed capacitance collected in parallel with a non-linear resistance see fig.I.14. They predict polymer OLED can be usefully modulated at frequencies as high as  $\sim 10^8 \text{ s}^{-1}$  [36]. In 2005, the Adachi group reported current density up to 1163A/cm<sup>2</sup> using a 5 $\mu$ s long electrical pulses allowing rise time of 4ns. The luminescence efficiency reach  $18 \times 10^6 \text{ Cd/cm}^2$  [37]. The same year, they achieved extremely-high-density steady state carrier injection and transport at 12,222 A/cm<sup>2</sup> into an CuPc based organic thin films using different high thermally conductive substrates (glass, sapphire, silicon) [12]. In 2011, the group of Karl Leo explored  $100 \mu\text{m} \times 100 \mu\text{m}$  small Alq3:DCM based OLED under high currents by transient electroluminescence on the nanosecond scale. They achieved 800 A/cm<sup>2</sup> using 50 ns electrical pulse with a rise time of 10 ns allowing temporal separation of singlet emission and singlet-triplet quenching [24]. In 2017, in our group, Zeng reported an electrical time response of as short as 2.1 ns and also shorter than the device optical decay time ( $9.8 \pm 0.2$  ns) with a break-down current density as high as 3.0 kA/cm<sup>2</sup> and EL as high as 12 W/cm<sup>2</sup> are measured with the fastest  $\mu$ -OLED [38]. In 2018, again in our group, Chime reported high-speed  $87 \mu\text{m} \times 120 \mu\text{m}$   $\mu$ -OLED mounted on coplanar waveguided electrodes exhibiting current density of 2kA/cm<sup>2</sup> showing a perceptible light response under ultra short electrical pulse duration of 9 ns with 2.1 ns rise-time. It demonstrates pulse duration in the range of the radiative lifetime of singlet excitons [39]. The technique was optimized further resulting in CPW  $\mu$ -OLEDs sustaining and responding appropriately both electrically and optically to ultra-short electrical pulses down to 2.5 ns only limited by the pulse generator. The electroluminescence peak brightness reaches 1.42 mW (9.5W/cm<sup>2</sup> and  $3.42 \times 10^6 \text{ Cd/m}^2$ ) [40]. In his thesis manuscript Chime reported current density up to 6 kA/cm<sup>2</sup> [41]. As a preliminary conclusion, both micrometric OLEDs and coplanar waveguide electrodes offer major advantages to achieve ultra-short pulses and high current densities. These experiments are listed in table 1.

*Table 1: pulsed OLED experiments*

Authors [reference]	Organic Compound	year	Pulse duration (ns)	Rise time (ns)	Current density (A/cm <sup>2</sup> )	Luminance efficiency Cd/m <sup>2</sup>
Heeger [33]	MEH-PPV	1992		50 ns	10 A/cm <sup>2</sup>	
Forrest [34]	Alq3:DCM or DCM2	2000	10μs		35 A/cm <sup>2</sup>	
Forrest [35]	Alq3:DCM or DCM2	2000	720ns	/	40 A/cm <sup>2</sup>	
Heeger [36]	PDOT / PPV	2002	200ns	12 ns	0.7 A/cm <sup>2</sup>	0.26 10 <sup>6</sup> Cd/m <sup>2</sup>
Adachi [37]	NPD /Alq3	2005	5μs	4 ns	1163 A/cm <sup>2</sup>	18 10 <sup>6</sup> Cd/m <sup>2</sup>
Adachi [12]	glass/CuPc	2005	1s	<1s	1053 A/cm <sup>2</sup>	1.5 10 <sup>6</sup> Cd/m <sup>2</sup>
	Sapphire/CuPc				4026 A/cm <sup>2</sup>	
	Silicon/CuPc				12,222 A/cm <sup>2</sup>	
	NPD/Alq3				514 A/cm <sup>2</sup>	
Leo [24]	Alq3:DCM	2011	50ns	10 ns	800 A/cm <sup>2</sup>	
Zeng [38]	Alq3:DCM	2017	15ns	2.1 ns	3 kA/cm <sup>2</sup>	1.6 10 <sup>6</sup> Cd/m <sup>2</sup>
Chime [39]	Alq3:DCM	2018	9ns	2.1 ns	2 kA/cm <sup>2</sup>	
Chime [40]	Alq3:DCM	2019	2.5ns	2 ns	1.73 kA/cm <sup>2</sup>	3.4 10 <sup>6</sup> Cd/m <sup>2</sup>
Chime [41]	Alq3:DCM	2017			6 kA/cm <sup>2</sup>	

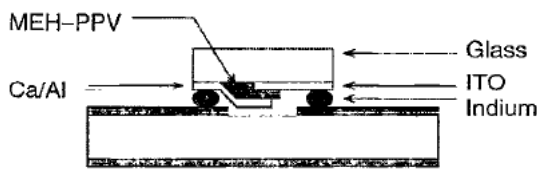


Figure I.12: Side view of the device geometry of a polymer OLED mounted on a microstrip line from [33]

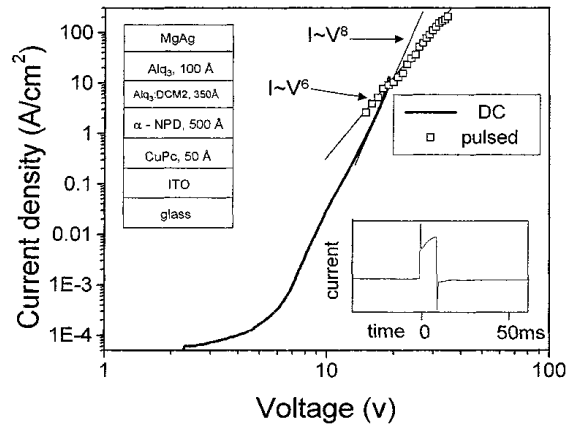


Figure I.13: Current-voltage characteristic of an OLED under dc and pulsed excitation. Bottom inset: current in the OLED as a function of time from [34]

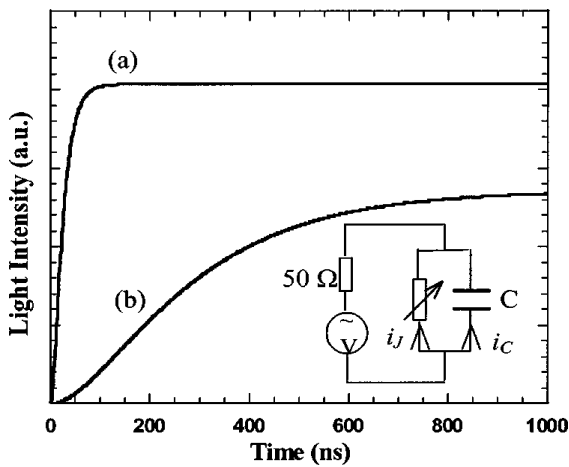


Figure I.14: Theoretical plot of the rising edge of EL emission; a) V=18 V, b) V=10 V. The equivalent circuit model is shown in inset from [36]

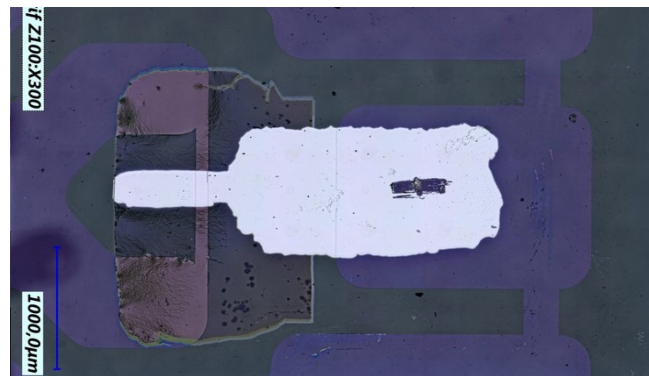


Figure I.15: Digital microscope image of a CPW μ-OLED : dark grey is the glass substrate, purple is the electrode (ITO), white is the aluminum cathode. The organic layer is visible with a light purple rectangle-like underlining the void and the 100μm large 1mm long anode arm from [40]



### I.3.2 Electrical modeling

The purpose of electrical modeling is to understand the dynamic behaviour of OLED device. This type of modeling has been the subject of several studies[42, 43, 44, 45, 46, 47,48]. Among them Chime et al. presented an electrical model for a fast-OLED used to demonstrate optical pulsed responses to electrical pulse excitation with duration down to 2.5 ns [39]. The equivalent circuit proposed by A. Chime in Fig.I.17 has been developed for ON-OFF operation under high pulse excitation. This model takes into account the physics and the topology of the OLED. The typical OLED with a stack of thin organic layers sandwiched between an ITO layer as the anode and an aluminum layer as the cathode, is used for this model and its equivalent electrical circuit is a combination of resistors and capacitors. The electrode resistances are respectively ( $R_{S1}$ ) and ( $R_{S2}$ ) for the ITO and aluminum electrodes. Note that the low conductivity of each bulk organic layers induced a resistance which we introduce as  $R_b$ . An equivalent parasitic capacitance ( $C$ ) is introduced to take into account two phenomena; junction capacitance resulted from the barriers between adjacent organic layers, and the low conductivity of organic materials making them to behave like dielectric materials between electrodes. To take into account the non-linear I-V diode characteristic a dynamic resistor ( $R_d$ ) is introduced. In ON-OFF regime, only two  $R_d$  values are necessary: the ON state  $R_d = R_{ON} + R_b$ , in the OFF state  $R_d = R_{OFF} + R_b$ .

In order to measure the OLED current  $I$ , a measurement resistor ( $R_{meas}$ ) is added as shown on Fig.I.17 and the relationship between  $I$  and the excitation voltage  $V_E$  is given by Eq(I.16);

$$\frac{dI(t)}{dt} + \left(1 + \frac{R_d}{R_{S1} + R_{S2} + R_{meas}}\right) \frac{1}{R_d C} I(t) = \frac{1}{R_{S1} + R_{S2} + R_{meas}} \left[ \frac{dV_E(t)}{dt} + \frac{1}{R_d C} V_E(t) \right] \quad \text{Eq. (I.16)}$$

with  $R_{ST} = R_{S1} + R_{S2} + R_{meas}$  solving Eq(I.16) under the assumption that  $dV_E/dt=0$  reads

$$I(t) = \frac{1}{R_d + R_{ST}} \left[ \frac{R_d}{R_{ST}} \exp\left(-\frac{R_d + R_{ST}}{R_{ST} R_d C} t\right) \right] V_E \quad \text{Eq. (I.17)}$$

The current  $I$  is the sum of the current flowing through the junction capacitor  $i_C$ , and the dynamical resistor  $i_D$  that reads;  $i_D(t) = \frac{1}{R_d + R_{ST}} \left[ 1 - \exp\left(-\frac{R_d + R_{ST}}{R_{ST} R_d C} t\right) \right] V_E$  Eq. (I.18)

The RC time constant  $\tau$  is expressed as follows:  $\tau = \frac{1}{\frac{1}{R_d} + \frac{1}{R_{S1} + R_{S2} + R_{meas}}} C$  Eq. (I.19)

This electrical model allows to simulate both the OLED current-density  $J(t)$  as a function of the excitation voltage  $V_E(t)$  and to quantify the time constant  $\tau$ . From equation I.19, the important parameters to reduce the time constant can be identified from which the geometry of the device can be optimized. Note that the dynamical resistance  $R_d$  appears as a key parameter at the same level than the serial resistances. Estimating the dynamical resistance from the operating point of the OLED on the I-V curve is not directly accessible. It requires to measure the characteristic I-V in DC regime, then calculate the slope of the characteristic and assuming that the later in high frequencies remain identical that in DC. This limitation suggests to upgrade toward a new electrical model free from the need to quantify the dynamical resistance.

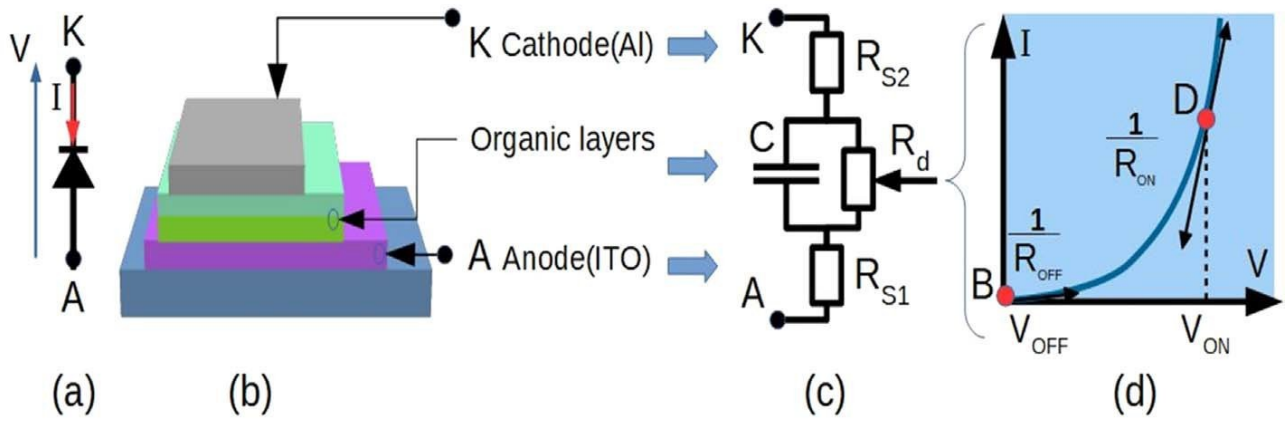


Figure I.16: Equivalent electrical circuit for an OLED in ON-OFF regime. a) device polarisation, b) device geometry and stack c) equivalent electrical circuit with a dynamical resistance  $R_d$ , d) The dynamical resistance is the inverse of the IV curve and reflects the OLED operating points (from[39])

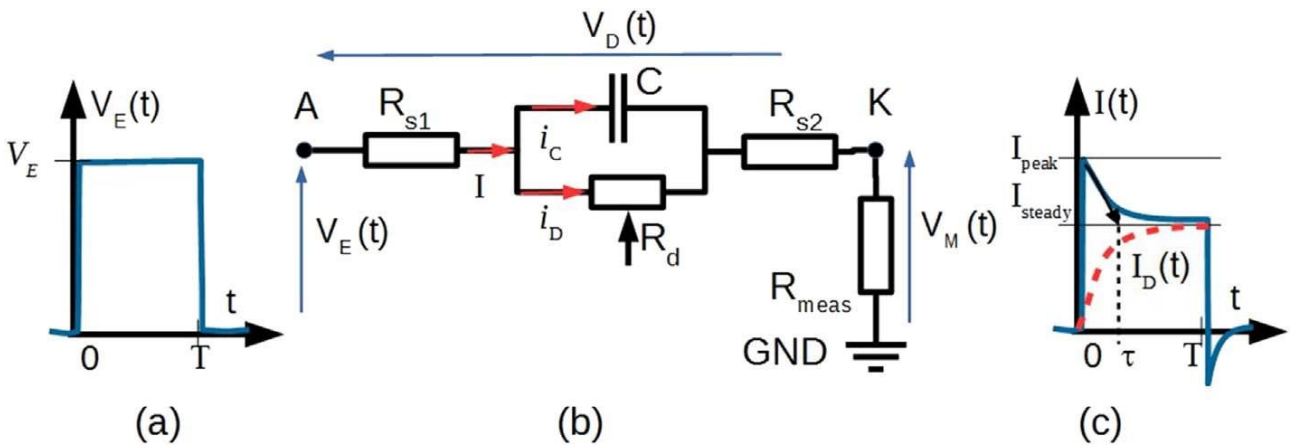


Figure I.17: Equivalent electrical circuit of an OLED and its use to model the electrical response to an impulse. a) input electrical pulse, b) equivalent electrical response, c) electrical response with an overshoot at turn on followed by a plateau (From[39])

### I.3.3 Spatial distribution of charge

Because we consider ultra-short pulses in the nanosecond scale shorter than the fluorescence decay time, it is legitimate to question the distribution of charges in the device. In 2003, Ruhstaller et al. Investigated transient electroluminescence at electrical pulse turn-on and found charge and recombination confinement effects at OLED internal interfaces see OLED stack on fig.I.18 [49];

At pulse onset, the holes penetrate into the device from the anode and accumulate first at the HTL and EML interface and then at the EML and EIL interface prior to penetration into the EIL. Subsequently electrons enter the device from the cathode and recombine with holes at the EML/EIL interface. The initial rise in recombination rate density leads to a rise of exciton density in EIL. Once the electrons enter the EML, the exciton density rises and eventually exceeds that of EIL this means light emission occurs first in the EIL/EML interface rather than the HTL/EML. Spatially, the recombination rate is strongly confined to internal interfaces rather than exclusively at the HTL/EML interface. They claim that the high current overshoot is due to the fast holes traversing the HTL and is not related to electrode charging effects. This study was performed numerically at the microsecond time scale and remains to be confirmed at the nanosecond time scale.

### I.3.4 Microwave electrodes

As mentioned above, Heeger was the first to introduce the association of microwave techniques with polymer OLED using microstrip lines as electrodes (fig.I.12 & fig.I.20.b) [33, 50]. Chime introduced rather coplanar waveguided electrodes proposed for the first time as an alternative to the microstrip lines by Wen [40, 41, 51]. It offer several advantages; great flexibility for the design and the fabrication and is of integration because ground plane and signal line are on the same plane.

The coplanar waveguide (CPW) electrodes consist of a central signal line (anode) located in the middle of two ground planes on the same side of dielectric substrate as shown on figure I.20.a.  $h$  and  $\epsilon_r$  respectively are the thickness and the relative dielectric permittivity of the glass substrate.

$W$  and  $t$  respectively are the width and the thickness of the conductive layer.  $G$  is the distance between the central line and the ground planes. These ground planes must be present on both sides of the central line and linked with each other either by an external circuit or by a wire.

For a given dielectric, the characteristic impedance of CPW reads:

$$Z_c = \frac{30 \pi}{\sqrt{\epsilon_{eff}}} \frac{K(k_0')}{K(k_0)} \quad \text{Eq.(I.20)}$$

is mainly given by the shape factor  $k$  defined by the ratios:

$$k = \frac{W}{W+2G} \quad \text{(I.21)} \quad \text{and} \quad h = \sqrt{1-k^2} \quad \text{Eq.(I.22)}$$

interval :  $\beta = \frac{\pi}{\ln\left(2 \frac{1+\sqrt{h}}{1-\sqrt{h}}\right)}$  Eq.(I.23)      when pour  $k < \frac{1}{\sqrt{2}}$

For the details of the characteristic impedance calculation, we refer the reader to Chime's thesis[41].

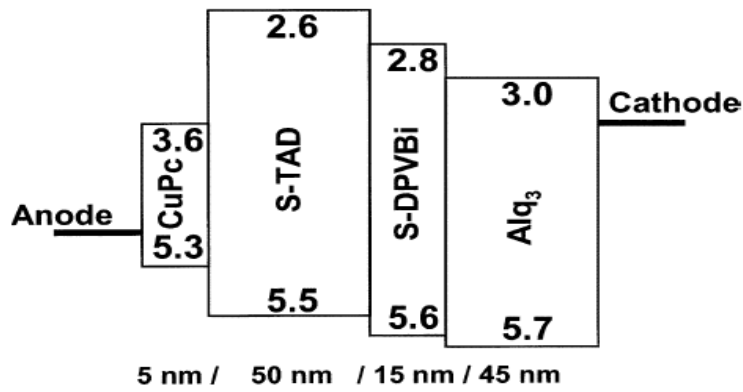


Figure I.18: Schematic energy level overview of the device structure for the blue-emitting OLED under investigation. The numbers indicate HOMO and LUMO level energies in electron-volts and the line below indicates the layer thicknesses (from [49])

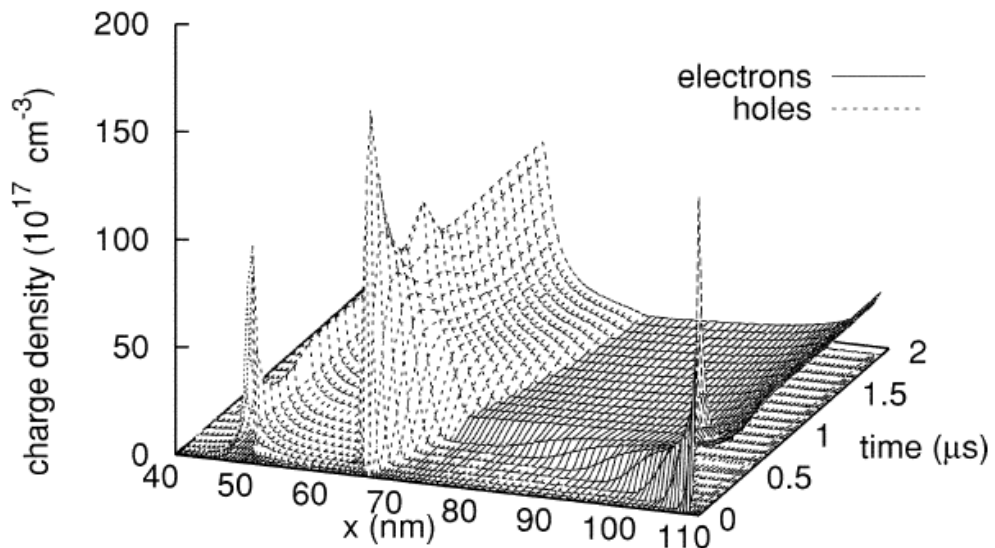


Figure I.19: Calculated internal hole (left) and electron (right) density profiles in a blue-emitting multilayer OLED as a function of time after turn-on. The internal interfaces between the three layers S-TAD/S-DPVBi/Alq are located at  $x = 50$  and  $65$  nm away from the anode (from [49]).

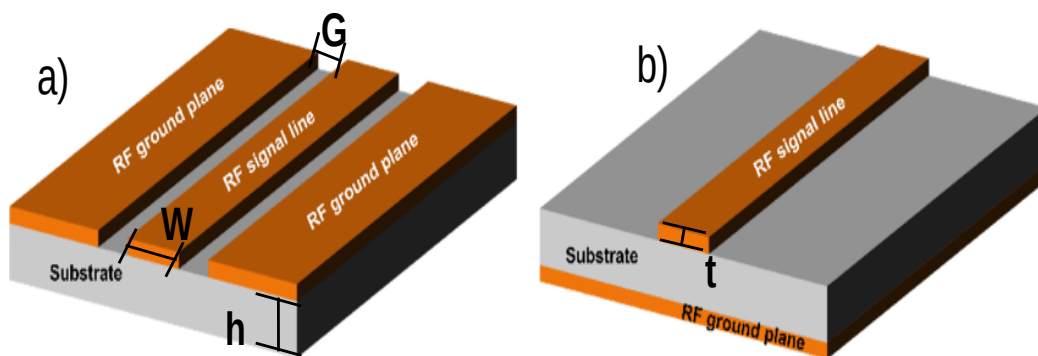


Figure I.20: Microwave electrodes: a): CPW electrodes, b): micro strip electrode [from 50]

## I.4. Basic laser concepts and state of the art of organic lasers

This section presents briefly the laser principle (sec. I.4.1 ) and the laser structure (sec. I.4.1.1 ) as basic concepts necessary to address the history of organic lasers (sec. I.4.2 ).

### I.4.1 Laser principle

#### I.4.1.1 Absorption, spontaneous and stimulated emissions

Lasers are based on three physical phenomena describing interaction between light and material; absorption, spontaneous emission, and stimulated emission

frequency selective and direction selective element (cavity) is added.

- **Absorption**

In the absorption phenomenon, a photon with the energy  $E = h\nu$  is absorbed by an atom or a molecule at equilibrium, promoting an electron from one energy level  $E_1$  to the energy level  $E_2 = E_1 + E$  (fig. I.21.a).

A way to address the absorption phenomenon at the material level, is to consider the Beer-Lambert law; in an absorbing medium, where the transmission intensity of light i.e the ratio between  $I$  the transmitted intensity and  $I_0$  the input intensity, varies exponentially with  $A$  the absorbance.

$A$  is the product of  $\alpha$  the absorption coefficient and  $d$  the length of propagation.

$$T = \frac{I_1}{I_0} = \exp^{-A} = \exp^{-\alpha d} \quad \text{Eq.(I.24)} \quad \text{the absorption coefficient expressed in } \text{cm}^{-1} \text{ or } \text{m}^{-1} .$$

The absorption coefficient appears as an imaginary part in the complex refractive index of a material  $n = n' + jn''$  Eq.(I.25) with  $n'' = \frac{\alpha}{2} \frac{c}{\omega}$  .

in the laser community, the notion of absorption cross section ( $\sigma [\text{cm}^2]$  ) is frequently used and reads:  $\sigma_a = \frac{1}{N} \frac{A}{d} = \frac{\alpha}{N}$  Eq.(I.26) where  $N$  is the molecular density.

Absorption constitutes losses for stimulated emission

- **Spontaneous emission**

In spontaneous emission, an excited electron in the energy level  $E_2$  decays to energy level  $E_1$  releasing a photon with an energy  $E = E_2 - E_1 = h\nu = hc/\lambda$  , where  $\nu$  is the frequency of the photons. The emitted photons are incoherent with no phase relationship (fig.I.21.b). The larger the energy bands, the broader the spontaneous emission spectrum.

- **Stimulated emission**

Einstein introduces the concept of stimulated emission in 1917 [52]. The stimulated emission is initiated by a photon initially present in the system which triggers the decay of an excited state emitting a second photon that maintains the same direction and phase as the initial photon (fig.I.21.c). The stimulated emission builds up from noise (spontaneous emission) if a frequency selective and direction selective optical elements (cavity) is added. The population inversion is an important condition to maintain the stimulated emission. This condition is easy to fulfill under an electrical excitation.

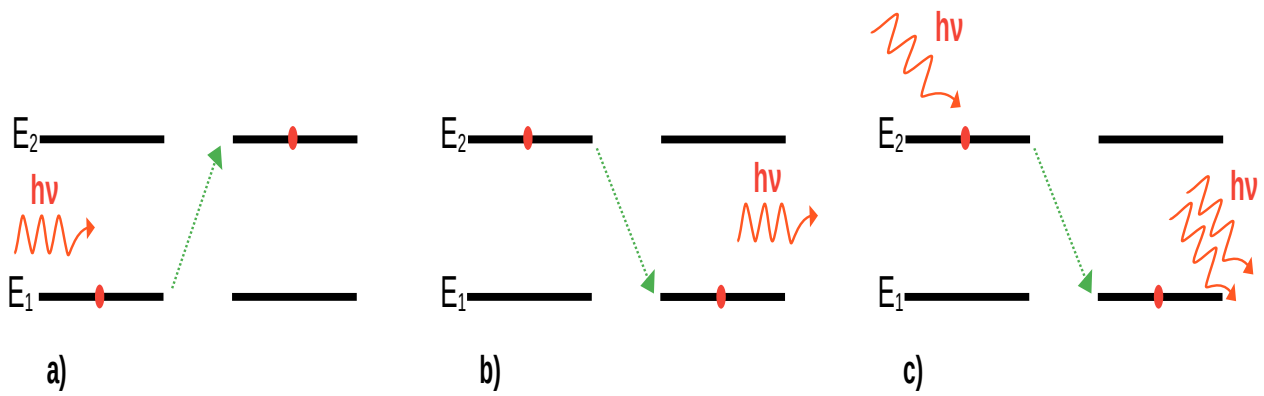


Figure I.21: Laser principles: a) absorption, b) spontaneous emission, c) stimulated emission

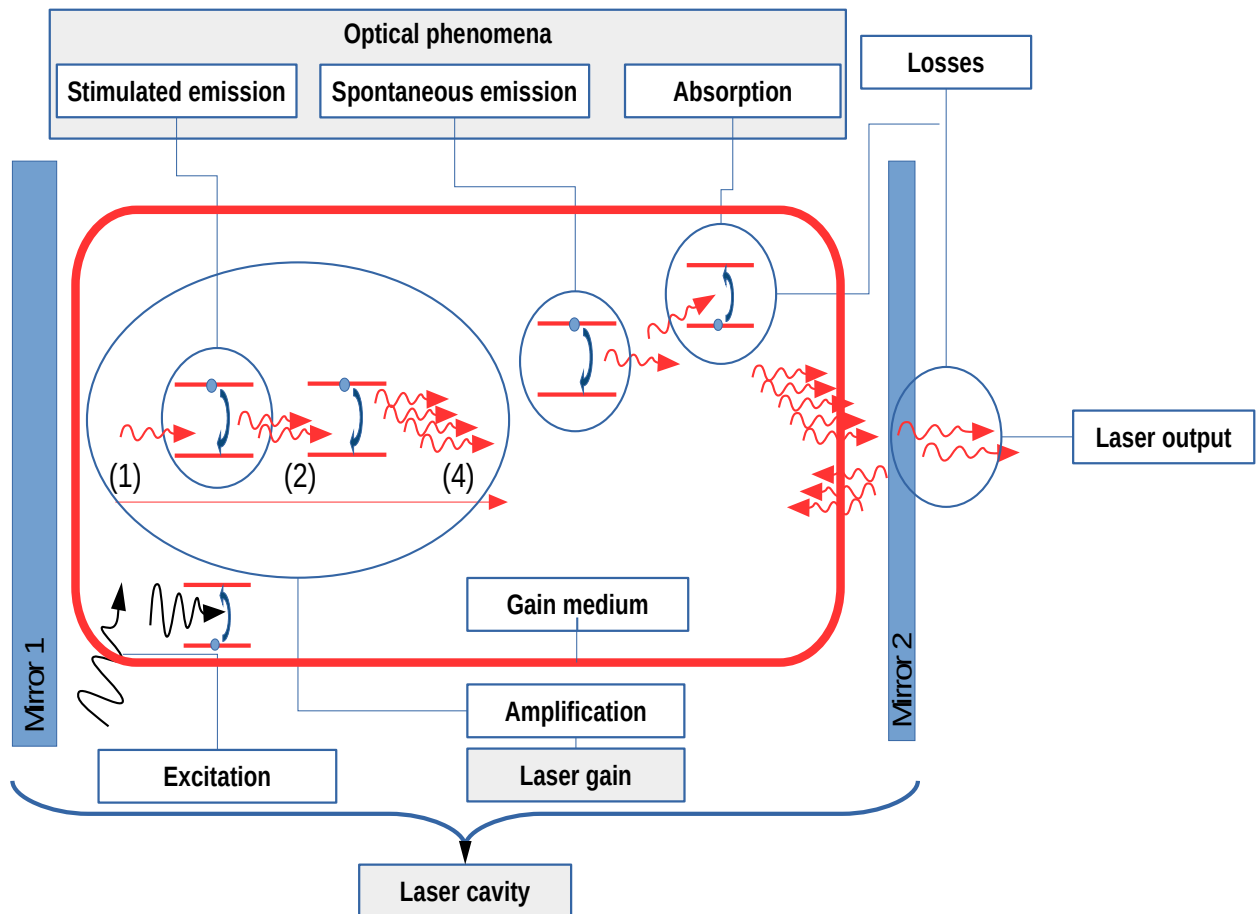


Figure I.22: Structure of laser

### I.4.1.1 Laser structure

Lasers are built from three basic bricks; a gain medium (section I.4.1.1.1 ), a cavity (section I.4.1.1.2 ), and an excitation source (section I.4.1.2 ) supplying energy to the system.

#### I.4.1.1.1 Gain medium

The gain medium provides amplification of the stimulated emission in a wavelength range corresponding to the energy bandgap of the material.

In organic thin films, the principle gain measurement method is called Variable Stripe Length (VSL) which have been proposed first for semiconductors [53]. The variation  $dI$  over a stripe length  $dz$  of the light intensity  $I$  emitted by a thin film gain medium with modal gain  $g$  pumped optically with an intensity  $I_{pump}$  reads [54]:

$$\frac{dI}{dz} = (A_{sp} N h \nu) \left[ \frac{\Omega(z)}{4\pi} \right] + g_{mod} I \quad \text{Eq.(I.27)}$$

where  $A_{sp}$  is the spontaneous emission rate,  $N$  is the excited state population density,  $h\nu$  is the photon energy,  $g_{mod} = \Gamma g - \alpha$  is the modal gain with  $g$  the (linear) gain in  $cm^{-1}$  of the material,  $\Gamma$  is the confinement factor, and  $\alpha$  is the propagation loss coefficient  $cm^{-1}$  (see section I.4.1.1 ),  $\Omega(z)$  is the solid angle of the emission of photons.

The exponential nature of the amplification of the stimulated emission appears in the solution:

$$I_{ASE}(z) = A_{sp} N h \nu \frac{\Omega(z)}{4\pi} \frac{1}{g_{mod}} \left( \exp^{g_{mod} z} - 1 \right) \quad \text{Eq.(I.28)}$$

In a linear regime, the (linear) gain coefficient  $g$  is proportional to the pump density  $I_{pump}$  :

$$g = K I_{pump} \quad \text{Eq.(I.29)} \quad \text{with K expressed in } cm W^{-1} .$$

The stimulated emission cross section  $\sigma_{em}$  (in  $cm^2$ ) is the ratio of the (linear) gain to the population density of the excited states  $N$  :

$$\sigma_{em} = \frac{g}{N} \quad \text{Eq.(I.30)}$$

From the linear gain  $g$ , the laser gain coefficients reads:

$$\xi_E = g \frac{c}{n} \frac{1}{N} \quad \text{Eq.(I.31)}$$

where  $n$  is the index of refraction in the material and  $c$  the light velocity, and  $N$  the density of excited states. The laser gain coefficient is also calculated from the cross section using the relation :

$$\xi_E = \frac{\sigma_{em} c}{n} \quad \text{Eq.(I.32)}$$

Table 2 gathers some examples of wavelength, linear gain, emission cross section, and laser gain coefficient of different organic materials allow in the guest:host configuration.

Table 2: Examples of wavelength, linear gain, emission cross section, and laser gain coefficient of different organic guest:host systems (Alq3:DCM, Alq3:DCM2, Alq3:DCJTb), and DCM, rhodamine 640 and BsB-Cz thin films

Compounds	$\lambda_{peak}$ (nm)	$g$ (cm <sup>-1</sup> )	Cross section (cm <sup>2</sup> )	Laser gain coeff. (cm <sup>3</sup> s <sup>-1</sup> )	Ref.
Alq3:DCM	595		$\sigma = 7.5 \times 10^{-16}$	$\xi = 1.4 \times 10^{-5}$	[55]
Alq3:DCM (2.8%)	605		$\sigma = 1.1 \times 10^{-16}$	$\xi = 2.0 \times 10^{-6}$	[56]
Alq3:DCM (2.5%)	618		$\sigma = 1 \times 10^{-16}$	$\xi = 1.8 \times 10^{-6}$	[57]
Alq3:DCM2 (1%)	612	30	$\sigma = 7.4 \times 10^{-17}$	$\xi = 1.3 \times 10^{-6}$	[58]
Alq3:DCM2 (3%)	626	89	$\sigma = 1.8 \times 10^{-16}$	$\xi = 3.2 \times 10^{-6}$	[58]
Alq3:DCM2 (6%)	637	138	$\sigma = 2.7 \times 10^{-16}$	$\xi = 4.8 \times 10^{-6}$	[58]
Alq3:DCJTb (2%)	660		$\sigma = 8.3 \times 10^{-16}$	$\xi = 1.5 \times 10^{-5}$	[59]
RH640 (5 wt%)	607		$\sigma = 1.39 \times 10^{-16}$		[54]
DCM	606		$\sigma = 2.47 \times 10^{-16}$		[54]
BsB-Cz	450			$\xi = 4.8 \times 10^{-6}$	[60]

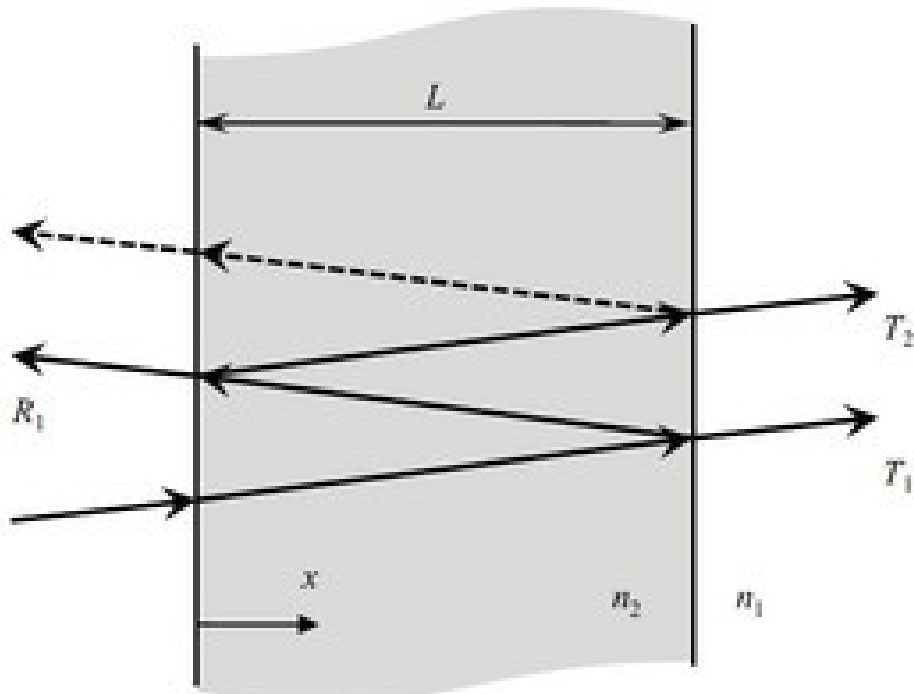


Figure I.23: Laser cavity principle



### I.4.1.1.2 Cavities

The role of the cavity is to select the frequency and the direction of the stimulated emission photons. The main categories of laser cavities are the Fabry-Perot type [61] with the vertical cavity surface emitting laser (VCSEL) [62] as a variant, the slab-waveguide [63], the 1D and 2D periodically modulated distributed feedback (DFB) [64] or photonic crystal [65] shown in fig.I.24.

- **Fabry-Perot**

It consists of two parallel mirrors  $M_1$  and  $M_2$  with reflection coefficient in intensities  $R_1$  and  $R_2$  spaced by a distance  $e$  and filled with a material with refractive index  $n$ . Its transmittance is given by the well-known Airy function;

$$A(\lambda) = \frac{1}{(1 + M \sin^2(\phi))} \quad \text{Eq.(I.33), with } M = 4 \frac{\sqrt{R_1 R_2}}{(1 - \sqrt{R_1 R_2})^2}$$

The quasi periodicity in wavelength of the Airy function is given by the free spectral range (FSR):

$$FSR = \Delta_\lambda = \frac{\lambda^2}{2ne} \quad \text{Eq.(I.34)}$$

The linewidth of the transmission peaks is  $\delta_\lambda = \frac{\Delta_\lambda}{F}$ , where  $F$  is the finesse given by

$$F = \frac{\pi (R_1 R_2)^{\frac{1}{4}}}{1 - (R_1 R_2)^{\frac{1}{2}}} \quad \text{Eq.(I.35). As a quality factor, the larger } F, \text{ the better the}$$

frequency selection of the cavity.

Fabry-Perot cavities are the archetype of the laser cavities on which historically the laser theories has been built; If a cavity of length  $L$  filled with a gain medium with  $g$  gain, and to obtain the threshold condition, the optical field reproduce itself after each round trip. Under continuous wave operating conditions, the amplitude and phase change accumulated by the optical field after one round trip reads:

$$\sqrt{R_1 R_2} \exp^{(g_{mod} L)} \exp\left(j \frac{2\pi nL}{\lambda}\right) = 1 \quad \text{Eq.(I.36)}$$

This equation condition can be split in to real and imaginary parts. The real part provides the threshold gain condition:

$$\sqrt{R_1 R_2} \exp^{(g_{mod} L)} = 1 \quad \text{Eq.(I.37) leading to the gain compensating the losses}$$

$$\Gamma g = \alpha + \frac{1}{2L} \ln\left(\frac{1}{R_1 R_2}\right) \quad \text{Eq.(I.38)}$$

While the imaginary part gives the condition of the lasing frequency:

$$\sin\left(\frac{2\pi nL}{\lambda}\right) = 0 \quad \text{Eq.(I.39)}$$

Defines the lasing wavelength  $\lambda_R$  :

$$\lambda_R = 2nL/m \quad \text{Eq.(I.40) with } m \text{ a longitudinal mode number}$$

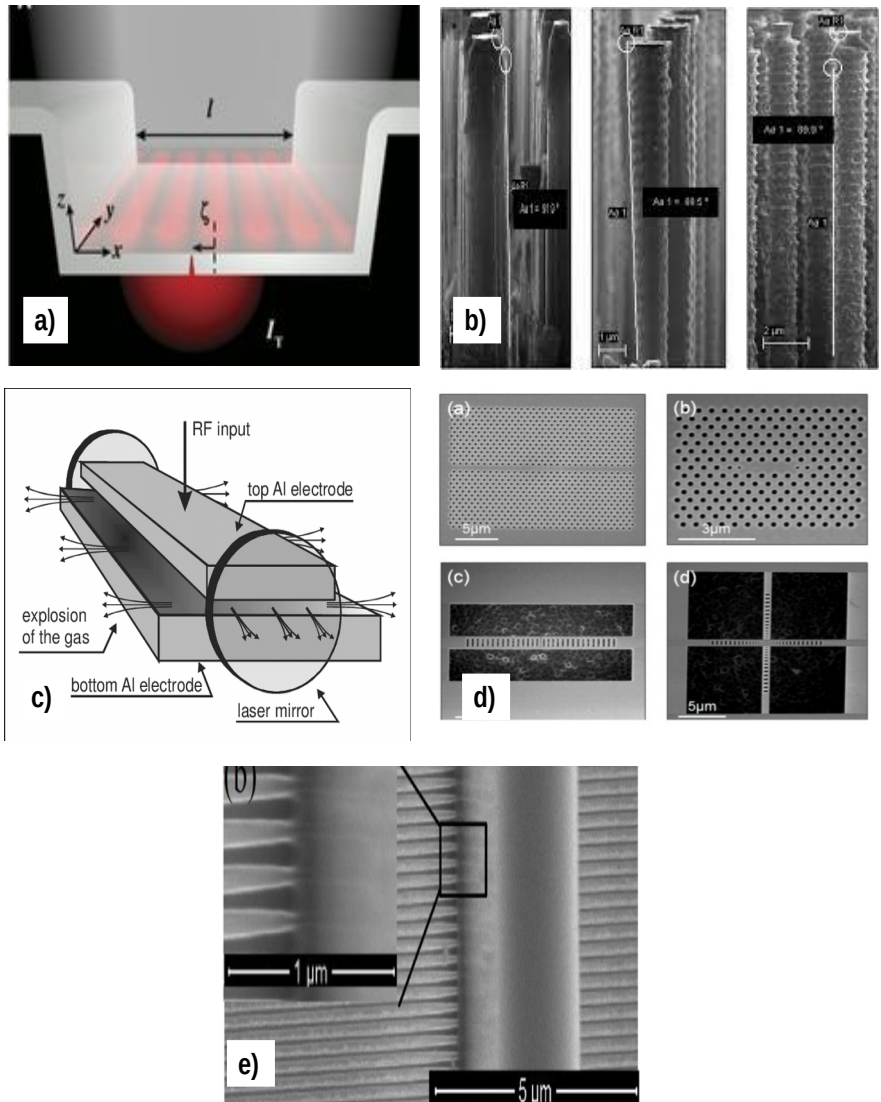


Figure I.24: Cavity types; a): Fabry Perot cavity, b): VCSEL cavity, c): slab waveguide cavity, d): crystal photonic cavity, e): DFB cavity [From 61,62,63,64,65]

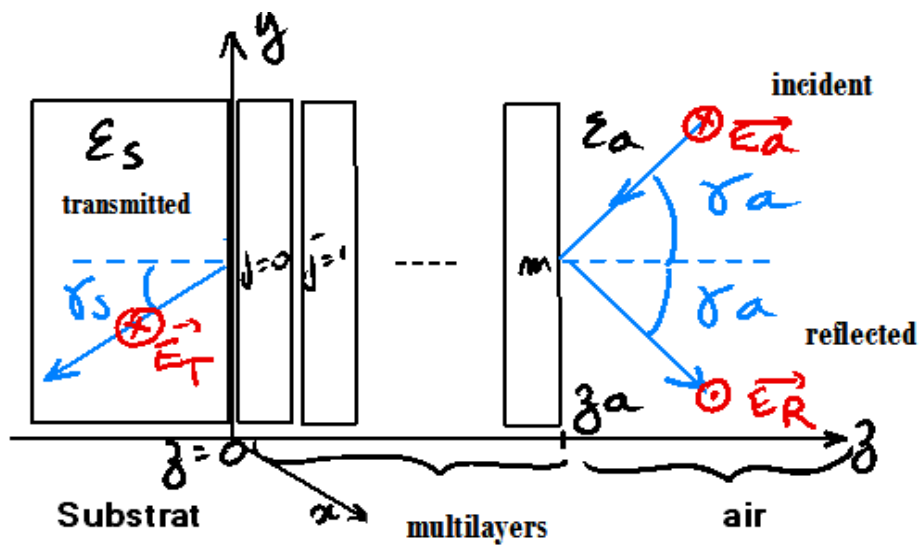


Figure I.25: Multilayers structure used to the transfer matrix method

- **VCSEL**

Vertical cavity surface emitting lasers are usually an integrated monolithic version of the Fabry-Perot cavity with a small mode volume leading to an enhancement or inhibition of the spontaneous emission via the Purcell effect which is added to the Fabry-Perot effect. Intensive research on organics VCSEL has been conducted in our group and for more details, we invite the reader to consult the work by Coens and Zeng [66, 67]

- **Slab-Waveguide**

In the slab waveguide type of cavity, the gain medium is a thin film where a frequency selection is obtained by the reduction of the waveguided modes. With the optical waveguide theory, it is possible to identify the allowed TE (and TM) optical waveguided modes and their effective index by solving the transcendental equation [68]:

$$h e = (m+1)\pi - \arctan\left(\frac{h}{p}\right) - \arctan\left(\frac{h}{q}\right) \quad \text{Eq.(I.41)}$$

where  $p = k_0 \sqrt{n_{\text{eff}}^2 - n_1^2}$ ,  $q = k_0 \sqrt{n_{\text{eff}}^2 - n_3^2}$ ,  $h = k_0 \sqrt{n_2^2 - n_{\text{eff}}^2}$  with  $k_0 = \omega \sqrt{\epsilon_0 \mu_0}$

The  $Y$  component of the TE mode electric field of the wave propagating in the  $z$  direction spreading over the different layers is defined for each layer as:

$$\begin{aligned} E_{y1} &= C_1 \exp^{px} \\ E_{y2} &= C_2 \cos(hx + \alpha) \\ E_{y3} &= C_3 \exp[-q(x-e)] \end{aligned} \quad \text{Eq.(I.42)}$$

$\Gamma$  the confinement factor as used in eq (I.27, I.38) is the fraction of the electric field in the confinement layer:

$$\Gamma = \frac{\int (E_{y2} dx)}{\int (E_{y1} dx) + \int (E_{y2} dx) + \int (E_{y3} dx)} \quad \text{Eq.(I.43)}$$

- **Distributed FeedBack cavities**

A Distributed FeedBack (DFB) cavity consists of a grating ie a periodic structure with an alternated sequence of two different materials with either gain or index contrast.

In a first approach, the frequency selection of a first order DFB can be expressed by the Bragg's law

$$\lambda_B = 2n\Lambda \quad \text{Eq.(I.44)}$$

where  $\Lambda$  is the period of the structure and  $n$  the index of the material. However, the Bragg's law does not apply for diffraction orders larger than 1 and other methods are necessary to model the cavity effect. Among these methods, the coupled wave theory and the transfer matrix formalism. For the coupled wave theory applied to polymer thin films to fabricate optically pumped DFB lasers, we refer the reader to the work by Sobel [69]. The transfer matrix formalism can be used to calculate the transmittance and the reflectance of multilayered optical thin films assuming layers infinite in both directions perpendicular to the direction of propagation. This is obviously not the case in the "planar" DFB structures, and it is a limit of this formalism. In the transfer matrix formalism, each  $j$  layer with a thickness  $d_j$  and refractive index  $n_j$  is modeled with an

elementary matrix  $M_j$  from which reflection and transmission from and to adjacent layers reads [70]:

$$M_j = \begin{pmatrix} \cos \phi_j & i \frac{1}{q_j} \sin \phi_j \\ i q_j \sin \phi_j & \cos \phi_j \end{pmatrix} \quad \text{Eq.(I.45)}$$

Where  $\phi_j = k n_j d_j \cos(\gamma_j)$  where  $k = 2\pi/\lambda$ , and  $\gamma_j$  is the angle of propagation of light chosen to 0 in our case.

For the S polarization,  $q_j = n_j \cos(\gamma_j)$  while for the P polarization  $q_j = n_j / \cos(\gamma_j)$ .

The matrix  $M_s$  of the stack made from the layers 1 to N is the product of the elementary matrix

$$M_s = \prod_N^1 M_j = M_N \cdot M_{N-1} \dots M_2 \cdot M_1 \quad \text{Eq.(I.46)}$$

$t(\lambda)$  the transmittance in amplitude of the stack reads:

$$t(\lambda) = 2 \frac{q_a}{q_a m_{11} + m_{12} q_s q_a + m_{21} + m_{22} q_s} \quad \text{Eq.(I.47)}$$

with  $m_{11}, m_{12}, m_{21},$  and  $m_{22}$  the components of the  $M_s$  matrix, and with  $q_a$  and  $q_s$  defined by  $q_x = n_x \cos(\gamma_x)$  in S polarization and  $q_x = n_x / \cos(\gamma_x)$  in P polarization with  $x = \{a, s\}$

#### I.4.1.2 Excitation sources

Excluding the chemical excitation [71], the main types of excitation sources present in the literature are the optical pumping and the electrical excitation. Optical pumping can be achieved with other lasers or flashlamps. The choice and challenge of this thesis being to develop an electrically excited organic laser, the remaining question is what is the difference between optical pumping and electrical excitation in terms of physical mechanisms? More precisely, which physical processes are beneficial and detrimental to the laser operation?

In (inorganic) semiconductor laser diodes, the population inversion condition is automatically fulfilled by direct excited states injection ie. electrons in the conduction band and holes in the valence band [72]. A priori this should remain true for the organic laser diode.

In organic semiconductors, a first major difference lies in the process of annihilation of excited states due to the presence of polarons. This will induce a decrease of the exciton population. A second difference is that the current injection increases both the radiative excitons (singlet) and the non-radiative excitons (triplet) whereas, under optical pumping the triplet population is fed via ISC a much slower mechanism.

To estimate the current density at laser threshold from the threshold value measured under optical pumping, the following equation given by is used [34, 73];

$$J_{th} = \frac{2 n_{th} \times q}{\eta_{rad} \times \tau_{rad}} \quad \text{Eq.(I.48)}$$

with  $n_{th}$  is the exciton density at the laser threshold,  $q$  is the electric charge,  $\eta_{rad}$  is the quantum efficiency (25% for the singlet), and  $\tau_{rad}$  is the emitted photon lifetime (5ns for DCM).

## I.4.2 State of the art of organic lasers

The literature lists only one example of lasing action in organic material under electrical excitation, whereas there are several example of organic lasers under optical excitation. We will screen some of them to identify the most relevant solutions for our objectives.

If the first laser was demonstrated by T. Mainman in 1960, the first organic laser was reported shortly after in 1966 almost simultaneously by two group; P.P. Sorokin et J.R. Lankard from the IBM laboratories at Yorktown Height in the USA and by Shaeffer and Schmidt from the Institute of physics and chemistry of the University of Marburg in Germany [74, 75]. The first group used a chloro-aluminum phtalocyanine dye (see Fig. I.26) in an ethyl-alcohol solution in an absorption cell placed in a cavity made of two flat mirrors (see Fig. I.27) and pumped with a ruby laser resulting in a laser threshold power density of about  $100\text{kW}/\text{cm}^3$ , while the second group used four dyes from the carbocyanine family in different solvent with a power threshold of  $100\text{kW}$ . This shows that although they were liquid-based, organic lasers take roots in the very beginning of the laser history. Note that another dye from the phtalocyanine family, the copper phtalocyanine is used as hole transporting layer in OLED.

They are closely followed by B.H. Soffer and B.B. McFarland who in 1967 present organic lasers based on rhodamine 6G (I.28) in ethanol but also in solid matrix of polymethylmethacrylate (PMMA) [76]. These first organic lasers have linewidths of 6 nm ( $Q = 95$ ) in a dielectric mirror cavity, and only 60 pm ( $Q = 9500$ ) when a first-order diffraction grating is added in the cavity. One first significant progress towards the organic laser diode is the possibility to solidify dyes dispersed in polymer matrixes as PMMA to obtain solid-state organic laser. This opens the possibility to get rid of the fluidic problems and to built even more compact lasers. Also, note that very early in the history of organic lasers, the introduction of a diffraction gratings in the cavity (See Fig. I.29) played a very important role in achieving high quality factors as well as wavelength tunability [77]. In 1968, shortly before Sorokin's group, Peterson and Snavely introduced flashlamp as a novel way to excite organic dyes in PMMA rods [78,79]

The nature of the losses in dye lasers has been discussed in detail in review articles by Snavely [80] Schäffer [81] and Stepanov and Rubinov [82], and it was shown among other things that the accumulation of triplet-states induces losses that limited the pulse duration up to  $0.1\mu\text{s}$ - to  $1\mu\text{s}$  preventing constant wave (CW) operation. By introducing triplets quencher (oxygen) the triplet lifetime was shortened to  $0.1\mu\text{s}$ , a time short enough to allow CW operation. The first CW operation of an organic dye solution laser was demonstrated by Peterson et al. in 1970 with Rhodamine 6G in water as a gain medium and with a short cavity made with two parallel sapphire-based dielectric mirrors so as to manage the thermal inhomogenities and reduce hot-spots. The laser threshold was  $3 \times 10^4 \text{ W}/\text{cm}^2$  and the full width at half maximum (FWHM) linewidth was 3nm resulting in a Q-factor  $Q \sim 200$  [83].

In 1970, H. Kogelnik and C.V. Shank introduced for the first time a solid-state organic laser with a novel type of cavity made of a periodic structure in which feedback is provided by backward Bragg scattering. In the so-called distributed feedback (DFB) laser, the gain medium consists of Rhodamine 6G dissolved in a gelatin films (Fig. I.31). Because nowadays DFB lasers are mainly associated with inorganic semiconductor lasers specially in the optical telecommunication field, it appears very surprising that the first DFB laser has in fact, been an organic one [84]. The same year, Kaminow replaced gelatin with polymethylmethacrylate PMMA [85].

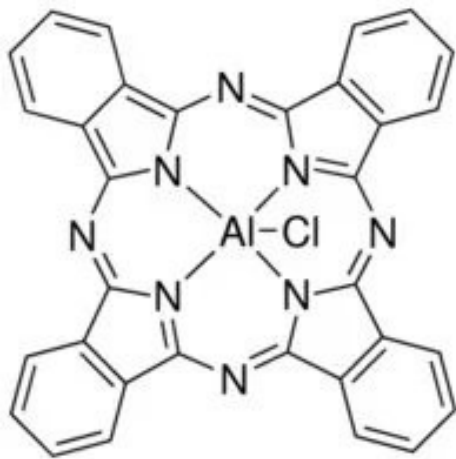


Figure I.26: Molecular structure of chloro-aluminium phthalocyanine. First organic gain medium used for the first dye (organic) laser.

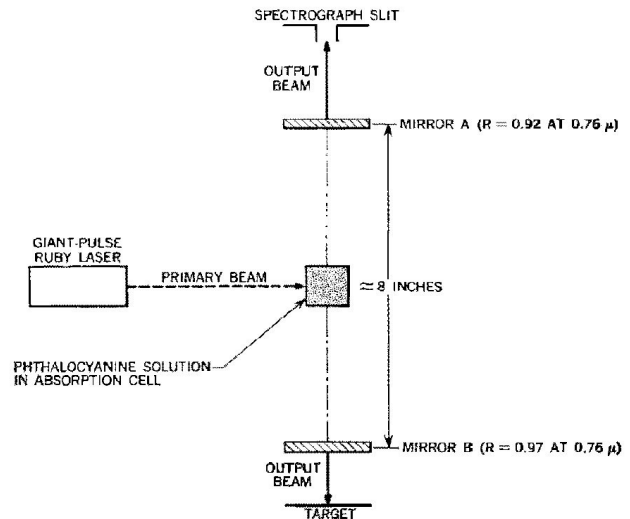


Figure I.27: Cavity structure of the first dye laser with flat dielectric mirror

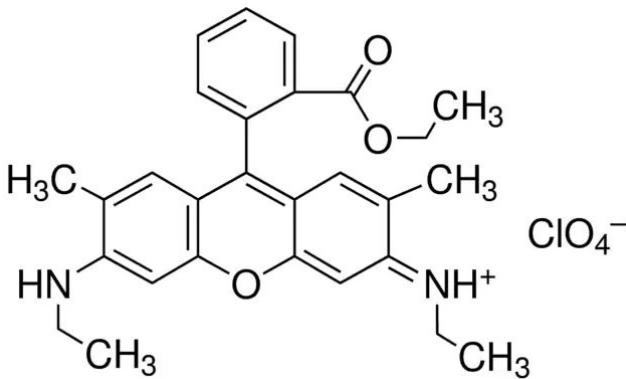


Figure I.28: Molecular structure of rhodamine 6G One of the most present laser dye in the literature

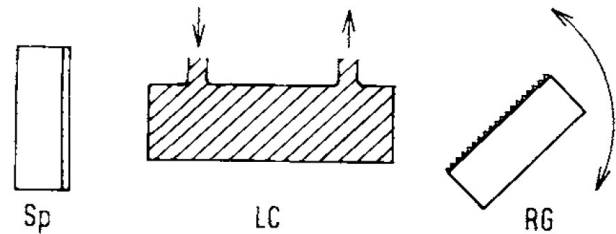


Figure I.29: Construction of a tunable laser cavity with a grating from Schaeffer [77]; Sp: laser mirror, LC, Laser cell, RG reflection grating, the curved double-headed arrow shows the direction of rotation of the grating for adjustment of the wavelength

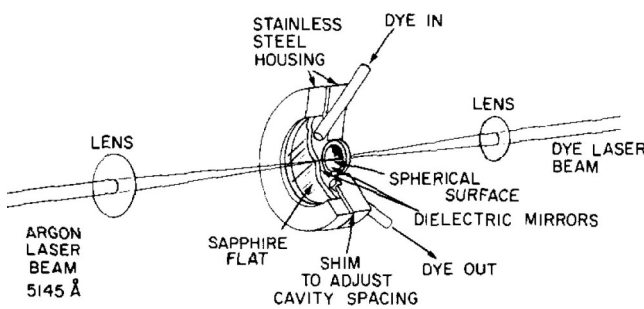


Figure I.30: Cavity structure of the first CW dye laser; The dielectric mirror are deposited on sapphire window instead of a glass window to improve the thermal management. The dye solution is circulating. Figure from [83]

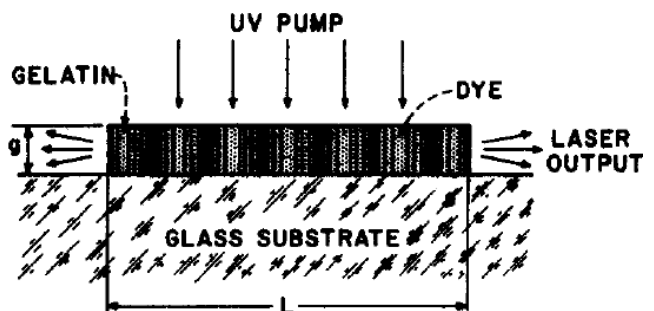


Figure I.31: Cross section of the first distributed feedback cavity consisting of dyed gelatin on a glass substrate irradiated with an interference pattern producing the periodic structure

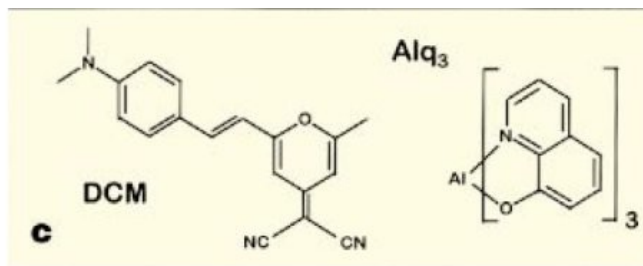
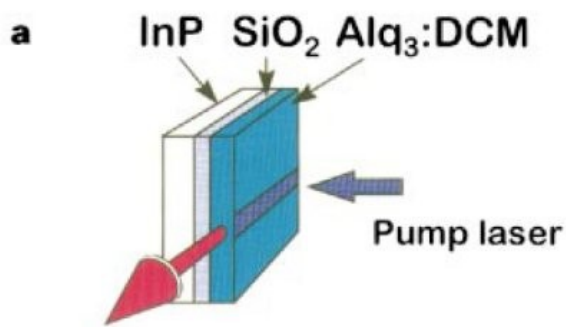
The development of highly transparent (low-loss) polymers such as PMMA (polymethyl methacrylate), HEMA (hydroxyethylmethacrylate) and ORMOSIL (organically modified silicate) constituted another important progress for solid state organic laser as it reduced the absorption losses and hence the laser threshold [86, 87, 88]. In 1995 Maslyukow et al. from the University of Moscow have investigated more systematically solid state lasers from different rhodamine dyes in different optimized PMMA matrices [89]. Pumping with a frequency-doubled Q-switched Nd:YAG laser (pulse duration 10ns), the flat dichroic mirror cavity produced laser output with FWHM of 6nm corresponding to a factor quality of  $Q \sim 100$  with a threshold laser below  $\sim 4 \text{ mJ/cm}^2$ .

In 1997, V. Kozlov and other collaborators of S. Forrest at Princeton University published in the journal Nature, evidence of laser emission in a vacuum-deposited organic thin layers composed of DCM2 co-evaporated with Alq3 [90]. The laser structure shown Fig. I.32 consists of 50nm of Alq3:DCM deposited on an InP substrate pre-coated with a 2  $\mu\text{m}$ -thick layer of SiO<sub>2</sub>, pumped by a 500ps optical pulses from a nitrogen laser (337nm) focused by a cylindrical lens into a 50  $\mu\text{m}$ -wide stripe. The laser threshold appeared to be as low as  $1.2 \mu\text{J/cm}^2$ . These dyes are actually OLED materials shaped in a stripe-type waveguide. Both materials co-evaporated in thin layers constitute a guest-host system introduced few years previously for OLEDs. This is a new step in the field of solid-state organic laser because this suppresses the distinction between dyes and OLED compounds named organic semiconductors. Further studies with planar microcavity made of a multilayered mirror and a metallic one, and with slab waveguide cavity lead for the first time to an estimation of the linewidth enhancement factor (Henri's factor) of  $\alpha \approx 2$  which appears to be lower than that of their inorganic counterparts [91, 92]. Among different gain media DCM, DCM2, Rhodamine 6G, CBP, perylene and coumarin 47, DCM2 exhibits the lowest threshold.

In 1997, Berggren et al. proposed an approach, based on energy transfer between molecular species (including DCM2), that lowers the threshold for stimulated emission using Förster Resonant Energy Transfer (FRET); an initial molecular excited state is generated in a host compound by absorption of light; this state is then resonantly and non-radiatively transferred down in energy between suitably matched dye molecules dispersed in the host, so ensuring that the absorption losses at the final emission wavelengths are very small [93]. A low absorbance at the emission wavelength(s) will mean that the optical gain and minimum pump power necessary for population inversion is lowered. The host serves mainly to physically separate the fluorescent dye molecules, which has the beneficial effect of hindering concentration quenching and increasing the quantum yield.

In 1998, Granlund et al. used a novel type of cavity (VCSEL see Fig. I.33) made of a polythiophene (polymer) layer sandwiched between two multilayered mirrors resulting in a microcavity with a Q-factor  $\sim 163$  and a laser threshold of  $120 \text{ nJ/cm}^2$  that was the lowest at the time [94]. The cavity is pumped with a 100 fs pulse at 530 nm delivered by an optical parametric generator amplifier OPG/OPA system pumped by an amplified Ti:Sapphire laser.

In 1999, Forrest et al. published a series of papers on the same topic with a prospective section on organic laser diode identifying issues with the low carrier mobilities of organic semiconductors, with the difficult trade-off between highly conductive and highly reflective electrodes, and the polaronic induced absorption [95]. He also calculated the Henri's factor for organic semiconductors [96]. The same year, Meier et al. reported lasing action from two-dimensional DFB in photonic crystal with 2,2'-biphenyl-5,5'-di-tert-butylphenyl-1,3,4-oxadiazole (PBD) doped with DCM or Coumarin 490 as a gain medium [97].



**Edge emission**

Figure I.32: Laser made from evaporated organic semiconductor (reprint from [91]); . a, Schematic of the laser structure and experimental set-up. c, Chemical structure of DCM and Alq3. DCM (4-(dicyanomethylene)-2-methyl-6-(4-dimethylaminostyryl)-4H-pyran) is a guest material, while Alq3 Tris(8-hydroxyquinoline)aluminum(III) is a host.

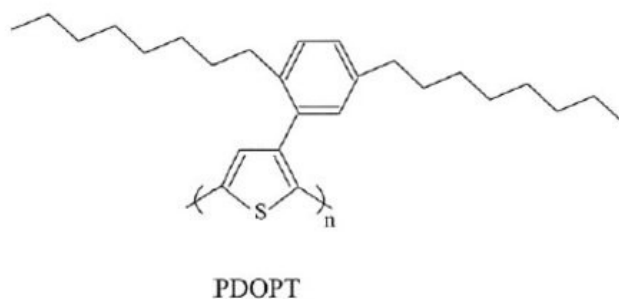
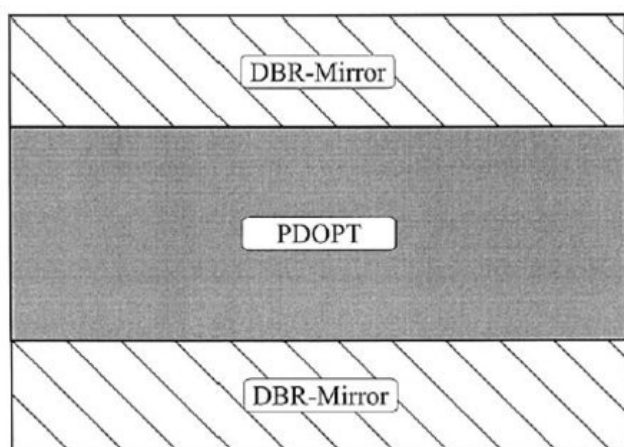


Figure I.33: VECSEL type of microcavity (left) , with polythiophene (PDOPT) molecular structure (right) reprint from [94]

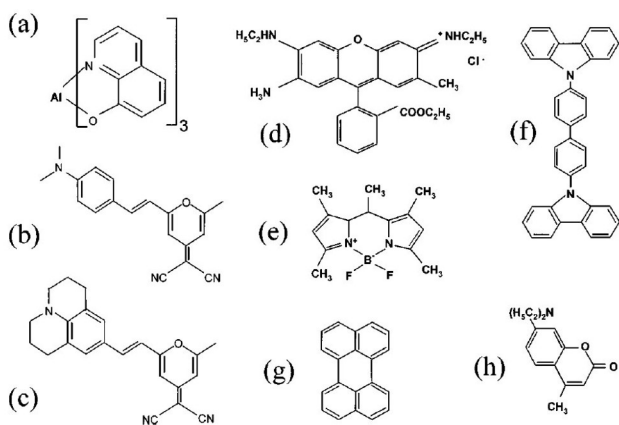


Figure I.34: Chemical structure formulas of a) Alq3, b) DCM, c) DCM2, d) rhodamine 6G, e) pyrromethane, f) CBP, g) perylene, h) coumarin 47. (from [91])

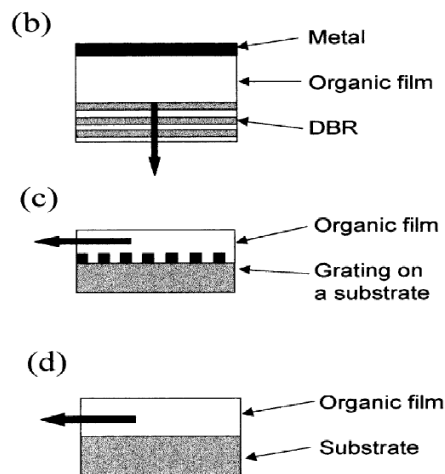


Figure I.35: (b) planar microcavity, (c) distributed feedback and (d) slab 3waveguide organic laser structures (solid arrows show the laser output beam).(From [95])



In 2000, several experiments using a DFB cavities were reported; Riechel et al presented a flexible polymer laser made from 1D and 2D periodically modulated substrate covered with LPPP as a gain medium as shown on Fig .I.26 [98]. It exhibited, 0.25nm narrow linewidth laser emission ( $Q \sim 1920$ ), for a 1.8nJ threshold corresponding to  $10 \mu\text{J}/\text{cm}^2$  with 2D DFB offering a lower threshold level than 1D-DFB (See Fig. I.37).

Kozlov in the group of Forrest, focused on Alq3:DCM as a gain medium but choose to placed it in a first-order DFB cavities. When pumped optically, it offered a laser threshold of  $0.2 \mu\text{J}/\text{cm}^2$ . The lasing thresholds of  $0.2 \mu\text{J}/\text{cm}^2$  observed in these double-heterostructure DFB organic semiconductor lasers (OSL) (Fig I.38) is significantly lower than that of Fabry–Perot OSL’s ( $1 \mu\text{J}/\text{cm}^2$ ) [90]. At threshold, the exciton density is estimated to  $n = 3 \times 10^{11} \text{cm}^{-2}$  and the equivalent current density to  $J = 80 \text{A}/\text{cm}^2$  calculated using the following equation:

$$j = \frac{2nq}{1/4} \frac{1}{\tau} \quad \text{Eq.(I.49)}$$

where  $q$  is the electron charge,  $\tau$  the DCM radiative lifetime is taken to 5ns,  $1/4$  is the ratio of radiative singlet excitons to the total number of excitons formed by electrical injection, and the factor of 2 accounts for two charges (electron and hole) needed to form an exciton. This level seems very low, probably because many losses have been underestimated. In the same paper they demonstrated experimentally current density up to  $35 \text{A}/\text{cm}^2$  under DC excitation in a structure similar to that of Fig. I.39.

In 2005, Samuel From University of Saint Andrews and Barnes from the University of Exeter, reported low threshold edge emitting polymer (MEH-PPV) distributed feedback laser [99]. The linewidth is estimated to 0.74nm and the threshold density to  $136 \mu\text{J}/\text{cm}^2$ .

In 2005, Koschorreck reported vertical emitting microcavity (VECSEL type) with Alq3:DCM in between multilayered mirrors exhibiting a Q-factor of 4500 and optically pumped by the frequency doubled output of a regenerative Ti:Sa amplifier providing pulses of 200fs [100]. They demonstrated a threshold of  $20 \mu\text{J}/\text{cm}^2$  instead of  $300 \mu\text{J}/\text{cm}^2$  in a previous experiment where the top mirror was an aluminium layer [92]. This is an indication of losses from a metallic cathode.

In 2005, Pisignano et al. investigated the emission properties of 1<sup>st</sup>-order and 2<sup>nd</sup>-order distributed-feedback (DFB) resonators based on an organic semiconductor patterned by a novel nanoimprinting technology achieving laser threshold of  $27 \mu\text{J}/\text{cm}^2$  and  $37 \mu\text{J}/\text{cm}^2$  and 1.1nm laser linewidth [101, 102].

Still in 2005, Rose et al. reported in nature laser action in organic polymers in different types of microcavities including DFB, ring microcavity around a fiber and using diphenylanthracene polymer as gain medium and with very surprisingly large laser linewidth  $\sim 8 \text{nm}$  whereas the laser threshold is among the lowest ever reported with  $40 \text{nJ}/\text{cm}^2$  [103].

In 2006, Yamamoto, reported the reduction of the laser threshold energy of the second-order DFB structure of [3-(2-benzothiazolyl)-7-(diethylamino)coumarin] (Coumarin 6) in a poly(N-vinylcarbazole) (PVCz) host matrix from  $300 \text{nJ}/\text{cm}^2$  by a factor of 30 to 50 compared with that in a polystyrene (PS) matrix ( $7.3 \text{mJ}/\text{cm}^2$ ). For both PVCz / Coumarin 6 and PS/Alq/ Coumarin 6, the effective energy transfer played a significant role for lowering the lasing threshold [104]. First order DFB microcavity exhibit lower threshold than second-order [105]

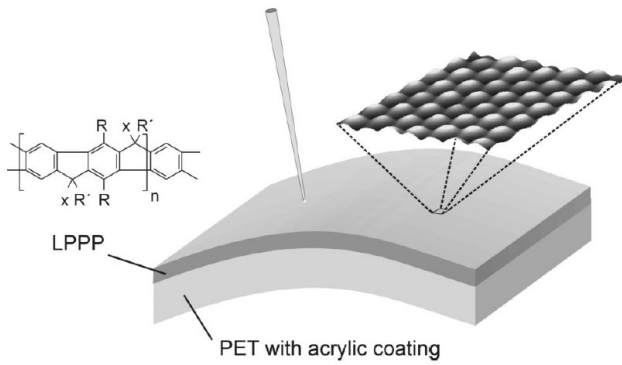


Figure I.36: flexible polymer laser. A film of the conjugated polymer LPPP is spin-coated onto a flexible substrate. The surface of the substrate has a periodic two-dimensional height modulation (From[98]).

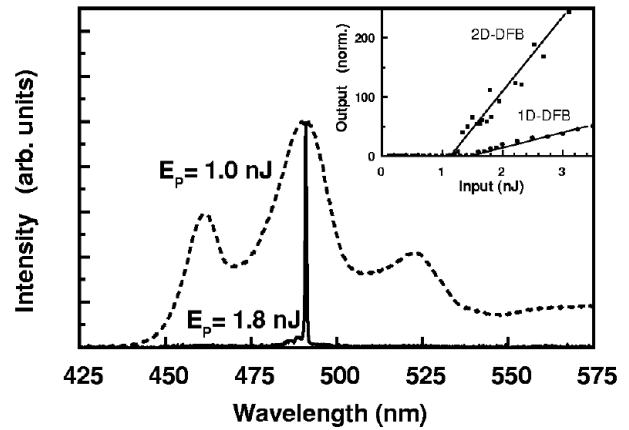


Figure I.37: Emission spectra of the 2D-DFB laser below (dashed line) and above laser threshold (solid line). The spectral half-width (FWHM) of the laser line is 0.25 nm.(From[98])

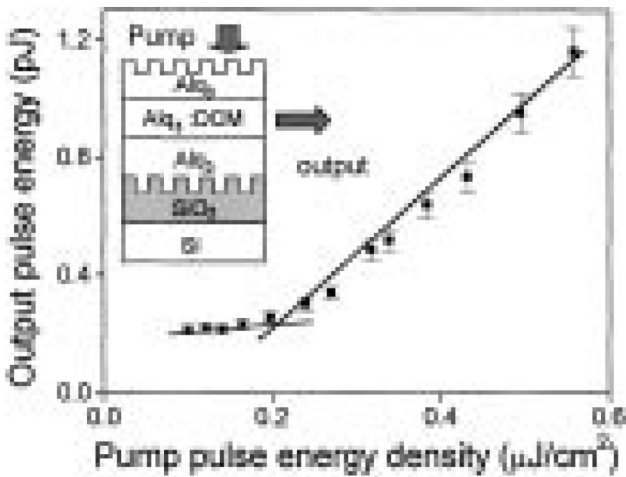


Figure I.38: DFB double heterostructure organic semiconductor laser (From [2])

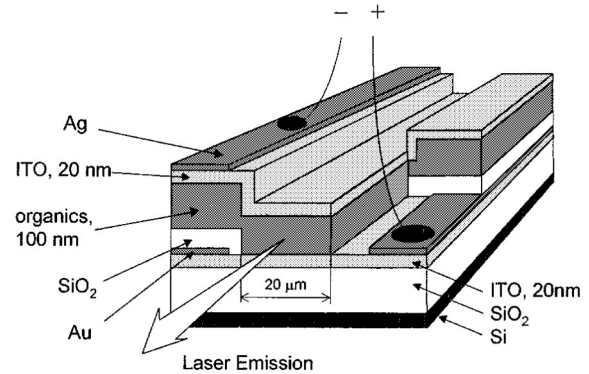


Figure I.39: Schematic of a waveguide OLED composed of a 100-nm-thick organic film and 20-nm-thick ITO contacts.(From [36])

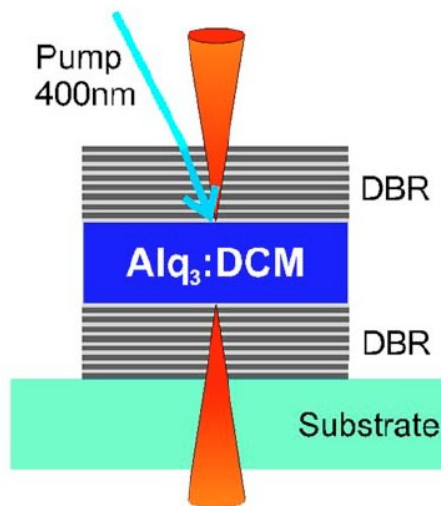


Figure I.40: vertical emitting Microcavity structure with an active layer of Alq<sub>3</sub>:DCM.(from [100])

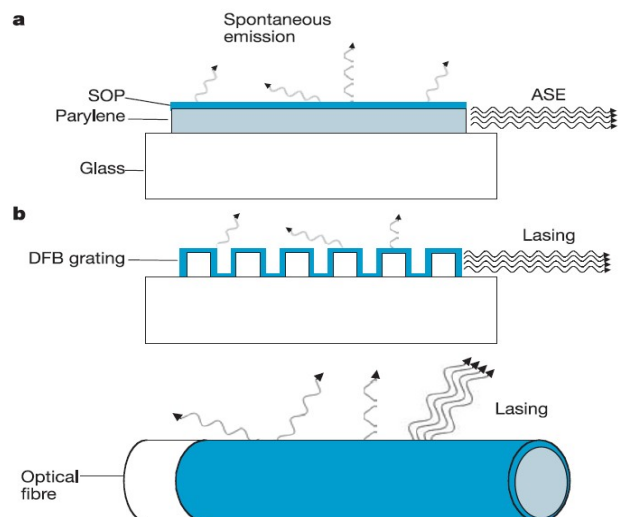


Figure I.41: Different types of microcavities presented in [103]

In 2006, C. Karnutsch, reported low threshold DFB polymer lasers based on a polyfluorene derivative [106]. In 2007, they improved their resonator, with a mixed-order grating design: A second-order Bragg scattering region that provides efficient vertical outcoupling of the laser radiation is surrounded by first-order scattering regions that give rise to strong feedback. Under optical pumping from a 10ns Q-switched Nd doped laser The laser threshold density is  $36\text{nJ/cm}^2$  is the lowest ever reported [107].

In 2009, Namdas et al proposed 1D and 2D imprinted DFB cavities on Quartz, ITO and Si wafer with SuperYellow as a gain medium, resulting in a threshold of  $3.6\mu\text{J/cm}^2$  [108]. Assuming no other optical losses, e.g., from carrier-induced absorption, an estimation of the equivalent current density given by the following equation is proposed;

$$J_{th} \approx \frac{N_0 q}{\Phi_{\text{int-el}} \tau_{\text{rad}}} \quad \text{Eq.(I.50)}$$

where  $N_0$  is density of photons at the lasing threshold (  $1 \times 10^{12} \text{cm}^{-2}$  ),  $q$  is electrical charge,  $\Phi_{\text{int-el}}$  is the internal quantum efficiency for the electroluminescence, and  $\tau_{\text{rad}}$  is the radiative lifetime of the excitons. Under the assumption of  $\Phi_{\text{int-el}} \approx 2.5\%$  ,  $\tau_{\text{rad}} \approx 5 \text{ns}$  and a carrier confinement in a 2nm thick zone the estimated current density is  $\sim 1.2 \text{kA/cm}^2$  . With 100nm thick confinement zone, the current density could jump up to  $60 \text{kA/cm}^2$ .

In 2009, Hirade from the Adachi's group demonstrate optically excited lasing by an organic semiconducting thin-film based on 2,7-bis[4-(N-carbazole)phenylvinyl]-9,9'-spirobifluorene (spiro-SBCz) as an active gain medium with a first-order distributed feedback (DFB) reflector. Lasing threshold is  $0.72 \pm 0.07 \mu\text{J/cm}^2$ , 83% lower than its threshold of amplified spontaneous emission ( $4.1 \pm 0.4 \mu\text{J/cm}^2$ ) [109].

Xia et al reported Low-Threshold Distributed-Feedback Lasers in silica grating Based on Pyrene-Cored Starburst Molecules with threshold of  $156\mu\text{J/cm}^2$ [110].

In 2014, Deotare with Bulovik proposed an ultracompact low-threshold laser with an Alq3:DCM host:guest molecular organic thin film gain layer. The device uses a photonic crystal nanobeam cavity (see Fig. I.44) which provides a high quality factor to mode volume (Q/V) ratio and increased spontaneous emission factor. Lasing is observed with a threshold of  $4.2 \mu\text{J/cm}^2$  when pumped by femtosecond pulses of  $\lambda = 400 \text{nm}$  [111].

In 2012, Gourdon in our group reported optically pumped organic two-dimensional planar photonic crystal H2 and L3 microcavity (See Fig. I.45) with Alq3:DCJTb (4-(dicyanomethylene)-2-t-butyl-6(1,1,7,7-tetramethyljulolidyl-9-enyl)-4H-pyran) laser gain medium with a laser threshold of  $9.7\mu\text{J/cm}^2$  [112, 113].

One year after the beginning of this doctoral work, the Adachi's group at the OPERA center from the Kyushu University in Japan have reported indications of stimulated emission in an organic hetero-structure under electrical excitation [114]. Many aspects of this pioneering work need to be explored further and confirmed; for example, the reported current threshold is as low as  $0.5\text{kA/cm}^2$ , the laser linewidth reduction is incomplete, and the quality factor of this mixed-order cavity structure (see fig. I.46) remains to be described in more details. But this give confidence that laser threshold under electrical excitation can be achieved.

The different experiments are listed in table 3.

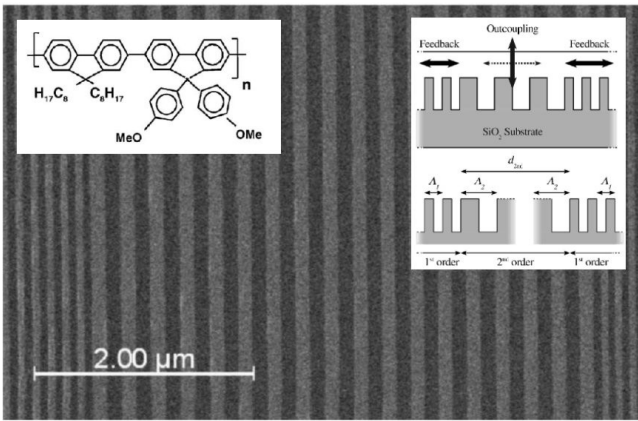


Figure I.42: Chemical structure of F8DP and a SEM picture of a mixed-order grating consisting of two 1st-order sections providing feedback and a 2nd-order region for vertical outcoupling. [107]

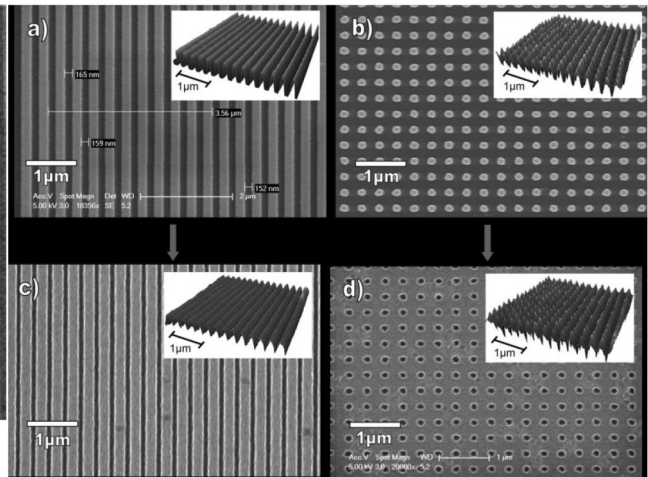


Figure I.43: from [108]

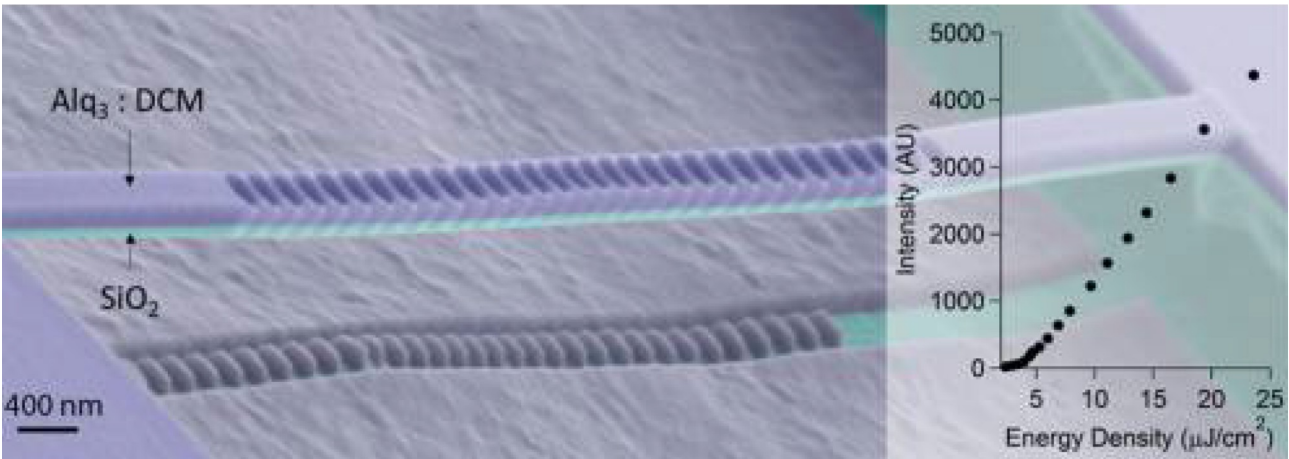


Figure I.44: Ultracompact photonic crystal nanobeam cavity [111]

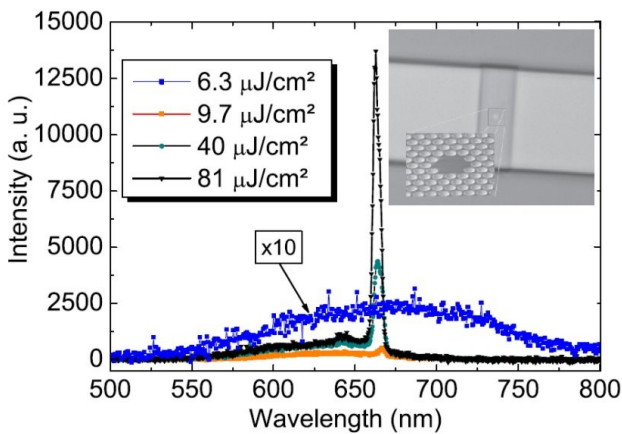


Figure I.45: Output spectra of the Alq3:DCJT B PhC for different pump energies. Inset: SEM image of the PhC microcavity.

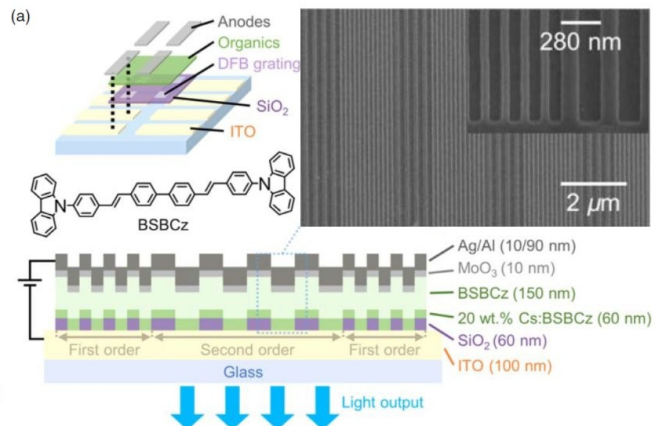


Figure I.46: Mixed order DFB cavity with BsB-Cz as laser gain medium

## I.5. Challenges towards the organic laser diode

In this section, we summarize the basic concepts and state of the art presented in the previous sections to identify the challenges of the design and realization of the organic laser diode. These challenges are analyzed successively according to the elementary bricks structuring a laser namely the gain medium (section I.5.1), the cavity (section I.5.2) and the excitation source (section I.5.3).

### I.5.1 Gain media

In the different experiments listed in table 3, several types organic gain media are used. To identify potential trends, for different organic gain media aggregated in three groups, we plot the laser threshold as a function of two parameters; firstly as a function of the quality factor (Fig I.47.a) and secondly as a function of the pulse duration of the optical pump (Fig. I.47.b). The three groups are:

- Host:Guest systems with Alq<sub>3</sub> as a host and with Rh6G, DCM, DCM2, or DCJTb as a guest (red circles)
- Other small molecules including non guest-host laser gain media (green squares)
- Polymers and blended polymers (blue triangles)

Figure I.47.a does not show a strong particular trend as a function of the quality factor because of several experiments spread over a large range of threshold energy density while with low Q-factors of about 100 (probably as a consequence of a too low resolution in the measurement of the laser linewidth). Apart from these experiments showing unexpectedly low threshold value with very small Q-factor, Alq<sub>3</sub>:Guest based Host:Guest systems (1<sup>st</sup> group) exhibit among the lowest threshold. Figure I.47.b presenting the laser threshold as a function of the pulse duration does not show a clear trend neither. Lowest threshold are observed for pulse duration in the 1-10ns range. One experiment with Alq<sub>3</sub>:Guest based Host:Guest systems (1<sup>st</sup> group) is among the lowest four threshold density.

As an intermediate conclusion, it appears that the gain media of the 1<sup>st</sup> group is the best choice because of low threshold energy density, and the number of experiments conducted with them.

### I.5.2 Laser cavities

We now analyze the impact of the cavity type on the laser threshold energy density plotted as a function of the quality factor (Fig I.47.c) and secondly as a function of the pulse duration of the optical pump (Fig. I.47.d). We distinguish the following five types of cavity; DFB microcavities (red stars), Fabry-Perot (green square), Photonic crystal (blue diamond), Slab-Waveguide (black square), and VCSEL (Yellow circle).

In Fig. I.47.c, among the six lowest threshold energy density, four of them have been obtained with DFB microcavities. The lowest laser threshold energy density is obtained with a DFB and a Q-factor of 6500. In Fig. I.47.d, the two lowest laser threshold energy density are obtained with DFB microcavities and pulse duration among the largest in the 1-10ns range.

The main conclusion from this bibliographic study, is therefore that Alq<sub>3</sub> doped with either Rh6G, DCM, DCM2 or DCJTb with a cavity of the DFB type is among the best choice to be considered. This configuration exhibits among the lowest with pulse excitation in the 1-10ns range, which is also compatible with electrical excitation.



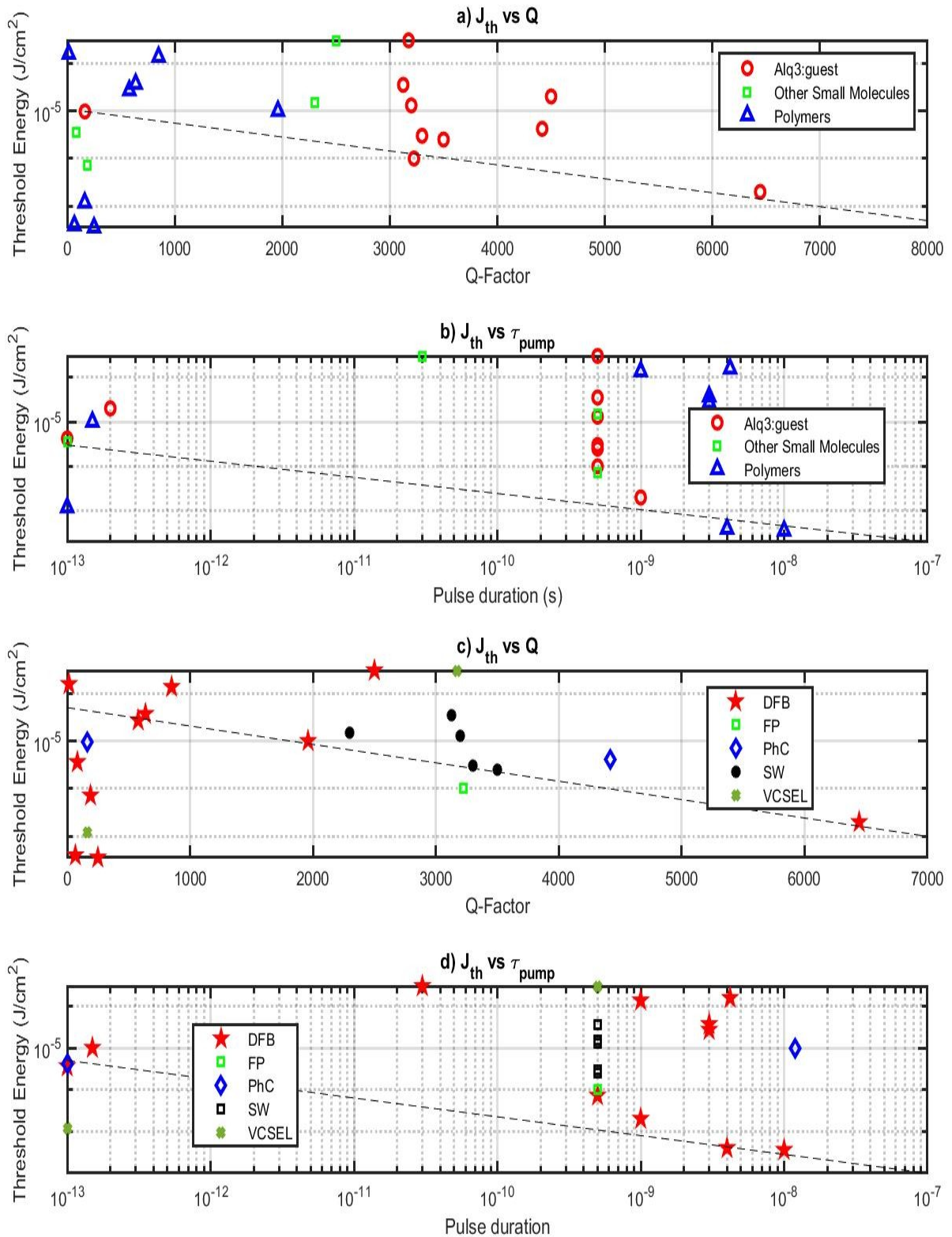


Figure I.47: Figures of merit showing the threshold energy density as a function of the quality factor (a, c) and of the pulse duration (b, d). a and b are displayed as a function of the types of organic gain media while c and d are displayed as a function of the type of cavity

### **I.5.3 Electrical excitation of organic materials**

From the experiments threshold values, it is possible to estimate the (equivalent) current density threshold value  $J_{Eq.Th.}$  needed to achieve the same level of excitation than provided by optical pumping using equation Eq.(I.48) . Note this equation assumes an electron-to-photon quantum efficiency of  $\eta=25\%$  whereas at high current density, the quantum efficiency in OLED is known to roll-off down to 0.1% or less [115, 116].

The equivalent current densities are presented in column 6 of table 3. The lowest laser threshold with a host:guest system is 87 A/cm<sup>2</sup> obtained by Kozlov et al. with quality factor as high as 6444 [90]. The lowest laser thresholds with DFB cavities are 17 A/cm<sup>2</sup> and 18 A/cm<sup>2</sup> obtained by Rose et al. and Karnutsch et al. with incredibly small Q-factors of 67 and 250 respectively [103, 107].

With a more relevant quantum efficiency of 0.1%, these values of the laser threshold are expected to increase by 250-fold reaching 21 kA/cm<sup>2</sup>, 4.2 kA/cm<sup>2</sup> and 4.5 kA/cm<sup>2</sup>.

The challenge of electrical excitation is therefore twofold, it is necessary to achieve both very high current density in OLED (~10 kA/cm<sup>2</sup>) and laser cavity with high quality factor (>5000).

Group, year [ref]	Organic gain medium	Cavity type	Q-factor or [laser linewidth (nm)]	Laser threshold (J/cm <sup>2</sup> )	Equivalent current density (A/cm <sup>2</sup> )	Lasing wavelength $\lambda_{em}$ (nm)	Pulse duration of excitation (ns)	$\lambda_{pump}$ (nm)
Maslyukov 1995 [18]	Rhodamines	Fabry-Perot	Q~100	4.0 mJ/cm <sup>2</sup>	1.7 MA/cm <sup>2</sup>	///	10 ns	///
Forrest 1997 [90]	Alq3:DCM	Fabry-Perot Stripe	[0.2nm]	1.0 $\mu$ J/cm <sup>2</sup>	434A/cm <sup>2</sup>	645	0.5 ns	337
Forrest 1998 [91]	Alq3:DCM	slab-waveguide	[0.2nm]	3.0 $\mu$ J/cm <sup>2</sup>	1 kA/cm <sup>2</sup>	615-660	0,5 ns	337
Forrest 1998 [91]	Alq3:DCM	VCSEL	[0.6nm]	300 $\mu$ J/cm <sup>2</sup>	130 kA/cm <sup>2</sup>	635	0,5 ns	337
Forrest 1998 [91]	Alq3:DCM2	slab-waveguide	[0.2nm]	2.5 $\mu$ J/cm <sup>2</sup>	1 kA/cm <sup>2</sup>	655-700	0,5 ns	337
Forrest 1998 [91]	Alq3:Rh6G	slab-waveguide	[0.2nm]	35 $\mu$ J/cm <sup>2</sup>	15 kA/cm <sup>2</sup>	610-625	0,5 ns	337
Forrest 1998 [91]	CBP: Coumarin47	slab-waveguide	[0.2nm]	15 $\mu$ J/cm <sup>2</sup>	7 kA/cm <sup>2</sup>	460	0,5 ns	337
Forrest 1998 [92]	Alq3:DCM	VECSEL	[0.2nm]	300 $\mu$ J/cm <sup>2</sup>	130 kA/cm <sup>2</sup>	635	0,5 ns	337
Granlund 1998 [94]	PDOPT	VECSEL	Q~163 [1.8nm]	120 nJ/cm <sup>2</sup>	82 A/cm <sup>2</sup>	655	100 fs	530
Forrest 1999 [95]	Alq3:DCM	Slab-waveguide	[0.2nm]	13 $\mu$ J/cm <sup>2</sup>	6 kA/cm <sup>2</sup>	640	0,5 ns	337
Riechel 2000 [114]	LPPP	1D and 2D DFB	Q~1960 [0.25nm]	10 $\mu$ J/cm <sup>2</sup> 200nJ/cm <sup>2</sup> / 1.5kW/cm <sup>2</sup>	5 kA/cm <sup>2</sup>	490	150fs	400
Kozlov 2000 [90]	Alq3:DCM or DCM2	DFB	Q~6444		87 A/cm <sup>2</sup>	644	1 ns	337
Samuel 2005 [99]	MEH-PPV	2D DFB	Q=850 [0.74nm]	136 $\mu$ J/cm <sup>2</sup>	93 kA/cm <sup>2</sup>	630	1 ns	532
Koschoreck 2005 [100]	Alq3:DCM	VCSEL	Q=4500	20 $\mu$ J/cm <sup>2</sup>	10 kA/cm <sup>2</sup>	624	200 fs	400
Pisignano 2005 [102]	Thiophene-based pentamer	Imprinted DFB	Q>637 [<1nm]	37 $\mu$ J/cm <sup>2</sup>	17 kA/cm <sup>2</sup>	580-660	3	355
Pisignano 2005 [101]	Oligothiophen	Imprinted DFB	Q~578 [1.1nm]	27 $\mu$ J/cm <sup>2</sup>	12 kA/cm <sup>2</sup>	636	3	355
Rose 2005 [103]	polymer	DFB	Q~67 [~8nm]	40nJ/cm <sup>2</sup>	17 A/cm <sup>2</sup>	535	4	337
Yamamoto 2006 [105]	PVCz:Coumarin6 Ps-Alq3:Coumarin6	Lloyd mirror tunable DFB	Q~2500	300 $\mu$ J/cm <sup>2</sup>	137 kA/cm <sup>2</sup>	516-546	30ps	355
Karnutsch 2006 [106]	Copolymer(BN-PFO)	1 <sup>st</sup> and 2 <sup>nd</sup> order DFB	Q~250 [~2nm]			447-460	10ns	390
Karnutsch 2007 [107]	polymer	Mixed order DFB	Q~250 [~2nm]	36nJ/cm <sup>2</sup>	18 A/cm <sup>2</sup>	452-460	10ns	390
Namdas 2009 [108]	SuperYellow	Imprinted 1 <sup>st</sup> and 2 <sup>nd</sup> order DFB	/	3.6 $\mu$ J/cm <sup>2</sup>	2 kA/cm <sup>2</sup>	582	100 fs	400
Hirade 2009 [109]	Spiro-SPCz	1 <sup>st</sup> -order DFB	[2.5nm]	720nJ/cm <sup>2</sup>	313 A/cm <sup>2</sup>	474	05.ns	337
Xia 2009 [110]	Pyrene-cored starbust	1D DFB	Q~15	156 $\mu$ J/cm <sup>2</sup>	76 kA/cm <sup>2</sup>	501	4.2ns	380
Deotare 2014 [111]	Alq3:DCM	Ph.C. Nanobeam	Q~4417 [0.14nm]	4.2 $\mu$ J/cm <sup>2</sup>	2 kA/cm <sup>2</sup>	618.5	100fs	400
Gourdon 2012 [112]	Alq3:DCJTb	Ph.C H2 microcavity	Q>165 [<4nm]	9.7 $\mu$ J/cm <sup>2</sup>	4 kA/cm <sup>2</sup>	662	12ns	355
Sandanayaka 2020 [114]	BsB-Cz	Mixed order DFB	Q unknown	NA	0.5kA/cm <sup>2</sup>	480nm	400ns	NA



## I.6. Conclusion

From the history of organic lasers, the electric pumping of organic gain media appears as an expected step in this long evolution that roots in the very beginning of the laser history with dye lasers, and with optically pumped solid-state organic lasers as an intermediate step.

The main historical challenge as it appears according to these reminders, is to excite electrically organic materials with large current density, whereas with pi- conjugation based intramolecular conductivity and with intermolecular hopping, there are known for their low mobility.

To complete this main challenge, according to the laser experiments conducted under optical pumping, the electrical excitation must be very intense of the order of 10 kA/cm<sup>2</sup> in the most favorable conditions.

The third challenge is then to create high-quality factor cavities essential for lowering electrical excitation densities to the lowest level obtain in this most favorable conditions.

The fourth challenge, deals with electrical excitation introducing specific mechanisms (which do not exist under optical pumping) such as the direct input of triplets (free from the ISC pathway) and as the annihilation of singlets under the effect of polarons. Understanding the impacts of these annihilation mechanisms requires further investigations.

In the view of these 4 challenges, choices are necessary at the electrical, optical and material level to progress toward the fabrication of organic laser diodes. Some of these choices are inspired by the bibliographic studies and previous research conducted in our group:

- Using Host:guest systems, we benefit from low optical absorption due to large Stoke shift.
- Host:guest systems can be incorporated into an organic heterostructure such as in OLEDs providing a very efficient way to inject current into a small molecule organic semiconductors.
- Under pulsed electrical excitation, current densities in the range of kA/cm<sup>2</sup> at the level of the laser threshold challenge can be achieved. With state of the art pulse durations, CPW electrodes offer an advantage in this area.
- Reducing OLED size down to the micrometric range induces a reduction of the electrical time constant allowing pulse generation at the nanosecond scale thus maximizing current densities. This unlock access to OLED dynamics at the fluorescence life time scale.
- DFB cavities appear as one of the best choice with quality factors up to the third challenge but also because of their compatibility with OLEDs. Among the most favorable conditions, Q factors above 5000 are desirable

## Reference

- [1] S. Schols, Device Architecture and Materials for Organic Light-Emitting Devices, Dordrecht : Springer Netherlands, 2011.
- [2] G. Stokes, On the change in Refrangibility of Light, *Philosophical Transactions of the Royal Society of London* **142** 463-562 (1852)
- [3] Valeur, and M. N. Berberan-Santos, Molecular Fluorescence: Principles and Applications, 2nd Ed. *Wiley-VCH* (2012)
- [4] J. R. Lacowicz, Introduction to Fluorescence, *Principles of Fluorescence Spectroscopy*, 3rd Ed. Springer US (2006) pp 3-6
- [5] B. Valeur, Introduction: On the Origin of the Terms Fluorescence, Phosphorescence, and Luminescence, In *New Trends in Fluorescence Spectroscopy: Applications to Chemical and Life Sciences*; B. Valeur, J. -C. Brochon, Eds.; Springer Series on Fluorescence Methods and Applications; Springer Verlag (2001) pp 3-6
- [6] P. Le Barny, "Électroluminescence des matériaux organiques. Principes de base", *Technique de l'Ingénieur*, N406, 2006.
- [7] W. Brütting, S. Berleb, et A. G. Mückl, « Device physics of organic light-emitting diodes based on molecular materials », *Organic electronics*, vol. 2, n° 1, pp. 1–36, 2001.
- [8] D.M. Pai. *J. Chem. Phys.* 52, p. 2285, 1970.
- [9] De Nevill Francis Mott, Edward A Davis, “*Electronic Processes in Non-Crystalline Materials*”, Dover Publication (2<sup>nd</sup> edition), 1964
- [10] A. Rose, *Physical Review* 97, 1538, 1955
- [11] P. E. Burrows and S. R. Forrest, “*Electroluminescence from trap-limited current transport in vacuum deposited organic light emitting devices*”, *Appl. Phys. Lett.* 64, 2285 (1994)
- [12] Hidetoshi Yamamoto, Hiroki Kasajima, Wataru Yokoyama, Hiroyuki Sasabe, and Chihaya Adachi, “*Extremely-high-density carrier injection and transport over 12000A/cm<sup>2</sup> into organic thin films*”, *Appl. Phys. Lett.* 86, 083502 (2005); <https://doi.org/10.1063/1.1866230>
- [13] Yifan Zhang, “*Excited State Interactions and Management in Organic light Emitting Diodes*”, Thesis of University of Michigan, March 7, 2014, <https://deepblue.lib.umich.edu/handle/2027.42/107267>
- [14] M.A. Lampert, “*Simplified Theory of Space-Charge-Limited Currents in an Insulator with Traps*”, *Phys. Rev.* 103, 1648, 1956, DOI:<https://doi.org/10.1103/PhysRev.103.1648>
- [15] M. Pope and C.E. Swenberg “*Electronic Processes in Organic Crystals and Polymers*”, 1999 Oxford university press
- [16] J. Kalinowski, “*Organic light-emitting diodes: Principles, characteristics, and processes*”, New York: Marcel Dekker, 2005.
- [17] Oleksandr Mikhnenko, Paul W.M. Blom, “*Exciton Diffusion in Organic Semiconductors*”, *Energy & Environmental Science* 8(7), May 2015, DOI:[10.1039/C5EE00925A](https://doi.org/10.1039/C5EE00925A)
- [18] M.V. der Auweraer, *Photophysics and photochemistry of molecular materials*, B-KULG0I12A
- [19] T. H. Förster, "Transfer mechanisms of electronic excitation", *Discuss. Faraday Soc.*, 27, pp. 7-17, 1959.
- [20] Selvin, P. R. ; Hearst, J. E. *Proc. Natl. Acad. Sci. U.S.A.*, 91, pp. 10024-10028, 1994.

## References

- [21] D. L. Dexter, "A theory of sensitized luminescence in solids", *Chem. Phys.*, vol. 21, n° 5, pp. 836-850, 1953.
- [22] S. Tokito and I. Tanaka, "Phosphorescent Organic Light-emitting Devices: Triplet Energy Management," *Electrochemistry*, vol. 76, no. 1, pp. 24–31, 2008, [10.5796/electrochemistry.76.24](https://doi.org/10.5796/electrochemistry.76.24).
- [23] Mikhail Y. Berezin and Samuel Achilefu, "Fluorescence Lifetime Measurements and Biological Imaging", *Chem Rev.* 2010 May 12; 110(5): 2641–2684. doi:[10.1021/cr900343z](https://doi.org/10.1021/cr900343z)
- [24] D. Kasemann, R. Brückner, H. Fröb, and K. Leo, Organic light-emitting diodes under high currents explored by transient electroluminescence on the nanosecond scale, *Phys. Rev B* 84, 115208 (2011), DOI: [10.1103/PhysRevB.84.115208](https://doi.org/10.1103/PhysRevB.84.115208)
- [25] M. Pope, H. P. Kallmann, and P. Magnante, *The Journal of Chemical Physics* 38, 2042 (1963).
- [26] C. Gartner et al., *J. Appl. Phys.* 101, 023107 (2007).
- [27] M. A. Baldo, R. J. Holmes, and S. R. Forrest, *Phys. Rev. B* 66, 035321 (2002).
- [28] M. A. Baldo, C. Adachi, and S. R. Forrest, *Phys. Rev. B* 62, 10967 (2000).
- [29] S. Reineke, K. Walzer, and K. Leo, *Phys. Rev. B* 75, 125328 (2007).
- [30] Y. Zhang et al., *Chem. Phys. Lett.* 495, 161 (2010).
- [31] N. C. Giebink, and S. R. Forrest, *Phys. Rev. B* 79, 073302 (2009).
- [32] R. G. Kepler et al., *Phys. Rev. Lett.* 10, 400 (1963).
- [33] D. Braun, D. Moses, C. Zhang, and A. J. Heeger, "Nanosecond transient electroluminescence from polymer light-emitting diodes," *Appl. Phys. Lett.*, vol. 61, no. 26, pp. 3092–3094, Dec. 1992, doi: [10.1063/1.107971](https://doi.org/10.1063/1.107971).
- [34] V. G. Kozlov *et al.*, "Structures for organic diode lasers and optical properties of organic semiconductors under intense optical and electrical excitations," *Quantum Electronics, IEEE Journal of*, vol. 36, no. 1, pp. 18–26, 2000.
- [35] N. C. Giebink and S. R. Forrest, "Temporal response of optically pumped organic semiconductor lasers and its implication for reaching threshold under electrical excitation," *Phys. Rev. B*, vol. 79, no. 7, p. 073302, Feb. 2009, doi: [10.1103/PhysRevB.79.073302](https://doi.org/10.1103/PhysRevB.79.073302).
- [36] J. Wang, R. G. Sun, G. Yu, and A. J. Heeger, "Fast pulsed electroluminescence from polymer light-emitting diodes," *Journal of Applied Physics*, vol. 91, no. 4, pp. 2417–2422, Feb. 2002, doi: [10.1063/1.1434545](https://doi.org/10.1063/1.1434545).
- [37] H. Nakanotani, T. Oyamada, Y. Kawamura, H. Sasabe, and C. Adachi, "Injection and Transport of High Current Density over 1000A/cm<sup>2</sup> in Organic Light Emitting Diodes under Pulse Excitation," *Japanese Journal of Applied Physics*, vol. 44, no. 6A, pp. 3659–3662, 2005, doi: [10.1143/JJAP.44.3659](https://doi.org/10.1143/JJAP.44.3659).
- [38] L. Zeng *et al.*, "Electrical and Optical Impulse Response of High-Speed Micro-OLEDs Under UltraShort Pulse Excitation," *IEEE Trans. Electron Devices*, vol. 64, no. 7, pp. 2942–2948, Jul. 2017, doi: [10.1109/TED.2017.2706723](https://doi.org/10.1109/TED.2017.2706723).
- [39] A. C. Chime, S. Bensmida, M. Chakaroun, M. W. Lee, H. Nkwawo, and A. P. A. Fischer, "Electrical modelling and design of ultra-fast micro-OLED with coplanar wave-guided electrodes in ON-OFF regime," *Organic Electronics*, vol. 56, pp. 284–290, May 2018, doi: [10.1016/j.orgel.2017.12.026](https://doi.org/10.1016/j.orgel.2017.12.026).
- [40] A. C. Chime, A. P. A. Fischer, S. Bensmida, J. Solard, M. Chakaroun, and H. Nkwawo, "Analysis of Optical and Electrical Responses of  $\mu$ -OLED With Metallized ITO Coplanar

## References

- Waveguide Electrodes Submitted to Nanosecond Electrical Pulses,” *IEEE Trans. Electron Devices*, vol. 66, no. 5, pp. 2282–2289, May 2019, doi: [10.1109/TED.2019.2905839](https://doi.org/10.1109/TED.2019.2905839).
- [41] CHIME Alex Chamberlain, “Etude théorique et expérimentale de micro-OLEDs rapides sur électrodes coplanaires en régime d’impulsions à haute densité de courant”, Thesis of Université Paris 13, Decembre 2017
- [42] C. Pinot et al., “Electrical modeling and numerical simulation of doped multilayer organic light-emitting diodes (OLEDs),” in *SID Symp. Dig. Tech. Papers*, vol. 38, n° 1, pp. 792–795, may 2007.
- [43] R. L. Lin, J.-Y. Tsai, D. Buso, and G. Zissis, “OLED equivalent circuit model with temperature coefficient and intrinsic capacitor,” in *Proc. IEEE Ind. Appl. Soc. Annu. Meeting*, pp. 1–8, 2014.
- [44] J. P. Bender, “SPICE modeling of ACTFEL devices and OLEDs,” M.S. thesis, Dept. Electr. Comput. Eng., Oregon State Univ., Corvallis, OR, USA, 2000.
- [45] J. H. Ahn et al., “Equivalent-circuit analysis of organic light emitting diodes by using the frequencydependent response of an ITO/Alq3/Al device,” *J. Korean Phys. Soc.*, vol. 46, n° 2, pp. 546–550, 2005.
- [46] J. Drechsel, M. Pfeiffer, X. Zhou, A. Nollau, and K. Leo, “Organic Mip-diodes by p-doping of amorphous wide-gap semiconductors: CV and impedance spectroscopy,” *Synth. Met.*, vol. 127, n° 1–3, pp. 201–205, 2002.
- [47] S. Nowy, W. Ren, A. Elschner, W. Lövenich, and W. Brütting, “Impedance spectroscopy as a probe for the degradation of organic lightemitting diodes,” *J. Appl. Phys.*, vol. 107, n° 5, pp. 054501-1–054501-9, 2010.
- [48] H. Park, H. Kim, S. K. Dhungel, J. Yi, S. Y. Sohn, and D. G. Jung, “Impedance spectroscopy analysis of organic light-emitting diodes fabricated on plasma-treated indium-tin-oxide surfaces,” *J. Korean Phys. Soc.*, vol. 51, n° 3, pp. 1011–1015, 2007.
- [49] Beat Ruhstaller, Tilman Beierlein, Heike Riel, Siegfried Karg, J. Campbell Scott, and Walter Riess, “Simulating Electronic and Optical Processes in Multilayer Organic Light-Emitting Devices”, *IEEE JOURNAL OF SELECTED TOPICS IN QUANTUM ELECTRONICS*, VOL. 9, NO. 3, MAY/JUNE 2003 723
- [50] Iannacci, Jacopo, “RF-MEMS Technology for High-Performance Passives The challenge of 5G mobile applications”, 2017, DOI: [10.1088/978-0-7503-1545-6](https://doi.org/10.1088/978-0-7503-1545-6)
- [51] C. P. Wen, Coplanar waveguide: A surface strip transmission line suitable for nonreciprocal gyromagnetic device applications, *IEEE Transactions on Microwave Theory and Techniques*, vol. 17, no. 12, pp. 1087–1090, 1969
- [52] Einstein, A. *Phy. Z.* 18, 121, 1917
- [53] Shaklee K.L., Nahory R.E., Leheny R.F., “Optical gain in semiconductors” *J. Lumin.*, 7, p. 284-309 (1973).
- [54] Iryna Gozhyk, “Polarization and gain phenomena in dye-doped polymer micro-lasers”, Thesis from Ecole normale superieures de Cachan, 2012
- [55] C. Gaertner, “Organic Laser Diodes: Modelling and Simulation”, Thesis Universitaet Karlsruhe (D), 2008
- [56] G. M. Akselrod, E. R. Young, K. W. Stone, A. Palatnik, V. Bulović, and Y. R. Tischler, “Reduced lasing threshold from organic dye microcavities,” *Phys. Rev. B*, vol. 90, no. 3, p. 035209, Jul. 2014, doi:

## References

- [57] P. B. Deotare, T. S. Mahony, and V. Bulović, "Ultracompact Low-Threshold Organic Laser," *ACS Nano*, vol. 8, no. 11, pp. 11080–11085, Nov. 2014, doi: [10.1021/nn504444g](https://doi.org/10.1021/nn504444g).
- [58] M Cehovski, S Döring, T. Rabea, R. Caspary, W Kowalsky, "Combined optical gain and degradation measurements in DCM2 doped Tris-(8-hydroxyquinoline)aluminum thin-films", SPIE Proceedings [SPIE SPIE Photonics Europe - Brussels, Belgium (Sunday 3 April 2016)] Organic Photonics VII - 9895(), 989508–. doi:10.1117/12.2227688
- [59] G. Barbillon, F. Gourdon, E. Cambriil, N. Fabre, A. M. Yacomotti, and S. Bouchoule, "SiNx/organic photonic crystal microcavity optimization for the fabrication of thin-film micro-laser," *Optics Communications*, vol. 325, pp. 15–22, Aug. 2014, doi: [10.1016/j.optcom.2014.03.067](https://doi.org/10.1016/j.optcom.2014.03.067).
- [60] Sandanayaka, A.S.D.; Matsushima, T.; Bencheikh, F.; Terakawa, S.; Potscavage, W.J., Jr.; Qin, C.; Fujihara, T.; Goushi, K.; Ribierre, J.-C.; Adachi, C. Indication of current-injection lasing from an organic semiconductor. *Appl. Phys. Express* 2019, 12, 061010, [doi:10.7567/1882-0786/ab1b90](https://doi.org/10.7567/1882-0786/ab1b90)
- [61] Wenqi Zhu et al., *Sci Adv* 2017; 3:e1700909
- [62] Kane Miller, Mingxiao Li<sup>1</sup>, Kevin M Walsh and Xiao-An Fu, "The effects of DRIE operational parameters on vertically aligned micropillar arrays", *J. Micromech. Microeng.* 23 (2013) doi:[10.1088/0960-1317/23/3/035039](https://doi.org/10.1088/0960-1317/23/3/035039)
- [63] Edward. F. Plinski\*, Dorota A. Wojaczek, Jerzy S. Witkowski, Pawel R. Kaczmarek, Piotr Kulczycki, Igor Tazbir, Andrzej B. Dobrucki, and Krzysztof M. Abramski, "Acoustics Processes in an RF excited CO<sub>2</sub> Waveguide Laser Pulsed Plasma", ICA 2004
- [64] Li, Qz., Huang, Yq., Ning, Jq. et al. InAs/GaAs Quantum Dot Dual-Mode Distributed Feedback Laser Towards Large Tuning Range Continuous-Wave Terahertz Application. *Nanoscale Res Lett* 13, 267 (2018), DOI: [10.1186/s11671-018-2674-3](https://doi.org/10.1186/s11671-018-2674-3)
- [65] Marina Radulaski, Thomas M. Babiniec, Sonia Buckley, Armand Rundquist, J Provine, Kassem Alassaad, Gabriel Ferro, and Jelena Vučković, "Photonic crystal cavities in cubic (3C) polytype silicon carbide films," *Opt. Express* 21, 32623-32629 (2013)
- [66] Anthony Coens, "Diode électroluminescente organique en microcavité verticale à miroirs diélectrique multicouche", Thesis from the Université Paris 13, 2013
- [67] Lei ZENG, "Étude théorique et expérimentale de  $\mu$ -OLED en régime impulsionnel à très haute densité de courant", Thesis from the Université Paris 13, 2016
- [68] Kawano, Kenji; Kitoh, Tsutomu, "Introduction to Optical Waveguide Analysis", John Wiley & Sons, Inc., 2001 July 01, DOI: [10.1002/0471221600](https://doi.org/10.1002/0471221600)
- [69] Frank Sobel, "Effet laser à contre réaction répartie (DFB) excité par voie optique dans les films minces polymères", Thesis from the Université d'Angers, 2001
- [70] Furman Sh.A., Tikhonravov A.V., "Basics of Optics of multilayer systems", Ed. Frontière, 1992, 137621540
- [71] J. Ultee, "Chemical Lasers and Their Applications", Volume 59 Numbers 6, June 1982, DOI: [10.1021/ed059p462](https://doi.org/10.1021/ed059p462)
- [72] Joseph T.Verdeyen, Thomas A.DeTemple, "Lasers", Reference Data for Engineers (Ninth Edition), Radio, Electronics, Computer, and Communications, Pages 41-1-41-20, 2002, [10.1016/B978-075067291-7/50043-1](https://doi.org/10.1016/B978-075067291-7/50043-1)

## References

- [73] G. F. Barlow et K. A. Shore, « Threshold current analysis of distributed feed-back organic semiconductor lasers », *IEE Proceedings - Optoelectronics*, vol. 148, n° 1, pp. 2–6, feb. 2001.
- [74] P. P. Sorokin and J. R. Lankard, “Stimulated Emission Observed from an Organic Dye, Chloro-aluminum Phthalocyanine,” *IBM J. Res. & Dev.*, vol. 10, no. 2, pp. 162–163, Mar. 1966, doi: [10.1147/rd.102.0162](https://doi.org/10.1147/rd.102.0162).
- [75] F. P. Schäfer, W. Schmidt, and J. Volze, “ORGANIC DYE SOLUTION LASER,” *Appl. Phys. Lett.*, vol. 9, no. 8, pp. 306–309, Oct. 1966, doi: [10.1063/1.1754762](https://doi.org/10.1063/1.1754762).
- [76] B. H. Soffer and B. B. McFarland, “CONTINUOUSLY TUNABLE, NARROW-BAND ORGANIC DYE LASERS,” *Applied physics letters*, vol. 10, p. 266, 1967.
- [77] F. P. Schäfer, “Organic Dyes in Laser Technology,” *Angewandte Chemie International Edition in English*, vol. 9, no. 1, pp. 9–25, 1970, doi: [10.1002/anie.197000091](https://doi.org/10.1002/anie.197000091).
- [78] O. G. Peterson and B. B. Snavely, “Stimulated emission from flashlamp-excited organic dyes in polymethyl methacrylate,” *Appl. Phys. Lett.*, vol. 12, no. 7, pp. 238–240, Apr. 1968, doi: [10.1063/1.1651972](https://doi.org/10.1063/1.1651972).
- [79] P. P. Sorokin, J. R. Lankard, V. L. Moruzzi, and E. C. Hammond, “Flashlamp-Pumped Organic-Dye Lasers,” *J. Chem. Phys.*, vol. 48, no. 10, pp. 4726–4741, May 1968, doi: [10.1063/1.1668055](https://doi.org/10.1063/1.1668055).
- [80] B. B. Snavely, “Flashlamp-excited organic dye lasers,” *Proceedings of the IEEE*, vol. 57, no. 8, pp. 1374–1390, Aug. 1969, doi: [10.1109/PROC.1969.7276](https://doi.org/10.1109/PROC.1969.7276).
- [81] F. P. Schäfer, “Organic Dyes in Laser Technology,” *Angewandte Chemie International Edition in English*, vol. 9, no. 1, pp. 9–25, 1970, doi: [10.1002/anie.197000091](https://doi.org/10.1002/anie.197000091).
- [82] B. I. Stepanov and A. N. Rubinov, “LASERS BASED ON SOLUTIONS OF ORGANIC DYES,” p. 17, *Sov. Phys. Usp.* 11 304 1968. DOI: [10.1070/PU1968V011N03ABEH003835](https://doi.org/10.1070/PU1968V011N03ABEH003835)
- [83] O. G. Peterson, S. A. Tuccio, and B. B. Snavely, “cw OPERATION OF AN ORGANIC DYE SOLUTION LASER,” *Appl. Phys. Lett.*, vol. 17, no. 6, pp. 245–247, Sep. 1970, doi: [10.1063/1.1653384](https://doi.org/10.1063/1.1653384).
- [84] H. Kogelnik and C. V. Shank, “STIMULATED EMISSION IN A PERIODIC STRUCTURE,” *Applied Physics Letters*, vol. 18, no. 4, p. 152, Feb. 1971, doi: [doi:10.1063/1.1653605](https://doi.org/10.1063/1.1653605).
- [85] I. P. Kaminow, H. P. Weber, and E. A. Chandross, “POLY(METHYL METHACRYLATE) DYE LASER WITH INTERNAL DIFFRACTION GRATING RESONATOR,” *Appl. Phys. Lett.*, vol. 18, no. 11, pp. 497–499, Jun. 1971, doi: [10.1063/1.1653511](https://doi.org/10.1063/1.1653511).
- [86] M. Dyumaev, A. A. Manenkov, A. P. Maslyukov, G. A. Matyushin, V. S. Nechitaïlo, and A. M. Prokhorov, “Transparent polymers: a new class of optical materials for lasers,” *Sov. J. Quantum Electron.*, vol. 13, no. 4, p. 503, Apr. 1983, doi: [10.1070/QE1983v013n04ABEH004204](https://doi.org/10.1070/QE1983v013n04ABEH004204).
- [87] M. D. Rahn and T. A. King, “Comparison of laser performance of dye molecules in sol-gel, polycom, ormosil, and poly(methyl methacrylate) host media,” *Appl Opt*, vol. 34, no. 36, pp. 8260–8271, Dec. 1995, doi: [10.1364/AO.34.008260](https://doi.org/10.1364/AO.34.008260).
- [88] J. C. Altman, R. J. Stone, F. Nishida, and B. S. Dunn, “Dye-activated ORMOSILS for lasers and optical amplifiers,” in *Sol-Gel Optics II*, Dec. 1992, vol. 1758, pp. 507–518. doi: [10.1117/12.132043](https://doi.org/10.1117/12.132043).
- [89] A. Maslyukov, S. Sokolov, M. Kaivola, K. Nyholm, and S. Popov, “Solid-state dye laser with modified poly (methyl methacrylate)-doped active elements,” *Applied optics*, vol. 34, no. 9, pp. 1516–1518, 1995.



## References

- [90] V. G. Kozlov, V. Bulović, P. E. Burrows, and S. R. Forrest, “Laser action in organic semiconductor waveguide and double-heterostructure devices,” *Nature*, vol. 389, no. 6649, pp. 362–364, Sep. 1997, doi: [10.1038/38693](https://doi.org/10.1038/38693).
- [91] V. G. Kozlov et al., “Study of lasing action based on Förster energy transfer in optically pumped organic semiconductor thin films,” *Journal of Applied Physics*, vol. 84, no. 8, pp. 4096–4108, Oct. 1998, doi: [doi:10.1063/1.368624](https://doi.org/10.1063/1.368624).
- [92] V. Bulović, V. G. Kozlov, V. B. Khalfin, and S. R. Forrest, “Transform-Limited, Narrow-Linewidth Lasing Action in Organic Semiconductor Microcavities,” *Science*, vol. 279, no. 5350, pp. 553–555, Jan. 1998, doi: [10.1126/science.279.5350.553](https://doi.org/10.1126/science.279.5350.553).
- [93] M. Berggren, A. Dodabalapur, R. E. Slusher, and Z. Bao, “Light amplification in organic thin films using cascade energy transfer,” *Nature*, vol. 389, no. 6650, Art. no. 6650, Oct. 1997, doi: [10.1038/38979](https://doi.org/10.1038/38979).
- [94] T. Granlund et al., “A polythiophene microcavity laser,” *Chemical Physics Letters*, vol. 288, no. 5–6, pp. 879–884, May 1998, doi: [10.1016/S0009-2614\(98\)00320-0](https://doi.org/10.1016/S0009-2614(98)00320-0).
- [95] V. G. Kozlov and S. R. Forrest, “Lasing action in organic semiconductor thin films,” *Current Opinion in Solid State and Materials Science*, vol. 4, no. 2, pp. 203–208, 1999.
- [96] V. G. Kozlov et al., “Study of lasing action based on Förster energy transfer in optically pumped organic semiconductor thin films,” *Journal of Applied Physics*, vol. 84, no. 8, pp. 4096–4108, Oct. 1998, doi: [doi:10.1063/1.368624](https://doi.org/10.1063/1.368624).
- [97] M. Meier et al., “Laser action from two-dimensional distributed feedback in photonic crystals,” *Applied Physics Letters*, vol. 74, no. 1, pp. 7–9, Jan. 1999, doi: [doi:10.1063/1.123116](https://doi.org/10.1063/1.123116).
- [98] S. Riechel et al., “A nearly diffraction limited surface emitting conjugated polymer laser utilizing a two-dimensional photonic band structure,” *Applied Physics Letters*, vol. 77, no. 15, pp. 2310–2312, Oct. 2000, doi: [doi:10.1063/1.1310207](https://doi.org/10.1063/1.1310207).
- [99] A. E. Vasdekis, G. A. Turnbull, I. D. W. Samuel, P. Andrew, and W. L. Barnes, “Low threshold edge emitting polymer distributed feedback laser based on a square lattice,” *Applied Physics Letters*, vol. 86, no. 16, p. 161102, 2005, doi: [10.1063/1.1898430](https://doi.org/10.1063/1.1898430).
- [100] M. Koschorreck, R. Gehlhaar, V. G. Lyssenko, M. Swoboda, M. Hoffmann, and K. Leo, “Dynamics of a high-Q vertical-cavity organic laser,” *Applied Physics Letters*, vol. 87, no. 18, pp. 181108–181108–3, Oct. 2005, doi: [doi:10.1063/1.2125128](https://doi.org/10.1063/1.2125128).
- [101] D. Pisignano et al., “First-order imprinted organic distributed feedback lasers,” *Synthetic Metals*, vol. 153, no. 1, pp. 237–240, Sep. 2005, doi: [10.1016/j.synthmet.2005.07.273](https://doi.org/10.1016/j.synthmet.2005.07.273).
- [102] D. Pisignano et al., “Emission properties of printed organic semiconductor lasers,” *Opt. Lett.*, vol. 30, no. 3, pp. 260–262, Feb. 2005, doi: [10.1364/OL.30.000260](https://doi.org/10.1364/OL.30.000260).
- [103] A. Rose, Z. Zhu, C. F. Madigan, T. M. Swager, and V. Bulović, “Sensitivity gains in chemosensing by lasing action in organic polymers,” *Nature*, vol. 434, no. 7035, Art. no. 7035, Apr. 2005, doi: [10.1038/nature03438](https://doi.org/10.1038/nature03438).
- [104] N. Tsutsumi and M. Yamamoto, “Threshold reduction of a tunable organic laser using effective energy transfer,” *J. Opt. Soc. Am. B*, vol. 23, no. 5, pp. 842–845, May 2006, doi: [10.1364/JOSAB.23.000842](https://doi.org/10.1364/JOSAB.23.000842).
- [105] N. Tsutsumi, A. Fujihara, and D. Hayashi, “Tunable distributed feedback lasing with a threshold in the nanojoule range in an organic guest-host polymeric waveguide,” *Appl. Opt.*, vol. 45, no. 22, pp. 5748–5751, Aug. 2006, doi: [10.1364/AO.45.005748](https://doi.org/10.1364/AO.45.005748).

## Reference

- [106] C. Karnutsch et al., “Low threshold blue conjugated polymer lasers with first- and second-order distributed feedback,” *Applied Physics Letters*, vol. 89, no. 20, p. 201108, Nov. 2006, doi: [doi:10.1063/1.2390644](https://doi.org/10.1063/1.2390644).
- [107] C. Karnutsch *et al.*, “Improved organic semiconductor lasers based on a mixed-order distributed feedback resonator design,” *Applied Physics Letters*, vol. 90, no. 13, pp. 131104–131104–3, Mar. 2007, doi: [doi:10.1063/1.2717518](https://doi.org/10.1063/1.2717518).
- [108] E. B. Namdas et al., “Low Thresholds in Polymer Lasers on Conductive Substrates by Distributed Feedback Nanoimprinting: Progress Toward Electrically Pumped Plastic Lasers,” *Advanced Materials*, vol. 21, no. 7, pp. 799–802, Feb. 2009, doi: [10.1002/adma.200802436](https://doi.org/10.1002/adma.200802436).
- [109] M. Hirade, H. Nakanotani, R. Hattori, A. Ikeda, M. Yahiro, and C. Adachi, “Low-Threshold Blue Emission from First-Order Organic DFB Laser Using 2,7-bis[4-(N-carbazole)phenylvinyl]-9,9'-Spirobifluorene as Active Gain Medium,” 2009, doi: [10.1080/15421400902938928](https://doi.org/10.1080/15421400902938928).
- [110] R. Xia, W.-Y. Lai, P. A. Levermore, W. Huang, and D. D. C. Bradley, “Low-Threshold Distributed-Feedback Lasers Based on Pyrene-Cored Starburst Molecules with 1,3,6,8-Attached Oligo(9,9-Dialkylfluorene) Arms,” *Adv. Funct. Mater.*, vol. 19, no. 17, pp. 2844–2850, Sep. 2009, doi: [10.1002/adfm.200900503](https://doi.org/10.1002/adfm.200900503).
- [111] P. B. Deotare, T. S. Mahony, and V. Bulović, “Ultracompact Low-Threshold Organic Laser,” *ACS Nano*, vol. 8, no. 11, pp. 11080–11085, Nov. 2014, doi: [10.1021/nn504444g](https://doi.org/10.1021/nn504444g).
- [112] F. Gourdon *et al.*, “Optically pumped lasing from organic two-dimensional planar photonic crystal microcavity,” *Applied Physics Letters*, vol. 100, no. 21, pp. 213304–213304–4, May 2012, doi: [doi:10.1063/1.4720178](https://doi.org/10.1063/1.4720178).
- [113] G. Barbillon, F. Gourdon, E. Cambril, N. Fabre, A. M. Yacomotti, and S. Bouchoule, “SiNx/organic photonic crystal microcavity optimization for the fabrication of thin-film micro-laser,” *Optics Communications*, vol. 325, pp. 15–22, Aug. 2014, doi: [10.1016/j.optcom.2014.03.067](https://doi.org/10.1016/j.optcom.2014.03.067).
- [114] A. S. D. Sandanayaka *et al.*, “Indication of current-injection lasing from an organic semiconductor,” *Appl. Phys. Express*, vol. 12, no. 6, p. 061010, Jun. 2019, doi: [10.7567/1882-0786/ab1b90](https://doi.org/10.7567/1882-0786/ab1b90).
- [115] C. Murawski, K. Leo, and M. C. Gather, *Adv. Mater.* 25, 6801 (2013), DOI: [10.1002/adma.201301603](https://doi.org/10.1002/adma.201301603)
- [116] K. Hayashi, H. Nakanotani, M. Inoue, K. Yoshida, O. Mikhnenko, T.-Q. Nguyen and C. Adachi, “Suppression of roll-off characteristics of organic light-emitting diodes by narrowing current injection/transport area to 50 nm”, *Appl. Phys. Lett.* 106, 093301 (2015); DOI: [10.1063/1.4913461](https://doi.org/10.1063/1.4913461)





# **Chapter II- Model, Design and Simulation**



## II. Model, Design and Simulation

In the previous chapter, we identify several challenges to be solved in order to reach stimulated emission in organic gain media under electrical excitation. These challenges can be faced if the following scientific paths are followed

- At the electrical level: Current-density in organic gain media large enough to reach laser threshold can be achieved under ultra-short pulsed electrical excitation. One has to identify the conditions under which these ultra-short electrical pulses can be generated in OLEDs.
- At the optical level: Distributed FeedBack - type cavity offers among the highest quality factor and still allows good current injection. As such, it appears to be the most suitable type. Under proper conditions on the geometry of the DFB structures, its wavelength selective profile can be adapted to match the material properties of the organic laser gain media.

### II.1. Introduction

This chapter aims to identify the above mentioned scientific path to reach the laser emission under electrical pumping. More precisely, the objectives are to quantify the above mentioned conditions, when it is possible, and translate them into design rules.

For the sake of simplicity, we split the design of the devices into three parts; namely the electrical level, the physical and material level, finally the optical level.

In section 2, we will consider the electrical level aiming the design of high-speed electrodes and organic devices to achieve ultra-short electrical responses and maximize the current density. In particular, we would like to extend Chime's work [1] to current density above  $6\text{kA/cm}^2$ .

We will then consider the physical level and investigate which material properties play a role in the stimulated emission process and how they affect the laser threshold. This requires to develop a laser theory for the organic laser diode which will be presented in section 3.

In section 4, we will consider the optical level, to build the design guidelines and to fabricate optical distributed Feedback cavities matching the material properties and with very high quality factors.

Finally, we will synthesize all the identified guidelines in the conclusion of this chapter.

## II.2. Electrical modeling

The goal of the electrical modeling is to understand and describe the OLED electrical dynamical behavior. It has been the subject of several recent studies [2,3,4,5,6,7,8,9]. Among these studies Chime et al. presented an electrical model for a fast-OLED used to demonstrate optical pulsed responses to electrical pulse excitation with duration down to 2.5 ns [10]. This model identified the important parameters to reduce the time constant as the serial resistance  $R_s$  allowing the optimize of the device geometry. However, the dynamical resistance  $R_d$  appears as a key parameter at the same level than the serial resistances. It is very difficult to estimate this parameter which limit the performance of this model and recommend us to find another electric model. With the help of this new or upgraded electrical model we hope to deduce the conditions and the key parameters to fabricate OLEDs able to respond efficiently to shorter electrical pulses with duration in the picosecond and nano-second range with increased current density up to several tens of kA/cm<sup>2</sup>. Finally we will determine the best geometry of the device circuitry to allow the excitation and measurements compatible with the high frequencies range involved in such ultra-short pulses.

### II.2.1. Improved equivalent electrical model

Here we present a new electrical model for ultra-fast OLEDs with three novelties: firstly, the impact of the measurement device is taken into account by adding the entry resistance of the oscilloscope together with its capacitance. Secondly the OLED barrier with its ideal diode-like behavior is replaced by a black box for which no restricting assumption is necessary. Thirdly, for the sake of completeness we introduce a shunt resistance to take into account potential current leaks.

Figure II.1 shows a typical OLED device with its anode connected to a pulse driver on the left side, and its cathode connected to an oscilloscope and its built-in measurement resistance across which the voltage is measured on the right and measurement side.

Figure II.2 presents a more detailed equivalent electrical circuit of the OLED:

- The serial resistances  $R_{s1}$  and  $R_{s2}$  are due to the electrode geometry and metal properties; The conduction in the bulk of the organic layers is implicit.
- The capacitance  $C$  results from the dielectric property of the organic layers sandwiched between electrodes and the energy barriers between the adjacent organic layers.
- A shunt resistor  $R_{shunt}$  that takes into account eventual leakage currents across the organic layer. This is the case when no hole blocking layer are included in the organic heterostructure resulting in hole current across. In an ideal OLED  $R_{shunt}$  is infinite assuming that no current leakage or a negligible one.
- The active part of the OLED that participates to the light emission is modeled with a black box. No restricting assumption is made on this active part as its characteristics are solely defined by the voltage  $V_d$  and the current  $I_d$  which are the unknown quantities to be solved.

Under the excitation voltage  $V_{exc}$ , the current  $I$  flowing through the OLED divides into  $I_s$  the leakage current flowing through  $R_{shunt}$ ,  $I_C$  the current flowing through the junction capacitance, and  $I_d$  the current through the active and useful part of the OLED participating to the light emission.

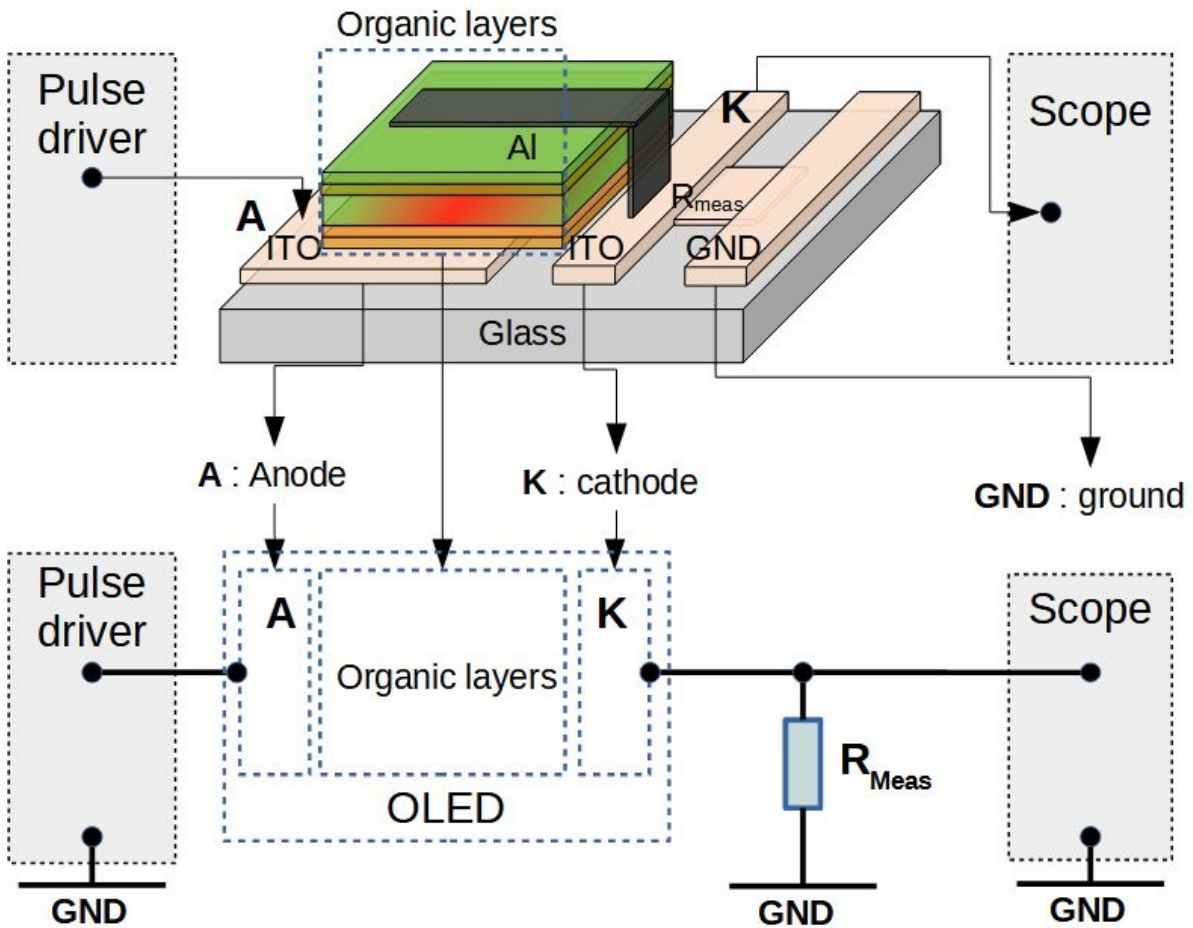


Figure II.1: The stack of the organic heterostructure is replaced by an equivalent electrical circuit with junction capacitance, and serial resistance

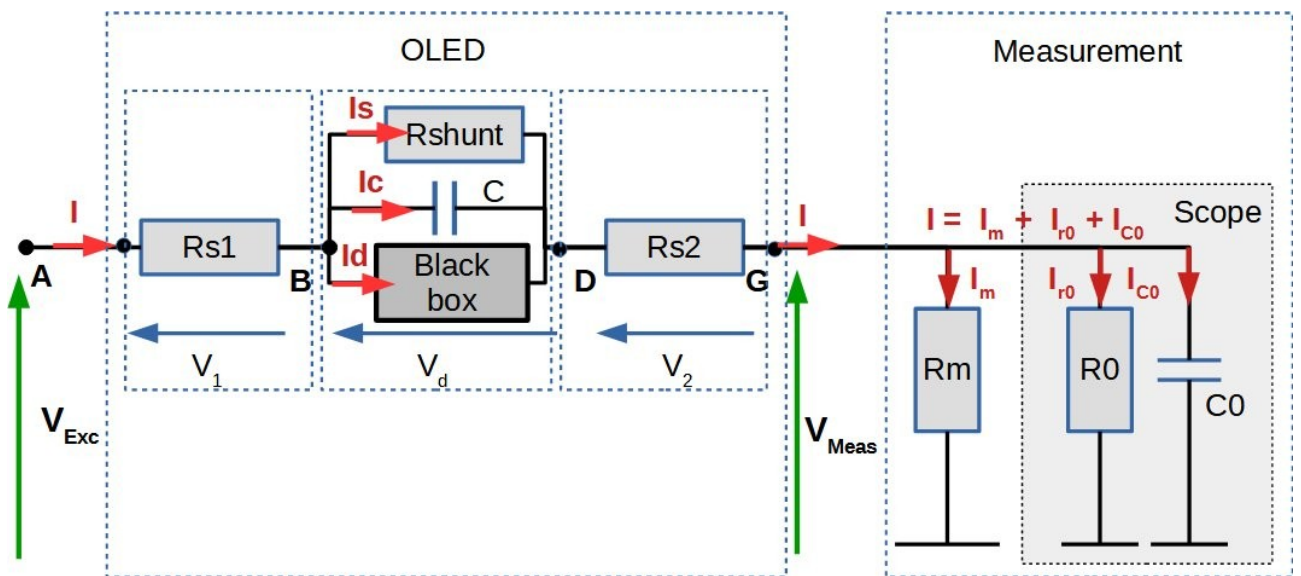


Figure II.2: Upgraded equivalent electrical model with the measurement tool taken into account

On the measurement side, a scope measures the voltage across the measurement resistance  $R_m$ .  $I_m$  and  $V_{meas}$  are respectively the current flowing through  $R_m$  and the voltage across it, while,  $I_{r0}$  and  $I_{C0}$  are the current in the resistance and capacitance of the scope respectively.

We apply Kirchhoff laws to the equivalent electrical circuit shown in Fig.II.2, on both the OLED side and the measurement side to solve the unknown quantities  $V_d$  and  $I_d$  while the known quantities are  $V_{exc}$  and  $V_{meas}$ .

$$I = I_d + I_c + I_s \quad \text{Eq. (II.1)} \quad \text{and} \quad I = I_m + I_{r0} + I_{C0} \quad \text{Eq. (II.2)}$$

$$I_s = \frac{V_d}{R_{shunt}} \quad \text{Eq. (II.3)} \quad \text{and} \quad I_m = \frac{V_{meas}}{R_m}, I_{r0} = \frac{V_{meas}}{R_0}, \text{Eq. (II.4), Eq. (II.5)}$$

$$I_c = \frac{dQ(t)}{dt} = C \frac{dV_d(t)}{dt} \quad \text{Eq. (II.6)} \quad \text{and} \quad I_{C0} = \frac{dQ_0(t)}{dt} = C_0 \frac{dV_{Meas}}{dt} \quad \text{Eq. (II.7)}$$

$$I = I_d + \frac{V_d}{R_{shunt}} + C \frac{dV_d(t)}{dt} \quad \text{Eq. (II.8)} \quad \text{and} \quad I = V_{meas} \left( \frac{1}{R_m} + \frac{1}{R_0} \right) + C_0 \frac{dV_{meas}(t)}{dt} \quad \text{Eq. (II.9)}$$

$$V_{Exc} = V_{Meas} + (R_{S1} + R_{S2})I + V_d \quad \text{Eq. (II.10)}$$

Using Eq.(2.2.8) and Eq.(II.9), the current flowing through  $R_d$  reads;

$$I_d = - \frac{V_d}{R_{shunt}} + V_{meas} \left( \frac{1}{R_m} + \frac{1}{R_0} \right) + C_0 \frac{dV_{meas}}{dt} - C \frac{dV_d(t)}{dt} \quad \text{Eq. (II.11)}$$

The voltage across the active layer is given by the following equation:

$$V_d = V_{Exc} - V_{Meas} - V_{Meas} (R_{S1} + R_{S2}) \left( \frac{1}{R_m} + \frac{1}{R_0} \right) - (R_{S1} + R_{S2}) C_0 \frac{dV_{meas}(t)}{dt} \quad \text{Eq. (II.12)}$$

On the bases of these equations,  $V_d$  and  $I_d$  are calculated from both measured quantities  $V_{meas}$  and  $V_{exc}$ , provided  $R_{shunt}$ ,  $R_m$ ,  $R_0$ ,  $C$ ,  $C_0$  are perfectly known.

The current which plays a major role in the light emission can thus be expressed as :

$$\begin{aligned} I_d = & -C \frac{dV_{Exc}(t)}{dt} - \frac{V_{Exc}}{R_{shunt}} \\ & + V_{meas} \left( \frac{1}{R_m} + \frac{1}{R_0} + \frac{1}{R_{shunt}} \left( 1 + (R_{S1} + R_{S2}) \left( \frac{1}{R_m} + \frac{1}{R_0} \right) \right) \right) \\ & + \frac{dV_{meas}(t)}{dt} \left[ C_0 \left( 1 + \frac{R_{S1} + R_{S2}}{R_{shunt}} \right) + C \left( 1 + (R_{S1} + R_{S2}) \left( \frac{1}{R_m} + \frac{1}{R_0} \right) \right) \right] \\ & + \frac{d^2 V_{meas}(t)}{dt^2} (R_{S1} + R_{S2}) C_0 C \end{aligned} \quad \text{Eq. (II.13)}$$

With

$$a = 1 + (R_{S1} + R_{S2}) \left( \frac{1}{R_m} + \frac{1}{R_0} \right) \quad \text{Eq. (II.14)} \quad \text{and} \quad b = \left( 1 + \frac{R_{S1} + R_{S2}}{R_{shunt}} \right) \quad \text{Eq. (II.15)} \quad \text{equation 13}$$

reads :

$$I_d = -C \frac{dV_{Exc}(t)}{dt} - \frac{V_{Exc}}{R_{shunt}} + V_{meas} \left( \frac{1}{R_m} + \frac{1}{R_0} + \frac{1}{R_{shunt}} a \right) + \frac{dV_{meas}(t)}{dt} [a C + b C_0] + \frac{d^2 V_{meas}(t)}{dt^2} (R_{S1} + R_{S2}) C_0 C \quad \text{Eq. (II.16)}$$

Eq.(II.16) is rewritten to let time constant appearing:

$$\frac{C}{(a C + b C_0)} \left( \frac{dV_{Exc}(t)}{dt} + \frac{V_{Exc}}{C R_{shunt}} \right) = - \frac{1}{(a C + b C_0)} I_d + \frac{d^2 V_{meas}(t)}{dt^2} \frac{(R_{S1} + R_{S2}) C_0 C}{(a C + b C_0)} + \frac{dV_{meas}(t)}{dt} + V_{meas} \frac{1}{\frac{1}{R_m} + \frac{1}{R_0} + \frac{1}{R_{shunt}} a} \quad \text{Eq. (II.17)}$$

From Eq.(II.17), different time constants appear;

$$\tau_1 = R_{shunt} (a C + b C_0) \quad \text{Eq. (II.18)}$$

$$\tau_2 = \frac{a C + b C_0}{\frac{1}{R_m} + \frac{1}{R_0} + \frac{1}{R_{shunt}} a} \quad \text{Eq. (II.19)}$$

under the assumptions that  $C_0$  is infinitely small and  $1/R_0 = 0$  it reads:

$$\tau_2' = \frac{C}{\frac{1}{(R_m + R_{S1} + R_{S2})} + \frac{1}{R_{shunt}}} \quad \text{Eq. (II.20)}$$

which is similar to the time constant calculated by Chime [11]

The time constant  $\tau_2$  reads as a function of the electrical model elements  $R_{S1}$ ,  $R_{S2}$ ,  $R_m$ ,  $R_{shunt}$  and  $C$  without  $R_d$ . The electrical time response of the device defined as the time required for  $I_d$  to approach its final value within 5% is simply

$$T_r \approx 3 \tau_2 \quad \text{Eq. (II.21)}$$

Since we intend to identify a path to minimize the time constant, one should consider the most relevant parameters: From equation II.19, the parameters to be taken into account are:

- The total serial resistance  $R_S = R_{S1} + R_{S2}$
- The OLED junction capacitance  $C$
- The shunt resistance  $R_{shunt}$
- The measurement resistance  $R_m$
- The oscilloscope input capacitance  $C_0$

The input resistance of the scope  $R_0$  is not relevant because it is fixed to  $50\Omega$  and cannot be varied.



## II.2.2. Numerical estimation of the time constant $\tau_2$

Figure II.3 with its four sub-figures present the  $\mu$ -OLED electrical time constant  $\tau_2$  for different values of the above mentioned 5 parameters  $R_s$ ,  $C$ ,  $R_{shunt}$ ,  $R_m$ ,  $C_0$ . To investigate the effect of every relevant parameters the plots are organized as follows: Four sub-plots corresponding to four different scenarios resulting from two values of  $C_0$  and two values of  $R_{shunt}$ :

- The oscilloscope capacitance takes two values:  $C_0 = 0.1\text{pF}$  and  $C_0 = 10\text{pF}$  which correspond to respectively very large ( $\sim 10\text{GHz}$ ) and a large ( $3\text{GHz}$ ) bandwidth of the scope,
- The leakage resistance  $R_{shunt}$  takes two values  $R_{shunt} = 1\text{k}\Omega$  and  $R_{shunt} = 1\text{M}\Omega$  corresponding respectively to the existence of a leakage current ( $10\text{mA}$  under  $10\text{V}$ ) and a micro leakage current barely measurable ( $1\mu\text{A}$  at  $10\text{V}$ ).

For each sub-figures, the time constant is plotted as a function of the measurement resistance  $R_m$  varying between  $R_m = 1\Omega$  and  $10\text{k}\Omega$  a value large enough to observe trends. It is plotted four times corresponding to four cases:

- The values of the capacitance  $C$  takes to value  $C = 0.1\text{pF}$  corresponding to a  $\sim 20 \times 20 \mu\text{m}^2$  active area OLED and  $C = 10\text{pF}$  corresponding to  $\sim 200 \times 200 \mu\text{m}^2$  active area OLED.
- The serial resistance  $R_s$  takes two values  $R_s = 10\Omega$  and  $R_s = 100\Omega$  chosen to be realistic in term of fabrication.  $R_s = 100\Omega$  is close to a value measured by Chime while  $R_s = 10\Omega$  is a more ambitious value but still reachable if an effort is devoted to optimize the OLED electrodes (metallization).

The resulting time constant range from few ps to few ns. The different curves show similar trends: The time constant increases with the measurement resistance  $R_m$  before it converge to a maximum for  $R_m \geq 500\Omega$ . Left sub-figures and right left figures appears similar in shape and span, which indicates that  $R_{shunt}$  plays a minor role within the range of values chosen for the parameters  $C$ ,  $C_0$ , and  $R_s$ . With the smaller value of the scope capacitance  $C_0 = 0.1\text{pF}$  the time constant spans on a larger range ( $\sim 2\text{ps}$  to  $\sim 2\text{ns}$ ) compare to  $C_0 = 10\text{pF}$  ( $10\text{ps}$  to  $2\text{ns}$ ). Obviously a scope with a large bandwidth is to be chosen to better discriminate the range of the time constant. The top-left figure shows time-constants curves distinct by up to tenfold factors for the different couples of  $R_s$  and  $C$ :

- With  $R_s = 100\Omega$  and  $C = 10\text{pF}$ , the time constant  $\tau_2$  range from  $1\text{ns}$  to  $1.5\text{ns}$  (see table 1). This is slightly above the targeted values.
- With  $R_s = 10\Omega$  and  $C = 10\text{pF}$ , the time constant  $\tau_2$  range from  $\sim 100\text{ps}$  to  $\sim 600\text{ps}$  (table II.1) which is fully compatible with ultra-high speed OLEDs, still with reasonable OLED active area. The challenge being to minimize the serial resistances one order of magnitude than what was done previously and keeping the measurement resistance preferably below  $R_m < 100$
- With  $R_s = 100\Omega$  and  $C = 0.1\text{pF}$ , the time constant  $\tau_2$  range from  $\sim 10\text{ps}$  to  $\sim 60\text{ps}$  (table 1). This is an acceptable range shorter than needed, but it would require a small OLED.
- With  $R_s = 10\Omega$  and  $C = 0.1\text{pF}$ , the time constant  $\tau_2$  range from  $\sim 1\text{ps}$  to  $\sim 10\text{ps}$  (table II.1) which is much less than needed and would require both very small OLED and efforts to reduce  $R_s$ .

This analysis indicates that from the theoretical point of view organic optoelectronic devices faster than those previously reported in the literature, in the picosecond range can be considered.

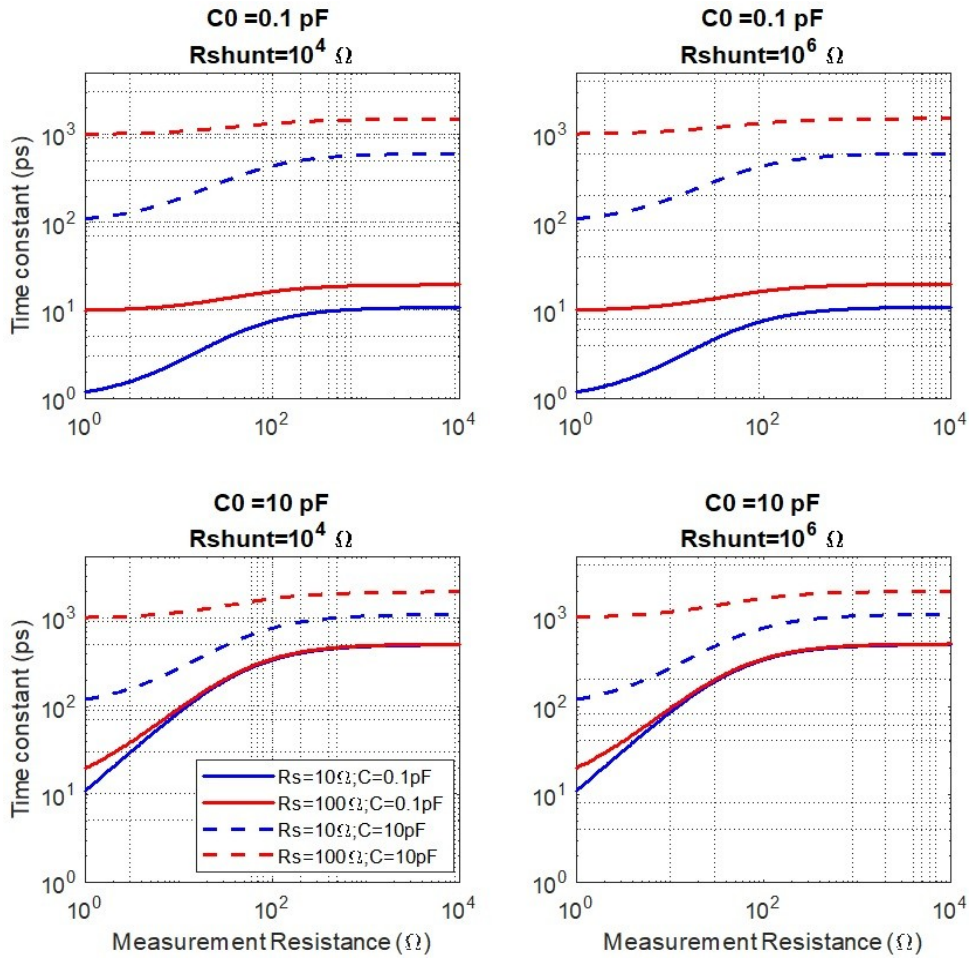


Figure II.3:  $\mu$ -OLED electrical time constant as a function of  $C$ ,  $C_0$ ,  $R_s$ ,  $R_{shunt}$ . And  $R_m$

$C_0$ (pF)	$R_{shunt}$ ( $\Omega$ )	$C$ (pF)	$R_s$ ( $\Omega$ )	$\tau_{2 \min}$	$\tau_{2 \max}$
0.1	$10^3$	10	100	917 ps	1307 ps
0.1	$10^3$	10	10	109 ps	568 ps
0.1	$10^3$	0.1	100	9 ps	18 ps
0.1	$10^3$	0.1	10	1 ps	10 ps
0.1	$10^6$	10	100	1010 ps	1500 ps
0.1	$10^6$	10	10	110 ps	600 ps
0.1	$10^6$	0.1	100	10 ps	20 ps
0.1	$10^6$	0.1	10	1 ps	11 ps
10	$10^3$	10	100	927 ps	1778 ps
10	$10^3$	10	10	118 ps	1037 ps
10	$10^3$	0.1	100	19 ps	490 ps
10	$10^3$	0.1	10	11 ps	479 ps
10	$10^6$	10	100	1020 ps	1995 ps
10	$10^6$	10	10	120 ps	1094 ps
10	$10^6$	0.1	100	20 ps	512 ps
10	$10^6$	0.1	10	11 ps	503 ps

### II.2.2.1. Numerical estimation of the maximum current-density

With the new electrical model, the diode current is presented as a function of excitation and measurement voltages. Because no assumption have been made on the current and the voltage across the active part of the OLED, but instead they are the unknowns to be calculated from the excitation voltage  $V_{exc}$  and the measurement voltage  $V_{meas}$ , the latter have both to be measured. For this reason we rely on the model built by Chime to estimate the OLED maximum current (Eq. II.16).

Based on the model presented by A. Chime and using the new parameters, the current-density can be presented as a function of  $R_d$ . According to this model the diode current starts with an initial turn-on peak current  $I_{peak}$  given by:

$$I_{peak} = \frac{V_E}{R_S + R_{meas}} \quad \text{Eq. (II.22)}$$

and when  $C$  is fully loaded, the initial current decreases toward a steady state current according to the following equation:

$$I_{steady} = \frac{R_S + R_{meas}}{R_d + R_S + R_{meas}} I_{peak} \quad \text{Eq. (II.23)}$$

In Fig.II.4 the current density is plotted as a function of the dynamical resistance  $R_d$  for three different OLED active areas  $A$  and for a maximum excitation voltage  $V_{exc} = 120V$ . The purpose of this study is to evaluate the impact of serial and measurement resistances on the "plateau" current density  $I_{steady}/A$ . This study is conducted with the following parameters:

- The serial resistance  $R_S$  is chosen from the conclusion of the previous study ( $R_S = 10 \Omega$ ) to which we add  $R_S = 15 \Omega$  in case  $R_S$  cannot be minimized down to  $10 \Omega$ .
- Four values of the measurement resistance are chosen  $R_m = 2\Omega, 5\Omega, 10\Omega$  or  $50\Omega$ .
- The OLED active area takes 3 values  $A_1 = 100 \times 100 \mu\text{m}^2$ ,  $A_2 = 50 \times 50 \mu\text{m}^2$  and  $A_3 = 25 \times 25 \mu\text{m}^2$

Figure II.4 shows that the current-density increases when the active area reduces, when the serial resistance reduces, as well as when the measurement resistance and dynamic resistance reduces.

The maximum current densities calculated with lower value of dynamical resistance  $R_d = 1\Omega$  ranges between  $J_d = 18.2 \text{ kA/cm}^2$  and  $J_d = 92.3 \text{ kA/cm}^2$  for A1, between  $J_d = 72.7 \text{ kA/cm}^2$  and  $J_d = 369.2 \text{ kA/cm}^2$  for A2 and above  $J_d = 290.9 \text{ kA/cm}^2$  for A3. A more realistic values estimated by Chime is  $R_d = 100\Omega$ , for which the current density varies between  $7.3 \text{ kA/cm}^2$  and  $10.3 \text{ kA/cm}^2$  for A1, between  $29.1 \text{ kA/cm}^2$  and  $42.9 \text{ kA/cm}^2$  for A2 and  $116.4 \text{ kA/cm}^2$  and  $171.4 \text{ kA/cm}^2$  for A3.

As a conclusion, the electrical time constant  $\tau_2$  decreases and the current density increases with the:

- Reduction of the measurement resistance  $R_m$
- Reduction of the serial resistance  $R_s$
- Reduction of the OLED capacitance  $C$  and oscilloscope capacitance  $C_0$
- Reduction of the active area  $A$

These results summarize the guidelines for the design and the fabrication of a new generation of ultra-fast  $\mu$ -OLED that will be presented in chapter 3.

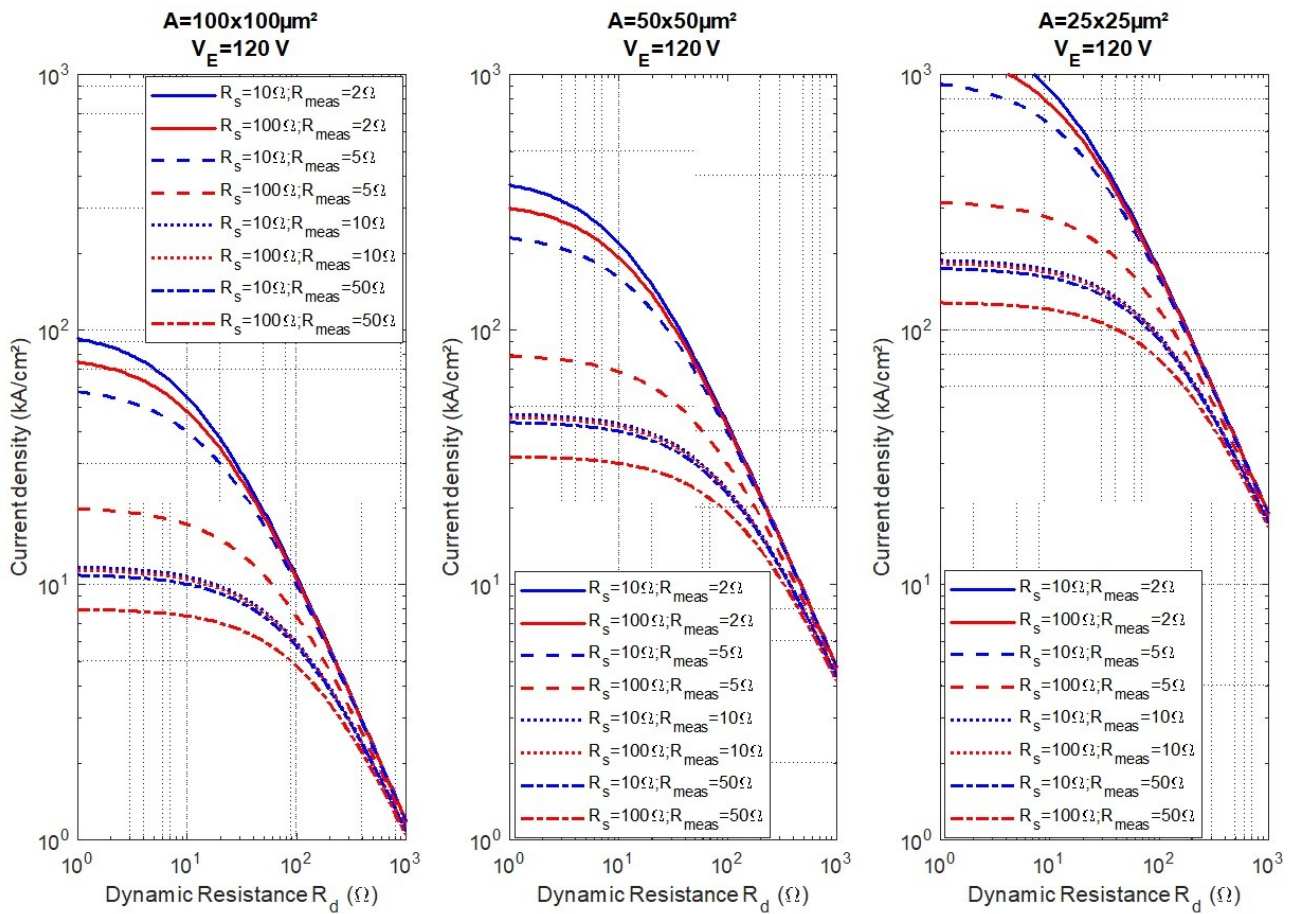


Figure II.4: Current density  $J_d=I_d/A$  for a 120 V excitation as a function of the dynamical resistance  $R_d$  for  $A=100 \times 100 \mu\text{m}^2$ ,  $A=50 \times 50 \mu\text{m}^2$  and  $A=25 \times 25 \mu\text{m}^2$ ,  $R_s=10 \Omega$  and  $R_s=15 \Omega$  and  $R_{\text{meas}}=2;5;10;50 \Omega$

### II.2.3. Design of coplanar waveguided electrodes (CPW)

When considering ultra-short pulses of duration  $T$ , one need to take into account the harmonics with frequencies multiple of  $1/T$  involved in the pulses. To deliver to the OLED the maximum of energy distributed in the different harmonics from a pulse generator, impedance matching on a large frequency range is to be implemented. Impedance matching between the pulse generator and the OLED ensure that the excitation pulses reach the active area of OLED without reflection or pulse distortion . The reflection coefficient is given by

$$\Gamma = \frac{Z_D - Z_C}{Z_D + Z_C} \quad \text{Eq. (II.24)}$$

where  $Z_D$  is the equivalent impedance of the device, and  $Z_C$  the characteristic impedance of the feeder line. The impedance matching issue is solved at two levels;

- at the generator level, the maximum power must be transmit from the generator to the feeder line. It's named the source matching
- at the receiver level, the emitting layer receives as much of this power from the line as possible. This is called load matching.

The reflection drives to the reduction of the incident energy of pulse directed to the OLED device. It has also the effect of distorting the pulse waveform by widening it and limiting the time response of OLED. To minimize the reflection wave requires the impedance matching or the modification of geometry of OLED electrodes and the excitation circuit to assure the continuity of impedance in the power lines on one hand, and on the other, impedance matching at the OLED level.

#### II.2.3.1. CPW structure

Proposed by A. Chime [11], the integration of the microwave engineering techniques to the high-speed OLED, is one solution to realize the impedance matching. The coplanar wave-guide (CPW) lines has been chosen as an alternative to microstrip line because it offers impedance matching on a wide frequencies range [12]. CPW line consists of three metal stripe placed on the same plane of a dielectric substrate with a thickness  $H$ . The central stripe conveys the signal while the two side stripes separated by a spacing  $G$  serve as ground planes. The coplanar line has several advantages: It has a great flexibility of design and fabrication to synthesize a given characteristic impedance. The mass and signal being on the same plane, it also shows ease of integration with other circuits without relying to metal connection and as such it facilitates realization of passive components; for example it allows integration of built-in resistance or more complex impedance. This type of line is perfectly suited for making the circuit on a glass substrate. The values  $W$  and  $G$  are chosen to obtain a characteristic impedance  $Z_C$  defined by:

$$Z_C = 30 \frac{\pi}{\sqrt{\epsilon_{\text{eff}}}} \times \frac{K(k_0')}{K(k_0)} \quad \text{Eq. (II.25)}$$

where  $K(k_x)$  is the complete elliptic integral of the first kind defined by:

$$K(k_x) = \int_0^{\pi} \frac{d\theta}{\sqrt{(1 - k_x^2 \sin^2(\theta))}} \quad \text{Eq. (II.26) where } k_x \text{ is either } k_0 \text{ or } k_1 \text{ are defined by:}$$

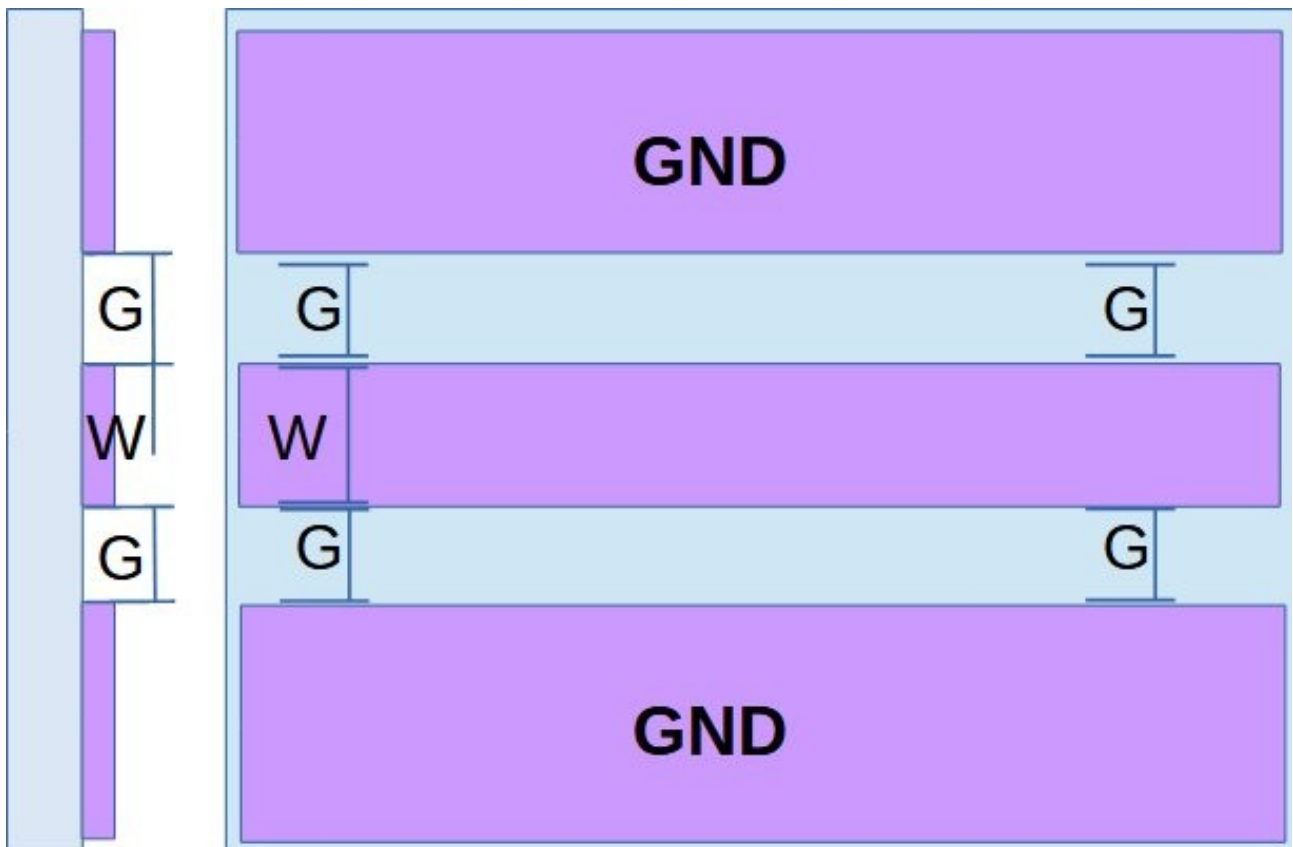


Figure II.5 Geometry of the coplanar waveguide. The conductive stripe are pink, the glass substrate is light blue.  $G$  is the gap between the central line and the ground stripes.

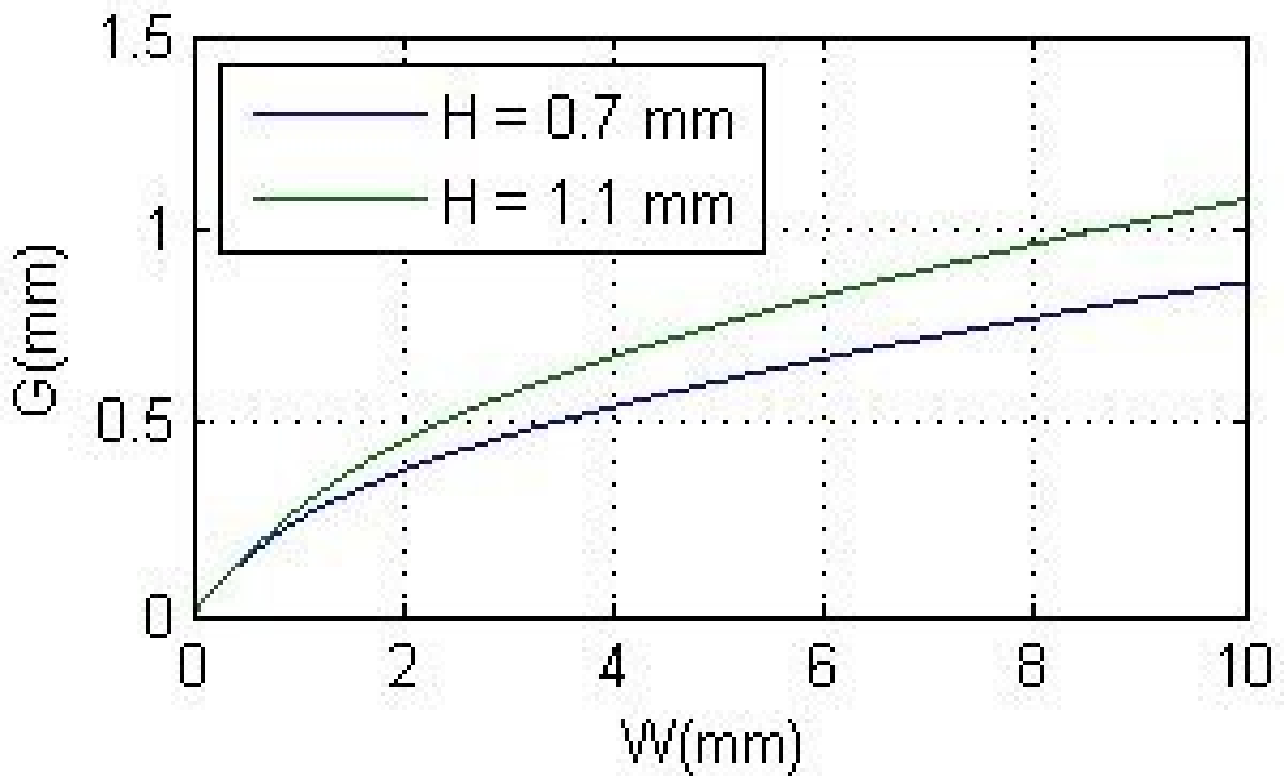


Figure II.6: Relationship between  $G$  and  $W$  for two different thickness of the glass substrate (from [ 10])

$$k_0 = \frac{W}{W+G} \quad \text{Eq. (II.27)} \quad \text{and} \quad k_1 = \frac{\sinh\left(\frac{\pi W}{4H}\right)}{\sinh\left[\frac{\pi(W+2G)}{4H}\right]} \quad \text{Eq. (II.28)}$$

and  $k_0'$  and  $k_1'$  are defined by  $k'_x = \sqrt{1-k_x^2}$ , with  $x = \{0,1\}$  Eq. (II.29)

$$\text{and} \quad \epsilon_{eff} = 1 + \frac{1}{2} \frac{K(k_0')}{K(k_0)} \times \frac{K(k_1')}{K(k_1)} \times (\epsilon_r - 1) \quad \text{Eq. (II.30)}$$

The relationship between W and G to achieved a characteristic impedance  $Z_c=50\Omega$  is plotted on fig.II.6. From this figure, a 700 $\mu\text{m}$  thick glass substrate ( $\epsilon_r=7.75$ ) with a gold central stripe of 1000 $\mu\text{m}$  should have a spacing  $G=243\mu\text{m}$  to the ground plane in order to exhibits a characteristic impedance  $Z_c=50\Omega$ .

$\epsilon$	$e_{\text{Glass}} (\mu\text{m})$	$W (\mu\text{m})$	$G (\mu\text{m})$	$Z_c$
7.75	700	1000	243	50 $\Omega$
7.75	700	1500	316	50 $\Omega$

### II.2.3.2. Design of the measurement resistance geometry

To increase the current density and decrease the time constant, the electrical model shows that the measurement resistance is to be minimized. Here we target measurement resistances below 10 $\Omega$ .

The measurement resistance are two builtin resistance added to the CPW as two ITO ribbons linking both ground plane with the cathode part of the central line as shown on figure II.7. Their resistance value R is defined by their geometry with a length G, and a section  $S= t \times d$  where t is the ITO thickness and d the width of the ribbons of shown on figure II.8.

$$R = \frac{\rho_{\text{ITO}} \times G}{d \times t} \quad \text{Eq. (II.31)}$$

where  $\rho_{\text{ITO}}$  is the resistivity of the Indium Tin Oxyde.

With both resistances R in parallel, and to achieve certain values of  $R_{meas}=R/2$  among  $\{5\Omega, 10\Omega\}$  a condition on the last undefined parameter, i.e. the width d of the ribbon is:

$$d = \frac{1}{2} \frac{\rho_{\text{ITO}} \times G}{(t R_{meas})} \quad \text{Eq. (II.32)}$$

The different values of the width d for two ITO thicknesses 140nm and 340nm and for two targeted values of  $R_{meas}$  5 $\Omega$  and 10 $\Omega$  are presented in table II.3.

### II.2.3.3. Estimation of the parasitic serial resistances

In order to control the size of the active are of the OLED, the layout invented by Chime et al, see figure II.9, is applied. This layout defines the size of the anode and the cathode and their cross section defines the device active area with a few micrometer accuracy.

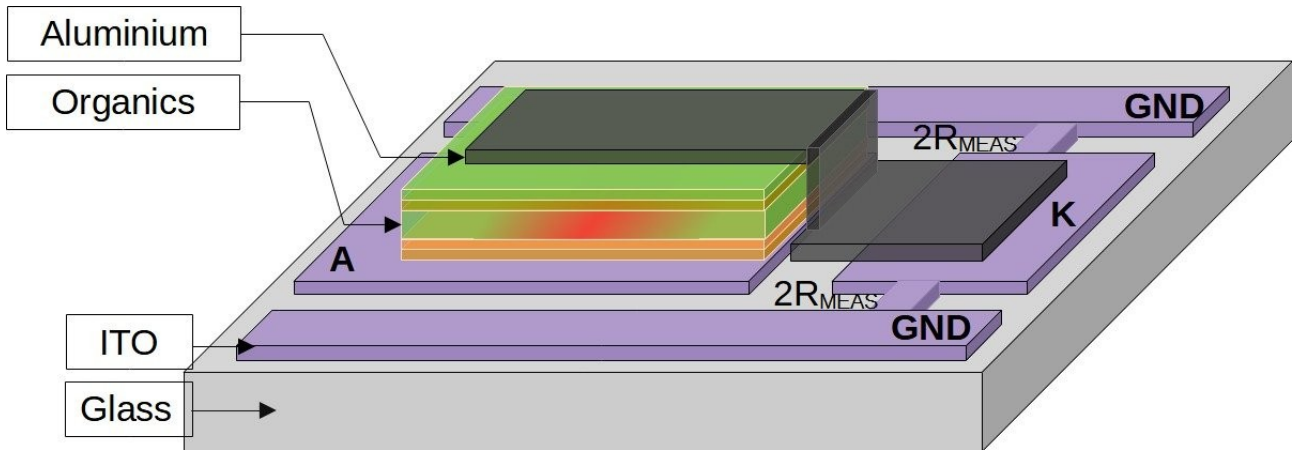


Figure II.7: Principle of the measurement resistances built-in the CPW

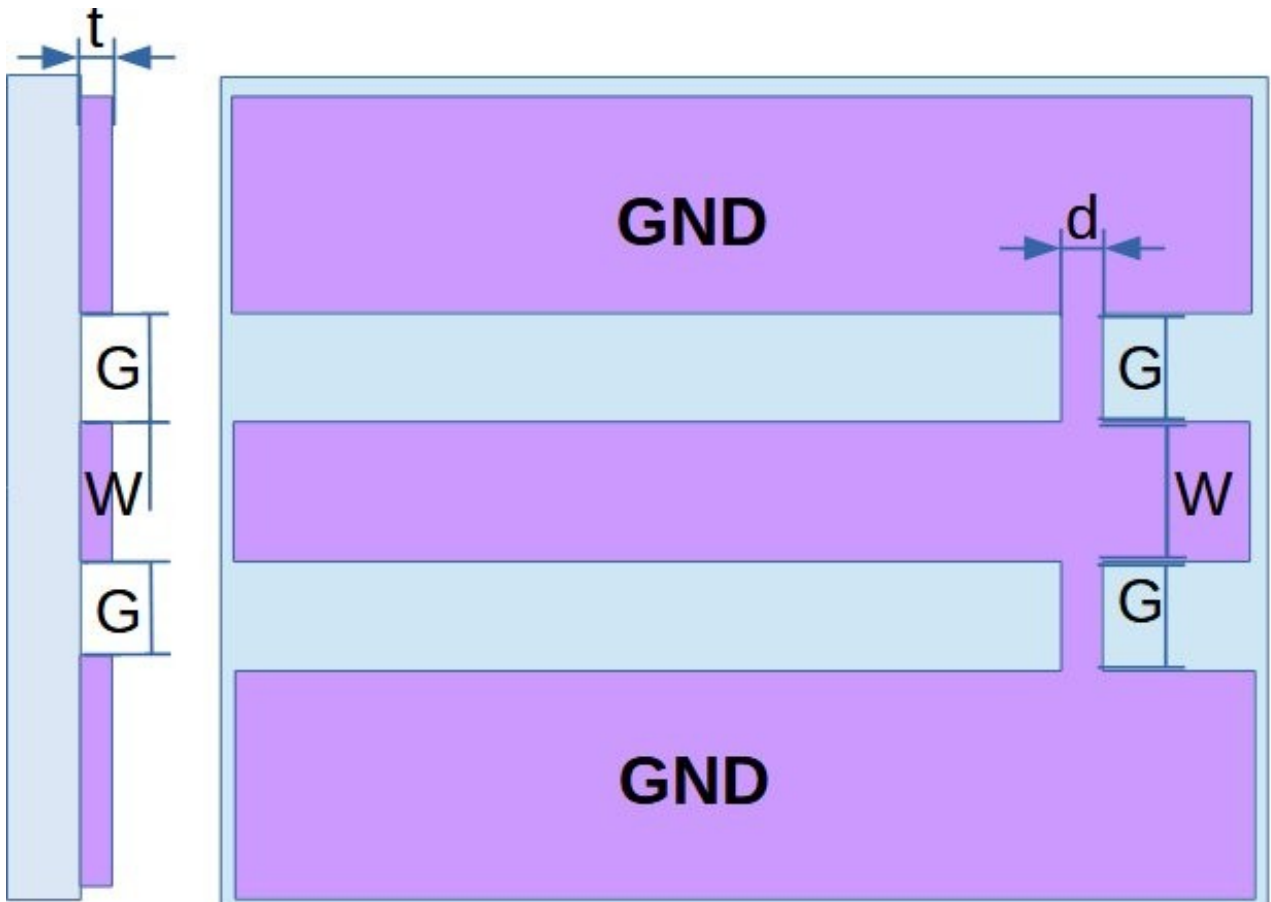


Figure II.8: Top view of the CPW and the geometry of the built-in measurement resistances

Table II.3: Geometry of the measurement resistances

$\rho_{ITO}$	G( $\mu\text{m}$ )	t ( $\mu\text{m}$ )	$R_{meas}$ $\Omega$	d ( $\mu\text{m}$ )
$10^{-4} \Omega \text{ cm}$	316	0.140	5 $\Omega$	564 $\mu\text{m}$
$10^{-4} \Omega \text{ cm}$	316	0.340	5 $\Omega$	232 $\mu\text{m}$
$10^{-4} \Omega \text{ cm}$	316	0.140	10 $\Omega$	282 $\mu\text{m}$
$10^{-4} \Omega \text{ cm}$	316	0.340	10 $\Omega$	116 $\mu\text{m}$
$10^{-4} \Omega \text{ cm}$	316	0.140	5.6 $\Omega$	500 $\mu\text{m}$
$10^{-4} \Omega \text{ cm}$	316	0.340	2.3 $\Omega$	500 $\mu\text{m}$



Firstly the central line is split into two parts; the anode side and the cathode side. Secondly, a void is created in the anode part. One side of the void is closed with a conductive and transparent anode ribbon (vertical on figure II.10) with a length  $L$  and a width  $V$ . the latter determining two of the limits of the active area. On top of the deposited organic layers, and perpendicular to the anode ribbon, a metallic horizontal cathode with a width  $H$  defines two other limits (see top Figure II.10).

The serial resistors are shown on the lower figure II.10 with the anode resistances  $r_{a1}$ ,  $r_{a2}$  and the cathode resistances  $r_{k1}$  and  $r_{k2}$ .

From the geometry, it is trivial to define the resistances on the cathode side and on the anode side:

On the anode side:

$$r_{a1} = \rho \frac{L_A}{Wt} \quad \text{Eq. (II.33)}$$

Eventually the anode part of the central line is covered with gold hence the resistivity is  $\rho = 2.4 \times 10^{-8} \Omega m$ .

$$r_{a2} = \rho_{ITO} \frac{\left(\frac{L-H}{2}\right)}{vt} \quad \text{Eq. (II.34)}$$

where  $\rho_{ITO}$  is the resistivity of conductive and transparent oxide, here indium tin oxyde (ITO  $\rho_{ITO} = 2.5 \times 10^{-6} \Omega m$  [13])

Here, both ITO resistance are in parallel and the total resulting resistance on the anode side is:

$$R_{S1} = r_{a1} + \frac{1}{2} r_{a2} = \rho \frac{L_A}{Wt} + \frac{1}{4} \rho_{ITO} \frac{L-H}{vt} \quad \text{Eq. (II.35)}$$

On the cathode side:

$$r_{k1} = \rho \frac{L_K}{Wt} \quad \text{Eq. (II.36)}$$

If the cathode is also partly covered with gold, the resistivity is  $\rho = 2.4 \times 10^{-8} \Omega m$ .

$$r_{k2} = \rho_{Al} \frac{X}{Ht} \quad \text{Eq. (II.37)}$$

where  $\rho_{Al}$  is the resistivity of aluminium ( $\rho_{Al} = 2.8 \times 10^{-8} \Omega m$ )

$$R_{S2} = r_{k1} + r_{k2} = \rho \frac{L_K}{Wt} + \rho_{Al} \frac{X}{Ht} \quad \text{Eq. (II.38)}$$

Tables II.5, II.4, II.6 and II.7 present the different values of serial resistances calculated from equations II.35 and II.38.

From Table II.5, it is shown that the serial resistance  $r_{A1}$  can be as high as  $71 \Omega$  if ITO is used. However, covering ITO with gold, allows to reduce the serial resistance  $r_{a1}$  down to  $1 \Omega$ .

From Table II.4, the serial resistance with 340nm thick ITO layer is as large as  $17 \Omega$ ,  $35 \Omega$  and  $72 \Omega$  respectively for  $100 \mu m$ ,  $50 \mu m$  and  $25 \mu m$  wide ITO ribbons respectively. The minimum total serial

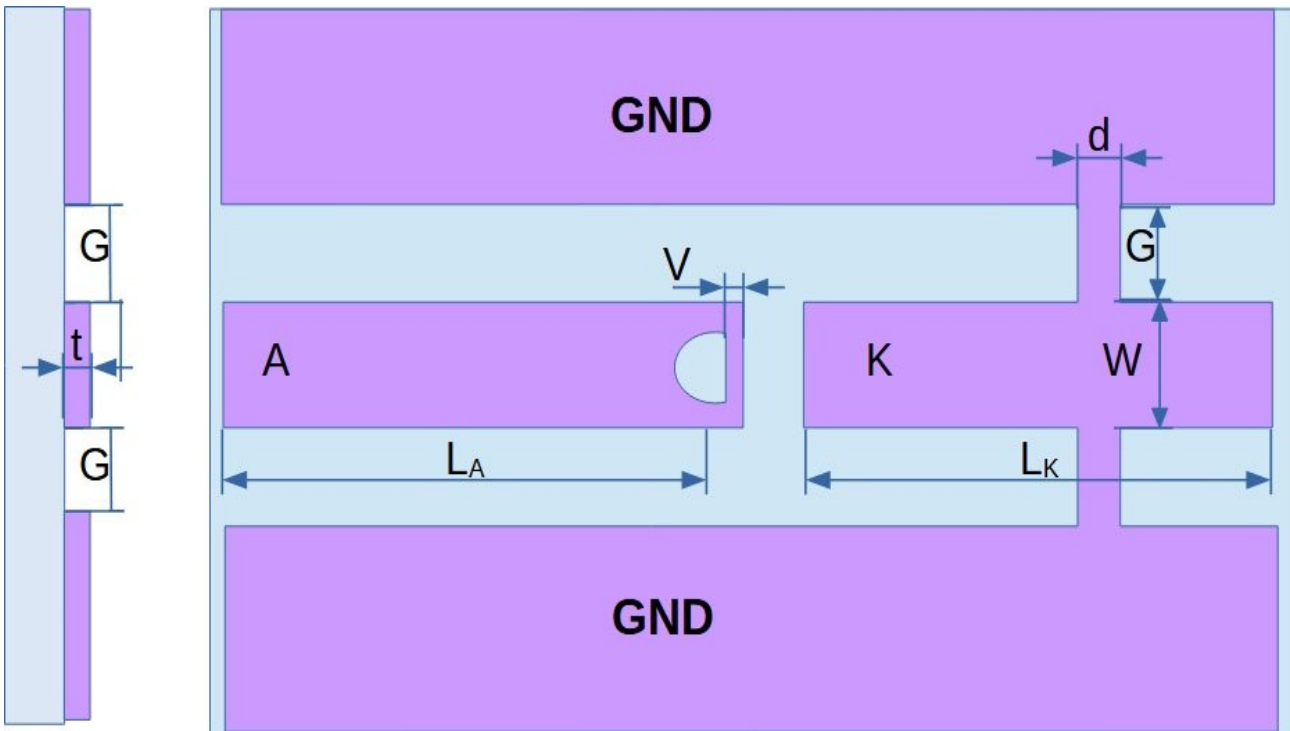


Figure II.9: Top view of the CPW electrodes with anode (A) and cathode (K) sections. A void is created in the anode section, leaving a vertical ribbon with a width  $V$ .

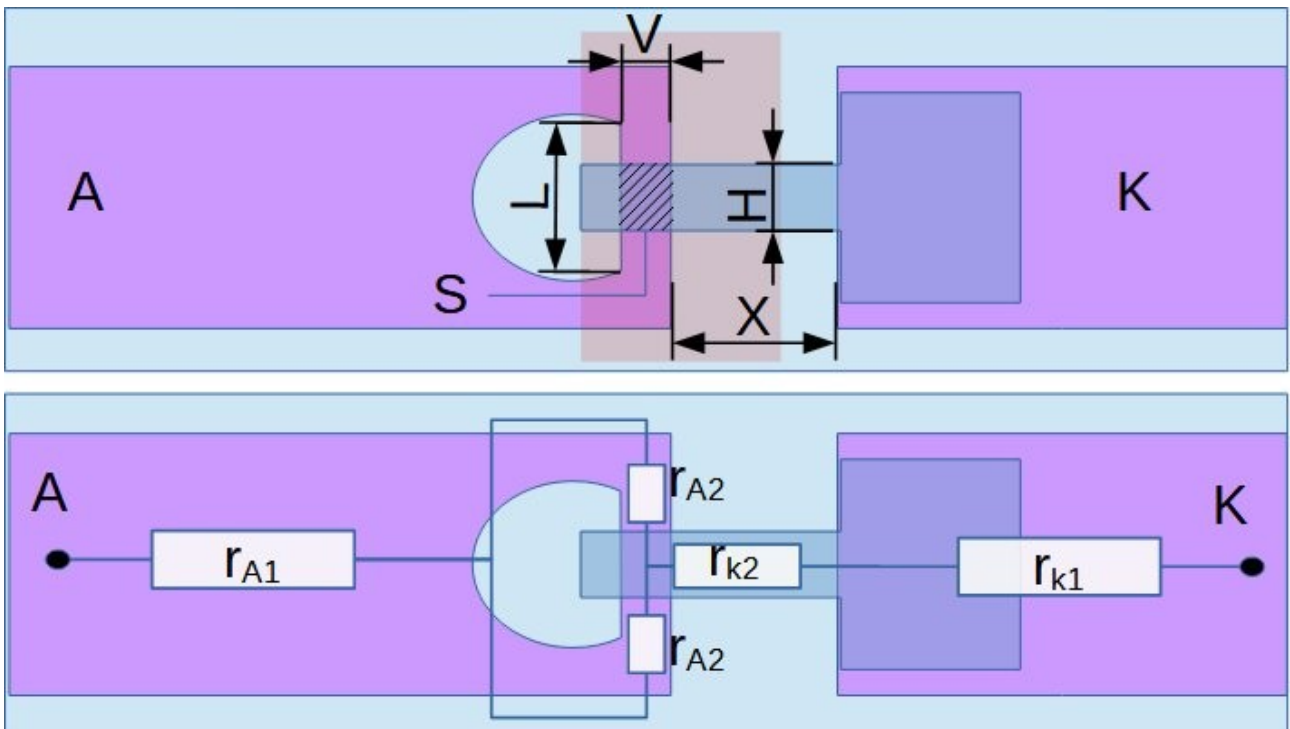


Figure II.10: Serial resistances. Top figure: Anode side (A), Cathode side (K),  $V$  width of the vertical ribbon,  $H$  width of the horizontal ribbon, their intersection defines the active area (S). Bottom figure; Serial resistances for each electrodes; on the anode side,  $r_{A1}$  is the serial resistance associated to the main part of the central line while  $r_{A2}$  are the the resistances associated to the vertical ribbon. On the cathode side,  $r_{k1}$  correspond to the main part of the central line, while  $r_{k2}$  correspond to the evaporated metallic horizontal ribbon (blue).

anode resistances are Rs1 respectively 18Ω, 36Ω and 73Ω respectively for 100μm, 50μm and 25μm wide ITO ribbons respectively.

From Table II.6, the serial resistance  $r_{k1}$  can be as low as 1Ω if it is metallized.

From Table II.7, the serial resistance  $r_{k2}$  can be as low as 0.3Ω, 0.7Ω, 2.1Ω for 100μm, 50μm and 25μm wide aluminum cathode ribbons respectively. The minimum total cathode serial resistances are Rs2 respectively 0.4Ω, 1Ω and 3Ω (1.7Ω, 2.4Ω and 3.8Ω) respectively for 100μm, 50μm and 25μm wide aluminum cathode ribbons respectively.

With gold metalization, the total serial resistances Rs1+Rs2 it is expected that they are minimized down to 18.5Ω, 37Ω and 76Ω (19Ω, 38Ω and 75Ω).

### II.2.3.4. Estimation of the parasitic capacitance

The parasitic capacitance  $C$  is estimated from the OLED active area  $A$  and the values of the capacitance per square meter  $C_M$  extracted from the literature and previous measurements.

$$C = C_M \times A \quad \text{Eq. (II.39)}$$

With  $A = H^2$ . From the literature, the surface capacitance ranges  $C_M = 28 - 35 \text{ nF cm}^{-2}$  [10]., The capacitances are in the ranges 2.8-35pF, 0.7-0.9pF and 0.2pF respectively with 100μm x 100μm, 50μm x 50μm and 25μm x 25μm active areas.

### II.2.3.5. Estimation of the time constant with the CPW geometry

The time constant for the most relevant above listed geometries calculated from Eq. (II.19), is presented in table II.9. It shows that with partial gold metalization of the anode and cathode and measurement resistance limited to 5.6Ω, the OLED with active sizes 100μm x 100μm, 50μm x 50μm and 25μm x 25μm exhibit electrical time constant below 100ps.

<b>Table II.4: Estimation of the serial resistance on the anode side</b> $r_{a2} = \frac{1}{2} \rho_{ITO} \frac{L-H}{vt}$					
t	v	L	H	$\rho$	$r_{a2}/2$
340 nm	100 μm	1000 μm	100 μm	$\rho_{ITO} = 2.5 \times 10^{-6} \Omega m$	17 Ω
340 nm	50 μm	1000 μm	50 μm	$\rho_{ITO} = 2.5 \times 10^{-6} \Omega m$	35 Ω
340 nm	25 μm	1000 μm	25 μm	$\rho_{ITO} = 2.5 \times 10^{-6} \Omega m$	72 Ω
140 nm	100 μm	1000 μm	100 μm	$\rho_{ITO} = 2.5 \times 10^{-6} \Omega m$	40 Ω
140 nm	50 μm	1000 μm	50 μm	$\rho_{ITO} = 2.5 \times 10^{-6} \Omega m$	85 Ω
140 nm	25 μm	1000 μm	25 μm	$\rho_{ITO} = 2.5 \times 10^{-6} \Omega m$	174 Ω
50 nm	100 μm	1000 μm	100 μm	$\rho_{ITO} = 2.5 \times 10^{-6} \Omega m$	113 Ω
50 nm	50 μm	1000 μm	50 μm	$\rho_{ITO} = 2.5 \times 10^{-6} \Omega m$	238 Ω
50 nm	25 μm	1000 μm	25 μm	$\rho_{ITO} = 2.5 \times 10^{-6} \Omega m$	488 Ω

<b>Table II.5: Estimation of the serial resistance on the anode side</b> $r_{a1} = \rho \frac{L_A}{Wt}$				
t	W	$L_A$	$\rho$	$r_{a1}$
340 nm	1500 μm	4000 μm	$\rho_{ITO} = 2.5 \times 10^{-6} \Omega m$	20 Ω
140 nm	1500 μm	4000 μm	$\rho_{ITO} = 2.5 \times 10^{-6} \Omega m$	48 Ω
50 nm	1500 μm	4000 μm	$\rho_{ITO} = 2.5 \times 10^{-6} \Omega m$	133 Ω

340 nm	1500 $\mu\text{m}$	4000 $\mu\text{m}$	$\rho_{Au} = 2.4 \times 10^{-8} \Omega\text{m}$	0.2 $\Omega$
150 nm	1500 $\mu\text{m}$	4000 $\mu\text{m}$	$\rho_{Au} = 2.4 \times 10^{-8} \Omega\text{m}$	0.5 $\Omega$
50 nm	1500 $\mu\text{m}$	4000 $\mu\text{m}$	$\rho_{Au} = 2.4 \times 10^{-8} \Omega\text{m}$	1 $\Omega$

**Table II.6: Estimation of the serial resistance on the cathode side**  $r_{k1} = \rho \frac{L_K}{Wt}$

t	W	$L_k$	$\rho$	$r_{k1}$
340 nm	1500 $\mu\text{m}$	2000 $\mu\text{m}$	$\rho_{ITO} = 2.5 \times 10^{-6} \Omega\text{m}$	10 $\Omega$
140 nm	1500 $\mu\text{m}$	2000 $\mu\text{m}$	$\rho_{ITO} = 2.5 \times 10^{-6} \Omega\text{m}$	24 $\Omega$
50 nm	1500 $\mu\text{m}$	2000 $\mu\text{m}$	$\rho_{ITO} = 2.5 \times 10^{-6} \Omega\text{m}$	67 $\Omega$
340 nm	1500 $\mu\text{m}$	2000 $\mu\text{m}$	$\rho_{Au} = 2.4 \times 10^{-8} \Omega\text{m}$	0.1 $\Omega$
140 nm	1500 $\mu\text{m}$	2000 $\mu\text{m}$	$\rho_{Au} = 2.4 \times 10^{-8} \Omega\text{m}$	0.2 $\Omega$
50 nm	1500 $\mu\text{m}$	2000 $\mu\text{m}$	$\rho_{Au} = 2.4 \times 10^{-8} \Omega\text{m}$	0.6 $\Omega$

**Table II.7: Estimation of the serial resistance on the cathode side**  $r_{k2} = \rho_{Al} \frac{X}{Ht}$

t	H	X ( $\mu\text{m}$ )	$\rho$	$r_{k2}$
340 nm	100 $\mu\text{m}$	375 $\mu\text{m}$	$\rho_{Al} = 2.8 \times 10^{-8} \Omega\text{m}$	0.3 $\Omega$
340 nm	50 $\mu\text{m}$	375 $\mu\text{m}$	$\rho_{Al} = 2.8 \times 10^{-8} \Omega\text{m}$	0.7 $\Omega$
340 nm	25 $\mu\text{m}$	375 $\mu\text{m}$	$\rho_{Al} = 2.8 \times 10^{-8} \Omega\text{m}$	2.1 $\Omega$
140 nm	100 $\mu\text{m}$	375 $\mu\text{m}$	$\rho_{Al} = 2.8 \times 10^{-8} \Omega\text{m}$	0.6 $\Omega$
140 nm	50 $\mu\text{m}$	375 $\mu\text{m}$	$\rho_{Al} = 2.8 \times 10^{-8} \Omega\text{m}$	1.5 $\Omega$
140 nm	25 $\mu\text{m}$	375 $\mu\text{m}$	$\rho_{Al} = 2.8 \times 10^{-8} \Omega\text{m}$	4.2 $\Omega$
50 nm	100 $\mu\text{m}$	375 $\mu\text{m}$	$\rho_{Al} = 2.8 \times 10^{-8} \Omega\text{m}$	1.2 $\Omega$
50 nm	50 $\mu\text{m}$	375 $\mu\text{m}$	$\rho_{Al} = 2.8 \times 10^{-8} \Omega\text{m}$	3 $\Omega$
50 nm	25 $\mu\text{m}$	375 $\mu\text{m}$	$\rho_{Al} = 2.8 \times 10^{-8} \Omega\text{m}$	8.4 $\Omega$

**Table II.8: Estimation of parasitic capacitance**

$C_M$	A	C
28 nF/cm <sup>2</sup>	100x100 $\mu\text{m}^2$	2.8pF
28 nF/cm <sup>2</sup>	50x50 $\mu\text{m}^2$	0.7pF
28 nF/cm <sup>2</sup>	25x25 $\mu\text{m}^2$	0.2pF
35 nF/cm <sup>2</sup>	100x100 $\mu\text{m}^2$	3.5pF
35 nF/cm <sup>2</sup>	50x50 $\mu\text{m}^2$	0.9pF
35 nF/cm <sup>2</sup>	25x25 $\mu\text{m}^2$	0.2pF

**Table II.9: Estimation of the time constant with  $C_0=1.5\text{pF}$ ,  $R_{shunt}=1\text{M}\Omega$ ,  $R_0=50\Omega$**

A	$a = 1 + (R_{S1} + R_{S2}) \left( \frac{1}{R_m} + \frac{1}{R_0} \right)$	$b = \left( 1 + \frac{R_{S1} + R_{S2}}{R_{shunt}} \right)$	$R_m$	RS	C	$\tau_2'$	$\tau_2$
100x100 $\mu\text{m}^2$	4.8	1.0	5.6 $\Omega$	19 $\Omega$	3.5pF	86ps	92ps
50x50 $\mu\text{m}^2$	8.5	1.0	5.6 $\Omega$	38 $\Omega$	0.9pF	39ps	46ps
25x25 $\mu\text{m}^2$	15.9	1.0	5.6 $\Omega$	75 $\Omega$	0.2pF	16ps	24ps
100x100 $\mu\text{m}^2$	9.6	1.0	2.3 $\Omega$	19 $\Omega$	3.5pF	75ps	78ps
50x50 $\mu\text{m}^2$	18.3	1.0	2.3 $\Omega$	38 $\Omega$	0.9pF	36ps	40ps
25x25 $\mu\text{m}^2$	35.1	1.0	2.3 $\Omega$	75 $\Omega$	0.2pF	15ps	19ps

## **II.3. An Organic Laser diode model**

### **II.3.1. Introduction**

In the current section, we consider the physical level and aim at investigating which material properties play a role in the stimulated emission process and how they affect the laser threshold. This requires to develop an overall understanding and description of the OLD mechanism provided by a unifying model. Such a model should be simple enough to facilitate its dissemination in different scientific communities, yet accurate enough to be useful in the establishment of design and fabrication rules. It should include electrical excitation instead of optical excitation and allow threshold estimation.

A first dynamical model has been introduced by Gärtner et al. [14]. Among the few dynamical models, Kasemann et al. proposed a simple rate equation model for the different exciton mechanisms in an OLED under pulsed electrical excitation, which provides a useful starting point [15]. However, it lacks inclusion of the micro-cavity and stimulated emission. The model introduced by Chua et al, does include the micro-cavity effect but pertains to optical pumping [16] and to time scales much longer than the nanosecond range considered in the current work.

In a very recent paper by Ahmad et al. [17] a theoretical and experimental investigation is reported of the polaron and exciton dynamics in Super Yellow OLEDs at high current-density nanosecond pulses. Apart from analysing the transient electrical current response of OLEDs to high voltage excitations, they focus on the dynamics of the spatial distributions of polaron charges, electric field and excitons and stimulated emission is not considered.

The goal is to set a first step toward a unified and simple model of the OLD that will be helpful in providing guidelines for the design and fabrication. As a second step and in coming chapter, the validity and accuracy of the model will be tested by confronting its predictability with measurements of an OLED with weak micro-cavity effect, under single-shot pulsed and intense electrical excitation in the nano-second range.

Contrary to Ahmad's work, we will deliberately assume for simplicity of the model that the densities of all constituents, i.e. polarons, excitons and photons, are uniformly distributed throughout the recombination zone with strict charge neutrality. Thus, our theory should be considered a first-order approximation.

As will be shown in Sec. 3.3, in case of electrical excitation the build-up of triplet excitons becomes dominant after a few nanoseconds, at the expense of singlet excitons, where the latter are essential for the optical gain. Therefore, lasing should be expected to occur within a few nanoseconds whereas this applies to a much lesser extent to optical pumping. Therefore this study will focus on short time range typically 1 to 20 ns.

A novelty of the current work is to introduce for the first time a laser model borrowed from the laser-dynamics field and to apply it to organic semiconductors in order to link the stimulated emission to the electrical excitation. The proposed OLD model can be applied to calculate the optical responses to electrical pulse excitations of guest-host system-based organic optoelectronic light sources and confront the predictions with the corresponding measured signal in the nano-

second time scale. Our model also provides a framework to analyze indications of lasing of the OLD and the required threshold current density [2].

The section is structured as follows: In section II.3.2. the OLD model is presented based on rate equations for the various relevant variables. The interplay between host and dopant guest molecules is explicitly addressed. In the various subsections II.3.2.1. to II.3.2.6. the different physical entities, i.e. polarons, singlet and triplet excitons in the host and dopant separately, and the photons are discussed. The optical gain is discussed in Sec. II.3.2.7. and an important factor, which plays a crucial role in the re-absorption of the (red) light emitted by the dopant singlet excitons is discussed in Sec. II.3.2.8. . In Sec. II.3.2.9. a few comments are given on the relation between the quality factor (Q) of the cavity and the corresponding photon lifetime. In Sec. II.3.3. numerical results are presented and compared for cases without cavity, i.e. for low-Q, and with a high-Q cavity. A numerical demonstration of light emission from an electrically driven OLD above laser threshold is given for the first time.

In section II.3.3.1. , laser threshold densities are calculated and predicted for two different values of the gain parameter and compared with that reported by Adachi's group [2]. The conclusion is given in section II.3.4. .

## II.3.2. The model

In the model we assume that the hole-type and electron-type polarons participate in charge transfer across the different organic layers and recombine in the emitting layer to form singlet and triplet excitons. The singlets can decay radiatively by photon emission, whereas radiative decay is Pauli-forbidden for the triplets.

We consider the situation where the emitting layer is composed of host molecules (the matrix), doped with a few percent of guest molecules (the dopant), where the excitonic states are quickly transferred from the host molecules to the singlet and triplet excitons of the dopant molecules by Förster transfer and in a less extent by Dexter transfer [18]. With a guest-host system like Alq<sub>3</sub>:Alq<sub>3</sub>:DCM, the host singlets have their optical transition in the green part of the spectrum (Alq<sub>3</sub>: ~520nm), whereas the dopant singlets provide both spontaneous and stimulated emission in the red spectrum (DCM: ~620nm). The idea is that the dopant-molecule ground states are easy to empty such that re-absorption of emitted light no longer hampers the optical gain, as it would do in case of host neat film.

The proposed OLD dynamical model is partially inspired on [14,15, 16, 19, 20, 21]. Equations read

$$\frac{dN_P}{dt} = \frac{J(t)}{ed} - \gamma N_P^2 \quad \text{Eq. (II.40)}$$

$$\frac{dN_S}{dt} = \frac{1}{4}\gamma N_P^2 + \frac{1}{4}\kappa_{TT} N_T^2 - (\kappa_{FRET} P_{0D} + \kappa_S + \kappa_{ISC}) N_S - \left( \frac{7}{4}\kappa_{SS} N_S + \kappa_{SP} N_P + \kappa_{ST} N_T \right) N_S \quad \text{Eq. (II.41)}$$

$$\frac{dN_T}{dt} = \frac{3}{4}\gamma N_P^2 + \kappa_{ISC} N_S + \frac{3}{4}\kappa_{SS} N_S^2 - (\kappa_{DEX T} P_{0D} + \kappa_T + \kappa_{TP} N_P) N_T - \frac{5}{4}\kappa_{TT} N_T^2 \quad \text{Eq. (II.42)}$$

$$\frac{dN_{SD}}{dt} = \kappa_{FRET} P_{0D} N_S + \frac{1}{4} \kappa_{TTD} N_{TD}^2 - (\kappa_{SD} + \kappa_{ISCD}) N_{SD} - \left( \frac{7}{4} \kappa_{SSD} N_{SD} + \kappa_{SPD} N_P + \kappa_{STD} N_{TD} \right) N_{SD} - \xi P_{HO} (N_{SD} - W N_{0D}) \quad \text{Eq. (II.43)}$$

$$\frac{dN_{TD}}{dt} = \kappa_{DEXT} P_{0D} N_T + \kappa_{ISCD} N_{SD} + \frac{3}{4} \kappa_{SSD} N_{SD}^2 - \kappa_{TD} N_{TD} - \frac{5}{4} \kappa_{TTD} N_{TD}^2 - \kappa_{TPD} N_{TD} N_P \quad \text{Eq. (II.44)}$$

$$\frac{dP_{HO}}{dt} = \beta_{sp} \kappa_{SD} N_{SD} + \left( \Gamma \xi (N_{SD} - W N_{0D}) - \kappa_{CAV} \right) P_{HO} \quad \text{Eq. (II.45)}$$

$$N_{0D} = N_{DOP} - N_{SD} - N_{TD} \quad \text{Eq. (II.46)}$$

$$P_{0D} = \frac{N_{0D}}{N_{DOP}} \quad \text{Eq. (II.47)}$$

where  $N_P$  is the polaron density,  $N_S$  the singlet and  $N_T$  the triplet population density, all in the host compound;  $N_{SD}$ ,  $N_{TD}$ , and  $N_{0D}$ , are the respective dopant singlet, triplet and ground-state population densities.  $P_{HO}$  is the photon density,  $J(t)$  the current density,  $d$  the active layer thickness and  $e$  the electron charge. Note that all densities in Eq. (II.41) to (II.47) are taken in the light-emitting layer.  $P_{0D}$  is the ratio of dopant ground-state molecules to the total number  $N_{DOP}$  of dopant molecules.  $W$  represents the overlap between the absorption spectrum  $S_{ABS}(\lambda)$  and the electroluminescence spectrum  $S_{EL}(\lambda)$  of the dopant,

$$W = \frac{\int S_{ABS}(\lambda) S_{EL}(\lambda) S_{CAV}(\lambda) d\lambda}{\int S_{EL}^2 S_{CAV}(\lambda) d\lambda} \quad \text{Eq. (II.48)}$$

where  $S_{CAV}(\lambda)$  is the cavity spectral shape.  $W$  accounts for the fraction of the dopant ground-state molecules that participate in the re-absorption of the emitted light. Note that  $W=1$  for identical spectra, else  $W < 1$ .

A first remark concerns the light emission by the host singlet excitons (green in case of Alq<sub>3</sub>). As we will show in subsection 3.3, the build-up of  $N_S$  remains relatively small, compared to  $N_{SD}$ . Moreover, no resonating structure is considered for the green light. Nevertheless, the host singlets will decay under spontaneous emission of green light. These emitted green photons are not considered in the rate equations.

As a second remark, note that the emission spectrum of an organic emitter is Stoke-shifted to the red by a few tens of nanometers from its absorption spectrum [22]. This implies that  $W$  will be quite small depending on the widths of the emission and absorption spectra. We estimate that in the weak micro-cavity limit with  $\kappa_{CAV}=3.0 \times 10^{14} \text{ s}^{-1}$ , we have  $W \approx 0.026$ , but as  $\kappa_{CAV}$  decreases with increasing cavity quality factor and the threshold for lasing is approached, the emitted spectrum will narrow dramatically, implying  $W$  to become much smaller. Therefore,  $W$  is a dynamical quantity and this will be studied in more detail in a future publication. Here, for the sake of simplicity, we will take  $W$  as a constant in the model. More about  $W$  will be discussed in subsection 3.2.8. The values of the various parameters in (II.40) to (II.47) are given in table 1 and explained in detail in the next subsections 3.2.1 to 3.2.7.

### II.3.2.1. The polaron differential equation

Equation II.40 describes the evolution of the polaron density with source term  $J(t) / (e d)$ , where  $e$  is the electron charge and  $d$  the thickness of the emitting layer. Polarons appear in two manifestations, positively charged hole-like polarons (density  $N_{p^+}$ ) and negatively charged electron-like polarons (density  $N_{p^-}$ ), where in view of assumed charge neutrality both populations are equal,  $N_{p^+} = N_{p^-}$ . Moreover, each neutral polaron pair recombines to form one exciton and leave behind one neutral molecule which occurs at the Langevin-recombination rate  $\gamma$  [23]. This recombination process drives the electrical current and leads to the sink term in Eq. II.40. In ref. 14 the value  $\gamma = 6.2 \times 10^{-12} \text{ cm}^3 \text{ s}^{-1}$  is evaluated. An approximate expression for  $\gamma$  based on the Poole-Frenkel model shows an exponential dependence of the polaron mobilities to the electric field  $F$  related to the excitation current [24]

$$\gamma = \frac{e}{\epsilon} (\mu_h + \mu_e) \approx \frac{e}{\epsilon} \mu_0 \exp\left(\frac{-E_a}{kT}\right) \exp\left(\frac{\delta\sqrt{F}}{kT}\right) \quad \text{Eq. (II.49)}$$

where  $\epsilon$  is the dielectric constant,  $\mu_h$  and  $\mu_e$  are the respective hole and electron mobility,  $\mu_0$  is the trap-free charge mobility,  $E_a$  the activation energy,  $\delta$  the Poole-Frenkel parameter,  $k$  the Boltzmann constant and  $T$  the temperature. In  $\text{Alq}_3$ , the mobility of electrons is much larger than that of holes, therefore  $\mu_h$  is neglected in first approximation [25]. According to Eq. II.49 we expect the value of  $\gamma$  to increase exponentially with increasing applied diode voltage. For this reason, a larger value is expected at the high current densities (and thus high excitation voltage of 100V or above) needed to reach the laser threshold. Under such conditions  $\gamma$  has not been measured, but we will propose a better estimation below in subsection 3.2.10, which is justified in chapter 4. In the pulsed excitation regime, with the voltage being switched from zero to a maximum and back to zero, an on-off approximation is applicable and a fixed value for  $\gamma$  can be assumed, although a dynamical expression may be preferred in other types of excitation.

### II.3.2.2. The host singlet-exciton equation

The first term on the right-hand side (r.h.s.) of Eq. II.41 is a source for the singlet excitons coming from the above-mentioned polaron recombination term. The factor  $1/4$  originates from the randomly injected spin statistics. The second term is a source term arising from triplet-triplet annihilation with generation rate  $k_{TT}$  [21]. All other terms are sink terms. The first sink term describes the Förster Resonance Energy Transfer (FRET) of singlet excitons from host to dopant molecules with a typical transfer time given by:

$$\tau_{FRET} = \frac{1}{\kappa_{FRET}} = \tau_d \left(\frac{a}{R_0}\right)^6 \quad \text{Eq. (II.50)}$$

where  $\tau_d$  is the host (donor) exciton lifetime,  $R_0$  is the Förster radius, and  $a$  is the average distance between the donor and the dopant (acceptor). It is approximated by half of the dopant molecule size,

$$a = \frac{1}{2\sqrt[3]{N_{DOP}}} \quad \text{Eq. (II.51)}$$

where  $N_{DOP} = C N_{MOL}$  is the molecular density of the guest (dopant),  $C$  its concentration and  $N_{MOL}$  the host density. In the case of the  $\text{Alq}_3$ :DCM guest-host system,  $\tau_d = 1/k_S = 12.5 \text{ ns}$ ,  $R_0 = 3.25 \text{ nm}$ , and  $a = 1.43 \text{ nm}$ , the estimated transfer time is  $\tau_{FRET} = 1/\kappa_{FRET} = 87 \text{ ps}$  and



$k_{\text{FRET}}=1.15 \times 10^{10} \text{ s}^{-1}$  [26,27]. FRET is among the fastest mechanisms involved in the current dynamics and as such constitutes the most dominant sink term in Eq. II.41. The probability  $P_{0D}$  accounts for the potential depopulation of the dopant ground state that would limit the energy transfer.

The second sink term describes the decay of the singlet exciton, modelled with the decay rate  $k_S$ . This rate is related to the fluorescence lifetime which is known to be very sensitive to the environment and therefore subject to large uncertainties [28, 29]. Indeed, the singlet exciton lifetime of a neat  $\text{Alq}_3$  film measured under optical pumping was found to be between 12.5 ns and 20 ns [30, 31, 32, 33, 34]. We choose the singlet lifetime of  $\text{Alq}_3$  as  $\tau_{\text{PL Alq}_3} = 12.5 \text{ ns}$ , and calculate the host decay rate  $k_S = 8.0 \times 10^7 \text{ s}^{-1}$  [35]. The third sink term accounts for the non-radiative de-excitation mechanism, the inter-system crossing (ISC), which is a spin-flip-induced intra-molecular energy transfer from singlet to triplet with a decay rate  $k_{\text{ISC}}$ . For  $\text{Alq}_3$  used as a host it is estimated to  $2.2 \times 10^4 \text{ s}^{-1}$  in the literature [36]. The last sink terms in Eq. II.41 describe the de-population of the host singlet density with different annihilation terms: singlet-singlet annihilation (SSA) with decay rate  $k_{\text{SS}}$ , singlet-polaron annihilation (SPA) with decay rate  $k_{\text{SP}}$ , and singlet-triplet annihilation (STA) with decay rate  $k_{\text{ST}}$  [15,14 ].

### II.3.2.3. The host triplet-exciton equation

The rate equation II.42 describes the variation of host triplet excitons. The first three terms in the r.h.s. are sources. The first is a contribution arising from the polaron recombination. With a 3/4 factor resulting from the spin statistics, this source term, when added to the first singlet source term in Eq. II.41, matches the first sink term for the polaron recombination in Eq. II.40. The second term describes the increase of  $N_T$  due to ISC in the same way as it decreases  $N_S$  in Eq. II.41. The third term corresponds to the creation of triplets due to singlet-singlet absorption (SSA). The fourth term summarizes all decay processes respectively due to Dexter transfer to dopant triplets, relaxation of the triplet excitons with decay time  $\tau_T=1/k_T$  [35] and triplet-polaron annihilation (TPA) [15]. Finally, the fourth term corresponds to triplet-triplet annihilation (TTA).

### II.3.2.4. The dopant singlet-exciton equation

The dynamics of the dopant-singlet density  $N_{SD}$  is described by Eq. II.43. The first term on the r.h.s. is the source as a result of the Förster energy transfer. This term matches the corresponding sink term in Eq. II.41. With the exception of the last term on the r.h.s., all other terms are the corresponding counterparts of terms in Eq. II.41.

In the first sink term, the dopant singlets decay radiatively at rate  $k_{SD}$ . For the  $\text{Alq}_3$ -DCM guest-host system we have taken the value  $k_{SD}=1.0 \times 10^9 \text{ s}^{-1}$  [15]. The last term describes the dopant singlet interaction with the photons due to stimulated emission with differential gain coefficient  $\xi$ . Here, the term  $(N_{SD} - WN_{0D})$  is the effective inversion of the dopant singlets.

### II.3.2.5. The dopant triplet-exciton equation

Rate equation II.44 describes the dopant triplet density  $N_{TD}$  variations. The first term matches the corresponding Dexter transfer term in Eq. II.42. The second term is the source resulting from the ISC matching the corresponding fourth term in Eq. II.43. The third term represents the decay of the dopant triplet density at rate  $k_{TD}$  by de-excitation, while other terms correspond to the absorption processes TTA ( $k_{TTD}$ ) and TPA ( $k_{TPD}$ ).

### II.3.2.6. The photonic equation

Rate equation II.45 accounts for the dynamics of the photon density  $PHO$ . The first term on the r.h.s. gives the spontaneous-emission contribution arising from the radiative recombination of the dopant singlets  $NSD$  at the rate  $k_{SD}$  where the spontaneous-emission factor  $\beta_{sp}$  is the fraction of emitted photons within the lasing mode.

The second term gives the stimulated-emission net rate, where  $(NSD - W \cdot N_{0D})$  is the effective inversion, as also mentioned in section 3.2.4.  $\Gamma$  is the confinement factor introduced to take into account the fact that only the part of the field wave-guided inside the gain medium is amplified. The last term on the r.h.s. accounts for the photon losses out of the cavity, with decay rate  $k_{CAV}=1/\tau_{CAV}$ , where  $\tau_{CAV}$  is the cavity photon lifetime. The net-amplification rate by stimulated emission is given by  $A_{STIM} = \Gamma \xi (N - SD - W N - 0 D) - k_{CAV}$ .

### II.3.2.7. The optical gain

The optical gain per unit length is given by

$$g = \frac{n\xi}{c} N_{SD} \quad \text{Eq. (II.52)}$$

where  $n$  is the index of refraction in the material and  $c$  the light velocity. In optical pumping experiments, the gain is given in terms of slope coefficient  $K$  such that:

$$g = K I_P \quad \text{Eq. (II.53)}$$

where  $I_P$  is the optical pump intensity. With the photon flux  $nIP / c$ , the equivalent excitation in terms of dopant-singlet excitons is

$$N_{SD} = I_P \frac{n\lambda_P}{hc^2} \quad \text{Eq. (II.54)}$$

where  $\lambda_P$  is the wavelength of the pump light and  $h$  the Planck's constant. Combining Eq. II.52, II.53, and II.54 we obtain

$$\xi = \frac{cg}{nN_{SD}} = K \frac{hc^3}{n^2\lambda_P} \quad \text{Eq. (II.55)}$$

It relates the gain parameter  $\xi$  to the slope coefficient  $K$  observed in optical pump experiments [20].

### II.3.2.8. More about the W-factor

Despite the Stoke shift, the normalized absorption spectrum  $S_{ABS}(\lambda)$  and the emission spectrum  $S_{EL}(\lambda)$  of the emitted light by the dopant show some overlap, which induces a residual re-absorption of the light emitted by the dopant singlet excitons  $NSD$ . With  $W$  representing the spectral overlap, (see [37]), the re-absorption rate per unit photon density equals  $\Gamma\xi W N_{0D}$ . Then, transparency is achieved when the available dopant singlet excitons  $NSD$  precisely cancel the re-absorption, i.e,

$$N_{SD|at\ transparency} = W N_{0D} \quad \text{Eq. (II.56)}$$

Note that the re-absorption of photons yields a source term for the dopant singlet population in Eq. II.43. In the bad-cavity limit, the reabsorption is maximal. When approaching the lasing threshold, the emission spectrum narrows, and  $W$  will become very small close to threshold and above.

### II.3.2.9. Relation between the quality factor and cavity lifetime $\tau_{CAV} = 1/k_{CAV}$

The losses resulting from the fraction of photons escaping the cavity per unit of time define a relationship between the cavity photon lifetime  $\tau_{CAV}$  and the corresponding quality factor  $Q$  which reads:

$$Q = \omega_0 \tau_{CAV}, \quad \text{Eq. (II.57)}$$

where  $\omega_0$  is the resonance frequency of the cavity mode. The cavity photon decay rate  $k_{CAV}$  can be expressed in the quality factor  $Q$  and the resonance wavelength in vacuum  $\lambda_0$  as

$$k_{CAV} = \frac{1}{\tau_{CAV}} = 2\pi \frac{c}{n \lambda_0} \frac{1}{Q} \quad \text{Eq. (II.58)}$$

At 620nm wavelength, a typical value for an OLED undergoing a parasitic weak microcavity effect is ( $Q \sim 6$ ) corresponding to a cavity decay rate of  $k_{CAV} \approx 3.0 \times 10^{14} \text{ s}^{-1}$ , and a photon life time in the cavity of  $\tau_{CAV} \approx 3 \text{ fs}$ . A reasonable value for the quality factor  $Q \approx 3000$  is achievable with a DFB-type of laser cavity and yields a cavity decay rate  $k_{CAV} \approx 5.4 \times 10^{11} \text{ s}^{-1}$  corresponding to a photon life time of  $\tau_{CAV} \approx 1.9 \text{ ps}$ .

**Table II.10: Model parameters**

Symbol	Name	Value	Ref.
<b>S</b>	OLED active area	$10^{-4} \text{ cm}^2$	
<b>d</b>	OLED active layer thickness	$380.0 \times 10^{-9} \text{ m}$	
<b>e</b>	Charge of the electron	$1.6 \times 10^{-19} \text{ C}$	
<b><math>\gamma</math></b>	Langevin recombination rate	$6.2 \times 10^{-12} \text{ cm}^3 \text{ s}^{-1}$	14
<b><math>N_{MOL}</math></b>	Molecular density	$2.1 \times 10^{21} \text{ cm}^{-3}$	
<b><math>K_{FRET}</math></b>	Förster transfer rate	$1.1 \times 10^{10} \text{ s}^{-1}$	27
<b><math>K_S</math></b>	Host singlet-exciton decay rate	$8.0 \times 10^7 \text{ s}^{-1}$	35
<b><math>K_{ISC}</math></b>	Host inter-system crossing rate	$2.2 \times 10^4 \text{ s}^{-1}$ to $1.0 \times 10^7 \text{ s}^{-1}$	21, 36
<b><math>K_{SS}</math></b>	Host singlet-singlet annihilation (SSA) rate	$3.5 \times 10^{-12} \text{ cm}^3 \text{ s}^{-1}$	15
<b><math>K_{SP}</math></b>	Host singlet-polaron annihilation (SPA) rate	$3.0 \times 10^{-10} \text{ s}^{-1}$	15,29
<b><math>K_{ST}</math></b>	Host singlet-triplet annihilation (STA) rate	$1.9 \times 10^{-10} \text{ cm}^3 \text{ s}^{-1}$	15
<b><math>K_{DEXT}</math></b>	Dexter transfer rate	$1.0 \times 10^{10} \text{ s}^{-1}$ to $5.0 \times 10^{15} \text{ s}^{-1}$	30
<b><math>K_T</math></b>	Host triplet decay rate	$6.5 \times 10^2 \text{ s}^{-1}$ - $4.0 \times 10^4 \text{ s}^{-1}$	15, 35
<b><math>K_{TP}</math></b>	Host triplet-polaron annihilation (TPA) rate	$2.8 \times 10^{-13} \text{ cm}^3 \text{ s}^{-1}$	15
<b><math>K_{TT}</math></b>	Host triplet-triplet annihilation (TTA) rate	$2.2 \times 10^{-12} \text{ cm}^3 \text{ s}^{-1}$	15
<b><math>K_{SD}</math></b>	Dopant singlet-exciton decay rate	$1.0 \times 10^9 \text{ s}^{-1}$	15, 31, 32
<b><math>K_{ISCD}</math></b>	Dopant inter-system crossing rate	$2.2 \times 10^4 \text{ s}^{-1}$ to $1.0 \times 10^7 \text{ s}^{-1}$	21, 36
<b><math>K_{SPD}</math></b>	Dopant singlet-polaron annihilation (SPA) rate	$3.0 \times 10^{-10} \text{ cm}^3 \text{ s}^{-1}$	15, 29
<b><math>K_{STD}</math></b>	Dopant singlet-triplet annihilation (STA) rate	$1.9 \times 10^{-10} \text{ cm}^3 \text{ s}^{-1}$	19
<b><math>K_{SSD}</math></b>	Dopant singlet-singlet annihilation (SSA) rate	$9.6 \times 10^{-13} \text{ cm}^3 \text{ s}^{-1}$	33
<b><math>K_{TD}</math></b>	Dopant triplet decay rate	$6.6 \times 10^2 \text{ s}^{-1}$	34
<b><math>K_{TTD}</math></b>	Dopant triplet-triplet annihilation (TTA) rate	$2.4 \times 10^{-15} \text{ cm}^3 \text{ s}^{-1}$	28
<b><math>K_{TPD}</math></b>	Dopant triplet-polaron annihilation (TPA) rate	$5.6 \times 10^{-13} \text{ cm}^3 \text{ s}^{-1}$	17, 28
<b><math>\Gamma</math></b>	Confinement factor	0.29	
<b><math>\xi</math></b>	Stimulated emission gain coefficient	$1.4 \times 10^{-5} \text{ cm}^3 \text{ s}^{-1}$	21
<b><math>k_{CAV}</math></b>	Cavity photon decay rate	$1\text{-}300 \times 10^{12} \text{ s}^{-1}$	
<b><math>\beta_{sp}</math></b>	Spontaneous emission factor	$< 10^{-4}$ - 0.15	
<b>C</b>	Dopant concentration	2%	
<b><math>N_{DOP}</math></b>	Density of guest molecules	$4.2 \times 10^{19} \text{ cm}^{-3}$	

### II.3.3. Dynamical response to pulsed electrical excitation

The current model is used first to calculate the dynamical responses of OLEDs under intense electrical pulsed excitations in different configurations. More precisely, we calculate the polaron ( $N_p$ ), host singlet and triplet ( $N_s$ ,  $N_T$ ), dopant singlet and triplet ( $N_{SD}$ ,  $N_{TD}$ ) and the photon ( $P_{HO}$ ) densities as functions of time on the basis of equations Eq. II.40 to II.47. The excitation is modelled with an intense electrical pulse with sigmoid shape, duration of 20 ns, and rise time of 100 ps. We consider a high-speed  $100 \times 100 \mu\text{m}^2$  ( $S = 1.0 \times 10^{-4} \text{ cm}^2$ )  $\mu$ -OLED with an 80 nm thick organic heterostructure that incorporates an Alq<sub>3</sub>:DCM guest-host system with  $\gamma = 1.3 \times 10^{-9} \text{ cm}^3\text{s}^{-1}$  and other parameter values as in table 1.

The first case investigated is an OLED with a residual weak micro-cavity effect ( $Q = 6$ ,  $k_{CAV} = 3.0 \times 10^{14} \text{ s}^{-1}$ ) and spectral overlap of  $W = 2.6\%$ . For this case, the peak current density is  $3.25 \text{ kA/cm}^2$  and the dynamical responses are plotted in fig. II.11.

Figure II.11.a, shows the electrical current density  $J(t)$  (blue solid line, left scale) and the polaron density  $N_p$  (cyan dash, right scale) as a function of time.

Figure II.11.b displays the host singlet  $N_s$  (green solid line) and triplet  $N_T$  (green dashes) densities.  $N_s$  increases with the pulse onset, reaches a first plateau at  $\sim 1.5 \times 10^{17} \text{ cm}^{-3}$  and increases again before reaching a second maximum at  $2.5 \times 10^{17} \text{ cm}^{-3}$ . Note that the maximum triplet density is nearly two orders of magnitude larger than for the singlets. After the maximum the triplet density decays due to the non-radiative recombination ( $k_T$ ) and the Dexter transfer to the dopants ( $k_{DEXT}$ ).

The time evolution of the dopant singlet  $N_{SD}$  and triplet  $N_{TD}$  population densities are shown in fig. II.11.c.  $N_{SD}$  (magenta solid line) increases quickly after the pulse onset, reaching a pronounced maximum at  $\sim 7.5 \times 10^{17} \text{ cm}^{-3}$  3 ns after the pulse onset, and decreases shortly after that to reach a value of  $5 \times 10^{16} \text{ cm}^{-3}$ , before vanishing after the end of the pulse. Note that  $N_{SD}$  at maximum is fivefold larger than the host-singlet maximum demonstrating a very efficient Förster transfer. Meanwhile  $N_{TD}$  (magenta dashes, right axis) increases steadily, reaches a plateau with a maximum  $> 4.0 \times 10^{19} \text{ cm}^{-3}$  and undergoes a very slow decay on a long (micro-second) time scale.

Figure II.11.d presents the photon density  $P_{HO}$  (red solid line, right scale) and the net amplification (blue solid curve, left scale) as a function of time.  $P_{HO}$  increases quickly, and  $\sim 2$  ns after the pulse onset it reaches a maximum at  $3.7 \times 10^{11} \text{ cm}^{-3}$ , then decays to the value  $2.5 \times 10^{10} \text{ cm}^{-3}$  until the end of the pulse and finally decays again.

As such, the photon density follows closely the singlet density which is a first strong indication that no laser action occurs. This is confirmed by the net-amplification rate (see sec.3.2.6)  $A_{STIM} = \Gamma \xi (N_{SD} - W N_{OD}) - \kappa_{CAV}$  which remains large and negative. The net-amplification should climb up to a value close to zero if lasing is to be reached.

The second case investigated consists of an OLED with a similar organic hetero-structure but with a high-quality factor micro-cavity ( $Q = 1800$ ,  $k_{CAV} = 1.0 \times 10^{12} \text{ s}^{-1}$ ), and a small spectral overlap  $W = 0.0015$ .

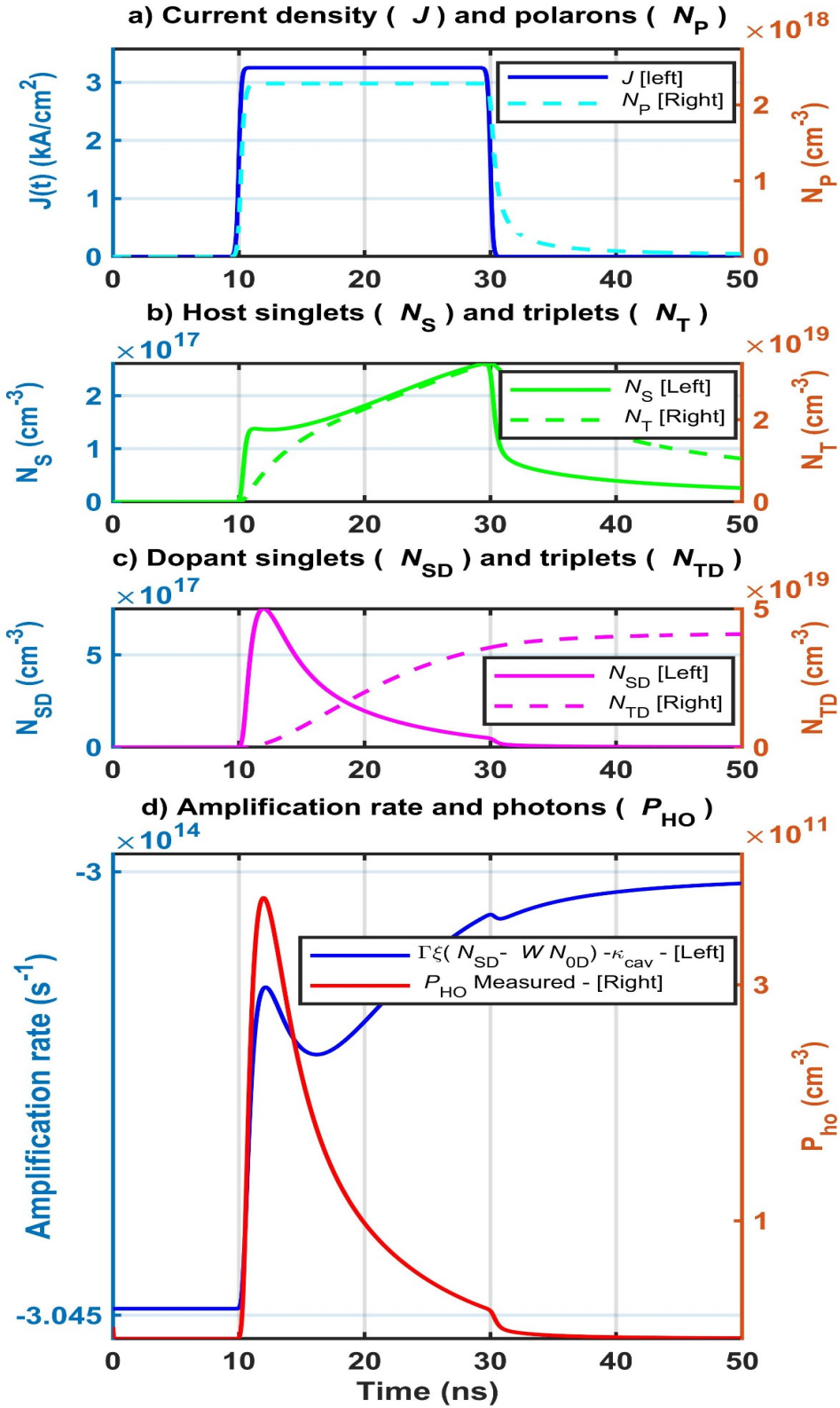


Figure. II.11: Dynamical response of a high-speed OLED with a weak microcavity effect submitted to a 20ns electrical pulse with intense current density ( $3.25 \text{ kA/cm}^2$ ), ( $Q = 6, k_{\text{cav}} = 3.0 \times 10^{14} \text{ s}^{-1}, \gamma = 1.3 \times 10^{-9} \text{ cm}^3 \text{ s}^{-1}, k_{\text{DEXT}} = 2.0 \times 10^8 \text{ s}^{-1}, k_{\text{ISC}} = k_{\text{ISCD}} = 2.2 \times 10^4 \text{ s}^{-1}, k_{\text{T}} = 6.5 \times 10^2 \text{ s}^{-1}, W = 2.6 \times 10^{-2}, \beta_{\text{sp}} = 0.15$ ).

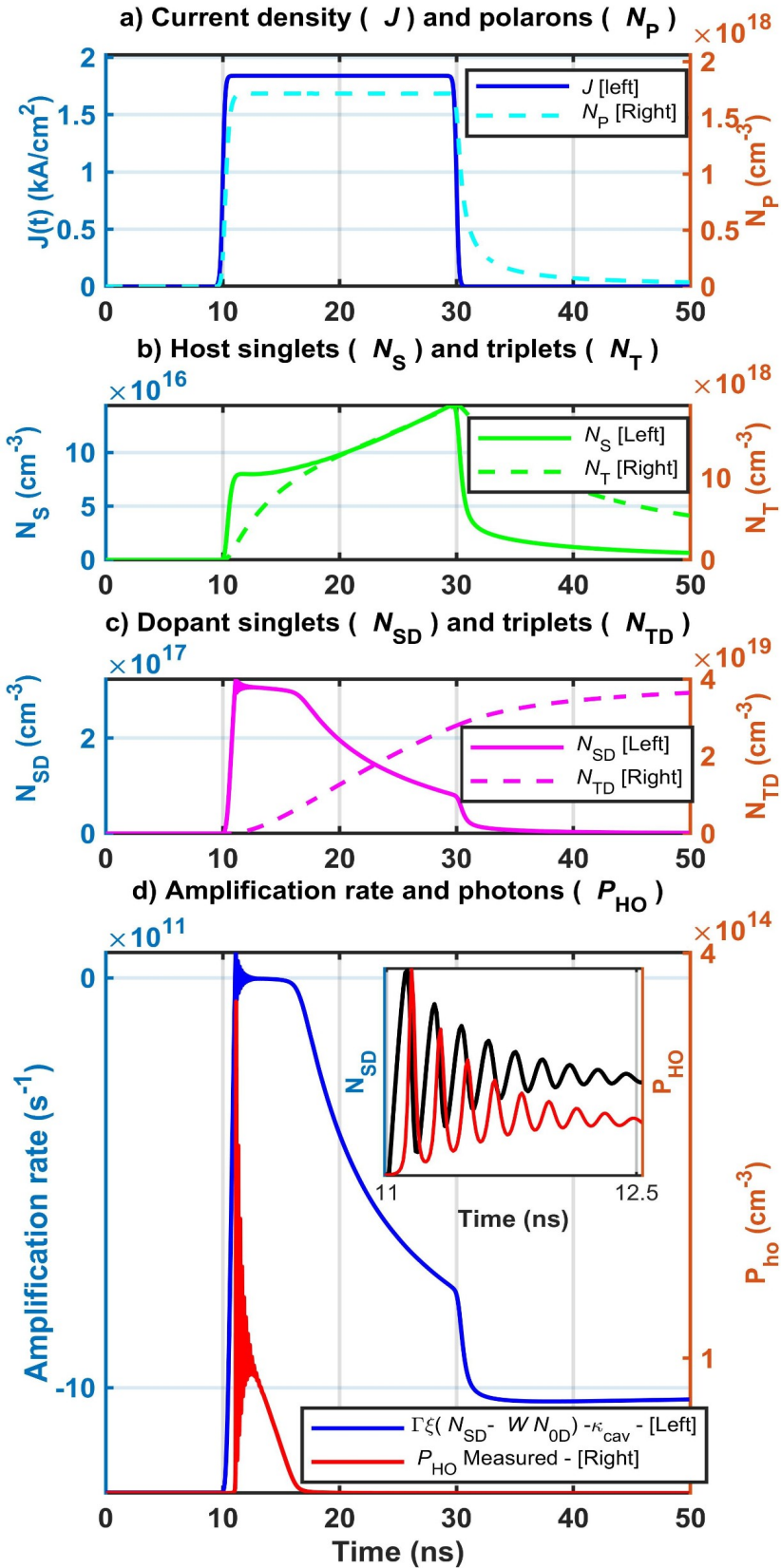


Figure. II.12: Dynamical response of an OLED with a high-quality factor  $Q=1800$  microcavity,  $k_{CAV} = 1.0 \times 10^{12} \text{ s}^{-1}$ , and peak current density  $J = 1.84 \text{ kA/cm}^2$ .  $\gamma = 1.3 \times 10^{-9} \text{ cm}^3 \text{ s}^{-1}$ ,  $k_{DEXT} = 2.0 \times 10^8 \text{ s}^{-1}$ ,  $k_{ISC} = k_{ISCD} = 2.2 \times 10^4 \text{ s}^{-1}$ ,  $k_T = 6.5 \times 10^2 \text{ s}^{-1}$ ,  $W = 1.5 \times 10^{-3}$   $\beta_{sp} = 5.0 \times 10^{-4}$ . Inset shows an oscillation of photons in quadrature with that of the dopant-singlet density.

The dynamical responses calculated with a peak current density of  $J = 1.84 \text{ kA/cm}^2$  are plotted in Fig. II.12 with the same color code as in Fig. II.11.

Figure II.12.a presents  $J(t)$  and  $N_p$  versus time. In Fig. 3.3.2.b the host triplet NT is seen to increase monotonously until the end of the pulse to  $1.8 \times 10^{19} \text{ cm}^{-3}$  which is more than 2 order of magnitude larger than the host singlet maximum ( $1.4 \times 10^{17} \text{ cm}^{-3}$ ). It decays very rapidly afterwards. In Fig.II.12.c the dopant singlets NSD increase sharply to a maximum of  $3.0 \times 10^{17} \text{ cm}^{-3}$ , reached 1.1 ns after the pulse onset, where it clamps for another 2ns before it decays slowly until the end of the pulse and then decays quickly again. The maximum of NSD is somewhat smaller than in the previous case of Fig. 3.3.1, as a consequence of the clamping, a first indication of lasing.

In Fig. II.12.d, the photon density starts with a steep rising flank, reaches a sharp maximum of  $3.6 \times 10^{14} \text{ cm}^{-3}$ , 1.1 ns after the beginning of the pulse and shows a damped GHz oscillation followed by a fast decay. The photon-density peak is three orders of magnitude larger than in the OLED case of Fig. II.12.d for a smaller current density. The net-amplification rate rises from  $-1.2 \times 10^{12} \text{ s}^{-1}$  up to a positive value ( $+6.1 \times 10^{10} \text{ s}^{-1}$ ) before slowly decaying during the excitation pulse down to  $-1.0 \times 10^{12} \text{ s}^{-1}$ . The positive value means that amplification of the light is taking place while the dopant exciton population clamps at its threshold value. This is a demonstration of lasing.

Note that the oscillations of the photon density become less damped when the electrical injected pulse amplitude increases. The inset of Fig. II.12.d. exhibits 6 GHz photon oscillations in quadrature with the oscillation of NSD. Such oscillations in the light intensity are typical for lasers described by two or more coupled rate-equations and are called relaxation oscillations [38]. For this reason, and on the basis of the proposed model, we predict the existence of GHz relaxation oscillations in OLDs lying at the origin of a large variety of dynamical behaviours similar to conventional semiconductor diode lasers [38].

In order to highlight the difference between spontaneous and stimulated emissions, fig.II.13 shows the net-amplification rate and photon density versus time for both the weak micro-cavity OLED case ( $Q = 6$ ) of fig. 3.3.1 and the high-Q micro-cavity case ( $Q = 1800$ ) of fig. II.12.

Three signatures of the lasing mechanism can be identified. Firstly, the clamping of NSD occurs during the maximum of emission for the high-Q case (magenta line) and not for the low-Q case (magenta dots) (fig. II.13.a). Secondly, the increase from a negative to a positive value close to zero of the net-amplification only occurs in the high-Q cavity case (blue solid line in fig. II.12.d). A third signature of lasing is the dramatic increase in the photon density by more than 3 orders of magnitude illustrating the difference between lasing (red solid line) and spontaneous emission (red dots) as shown in fig. II.13.b.

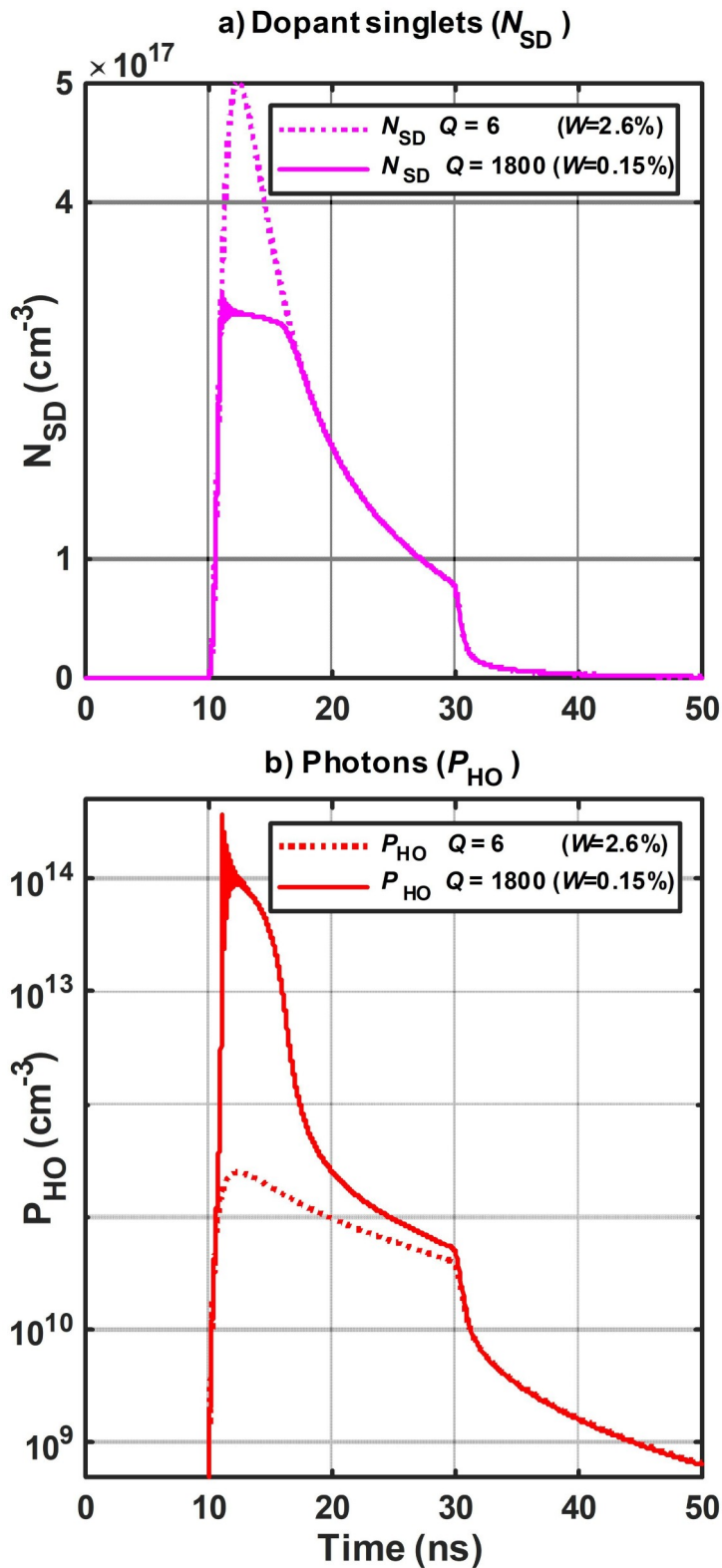


Figure. II.13: Comparison between spontaneous and stimulated emission high-lighting the signatures of lasing. a) Singlet densities versus time for the low-Q micro-cavity (magenta dotted line) and high-Q micro-cavity (magenta solid line). Note the clamping of  $N_{SD}$  in the high-Q case. b) Photon densities versus time for the low-Q (red dotted line) and high-Q micro-cavity (red solid line). Note the logarithmic scale.



### II.3.3.1. Threshold estimation

The laser threshold will be estimated for the Alq<sub>3</sub>:DCM guest-host system for two different gain values. The first is for  $\xi_1 = 1.4 \times 10^{-5} \text{ cm}^3 \text{ s}^{-1}$  as in Table 1 and 2 and the second for  $\xi_2 = 4.8 \times 10^{-6} \text{ cm}^3 \text{ s}^{-1}$ , a gain value similar to that of BsB-Cz(4,4'-bis[(N-carbazole)styryl]-biphenyl), which is the gain medium in the experiment reported by Adachi's group [2]. Although BsB-Cz is not a guest-host system, Förster transfer is so fast (87 ps) that we assume in lowest approximation the guest to be "transparent". In both cases all other model parameters are those given in Tables 2, column 2 for OLED 1 except  $k_{ST} = 1.0 \times 10^{-12} \text{ cm}^3 \text{ s}^{-1}$  and  $k_{STD} = 1.0 \times 10^{-12} \text{ cm}^3 \text{ s}^{-1}$ . The amplitude of the sigmoid shaped pulsed current density is varied from 0.1 kA/cm<sup>2</sup> to 10 kA/cm<sup>2</sup> close to the maximum current density achieved in this study. For each of the applied current amplitudes, we integrate the photon densities over the pulse duration. Figure II.14 displays the calculated L-I curves in a log-log plot for 4 different values of the Q-factor,  $Q_1 = 1,000$  (black),  $Q_2 = 3,000$  (dark blue),  $Q_3 = 10,000$  (light blue),  $Q_4 = 30,000$  (green) and two different values for  $W$  (i.e.  $W_1 = 1.5 \times 10^{-3}$  (dashes) and  $W_2 = 0$  (solid lines)). Figure II.14.a shows the first case (Alq<sub>3</sub>:DCM as gain medium; parameters as in Table 2) while Figure 3.4.1.b presents the second case with a gain coefficient equal to that of BsB-Cz and reduced singlet-triplet absorption  $k_{ST} = 1.0 \times 10^{-12} \text{ cm}^3 \text{ s}^{-1}$  and  $k_{STD} = 1.0 \times 10^{-12} \text{ cm}^3 \text{ s}^{-1}$  [2]. The S-shaped curves in log-log scale are typical of laser characteristics. The laser threshold current is defined as the inflexion point of the L-I curve. In the first case, with  $W_1 = 1.5 \times 10^{-3}$  the laser thresholds are estimated as  $J_{th4\_1} = 0.18 \text{ kA/cm}^2$  for  $Q_4 = 30,000$ ;  $J_{th3\_1} = 0.28 \text{ kA/cm}^2$  for  $Q_3 = 10,000$ ;  $J_{th2\_1} = 0.63 \text{ kA/cm}^2$  for  $Q_2 = 3,000$  and  $J_{th1\_1}$  is predicted  $1.78 \text{ kA/cm}^2$ . With  $W = 0$ , the threshold currents are lower with  $J_{th4\_0} = 0.04 \text{ kA/cm}^2$  for  $Q_4 = 30,000$ ;  $J_{th3\_0} = 0.11 \text{ kA/cm}^2$  for  $Q_3 = 10,000$ ;  $J_{th2\_0} = 0.44 \text{ kA/cm}^2$  for  $Q_2 = 3,000$ , while  $J_{th1\_0} = 1.58 \text{ kA/cm}^2$ . We recall the significance of  $W$  (see Sec, 3.2.8). Above threshold  $W \sim 0$ , whereas below threshold a value  $>0$  applies. Hence, the real threshold will lay somewhere between the two values obtained for each  $Q$ . In Fig. II.14.b, for  $W = 1.5 \times 10^{-3}$  (solid curves), the respective thresholds are  $J_{th4} = 0.19 \text{ kA/cm}^2$ ,  $J_{th3} = 0.36 \text{ kA/cm}^2$ ,  $J_{th2} = 0.89 \text{ kA/cm}^2$  and  $J_{th1} = 2.37 \text{ kA/cm}^2$ . With  $W = 0$  (dashed curves), the threshold currents are lower with  $J_{th4} = 0.08 \text{ kA/cm}^2$ ,  $J_{th3} = 0.25 \text{ kA/cm}^2$ ,  $J_{th2} = 0.8 \text{ kA/cm}^2$  and  $J_{th1} = 2.35 \text{ kA/cm}^2$ . As a first conclusion, we obtain a laser threshold as low as  $0.54 \text{ kA/cm}^2$  with a gain coefficient equal to that of BsB-Cz as gain medium and for the smaller values for  $\kappa_{ST}(D)$  ( $1 \times 10^{-12} \text{ cm}^3 \text{ s}^{-1}$  [39]), like in the experiment of Adachi's group, provided that the quality factor is in the range  $3,000 < Q < 10,000$  and without residual absorption ( $W = 0$ ). To investigate further this finding, we show in Fig. II.15 a log-log plot of the threshold current density as a function of the quality factor for two values of  $W$ , i.e.  $1.5 \times 10^{-3}$  (dashed line) and  $0$  (solid line) Red curves are for  $\xi_1 = 1.4 \times 10^{-5} \text{ s}^{-1}$  (Alq<sub>3</sub>:DCM) and blue curves for  $\xi_2 = 4.8 \times 10^{-6} \text{ s}^{-1}$ . (BsB-Cz). Obviously, these curves confirm the decrease of the threshold current density with the increase of the quality factor  $Q$ . Two different types of decreasing functions can be distinguished. For  $W_2 = 0$ , the functions (blue and red solid lines) show a continuous linear decrease (in log-log scale), whereas for  $W_1 = 1.5 \times 10^{-3}$  (red and blue dashed lines) the function exhibits a saturation towards  $0.13$ - $0.15 \text{ kA/cm}^2$ . This saturation occurs when the residual absorption loss annihilates the benefice of a higher quality factor. From Fig. II.15, one can identify more precisely the conditions to obtain a threshold current density as low as  $0.54 \text{ kA/cm}^2$ : In the first case, with Alq<sub>3</sub>:DCM as a gain medium, the quality factor is to exceed  $Q_1 \sim 2,100$  with  $W = 0$ , and  $Q_1 \sim 3,100$  with  $W_1 = 1.5 \times 10^{-3}$ . In the second case, with BSB-Cz gain value and reduced STA, the quality factor

is to exceed  $Q_2 \sim 4,300$  with no residual absorption ( $W = 0$ ) and  $Q_2 \sim 5,500$  for  $W_1 = 1.5 \times 10^{-3}$ .

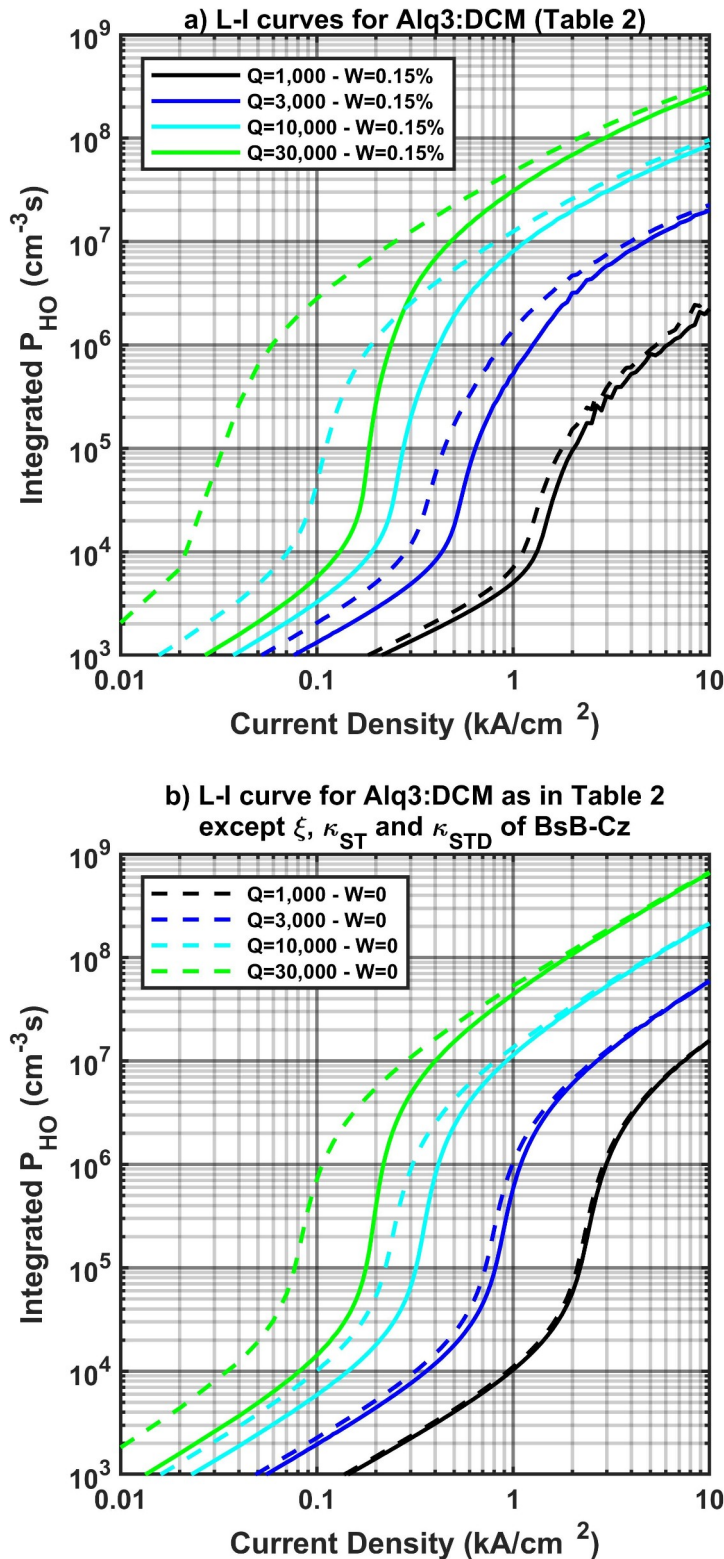


Figure. II.14: Light-current curve as a function of the quality factor for different gain media. a) Gain medium is Alq<sub>3</sub>:DCM guest-host system with  $\xi_1 = 14 \times 10^6 \text{ cm}^3 \text{ s}^{-1}$ . b) Gain coefficient  $\xi_2 = 4.8 \times 10^6 \text{ cm}^3 \text{ s}^{-1}$ ,  $\kappa_{ST} = 1 \times 10^{-12} \text{ cm}^3 \text{ s}^{-1}$ ,  $\kappa_{STD} = 1 \times 10^{-12} \text{ cm}^3 \text{ s}^{-1}$  as for BsB-Cz [2]. Solid lines are with  $W_1 = 1.5 \times 10^{-3}$  and dashed lines with  $W_2 = 0$ .

### II.3.4. Conclusion on the model

We have established a new model based on rate equations for the dynamics of the spontaneous and stimulated emission of a red emitting OLD. The model, which is also valid for OLEDs with small quality factors, takes account of the guest-host system, where the host-singlet excitons form a reservoir from which the dopant-singlet excitons are delivered. A key parameter  $W$  was introduced to take into account the residual absorption resulting from the partial overlapping of the (broad) absorption and (narrow) emission spectra.

On the basis of the proposed model, we simulate the dynamical responses of different OLEDs to a sigmoid-like pulsed electrical excitation with a duration of 20ns and various peak current amplitudes. The calculated time responses include the population densities of polarons, of host singlets and triplets, of dopant singlets and triplets, and of photons. The dynamical behaviours of OLEDs in a low-Q cavity on the one hand and in a high-Q cavity with  $Q = 1,800$ , on the other hand, are simulated and compared.

The predicted optical response of the high-Q OLED exhibits (a) a sudden dramatic increase of the photon density for a duration much smaller than that of the electrical excitation with (b) a damped oscillation in the GHz regime and (c) clamping behaviour for the dopant-singlet density. This is reminiscent of laser action and leads us to predict the existence of relaxation oscillations in OLDs very similar to those reported and extensively studied in conventional III-V laser diodes [38].

The comparison between OLED and OLD highlights three signatures of the lasing phenomenon. Firstly, the optical response after the pulse onset is orders of magnitude larger in the laser case than in the OLED case. Secondly the dopant singlet density is clamped during the lasing action and, thirdly, the sign of the net-amplification changes from negative to positive. The light-current curves have been calculated for different values of the quality factor, and for two different organic gain media, ie Alq<sub>3</sub>:DCM and BsB-Cz. On the basis of the parameter set used for Fig. 3.3.2 and with  $\xi^2 = 4.8 \times 10^{-6} \text{ cm}^3 \text{ s}^{-1}$ , we predict for the latter organic compound a laser threshold as low as  $0.54 \text{ kA cm}^{-2}$  if the quality factor is taken as  $Q = 4,300$  and provided that there is no residual absorption ( $W = 0$ ). Therefore, the model confirms the possibility of the threshold-current density of  $540 \text{ A/cm}^2$  observed in the recent first experimental indication of lasing in an OLED [2].

Finally, as a guide-line for the fabrication of OLDs, we show the predicted laser threshold as a function of the quality factor for different configurations.

Among the different parameters to be identified to fabricate the organic diode laser, several points needs to be clarified further such as the choice of the optimal laser gain medium and the maximum Q factor that can be achieved with a DFB cavity.

Current density at threshold ( $J_{th}$ ) vs quality factor ( $Q$ )

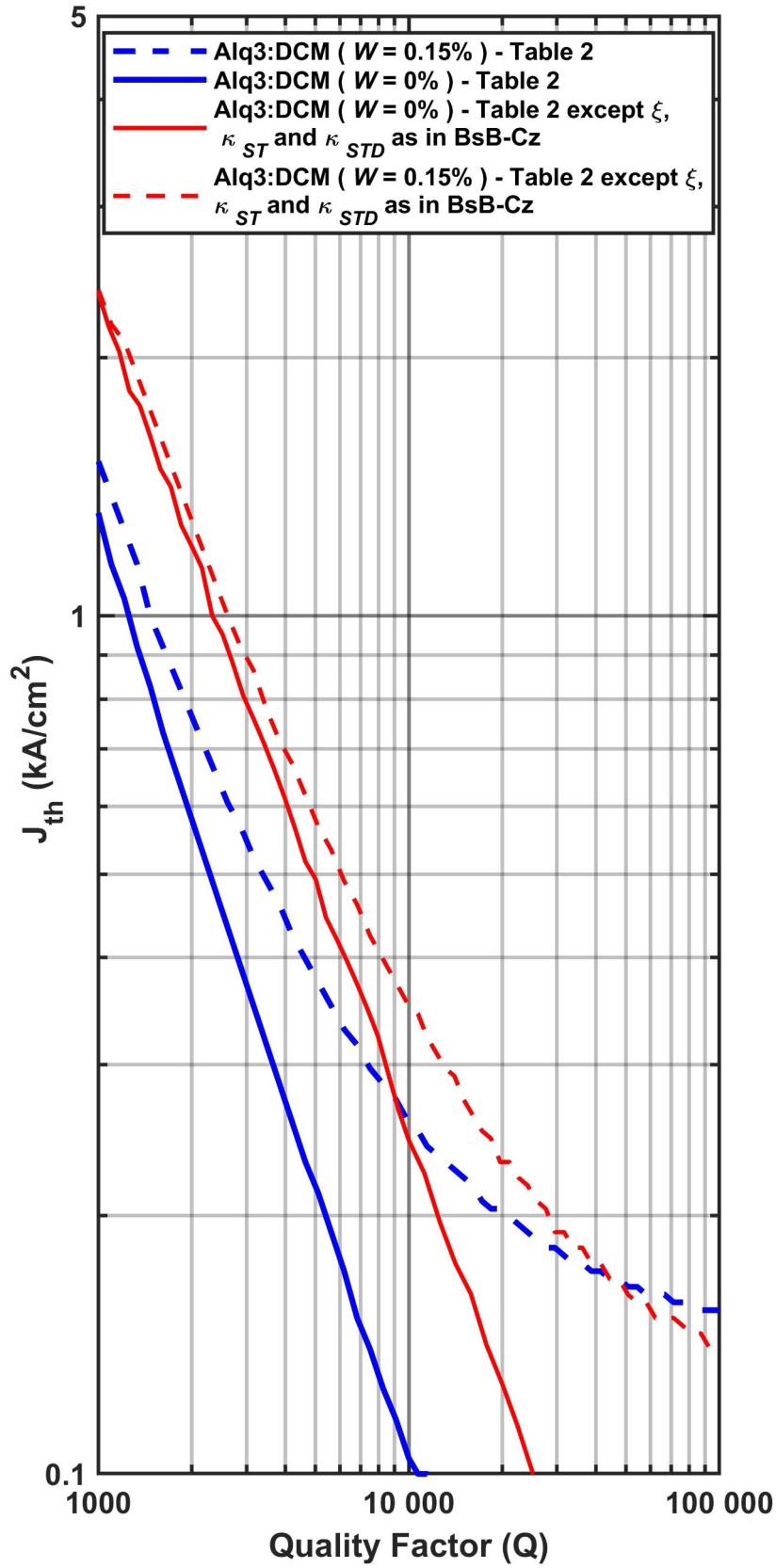


Figure. II.15: Threshold current density as a function of the quality factor  $Q$  for the two cases of Fig. 7.a and 7.b.

## II.4. Optical design

### II.4.1. Objectives

This section is dedicated to the design of the optical part of the organic laser diode. This includes the choice of the optimal organic gain medium from its gain and its losses, and the optimal design of the laser cavity geometry.

The relevant parameters are those present in equation II.45:

$$\frac{dP_{HO}}{dt} = \beta_{sp} \kappa_{SD} N_{SD} + \left( \Gamma \xi (N_{SD} - W N_{0D}) - \kappa_{CAV} \right) P_{HO}$$

In that equation, we focus on the stimulated emission term that is the second right-hand-side term where four parameters can be identified ;

- The confinement factor  $\Gamma$  that depend on the waveguide geometry and the central wavelength considered
- The gain coefficient that depends on the chosen material only :  $\xi = \frac{cg}{n N_{SD}} = K \frac{hc^3}{n^2 \lambda_p}$  Eq.II.55
- The residual absorption  $W$  depends on the chosen material and in a less extend to the cavity profile.
- The cavity photon decay rate is related to the quality factor of the cavity by eq. II.57:  $Q = \omega_0 \tau_{CAV}$  where  $\kappa_{CAV} = \frac{1}{\tau_{CAV}} = 2\pi \frac{c}{n \lambda_0} \frac{1}{Q}$  Eq. II.58. It depends on the waveguide geometry and the cavity geometry and on  $\lambda_0$  the central wavelength which is the first input parameter to consider in order to design a DFB cavity.

The dependence of these parameters to the input parameters is presented in the table below

	Material	$\lambda$	Waveguide geometry	Cavity geometry
Gain coefficient $\xi$	✓			
Confinement factor $\Gamma$		✓	✓	
Residual absorption $W_0$	✓			(✓)
Cavity photon decay rate $K_{cav}$		✓	✓	✓

Owing to these dependencies and potential time-consuming multiple-parameter calculations, the order in which the different parameters will be studied needs to be carefully considered.

Because of a single dependence, the parameter to be considered first is the gain coefficients  $x$ . We will therefore compare materials (section II.4.2. ) on the basis of their gain coefficients  $x$  (section II.4.2.1. ), before comparing their residual absorption (section II.4.2.2. ). From the selected laser gain material, the resonance wavelength  $\lambda$  of the laser (central wavelength) will be defined. On the basis of this wavelength, the OLED stack will be investigated from the optical waveguide point of view (section II.4.3. ) so as to maximize the confinement factor. Finally, with this new geometrical inputs, together with the calculated effective index, the cavity geometry will be defined and its quality factor  $Q$  will be calculated (section II.4.5. ).

## II.4.2. Laser gain material

The current study focuses on red-emitting materials for a double reason: Firstly, the larger the wavelength, the larger the patterns, and thus the easier to fabricate. Secondly, silicon photodiodes exhibit a slightly larger responsivity in the red range for example the responsivity of APD430A2 in 600nm is equal to 50A/W while in 400nm it equals to 22A/W.

Also, the research group has summ up experiences with different red laser material:

- Alq<sub>3</sub> doped with 2% in weight of DCJTb has been used with photonic crystal cavity [39]
- Alq<sub>3</sub> doped with 2% in weight of DCM2 has been used with multilayered microcavity [40]

As mentioned in the previous paragraph, the objective is to choose the laser gain material offering the lowest laser threshold. If one consider several cavities characterized by the same photon decay rate  $K_{cav}$ , but filled with different laser gain material, the threshold will be determined by the term :

$$\Gamma \xi (N_{SD} - W N_{0D}) \quad \text{Eq. (II.59)}$$

In order to choose the most relevant laser gain materials, one need to compare their intrinsic properties ie their gains and their absorption losses:

- The gain is the product of  $\xi \times N_{SD}$  , Laser materials can be compared and sorted as a function of the larger laser gain coefficient  $\xi$  . The comparison of the different material as a function of their gain will be presented in section. II.4.2.1. .
- The material-related-losses are related to the term  $\xi \times W \times N_{0D}$  . Laser materials can also be compared and sorted as a function of the lowest residual absorption  $W$  and then  $\xi \times W$  . However, the residual absorption defined in eq. II.48 depends on the filter profil  $S_{CAV}(\lambda)$  which prevents it to express solely an intrinsic property of the materials. For this reason, a new expression of the intrinsic residual absorption will be derived in II.4.2.2. . The idea is to define a quantity related to the material only and independent of the cavity profile. We will introduce the intrinsic residual absorption  $W_i$  to be defined.

### II.4.2.1. Laser gain coefficient of different organic compounds

The considered red electroluminescent materials known respectively as DCM, DCM2 and DCJTb are shown respectively on fig. II.16a, b, and c. Figure II.16.d. presents the blue laser gain medium used by Adachi's Group for the sake of comparison [2].

- DCM stands for 4-(Dicyanomethylene)-2-methyl-6-(4-dimethylaminostyryl) -4H-pyran. Its molecular weight is 303.36 g/mol and its molecular structure is presented in fig. II.16.a.
- DCM2 stands for [2-methyl-6-[2-(2,3,6,7-tetrahydro-1H,5H-benzo[*ij*]quinolizin-9-yl) ethenyl]-4Hpyran-4-ylidene] propane-dinitrile. The molecular weight is 355.43 g/mol and its structure is presented in fig. II.16.b.
- DCJTb stands for 4-(dicyanomethylene)-2-t-butyl-6(1,1,7,7-tetramethyljulolidyl-9-enyl)-4H-pyran. The molecular weight is 453.62 g/mol and its molecular structure is presented in fig.II.16.c.
- BsB-Cz stands for 4,4'-Bis (4- (9H-carbazol-9-yl) styryl) biphenyl. The molecular structure is presented in fig. II.16.c. The molecular weights of the molecules is 688.86 g/mol.

Different laser gain coefficient extracted from the literature or calculated from it are presented in table 11. The laser gain coefficient is calculated from the linear gain  $g$  in  $\text{cm}^{-1}$  :

$$\xi = g \frac{c}{n} \frac{1}{N_{SD}} \text{ Eq. (II.60)}$$

where  $n$  is the index of refraction in the material and  $c$  the light velocity, and  $N_{SD}$  the density of excited states. The laser gain coefficient is calculated from the cross section by :

$$\xi = \frac{\sigma \times c}{n} \text{ Eq. (II.61)}$$

Akselrod et al, reported a laser experiment with  $\text{Alq}_3$  doped with 2.8% of DCM and a cross section of  $\sigma = 1.1 \times 10^{-18} \text{ cm}^2$  corresponding to a laser gain coefficient of  $\xi = 1.9 \times 10^{-6} \text{ cm}^3 \text{ s}^{-1}$  [41]. Deotare et al, reported an ultracompact low-threshold laser with  $\text{Alq}_3$  doped with DCM at 2.5%, based on a photonic crystal nanobeam cavity. The cross section is estimated to  $\sigma = 1 \times 10^{-16} \text{ cm}^2$  corresponding to a laser gain coefficient of  $\xi = 1.8 \times 10^{-6} \text{ cm}^3 \text{ s}^{-1}$  [42]. These values are slightly less than the value  $\xi = 1.4 \times 10^{-5} \text{ cm}^3 \text{ s}^{-1}$  reported by Gärtner [21].

Cehovski et al reported a laser experiment with  $\text{Alq}_3$  doped with different concentrations of DCM2 showing an increase of the laser gain coefficient from  $30 \text{ cm}^{-1}$  to  $89 \text{ cm}^{-1}$  and  $138 \text{ cm}^{-1}$  when the concentration is increased from 1% to 2% and 6% [43]. This corresponds to a laser gain coefficient in the range  $1.3 \times 10^{-6} \text{ cm}^3 \text{ s}^{-1}$  to  $4.8 \times 10^{-6} \text{ cm}^3 \text{ s}^{-1}$  .

Experiments with  $\text{Alq}_3$ :DCJTb are more rare. In 2014, Barbilon et al, reported an organic laser experiment with a SiN photonic crystal cavity filled with  $\text{Alq}_3$  doped with 2% of DCJTb from which the stimulated cross section was estimated to  $\sigma = 8.3 \times 10^{-16}$  . The corresponding estimated laser gain coefficient is  $\xi = 1.5 \times 10^{-5}$  .

For the sake of comparison BSB-Cz show a laser gain coefficient of  $\xi = 4.8 \times 10^{-6} \text{ cm}^3 \text{ s}^{-1}$  [2].

DCJTb appears to offer the largest laser gain coefficient  $\xi = 1.5 \times 10^{-5}$  slightly more than DCM with  $\xi = 1.4 \times 10^{-5}$  , and than DCM2 with  $\xi = 4.8 \times 10^{-6}$  . In any case, DCJTb, DCM and DCM2 exhibit larger laser gain coefficient than BSB-Cz. The difference in the laser gain coefficient is not large as all the parameter exhibits the same order of magnitude. The influence of the concentration has not been explored for all parameters, but from DCM2 it appears that the increase in the concentration in the range 1%-6% increases slightly the laser gain coefficient by less than a four-fold. We can conclude that the choice of a red dye among others solely from their laser gain coefficient will not to be decisive to reduce the laser threshold.

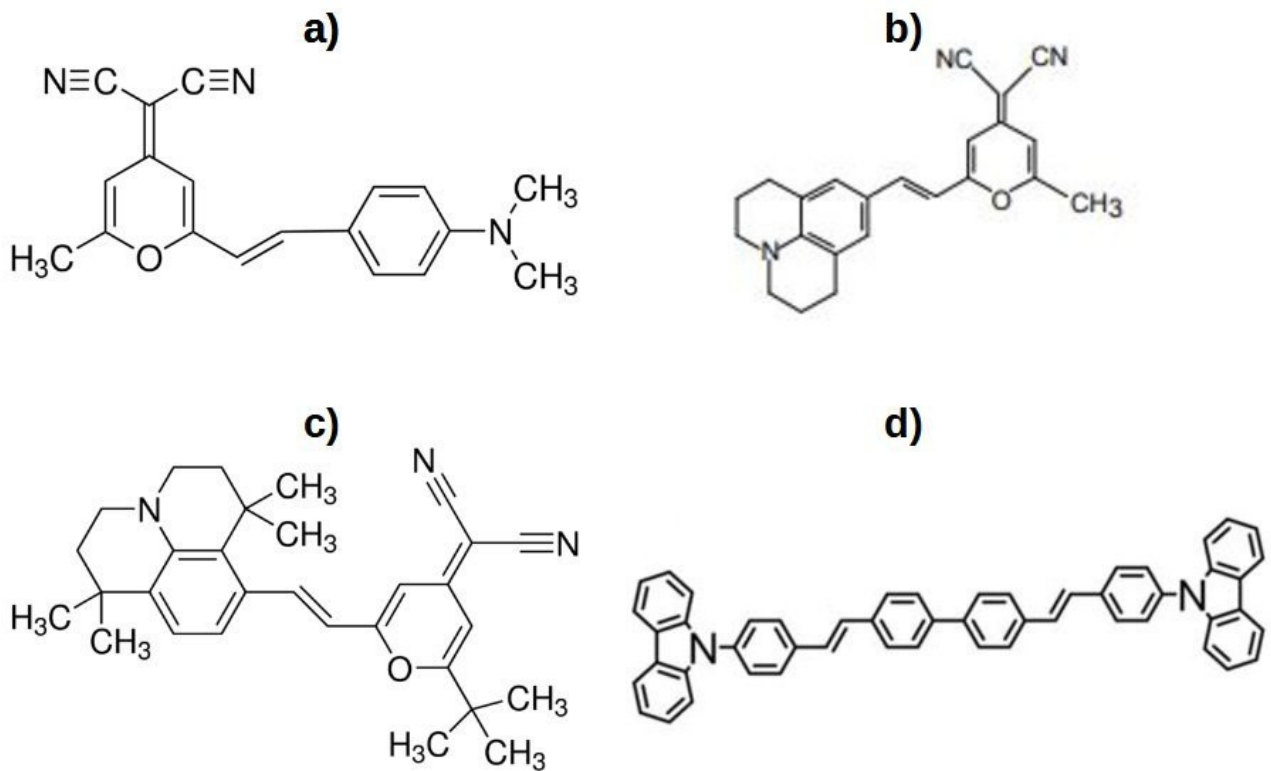


Figure. II.16: Different organic compounds used as laser gain medium: a) DCM, b) DCM2, c) DCJTB, d) BsB-Cz. Dcm, DCM2 and DCJTB are red emitting material, while BsB-Cz is a blue emitting material.

Table II.12: Laser gain coefficient of different organic compounds Calculated with  $n=1.65$

Compounds	$\lambda_{peak}$ (nm)	g (cm <sup>-1</sup> )	Cross section (cm <sup>2</sup> )	Laser gain coeff. (cm <sup>3</sup> s <sup>-1</sup> )	References
Alq <sub>3</sub> :DCM	595		$\sigma = 7.5 \times 10^{-16}$	$\xi = 1.4 \times 10^{-5}$	[21]
Alq <sub>3</sub> :DCM (2.8%)	605		$\sigma = 1.1 \times 10^{-16}$	$\xi = 2.0 \times 10^{-6}$	[41]
Alq <sub>3</sub> :DCM (2.5%)	618		$\sigma = 1 \times 10^{-16}$	$\xi = 1.8 \times 10^{-6}$	[42]
Alq <sub>3</sub> :DCM2 (1%)	612	30	$\sigma = 7.4 \times 10^{-17}$	$\xi = 1.3 \times 10^{-6}$	[43]
Alq <sub>3</sub> :DCM2 (3%)	626	89	$\sigma = 1.8 \times 10^{-16}$	$\xi = 3.2 \times 10^{-6}$	[43]
Alq <sub>3</sub> :DCM2 (6%)	637	138	$\sigma = 2.7 \times 10^{-16}$	$\xi = 4.8 \times 10^{-6}$	[43]
Alq <sub>3</sub> :DCJTB (2%)	660		$\sigma = 8.3 \times 10^{-16}$	$\xi = 1.5 \times 10^{-5}$	[44]
BsB-Cz	450			$\xi = 4.8 \times 10^{-6}$	[2]



## II.4.2.2. Residual absorption

### II.4.2.2.1. Objectives and method

In section II.3. we proposed an organic laser diode model and identified some key parameters playing a role in the laser dynamics and in the laser threshold (singlet-triplet annihilation rate  $\kappa_{st}$ , singlet-polaron annihilation rate  $\kappa_{sp}$  ...) among which the residual absorption  $W$  is a source of losses [45].

The residual absorption invention results from the difference in the absorption phenomenon in the conventional laser and in the organic laser diode. The organic laser gain media exhibit a stronger Stoke-shift between the absorption and the electroluminescence spectra than their inorganic counterparts, resulting in a smaller overlap between the emission of the spectra. Therefore a coefficient  $W$  is introduced in the proposed organic laser diode model to take account of the smaller fraction of the ground state population that can reabsorb the emitted light.

In the current study, we aim at choosing organic gain media from their impact on the laser threshold due to their residual absorption. More precisely, we aim at comparing some organic laser gain media by measuring their absorption and emission spectra and calculate their respective residual absorption. From that we will estimate the impact of the residual absorption on the laser threshold.

This section is organized as follows: In subsection II.4.2.2.2. we define more systematically the intrinsic residual absorption  $W_i$ , in subsection II.4.2.2.3. we present the absorption and emission spectra of the organic compounds listed in the previous section II.4.2. . Finally in section II.4.2.2.4. we calculate their respective residual adsorptions before we compare and discuss them.

### II.4.2.2.2. Theory of the residual absorption and intrinsic residual absorption

An expression for the residual absorption  $W$  is derived as follows:

Figure II.17 sketches the electroluminescence spectrum  $S_E(\lambda)$  of an organic material normalized to its maximum ie,  $S_E(\lambda_E)=1$ . Such an organic material also present an absorption spectrum  $S_{abs}(\lambda)$  normalized to its maximum such that  $S_{ABS}(\lambda_{ABS})=1$ . We consider that this organic material behaves as a laser gain material located in a laser cavity which transmission spectrum  $S_{CAV}(\lambda)$  exhibits a resonance peak at  $\lambda_{Res}$  and it is normalized with:

$$\int S_{CAV}(\lambda) d\lambda = 1 \quad \text{Eq. (II.62)}$$

The normalized spectral distribution of the photon density in the laser mode  $p_{HO}(t, \lambda)$  in the active layer at time  $t$  is that of the electroluminescence spectrum  $S_E(\lambda)$  filtered by the cavity profile  $S_{CAV}(\lambda)$  and it reads:

$$p_{HO}(t, \lambda) = P_0(t) \frac{S_{CAV}(\lambda) S_E(\lambda)}{\int S_{CAV}(\lambda) S_E(\lambda) d\lambda} \quad \text{Eq. (II.63)}$$

where  $P_0(t)$  is the total photon density satisfying

$$P_0(t) = \int p_{HO}(t, \lambda) d\lambda \quad \text{Eq. (II.64)}$$

Provided that the stimulated emission phenomenon occurs, the rate of stimulated emission photon density  $d p_{HO}/dt|_{Stim.Em.}$  in the wavelength interval  $d\lambda$  centered at a given wavelength  $\lambda$  is proportional firstly to the density of the available singlet excitons NSD that recombine and are distributed spectrally among the different vibrational sub-levels following the normalized

electroluminescence spectra  $SE(\lambda)$ , and secondly to the (stimulating) photons with density  $p_{HO}(t, \lambda)$ :

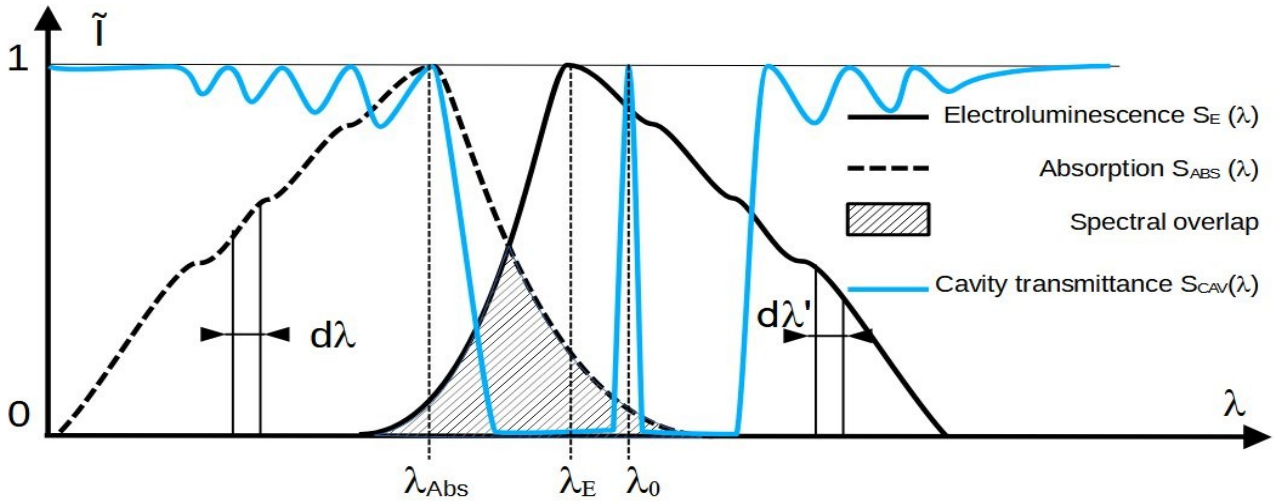


Figure. II.17: Absorption  $S_{ABS}(\lambda)$  (dashed line) and emission  $S_E(\lambda)$  (solid line) spectra of an organic material with a cavity spectral profile  $S_{CAV}(\lambda)$  (solid blue line). Spectral overlap between the emission and absorption (shaded area).

$$\left. \frac{d p_{HO}(t, \lambda)}{dt} \right|_{Stim.Em.} d \lambda = \xi_E N_{SD}(t) S_E(\lambda) p_{HO}(t, \lambda) d \lambda \quad \text{Eq. (II.65)}$$

where  $\xi_E$  is a gain coefficient and  $S_E(\lambda)$  is the electroluminescence spectrum normalized to  $S_E(\lambda_E)=1$ . Substituting into gives:

$$\left. \frac{d p_{HO}(t, \lambda)}{dt} \right|_{Stim.Em.} d \lambda = \xi_E P_0(t) \frac{N_{SD}(t) S_E(\lambda)^2 S_{CAV}(\lambda)}{\int S_{CAV}(\lambda) S_E(\lambda) d \lambda} d \lambda \quad \text{Eq. (II.66)}$$

Similarly, the rate of re-absorbed photon density  $\left. d p_{HO}/dt \right|_{Re.Abs.}$  is proportional to the available ground state density  $N_{0D}$ , to the absorption spectra  $S_A(\lambda)$  and to the density of photons  $p_{HO}(t, \lambda)$ :

$$\left. \frac{d p_{HO}(t, \lambda)}{dt} \right|_{Re.Abs.} d \lambda = \xi_A N_{0D}(t) S_A(\lambda) p_{HO}(t, \lambda) d \lambda \quad \text{Eq. (II.67)}$$

where  $\xi_A$  is the absorption coefficient at maximum absorption and  $S_A(\lambda)$  is the absorption spectrum normalized to  $S_A(\lambda_A) = 1$ . Combining into gives:

$$\left. \frac{d p_{HO}(t, \lambda)}{dt} \right|_{Re.Abs.} d \lambda = \xi_A P_0(t) N_{0D}(t) \frac{S_A(\lambda) S_{CAV}(\lambda) S_E(\lambda)}{\int S_{CAV}(\lambda) S_E(\lambda) d \lambda} d \lambda \quad \text{Eq. (II.68)}$$

The net stimulated emission is the difference between Eq. II.66 and Eq. II.68 to be integrated:

$$\int \left. \frac{d p_{HO}(t, \lambda)}{dt} \right|_{Net.Stim.} d \lambda = \int \left( \left. \frac{d p_{HO}(t, \lambda)}{dt} \right|_{Stim.Em.} - \left. \frac{d p_{HO}(t, \lambda)}{dt} \right|_{Re.Abs.} \right) d \lambda = P_0(t) \int \left[ \xi_E N_{SD}(t) S_E(\lambda) - \xi_A N_{0D}(t) S_A(\lambda) \right] \times \frac{S_E(\lambda) S_{cav}(\lambda)}{\int S_{CAV}(\lambda) S_E(\lambda) d \lambda} d \lambda \quad \text{Eq. (II.69)}$$

(Eq. 1) We introduce  $M_E$  and  $M_A$  as

$$M_E = \frac{\int S_E(\lambda) S_E(\lambda) S_{CAV}(\lambda) d\lambda}{\int S_E(\lambda) S_{CAV}(\lambda) d\lambda} \text{ Eq. (II.70)}$$

and

$$M_A = \frac{\int S_A(\lambda) S_E(\lambda) S_{CAV}(\lambda) d\lambda}{\int S_E(\lambda) S_{CAV}(\lambda) d\lambda} \text{ Eq. (II.71)}$$

with

$$P_{HO|Net.Stim}(t) = \int p_{HO|Net.Stim}(t, \lambda) d\lambda \text{ Eq. (II.72)}$$

simplifies to:

$$\frac{dP_{HO}(t)}{dt} |_{Net.Stim} = P_0(t) [\xi_E M_E N_{SD}(t) - \xi_A M_A N_{OD}(t)] \text{ Eq. (II.73)}$$

Factorizing  $\xi_E M_E(\lambda)$ , the term in front of  $N_{OD}$  becomes:

$$W = \frac{\xi_A M_A}{\xi_E M_E} \text{ Eq. (II.74)}$$

it is the fraction of the ground state participating to the re-absorption.

The final rate equation for the photon density in the laser mode reads

$$\frac{dP_{HO}(\lambda)}{dt} = P_0 \xi_E M_E [N_{SD} - W N_{OD}] \text{ Eq. (II.75)}$$

In order to compare the material independently of the laser cavity, we consider the case where the cavity profile do no exhibit any selection (I.e; a flat function) thus  $S_{cav}(\lambda)$  is a constant independent of  $\lambda$  :

$$S_{cav}(\lambda) = S_{cav} \text{ Eq. (II.76)}$$

$M_E$  and  $M_A$  simplify to :

$$M_E = \frac{S_{CAV} \int S_E(\lambda) S_E(\lambda) d\lambda}{S_{CAV} \int S_E(\lambda) d\lambda}$$

and,

$$M_A = \frac{S_{CAV} \int S_A(\lambda) S_E(\lambda) d\lambda}{S_{CAV} \int S_E(\lambda) d\lambda}$$

Finally, without cavity filtering, the ratio  $M_A/M_E$  reads

$$W_i = \frac{\int S_A(\lambda) S_E(\lambda) d\lambda}{\int S_E(\lambda) S_E(\lambda) d\lambda} \text{ Eq. (II.77)}$$

In the special case of a constant cavity profile, the residual absorption is related to the material properties only, and not to the cavity. We call Intrinsic Residual Absorption the term  $W_i$  that opens the possibility to compare the material with each other.



Figure. II.18: Photoluminescence of 5 organic compounds diluted in chloroform (1 $\mu$ mol/ml), from left to right chloroform, BsB-Cz, Alq<sub>3</sub>Alq<sub>3</sub>, DCM, DCM2, DCJTb exposed to UV light from a LED emitting at 405nm.

**Table II.13: List of samples Samples number(peak wavelength)**

Type of samples	DCM	DCM2	DCJTb	BsB-Cz
Solution; 1 $\mu$ mol/ml in 5 ml of chloroform	#1	#5	#9	#13
Type 1 organic heterostructure: m-MTDATA (35nm)/NPD (15nm)/Alq <sub>3</sub> :Dopant(1%) (35nm)/Alq <sub>3</sub> (25nm)/LiF(1nm)/Al (300nm)	#2	#6	#10	
Type 2 organic heterostructure: m-MTDATA (35nm)/NPD (15nm)/Alq <sub>3</sub> :Dopant(2%) (35nm)/Alq <sub>3</sub> (25nm)/LiF(1nm)/Al (300nm)	#3	#7	#11	
Type 3 organic heterostructure: m-MTDATA (35nm)/NPD (15nm)/Alq <sub>3</sub> :Dopant(4%) (35nm)/Alq <sub>3</sub> (25nm)/LiF(1nm)/Al (300nm)	#4	#8	#12	
Type 4 organic heterostructure: NPD (60nm)/ BsB-Cz (150nm)				#14

#### II.4.2.2.3. Absorbance and electroluminescence spectra

The spectra reported in the literature are very often measured in different solvent and the luminescence spectra differ from one to another. More rarely, luminescence spectra are measured with the materials in thin film and even in this shape, significant differences in the spectra appear from one experiment to another leading to questioning the quality or the purity of the compounds from one experiment to another [46]. Because the ultimate goal is to be able to build organic laser diodes with the organic gain material evaporated in the emitting layer of an organic hetero-structure, we aim at calculating the residual absorption of the materials in the form of a solid state (ie thin layer). Therefore, new measurements of the luminescence and the absorption spectra of the compounds that will be used for making the devices are required. More precisely, we aim at measuring both the photoluminescence observed under optical excitation and electroluminescence measured under electrical excitation. The latter requires OLED fabrication. Different samples are then prepared :

- Solution are prepared at a molar concentration of 1  $\mu\text{mol/ml}$  mixed in 5 ml of chloroform. Chloroform is used for the sake of comparison with [46]. Before measurement, the samples are preliminary centrifugated so as to decant the undissolved particles and only the colloid-free part of the solution is withdrawn and used for measurements. This prevent base line errors particularly in the 600-900nm wavelength range. Chloroform has been preferred over ethanol and anisole because of less colloids and less absorption. Four solutions have been prepared containing DCM, DCM2, DCJTb and BSB-Cz.
- To acquire the electroluminescence spectra four types of organic heterostructure (OLED) are evaporated under a vacuum of  $8 \cdot 10^{-8}$  Torr with a deposition rates are  $<0.2\text{nm/s}$  on 0.7mm glass substrate covered with a 140nm thick ITO Layer. DCM, DCM2, and DCJTb named 'Dopant' in the following heterostructures are evaporate at a lower rate.
  - Type 1 consists of m-MTDATA (35nm)/NPD (15nm)/ Alq<sub>3</sub>:Dopant (35nm)/ Alq<sub>3</sub>(25nm)/ LiF(1nm)/Al (300nm). Doping is 1%
  - Type 2 consists of m-MTDATA (35nm)/ NPD (15nm)/ Alq<sub>3</sub>:Dopant (35nm)/ Alq<sub>3</sub>(25nm)/ LiF(1nm)/Al (300nm). Doping is 2%
  - Type 3 consists of m-MTDATA (35nm)/ NPD(15nm)/ Alq<sub>3</sub>:Dopant (35nm)/ Alq<sub>3</sub>(25nm)/ LiF(1nm)/Al (300nm). Doping is 4%
  - Type 4 organic heterostructure consisting of NPD (60nm)/ BSB-Cz (150nm)

The measurements are carried out with the following instruments:

- Absorption spectra are acquired with a Jasco V-630 spectrophotometer (300-900nm).
- Photoluminescence is measured with a UV-Vis spectrofluorimeter Fluorimax4+ (Horiba)
- Electroluminescence is measured with a homemade OLED characterization setup including an Ocean Optics 2000 spectrophotometer. Measurement are performed under a bias voltage of 10V. The integration time to acquire noise-minimized spectra is 3 seconds.

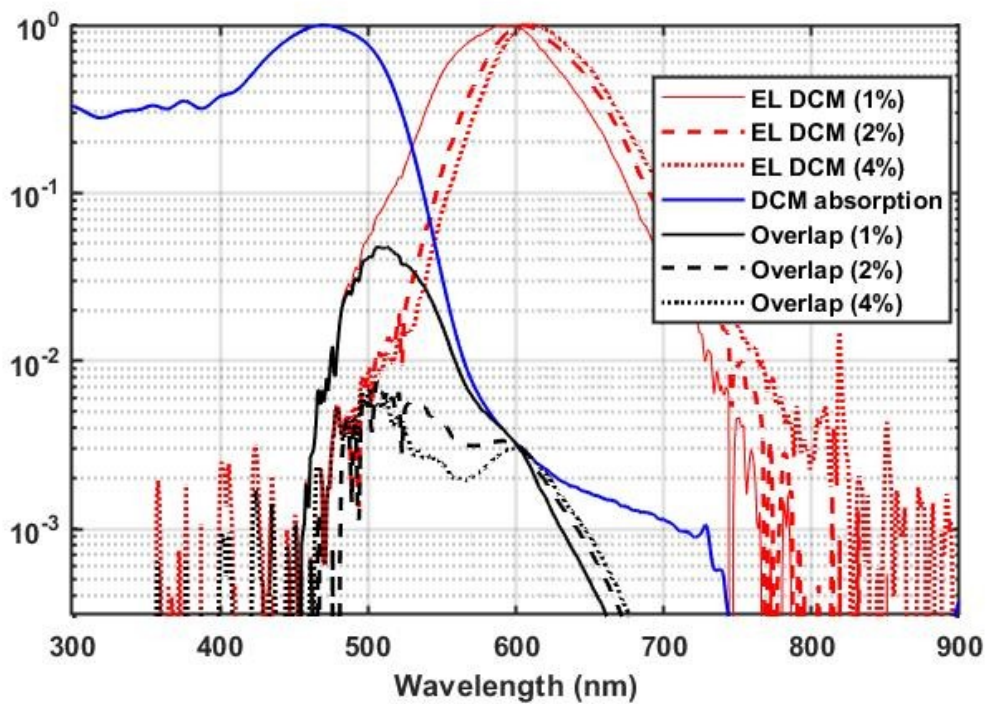
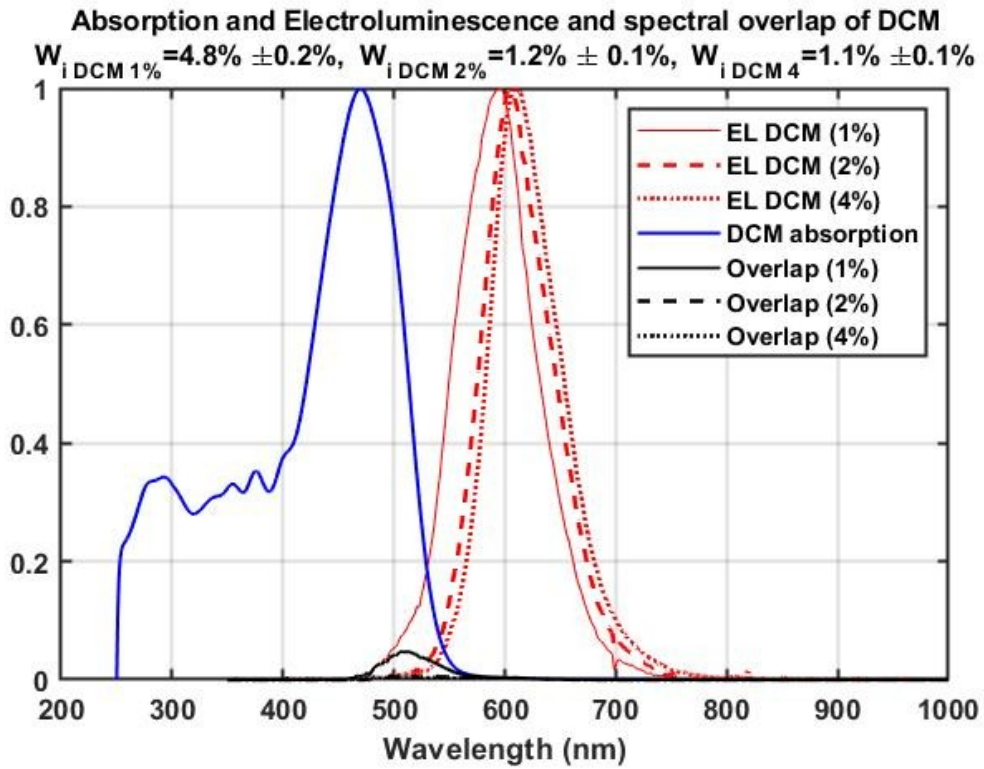


Figure. II.19: Absorption (blue), Electroluminescence (red) spectra of DCM. Product of both spectra in black. Top figure is in linear scale, bottom figure is in logarithmic scale. Absorption (blue solid line) measured from sample #1. Emitting layer is  $Alq_3Alq_3$  doped with DCJTb 1% (red solid line - sample #2), 2% (red dashed line - sample #3), 4% (red dash-dot line - sample #4)

Figure II.19 presents the absorption spectrum of DCM measured in solution (sample #1) plotted in blue, and the electroluminescence spectra of the samples with a 1% concentration of DCM in Alq<sub>3</sub>, (sample #2) plotted in red solid line, with a 2% concentration plotted in red dash line (sample #3) and with a 4% concentration plotted in red dash-dot (sample #4). The red shifts of the peak wavelength with the DCM concentration are clearly visible with maxima respectively at 595nm, 605nm and 608nm for respectively 1%, 2% and 4% of DCM in Alq<sub>3</sub>. The products  $S_A(\lambda) \times S_E(\lambda)$  of the absorption spectrum  $S_A(\lambda)$  by the electroluminescence spectra  $S_E(\lambda)$  for the different concentration corresponding to the so-called "overlap" are plotted in black: The black solid line curve corresponds to a concentration of 1%, while the black-dash curve correspond to that of the 2% concentration, and the black dash-dot curve correspond to that of the 4% concentration. In the linear scale only the 1% concentration case is visible. The logarithmic scale is necessary to compare the overlap functions; the three curves are clearly visible with the highest maximum obtained with the 1% concentration, the second highest maximum obtained with the 2% shortly ahead from the 4% case maximum.

Figure II.20 presents the DCM2 spectra, with the absorption spectrum measured in solution (sample #5) and plotted in blue, and with the electroluminescence spectra of DCM2 in red with a 1% concentration in Alq<sub>3</sub> (sample #6) plotted in red solid line, with a 2% concentration plotted in red dash line (sample #7) and with a 4% concentration plotted in red dash-dot (sample #8). The electroluminescence peak wavelengths are respectively 621nm, 633nm and 642nm respectively for 1% concentration of DCM2 in Alq<sub>2</sub>, 2% and 4%. This illustrates the red shift of the peak wavelength when the concentration increases. The black solid lines correspond to the products  $S_A(\lambda) \times S_E(\lambda)$  called "overlap" for the different concentration; 1% corresponds to the black solid line, while the black dash curve corresponds to that of the 2% concentration, and the black dash-dot curve correspond to that of the 4% concentration. Again, in the linear scale only the 1% concentration case is visible. In the logarithmic scale, the three curves are clearly visible with the highest maximum obtained with the 1% concentration, the second highest maximum obtained with the 2% and the third obtained with the 4% case maximum.

Figure II.21 presents the DCJTB spectra with the same color code as in previous figures; the absorption spectrum measured in solution (sample #9) (blue), the electroluminescence spectra of DCJTB with a 1% (sample #10) (red solid line), with a 2% (sample #11) (red dashed line) and with a 4% concentration plotted in red dash-dot (sample #12). The electroluminescence peak wavelengths are respectively 624nm, 634nm and 636nm for respectively 1%, 2% and 4% cases. Again, this illustrates the red shift of the peak wavelength when the concentration increases. The products  $S_A(\lambda) \times S_E(\lambda)$  is plotted in black for the different concentration; 1% corresponds to the black solid line, while the black dash curve corresponds to that of the 2% concentration, and the black dash-dot curve correspond to that of the 4% concentration. The logarithmic scale shows clearly the three curves with the highest maximum obtained with the 1% concentration. Note that the noise of the overlaps curves exists mainly in the wavelength range below 550nm.

Figure II.22 presents the BsB-Cz spectra with the same color code as in the previous figures; the absorption spectra is in blue (sample #13), the photoluminescence is in red (sample #14). The spectral overlap expressed by the product of the absorption and photoluminescence spectra  $S_A(\lambda) \times S_E(\lambda)$  clearly exhibit a curve with a much larger maximum than for previous materials specifically in the linear regime.



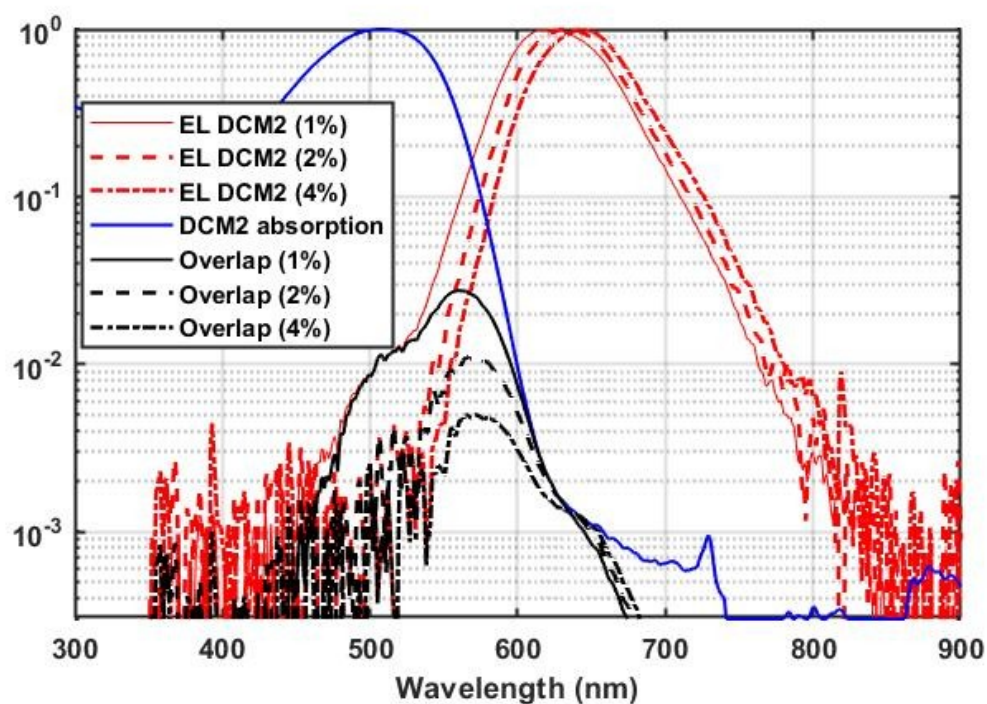
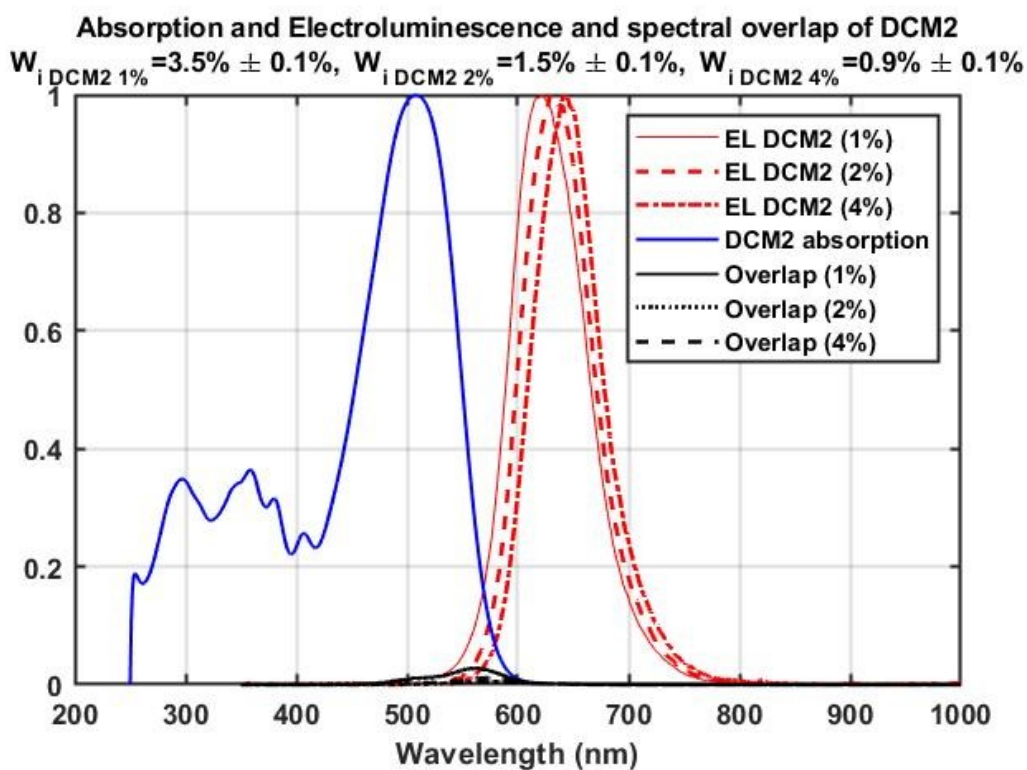


Figure. II.20: Absorption (blue), electroluminescence (red) spectra of DCM2. Product of both spectra in black. Top figure is in linear scale, bottom figure is in logarithmic scale. Absorption (blue solid line) measured from sample #5. Emitting layer is  $Alq_3Alq_3$  doped with DCM2 1% (red solid line- sample #6), 2% (red dashed line- sample #7), 4% (red dash-dot line- sample #8)



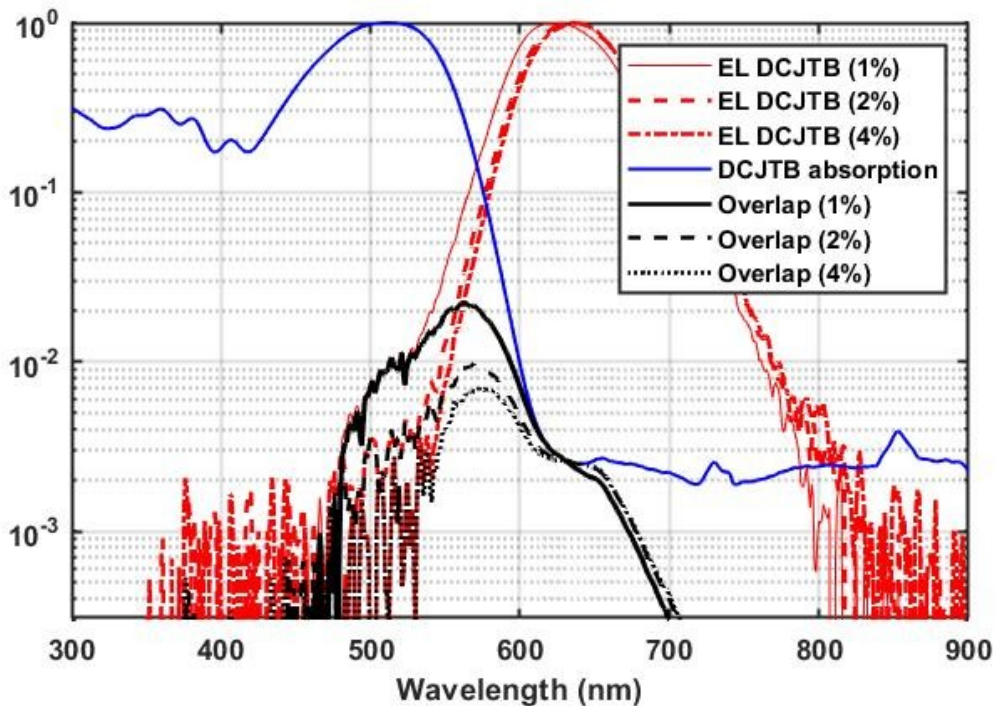
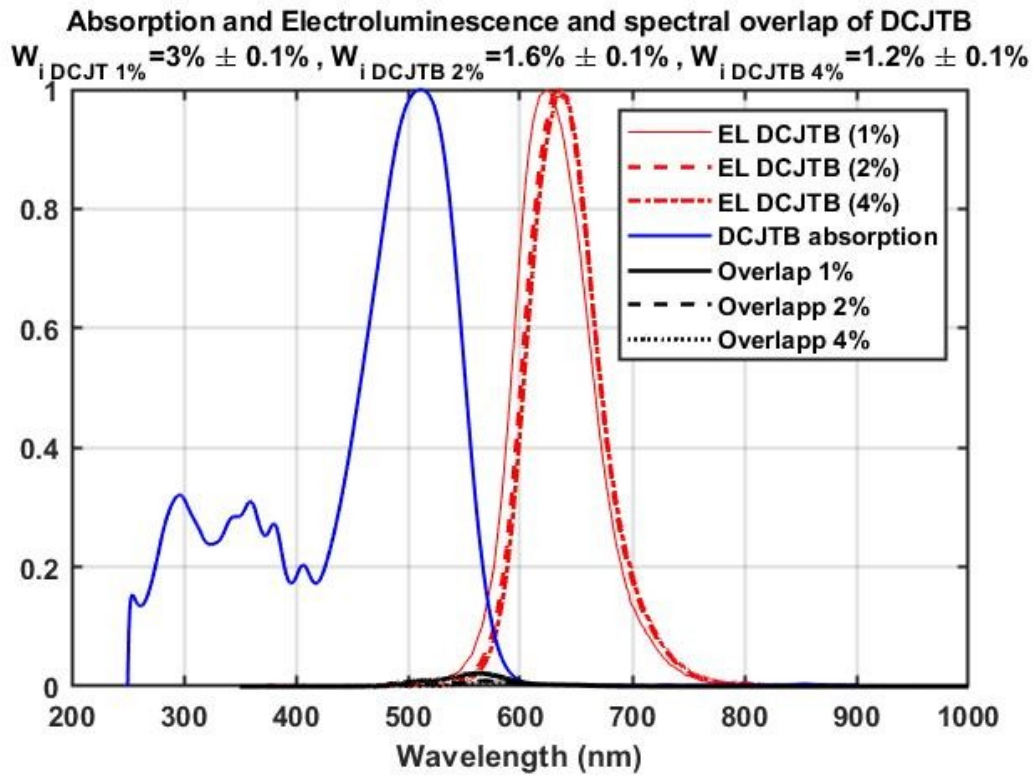


Figure. II.21: Absorption (blue), electroluminescence (red) spectra of DCJTB. Product of both spectra in black. Top figure is in linear scale, bottom figure is in logarithmic scale. Absorption (blue solid line) measured from sample #9. Emitting layer is  $Alq_3Alq_3$  doped with DCJTB 1% (red solid line - sample #10), 2% (red dashed line - sample #11), 4% (red dash-dot line - sample #12)

Absorption, Photoluminescence  
and spectral overlap of BsB-Cz  
Residual Absorption :  $W_i=13.5\%$

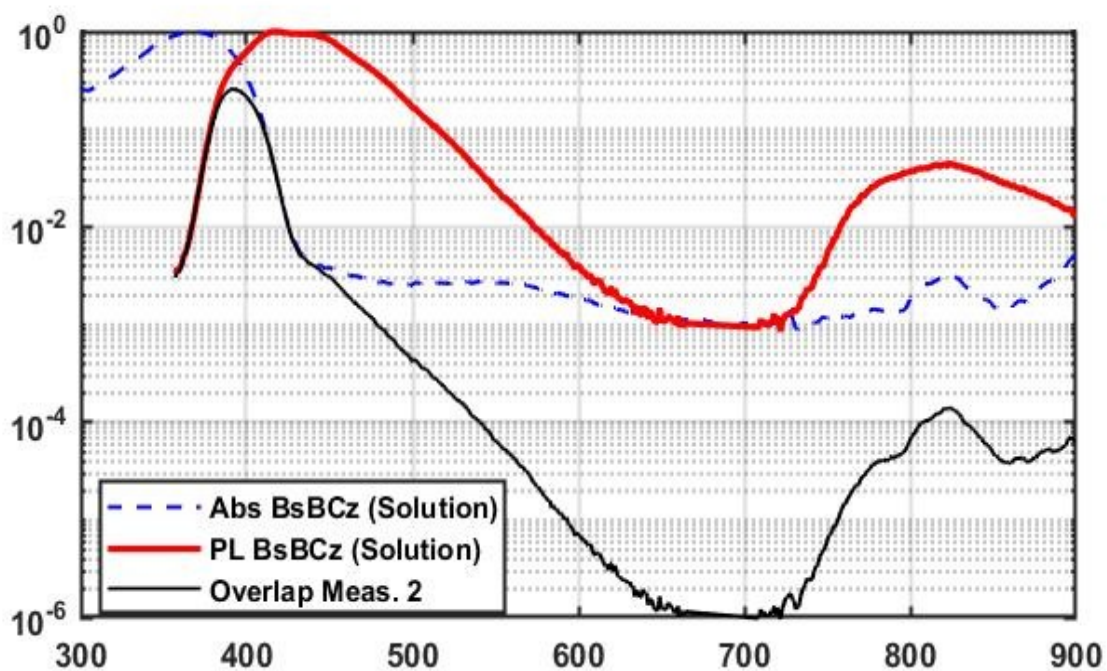
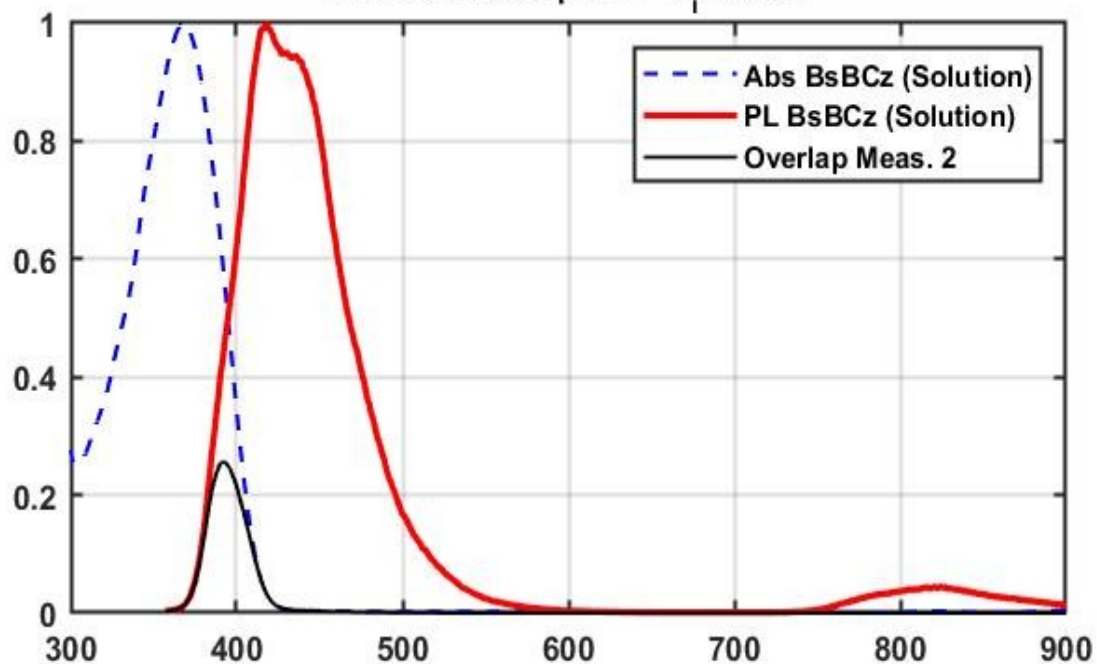


Figure. II.22: Absorption (dashed blue), photoluminescence (red), and spectral overlap (black) for BsB-Cz. Top figure is in linear scale, bottom figure is in logarithmic scale. Absorption (blue solid line) measured from sample #13.

#### II.4.2.2.4. Residual absorption calculation

We analyze first the products of the absorption spectrum  $S_A(\lambda)$  by the electroluminescence spectra  $S_E(\lambda)$  for the different concentration. They are plotted in black in figures II.19, II.20, and II.21 and it reads  $S_A(\lambda) \times S_E(\lambda)$ .

This is part of the numerator of eq. II.77: 
$$W_i = \frac{\int S_A(\lambda) S_E(\lambda) d\lambda}{\int S_E(\lambda) S_E(\lambda) d\lambda}$$

These spectra-like allow both a quantitative and a qualitative approach and a comparison of the residual absorption of the different materials and the different concentration. Although or because they are plotted for a systems without a cavity ( $S_{\text{CAV}} = \text{constant}$  is a flat cavity that exhibits no frequency selection) they are also interested to identify wavelengths for which the residual absorption is less impacting the systems. These spectra-like illustrates a physical meaning of the residual absorption. However, it is to be remembered that the residual absorption is a dynamical quantity that recover all its meaning when selective cavity spectral profile is included.

Table II.14 summarizes the residual absorption values  $W_i$  for different concentrations of DCM, DCM2 and DCJTB as well as for neat BsB-Cz calculated using eq. II.77. Note, that the residual absorption for the DCM, DCM2 and DCJTB are calculated with electroluminescence spectra whereas that of the BSB-Cz is measured from the photoluminescence. The lowest values of  $W_i$  are obtained for the highest concentrations as a result of a larger Stocke shift of the electroluminescence with respect to the absorption spectrum when the concentration is increased.

Apart from the previous remark, no easy other trends emerge from the table II.14. Indeed, at the lowest concentration (1%) DCJTB offers the lowest residual absorption with  $w_i = 2.98 \pm 0.03\%$ . For a concentration of 2%, DCM presents the lowest residual absorption  $w_i = 1.19 \pm 0.03\%$ , while for a concentration of 4%, DCM2 presents the lowest residual absorption with  $w_i = 0.86 \pm 0.03\%$ . From table II.14, the lowest value is obtained with 4% of DCM2 in Alq<sub>3</sub>, and the second lowest value is obtained with a concentration of 4% of DCM. The impact of the residual absorption on the laser threshold is illustrated figure II.23. It shows a set of curves plotting the threshold current density as a function of the quality factor calculated for different residual absorption values ranging from 0% to 10%. More precisely, it is computed using the set of equations II.40-II.47 for  $W_0 = \{0\%, 0.15\%, 1\%, 2\%, 5\%, 8\%, 10\%\}$ .

Figure II.23 shows that at a given value of the quality factor  $Q$ , even low values  $W_0$  of the residual absorption induce a large change of  $J_{th}$  the threshold current density compared to  $W_0 = 0\%$ . For example, at  $Q = 1000$ , the current density is  $J_{th1} = 1.3 \text{ kA/cm}^2$  for  $W_{01} = 0\%$  and  $J_{th2} = 2.8 \text{ kA/cm}^2$  for  $W_{02} = 1\%$  and even  $J_{th3} = 4.5 \text{ kA/cm}^2$  for  $W_{03} = 5\%$ . Larger values of the residual absorption  $W_0$  potentially rises up the threshold current density beyond the available current density budget. Note also that, the larger the  $Q$ -factors, the larger the increase of the threshold current density with the residual absorption  $W_0$ .

If the residual absorption is the only criterium considered to choose for an organic laser gain material, DCM2 is to be chose first and DCM would be a second choice. This is different from the conclusion inherited from table II.12 where DCJTB exhibits the highest laser gain coefficient and DCM the second highest. As the laser gain coefficient  $\xi$  and the residual absorption  $w_i$  are parameters leading to different conclusion, another but more synthetic criterium is necessary to choose for a laser gain material among the different material listed above.

Material	Absorption ( $\lambda_{peak}$ )	$W_{i1}$ (1% concentration)	$W_{i2}$ (2% concentration)	$W_{i4}$ (4% concentration)	$W_{ineat}$
DCM	(472nm)	4.8±0.2% (596nm)	1.2±0.1% (605nm)	1.1±0.1% (608nm)	
DCM2	(508nm)	3.5±0.1% (621nm)	1.5±0.1% (633nm)	0.9±0.1% (642nm)	
DCJTB	(509nm)	3.0±0.1% (624nm)	1.6±0.1% (634nm)	1.2±0.1% (636nm)	
BsB-Cz	(368nm)				13.5% (418nm)

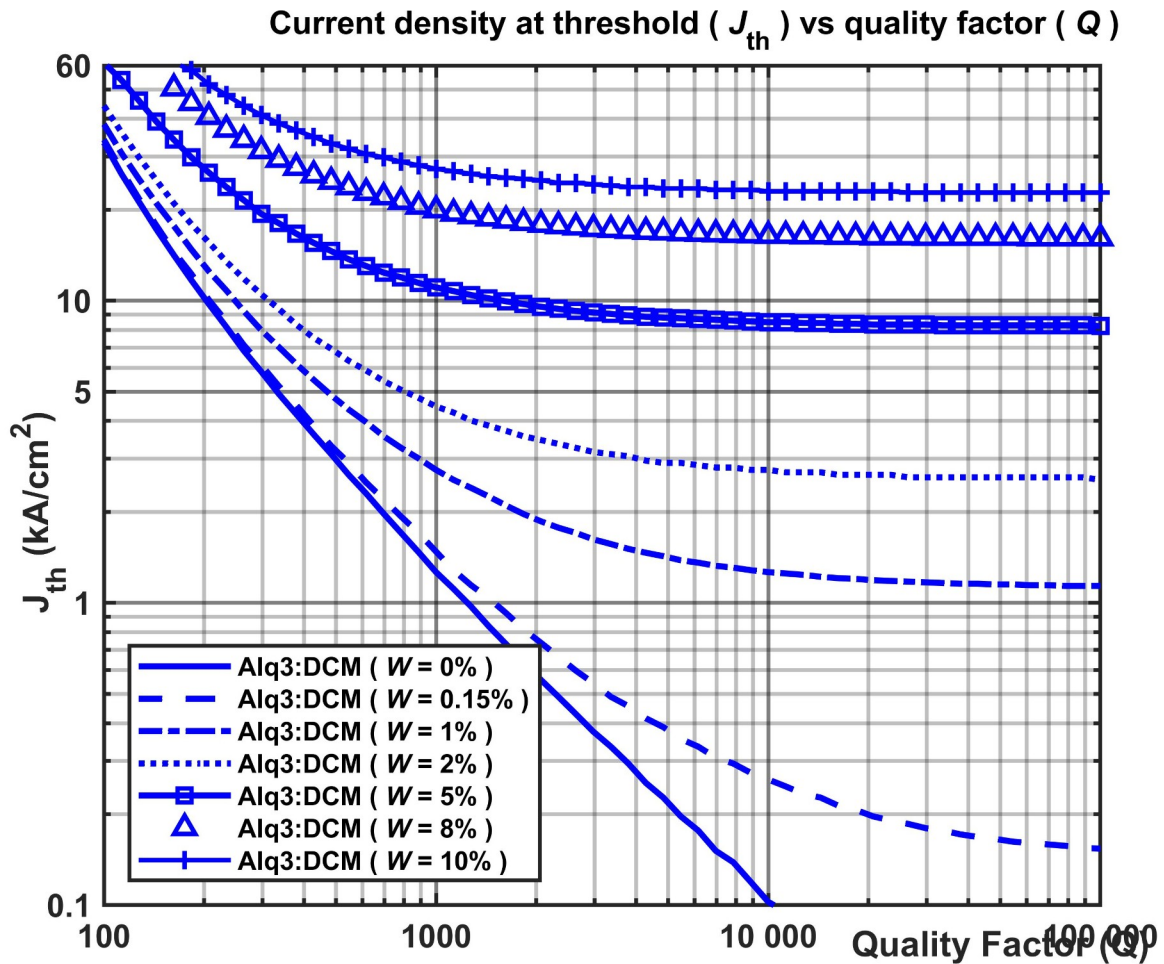


Figure. II.23: Figure of merit

#### II.4.2.2.5. The effective gain

Following the previous conclusions that shows the difficulty to identify the best candidate as a laser gain material among the DCM, DCM2, and DCJTB from either the laser gain coefficient alone or the residual absorption alone, we have gathered the data and plotted them on figures II.24.

Figure II.24.a presents the laser gain coefficient as a function of the concentration C in % for DCM (red), DCM2 (magenta) and DCJTB (blue). Clearly, DCJTB offer the best gain coefficient. Note that, in the case of DCJTB the different values for the 1%, 2% and 4% concentration are interpolations from the single value identified from the literature to which the origine has been added (zero laser gain coefficient for a zero concentration:  $(C=0, \xi=0)$  .

Figure II.24.b presents the residual absorption  $W_i$  as a function of the concentration C in % again for DCM (red), DCM2 (magenta) and DCJTB (blue). In this case, no material emerge clearly as the best candidate because  $W_i$  values are both close to each other and the it changes with the concentration C.

Because the previous conclusion are contradictory, we conduct the investigation further and we plotted in fig. II.24.c the produc  $\xi \times W_i$  of the laser gain coefficient  $\xi$  by the residual absorption  $W_i$  as a function of the concentration C again for DCM (red), DCM2 (magenta) and DCJTB (blue). The product  $\xi \times W_i$  appear in equation II.59 with a minus sign, and therefore the minimum of the absolute value is to be sought. With this criterium, DCM appears to be the best laser material candidate shortly ahead from the DCM2 in the 2% concentration case. But here again the difference is not large and the conclusion appear fragile.

The effective gain  $G_{eff} = \xi(N_{SD} - W_i N_{0D})$  (Eq. II.59) is a more complete parameter to seek for a conclusion. The effective gain  $G_{eff}$  is plotted in fig. II.24.d as a function of the concentration C in % for DCM (red), DCM2 (magenta) and DCJTB (blue) under the following conditions:

- The laser gain coefficient  $\xi$  is interpolated from fig. II.24.a for the concentration values  $C=1\%$ ,  $C=2\%$ , and  $C=4\%$  of the.
- The dopant singlet density is kept constant to  $N_{SD} = 5.8 \times 10^{17} \text{ cm}^{-3}$  corresponding to a current of  $3.5 \text{ kA/cm}^2$  estimated in a linear approximation from fig. II.13.
- The residual absorption values are interpolated from fig. II.24.b.
- The ground state population density  $N_{0D}$  is approximated to:

$$N_{0D} = N_{mol} \times C \quad \text{Eq. (II.78)}$$

where  $N_{Mol} = 2.1 \times 10^{21} \text{ cm}^{-3}$  is the host ( $\text{Alq}_3$ ) population density in accordance with the table II.9 and where C is the concentration of dopant relative in  $\text{Alq}_3$ .

The chosen value of the current density  $J=3.5 \text{ kA/cm}^2$  corresponds in linear approximation to the singlet density  $N_{SD}=5.8 \times 10^{17} \text{ cm}^{-3}$  . Note that the current density value has been chosen from the simulation presented in fig. II.13 because the threshold is reached with it. **Under theses approximations that are valid below threshold, zero or positive values of the effective gain  $G_{eff}$  are reached first with the DCM at a concentration of 2%.**



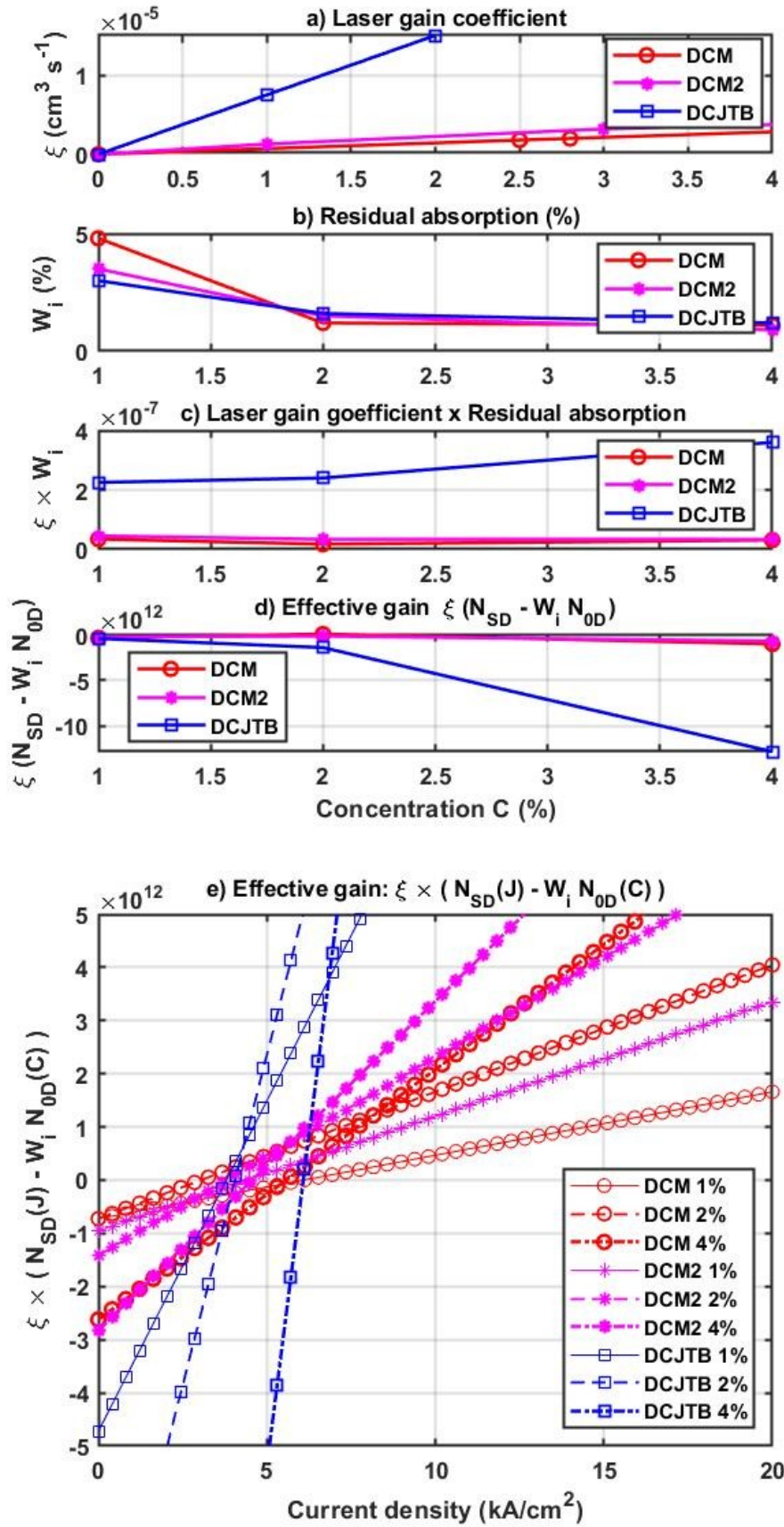


Figure. II.24: Graphical analysis of the laser gain coefficient , the residual absorption and the effective gain

This approximation is valid below threshold, because at threshold and above, the singlet density  $N_{SD}$  clamps and current density  $J$  and singlet density  $N_{SD}$  are decoupled from each other as illustrated in fig. II.13.a. As these curves are dependent on the current density  $J$ , and for the sake of completeness, we plotted the effective gain  $G_{Eff}$  as a function of  $J$  in fig. II.24.e. It is computed under the following approximations: Using a linear approximation, the dopant singlet density  $N_{SD}$  is related to the current density  $J$  by:

$$N_{SD}(J) = N_{SD}(J_{Th0}) / J_{Th0} \times J \quad \text{Eq. (II.79)}$$

where  $N_{SD}(J_{Th0}) = 3 \times 10^{17} \text{ cm}^{-3}$ , and  $J_{Th0} = 1.81 \text{ kA/cm}^2$ .

Again, this linear approximation is valid below threshold, as at threshold and above threshold the singlet density clamps and current density and singlet density are not function of each other any more as illustrated in fig. II.13. From fig. II.24.d, the effective gain  $G_{Eff}$  of DCM with a 2% concentration (red dashed line with circle markers) exhibits the lowest current density ( $J = 3.2 \text{ kA/cm}^2$ ) for which the effective gain becomes positive. **For these reasons, and in the context of the large approximations, the DCM with a concentration of 2% appears to be the best candidate as a laser gain material. For the rest of the study, we will focus on DCM with a 2% concentration as laser gain material, and will use the peak wavelength  $\lambda_{peak} = 605 \text{ nm}$  to design the laser cavity.**

A more systematical study with more values of the concentration would probably reveal that a lower threshold can be obtained for another value, but the effort is not worth it because the evaporation process of OLED (see chapter 3) do not allow a resolution on the concentration smaller than 1%. Note that with the introduction of the linear dependence on the current density  $J$  of the singlet density  $N_{SD}$  based on Eq. II.79, and of the linear dependence on the concentration  $C$  of the ground state density  $N_{0D}$  based on Eq. II.78, the effective gain reads:

$$G_{eff} = K \times J - \beta_0 \quad \text{Eq. (II.80)}$$

where  $K$  is the slope that reads:

$$K = \xi \frac{N_{SD}(J_{Th0})}{J_{Th0}} \quad \text{Eq. (II.81)}$$

and where  $\beta_0$  is the y-intercept that reads:

$$\beta_0 = -\xi W_i C N_{Mol} \quad \text{Eq. (II.82)}$$

From equation II.82, the y-intercept  $\beta_0 = -\xi W_i C N_{Mol}$  decreases when the laser gain coefficient  $\xi$  increases and when the concentration increases. This explain the relative position of the three blue curves corresponding to the DCJTB. This explains also why the y-intercept for 4% of DCJTB (thick blue dash-dot line) is below the y-intercept for 2% of DCJTB (blue dash line) itself below the 1% of DCJTB (thib blue solid line) and below the other y-intercept for the other material DCM and DCM2 as shown in figure II.24. This ranking corresponds more or less to that of fig. II.24.c where the highest product  $\xi \times w_i$  is observed for DCJTB whatever the concentration is. Note that, data with the DCJTB are inherited from one single value of the laser cross section extracted from the literature [44]. Without confirmation of the order of magnitude of the stimulated emission cross section or of the laser gain coefficient by other study. the reliability of the value  $\xi_{DCJTB}$  is at stake.

### II.4.3. OLED structure from the optical waveguide point of view

This section is dedicated to the design of the OLED stack including the ITO layer. More precisely, the objective is to estimate the optimal value of the ITO layer thickness and of the organic layer heterostructure to maximize the confinement factor  $\Gamma$ .

#### II.4.3.1. Objectives and method

The considered parameter is the confinement factor  $\Gamma$  to be investigated as a function of the different layer thicknesses. The confinement factor  $\Gamma$  is calculated using a 1-D mode solver for optical dielectric multi-layer slab waveguides available on the website <https://www.computational-photonics.eu>. This applet calculates the effective indices of guided modes and screen the corresponding optical fields. Apart from the structure, the script requires to specify the vacuum wavelength and the polarization. The input mask of the script consists of a stack of N-layers between the substrate and the superstrate as shown on Fig.II.25 (left). The considered geometry is a stack of different layers defined by their thicknesses  $t_i$  and the real part of their refractive index  $n_i$ . The x direction is perpendicular to the film plane and the light is propagated along the Z direction. Along the y direction the refractive index profile and the fields supposed to be constant and infinite. On the basis of the Helmholtz equation, the script calculates different parameters like the propagation constant  $\beta$ , the effective index :

$$n_{eff} = \beta / k \quad \text{Eq. (II.83)}$$

where  $k = 2\pi/\lambda$  is the vacuum wavenumber associated with the specified vacuum wavelength  $\lambda$ ,

$$\text{the normalized effective permittivity } B = \frac{(n_{eff}^2 - n_{min}^2)}{(n_{max}^2 - n_{min}^2)} \quad \text{Eq. (II.84)}$$

with the maximum refractive index  $n_{max}$  of all layers.  $n_{min}$  denotes the largest of the substrate and cover refractive indices,

$$\text{the coupling lengths } L_c = \frac{\pi}{|\beta_0 - \beta_1|} \quad \text{Eq. (II.85)},$$

and the confinement factor  $\Gamma$  as a function of the geometry of the waveguide section for the different TE and TM polarizations. The program solves and plots the electric fields, the magnetic fields, their absolute value, the poynting vector and the energy density as shown in Fig.II.26. The effective index can be scanned as a function of one of the following parameters: vacuum wavelength  $\lambda$ , the refractive indices  $n_s$ ,  $n_c$  and  $n_{LN}$  of the substrate, the cover and the interior layers and its thickness  $t_{LN}$ .

#### II.4.3.2. Considered stack

The considered stack is illustrated in Fig.II.25 (right) and consists of 4 layers; a glass substrate ( $n_s=1.45$ ), an ITO conductive and transparent layer ( $n_{L1}=1.9$ ), organic layers taken as a one single layer with the average refractive index ( $n_{L2}=1.7$ ), and the superstrate ( $n_0=1$ ).



### II.4.3.3. Confinement factor

In sub-section II.4.3.3.1. , we present both the apparition of the different modes and the confinement factor as a function of ITO thickness. Once the optimum ITO thickness has been identified, we keep it constant and investigate the effect of the thickness of organic layers on the confinement factor ( II.4.3.3.2. ). Finally, we will concluded on the optimum waveguide geometry to maximize the confinement factor.

#### II.4.3.3.1. Role of the ITO thickness on the confinement factor

The ITO as a transparent and conductive layer, it is both the anode of OLED, but also with its refractive index  $n_{L1}=1.9$  higher than that of the organic layer (  $n_{L2}=1.7$  ) it can guide light. For this reason we study the effect of its thickness on the confinement factor. The organic layer thickness is set arbitrary constant to  $t_{L2}=100\text{nm}$  and the ITO thickness  $t_{L1}$  is varied. Using the 1D solver the confinement factor is calculated for the different layer thicknesses and for each mode (TE and TM).

As a prerequisite, the existence of the different TM and TE modes is verified, quantified as function of the ITO thickness and plotted in Fig. II.27 (top). As commonly known, the number of modes increases with the ITO thickness and the occurrence of an additional TM modes is always shifted to larger thickness compared to the occurrences of an additional TE mode. An important results is that up to an ITO thickness of 250nm, only one TE mode and one TM mode exist. In order to design a single mode (single TE and single TM mode) laser, with the current structure (Organic thickness is 100nm) one has to keep the ITO thickness below 250nm. This excludes a priori the substrates with 340nm thick ITO layers, but this is to be confirmed with new calculations for organic layer thicknesses different from  $t_{L2}=100\text{nm}$ .

To define the optimal thickness of ITO layer, we focus on the first mode of TE ( $TE_0$ ) disregarding the TM mode, and we plot the confinement factor in the organic layer as a function of ITO thickness as shown in Fig. II.27(bottom). Note that the confinement factor presents a clear maximum at  $\Gamma=0.31$  for a ITO layer thickness between 50nm and 55nm and decays for larger ITO thicknesses.

Note that  $t_{L1}=50\text{nm}$  is a much thinner ITO layer thickness than usually considered with the substrates available for conventional OLED (340nm or 140nm). Also, in sections II.2.3.2. , and II.2.3.5. dedicated to the optimization of the device from the electrical point of view, we demonstrated that the higher the ITO thickness the smaller the serial and measurement resistances which in turn reduces the time constant allowing much larger current density in the OLED and a better budget to reach the laser threshold. A complicated trade-off is therefore necessary to both maximize the confinement factor and keep the electrical time constant as low as necessary. In the following studies three types of substrates with three different thicknesses are to be considered; 50nm, 140nm and 340nm although the latter is probably not relevant.

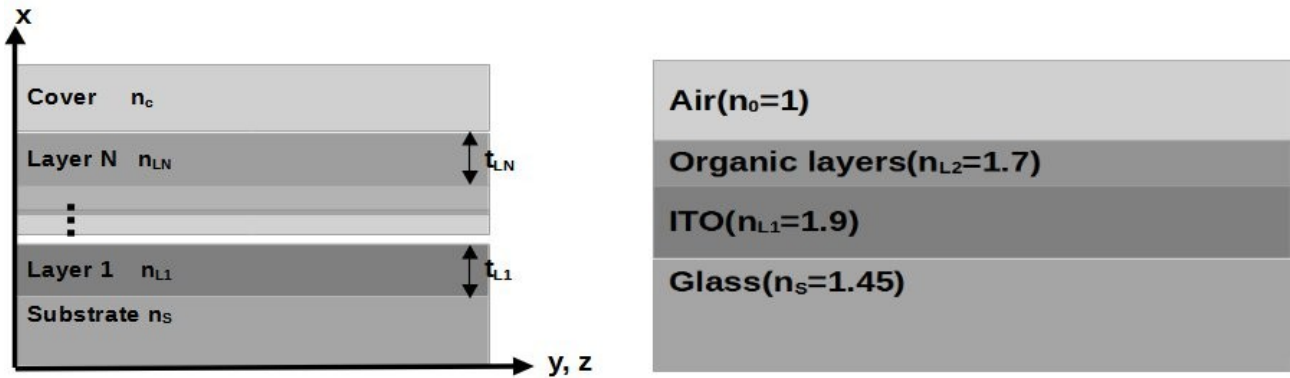


Figure. II.25: OLED stack from the optical waveguide point of view: (Left) principle of the stack for the study of the electrical field and the confinement factor, (Right) OLED stack considered in the current study: glass substrat ( $n_s=1.45$ ), ITO layer ( $n_{L1}=1.9$ ), organic layers ( $n_{L2}=1.7$ ), superstrate ( $n_0=1$ )

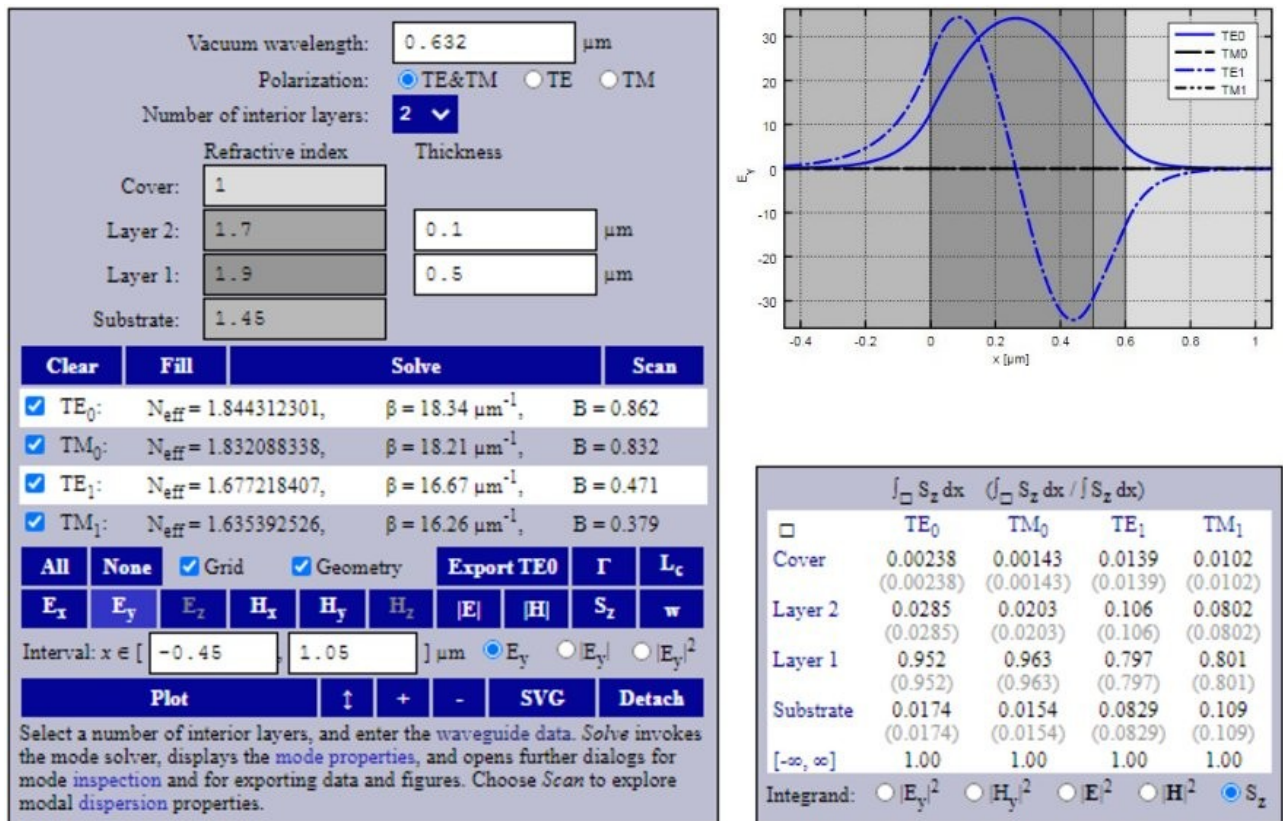


Figure. II.26: Overview of the result windows of the 1-D solver of the optical waveguide: (Left) definition of the structure and basic calculation), (upper right) Electrical field in the TE and tM polarization as function of the stack thickness, (lower right) integrand of the TE and TM fields

#### II.4.3.3.2. Role of the Organic layer thickness on the confinement factor

In a second step, we study the confinement factor of the TE mode in the organic layer as a function of organic layer thickness  $t_{L2}$  for the three thicknesses defined above ( $t_{L1} = 50\text{nm}$ ,  $140\text{nm}$  and  $340\text{nm}$ ).

Firstly, we performed the calculations for the  $TE_0$  polarization. Figure II.28 display the confinement factor for ITO thicknesses of  $50\text{nm}$  (green solid line)  $140\text{nm}$  (blue solid line) and  $340\text{nm}$  (red solid line). As shown in fig.II.28, the confinement factor values for the  $TE_0$  reach plateau values saturating at  $0.121$ ,  $0.577$  and  $0.999$  respectively for ITO thicknesses of  $340\text{nm}$ ,  $140\text{nm}$  and  $50\text{nm}$  respectively. These plateau values of the confinement factor are reached for organic layer thicknesses from  $\sim 500\text{nm}$ ,  $\sim 2\mu\text{m}$  and  $\sim 4\mu\text{m}$  respectively. The thicknesses above  $1\mu\text{m}$  are irrelevant for organic heterostructures because efficient organic heterostructures are usually about  $100\text{nm}$  thicn. That is the following studies will focus onto organic thicknesses less than  $1\mu\text{m}$  which is already a very large value for an organic heterostructures.

FigureII.29 presents the confinement factor as a function of organic layer thickness for different polarization mode TM (blue, cyan and magenta) and TE (red, black and green) for ITO thickness  $340\text{nm}$  (left figure),  $140\text{nm}$  (middle figure) and  $50\text{nm}$  (right figure).

- In the  $340\text{nm}$  case, the confinement factors reach  $0.12$  and  $0.16$  for an organic layer thickness of  $t_{L2}=1\mu\text{m}$  respectively for the  $TE_0$  and  $TM_0$  modes.
  - With a thickness of  $t_{L2}=200\text{nm}$ , the  $\Gamma$  values of the  $TE_0$  and  $TM_0$  modes as low as  $0.09$  and  $0.10$ . With the  $TE_0$  and  $TM_0$  modes, the  $TE_1$  and  $TM_1$  also coexist and the latter reach  $\Gamma$  values of  $0.37$  and  $0.33$  respectively for  $t_{L2}=200\text{nm}$ . In such a situation it is very likely that the  $TE_1$  and  $TM_1$  will reach the condition for lasing before  $TE_0$  and  $TM_0$ .
  - With a thickness of  $t_{L2}=125\text{nm}$  corresponding to a quarter wavelength thick organic heterostructure, the  $\Gamma$  values of the  $TE_0$  and  $TM_0$  modes as low as  $0.07$  and  $0.06$  while that of the  $TE_1$  an  $TM_1$  are  $0.23$  and  $0.16$  respectively.
  - With a thickness of  $t_{L2}=100\text{nm}$  corresponding to an average OLED thickness, the  $\Gamma$  values of the  $TE_0$  and  $TM_0$  modes as low as  $0.06$  and  $0.04$  while that of the  $TE_1$  an  $TM_1$  are  $0.18$  and  $0.11$  respectively.
- In the  $140\text{nm}$  case, the  $TE_1$  and  $TM_1$  modes exist starting from  $t_{L2}=275\text{nm}$  which leaves a organic layer thickness large enough to find an organic heterostructure with a realistic thickness.
  - With a thickness of  $t_{L2}=200\text{nm}$ , the  $\Gamma$  values of the  $TE_0$  and  $TM_0$  modes as low as  $0.34$  and  $0.38$ .
  - With a thickness of  $t_{L2}=125\text{nm}$ , the  $\Gamma$  values of the  $TE_0$  and  $TM_0$  modes as low as  $0.25$  and  $0.22$ .
  - With a thickness of  $t_{L2}=100\text{nm}$ , the  $\Gamma$  values of the  $TE_0$  and  $TM_0$  modes as low as  $0.21$  and  $0.17$ .
- In the  $50\text{nm}$  case, the  $TE_0$  and  $TM_0$  modes do not coexist with other modes below  $400\text{nm}$ . More over the  $TE_0$  and  $TM_0$  curves are located above the  $TE_1$ ,  $TM_1$  themselves above the  $TE_2$  and  $TM_2$ . Lasing conditions are therefore more favorable for the  $TE_0$  and  $TM_0$ .
  - With a thickness of  $t_{L2}=200\text{nm}$ , the  $\Gamma$  values of the  $TE_0$  and  $TM_0$  modes as large as  $0.56$  and  $0.49$ .

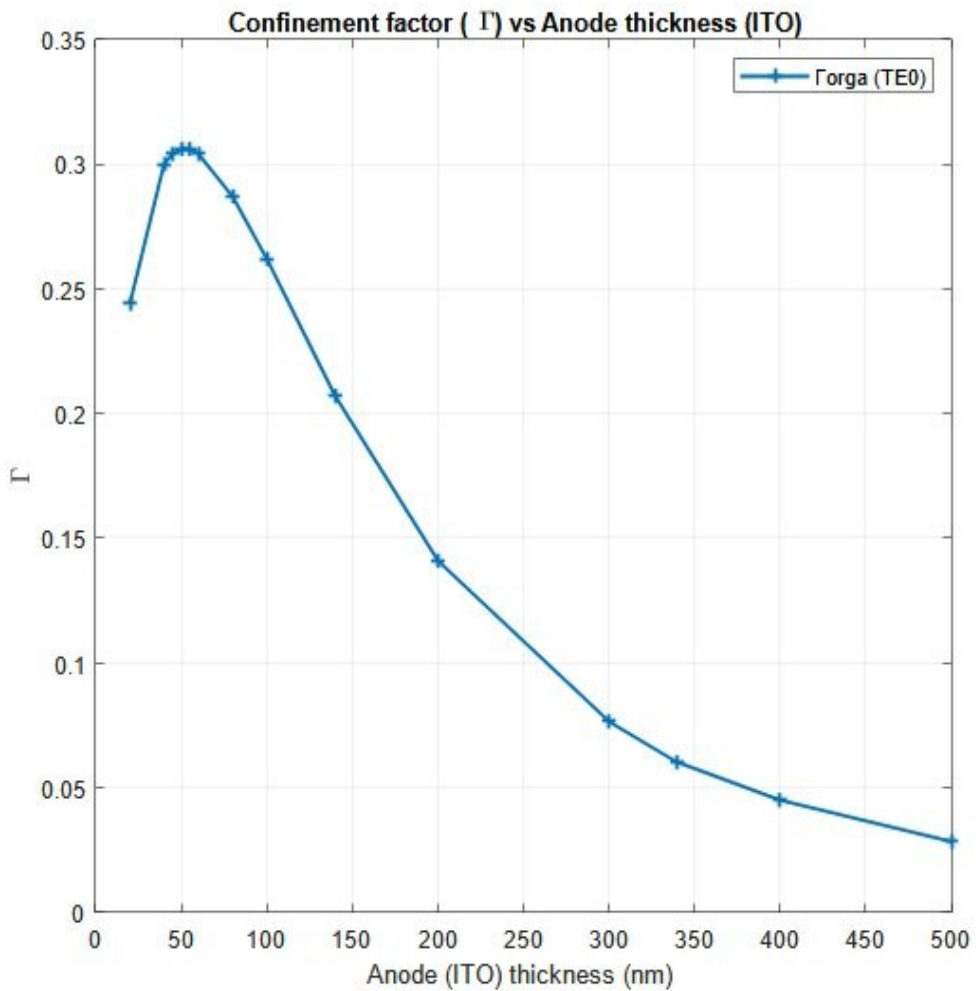
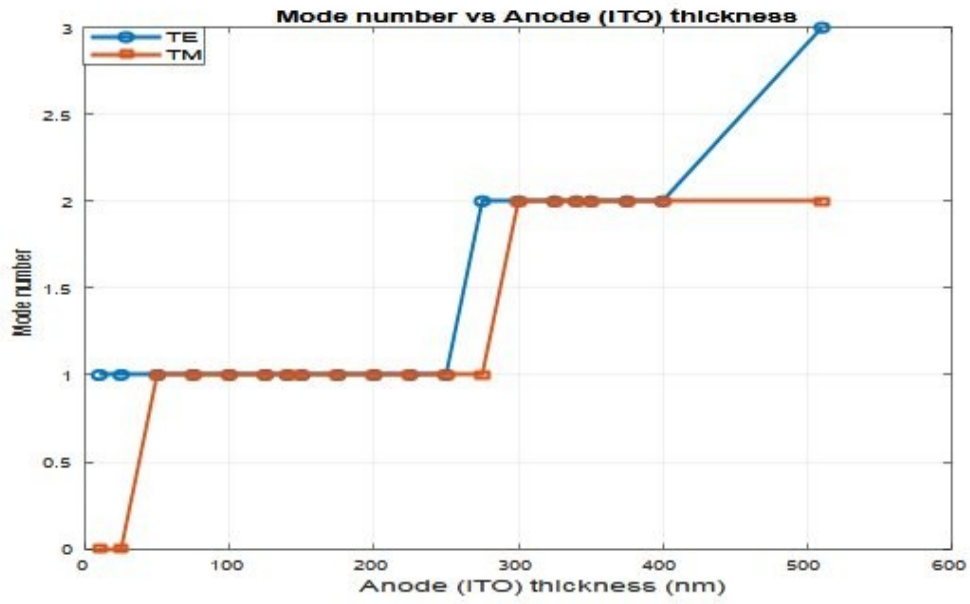


Figure. II.27: Confinement factor study: (top) number of TE and TM modes as a function of the ITO layer thickness, (bottom) confinement factor  $\Gamma$  as function of the ITO thickness

- With a thickness of  $t_{L2}=125\text{nm}$ , the  $\Gamma$  values of the TE0 and TM0 modes are as large as 0.39 and 0.19. The TE0 confinement factor being almost twice that of the TM0, it will be favoured for lasing over the TM0.
- With a thickness of  $t_{L2}=100\text{nm}$ , the  $\Gamma$  value of the TE0 is as large as 0.31 while that of the TM0 modes is as low 0.08. Again in this case the TE0 confinement factor is much larger (fourfold) than that of the TM0, favouring the TE0 for lasing.

As a preliminary conclusion, the best configurations are found with an ITO thickness as low as 50nm. Note that, for this configuration, the confinement factor for TE0 and TM0 are still higher than the other modes. For the three organic layer thicknesses ( $t_{L2}=200\text{nm}$ , 125nm and 100nm) the TE0 modes exhibit larger values of the confinement factors than the TM0. The TE0  $\Gamma$  value increase with the organic layer thickness  $t_{L2}$ .

#### II.4.3.3. Conclusion on the optimal layer thicknesses from the confinement factor

Table 2.14 presents the confinement factor for different cases with different ITO thicknesses and organic thicknesses. The organic thickness of 100nm is chosen because it is close to a standard OLED thickness. The thickness of 125nm was reported by Coens for a quarter wavelength emission layer thickness and with which current density above  $1000\text{mA}/\text{cm}^2$  in DC regime was obtained in an undoped organic heterostructure [40]. This is an indication that despite a slightly larger OLED thickness electrical performances remain. The thickness of 200nm has been reported by Adachi's group with a doped (PIN) heterostructure type thus with an enhance mobility offering better electrical performance than undoped OLEDs [2].

For the same organic layer thickness the increase of ITO the thickness leads to a decrease of the confinement factor and eventually to an increase in the modes number (TE and TM). On the other hand, the increase in the thickness of the organic layers enhances the confinement factor.

As a conclusion, the higher confinement factor ( $\Gamma=0.57$ ) is obtained for the couple of ITO and organic layer thicknesses ( $t_{L1}=50\text{nm}$ ,  $t_{L2}=200\text{nm}$ ) which we will consider as the best optimum in what follows.

As an undoped 200nm thick organic heterostructure may suffer from electrical performances far from the state of the art, a second optimum to be considered is with the couple of ITO and organic layer thicknesses ( $t_{L1}=50\text{nm}$ ,  $t_{L2}=125\text{nm}$ ) offering  $\Gamma=0.39$ . In this case, the confinement factor difference between the TE0 and the TM0 modes, is expected to favour the TE0 more clearly than with the first optimum.

**Table II.15: Summary of the  $\Gamma$  values for the different cases**

ITO thickness $t_{L1}$ (nm)	Organic thickness $t_{L2}$ (nm)	$\Gamma$			
		TE0	TM0	TE1	TM1
50	200	0.565	0.487	-	-
	125	0.385	0.19	-	-
	100	0.306	0.0882	-	-
140	200	0.339	0.38	-	-
	125	0.247	0.226	-	-
	100	0.207	0.166	-	-
340	200	0.097	0.106	0.367	0.334
	125	0.073	0.065	0.231	0.163
	100	0.061	0.049	0.183	0.107

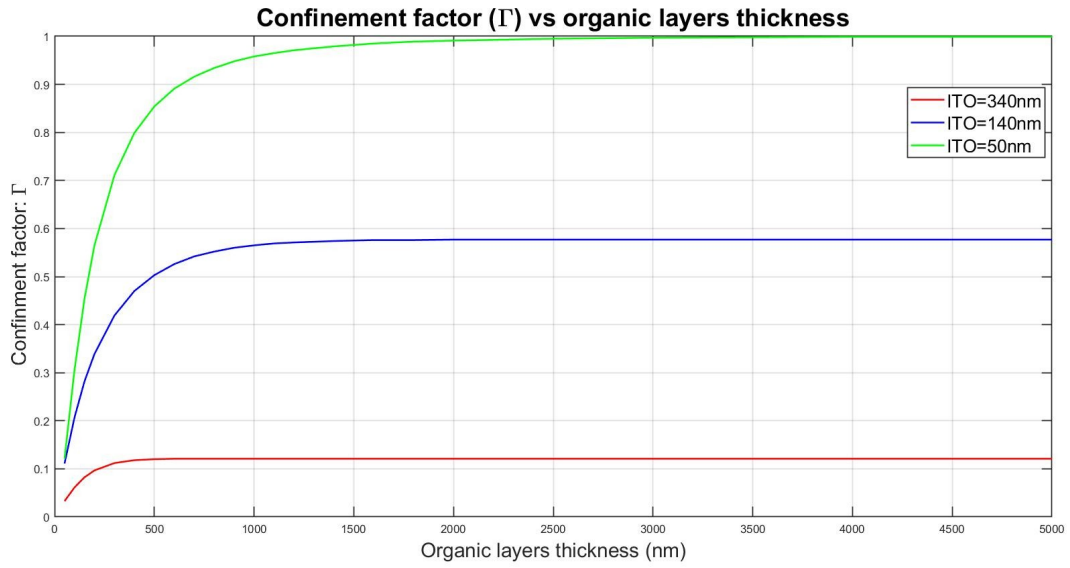


Figure. II.28: Confinement factor as a function of the organic layer thickness: Confinement factor of TE0 in organic layer vs organic layer thickness for ITO thickness; 340nm (red), 140nm (blue), 50nm (green)

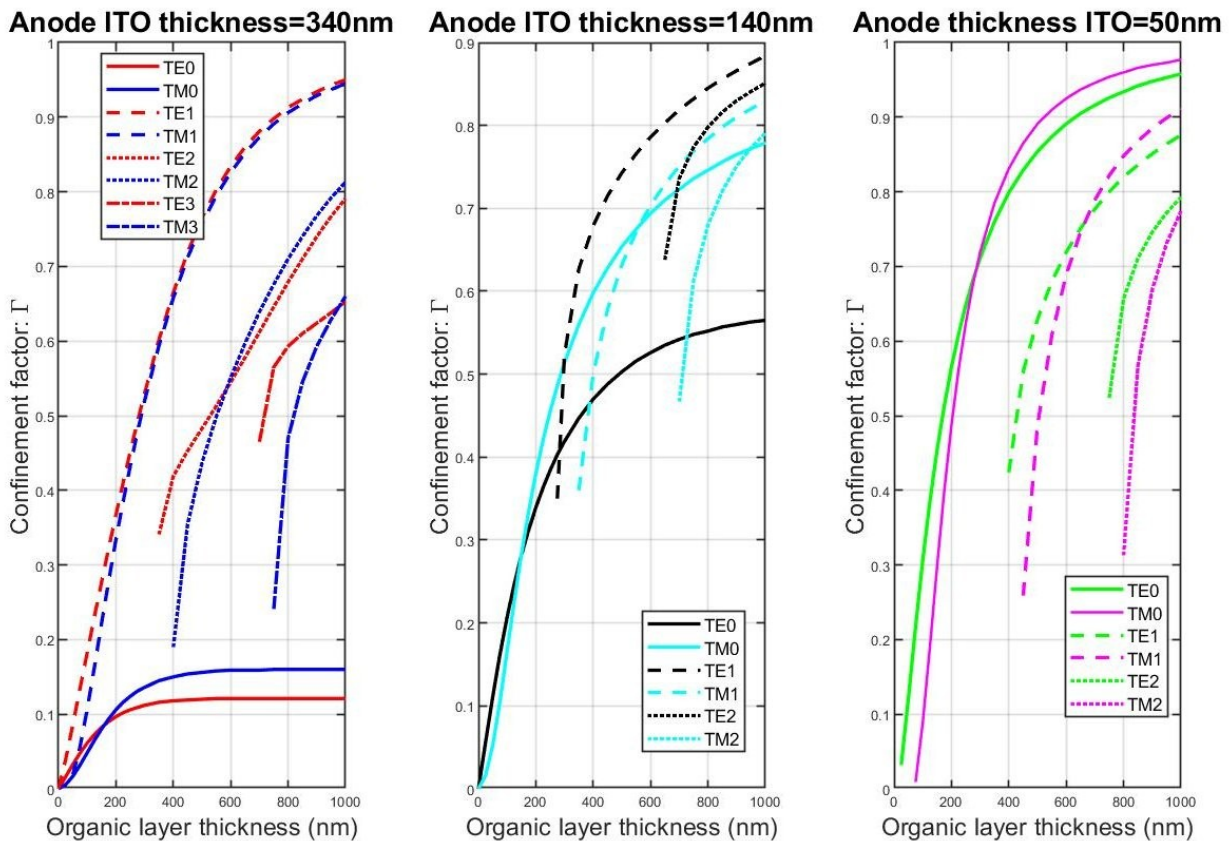


Figure. II.29: Confinement factor in organic layer vs organic thickness for ITO thickness ; 340nm (red (TE) and blue(TM)), 140nm (black(TE) and cyan(TM)) and 50nm (green(TE) and magenta(TM))

## II.4.4. Laser cavity design

This section is dedicated to the design of the DFB cavity. The calculation of the cavity profile based on the matrix transfer method requires to know the effective index  $n_{eff}$  and the index contrast  $\Delta n_{eff}$  of the considered multilayered system.

### II.4.4.1. Objectives and method

The first step is to calculate the above mentioned parameters ie the effective index  $n_{eff}$  and the index contrast  $\Delta n_{eff}$  on the structure

For this calculation, we use the same 1D solver of the electrical and magnetic field of the optical waveguide than in the section II.4.4.2. .

### II.4.4.2. Study of the effective index

The effective index  $N_{eff}$  can be defined as the propagation constant  $\beta$  in the waveguide divided by the free space propagation constant  $k$ .

$$N_{eff} = \frac{\beta}{k}$$

where  $k = \frac{2\pi}{\lambda}$  is the vacuum wavenumber associated with the specified vacuum wavelength  $\lambda$

There can be several effective indices depending on the modes that are excited in the waveguide. The effective index is one of the key parameter in guided propagation. The effective index depends on the wavelength and the mode in which light propagates.  $N_{eff}$  is not just a material property but is depended on the geometry of the waveguide as the thickness of the waveguide. Using the “OMS” script, we study the relationship between the effective index called also modal index and the waveguide geometry parameters.

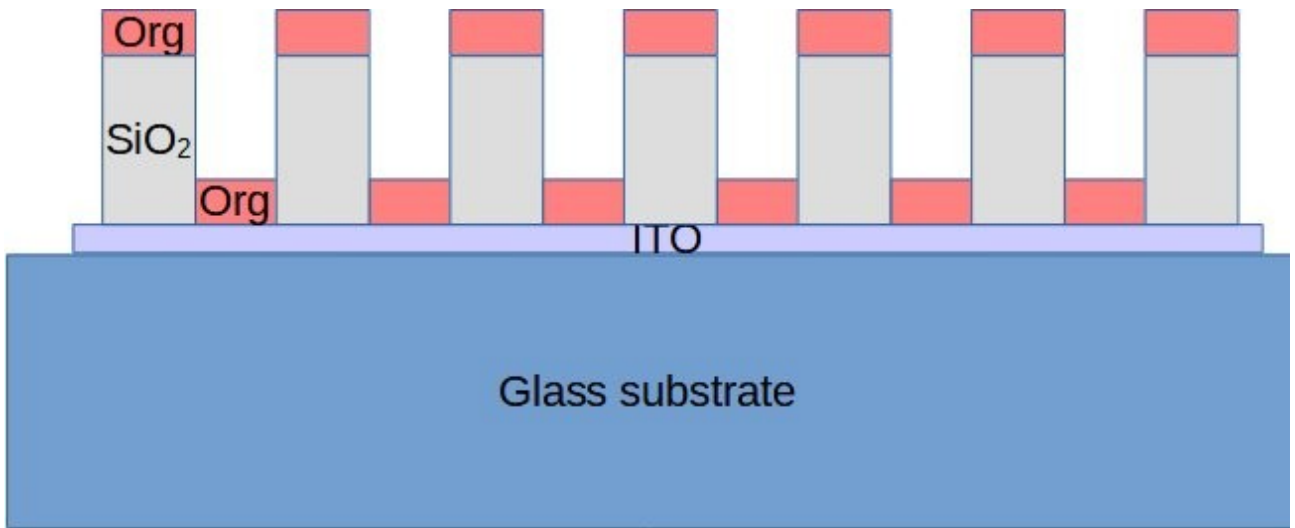
In the DFB cavity consists of a succession of  $\text{SiO}_2$  insulating lines deposited on the ITO conductive layer and separated by the organic layers. In a point of view of the waveguide thickness, two types of sections can be distinguished:

- Large thickness and low effective index ( $n_L$ ) sections as shown on Fig.II.30(b) consisting of an ITO layer with a thickness  $t_1$  and a refractive index  $n_1$ , covered with a  $\text{SiO}_2$  layer with a thickness  $t_2$  and a refractive index  $n_2$  and on top of which an organic layer is deposited with a thickness  $t_3$  and a refractive index  $n_3$ . The superstrate is air with refractive index  $n_0$ .
- Small thickness with high effective index ( $n_H$ ) sections as shown on Fig.II.30(c) consisting of an ITO layer with a thickness  $t_1$  and a refractive index  $n_1$ , covered with an organic layer with a thickness  $t_3$  and a refractive index  $n_3$ . The superstrate is air.

The low effective index ( $n_L$ ) and high effective index ( $n_H$ ) can be calculated for the different cases summarized in the table 2.14 with two parameters:

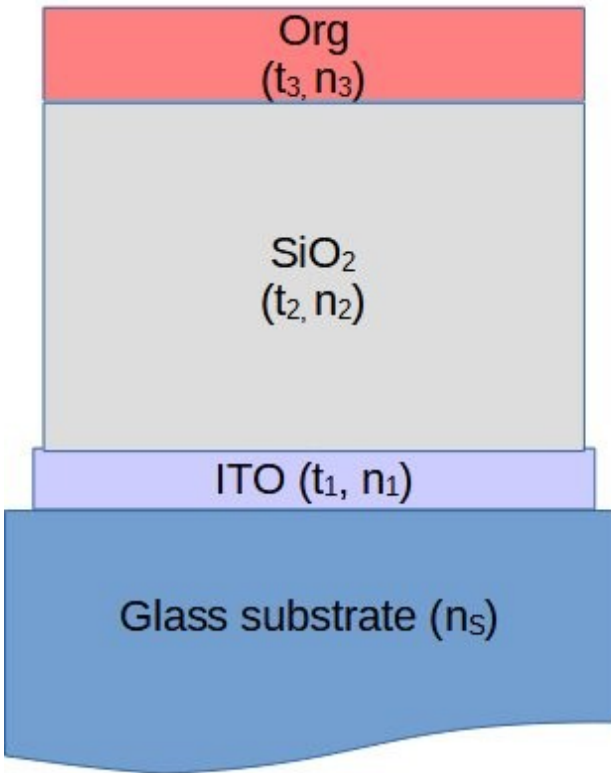
- The ITO thickness 340nm, 140 nm or 50nm.
- The organic layer thickness with either 200nm, 125nm or 100nm.

The  $\text{SiO}_2$  thickness is a new parameter to investigate which gives a new degree of freedom in the design of the DFB structure.

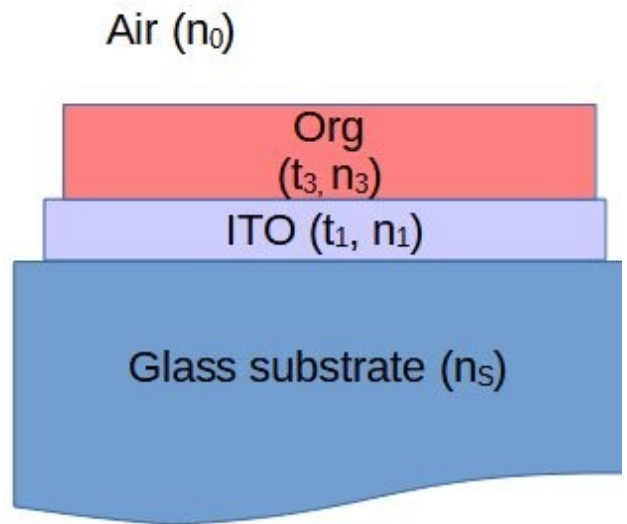


Air ( $n_0$ )

**a)**



**b)**



**c)**

Figure. II.30: DFB cavity and multilayered waveguide. a) DFB structure with periodic SiO<sub>2</sub> layer as both insulating and low index material b) Detail of the type 1 section with the SiO<sub>2</sub> layer resulting in low effective index  $n_L$  (a) Detail of the type 2 section without the SiO<sub>2</sub> layer resulting in an high effective index (b)



In the coming sections, we will evaluate, as a first step (§ II.4.4.2.1. ), the high and the low refractive indexes on the one hand and the parameters of the waveguide geometry such as the thickness of the different layers (ITO, organic and SiO<sub>2</sub>) on the other hand. In a second step (§ II.4.4.2.2. ), we will calculate the effective index contrast as a function of the SiO<sub>2</sub> thickness.

#### II.4.4.2.1. High effective index

The effective index  $n_H$  is calculated using the structure shown on FigII.30.c. Figure II.31 presents the high effective index for the TE<sub>0</sub> mode as a function of the organic layer thickness for an ITO thickness of 340nm (red), 140nm (blue) and 50nm (green). The effective index  $n_H$  increases when both the organic and the ITO layers thickness increase before reaching a plateau. For ITO thickness of 340nm, the plateau value  $n_H=1.813$  is reached for an organic layer thickness of 310nm. For 140nm of ITO, the effective index reaches  $n_H=1.716$  and remain constant above an organic layer thickness of 660nm. For 50nm of ITO, the plateau value is not reached below 1 $\mu$ m. The higher value of the effective index  $n_H=1.698$  is obtained starting from 3 $\mu$ m of the organic thickness (out of scale of figureII.31).

Figure II.32 presents the different effective index for different TE and TM modes as a function of the organic layer thickness, for the three different ITO thickness (340nm, 140nm and 50nm). As demonstrated previously, depending on the thickness of ITO, several TE and TM modes coexist. The general phenomenon is that the effective index  $n_H$  increases with both the ITO and the organic layers thickness. In the three cases of ITO thicknesses, the TE modes exhibit larger effective index values than the TM modes.

- In the 340nm case (figure II.31.left), the several TE and TM modes coexist for all the organic layer thicknesses. This means that in this case, lasing would probably be multimode. The highest effective index value  $n_H=1.813$  is obtained with the TE<sub>0</sub> mode. It is as large as  $n_H=1.806$  for  $t_3=100$ nm,  $n_H=1.809$  for  $t_3=125$ nm and  $n_H=1.811$  for  $t_3=200$ nm.
- For an ITO thickness  $t_1=140$ nm (figure II.31.middle), the TE<sub>1</sub> and TM<sub>1</sub> modes exist starting from  $t_3=270$ nm and  $t_3=320$ nm respectively. The  $t_3=270$ nm value allows a much larger range for the organic heterostructure thickness than what is needed from was reported by the Adachi's group with 200nm [2]. The highest effective index value  $n_H=1.717$  is obtained with the TE<sub>0</sub> mode which is 95% of the plateau value obtained with the 340nm case. The effective index for the TE<sub>0</sub> mode is as large as  $n_H=1.67$  for  $t_3=100$ nm,  $n_H=1.680$  for  $t_3=125$ nm and  $n_H=1.696$  for  $t_3=200$ nm and there is a significant index difference with the TM<sub>0</sub> mode with  $n_H=1.588$  for  $t_3=100$ nm,  $n_H=1.607$  for  $t_3=125$ nm and  $n_H=1.645$  for  $t_3=200$ nm. this is favorable to the TE<sub>0</sub> modes in the context of mode competition for lasing.
- For an ITO thickness  $t_1=50$ nm (figure II.31.right), the TE<sub>1</sub> and TM<sub>1</sub> modes exist starting from  $t_3=380$ nm and  $t_3=430$ nm respectively. Again this allow a rang larger than what is needed for an organic heterostructure thickness. The effective index for the TE<sub>0</sub> mode is  $n_H=1.526$  for  $t_3=100$ nm,  $n_H=1.546$  for  $t_3=125$ nm and  $n_H=1.591$  for  $t_3=200$ nm. Note these values are close to that of glass. The index difference with the TM<sub>0</sub> mode is respectively  $\Delta n_H = 0.067$ ,  $\Delta n_H = 0.074$ ,  $\Delta n_H = 0.058$  which is favorable to the TE<sub>0</sub> modes in the context of mode competition for lasing.

At this stage of the reasoning, the 340nm case offering the largest values for  $n_H$  seems the most interesting.

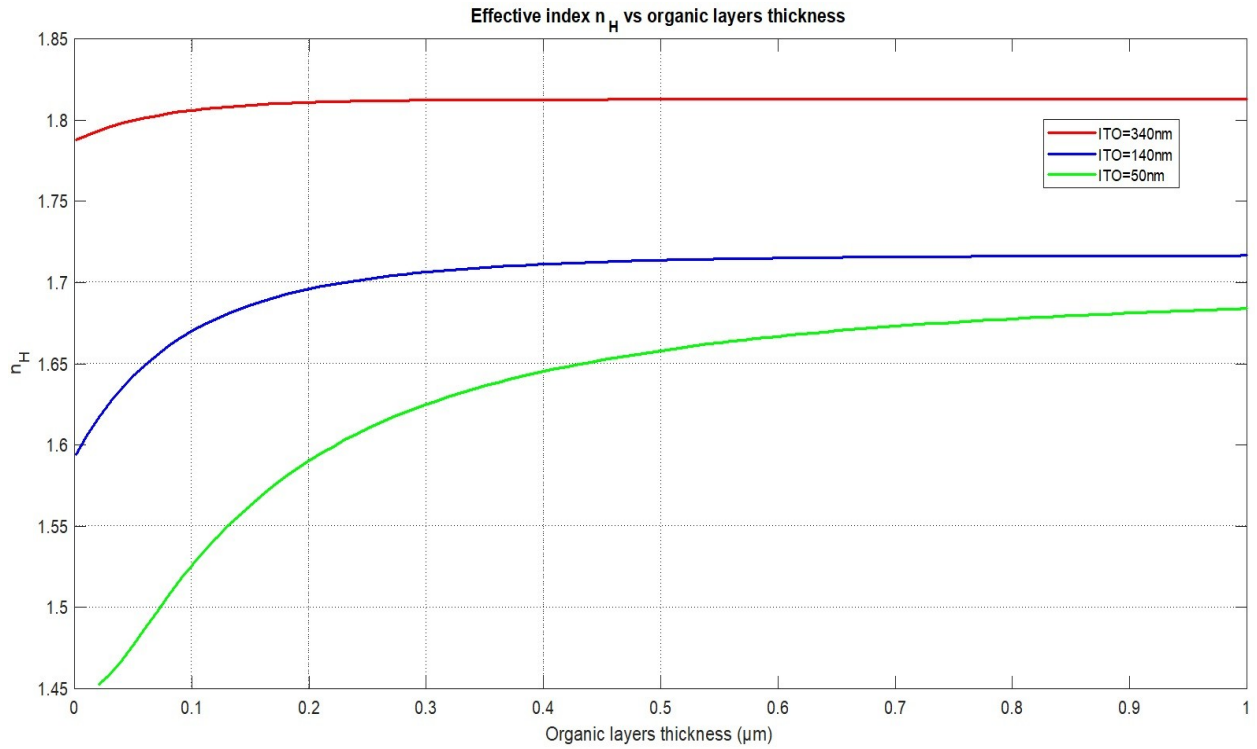


Figure. II.31: Effective index  $n_H$  of the type 2 section versus the organic layer thickness for ITO thickness; 340nm (Red), 140nm (blue) and 50nm (green)

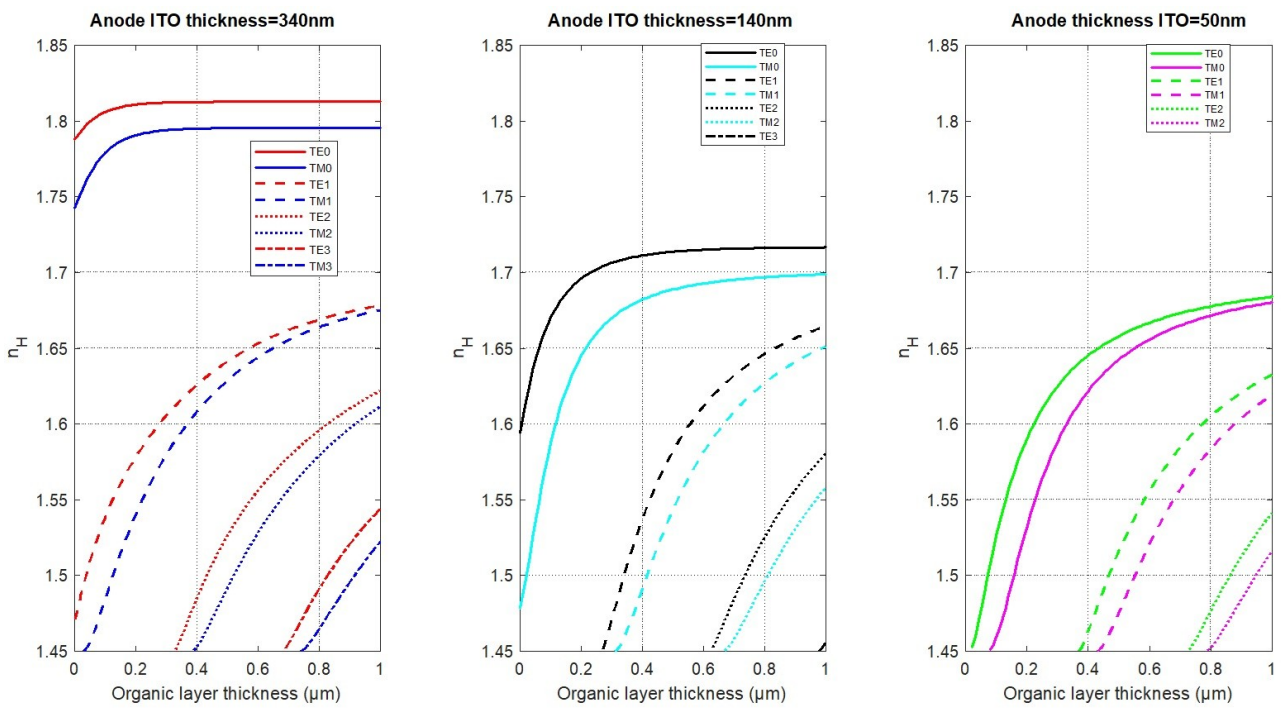


Figure. II.32: Effective index in organic layer vs organic thickness for ITO thickness ; 340nm (red (TE) and blue(TM)), 140nm (black(TE) and cyan(TM)) and 50nm (green(TE) and magenta(TM))

#### II.4.4.2.2. Low effective index

We call low effective index, the one calculated with the type 2 section presented Fig.II.30.

As shown on Fig. II.30.a the DFB cavity is made with an electrical silica insulation layer patterned with lines periodically arranged on the ITO layer. The section corresponding to the stack on top of a silica insulating line is the effective index to be calculated called low effective index  $n_L$ .

In this sub-section, we focus on the calculation of the effective index  $n_L$  as a function of the thickness of the silica ( $\text{SiO}_2$ ) layer thickness and aim at identifying the conditions for obtaining the lowest effective indexes. These calculations are performed for the  $\text{TE}_0$  mode only and is repeated for three values of the ITO thickness and three values of organic layer thickness as explained in II.4.3.3.3. .

Figure II.33 presents the effective index  $n_L$  as a function of the  $\text{SiO}_2$  thickness for different ITO thicknesses: 340nm (red), 140nm (blue) and 50nm (green). For each ITO thickness, the effective index is calculated for organic layer thickness of 100nm (solid lines), 125nm (dashed lines) and 200nm (dotted lines).

Figure II.33 shows 3 series of curves showing that the low effective index  $n_L$  decreases when the  $\text{SiO}_2$  thickness  $t_2$  increases. Lower plateaus are reached for  $t_2 > 200\text{nm}$ , 300nm and 500nm respectively  $n_L = 1.797$ ,  $n_L = 1.639$  and  $n_L = 1.493$  for the ITO thicknesses of 340nm, 140nm and 50nm respectively. Moreover, the low effective index  $n_L$  increases from  $\sim 1.55$ , to  $\sim 1.67$  and to  $\sim 1.8$  when the ITO thickness increases from 50nm, 140nm and 340nm respectively. The increase of the organic layer thickness also increases the low effective index  $n_L$ . A preliminary conclusion is that the lowest effective index are obtained with an ITO thickness  $t_1 = 50\text{nm}$  and with the lowest possible organic layers.

Note that the  $n_L$  differences between the 100nm, 125nm and 200nm cases increase with lower ITO thickness  $t_1$ .

#### II.4.4.2.3. Effective index contrast and conclusion

This sub-section is dedicated to the calculation of index contrast  $\Delta_{neff}$  between the effective index  $n_H$  and  $n_L$ :  $\Delta_{neff} = n_H - n_L$ . The effective index contrast is one of the key parameters to define the quality factor of the laser cavity. Indeed, a lower effective index contrast causes a lower reflectivity of the mirror and thus a smaller quality factor and as a consequence it decreases the amplification rate enhancing the laser threshold. The goal of this study is therefore to identify the optimum waveguide geometry offering the higher effective index contrast  $\Delta_{neff}$ . It is evaluated as a function of  $\text{SiO}_2$  layer thickness  $t_2$  for the nine combinations of ITO and organic layer thickness  $t_1$  and  $t_3$ .

Figure II.34 presents the effective index contrast  $\Delta_{neff}$  as a function of the  $\text{SiO}_2$  layer thickness  $t_2$  plotted on a logarithmic scale for three ITO layer thicknesses  $t_1 = 50\text{nm}$  (green), 140nm (blue) and 340nm (red) and for three organic layer thicknesses  $t_3 = 100\text{nm}$  (solid line), 125nm (dashed line) and 200nm (dotted line). The trends of the different curves show an increase of the effective index contrast  $\Delta_{neff}$  from zero to higher values up to 0.07 when the  $\text{SiO}_2$  layer thickness  $t_2$  is increased and when the ITO layer thickness is decreased.

- For the 340nm case the highest index contrast is  $\Delta_{neff} = 0.016$  obtained with an organic layer thickness  $t_3 = 200\text{nm}$ .

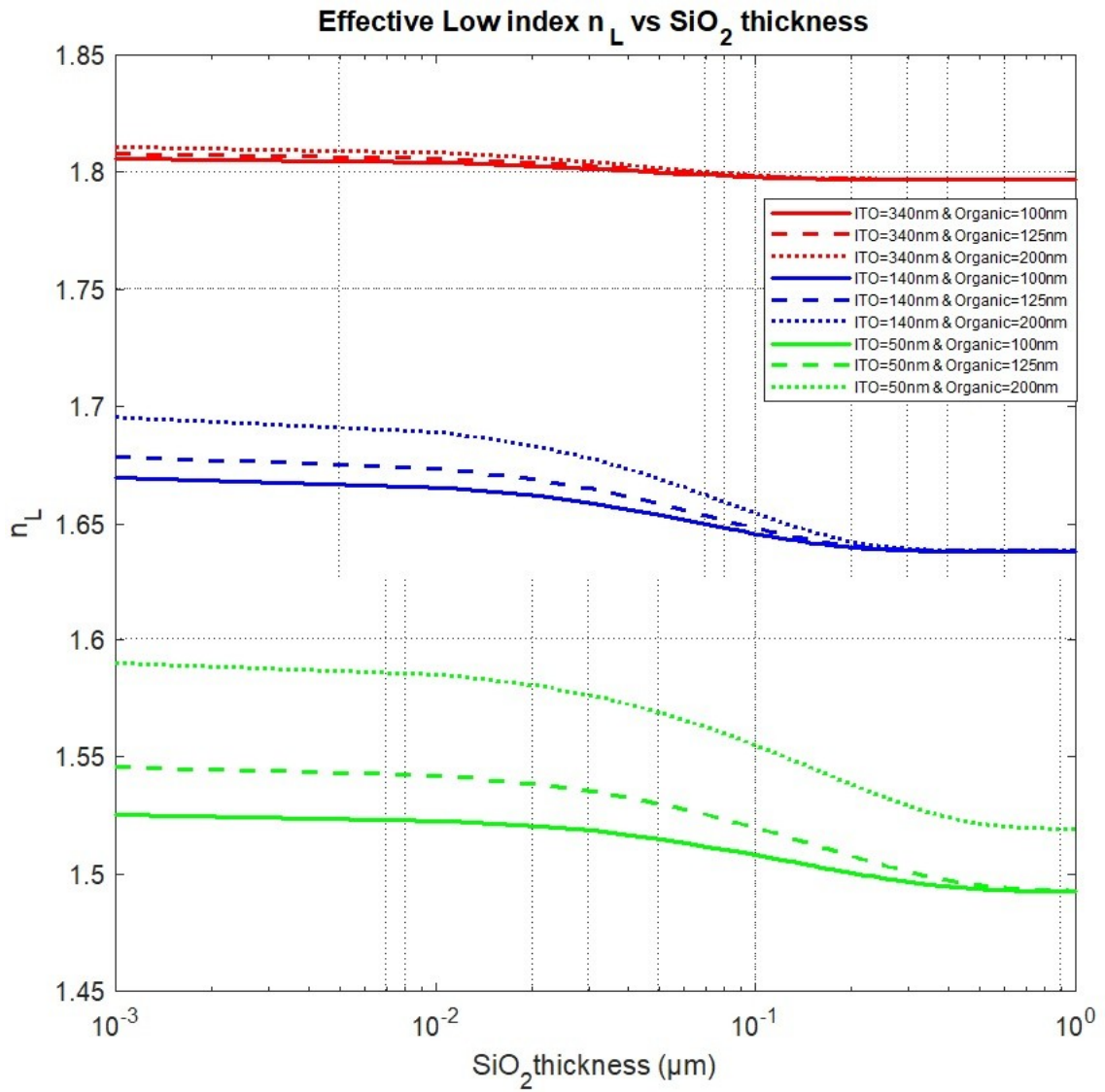


Figure. II.33: Effective index  $n_L$  versus  $\text{SiO}_2$  layer thickness for different ITO thickness; 340nm (red), 140nm (blue) and 50nm (green) and for different organic thickness; 100nm (solid lines), 125nm (dashed lines) and 200nm (dotted lines)

- For the 140nm case the highest index contrast is  $\Delta_{neff} = 0.057$  obtained with an organic layer thickness  $t_3=200\text{nm}$ . For SiO<sub>2</sub> layer thicknesses of  $t_2= 100\text{nm}$ ,  $t_2= 50\text{nm}$ , the index contrasts is large than that for the  $t_1=50\text{nm}$  case and are  $\Delta_{neff} = 0.042$  ,and  $\Delta_{neff} = 0.027$  respectively.
- 1. For the 50nm case the highest index contrast is  $\Delta_{neff} = 0.071$  obtained with an organic layer thickness  $t_3=200\text{nm}$ . For SiO<sub>2</sub> layer thicknesses of  $t_2= 300\text{nm}$ ,  $t_2= 100\text{nm}$ ,  $t_2= 50\text{nm}$  (Achievable SiO<sub>2</sub> thickness to be obtained with a HSQ photoresist), the index contrasts are  $\Delta_{neff} = 0.061$  ,  $\Delta_{neff} = 0.035$  and  $\Delta_{neff} = 0.021$  respectively.

Table 2.15 summarizes the values of high effective index  $n_H$ , low effective index  $n_L$  and effective index contrast  $\Delta_{neff}$  for nine different combination based on;

- Three values of the ITO layer thicknesses 340nm, 140nm and 50nm.
- Three thicknesses of the organic layer 100nm, 125nm and 200nm.
- Three SiO<sub>2</sub> layer thicknesses (300nm, 100nm and 50nm). This choice is based on the capacity of the fabrication.

The highest index contrast is  $\Delta_{neff} = 0.061$  obtained with  $t_1=50\text{nm}$ ,  $t_2=300\text{nm}$  and  $t_3=200\text{nm}$  which we will consider to be the optimum case in what follows.

As a conclusion, we highlight three design rules:

1. The thinner the ITO thickness  $t_1$  the higher the index contrast. The 340nm case can be discarded because of the lowest index contrasts. The 50nm is to be preferred as it offers among the highest index contrasts.
2. The thicker the SiO<sub>2</sub> layer  $t_2$  is, the higher the index contrast is. The case with 50nm of SiO<sub>2</sub> can be discarded.
3. The thicker the organic layer  $t_3$ , the higher the index contrast. The optimal thickness will depends on the emission wavelength because a quarter wavelength optical thickness is to be targeted to achieve the most efficient emission. The emitting layer being to be located at the belly of a transversal standing wave.

Note that for  $\lambda=625\text{nm}$  , and in the case ( $t_1=140\text{nm}$ ,  $t_2=300\text{nm}$  and  $t_3=100\text{nm}$ ) the effective index being  $n_L=1.638$ , a quarter wavelength optical thickness of 155nm leads to a geometrical thickness  $d=95\text{nm}$  not far from  $t_3$ .

The same calculation for the above so called optimum case leads to a larger difference with the quarter wavelength optical thickness.

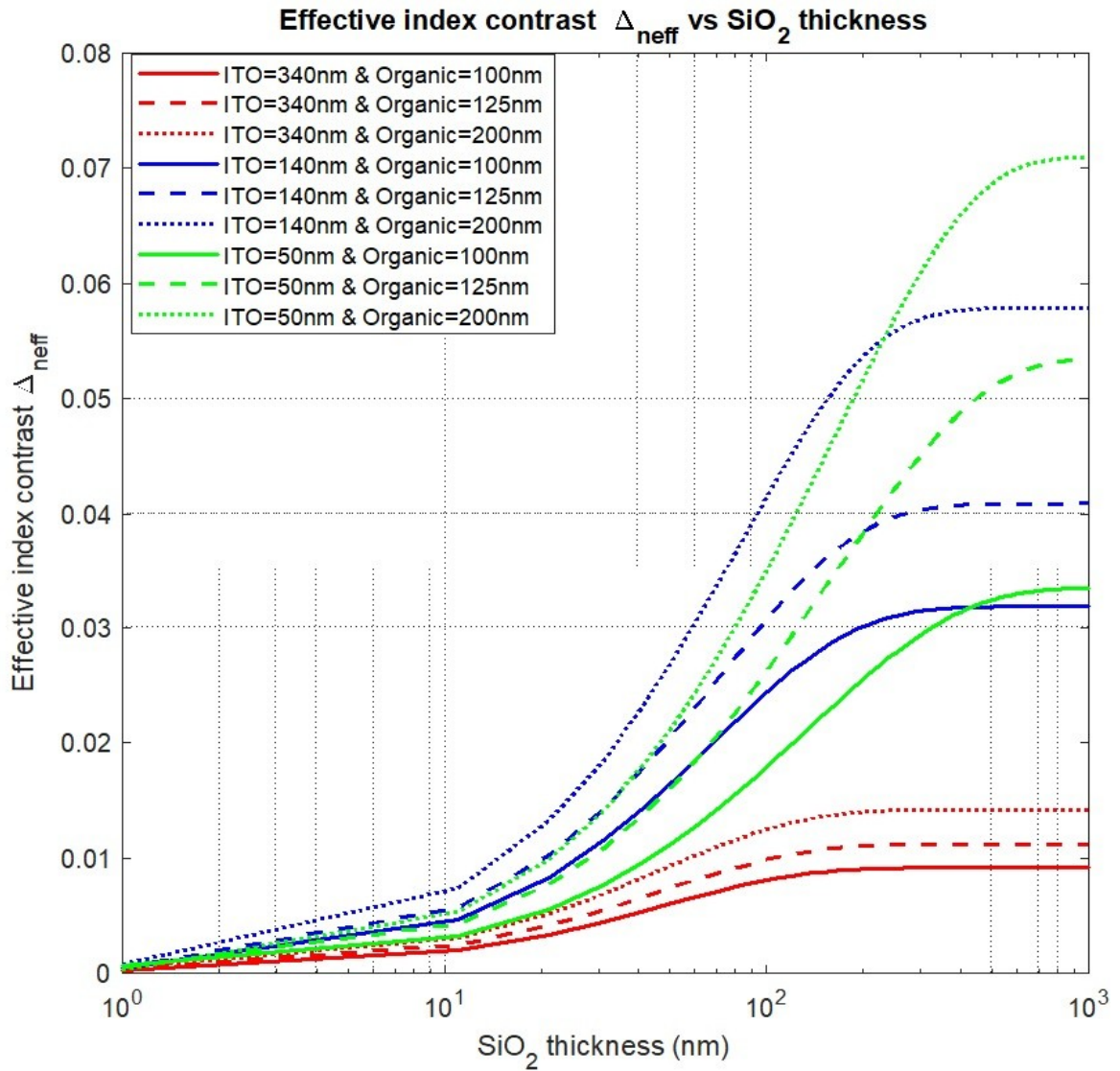


Figure. II.34: Effective index contrast vs SiO<sub>2</sub> layer thickness for ITO thickness; 340nm (Red), 140nm (blue) and 50nm (green) and organic thickness; 100nm (continued line), 125nm (discontinued line) and 200nm (point line)

ITO thickness $t_1$ (nm)	Organic thickness $t_3$ (nm)	$n_H$	$n_L$			$\Delta_{neff}$		
			SiO <sub>2</sub> thickness $t_2$ (nm)			SiO <sub>2</sub> thickness $t_2$ (nm)		
			50	100	300	50	100	300
50	100	1.526	1.515	1.508	1.497	0.0107	0.0175	0.029
	125	1.546	1.530	1.519	1.501	0.016	0.026	0.045
	200	1.590	1.569	1.555	1.529	0.021	0.035	0.061
140	100	1.670	1.654	1.646	1.638	0.016	0.024	0.031
	125	1.679	1.659	1.648	1.639	0.021	0.031	0.040
	200	1.696	1.669	1.655	1.639	0.027	0.041	0.057
340	100	1.806	1.799	1.798	1.797	0.006	0.008	0.009
	125	1.808	1.800	1.798	1.797	0.007	0.009	0.011
	200	1.811	1.802	1.799	1.797	0.009	0.012	0.014

## II.4.5. Design of the distributed feedback cavity

This section is dedicated to the design of a distributed feedback (DFB) laser cavity. More precisely we aim at identify the optimal geometry maximizing the quality factor.

### II.4.5.1. Objectives and methods

The Matrix transfer method is used to calculate the reflectance considering the DFB cavity is a periodic stack (grating) with alternation of high index and low index materials. Each layer of the stack is considered infinite in the x and y directions while the incident light propagate in the z direction as shown in fig. II.35. The assumption of layers infinite in the x and y direction is strong because, in reality the optimal thickness of the type1 and type2 sections presented in fig. II.30 are only few hundred of nanometers as summarized in table 2.15. For this reason, we plan to compute a 3D-FDTD analysis to confirm the results obtained with the matrix transfer method.

The targeted DFB laser cavity apriori consist of a left mirror (Mirror 1) and a right mirror (Mirror 2) surrounding a defect zone. In conventional laser the gain medium is located in between the mirrors (Defect zone), whereas in our case, the gain medium will be distributed along the structure as part of the high index layers (orange in Fig. II.36).

The study is split into three parts:

- As first step, we will consider a single mirror and will investigate how the reflectance evolves with the number N of pairs.
- In a second step, we will introduce defects in between mirrors. We will then investigate the quality factor for different defects and search how to maximize it.
- We will confirm this results with a 3D FDTD calculation

### II.4.5.2. Single multilayered (DFB) mirror

In this first step we consider a single mirror made of N pairs of quarter wavelength ( $\lambda/4$ ) layers of high index ( $n_H$ ) and low index ( $n_L$ ), the central wavelength  $\lambda_c=605nm$  corresponding to the peak wavelength of the DCM. (A similar reasoning would apply for other wavelength and other materials). Each mirror starts and ends with high index layers, and thus is made of N pairs and a single high index layer as shown on Fig. II.36. We neglect the absorption, thus each layer is characterized by a pure real index. In absence of absorption, the reflectance R and the transmittance T in intensity are link by the trivial relationship  $R+T=1$  as shown on Fig. II.37. The transmittance T and the reflectance R have been calculated with N=100 pairs (plus a high index layer) for the different index contrasts listed in table 2.15 to which we added  $\Delta_{neff} = 0.25$  corresponding to the index difference between the bulk organic material  $n=1.7$  and that of the  $SiO_2$   $n=1.45$ . The different reflectances presented in Fig. II.37 exhibit band-pass properties with the largest values of the reflexion in wavelength ranges  $\Delta\lambda$  centered on  $\lambda_c=605nm$ . Transmittances exhibits notch-filters properties with the same bandwidth  $\Delta\lambda$ . In some cases the bandwidth  $\Delta\lambda$  are the one dimensional equivalent to the forbidden bandgap of photonic crystals.

From fig. II.37 the width  $\Delta\lambda$  of the forbidden bandgaps can be compared for the different index contrasts:



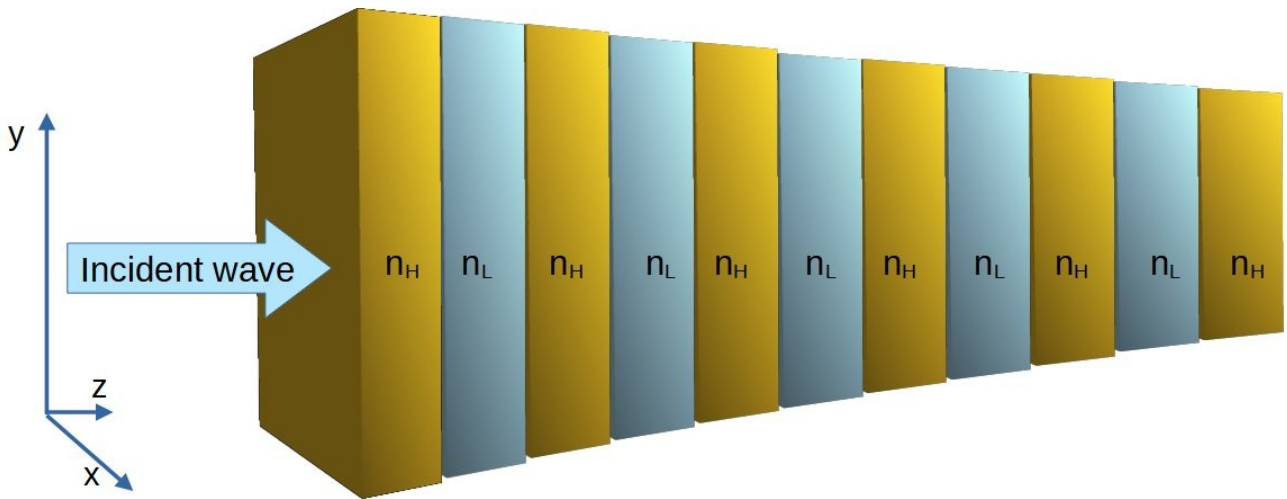


Figure. II.35: Stack used to calculate transmittance and reflectance with the matrix transfer method

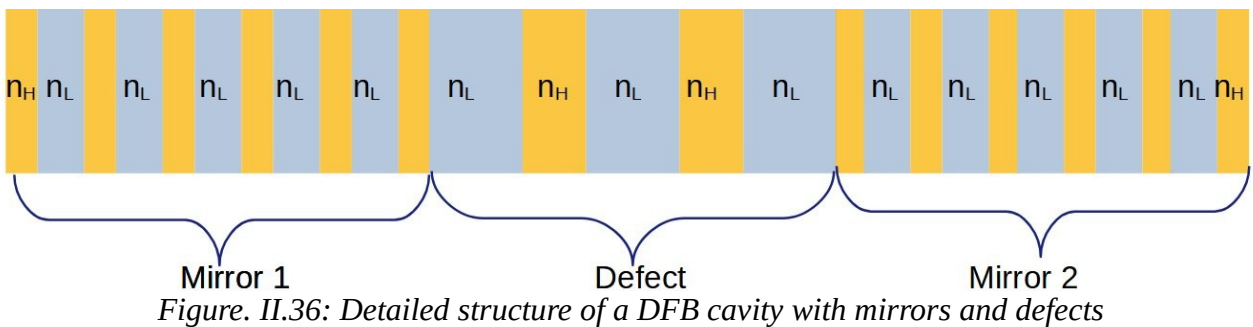


Figure. II.36: Detailed structure of a DFB cavity with mirrors and defects

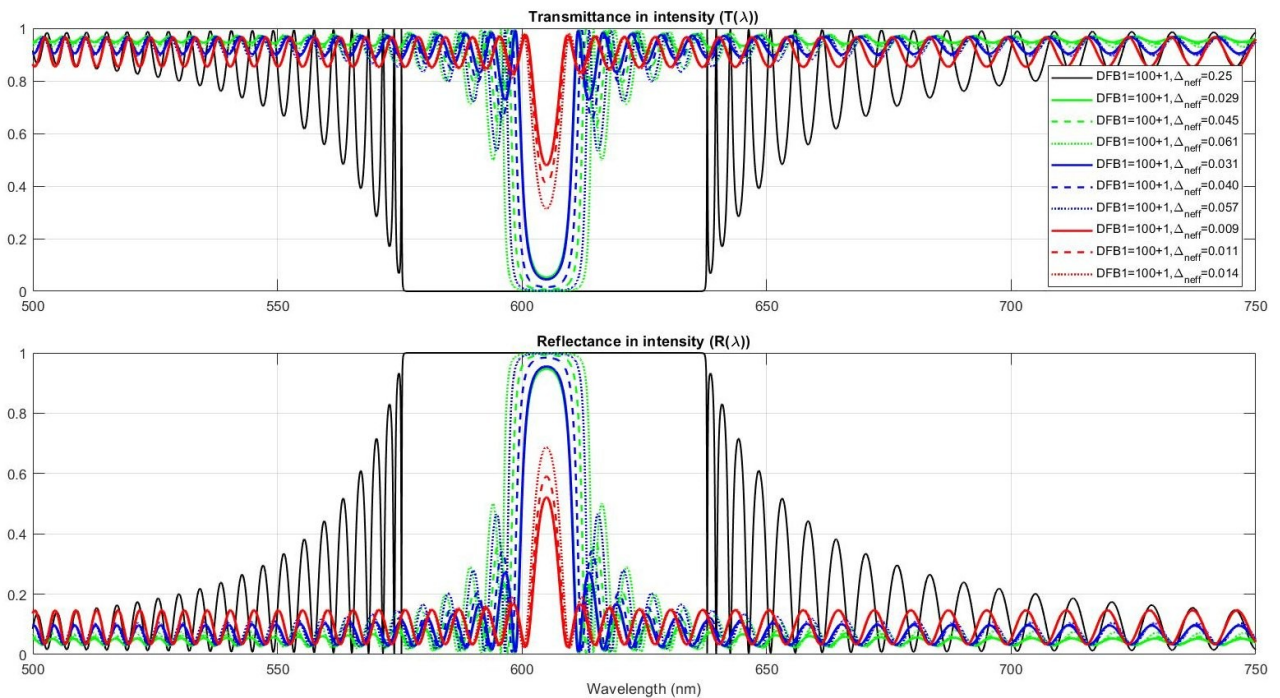


Figure. II.37: Transmittance  $T(\lambda)$  (top) and reflectance  $R(\lambda)$  (bottom) calculated for  $N=100$  pairs (+1 high index layer) and for the different index contrasts listed in table 2.15:  $\Delta_{neff}=0.25$  (black) offers the largest forbidden bandgap.  $R$  and  $T$  calculated for  $t_1=50\text{nm}$  and  $t_2=300\text{nm}$  (green),  $R$  and  $T$  calculated for  $t_1=140\text{nm}$  and  $t_2=300\text{nm}$  (blue).  $R$  and  $T$  calculated for  $t_1=340\text{nm}$  and  $t_2=300\text{nm}$  (red).



- $T_1(\lambda)$  is the transmittance of the multilayered mirror calculated with the large index contrast  $\Delta_{neff} = 0.25$ . Light transmission is close to zero from 589nm to 654nm, resulting in a full width at half maximum (FWHM) bandwidth of  $\Delta\lambda_1 = 65\text{ nm}$ .
- $T_2(\lambda)$  is the transmittance calculated with the index contrast  $\Delta_{neff} = 0.061$  corresponding to the optimum index contrast listed in table 2.15 (ITO thickness is  $t_1=50\text{nm}$ , SIO2 thickness is  $t_2=300\text{nm}$  and the thickness of the organic layers is  $t_3=200\text{nm}$ ). The calculated FWHM bandwidth is  $\Delta\lambda_2 = 18\text{ nm}$ .
- For the index contrasts  $\Delta_{neff} = 0.057$ ,  $\Delta_{neff} = 0.045$ , and  $\Delta_{neff} = 0.040$  respectively the FWHM bandwidth are  $\Delta\lambda_3 = 15\text{ nm}$ ,  $\Delta\lambda_4 = 14\text{ nm}$ , and  $\Delta\lambda_5 = 12\text{ nm}$  respectively.
- For the index contrast,  $\Delta_{neff} = 0.014$ ,  $\Delta_{neff} = 0.011$ , and  $\Delta_{neff} = 0.009$  the transmittance and reflectances are plotted in red in Fig. II.37. For these values, and in the case  $N=100$ , the FWHM bandwidths of the reflectance can be calculated but the corresponding peak values hardly exceed 0.6, which indicates no forbidden bandgap exists.

A trend can be identified; the width of the reflectance become narrower when the index contrast reduces. This is similar to what is observed with two dimensional photonic crystal with the forbidden bandgap depending on the index contrast.

Note that, the forbidden bandgap  $\Delta\lambda_2 = 18\text{nm}$  corresponding to the maximum calculated in table 2.15 is about 4 times narrower than the full width at half maximum (FWHM) of the electroluminescence spectra of the dopant which is about 80nm (see Fig. II.19). The laser cavity will therefore be efficient only on a small spectral range of the laser gain spectra and very likely spontaneous emission and stimulated emission will occur simultaneously.

We will now investigate the effect of the number  $N$  of pairs on the width  $\Delta\lambda$  of the reflectance windows from which we will estimate the forbidden bandgap. The number of pairs is varied from  $N=2$  (+1 layer) to 210 pairs (+1 layer), and for each number  $N$  of pairs the reflectance is calculated for  $\Delta_{neff}=0.25$  and for the nine different index contrasts value listed in the last column of table 2.15. The width in wavelength of the windows for which the reflectances is maximum can be estimated at half maximum giving a range  $\Delta\lambda$  from which the forbidden bandgap can be estimated. The result is plotted fig.II.38. The different width  $\Delta\lambda$  of the reflectance windows calculated as a function of  $N$  for the nine index contrasts of last column of table 2.15 are presented in the left axis, while the maximum of the reflectance windows correspond the right axis of top fig. II.38. The amplitudes of the reflectance calculated for  $\Delta_{neff} = 0.061$ ,  $\Delta_{neff} = 0.057$ ,  $\Delta_{neff} = 0.045$ ,  $\Delta_{neff} = 0.040$ ,  $\Delta_{neff} = 0.031$ , and  $\Delta_{neff} = 0.029$  exceed 0.95 for  $N \geq 100$ , while for lower index contrast the amplitudes of the reflectance do not exceed 0.95 even for pair numbers  $N$  as large as 200. On the bottom figure II.38 are plotted the width  $\Delta\lambda$  in the cases  $R \geq 0.95$  as an estimation of the forbidden bandgap. It shows a small decrease of the width  $\Delta\lambda$  of the forbidden bandgap with the number  $N$  of pairs.

We have checked numerically that for large numbers of pairs ( $N \gg 25$ ) mirrors starting and ending with low index ( $n_L$ ) layers exhibit similar (but slightly smaller) width of the forbidden bandgap than those starting and ending with high index layers ( $n_H$ ).

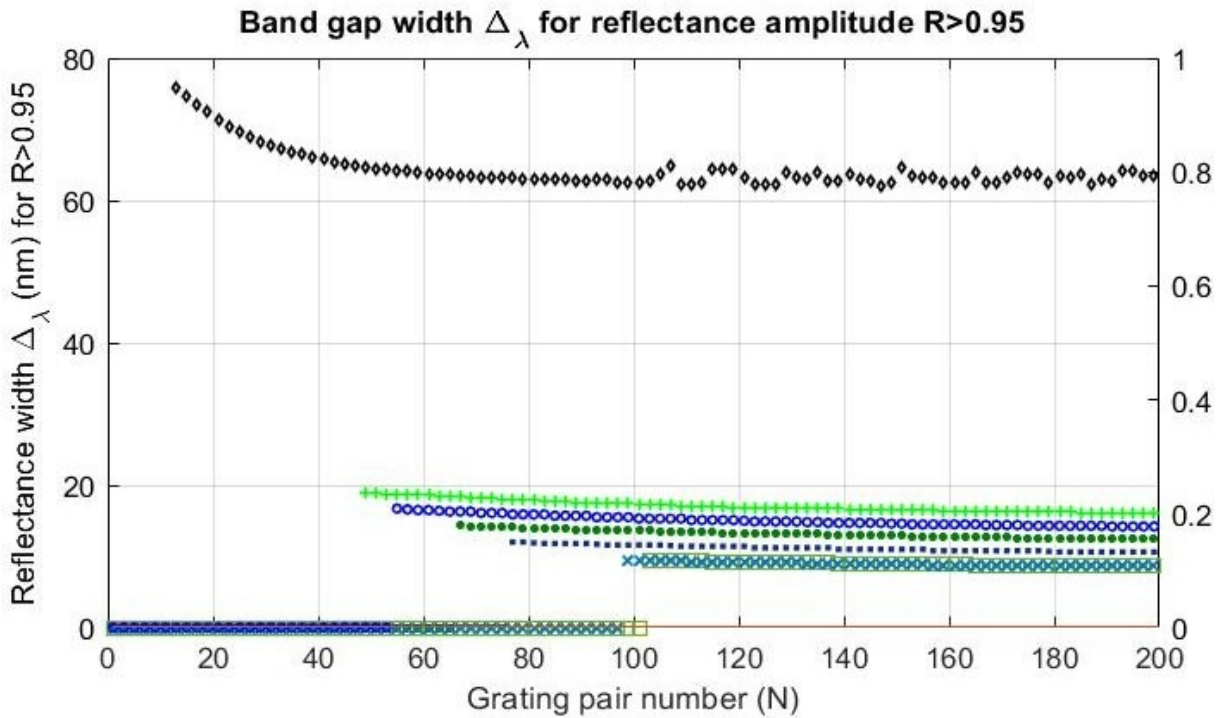
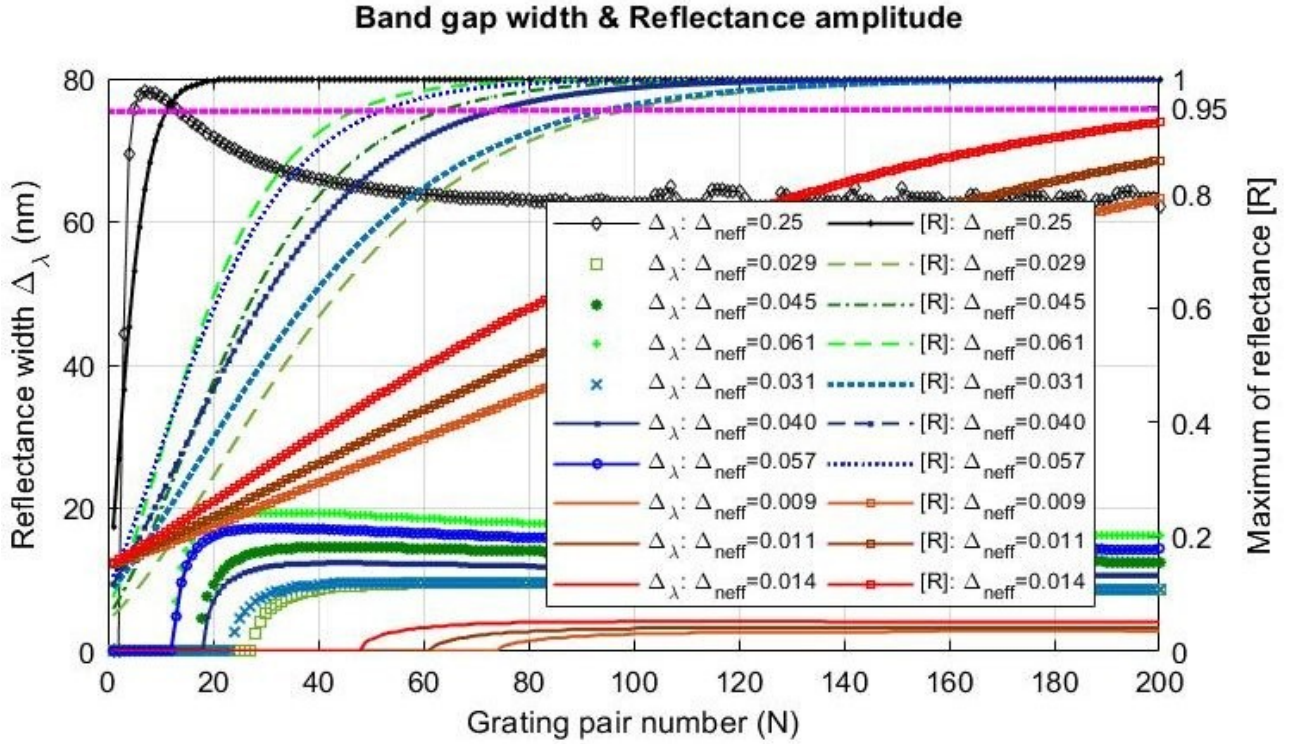


Figure. II.38: Width FWHM of the reflectance windows as a function of the number  $N$  of pairs of layers. (top) Width of the reflectance windows calculated for nine index contrasts (left axis) and the peak wavelength of the reflectance windows for the same nine index contrasts (right axis). (bottom) values of the full width at half maximum (FWHM) of the reflectance windows as a function of the number  $N$  of pairs for peak reflectance above 0.95. With the “bulk” index contrast  $\Delta_{neff} = 0.25$  the forbidden bandgap converges to  $\Delta\lambda_1 = 65\text{nm}$  when  $N > 100$ . For  $\Delta_{neff} = 0.061$  the forbidden bandgap is 18nm and 16nm for  $N=80$  and 200 pairs respectively.

### II.4.5.3. Cavities consisting of DFB mirrors and defects in between

As a second step, we investigate DFB cavities designed with the following rules:

- Cavities are made of a left and a right mirrors with a defect in between (See Fig. II.39)
- Mirrors (light yellow and light grey Fig. II.39) are made of  $N$  pairs of quarter wavelength ( $\lambda/4$ ) layers alternatively of high-index ( $n_H$ ) and low-index ( $n_L$ ), where  $\lambda$  is the considered central wavelength. Each mirror starts and ends with high index layers ( $n_H$ ), and thus is made of  $2N+1$  layers. This is particularly important when the number  $N$  of pairs is small ( $<10$ ).
- Defect (darker grey and yellow Fig. II.39) are made of high index ( $n_H$ ) and low index ( $n_L$ ) with a total optical thickness that is an odd number of half-wavelength such that after one round-trip the accumulated phase is a multiple of the wavelength resulting in a constructive interference. Because mirrors starts and ends with a high-index layers, defects have to starts and ends with a low index layer ( $n_L$ ). The smallest defect is a single half-wavelength layer made of low index ( $n_L$ ) as in Fig. II.39.a). Different types of defects can be distinguished:
  - The defect starts and ends with a half-wavelength optically thick low-index ( $n_L$ ) layer as in Fig. II.39.a,b,c. In between the starting and ending half-wavelength optically thick low-index ( $n_L$ ) layers, three main manners to arrange other layers have been identified:
    - an even number of half-wavelength thick low-index layers (See Fig. II.39.a)
    - an odd number of half-wavelength thick high-index layers (See Fig. II.39.b)
    - an alternation of half-wavelength thick high-index ( $n_H$ ) and low-index ( $n_L$ ) layers. With a total optical thickness equal to  $2M+1$  where  $M$  is the number of pairs of high-index ( $n_H$ ) and low-index ( $n_L$ ) layers (See Fig. II.39.c).
  - The defect starts and ends with a quarter-wavelength optically thick low index ( $n_L$ ) layers (Fig. II.39.d). Because both starting and ending quarter-wavelength optically thick low index ( $n_L$ ) layers accumulate a half-wavelength phase, an even number of half-wavelength thick high-index layers ( $n_H$ ) is to be inserted.

The different cavities with the different types of defect all exhibits resonances as shown on fig. II.39. The resonances are centered at the central wavelength  $\lambda_c=605nm$  with  $\delta\lambda$  full width at half maximum (FWHM). This is an indication that they are suitable as laser cavity centered on the maximum DCM electroluminescence maximum.

The type c of defects consisting of an alternation of half-wavelength thick high-index ( $n_H$ ) and low-index ( $n_L$ ) layers constitute a second order grating. It is sometimes called “DFB2” in the text below. The advantage of defects made with second order grating is to provide scattering in the direction perpendicular to the plan of the grating at the wavelength of resonance. This offer the possibility to measure the device light intensity more easily.

Note that, with a defect made with an alternation of half-wavelength thick high-index ( $n_H$ ) and low-index ( $n_L$ ) layers as in fig. II.39.c, the FWHM reflectance window (forbidden bandgap) is enlarged (see dotted blue curve Fig. II.40). For example with  $N=50$  pairs and  $M=5$  for a second order grating type of defect,  $\Delta\lambda = 90nm$  which is an increase of 50% compared to the reference spectrum extracted from Fig. II.37. The reference spectrum is plotted again with a blue thick solid line in Fig. II.40. This enhancement of the FWHM of the forbidden bandgap is advantageous for a reduction of the spontaneous emission components of the spectra with respect to that of the stimulated emission allowing potentially a less noisy detection of the stimulated emission components.

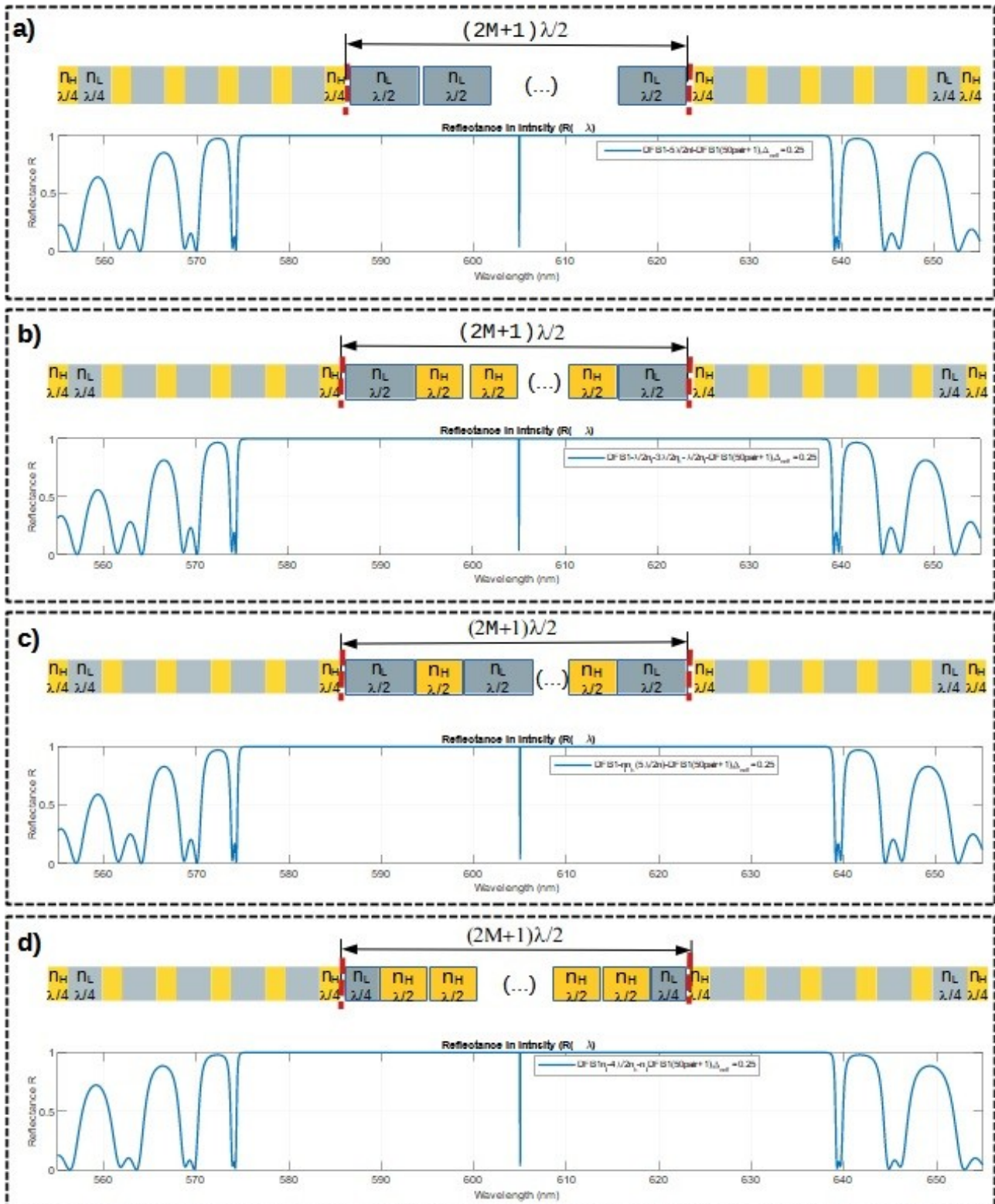


Figure. II.39: Different types of cavity with different types of defects: a) an even number of half-wavelength thick low-index layers, b) an odd number of half-wavelength thick high-index layers, c) an alternation of half-wavelength thick high-index ( $n_H$ ) and low-index ( $n_L$ ) layers.

#### II.4.5.4. Quality factor of DFB cavities

The quality factor of the passive (empty) cavity can be calculated from  $\delta \lambda$  the full width at half maximum (FWHM) of the resonance:

$$Q = \frac{\lambda_c}{\delta \lambda} \quad \text{Eq. (II.86)}$$

For example, with left and right mirrors made of  $N=50$  pairs plus one  $n_H$  layer, and a second order grating (type c of defect) with  $M=5$  exhibits a FWHM resonance  $\delta \lambda = 1.6 \text{ nm}$  resulting in quality factor  $Q=387$  (See Fig.II.40).

To compare the different configurations and identify the most relevant one, we compare the quality factors  $Q$  for the different index contrast and for each type of defect in Fig. II.41. Using the matrix transfer method we compute the transmittance varying the pair number  $N$  varies between 1 and 200, while the pairs of defect is fixed to  $M=2$  (5 layers), and calculate the FWHM resonance linewidth. The quality factor is plotted with a logarithmic scale as a function of  $N$  the pairs in each mirror.

First of all, it is to be noted that the quality factors increases with  $N$  the number of pairs. The slope in logarithmic scale appears linear, meaning an exponential increase. The “slope” is different for the different index contrast ( $\Delta_{neff} = 0.25$ , black,  $\Delta_{neff} = 0.061$  green,  $\Delta_{neff} = 0.057$  blue,  $\Delta_{neff} = 0.014$  red). The better the index contrast, the larger the slope of the quality factor is.

With these simulation performed without absorption, quality factors in excess of  $Q > 1000$  are obtained with  $N > 51$  (respectively  $N > 65$ , and  $N > 87$ ) for  $\Delta_{neff} = 0.061$  green, (respectively  $\Delta_{neff} = 0.057$  blue,  $\Delta_{neff} = 0.014$  red).

For  $\Delta_{neff} = 0.061$  (green), quality factors over  $Q \geq 3000$  and  $Q \geq 5000$  are obtained with  $N \geq 66$  and  $N \geq 72$ . For  $\Delta_{neff} = 0.057$  (blue), quality factors over  $Q \geq 3000$  and  $Q \geq 5000$  are obtained with  $N \geq 73$  and  $N \geq 81$ .

Quality factors in excess of  $Q > 1,000,000$  can be obtained with  $N > 141$  and  $N > 157$  respectively for  $\Delta_{neff} = 0.061$  (green) and  $\Delta_{neff} = 0.057$  (blue) respectively.

The quality factor barely exceeds  $Q=1000$  for  $N=200$  in the less favorable case with  $\Delta_{neff} = 0.014$ .

The quality factors barely change as a function of the type of defect. Indeed whatever the different index contrast is, the defect cavities types a, c and d are superimposed; The type b is slightly lower than the other types but the difference is small and thus is not an obstacle.

These results were obtained without taking into account the absorption of ITO and of SiO<sub>2</sub>. The absorption of the organic semiconductors is not taken into account in the calculation of the reflectance, but it is present in the organic laser diode model with  $W_0$  the residual absorption. This leads to overestimate the quality factor. To take the effect of the absorption into account in order to maximize the quality factors, the number  $N$  of pairs should be increased.

Note that the transfer matrix method do not take into account the diffraction perpendicular to the plane of the grating and a such overestimate the quality factor.



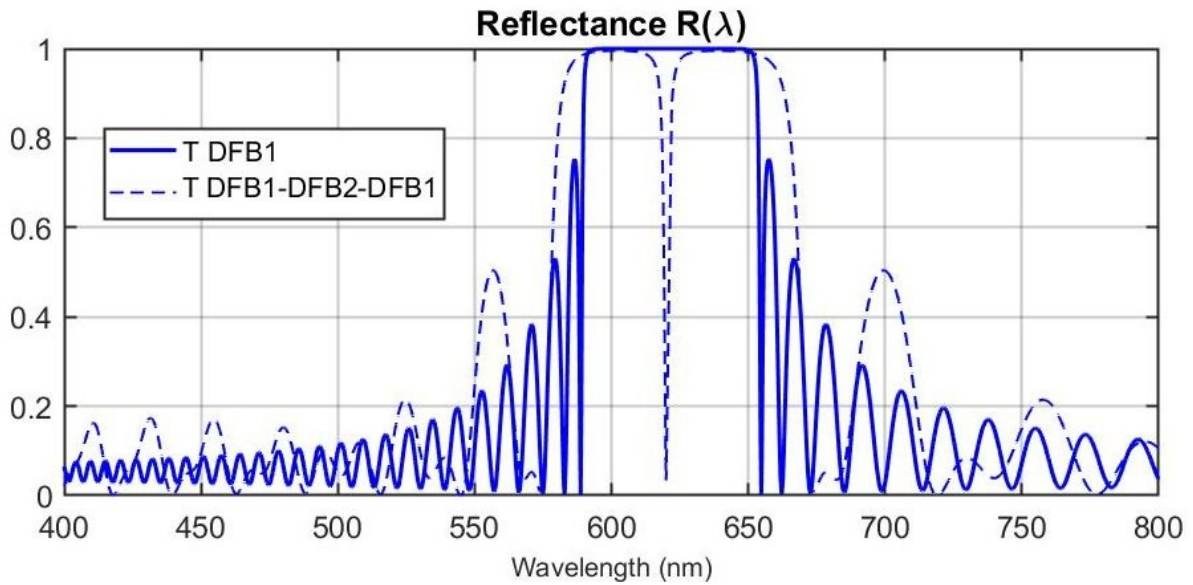


Figure. II.40: Reflectance of a single mirror (DFB1) (blue solid line) and two mirrors (DFB1) surrounding defects (DFB2) (thin blue dashed line)

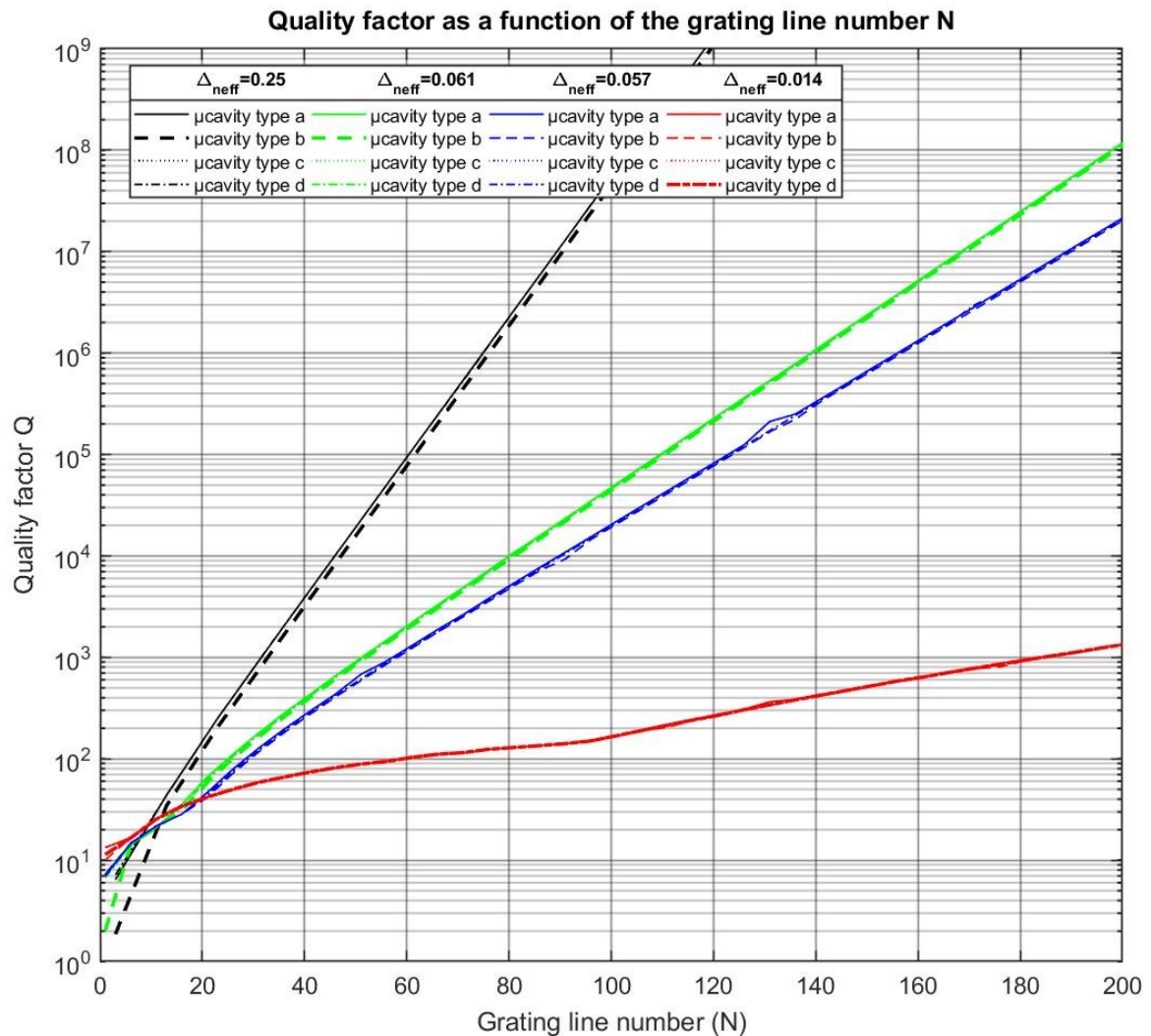


Figure. II.41 : Quality factor of the different type of cavities with different types of defects a a function of the number of pairs in the mirrors

### II.4.5.5. Finite-difference time domain analysis and confirmation

To confirm the calculation done with the transfer matrix formalism, we performed Finite Difference Time Domain (FDTD) calculations using Rsoft.

#### II.4.5.5.1. FDTD method

The finite difference time domain method, introduced by K.S.Yee in 1966 [], is a sophisticated and powerful numerical tool for modeling nano-optical devices. This method solves Maxwell's equations directly by taking into account the finite size of the structure. FDTD allows the study of the light propagation in any type of geometry. It enables a modeling of the electromagnetic field inside the structure as a function of time but real-space analysis or spectral response is also possible using the Fourier transform of the signal. The FDTD technique is based on the Maxwell equations in the case of a linear and isotropic medium in a charge free space. In Cartesian coordinates, Maxwell's equations are written into 6 equations. We present 2 of these equation as follows:

$$\frac{\partial H_x}{\partial t} = -\frac{1}{\mu} \left( \frac{\partial E_y}{\partial z} - \frac{\partial E_z}{\partial y} \right)$$

$$\frac{\partial E_y}{\partial t} = -\frac{1}{\epsilon} \left( \frac{\partial H_x}{\partial z} - \frac{\partial H_z}{\partial x} \right)$$

with  $\mu$  is the magnetic permeability and  $\epsilon$  is the electrical permittivity of the medium.

The FDTD method is based on the discretization of space-time of these equations by the Yee lattice method.

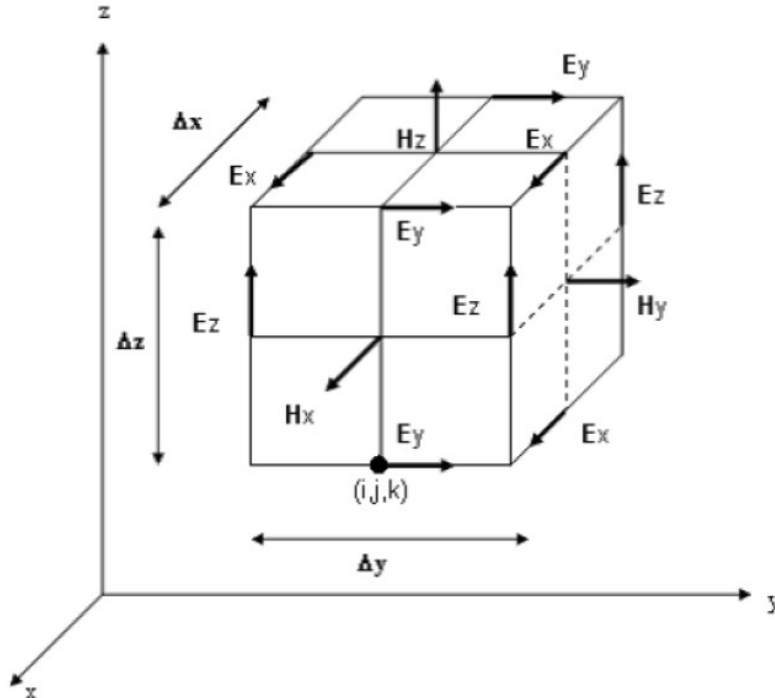


Figure. II.42: Yee lattice used in the FDTD method. The electrical field components are aligned along the edges of this cubic unit cell and the magnetic field components are normal to the cell faces

Maxwell's equations describe the evolution of electrical  $\vec{E}$  and magnetic  $\vec{H}$  fields as a function of the time by step of  $\Delta t$  and also as a function the space which is discretized by steps of  $\Delta x$ ,  $\Delta y$  and  $\Delta z$ . The  $\vec{H}$  components are calculated at points offset by half spatial step according to the calculation points of the  $\vec{E}$  components as presented on fig.II.42. In time domain, the components of  $\vec{E}$  field are determined at  $t=n\Delta t$ , where n is an integer and  $\vec{H}$  the field components are calculated at  $t=\left(n+\frac{1}{2}\right)\Delta t$ . The components of the electrical fields are calculated at  $t=(n+1)\Delta t$  as a function of the same component at  $t$  and the components of the next field at  $t=\left(n+\frac{1}{2}\right)\Delta t$  and the component of  $\vec{H}$  field at  $t=\left(n+\frac{1}{2}\right)\Delta t$  is equal to the same component at  $t=\left(n-\frac{1}{2}\right)\Delta t$  plus the  $\vec{E}$  field component at  $t$  as presented by fig.II.43. This spatio-time discretisation is interpreted into the Maxwell system by

$$H_{x(i,j,k)}^{n+\frac{1}{2}} = H_{x(i,j,k)}^{n-\frac{1}{2}} + \frac{\Delta t}{\mu \Delta z} (E_{y(i,j,k)}^n - E_{y(i,j,k-1)}^n) - \frac{\Delta t}{\mu \Delta y} (E_{z(i,j,k)}^n - E_{z(i,j-1,k)}^n)$$

$$E_{x(i,j,k)}^{n+1} = E_{x(i,j,k)}^n + \frac{\Delta t}{\epsilon \Delta y} (H_{z(i,j+1,k)}^{n+\frac{1}{2}} - H_{z(i,j,k)}^{n+\frac{1}{2}}) - \frac{\Delta t}{\epsilon \Delta z} (H_{y(i,j,k+1)}^{n+\frac{1}{2}} - H_{y(i,j,k)}^{n+\frac{1}{2}})$$

where n is the step of time discretization, i, j and k are an integers presented the nodes position of the mesh in x, y and z directions. The evolution of the electromagnetic field as a function of time is therefore calculated at each point of the mesh by an iterative temporal process with  $\Delta t$  is the step time and the  $\Delta x, \Delta y$  and  $\Delta z$  are the spatial steps

The electromagnetic fields are calculated at each point of cell and over a fixed number of steps. The computation time is therefore proportional to the number of temporal and spatial discretization points. This condition make the FDTD method use very wide memory which results a long calculation times. The precision of the calculation is depended on the number of the time and spatial points discretization.

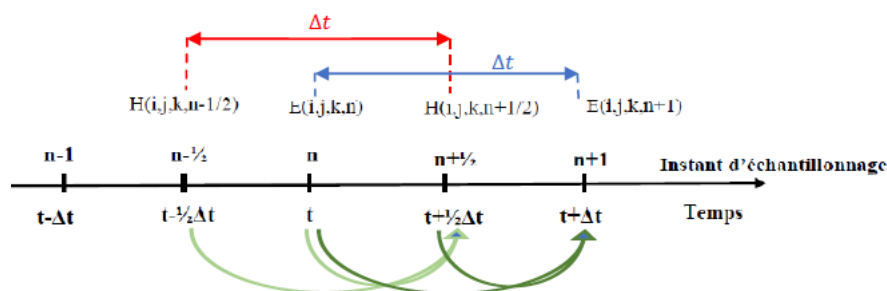


Figure. II.43: Time discretization



### II.4.5.6. Presentation of structure and parameters

The objective of this study is to evaluate differently the response of the  $\mu$ -cavity with a type c defect as presented in section II.4.5.3. . We aim at simulating the light propagation within this structure on the basis of a FDTD method. Here we use the Fullwave software from the Photonic Suite edited by Rsoft. The longitudinal (z axis) structure drawing in the Rsoft CAD is presented in Fig.II.44: The  $\mu$ -cavity consists of two first-order grating mirrors separated by a second order grating as a defect. In agreement with fig.II.39.c, the  $\mu$ -cavity is an alternate of quarter-wavelength lines of SiO<sub>2</sub> and of organic layers patterned on an ITO layer covering a glass sample. A longitudinal section ( X and , Z axis) is shown fig .II.45.a. The structure is supposed to be infinite in the y direction. Two types of parameters have to be considered; geometric parameters (§ II.4.5.6.1. ) and numerical parameters (§ II.4.5.6.2. ).

#### II.4.5.6.1. Geometric parameters

Geometric parameters are related to the design and to the materials properties of the structure. The main parameters are;

- The refractive index: While using the Fullwave software, a background refractive index is first introduced. In our case, we consider  $n_0=1$  for air as the background refractive index. Fullwave refer to the different refractive indexes of the different materials of the structure using the index differences  $\Delta n_i$  to the background refractive index:  $\Delta n_i = n_i - n_0$ . The index difference is plotted Fig. II.45.b.
- In this study, we use the bulk indexes,  $n_{\text{Glass}}$ ,  $n_{\text{ITO}}$ ,  $n_{\text{SiO}_2}$  and  $n_{\text{Orga}}$  for respectively glass substrate, ITO layer, SiO<sub>2</sub> layer and organic layers as in column3 of table II.16:
- The thickness of each layer:  $e_{\text{Glass}}$ ,  $e_{\text{ITO}}$ ,  $e_{\text{SiO}_2}$  and  $e_{\text{Orga}}$  corresponding to respectively the glass substrate, the ITO layer, the SiO<sub>2</sub> layer and the organic layers are that presented in the fourth column of table II.16:
- The width of the organic lines ( $w_{\text{Orga}}$ ) and the SiO<sub>2</sub> lines ( $w_{\text{SiO}_2}$ ) are calculated by the Fulwave software on the basis of the Bragg equation:  $W_i = \lambda_{\text{res}} / 4 n_i$
- The number N of periods of pairs of lines in the mirrors is a software parameter that can be varied. The defect geometry is introduced via its length L.

The following table presents the geometric parameters used for the FDTD study.

Central wavelength	Materials	Refractive index	thickness
620nm or 632nm	Glass sample	1.45	700 $\mu$ m
	ITO layer	1.9	50nm 140nm 340nm
	SiO <sub>2</sub>	1.45	200nm
	Organic	1.7	125nm

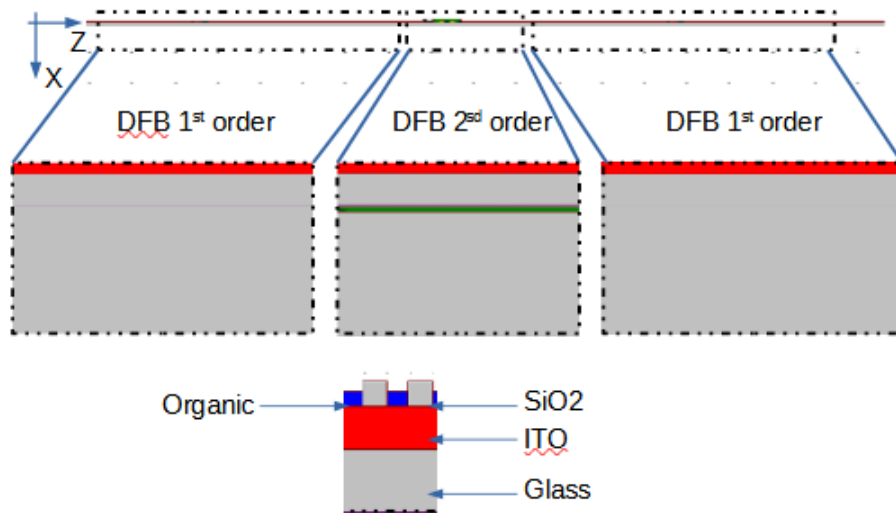


Figure. II.44:  $\mu$ cavity structure designed to be using in FDTD method

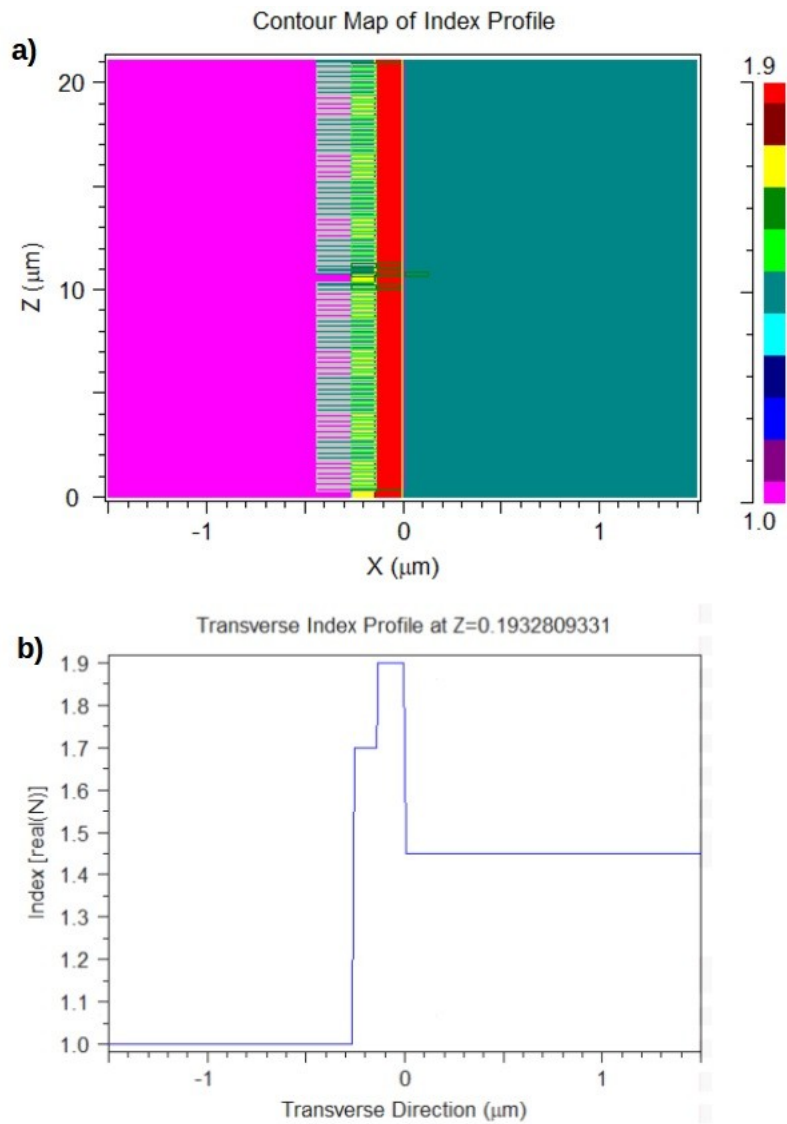


Figure. II.45: Refractive index profile

#### II.4.5.6.2. Numerical parameters

The FDTD algorithm requires numerical simulation parameters to solve Maxwell's equations for an electromagnetic fields in a structure as a function of time and space. The main numerical parameters are:

- **The spatial simulation domain**

The  $x \in (x_{min}, x_{max})$ ,  $y \in (y_{min}, y_{max})$  and  $z \in (z_{min}, z_{max})$  domains define the spatial area to be simulated. They should be large enough to include the structure and the different fields including the evanescent one. In our case the computational domains are  $x \in [-1.5, 1.5]$  and  $z$  presents the width of the structure. Note that the zero for  $x$  represents the Glass/ITO interface .

- **The boundary condition**

The perfect matched layer (PML) [47] is used as an absorbing boundary that eliminates the wave propagation outside of the spatial domain. This layer prevents the wave reflection resulting from index differences presents outside from the spatial interval. In this study the PML is equal to  $0.5 \mu\text{m}$  as shown in Fig. II.46.

- **Spatial grid size**

The spatial resolution is controlled by the number of steps per unit of space. It's called spatial grid size. To produce a precise and perfect simulation, the spatial grid can be chosen as a function of the wavelength in the materials and as a function of the geometry of the structure. The spatial grid size  $\Delta x, \Delta y, \Delta z$  must be less than  $\lambda/10$  . In our case, we use  $\Delta x = \Delta y = \Delta z = 0.01$  which is available for all visible range of wavelength.

- **Time simulation domain**

This method solves the electromagnetic fields as a function of time. The simulation starts at  $t=0$  and when the convergence of computational is detected using the convergence criterion the simulation stopped. When this condition is not automatically reached, we need to define the end of the simulation with a stop time. The stop time sets the time domain of the simulation. To produce an accurate simulation the time domain must be large enough.

- **Time grid size**

The time resolution is controlled by the time step  $\Delta t$  which must satisfy the Courant-Friedrichs-Lewy rule to obtain a stable simulation. The FDTD method is stable when the following condition

is fulfilled:  $\Delta t < \frac{1}{c \sqrt{\frac{1}{\Delta x^2} + \frac{1}{\Delta y^2} + \frac{1}{\Delta z^2}}}$  where  $c$  is the velocity of light. Fullwave enforce this

condition for each simulation.

- **Excitation source**

The excitation source consists of both a spatial and a temporal term such as  $\Phi(\vec{r}, t) = \sqrt{P_i} f_i(\vec{r}) g_i(t) e^{i\phi_i t}$  where  $P_i$  and  $\phi_i$  are the power and the phase of the source with  $f_i(\vec{r})$  the spatial component and  $g_i(t)$  the temporal component. It also called the launch field. It can be a field source, current source or enclosed source. The launch type is used to get the same conditions as in our device is a light source which is located in the defect.

- **The monitor**

Monitors record the information or response of the fields as a function of time or frequency. This information can be a power or intensity density. With this output from the simulation we analyze the response of the structure. In our case, we study the forbidden band gap of the  $\mu$ -cavity, the existence of light coupled normal/ perpendicularly to the structure and the quality factor. Depending on the objective of the study, the monitor is located either in the mirrors, or in the defect or in the glass substrate. We use only power density monitors.

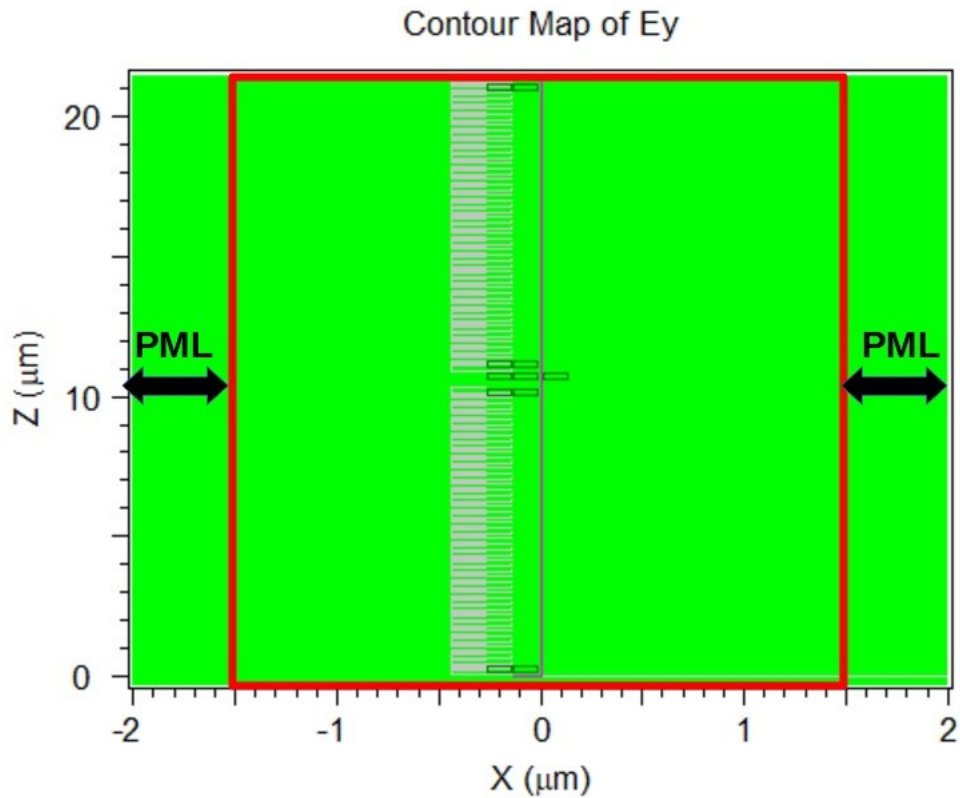


Figure. II.46: the red rectangle presents the simulation zone with the PML part

#### II.4.5.7. 2D studies

The objectives of this study are, firstly to confirm the existence of the forbidden band gap, secondly to identify the optimal  $\mu$ -cavity structure that offers the highest quality factor  $Q = \frac{\lambda_{res}}{\Delta\lambda}$  and finally to check if with the type defects..

- **Forbidden band gap study**

For this first study, we simulate a  $\mu$ -cavity with a type c defect and with an ITO thickness of 340nm, a SiO<sub>2</sub> thickness of 200nm and a thickness of the organic layers of 125nm. We draw 250 pairs of SiO<sub>2</sub> and Organic lines separated by a defect consisting of 7 pairs plus one of second-order grating. The central wavelength used to define the width of organic and SiO<sub>2</sub> line using the brag relationship is 620 nm. Figure.II.47 presents the spectra recorded by a monitor placed in the organic line of defect. We observe a first photonic forbidden bandgap from 606 nm to 614 nm and a second one from 652 nm to 657 nm. In each forbidden bandgap intense resonance peaks centered in the middle of each bandgap located at at 610 nm and 655 nm exist. This is to be related to the existence of several Transverse modes guided by the ITO.

- **Quality factor as a function ofn the ITO thickness**

Secondly we study the quality factor as a function of the ITO electrode thickness so as to confirm its optimal thickness. We use the same structure simulated as in the previous study except for the free space wavelength set to 632 nm. Fig.II.48 shows how the quality factors evolves as a function of the ITO layer thickness with a maximum for 50 nm in agreement with the study based on the transfer matrix method. Note that the quality factor hardly exceed 400. This is due to the stop time set to 500  $\mu$ s for this simulation is 500 $\mu$ s that results in a low frequency resolution.

To confirm that higher Q-factor can be achieved, Q factors are then calculated as a function of the number of line in the grating (DFB mirrors) with a larger stop time equal to 1000 and an ITO thickness equal to the standard ITO thickness of 140 nm. Figure.II.49 presents that the Q factor increases with the line number up to 1800 and then saturates. Again this saturation is a result of the not-large-enough time resolution.

- **Vertical coupling of light**

In the third study, we verify the diffraction of light perpendicular to the structure. The considered structures consists of  $\mu$ cavity with a type c defect. The width of the lines are calculated on basis of free space wavelength equal to 620 nm. The ITO thickness is equal to 140 nm and the monitor located 1  $\mu$ m away for the defect in the glass sample records the field information.

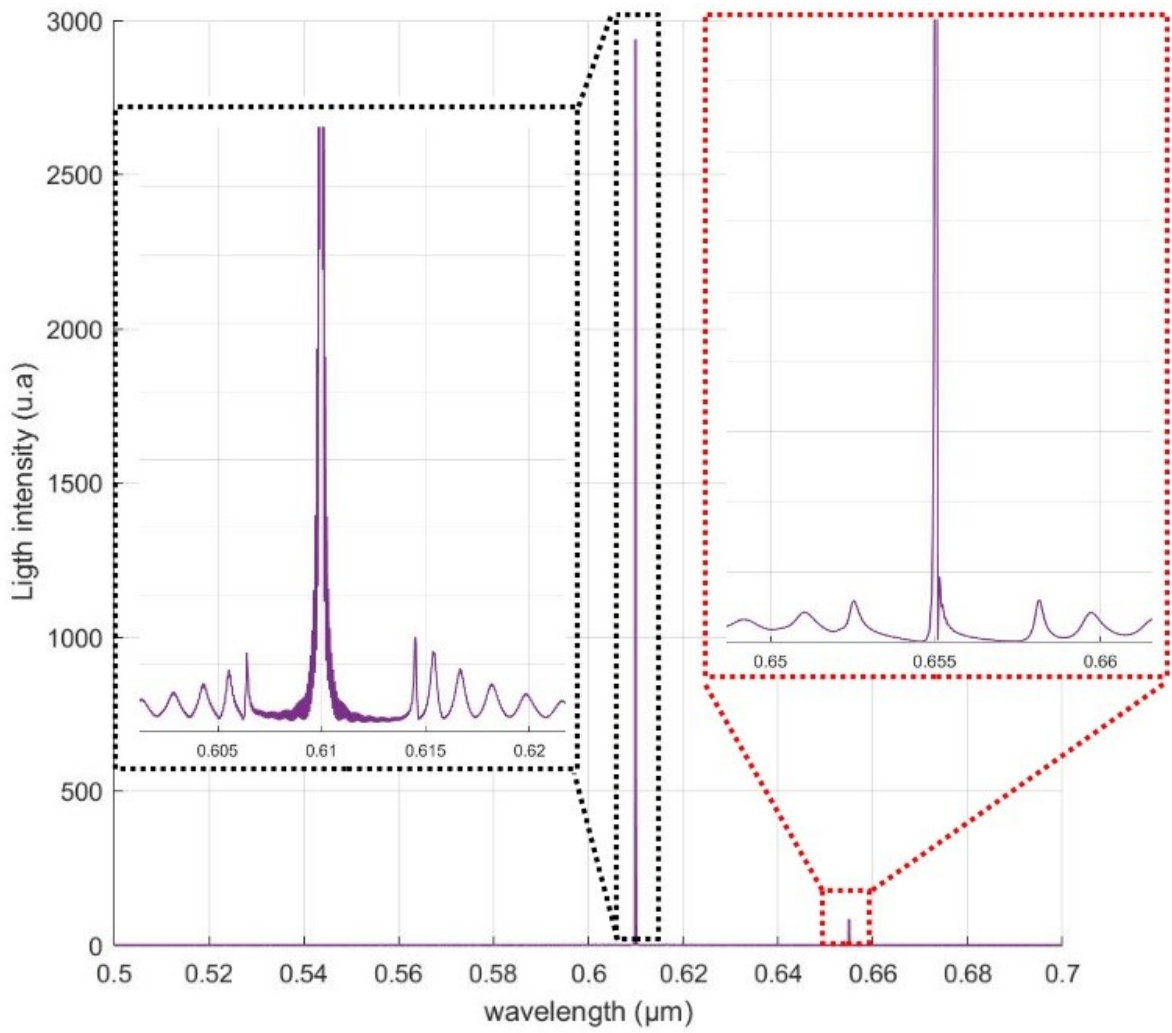


Figure. II.47: Response of  $\mu$ cavity type c: it presents two modes with presence of forbidden band gap with a resonance pic at 614nm (black rectangle) and 655nm (red rectangle)

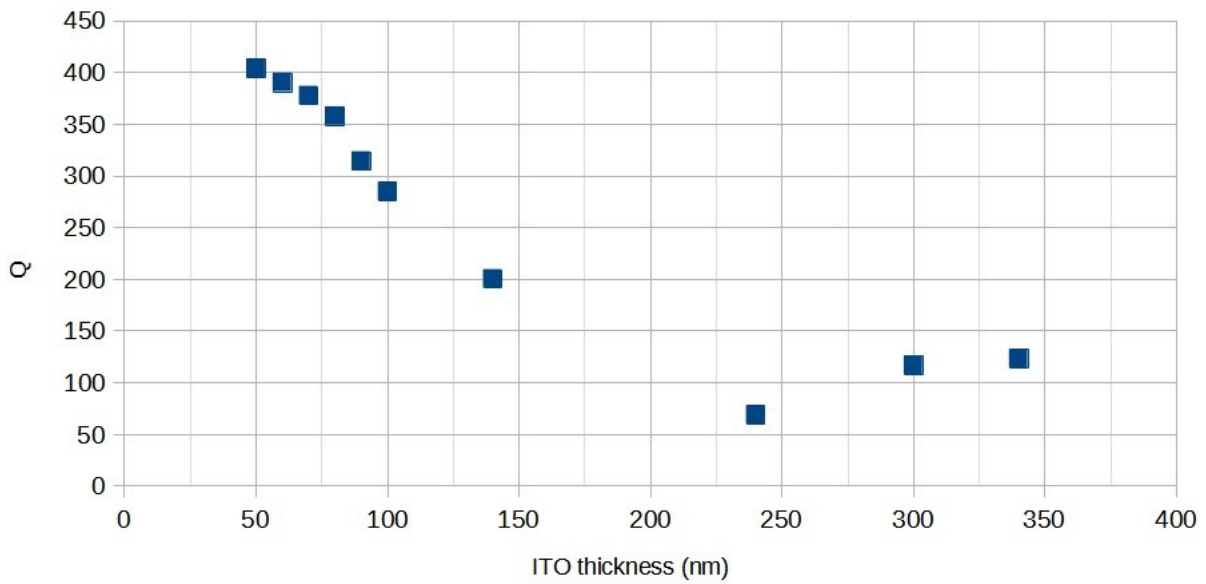


Figure. II.48: Quality factor ( $Q$ ) as a function of ITO thickness

Figure.II.50 presents the spectra calculated from the field record with the monitor in the glass substrate. When a second order defect (type C) is included in the structure, a resonance peak at 652.2 nm is observed. This is a clear confirmation that light is diffracted in the direction perpendicular to the axis when a second order grating is introduced as a defect in the  $\mu$ -cavity. With a stop time equal to 10000, and real values for the refractive index (no absorption) the previous structure offers a Q factor as high as 16650. Note that all these studies are performed with the bulk refractive index.

## II.5. Conclusions on the electrical, material and optical designs.

To conclude this chapter, we present a synthesis of our studies divided in three types of design rules; first the electrical design rules, secondly the choice of laser gain materials and finally design rules related to the laser cavity.

From the electrical perspectives, the objective is to design ultra-high-speed OLEDs so as to, first, be able to emit nanoseconds and sub-nanosecond light pulses and, second, to reach ultra-high current density up to tens of kA/cm<sup>2</sup>. Regarding ultra-high-speed organic optoelectronic devices, we predicted that electrical time constant  $\tau_2$  equal or shorter than 100 ps are possible. Regarding the current density we predict that values up to 50 kA/cm<sup>2</sup> can be reached. On the basis of a dynamical electrical model improved for the occasion, we identify conditions to make it feasible.

The following **design rules 1** deal with the electrical time response to be  $\tau_2 \leq 100 \text{ ps}$ . The conditions on the electrical response time can be identified from eq. II.20 :

$$\tau_2' = \frac{C}{\frac{1}{(R_m + R_{S1} + R_{S2})} + \frac{1}{R_{Shunt}}}$$

- **Design Rule 1a:** The OLED capacitance  $C$  is minimized (ideally below 5pF). This is achievable via the reduction of the active area  $A$ . We choose to work with the active areas  $100 \times 100 \mu\text{m}^2$ ,  $50 \times 50 \mu\text{m}^2$  and  $25 \times 25 \mu\text{m}^2$  resulting in capacitance down to  $C_1 = 2.8 \text{ pF}$ ,  $C_2 = 0.9 \text{ pF}$  and  $C_3 = 0.2 \text{ pF}$  respectively.
- **Design Rule 1b:** The sum of the measurement resistance  $R_m$  and the serial resistance  $R_s$  is to be minimized ideally below  $\tau_2 / C_i$ . ( $\sim 30 \Omega$ ) calculated for  $A = 100 \times 100 \mu\text{m}^2$ .

The **design rules 2** deal with the maximum achievable current density. Its plateau value is given by eq. II.22 and II.23;

$$I_{steady} = \frac{V_E}{R_d + R_s + R_m}$$

The current is maximized when the sum  $R_d + R_s + R_m$  is minimized. With the parameters presented in table II.17 current density  $J_d$  as high as several tens of kA/cm<sup>2</sup> are achievable for low values of  $R_d$  (ideally below  $100 \Omega$ ). This corresponds to operating points with large excitation voltages. Then  $R_s + R_m$  is to be minimized at the level of  $R_d$  or below.

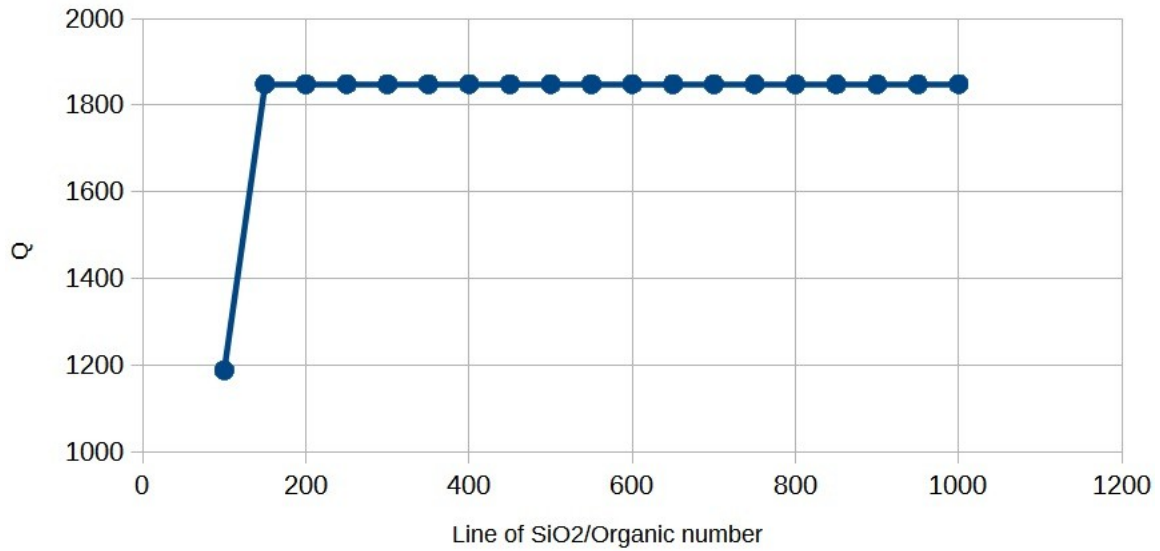


Figure. II.49: Quality factor (Q) as a function of line number of mirrors

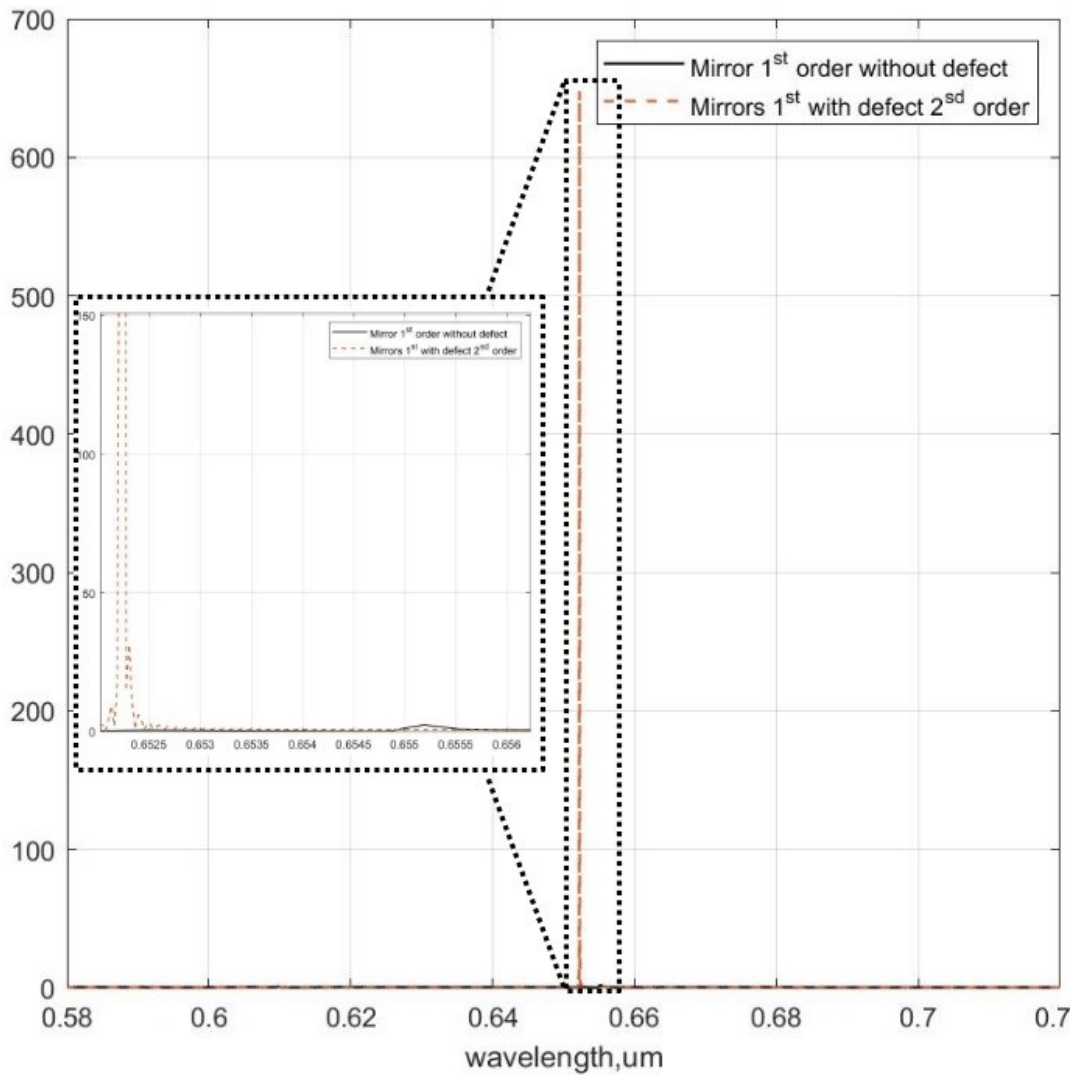


Figure. II.50: The response of mirrors without defect (black solid line) and with defect type DFB second order (orange dash line) in the glass sample. In the black rectangle, we present a zoom of the response to prove that only with defect type DFB second order the wave is coupled perpendicularly to the propagation of the wave in mirrors



- **Design Rule 2a:** The measurement resistance  $R_m$  is minimized but is to remain large enough to allow measurements of the current of the order of  $J_{min}=1 \text{ kA/cm}^2$  flowing across the OLED with a relative accuracy of 1%. With an oscilloscope offering a resolution of  $V_{res} = 1 \text{ mV}$ , and a current to be measured of  $I_{min}=A.J_{min}/100$ , the measurement resistance  $R_m=100 V_{res}/(A J_{min})$  becomes  $\geq 1\Omega$  (respectively  $4\Omega$  and  $16\Omega$ ) for  $100 \times 100 \mu\text{m}^2$  (respectively for  $50 \times 50 \mu\text{m}^2$  and  $25 \times 25 \mu\text{m}^2$ )
- **Design Rule 2b:** The serial resistance  $R_s$  is then minimized ideally below  $\sim 85\Omega$ .  $R_s$  is minimized when the thickest ITO layers (340nm) is used and with partial gold metalization of the anode and cathode except zones where transparent and conductive electrode are needed.

The **design rules 3** deal with the use of a coplanar waveguide (CPW) electrodes as introduced by Chime. This reduce pulse reflection and minimize its distorsion [10,11,12].

- **Design Rule 3a:** Cathodes and anodes are made of a strip line with a width  $W$ . We choose  $W=1500\mu\text{m}$  to offer enough room for the rest of the fabrication
- **Design Rule 3b:** Two ground planes both sides of the central anodes and cathode strip are place apart from the central line by a distance  $G=316$  resulting in a  $50\Omega$  characteristic impedance
- **Design Rule 3c:** Built-in resistors  $2 \times R_m$  link the cathode central strip line with the ground planes.  $R_m=2.3 \Omega$  when using a width  $d=500\mu\text{m}$  which is approximately the same order of mangitude than calculated in 2.aThe optimal electrical parameters and the geometry of the CPW electrodes are summarized in table II.17.

$e_{\text{Glass}}$ ( $\mu\text{m}$ )	$t$ (nm)	$W$ ( $\mu\text{m}$ )	$G$ ( $\mu\text{m}$ )	$d$ ( $\mu\text{m}$ )	$L$ ( $\mu\text{m}$ )	$X$ ( $\mu\text{m}$ )	$A$ ( $\mu\text{m}^2$ )	Estimation of the electrical time constant (ps)	Estimation of the maximal Current Density for $R_d=100\Omega$
700	340	1500	316	500	1000	375	100x100	78ps	10kA/cm <sup>2</sup>
							50x50	40ps	40kA/cm <sup>2</sup>
							25x25	19ps	171kA/cm <sup>2</sup>

From the material point of view, our conclusion are inherited from the new Organic laser diode dynamical model based on 6 coupled differential equations that include electrical excitation, polarons, singlet and triplet population of a host, singlet and triplet population of a guest, and a photonic equation as presented in section II.3. . Based on this model, simulations have been launched that uses a set of more than 20 parameters reflecting both the material properties including Langevin recombination, singlet lifetime, triplet lifetime, STA, SPA, TTA, ISC, ... and cavity properties including photon cavity lifetime, confinement factors... The model includes the concept of residual absorption that has been proposed for the occasion for the purpose to take into account the frequency-selective limited reabsorption of photons by the Stoke-shifted ground state population.

On the basis of this model, and parameters extracted from the literature for DCM as a guest in Alq<sub>3</sub> as a host, we predict that stimulated emission occurs under pulse electrical excitation during a time

window of 7ns after the turn on provided the quality factor is  $Q \geq 1800$ . Under these condition the current density is predicted in excess of the laser threshold at 3.5 kA/cm<sup>2</sup>.

Also with the help of the model, we highlight the importance of the residual absorption. Together with the effective gain they constitute two of the key parameters to choose the laser gain material although other parameter related to STA and SPA play a role and need to be investigated further.

- **Design Rule 4a:** Gain material is chosen on the basis of its residual absorption and laser gain coefficient so has to minimize the current density  $J_d$  to achieve the first positive net gain  $G_{eff}$ . With this choice, DCM with a concentration of 2% as a host material in Alq<sub>3</sub> as a the guest material systems offers the lowest current density (about 3.2 kA/cm<sup>2</sup>) to overcome the reabsorption losses. DCM with a concentration of 2% exhibits a maximum of electroluminescence at  $\lambda_{res}=605$  nm, defines the resonance wavelength of the future laser cavity. It has been observed that concentration of 4% of DCJTb in Alq<sub>3</sub> shows a larger slope but also requires a much higher current density which complicate the task. (Additional design rules will need to be established to take into account other material parameters like SPA and STA in the choice of parameters).
- **Design Rule 4b:** The resonance wavelength is defined by the maximum of electroluminescence of the chosen material at the chosen concentration

Our conclusions on the laser cavity design rules are based on an optical waveguide analysis and on the transfer matrix method. With optical waveguide analysis we identify the conditions on the OLED stack including the ITO layer to maximize the confinement factor  $\Gamma$  (Design Rules 5). We conclude that with an ITO layer as thin as  $t_{L1}=50$  nm and an Organic layer as thick as  $t_{L2}=200$  nm (respectively 125 nm) a confinement factor as large as  $\Gamma=0.565$  (respectively 0.39).

- **Design Rule 5a:** Minimize the thickness of the high-index Transparent and conductive electrodedown to 55 nm
- **Design Rule 5b:** From the Transfer Electric mode point of view, the confinement factor is maximize in the organic layers when their total thickness is maximized. An empirical trade-off with the optimal OLED thickness resulting from the charge transport is necessary which leads to choose thickness in the range 125 nm to 200 nm

The use of the transfer matrix method, was to identify three conditions on the laser cavity; firstly, enlarging the width of the reflectance of the mirrors (forbidden bandgap) to cover the largest part of the electroluminescence spectrum of the chosen material (Design Rule 6), secondly, maximizing quality-factors ideally as high as several thousands (Design Rule 7), and finally, coupling the light in the direction perpendicular to the plan of the cavity for measurement (Design Rule 8).

- **Design Rule 6.a:** We use mirrors made with first order DFB gratings offering among the highest reflectivity. DFB Mirrors are made of gratings with quarter-wavelength alternated high effective index  $n_H$  and low effective index  $n_L$  lines:
- **Design Rule 6.b:** To enlarge the width of their forbidden bandgap, an optimal set of the ITO, SiO<sub>2</sub> and Organic layers thicknesses chosen to maximize the index contrast  $\Delta n_{eff} = n_H - n_L$  is to be identified. The identified optimal structure consists of an ITO thickness of 55 nm (chosen from Design Rule 5a), of a thickness of the organic layers in the range 125-200 nm and of a SiO<sub>2</sub> thickness of 300 nm. The resulting effective index contrast

is  $\Delta_{\text{neff}}=0.061$  for an organic layer thickness of 200 nm and is  $\Delta_{\text{neff}}=0.045$  for an organic layer thickness of 125nm. Note that the index contrast is much smaller than that of the bulk materials around 0.25.

- **Design Rule 6.c:** On the basis of the effective indices chosen from the Design Rule 6a, the width of the lines with high effective index is  $\Lambda_1=95\text{ nm}$  and the width of that of low effective-index is  $\Lambda_2=99\text{ nm}$  . It is predicted that this mirror offers a FWHM reflectance of  $\Delta\lambda = 20\text{ nm}$  .
- **Design Rule 7a:** Maximizing the quality factor of cavity. We chose the DFB mirrors to be separated by multiple of half-wavelength line defects.
- **Design Rule 7bc:** To achieve quality factors above 3000, at least  $N \geq 66$  pairs are required. Note that all this studies are made without absorption so in reality N is to be increased and we propose to use at least  $N=80$ .
- **Design Rule 8:** To extract light perpendicular to the plan of the cavity, we propose a defect made of half wavelength alternated high effective index  $n_H$  and low effective index  $n_L$  lines such as a second order DFB grating. The micro-cavity will then consists of a left and right first-order DFB mirror made with  $N=80$  alternated pairs of Organic and SiO<sub>2</sub> layers separated by a second order DFB grating made of  $M (<10)$  pairs of SiO<sub>2</sub> and organic layers.

The design rules are summarized on fig. II.51.

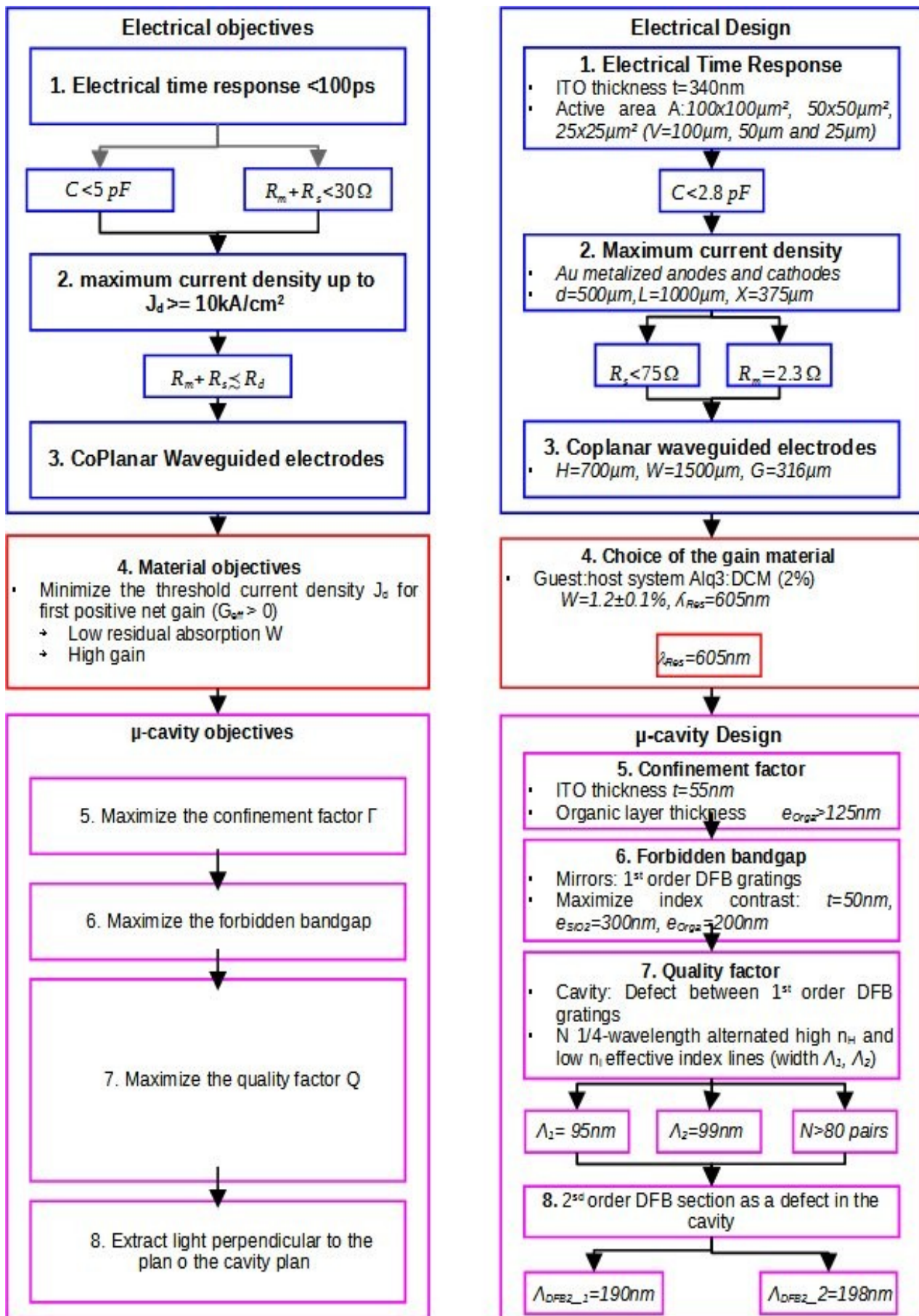


Figure. II.51 : Organigram showing choices and the resulting laser cavity geometry

## References

- [1] CHIME Alex Chamberlain, “Etude théorique et expérimentale de micro-OLEDs rapides sur électrodes coplanaires en régime d'impulsions à haute densité de courant”, Thesis of Université Paris 13, Decembre 2017
- [2] A. S. D. Sandanayaka et al., “Indication of current-injection lasing from an organic semiconductor,” *Appl. Phys. Express*, vol. 12, no. 6, p. 061010, May 2019, [doi: 10.7567/1882-0786/ab1b90](https://doi.org/10.7567/1882-0786/ab1b90)
- [3] C. Pinot et al., “Electrical modeling and numerical simulation of doped multilayer organic light-emitting diodes (OLEDs),” in *SID Symp. Dig. Tech. Papers*, vol. 38, n° 1, pp. 792–795, may 2007.
- [4] R. L. Lin, J.-Y. Tsai, D. Buso, and G. Zissis, “OLED equivalent circuit model with temperature coefficient and intrinsic capacitor,” in *Proc. IEEE Ind. Appl. Soc. Annu. Meeting*, pp. 1–8, 2014.
- [5] J. P. Bender, “SPICE modeling of ACTFEL devices and OLEDs,” M.S. thesis, Dept. Electr. Comput. Eng., Oregon State Univ., Corvallis, OR, USA, 2000.
- [6] J. H. Ahn et al., “Equivalent-circuit analysis of organic light emitting diodes by using the frequencydependent response of an ITO/Alq<sub>3</sub>/Al device,” *J. Korean Phys. Soc.*, vol. 46, n° 2, pp. 546–550, 2005.
- [7] J. Drechsel, M. Pfeiffer, X. Zhou, A. Nollau, and K. Leo, “Organic Mip-diodes by p-doping of amorphous wide-gap semiconductors: CV and impedance spectroscopy,” *Synth. Met.*, vol. 127, n° 1–3, pp. 201–205, 2002.
- [8] S. Nowy, W. Ren, A. Elschner, W. Lövenich, and W. Brütting, “Impedance spectroscopy as a probe for the degradation of organic lightemitting diodes,” *J. Appl. Phys.*, vol. 107, n° 5, pp. 054501-1–054501-9, 2010.
- [9] H. Park, H. Kim, S. K. Dhungel, J. Yi, S. Y. Sohn, and D. G. Jung, “Impedance spectroscopy analysis of organic light-emitting diodes fabricated on plasma-treated indium-tin-oxide surfaces,” *J. Korean Phys. Soc.*, vol. 51, n° 3, pp. 1011–1015, 2007.
- [10] A. C. Chime, A. P. A. Fischer, S. Bensmida, J. Solard, M. Chakaroun, and H. Nkwawo, “Analysis of Optical and Electrical Responses of  $\mu$ -OLED With Metallized ITO Coplanar Waveguide Electrodes Submitted to Nanosecond Electrical Pulses,” *IEEE Trans. Electron Devices*, vol. 66, no. 5, pp. 2282–2289, May 2019, [doi: 10.1109/TED.2019.2905839](https://doi.org/10.1109/TED.2019.2905839).
- [11] A. C. Chime, S. Bensmida, M. Chakaroun, M. W. Lee, H. Nkwawo, and A. P. A. Fischer, “Electrical modelling and design of ultra-fast micro-OLED with coplanar wave-guided electrodes in ON-OFF regime,” *Organic Electronics*, vol. 56, pp. 284–290, May 2018, [doi: 10.1016/j.orgel.2017.12.026](https://doi.org/10.1016/j.orgel.2017.12.026).
- [12] C. P. Wen, Coplanar waveguide: A surface strip transmission line suitable for nonreciprocal gyromagnetic device applications, *IEEE Transactions on Microwave Theory and Techniques*, vol. 17, no. 12, pp. 1087– 1090, 1969.
- [13] Y. Wu *et al.*, “Resistivity and oxygen content of indium tin oxide films deposited at room temperature by pulsed-laser ablation,” *Journal of Applied Physics*, vol. 86, no. 2, pp. 991–994, Jul. 1999, [doi: 10.1063/1.370864](https://doi.org/10.1063/1.370864).

## References

- [14] C. Gartner, C. Karnutsch, C. Pflumm, and U. Lemmer, “Numerical Device Simulation of Double-Heterostructure Organic Laser Diodes Including Current-Induced Absorption Processes,” *IEEE Journal of Quantum Electronics*, vol. 43, no. 11, pp. 1006–1017, Nov. 2007, doi: [10.1109/JQE.2007.905021](https://doi.org/10.1109/JQE.2007.905021).
- [15] D. Kasemann, R. Brückner, H. Fröb, and K. Leo, “Organic light-emitting diodes under high currents explored by transient electroluminescence on the nanosecond scale,” *Phys. Rev. B*, vol. 84, no. 11, p. 115208, 2011, doi: [10.1103/PhysRevB.84.115208](https://doi.org/10.1103/PhysRevB.84.115208).
- [16] S.-L. Chua, B. Zhen, J. Lee, J. Bravo-Abad, O. Shapira, and M. Soljačić, “Modeling of threshold and dynamics behavior of organic nanostructured lasers,” *J. Mater. Chem. C*, vol. 2, no. 8, pp. 1463–1473, Jan. 2014, doi: [10.1039/C3TC31870B](https://doi.org/10.1039/C3TC31870B).
- [17] V. Ahmad, J. Sibus, M. Greenberg, A. Shukla, B. Philippa, A. Pivrikas, G. Vamvounis, R. White, S.-C. Lo, and E.B. Namdas, *Nat Commun* **11**, 4310 (2020).
- [18] A. A. Shoustikov, Yujian You, and M. E. Thompson, “Electroluminescence color tuning by dye doping in organic light-emitting diodes,” *IEEE J. Select. Topics Quantum Electron.*, vol. 4, no. 1, pp. 3–13, Feb. 1998, doi: [10.1109/2944.669454](https://doi.org/10.1109/2944.669454).
- [19] N.C. Giebink and S.R. Forrest, “Temporal response of optically pumped organic semiconductor lasers and its implication for reaching threshold under electrical excitation”, *Physical Review B* 79, 073302, 2009. [10.1103/PhysRevB.79.073302](https://doi.org/10.1103/PhysRevB.79.073302)
- [20] I. Gozhyk, “Polarization and gain phenomena in dye-doped polymer micro-lasers”, Thesis Ecole normale superieure de Cachan (F), 2012
- [21] C. Gaertner, “Organic Laser Diodes: Modelling and Simulation”, Thesis Universitaet Karlsruhe (D), 2008
- [22] J. R. Gispert, *Coordination Chemistry*. (2008). Wiley-VCH. p. 483. ISBN 3-527-31802-X <https://doi.org/10.1002/aoc.1550>
- [23] P. Langevin, *Ann. Chim. Phys.* 28,433,1903
- [24] Kao, K. C. *Dielectric Phenomena in Solids*; Elsevier Academic Press: San Diego, 2004. Hardcover ISBN: 9780123965615
- [25] P. Juhasz, J. Nevrel, M. Micjan, M. Novota, J. Uhrík, L. Stuchlikova, J. Jakabovic, L. Harmatha and M. Weis, “Charge injection and transport properties of an organic light-emitting diode,” *Beilstein J. Nanotechnol.*, vol. 7, no. 1, pp. 47–52, Jan. 2016, doi: [10.3762/bjnano.7.5](https://doi.org/10.3762/bjnano.7.5).
- [26] N. Tsutsumi and T. Hinode, “Tunable organic distributed feedback dye laser device excited through Förster mechanism,” *Appl. Phys. B*, vol. 123, no. 3, p. 93, Mar. 2017, doi: [10.1007/s00340-017-6679-x](https://doi.org/10.1007/s00340-017-6679-x).
- [27] V. G. Kozlov, V. Bulovic, P.E. Burrows, M. Baldo, V.B. Khalfin, G. Parthasaraty, S.R. Forrest, Y. You, E. Thompson., “Study of lasing action based on Förster energy transfer in optically pumped organic semiconductor thin films,” *J. Appl. Phys.*, vol. 84, no. 8, p. 14, 2014. [doi.org/10.1063/1.368624](https://doi.org/10.1063/1.368624)

## References

- [28] U. Noomnarm and R. M. Clegg, "Fluorescence lifetimes: fundamentals and interpretations," *Photosynth Res*, vol. 101, no. 2–3, pp. 181–194, Sep. 2009, doi: [10.1007/s11120-009-9457-8](https://doi.org/10.1007/s11120-009-9457-8).
- [29] M. A. Omary and H. H. Patterson, "Luminescence, Theory," in *Encyclopedia of Spectroscopy and Spectrometry*, Elsevier, 2017, pp. 636–653. DOI: 10.1016/B978-0-12-803224-4.00193-X
- [30] C.W. Tang, S.A. VanSlyke, C.H. Chen, *J. Appl. Phys.* 65 (1989) 3610 "Electroluminescence of doped organic thin films," *Journal of Applied Physics*, vol. 65, no. 9, p. 3610, May 1989, doi: [doi:10.1063/1.343409](https://doi.org/10.1063/1.343409)
- [31] I. Sokolik, R. Priestley, A. D. Walser, R. Dorsinville, and C. W. Tang, "Bimolecular reactions of singlet excitons in tris(8-hydroxyquinoline) aluminum," *Appl. Phys. Lett.*, vol. 69, no. 27, pp. 4168–4170, Dec. 1996, doi: [10.1063/1.116974](https://doi.org/10.1063/1.116974). <https://doi.org/10.1063/1.116974>
- [32] A.D. Walser, R. Priestley, R. Dorsinville, "Temperature dependence of the singlet excited state lifetime in  $\text{Alq}_3\text{Alq}_3$ ," *Synthetic Metals*, vol. 102, no. 1, pp. 1552–1553, Jun. 1999, doi: [10.1016/S0379-6779\(98\)00558-X](https://doi.org/10.1016/S0379-6779(98)00558-X).
- [33] S. Fujita, T. Nakazawa, M. Asano, and S. Fujita, "Comparative Study of Photoluminescence Dynamics of Tris(8-hydroxyquinoline) Aluminum-Based Organic Multilayer Structures with Different Types of Energy Lineups," *Jpn. J. Appl. Phys.*, vol. 39, no. 9R, p. 5301, Sep. 2000, doi: [10.1143/JJAP.39.5301](https://doi.org/10.1143/JJAP.39.5301).
- [34] S. Kundu, K. Fujihara, T. Okada, and M. Matsumura, "Excitation Migration from Photoexcited Tris(8-hydroxyquinolino)aluminium to Quinacridone in Codeposited Thin Films," *Jpn. J. Appl. Phys.*, 39, 9R, (2000) 5297 doi: [10.1143/JJAP.39.5297](https://doi.org/10.1143/JJAP.39.5297).
- [35] T. Mori, K. Obata, K. Miyachi, T. Mizutani, and Y. Kawakami, "Fluorescence Lifetime of Organic Thin Films Alternately Deposited with Diamine Derivative and Aluminum Quinoline," *Jpn. J. Appl. Phys.*, vol. 36, no. 12R, p. 7239, Dec. 1997, doi: [10.1143/JJAP.36.7239](https://doi.org/10.1143/JJAP.36.7239).
- [36] S. Zhang, J. Song, T. Kreouzis, and W. P. Gillin, "Measurement of the intersystem crossing rate in aluminum tris(8-hydroxyquinoline) and its modulation by an applied magnetic field," *Journal of Applied Physics*, vol. 106, no. 4, p. 043511, Aug. 2009, doi: [10.1063/1.3204015](https://doi.org/10.1063/1.3204015).
- [37] C.-W. Chang, Y.-T. Kao, and E. W.-G. Diau, "Fluorescence lifetime and nonradiative relaxation dynamics of DCM in nonpolar solvent," *Chemical Physics Letters*, vol. 374, no. 1–2, pp. 110–118, Jun. 2003, doi: [10.1016/S0009-2614\(03\)00645-6](https://doi.org/10.1016/S0009-2614(03)00645-6).
- [38] J. Ohtsubo, *Semiconductor Lasers: Stability, Instability and Chaos*, 3rd ed. Berlin Heidelberg: Springer-Verlag, 2013.
- [39] F. Gourdon *et al.*, "Optically pumped lasing from organic two-dimensional planar photonic crystal microcavity," *Appl. Phys. Lett.*, vol. 100, no. 21, p. 213304, May 2012, doi: [10.1063/1.4720178](https://doi.org/10.1063/1.4720178).
- [40] A. Coens *et al.*, "Experimental optimization of the optical and electrical properties of a half-wavelength-thick organic hetero-structure in a Micro-cavity," *Opt. Express, OE*, vol. 20, no. 28, pp. 29252–29259, Dec. 2012, doi: [10.1364/OE.20.029252](https://doi.org/10.1364/OE.20.029252).



## References

- [41] G. M. Akselrod, E. R. Young, K. W. Stone, A. Palatnik, V. Bulović, and Y. R. Tischler, "Reduced lasing threshold from organic dye microcavities," *Phys. Rev. B*, vol. 90, no. 3, p. 035209, Jul. 2014, doi: [10.1103/PhysRevB.90.035209](https://doi.org/10.1103/PhysRevB.90.035209).
- [42] P. B. Deotare, T. S. Mahony, and V. Bulović, "Ultracompact Low-Threshold Organic Laser," *ACS Nano*, vol. 8, no. 11, pp. 11080–11085, Nov. 2014, doi: [10.1021/nn504444g](https://doi.org/10.1021/nn504444g).
- [43] M. Cehovski, S. Döring, T. Rabea, R. Caspary, W. Kowalsky, "Combined optical gain and degradation measurements in DCM2 doped Tris-(8-hydroxyquinoline)aluminum thin-films", SPIE Proceedings [SPIE SPIE Photonics Europe -Brussels, Belgium (Sunday 3 April 2016)] Organic Photonics VII - 9895, 989508-. doi:10.1117/12.2227688
- [44] G. Barbillon, F. Gourdon, E. Cambri, N. Fabre, A. M. Yacomotti, and S. Bouchoule, "SiNx/organic photonic crystal microcavity optimization for the fabrication of thin-film micro-laser," *Optics Communications*, vol. 325, pp. 15–22, Aug. 2014, doi: [10.1016/j.optcom.2014.03.067](https://doi.org/10.1016/j.optcom.2014.03.067).
- [45] A. Ouirimi, A. C. Chime, N. Loganathan, M. Chakaroun, A. P. A. Fischer, and D. Lenstra, "Threshold estimation of an organic laser diode using a rate-equation model validated experimentally with a microcavity OLED submitted to nanosecond electrical pulses," *Organic Electronics*, vol. 97, p. 106190, Oct. 2021, doi: [10.1016/j.orgel.2021.106190](https://doi.org/10.1016/j.orgel.2021.106190).
- [46] Y. Oyama, M. Mamada, A. Shukla, E. G. Moore, S-C. Lo, E. B. Namdas, C. Adachi, "Design Strategy for Robust Organic Semiconductor Laser Dyes," *ACS Materials Lett.*, vol. 2, no. 2, pp. 161–167, Feb. 2020, doi: [10.1021/acsmaterialslett.9b00536](https://doi.org/10.1021/acsmaterialslett.9b00536).
- [47] J.P. Berenger, "A Perfectly Matched Layer for the Absorption of Electromagnetic waves" *J. Comput. Phys.*, **114**, 185 (1994)





# **Chapter III – Fabrication**



# III. Fabrication

## III.1. Introduction

This chapter is dedicated to the description of the fabrication process. For the sake of clarity, the whole process is split in four main sub-processes: After a quick presentation of the different substrates used for the fabrication listed in section III.2, we will present the design of the masks in section III.3 In section III.4, we report the patterning of the CPW electrodes in section III.5, the fabrication of the DFB laser cavity is detailed and finally in section III.6 the OLED organic heterostructures are presented.

The four main sub-processes necessary to perform the fabrication of the devices and their sub-tasks are illustrated in fig.III.1

- Sub-process 0: Mask design:

In chapter 2, we established guidelines to both reduce the OLED electrical time constant and to enhance the maximum current density sustainable by the OLED.

- The geometry of the coplanar waveguide introduced by A. Chime with a gap  $G=316\mu\text{m}$  between the anode and cathode strip of width  $w=1000\mu\text{m}$  has been retained [1].
- To reduce the measurements resistance  $R_{\text{meas}}$  further from A. Chime devices, a new geometry is to be implemented. Together with the CPW geometry they will define the Mask 1 (etching mask).
- To reduce further the serial resistances  $R_s$  compared to previous studies [1], two modifications have been introduced: firstly the size of the anode has been shrunk, and secondly a more careful and accurate metallization of the ITO layer has been implemented. The shrinkage is implemented in Mask 1 while the metallization is implemented with a new step that uses a new mask (Mask 2 Metallization mask).
- In chapter 2, we also highlight the importance of the confinement factor and the optimization of the index contrast in the DFB cavity in the reduction of the laser threshold. This requires another mask dedicated to the thinning of the active area down to 55 nm (Mask 3 – Thinning masks).

- A first shadow mask dedicated to the organic layer deposition is defined (Organic hollow mask – Mask 4).
- To achieve a better accuracy on both the shape of the cathode and its positioning with respect to the active area, a hollow mask is introduced as Mask 5. Alignment marks and overlay marks (respectively) are also introduced in Mask 1 and in Mask 2, and counter-overlay marks are reproduced on mask 5 (respectively).
- Sub-process 1: Electrodes patterning: The electrode patterning is done in two main steps:
  - Firstly, the ITO layer is dry etched using the specific geometry defined by Mask 1. (Step 1.1 to 1.6)
  - Secondly, partial gold-coating is performed using the metalization mask (Mask 2). (Step 1.7 to 1.11)
- Sub-process 2: DFB-Cavity fabrication: The laser cavity is fabricated on the active area (optionally with a thinner ITO layer) on the ITO anode previously patterned and metalized in step 1.
  - Optionally, but prior to the DFB-cavity fabrication, and so as to maximize the confinement factor in accordance with Design Rule 5 and to enlarge the forbidden bandgap in agreement with Design Rule 6 defined in chapter II, the ITO-based anode active area will be thinned by dry etching after a photolithography step using mask 3 (thinning mask). (Step 2.1 to 2.5)
  - The main part of sub-process 2 consists of 4 steps (2.6 to 2.9) that will be described more in details in section III.4. The most important step is based on e-beam lithography which is the most adequate patterning techniques to achieve the ~100 nm resolution identified in chapter 2 for the fabrication of DFB laser cavities.
- Sub-process 3: OLED deposition: The organic hetero-structure is deposited using vacuum deposition techniques. The main improvement in the OLED deposition deals with the use of high-resolution hollow-masks. A new generation of hollow mask providing both a better than  $\pm 50 \mu\text{m}$  accuracy in the positioning of the metallic cathode with respect to the active area with the DFB cavity and a better than  $5 \mu\text{m}$  resolution in the metallic cathode shape.

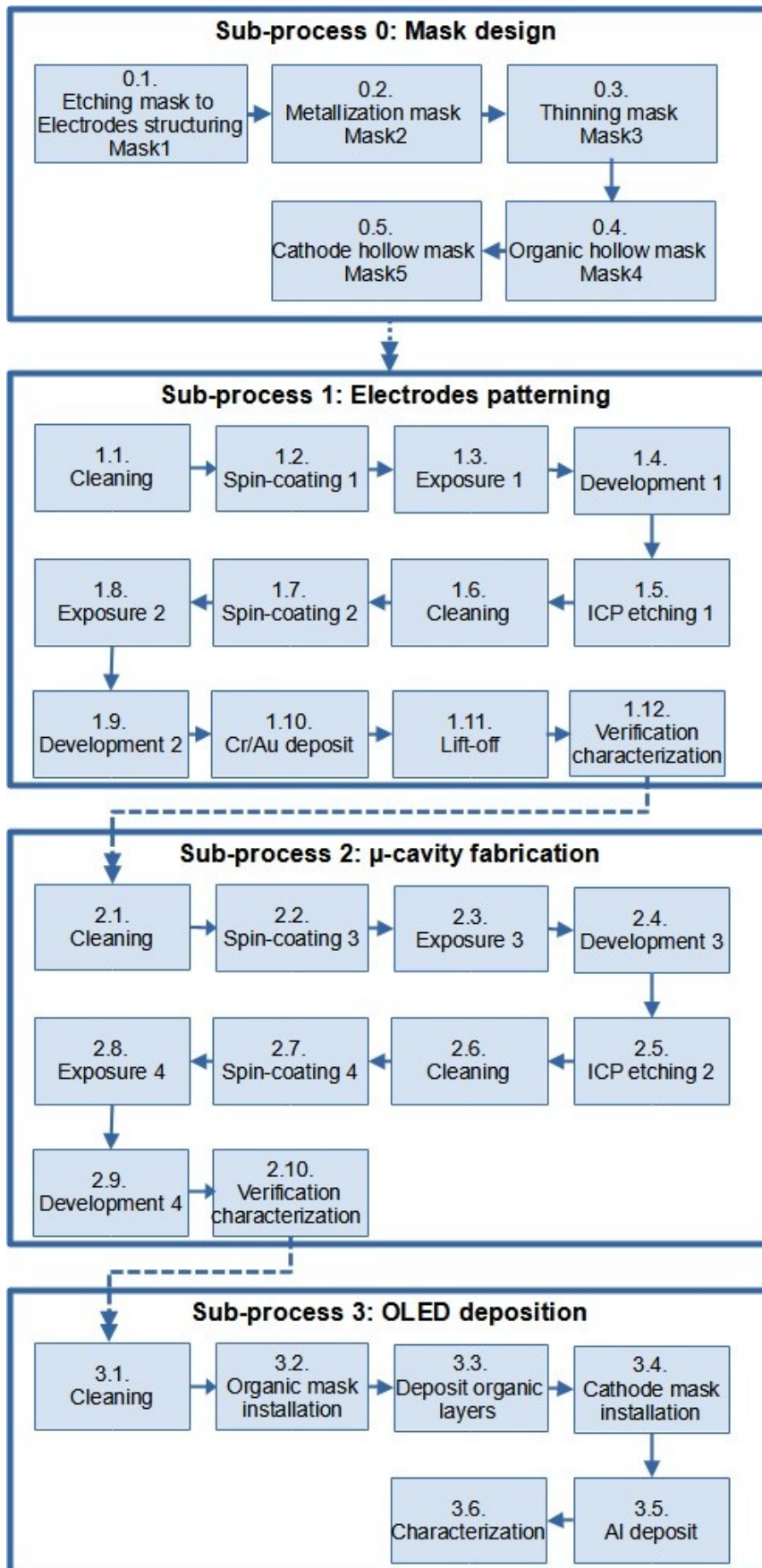


Figure III.1: Device fabrication steps

### III.2. Substrates dimensions, properties and samples

The substrates are glass slides with a dimensions of 25 mm x 17 mm and with a thickness of 700  $\mu\text{m}$ . The substrate are covered on one face with an ITO coating. These samples were provided by LUMTEC- Luminescence Technology Corp, Taiwan. The refractive index of the ITO layer is between 1.8 and 2.1 in the literature.

- Two different ITO thicknesses ( $t_{\text{ITO}}$ ) are used 340 nm and 140 nm
  - ITO thickness of  $t_{\text{ITO}} = 340$  nm presents a resistance of 5  $\Omega/\text{sq}$ .
  - ITO thickness of  $t_{\text{ITO}} = 140$  nm offers a resistance of 15  $\Omega/\text{sq}$ .

Each sample is divided into two columns each of them contains 3 rows of OLEDs as shown in Fig.III.2. Column A is dedicated to the fabrication of the cavities whereas the column B is used for the reference OLEDs without cavities. First row corresponds to 100x100  $\mu\text{m}^2$  OLED, while second and third row corresponds to 50x50  $\mu\text{m}^2$  and 25x25  $\mu\text{m}^2$  respectively.

- The width V of the ITO anode arms varies from 100 $\mu\text{m}$ , 50 $\mu\text{m}$  to 25 $\mu\text{m}$
- The width H of Al cathode takes also three values 100 $\mu\text{m}$ , 50 $\mu\text{m}$  and 25 $\mu\text{m}$ . For some samples the width H is identical whatever the V value is.

The different types of devices are summarized in table III.1 and grouped as Type 1 for the 340nm thick ITO coating, and Type 2 for the 140nm thick ITO coating.

OLED are labeled using the following code:

$t_{\text{ITO}} - \text{V-H-T-C}$

For example 340-100-100-T-A corresponds to a 100x100  $\mu\text{m}^2$  OLED in Column A on a 340nm ITO coating thinned to 55 nm

The thinner layer of ITO is intended for a larger confinement factor at the expense of a higher resistivity, hence a higher serial resistance thus a lower maximum current density.

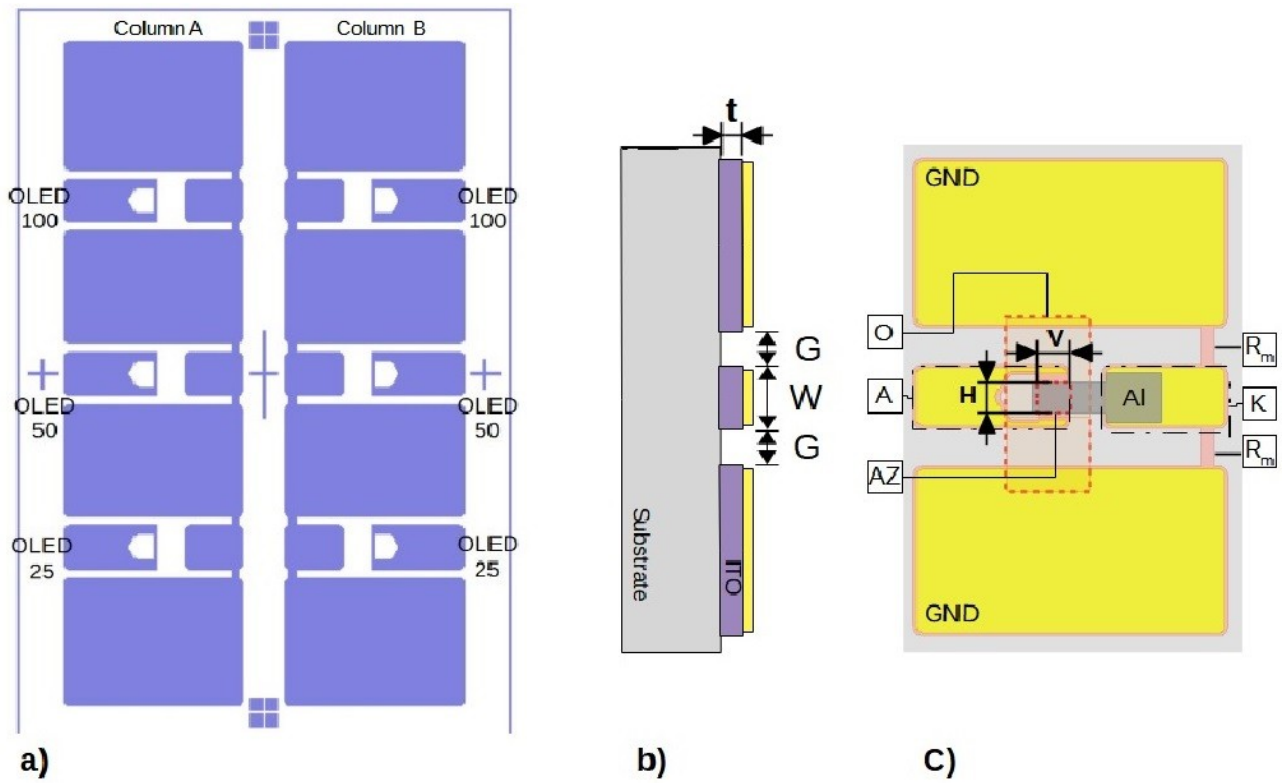


Figure III.2: Diagram of sample: a) Top view of sample: 2 columns A and B, 6 OLEDs with width of anode  $V=[100, 50, 25]\mu\text{m}$ , b): Section view of an OLED, c): Top view of an OLED: Anode side (A), Cathode side (K),  $V$  width of the vertical ribbon,  $H$  width of the horizontal ribbon

Table III.1: Different types of sample and geometry

	$t_{\text{TIO}}$ (nm)	$R_{\text{meas}}$ ( $\Omega$ )	$V$ ( $\mu\text{m}$ )	$H$ ( $\mu\text{m}$ )		Thinned		Column
Type 1	340	3	100 50 25	100		T	F	A B
Type 2	140	15	100 50 25	100	100 50 25			A B



### III.3. Mask Design

The design of masks corresponds to the sub-process 0 of Fig.III.1. Physical quantities such as resistances, capacitances, active surfaces and thicknesses identified and defined at the design stage in Chapter 2 are geometrically translated into different types of masks such as masks for photolithography, and hollow masks both types at scale one. Photolithography masks consist of a patterned chrome coating on silica substrates transparent to UV light. Hollow masks are thin metal or silicon membranes in which openings are cut sometimes at the micrometric scale. In the following sections, the patterns of the different masks are presented through their layout designed using Clewin software by Wieweb.

#### III.3.1 Etching mask

The pattern of the etching mask (Mask 1) as shown in purple in Fig.III.3.a corresponds to parts where the ITO coating will remain after etching. It presents six sets of CPW electrodes made of 1500  $\mu\text{m}$  wide central strips separated by a gap  $G=316 \mu\text{m}$  from large ground planes. Each central line is split (vertically in fig.III.3) into an anode and a cathode and the distance between them is  $L=370\mu\text{m}$ . Cathodes present a nail-like void closed by a horizontal arm with a width  $V=100 \mu\text{m}, 50 \mu\text{m},$  or  $25 \mu\text{m}$  as shown in zoomed fig..III.3.b, III.3.c and III.3.d respectively. On the anode side the central line is linked to both ground planes with two short tracks playing the role of resistors. The length of the anode arm is  $V=1000 \mu\text{m}$ . The width  $d$  of the short tracks is 500  $\mu\text{m}$  resulting in a theoretical measurement resistance of  $R_{meas}=5.6 \Omega$  and  $R_{meas}=2.3 \Omega$  respectively for ITO coating thickness of 140nm and 340nm. In addition, the etching mask contains three types of markers with different sizes: Millimeter marker are used to align manually the patterned substrates with the hollow masks as will be presented in section III.3.4. It also contains a sub millimeter-meter marks around the anode arms used for the alignment of the  $\mu$ -cavity during the sub-process 2. Finally micrometer cross-marks are used to align the different photolithography steps with respect to each.

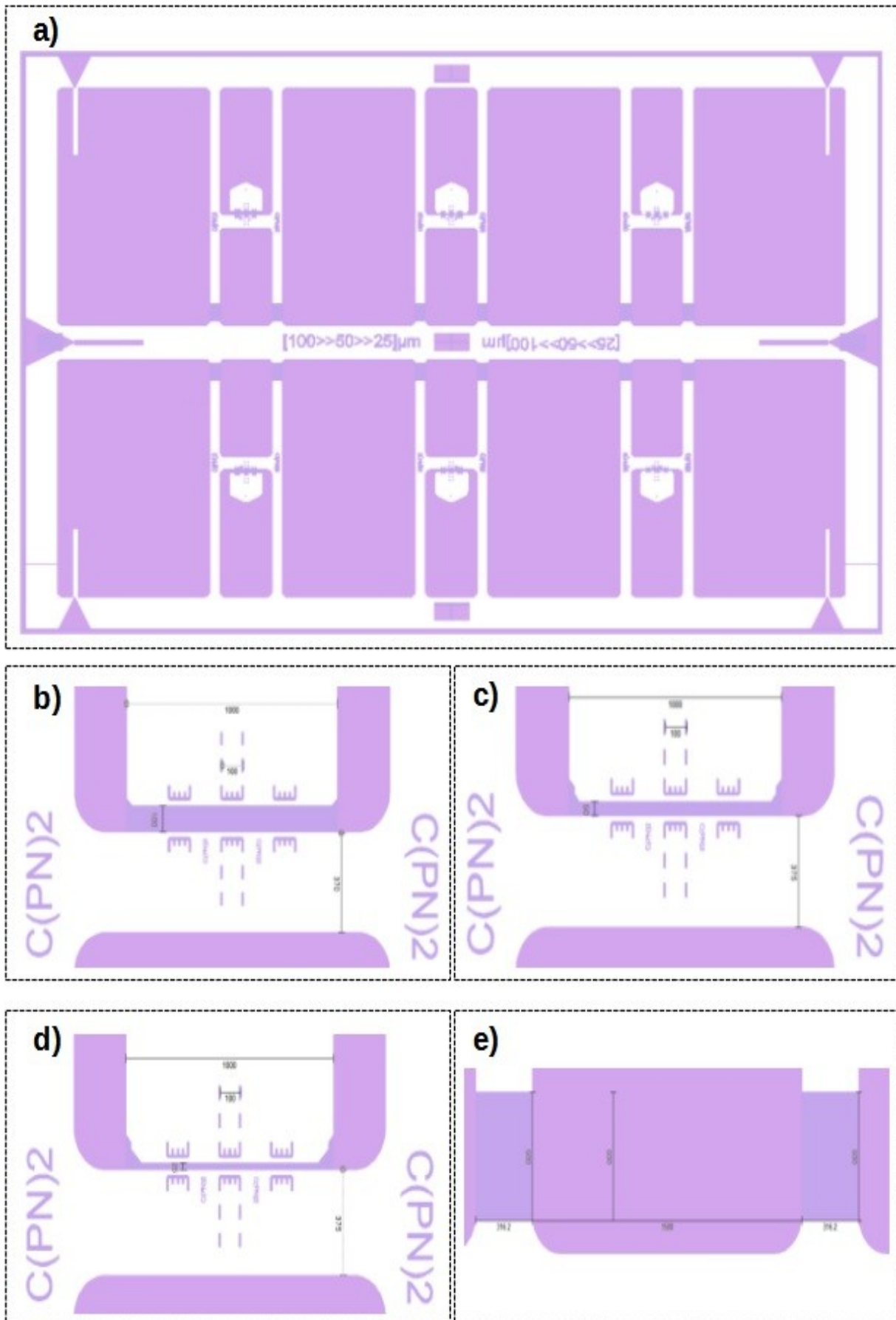


Figure III.3: Mask 1: ITO etching; Electrodes and measurement resistance structuring; a): Global etching mask, b): ITO anode with width  $100 \mu\text{m}$ , c): ITO anode with width  $50 \mu\text{m}$ , d): ITO anode with width  $25 \mu\text{m}$  and d): Measurement resistance  $R_{\text{meas}}$

### III.3.2 Metalization mask

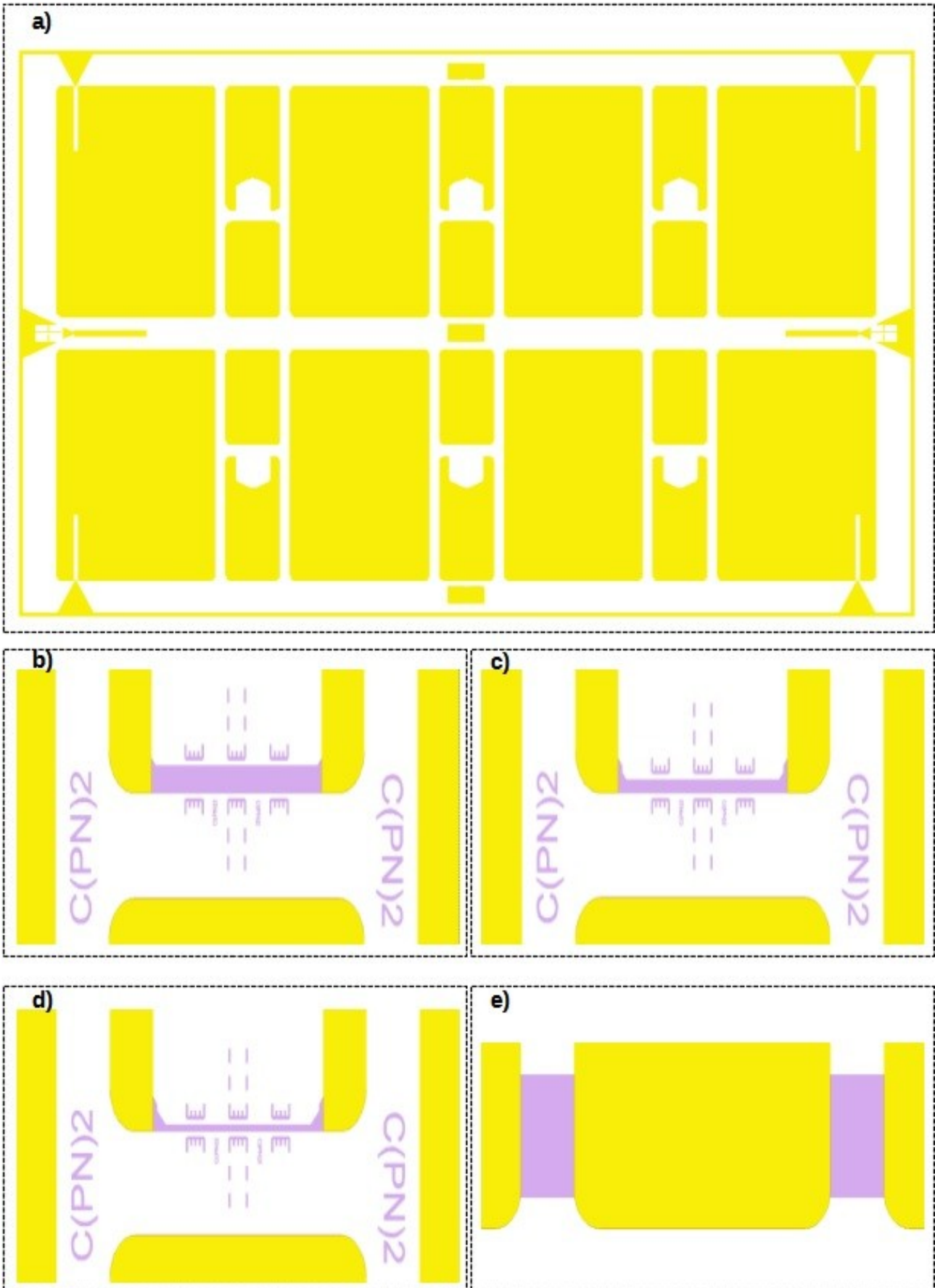
Figure.III.4.a presents the metalization mask (Mask 2) with the areas to be metalized shown in yellow. The purpose of this mask is to coat with gold the ITO except for two types of parts: firstly, the anode arms that are 100  $\mu\text{m}$ , 50  $\mu\text{m}$  and 25  $\mu\text{m}$  wide presented in purple in fig.III.4.b, c, d respectively that are to remain transparent for allowing the light emitted by the OLED to pass through the substrate. The purple parts belonging to the etching mask layout and that represent ITO free from metalization appear when the etching mask layout is placed underneath the layout of the metalization mask. Secondly, two small parts linking the cathodes and their surrounding ground planes as shown fig.III.4.e are to remain un-coated to reach the targeted measurement resistances of several ohms defined in section 2.3.4. If metalized, the resistances would be too small. Their dimensions are those defined for the etching mask in previous section with short tracks  $d=500 \mu\text{m}$  and length  $G=316 \mu\text{m}$  wide resulting in a theoretical measurement resistance of  $R_{meas}=5.6 \Omega$  and  $R_{meas}=2.3 \Omega$  respectively for ITO coating thickness of 140 nm and 340 nm

Except for these measurement resistances, the goal of the metalization step is to reduce the serial resistance much below 100  $\Omega$ . A reduction by a tenfold factor of the parasitic serial resistances compared to that obtained in previous version of the CPW electrodes is targeted.

The etching mask also contains only two types of the above mentioned markers;

- the millimeter markers for the manual alignment of the hollow masks,
- and the micrometer cross-shaped markers dedicated to mask alignment and present in the left and right triangles on the horizontal middle axis.

The metalization mask is drawn for negative photoresists. After development of the negative photoresist, a thin layer of gold is to be evaporated onto the sample, before application of a lift-off process will locally remove the gold coating in the white and purple parts of Fig.III.4.



### III.3.3 Thinning mask

The thinning mask (Mask 3) is used to optimize the confinement factor and the effective index contrast as mentioned in section 4.3.3 and section 4.4.2 of chapter 2. It is a lithography mask used to etch and thin locally part of the ITO anode arm. A local thinning is performed in the middle of the arms of each anode to obtain a 200 $\mu\text{m}$  wide part with residual thickness of 55 nm where the active area of the OLED with organic layers and aluminum cathode and eventually the microcavity are to be located

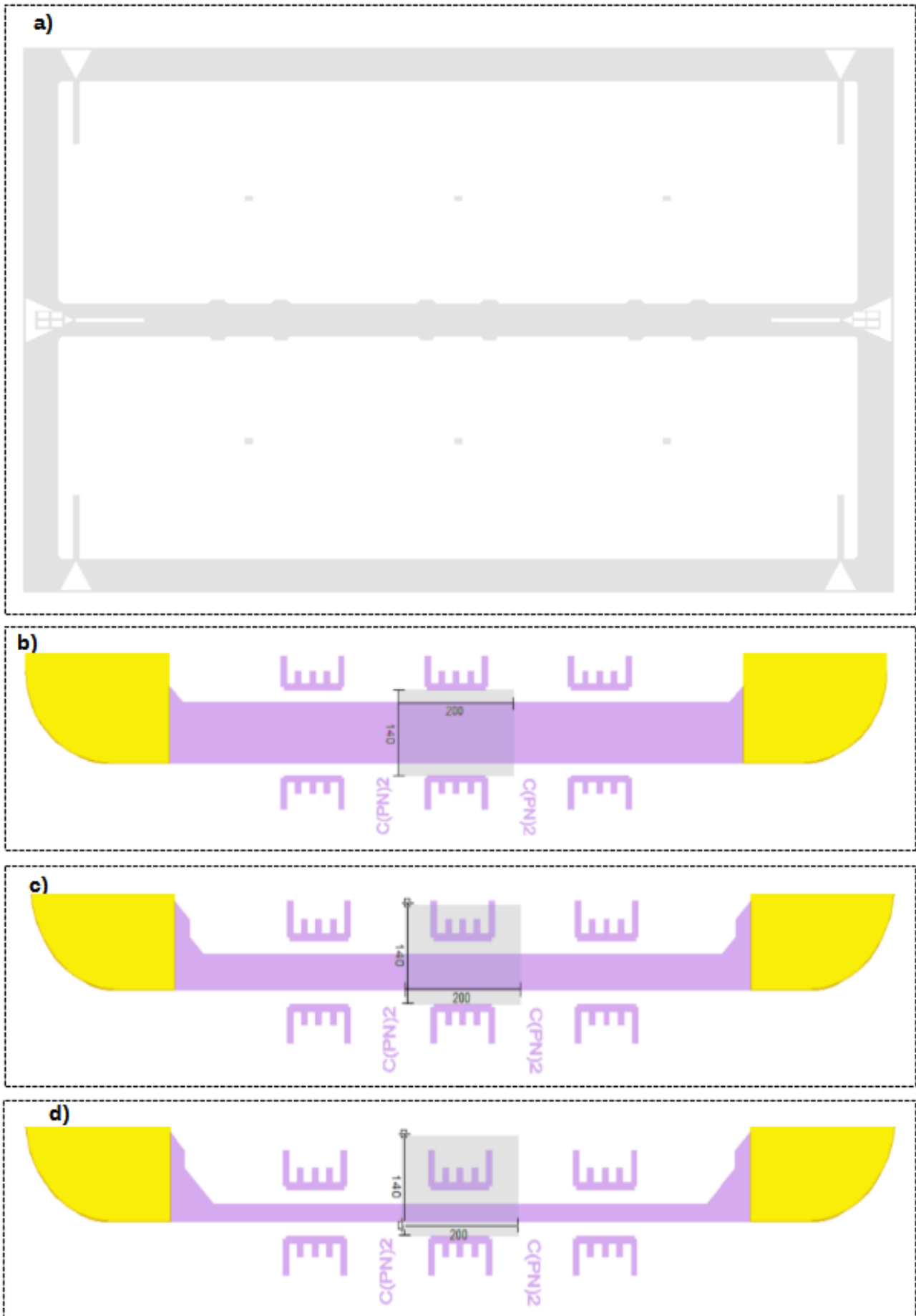
Figure III.5.a shows an overview of the thinning mask. It consists of six  $\mu$ -areas (200  $\mu\text{m}$  x 150  $\mu\text{m}$ ) located in the center of the anode arms to be partially etched.

The width of 200  $\mu\text{m}$  has been chosen for two reasons; Firstly, it has to be large enough to host the active areas. To take into account potential misalignment of the cavity, the width of the thinning zone is chosen to 150  $\mu\text{m}$  to be larger than the largest anode arm (100  $\mu\text{m}$ ). Also to be tolerant to errors in the manual alignment of hollow masks with respect to the active area, it has to be larger than the width of the aluminum cathode. Therefore the length of the thinning zone is set to 200  $\mu\text{m}$ . Secondly it has to be compatible with the dimension of the elementary field stitching of the e-beam lithography system.

The thinning mask also contains two types of the above mentioned markers;

- the millimeter markers for the manual alignment of the hollow masks,
- the micrometer cross-shaped markers dedicated to mask alignment and present in the left and right triangles on the horizontal middle axis.

The etching mask, the metalization mask and the thinning masks are fabricated by Femto-st.



### **III.3.4 Hollow masks**

Hollow masks are thin self-supporting membranes with opening through which material streams can be evaporated. The purpose of hollow masks is to deposit locally by vacuum evaporation organic materials and aluminum to certain zones of the samples.

We distinguish two different hollow masks: A hollow mask for the deposition of organic materials, and another hollow mask for the deposition of the aluminum cathode:

#### **III.3.4.1 Hollow masks for organic materials**

The layout of the hollow mask dedicated to organic materials deposition is shown Fig.III.6. An overview is shown Fig. III.6.a. It consists of six 1.5 mm by 3 mm rectangular openings centered on the anode arms as presented in fig.III.6.b, c and d. The dimensions of the hollows are chosen large enough such that errors in the alignment would have no impact on the layer thicknesses. Part of the ground planes, part of the cathode, and part of the metalized anode arms are covered with organic material without consequence on the capacitance of the device if the aluminum cathode remain small.

The alignment of the hollow mask with the patterns defined from previous mask (Mask,1, Mask 2) and more specifically from the thinning mask (Mask3) with the smallest patterns (200  $\mu\text{m}$  long x 100 or 50 or 25  $\mu\text{m}$  wide active areas) is to be done manually and with naked eyes. The errors in positioning can therefore be very large. To facilitate the alignment and minimize the errors, the hollow mask includes 8 triangular (1 mm base – 1 mm height) hollow overlay markers extended by 2 mm long and 150  $\mu\text{m}$  wide slits so as to be visible with naked eyes and so as to be superimposed with similar but metalized marks as defined from Mask 2.

The hollow masks made of 170  $\mu\text{m}$  thick electro-deposited nickel membrane are fabricated by “VECO-France” from the layout designed using Clewin software by Wieweb.



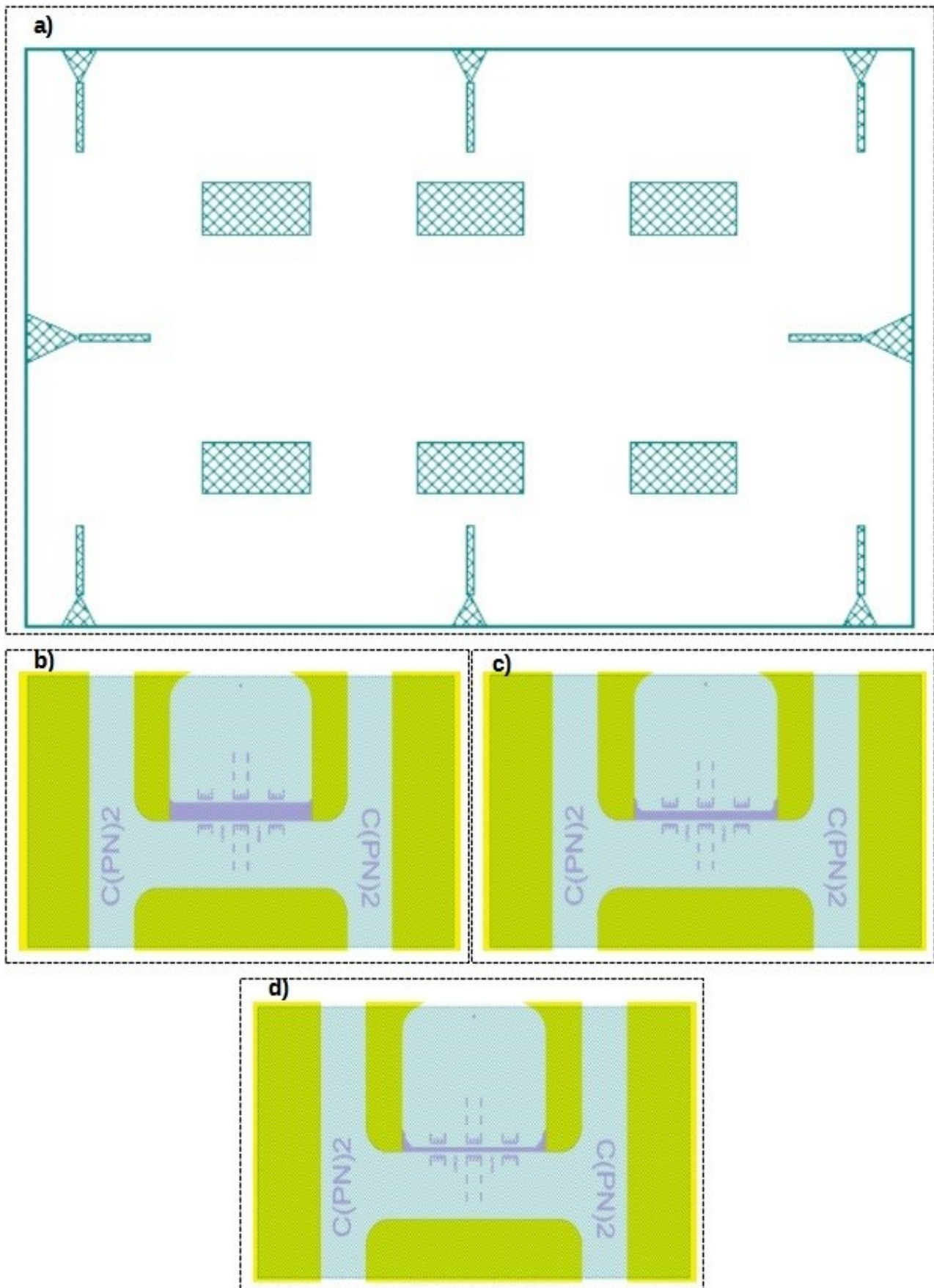


Figure III.6: Mask 4: Organic hollow mask; a): Global view of mask, b, c and d show the zoom of the hollow mask of organic for 3 OLEDs 100, 50 and 25  $\mu\text{m}$  respectively



### III.3.4.2 Hollow masks for aluminum cathode

This hollow mask is also a 170  $\mu\text{m}$  thin self-supported electro-deposited nickel membrane that is placed a few millimeters against the OLED substrate and through which aluminum vapors will be evaporated to form localized cathodes. The accuracy of the hollow masks is around of some micrometers. The mask is placed as close as possible to the substrate to prevent the cone of non-directive flow of aluminum vapors from blurring the electrode contours. The smaller a dimension of an electrode is the more important it is to reduce this parallax effect.

Figure III.7 shows the layout and zooms of the hollow mask used to evaporate the aluminum cathodes. In fig. III.7.a, six hollow cathode patterns and height hollow markers are shown in blue.

Cathode patterns are made of two parts: firstly a part of 800 $\mu\text{m}$  wide to overlap with the cathode part of the central track of the CPW electrodes so as to maximize the electrical contact as shown in Fig. III.7.b. Secondly, a thin vertical arm 100 $\mu\text{m}$ , 50 $\mu\text{m}$  or 25 $\mu\text{m}$  wide and 800  $\mu\text{m}$  long crossing the horizontal anode shown in purple in Fig. III.7.c, d, and e. The latter show only the 100  $\mu\text{m}$  wide arms. The length of the arms is long enough to make sure a part of the aluminum cathode do overlap the ITO anode despite misalignment errors.

Overlay markers are made of hollow triangles continued with 200 $\mu\text{m}$  wide hollow slits used for manual alignments with previous overlay marks in particular with the overlaymarks metalized with gold from the metalization step.

With this mask the cathode layer is expected to be deposited with a precision much better than 200  $\mu\text{m}$  and the active area is expected to be positioned with the same accuracy in the middle of the horizontal ITO anode arm.

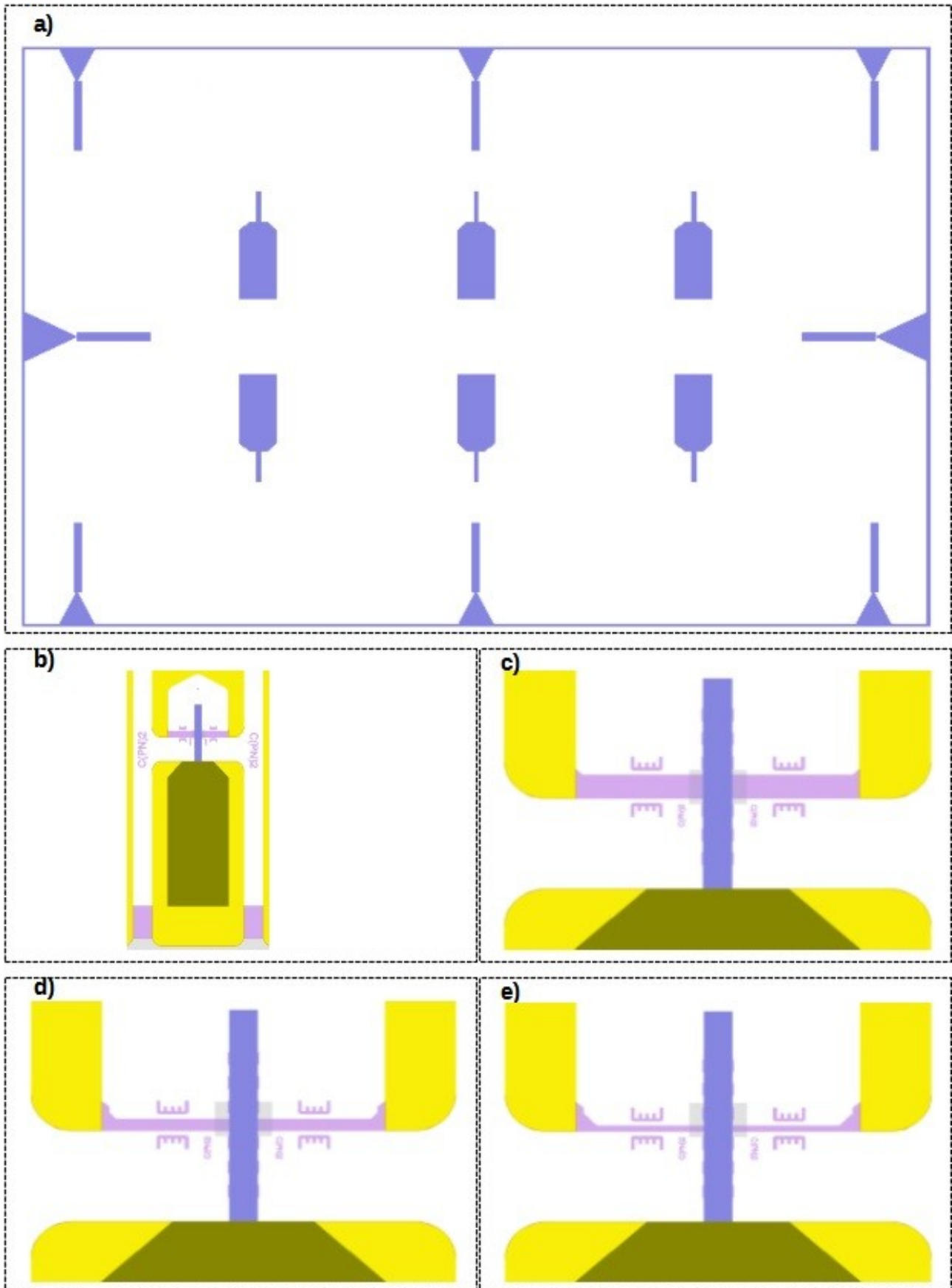


Figure III.7 : Mask 5: Cathode hollow mask for rectangular OLED; a): Global view of mask, b, c, d and e show the hollow mask of cathode (width =  $100\mu\text{m}$ ) for 3 OLEDs 100, 50 and  $25\mu\text{m}$  respectively

### **III.4. Electrodes patterning**

The electrode patterning corresponds to the sub-process 1 of Fig. III.1. It consists of twelve consecutive steps presented below.

#### **III.4.1 Cleaning**

This step consists of a chemical treatment of the ITO coatings for the purpose of removing contaminants. This process identified as step 1.1 in Fig. III.1 is performed in a laminar flow hut and consists of 3 tasks:

- Immersing the ITO coated glass substrates in an ultrasonic bath of acetone for 5min. This removes traces of grease, then ethanol
- A second ultrasonic bath in isopropanol eliminates all organic traces of other solutions.
- Eventually, a UV-Ozone cleaning provides a better adhesion of surface by a changing of surface energy.

#### **III.4.2 Photolithography**

The photolithography step is identified as tasks 1.2, 1.3 and 1.4 in Fig. III.1 is one of the essential steps. The purpose; is to transfer a predefined pattern from a photolithography mask onto the substrate via a photoresist. Here we will use the etching mask defined in section III.3.1. The lithography is the set of three elementary tasks:

- Substrate coating; It consists in coating a substrate with a layer of resist. Resists are either electron sensitive or photons sensitive (photoresists). There are two types of photoresists; positive or negative
- Insulation: A photolithography mask is then placed on the substrate with its pattern plated against the photosensitive resin. This is operated with a mask aligner. The set is then exposed to UV light issued from a UV light source embedded in the mask-aligner. The pattern is then positively or negatively transferred into the photoresist depending on whether the photoresist is positive or negative.
- Development, It consists in revealing the latent image by selective dissolution of the sensitive layer. When properly exposed and developed, the patterns show-up in the full thickness of the photoresist.

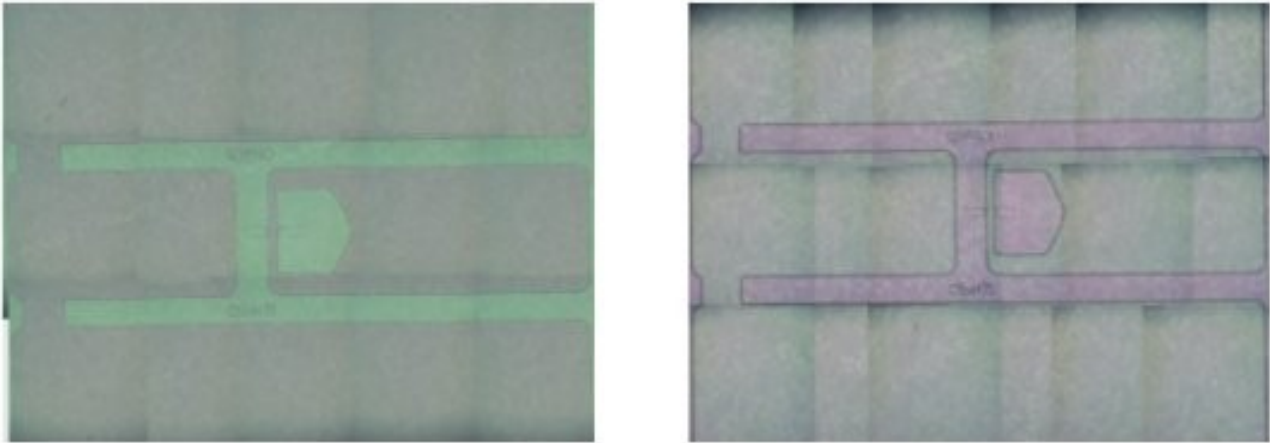


Figure III.8: Appearance of the samples after the photolithography step (Task 1.2 to 1.4). Left sample with 140nm of ITO, right with an ITO thickness of 340nmPr. Grey is the patterned photoresist, green (left) and purple(right) are parts with ITO free from photoresist.

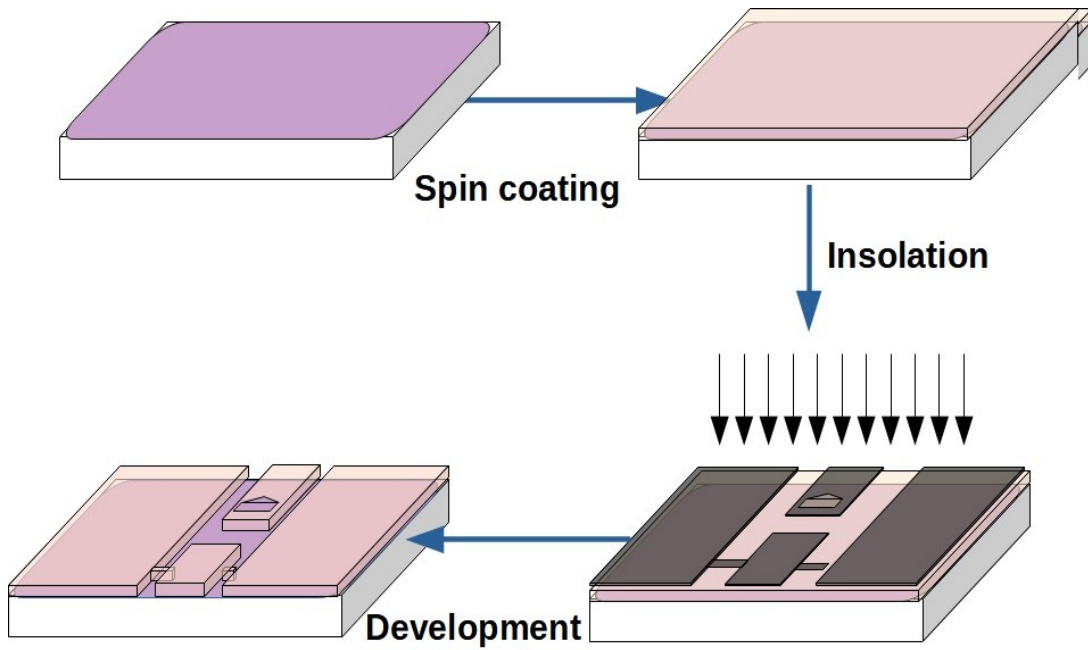


Figure III.9: Schematics of the photolithography task 1.2 of fig. III.1

- At this stage

In our case, we need to transfer patterns with the smallest dimension being 25  $\mu\text{m}$ .

The coating of the ITO anodes, is performed with the positive photoresist AZ1518 for the samples with an ITO thickness of 140 nm and with the positive photoresist AZ4533 for the samples with an ITO thickness of 340 nm. This is because the thickness of the photoresists is to be thicker than that of the ITO so as to fully protect the ITO coating during the etching step since etching rate of the photoresist is higher than that of the ITO.

After alignment of the etching mask (Mask 1) with a MJB4 mask-aligner from Karl Suss, the photoresist is exposed through the mask (Mask 1) with a UV Hg lamp (i-line  $E=14.3\text{mW}$ ) during 12.7 s for the AZ1518 and 27,8 s for the AZ4533.

Finally, the pattern is revealed in the photoresist; the substrate is immersed in a development solution of AZ351B diluted in deionized water with a concentration 1:4 during 1 min. To stop the chemical reaction the substrate is immersed in “deionized” water for 1 min. At this stage the sample is a glass substrate entirely covered with a 140 nm (or 340 nm) ITO coating, on top of which a photoresist layer is patterned according to the etching mask (Mask 1 -See Section III.3.1 )

### **III.4.3 Etching**

The etching step is identified as tasks 1.5 and 1.6 in Fig. III.1. The purpose of the etching is to transfer the photoresist pattern into the ITO layer as shown on Fig. III.10. Preliminary, the sample is post baked in order to densify the photoresist (not shown in Fig III.1). There is two family of etching processes; chemical or wet etching using a chemical solution , and dry etching where the material is sputtered and etch with reactive ions or a vapor phase etchant. It can be divided into four distinct classes known as ion beam etching (IBE), vapor phase etching (VPE) and reactive ion etching (RIE) and inductively coupled plasma (ICP).

In this work, we use the fourth dry etching technique called ICP and we apply it using the 200IL model from the manufacturer CORIAL. It has the advantage of favoring a vertical engraving profile because it combines a chemical etching effect (plasma) and a strong physical etching effect (ionic bombardment) which is very anisotropic. But without selectivity.

This process has been established on the basis of a bibliographic study improved experimentally with a try-and-error approach. ICP etching of ITO coating with  $\text{Ch}_4/\text{Cl}_2$  has been reported by Rong Fang et al but a more systematical study identified the best ITO/Photoresist etching selectivity with

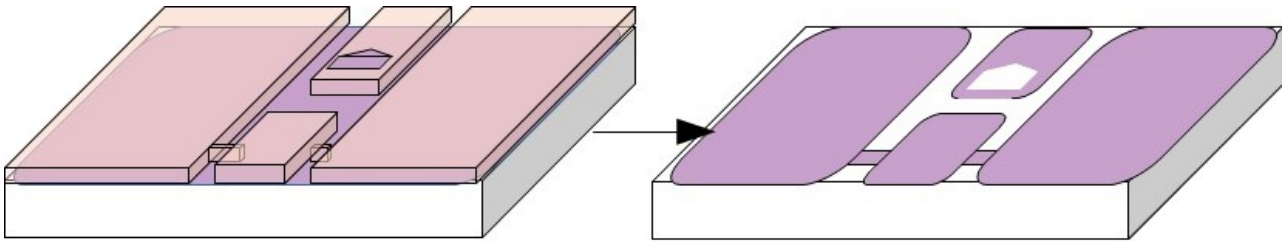


Figure III.10: Scheme of etching step

Table III.2: ITO etching recipe

Pressure [mTorr]	T [°C]	RF power [W]	LF power [W]	Cl <sub>2</sub> flow [sccm]	C <sub>2</sub> H <sub>4</sub> flow [sccm]	Ar flow [sccm]	He flow [sccm]
10	20	200	300	30	7	50	10

Table III.3: ITO etching parameters

Sample	ITO thickness [nm]	Resin	Resin thickness [μm]	Etching time [s]
Ech 1	340	AZ1518	4,2	240
Ech 2	140	AZ4533	2,4	90

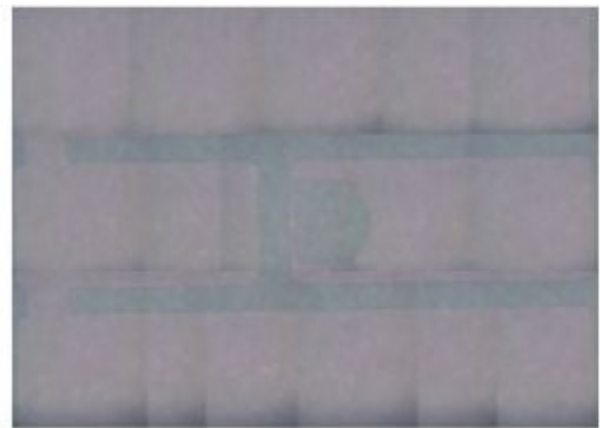
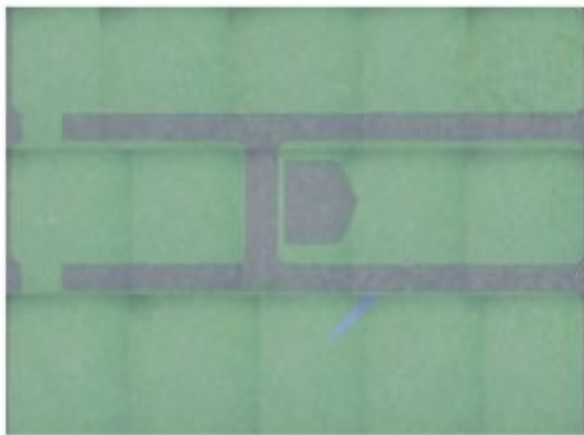


Figure III.11: Top view of samples with 140nm (left) and 340nm (right) thick ITO layer after etching

HI/Ar [2,3]. Chime used a  $\text{Ch}_4/\text{Cl}_2$  based plasma to etch 340 nm thick ITO coating covered with AZ1518 photoresist[2]. We use the same recipe made with chlorinated gases and with the parameters presented in table III.2. From a rule of thumb, and an optimization obtained by try-and-error approach to limits under-etching and over-etching, the etching time is set to 90s for the 140nm thick ITO coating covered with AZ4533 that has replaced AZ1518 to take into account the selectivity.

The etching time corresponding to the desired etching depth and the correct thickness of the resin mask is found after a calibration step performed using different etching time for each type of samples. The table III.3 presents the different parameters for each type of sample

After etching, the sample is cleaned (Task 1.5) with acetone, ethanol and isopropanol with the same process described in section III.4.1, before observation under an optical microscope Leica DM8000 to check if the pattern is correct or if there is over-engraving or under-engraving.

#### **III.4.4 Metalization**

The metalization step is identified as tasks 1.7, 1.8, 1.9, 1.10 and 1.11 in Fig. III.1. This step consists in depositing a chrome/gold double layer on the patterned ITO except on active regions and integrated built-in resistances. The whole process is illustrated in Fig. III.12 with ITO in purple, photoresist in pink, metalization mask in dark grey, and gold in yellow. First, a photolithography step is performed with 3000 rpm spin-coating of AZ1518 photoresist (task 1.7), i-line exposure for 12.7 seconds through the metalization mask (Mask 2) (Task 1.8) and development with a solution of AZ351B diluted in deionized water with a concentration 1:4 during 60 seconds (Task 1.9). We use the same parameters as in § III.4.2 but with AZ1518 as a photoresist. Secondly 10 nm of chromium is deposited by thermal evaporation before 50nm of gold (Task 1.10). After the metal evaporation, the Cr/Au metallic film is uniformly covering the sample including regions with the AZ1518 photoresist. Thirdly, the AZ1518 photoresist is removed by immersing the sample in solvent, as a last step of a lift-off process (Task 1.11). The final substrate, is partially covered with the Cr/Au metallic layer. At this stage the sample resemble that of fig III.13 left (respectively right) for samples with 140nm ITO (respectively 340nm).

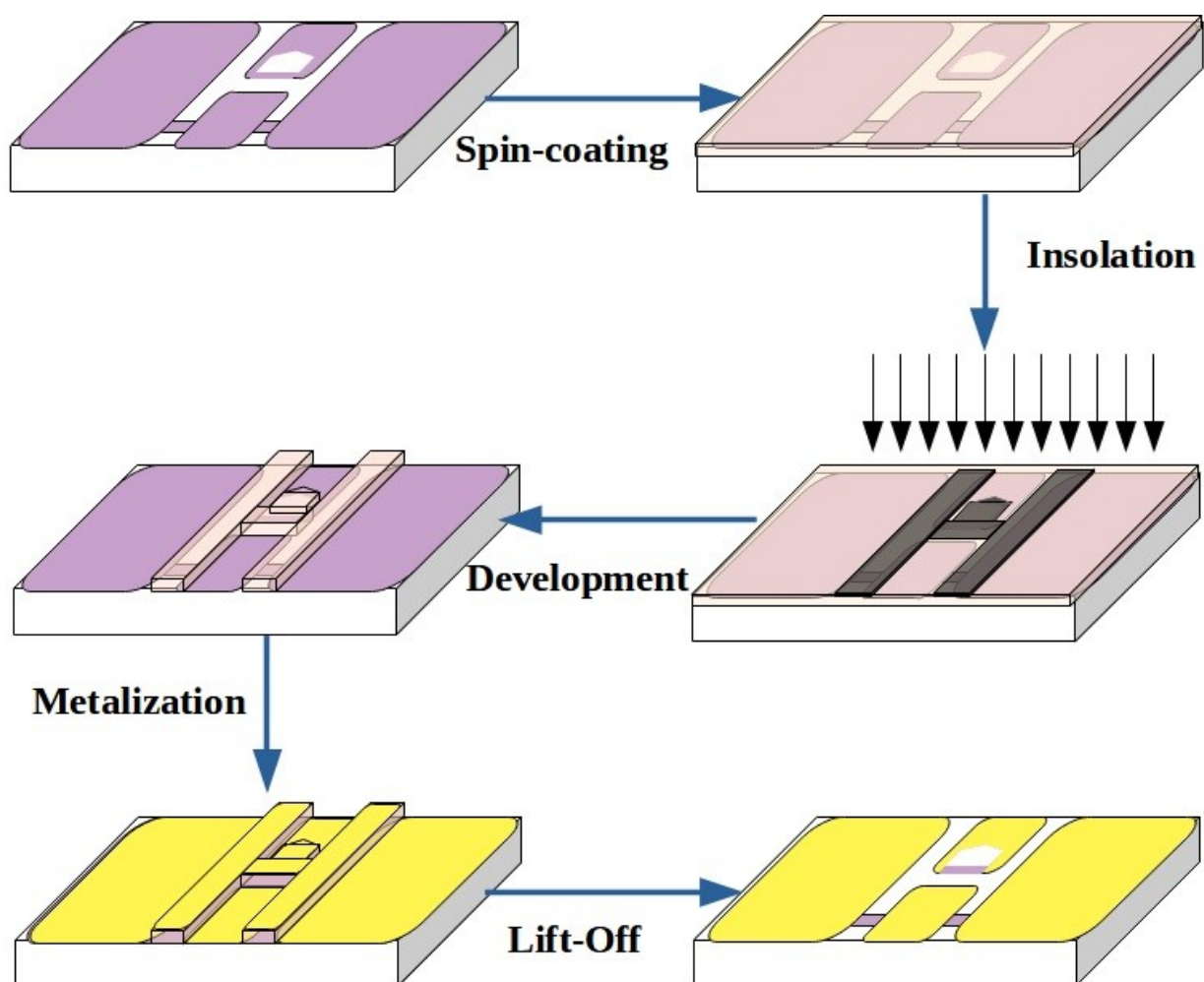


Figure III.12: Metalization steps : Spin-coating of AZ1518 photoresist (Task 1.7), Exposure for 12.7s (Task 1.8), Development with a solution of AZ351B diluted in deionized water with a concentration 1:4 during 1min (Task 1.9), Metal deposition of 10nm of Cr and 50nm of Au (Task1.10), and lift-off

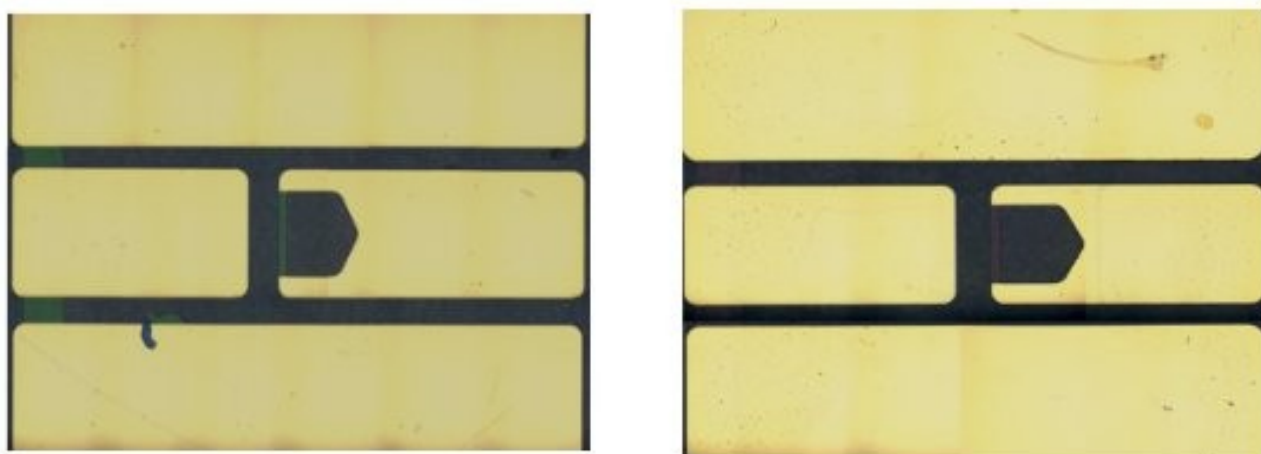


Figure III.13: top view of samples after metalization



## III.4.5 Validation

### III.4.5.1 Optical inspection and validation

After each step we characterize the substrate using an optical microscope Leica DM8000 to check the alignment of the etching mask (Mask 1) and the metalization mask (Mask 2). The top views after each step for the two types of samples  $t_{\text{ITO}}=140$  nm (left) and  $t_{\text{ITO}}=340$  nm (right) are shown after the photolithography step (fig.III.8.a), etching step (fig.III.11) and metalization step (fig.III.13).

### III.4.5.2 Electrical validation

In order to verify that the manufactured samples exhibit the intended properties, the corresponding electrical properties have to be checked, For this purpose, a dedicated sample is fabricated according to the above described steps on top of which an aluminum cathode is deposited ( without the organic layers) as shown in the Fig.III.14. In this section, we focus on the DC and AC measurements of the serial resistances and the measurement resistances.

In DC regime they can be measured with a probe station, needle like probes and an ohmmeter. The measurements resistances  $2R_m$  are measured by probing across point A and B or A and B' (see fig. III.14). Two types of serial resistances are distinguished;  $R_{\text{SC}}$  on the cathode side that is mainly induced by the long aluminum cathode (gray on Fig. III.14) and  $R_{\text{SA}}$  on the anode side that is mainly induced by the thin ITO anode stripe (horizontal green stripe aside point C in Fig III.14). The serial resistances  $R_{\text{SC}}$  is measured by probing between the A and C (see lower left photo of Fig III.14, while  $R_{\text{SA}}$  is measured with the probes in C (as in upper right photo of Fig III.14) and D (as in lower right photo of Fig III.14).

The value of  $R_{\text{SC}}$  varies slightly with positioning errors of the hollow positioning mask (Mask4) between  $R_{\text{SC}}=10$  Ohms and  $R_{\text{SC}}=17$  Ohms.

The values of  $R_{\text{SA}}$  varies with the width of the thin ITO anode stripe that takes the values  $25\mu\text{m}$ ,  $50\mu\text{m}$ , and  $100\mu\text{m}$ . resulting in  $R_{\text{SA1}}=22$ .Ohms,  $R_{\text{SA2}}=33$ .Ohms,  $R_{\text{SA3}}=51$ .Ohms,

The values measured for the measurement resistance are in the range of the targeted values, slightly smaller than the 50ohm limit defined in chapter II. This is a first indication that the design and the fabrication of the sample are relevant.

The values measured for the serial resistances is slightly above the targeted value of 200ohm.

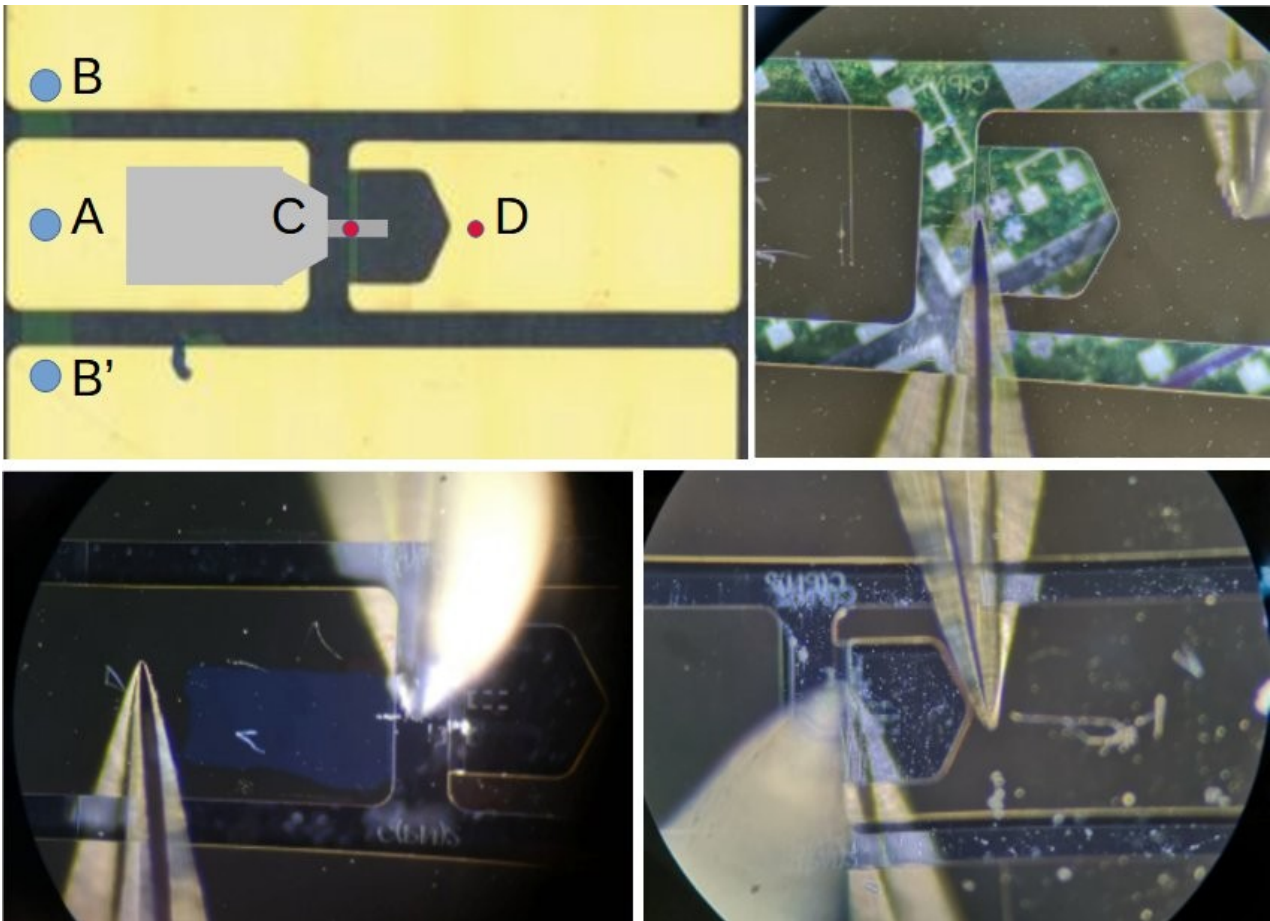


Figure III.14: Probing of resistances in DC regime. upper-left) Top view of the sample with a schematic of the probe positioning.

Table III.4: Measurement resistance and serial resistance of different OLED with 140nm of ITO as an anode

Parameters	OLED size ( $\mu\text{m}^2$ )		
	100X100	50X100	25X100
$R_{\text{measurement}} (\Omega)$	5.2±0.2		
$R_{\text{serial}}(\Omega)$	34±5	43±9	68±14

Table III.5: Measurement resistance and serial resistance of different dimensions of OLED with 340nm of ITO as an anode

Parameters	OLED size ( $\mu\text{m}^2$ )		
	100X100	50X50	25X30
$R_{\text{measurement}} (\Omega)$	3.7±0.1		
$R_{\text{serial}}(\Omega)$	NA		

AC measurements of the impedance is accessible through the reflection coefficient on 1-port of a Vector Network Analyzer (VNA(S11 parameters)). With the dedicated samples describe in the previous paragraph, it is possible to measure the S11 parameter both on the cathode and anode sides and calculate both the measurement resistances and the serial resistances for different modulation frequency.

After the calibration of the measurement setup that uses a 2000  $\mu\text{m}$  pitch ground-signal-ground (GSG) probe and a VNA with a dedicated calibration kit,(Short, Load, Open), the device is measured twice; firstly the probe for the measurement of the S11 parameter on the cathode side is positioned as shown in green in the figure.III.15. To measure the measurement resistance the probe is positioned on the anode side as shown with red stars in Fig.III.15 b. The VNA measures the complex reflection coefficient  $\Gamma$ . from which the impedance value is calculated on the basis of Eq. 4 using a Matlab script..The results are plotted on the Smith diagram shown in fig.III.16 and fig.III.17 respectively for the substrates coated with 140nm and 340nm (respectively) of ITO. These figures present the impedance (solid line) and the total impedance (discontinued line). The real part of Z corresponds to the resistance value.

$$Z = Z_c \left[ \frac{(1 + \Gamma)}{(1 - \Gamma)} \right] \quad \text{eq 4}$$

Where  $Z_c$  is the characteristic impedance and  $\Gamma$  the reflection coefficient. The serial resistance is calculated from the difference between the total resistance and the measurement resistance. Table III.6 and table III.7 present the different values of the measurement resistances  $R_m$  and serial resistances  $R_s$ .

Parameters	Frequency	OLED dimension ( $\mu\text{m}$ )				
		100X100	50X100	25X100	50X50	25X30
$R_{\text{measurement}} (\Omega)$	10kHz	4.65 $\pm$ 0.05	4.76 $\pm$ 0.09	4.83 $\pm$ 0.19	4.69 $\pm$ 0.16	4.71 $\pm$ 0.07
	1GHz	5.36 $\pm$ 0.03	5.24 $\pm$ 0.07	5.28 $\pm$ 0.02	5.29 $\pm$ 0.05	5.27 $\pm$ 0.05
	3GHz	6.41 $\pm$ 0.38	6.36 $\pm$ 0.47	6.36 $\pm$ 0.47	6.40 $\pm$ 0.14	8.29 $\pm$ 1.96
$R_{\text{serial}}(\Omega)$	10kHz	34.17 $\pm$ 0.70	65.49 $\pm$ 0.61	134.31 $\pm$ 2.79	69.70 $\pm$ 2.57	136.71
	1GHz	37.14 $\pm$ 0.67	49.52 $\pm$ 9.06	117.49 $\pm$ 5.57	55.88 $\pm$ 0.56	114.56 $\pm$ 5.12
	3GHz	59.35 $\pm$ 0.52	50.66 $\pm$ 8.62	82.18 $\pm$ 16.17	60.25 $\pm$ 0.91	66.93 $\pm$ 2.99

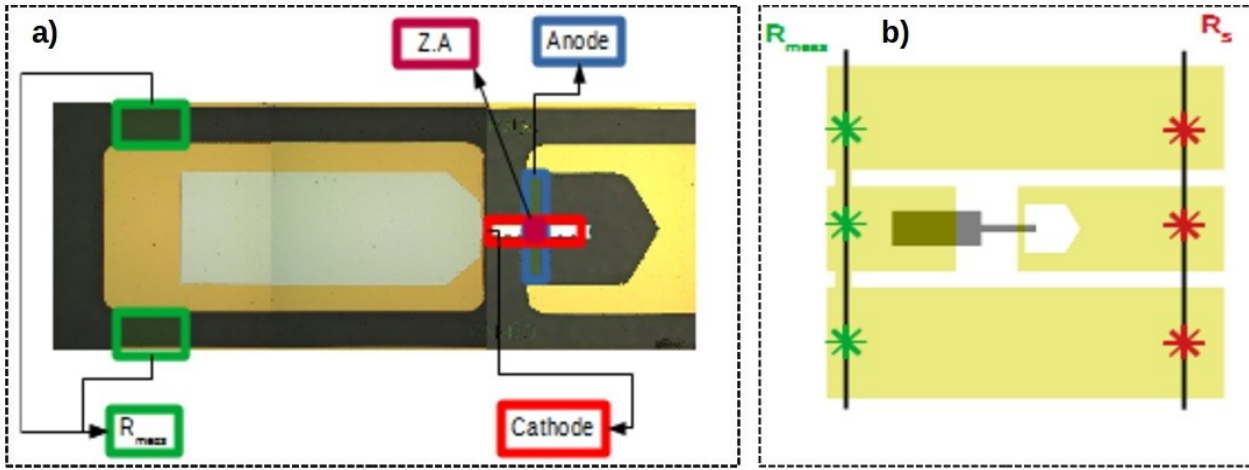


Figure III.15: Top view of a coplanar waveguide electrodes (a) and positioning of the probe; green measurement of the measurement resistance (b)

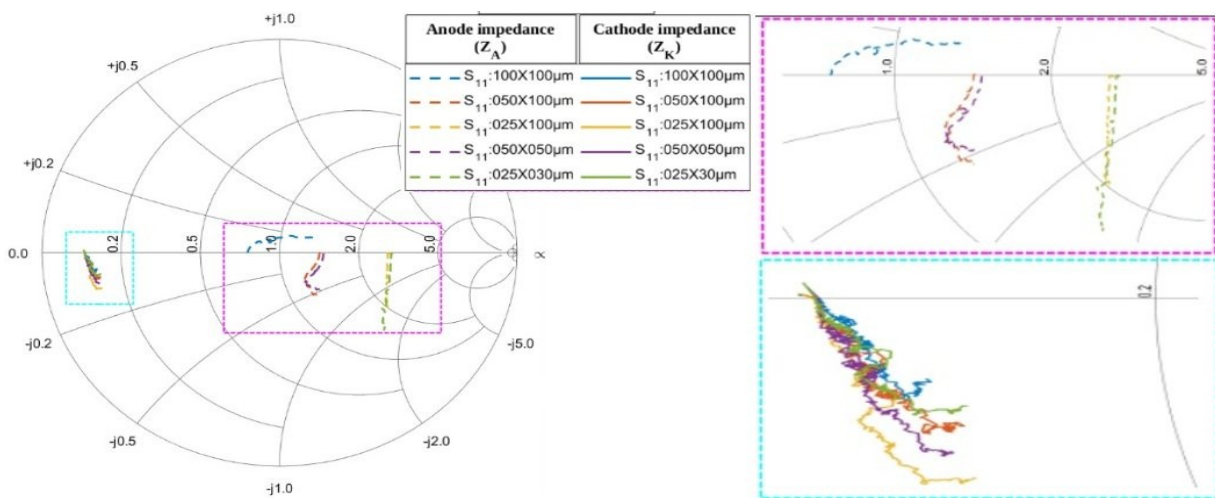


Figure III.16: Smith diagram of reflection coefficient for samples with 140nm thick ITO anode: the cyan inset :  $S_{11}$  parameter on the cathode side, magenta inset:  $S_{11}$  parameters on the anode side

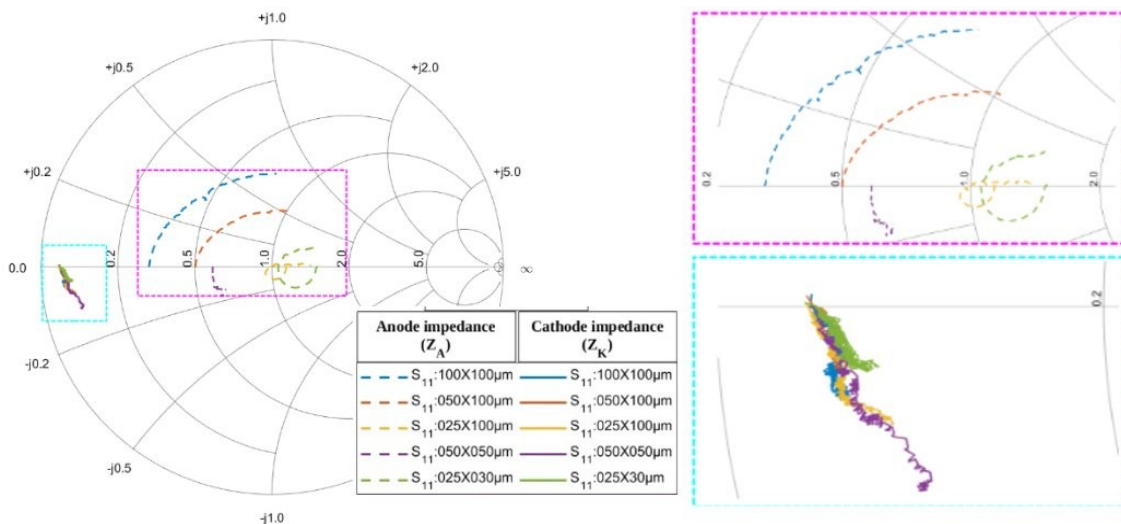


Figure III.17: Smith diagram of reflection coefficient for substrate with 340nm of ITO: the cyan rectangle present the  $S_{11}$  parameter in cathode part, the magenta rectangle presents the  $S_{11}$  parameter in anode part

Parameters	Frequency	OLED dimension ( $\mu\text{m}$ )				
		100X100	50X100	25X100	50X50	25X30
$R_{\text{measurement}} (\Omega)$	10kHz	2.15 $\pm$ 0.10	2.12 $\pm$ 0.11	2.05 $\pm$ 0.13	2.07 $\pm$ 0.11	2.13 $\pm$ 0.08
	1GHz	2.49 $\pm$ 0.07	2.61 $\pm$ 0.13	2.49 $\pm$ 0.12	2.52 $\pm$ 0.13	2.67 $\pm$ 0.04
	3GHz	3.48 $\pm$ 0.77	3.65 $\pm$ 0.61	3.71 $\pm$ 0.96	3.96 $\pm$ 0.88	4.01 $\pm$ 0.56
$R_{\text{serial}}(\Omega)$	10kHz	14.11 $\pm$ 0.91	23.54 $\pm$ 0.22	38.92 $\pm$ 6.44	36.41 $\pm$ 5.05	81.19 $\pm$
	1GHz	16.06 $\pm$ 0.31	21.29 $\pm$ 1.00	36.78 $\pm$ 0.46	36.84 $\pm$ 0.75	38.37 $\pm$ 1.06
	3GHz	32.23 $\pm$ 0.81	41.81 $\pm$ 2.24	55.92 $\pm$ 0.69	47.02	58.18 $\pm$ 0.23

### III.5. $\mu$ -cavity patterning

As defined previously in chapter II, the micro-cavity consists of a first order grating made of 300 nm thick  $\text{SiO}_2$  quarter-wavelength lines to select a resonance wavelength of  $\lambda = 605\text{nm}$  (DCM) as a first choice (and  $\lambda = 624\text{nm}$  for a second choice with DCJT).

Depending on the considered ITO thickness, the effective indices differ, and consequently the width  $l_L$  of the  $\text{SiO}_2$  lines vary as indicated in table III.8. The spacing between lines  $l_H$  is to be filled with organic materials and vary also.

	$\text{SiO}_2$ thickness (nm)	ITO thickness (nm)	Line type	Refractive index (index contrast)	First order line width $l_L$ or spacing $l_H$ (nm)	Second order line width $2l_L$ or spacing $2l_H$ (nm)	First order DFB1 Period (nm)	Second order DFB2 Period (nm)	DFB1 => DFB2 Period (nm)	
Bulk refractive index	300	140 & 340	Organic line $n_H$	1.7 (0.25)	$l_H = 91$	$2l_H = 182$	198	396	289	
			$\text{SiO}_2$ line $n_L$	1.45	$l_L = 107$	$2l_L = 214$				
Effective index		340	340	Organic line $n_H$	1.81 (0.03)	$l_H = 86$	$2l_H = 171$	173	344	258
				$\text{SiO}_2$ line $n_L$	1.79	$l_L = 87$	$2l_L = 173$			
		140	140	Organic line $n_H$	1.68 (0.04)	$l_H = 92$	$2l_H = 185$	187	374	280
				$\text{SiO}_2$ line $n_L$	1.64	$l_L = 95$	$2l_L = 189$			
50	50	Organic line $n_H$	1.55 (0.05)	$l_H = 100$	$2l_H = 200$	203	406	303		
		$\text{SiO}_2$ line $n_L$	1.50	$l_L = 103$	$2l_L = 206$					

The table III.8, clearly indicates that the DFB grating periods are about 200 nm. Several requirements must be taken into account in the fabrication of DFB micro-cavities, in particular the control of the dimensions of the patterns as small as 200 nm. In order to obtain, on one hand a band gap centered around the targeted wavelength ( $\lambda = 605\text{nm}$  DFB 1), and on the other hand, a vertical laser emission at the desired wavelength the relative accuracy must be about 1% to achieve  $\lambda =$

605±6nm. This  $\mu$ -cavity must cover the OLED active area (100, 50 or 25 X 200  $\mu$ m). In our case, and accorded to this exigences, the electron beam lithography is the technique that offers the best solutions in term of size and resolution although 1% accuracy is hard to achieve.

### **III.5.1 Scanning electronic lithography :**

The electron-beam lithography is one of the most accurate nano-patterning technique used to transfer the smallest patterns. As photolithography, the scanning electronic lithography consists a set of three steps; the substrate coating with an electron-sensible resist, exposure with an accelerated electron beam whose wavelength is between 0.4nm and 20nm hence the higher resolution compared to the photolithography, and finally the development of the pattern the resist.

#### **III.5.1.1 Principle of Scanning electron lithography:**

It uses a focused beam of accelerated electrons controlled by a system to reproduce the pattern on an electron-sensitive film. The pattern mask is drawn with a software in a sequential way. Indeed, the writing is done point by point which explains the high resolution. In general, the scanning electronic lithography system consists of a scanning electronic microscope column (SEM column), a beam blanker which allows to block the electron beam so as to shift the position of a motorized sample holder associated with an accuracy better than  $\lambda/10$  thanks to a laser interferometer.

##### **● SEM column**

The essential scanning electronic microscope components include

- Electron gun: it consists of an electron source. There are two types of electron source; the conventional source use tungsten filaments or lanthanum hexaboride single crystal tips, and field emission (FE) sources use a cold cathode or a Schottky emitter. The thermal FE sources provide both better imaging and lithography in terms of brightness (current density), probe size and low dispersion.
- Electron lenses to focus the beam. It consists of an alignment system to center the beam in the SEM column, a condenser lenses to minimize the electron source size, a deflector coils to produce the beam sweep on the sample surface, a stigmatist to correct the astigmatism of the beam and a diaphragm to define the aperture angle of the beam.
- Detectors to produce the image of the substrate using an image analysis system.
- Vacuum system to achieve a secondary vacuum in the working chamber and a high secondary vacuum int the electron gun.

### ● **Pattern design**

To design the pattern, a computer aided design (CAD) software will be used. With this method any shape can be designed, interfaced and issued in GDSII format. The design of the pattern consists in defining not only the shape but also the size and the positions of the pattern elements. To successfully the pattern design, some constraints of the writing system have to be considered such as the size of the writing field. This latter is the area to be exposed to the electron beam. The choice of its size defines the so called pixel size which is related to the resolution. Indeed the width of a pixel is equal to the writing field size divided by the number of pixel. Note that the resolution increases when the field size is reduced. If an area larger than the field size is desired, several fields can be positioned next to each other provided that the field edges are aligned with each other. This method is known as field stitching.

### ● **Pattern exposure**

The resist will be selectively exposed to electron through the digital mask pixel after pixel for a certain time called *Dwell time*. When the beam moves for a certain distance called step size, it is cut by the beam blanker. Electrons react with the resist and modify its molecular structure which changes the solubility of material. Leaving a latent image, the resist can be selectively dissolved to let the pattern appearing. To successfully the resist expose, some main parameters as the type of resist, and the dose have to be known.

- **Resist** is an electron sensitive organic polymer which coats the substrate generally by spin coating. This material reacts with the electron and depending on the type of resist positive or negative, the sensitive material will be degraded or strengthened respectively.
- **Dose** is the charge per unit area delivered to the resist ( $\mu\text{C}/\text{cm}^2$ ). It is one of the key parameters of the electron-beam lithography. To define it, we must measure the probe current which is dependent on the acceleration voltage of electron and the beam diameter. The optimal dose is determined by try and error method for which the size of the patterns is transferred to the sample with dimensions closest to the original mask.

#### **III.5.1.2 Fabrication parameters**

At this step (Step 2.7 in Fig. III.1) we use the hydrogen silsesquioxane (HSQ) as a negative and electro-sensitive resist[4,5]. It's one of the highest resolution e-beam resist available (<10 nm). Commercially, this product is manufactured by Dow Corning (DuPont) and is known as Fox16. It is very sensitive to the surface condition of the sample that's why we need to do a cleaning step with a UV-ozone treatment before use. The HSQ resist is deposited by spin-coating at 6000 rpm.

Immediately after deposition, annealing is performed at 85 °C for 10 min to harden the HSQ layer. The thickness of this film is in this case around 300 nm. Then the sample is loaded in the vacuum chamber of scanning electron microscopy (SEM) which from Pioneer (Raith) (Fig. III.19). The sample is fixed to a translation plate as presented in fig.III.18, that moves in x and y defining the written coordinates and in z to find the working distance between the electron beam and the sample.

The choice of different parameters depends on mask requirements, resist properties, and technological limits. As indicated in chapter II, the considered micro-cavity consists of DFB grating. To define the adequate parameters, to fabricate the  $\mu$ -cavity, we study the different main parameters as the dose, the area step, the time of development. For these studies, we chose as an accelerated voltage equal to 20 kV, diaphragm aperture equal to 15  $\mu$ m, work distance depending on ITO thickness is around 6.5 mm and a pitch current between 60 and 80 pA. As in photolithography, the sample is immersed in an alkaline solution to reveal the patterns. This step depends of the rate of dissolution of the photoresist polymer, of the time of development, of the temperature bake, of the resist thickness and of the pattern dimension. The process parameters is to be optimized carefully to achieve the accuracy needed for the targeted structure. The goal is to pattern lines of SiO<sub>2</sub> with a width  $l_L$  separated from each other by a spacing  $l_H$  defined in table III.8. The unexposed resist lying in between lines is to be eliminated systematically avoiding under-development (negative resist). On the contrary, over-development will increase the spacing  $l_H$  and reduce the line width  $l_L$ . Therefore we decided to conduct a systematical and careful study of the different parameters of process including the effect of development time. At this stage, the following studies are conducted with substrates plainly covered with ITO and without CPW electrodes.

- **Solution study**

The solution using to reveal the patterns consists of a tetramethylammonium hydroxide dissolved in water. This developer is commercialized by Rohm and Haas electronic materials as a MF CD-26 developer. The developer product a chemical reaction with the molecules of the resist to eliminate the unexposed areas but this reaction taking place in an aqueous environment can produce an insoluble film and stop the development [6]. For this reason one add 4% of NaCl to the solution as a catalyzer. The resulting developer solution contains MFCD-26 (TMAH 2,5%): H<sub>2</sub>O + 4% NaCl.

- **Dose study**

We consider three different samples with three thickness of ITO (55 nm, 140 nm, 340 nm). The thickness difference of the transparent and conductive layer causes a difference in the distribution of the electron charge during the exposure. This difference leads to different optimal doses necessary to



achieve the same pattern. Figures. III.20, III.21 and III.22 present the SEM observations of the electron-beam lithography using a mask with lines width of 107nm and spacing of 91 nm and doses of  $400 \mu\text{C}/\text{cm}^2$ ,  $600 \mu\text{C}/\text{cm}^2$  and  $800 \mu\text{C}/\text{cm}^2$ . Figure.III.23 confirms that the optimal dose depends on the thickness of the ITO layer. Preliminary conclusion shows that the optimal charge per area for the samples with the different thickness 340 nm, 140 nm and 50 nm of ITO coating respectively are  $500 \mu\text{C}/\text{cm}^2$ ,  $600 \mu\text{C}/\text{cm}^2$  and  $620 \mu\text{C}/\text{cm}^2$  respectively.



Figure III.18: Sample fixed to a translation plate



Figure III.19: Photo of the Raith scanning electronic lithography system in C(PN)2

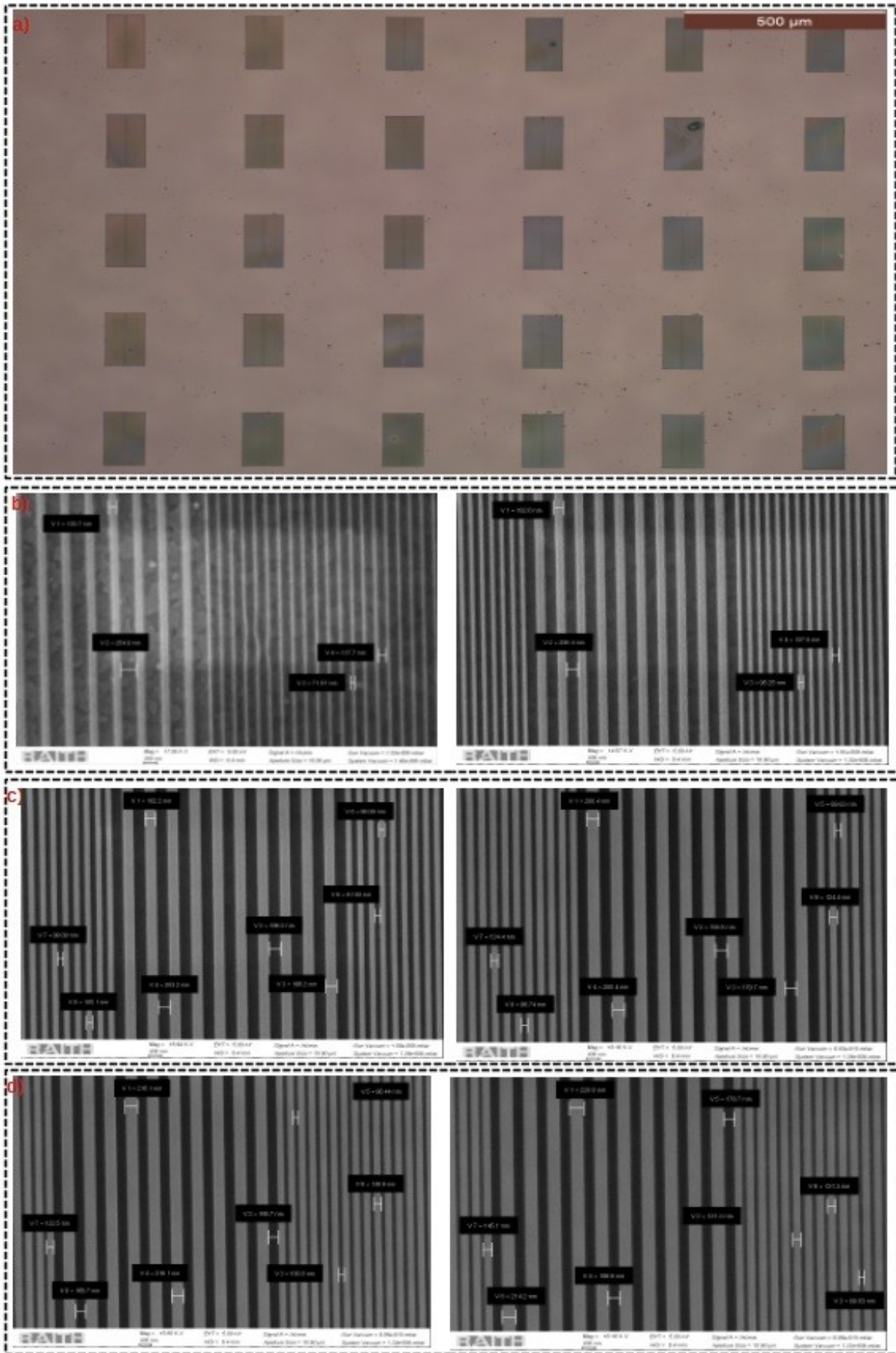


Figure III.20: Dose test for samples with 340nm thick ITO coating; a) Optical microscope image for the sample, b) SEM image for  $400\mu\text{C}/\text{cm}^2$ , c) SEM image for  $600\mu\text{C}/\text{cm}^2$ , d) SEM image for  $800\mu\text{C}/\text{cm}^2$

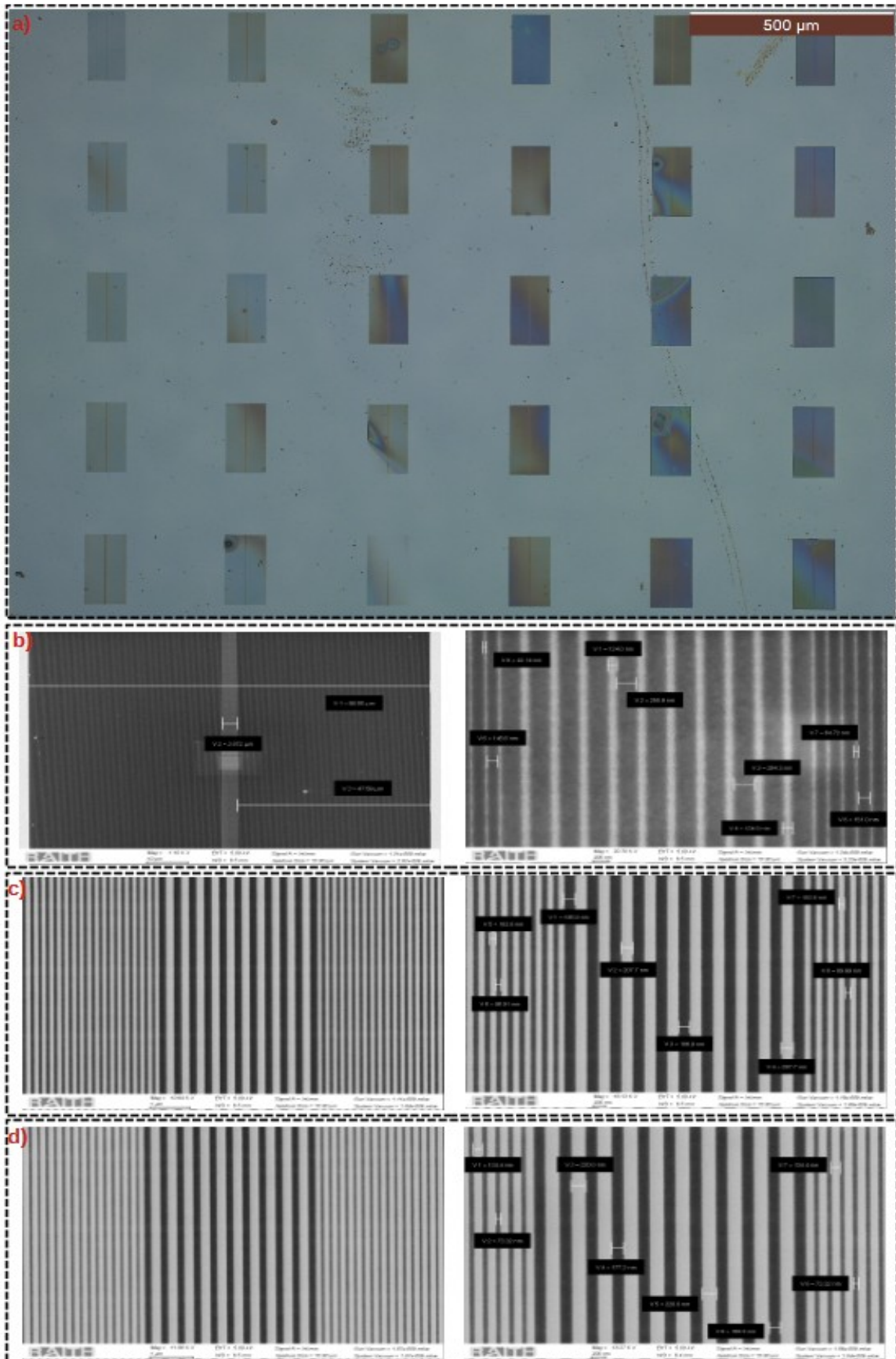


Figure III.21 : Dose test for sample with 140nm thick ITO coating; a) Optical microscope overview of the sample with the different doses, b) SEM image for  $400\mu\text{C}/\text{cm}^2$ , c) SEM image for  $600\mu\text{C}/\text{cm}^2$ , d) SEM image for  $800\mu\text{C}/\text{cm}^2$



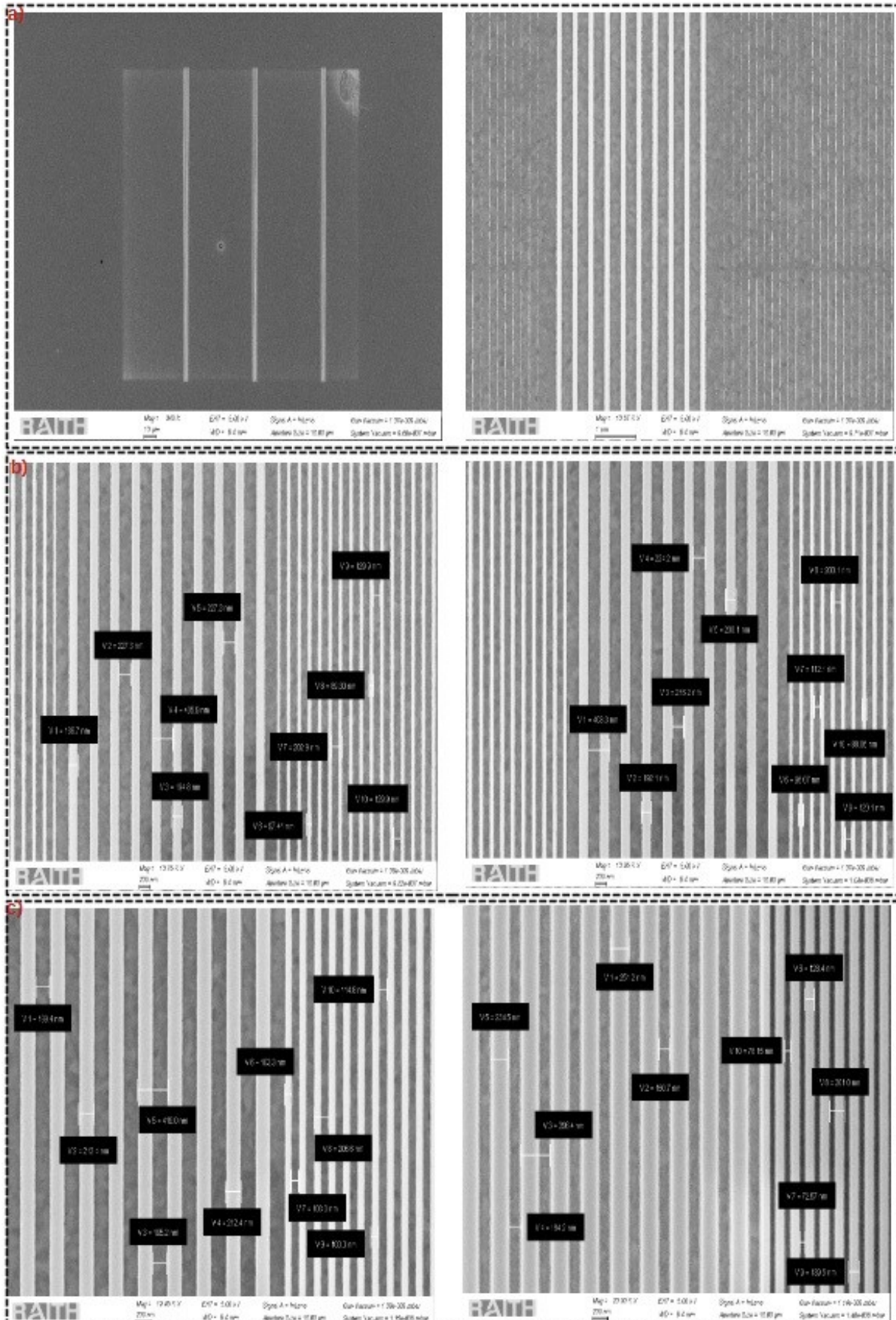


Figure III.22: Dose test for sample with 50nm thick ITO coating; a) SEM image for  $400\mu\text{C}/\text{cm}^2$ , b) SEM image for  $500\mu\text{C}/\text{cm}^2$ , c) SEM image for  $700\mu\text{C}/\text{cm}^2$

- **Time development study**

For this study, we use a pattern with  $l_L = 114\text{nm}$  and a spacing  $l_H = 97\text{nm}$ . For several doses from 400 to 800  $\mu\text{C}/\text{cm}^2$ , we study the impact of the development time on the pattern accuracy. The graph of fig. III.24 shows the measured line width  $l_L$  and the spacing  $l_H$  as a function of doses from 400  $\mu\text{C}/\text{cm}^2$  to 800  $\mu\text{C}/\text{cm}^2$ , for different development times (20 min, 40 mn, and 60 min). The optimal development time is to 40 minutes.

- **Area step study**

We next studied the impact of the area step. The area step defines the elementary shift of the e-beam used to increment its position and go through the pattern. Figure III.25 shows two patterns obtained respectively with a 0.2  $\mu\text{m}$  and a 0.02  $\mu\text{m}$  area steps. Obviously the smaller area step exhibits a more accurate pattern at a cost of a longer writing time.

- **Write field**

The write field is the maximum area writable by the e-beam. The smallest pattern size thus the write field, is to be at least larger or equal to the larger step OLED active area of 100  $\mu\text{m} \times 100 \mu\text{m}$ . Insufficient accuracy in the positioning of the pattern on the ITO cathode may leave the cathode free from the pattern resulting in an OLED section without cavity and eventually spontaneous emission parasiting coherent light observation. Thus uncertainty in the positioning of the pattern with respect to the CPW electrodes requires the write field to be at least equal to the width of cathode plus the uncertainty in the positioning. Thus dimensions of the write field of 200  $\mu\text{m} \times 200 \mu\text{m}$  become desirable. It can be done in two manner, firstly with a single 200x200  $\mu\text{m}$  write field at a cost of reduced resolution, or secondly with four elementary 100x100  $\mu\text{m}^2$  write fields paving a 200x200  $\mu\text{m}^2$  field. The later solution requires field stitching for accurate alignment of the pattern but offers a better resolution at a cost of a longer writing time. We were forced to choose the first solution and use a write field of 200  $\mu\text{m} \times 200 \mu\text{m}$  without stitching (because of a trouble shooting on the laser interferometer stage making the stitching unavailable for month)). Figure.III.26 shows that without stitching a misalignment is induced a the junction of the field.

Positioning the pattern in the center of the arm of the ITO CPW electrodes with sufficient accuracy requires a dedicated approach; We use the markers etched in the ITO coating during step 1.5 to position the pattern in the anode arms as shown in the fig. III.27. Note that with samples etched with CPW electrodes, the conductivity may varies locally depending on the geometry. As a consequence, optimal doses are different from that with plain ITO coating; for sample with 340 nm, 140 nm and 50 nm ITO coating, the optimal dose respectively are 480  $\mu\text{C}/\text{cm}^2$ , 580  $\mu\text{C}/\text{cm}^2$  and 600  $\mu\text{C}/\text{cm}^2$ .

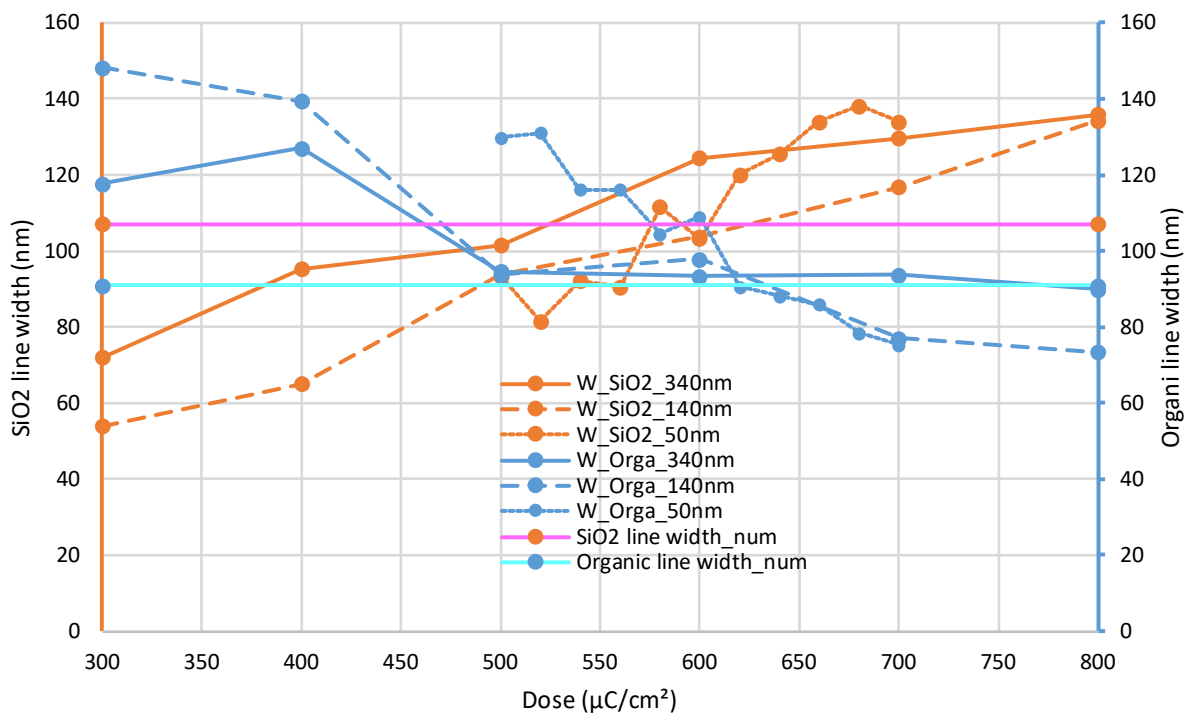


Figure III.23: Line width  $l_L$  and spacing  $l_H$  as a function of the dose of exposure: Orange curves and dots lines for correspond to the width  $l_L$  of the SiO<sub>2</sub> lines. B, blue curves and dots lines corresponds to the spacing  $l_H$ ; solid curves for 340nm thick of ITO coating, discontinued lines for 140nm thick of ITO coating, dash lines for correspond to with 50nm thick of ITO coating., Magenta line is the targeted value  $l_L$  (of SiO<sub>2</sub> line width) and cyan line is the targeted spacing  $l_H$ .

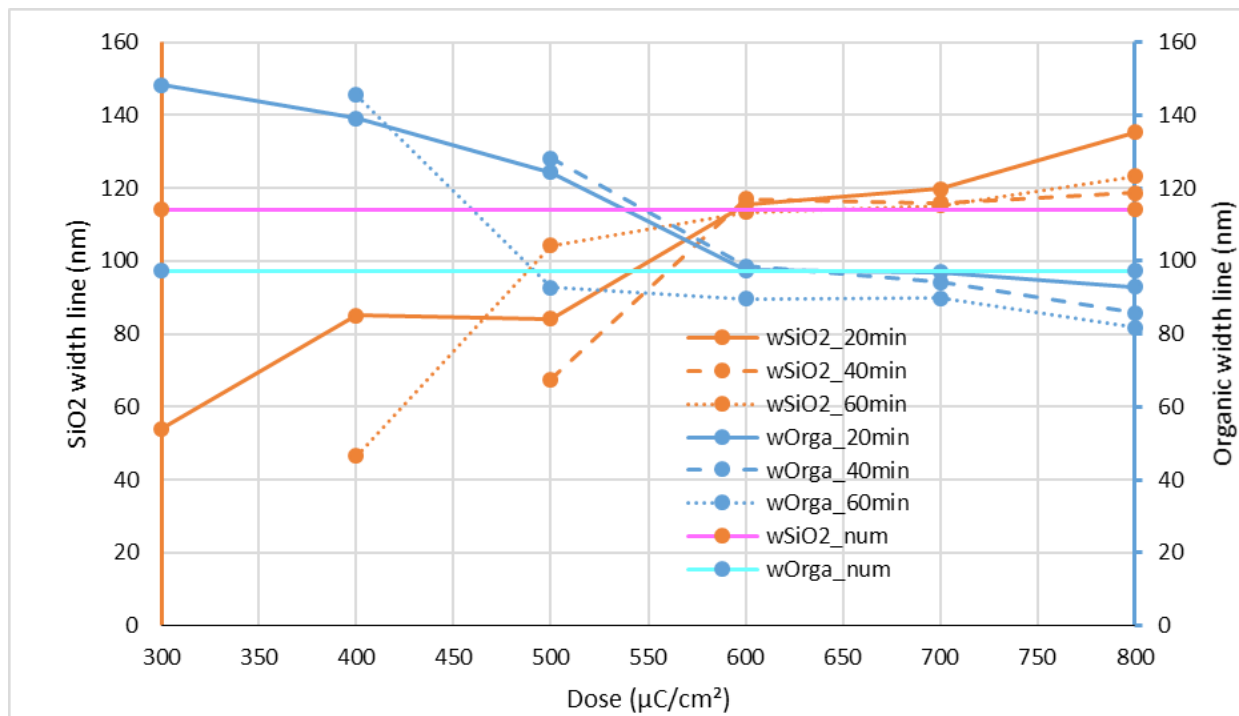


Figure III.24: Line width  $l_L$  and spacing  $l_H$  as a function of the dose for different development times: Orange curves for the width  $l_L$  of SiO<sub>2</sub> lines, blue lines for the spacing; solid line for 20minutes, discontinued lines 40minutes, dash lines for 60minutes, magenta line presents the targeted value  $l_L$  while cyan line corresponds to the targeted spacing  $l_H$ .

The table III.9 summarize the electron beam lithography parameters used for the fabrication of DFB  $\mu$ cavity in the center of the anode arms as step 2.8 and 2.9 in Fig. III.1.

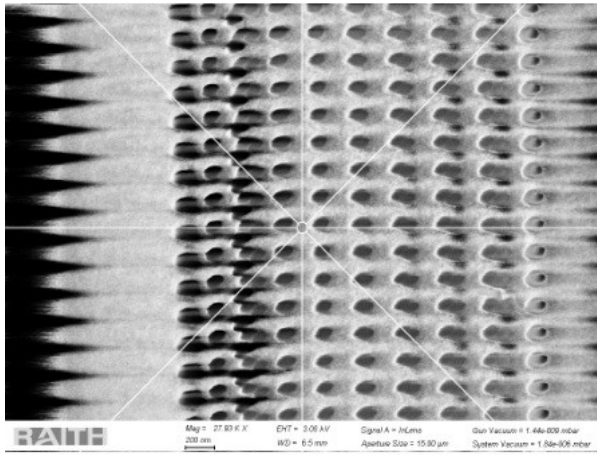
<b>Table III.9: Electron beam lithography parameters</b>	
<b>Area write field</b>	200 $\mu\text{m}$ x 200 $\mu\text{m}$
<b>Area step</b>	0.02 $\mu\text{m}$
<b>Acceleration voltage</b>	20 kV
<b>Diaphragm diameter</b>	15 $\mu\text{m}$
<b>Working distance</b>	6.5 mm
<b>Pitch current</b>	Between 60 and 80 pA
<b>Dose</b>	480 $\mu\text{C}/\text{cm}^2$ for 50 nm of ITO 580 $\mu\text{C}/\text{cm}^2$ for 140 nm of ITO 600 $\mu\text{C}/\text{cm}^2$ for 340 nm of ITO
<b>Developer</b>	MFCD26:H <sub>2</sub> O +NaCl (1:1, 4% of NaCl)
<b>Time development</b>	40 minutes

### III.5.2 Preliminary observation and validation

After fabrication, the patterns are observed and checked with different types of microscope (Step 2.10 in Fig. III.1. We also investigate the response of the  $\mu$ -cavity when illuminated with a laser beam.

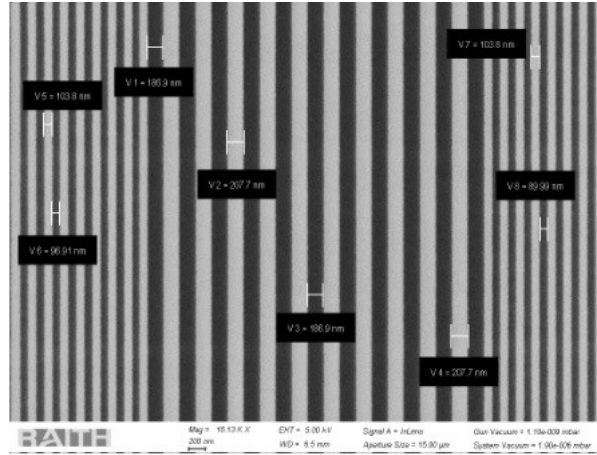
#### III.5.2.1 Structure observation

To verify the position and the dimension of the structure we use an optical microscope Leica DM8000 (Fig III.27) and a scanning electron microscope as presented in fig.III.28.a. To verify that the spacing are clean and free from resist an atomic force microscope in contact mode is used to analyze the conductivity of the surface. Figure.III.28.b presents the AFM observation and the first and the second orders of the DFB cavity can clearly be distinguished. Finally with a digital microscope (Keyence), we observed the diffraction of the DFB when illuminated with a 632nm red laser(Fig.III.30). It is observed that the second order section of the grating couples the light out in the perpendicular direction of the  $\mu$ -cavity plan whereas the first order barely does.



0.2

Figure III.25: Area step test



0.02

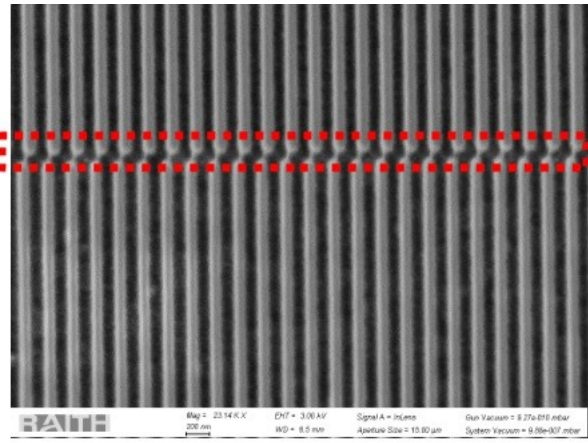
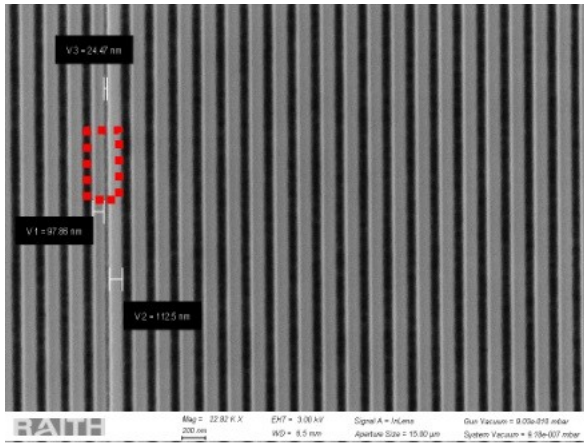


Figure III.26: Stitching step

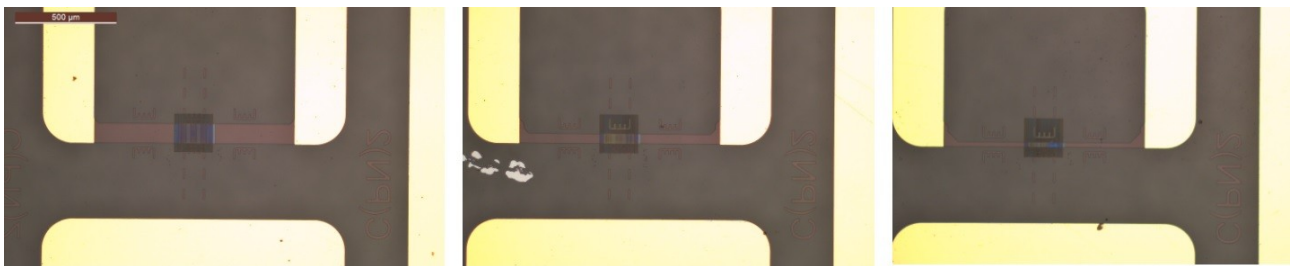


Figure III.27: Optical microscope characterization of a definitive sample



### III.5.2.2 Indication of second order diffraction

To check for the effective coupling out of the plan of the second order grating, we fabricate on a glass sample covered with a 140 nm ITO coating partially etched down to 50 nm, a pattern made of 17 sections: First (Section1) and last sections (Section17) are a 50 periods of second  $\Lambda_2$  order gratings with line width of  $2l_L=208$  nm and a spacing of  $2l_H=214$  nm. Second section (Section 2) is made of 50 periods  $\Lambda_1$  first order grating with line width of  $l_L=104$  nm and a spacing of  $l_H=107$  nm. Third section (S3) is made of 11 periods of a second order grating with  $2l_L=208$  nm and  $2l_H=214$  nm. Fourth section (Section 4) is identical to second section. Section2, S3 and Section 4 constitute an intermediate pattern repeated 5 times (up to Section 16). The longitudinal section of the multi-section pattern is shown Fig III.29.III.29. The corresponding resonance wavelength is 629 nm close to the emission wavelength of a red diode laser at 632 nm injected from the right side in the glass substrate. A top view of the sample under ambient illumination and without laser injection is shown in Fig III.30. left where the 25  $\mu\text{m}$  width ITO horizontal stripe exhibits two colors; on the left part, the 50nm thick stripe is light purple-blue, whereas on the right part the 140 nm thick ITO stripe is dark-rose. The 200  $\mu\text{m}\times 200 \mu\text{m}$  pattern overlaps the stripe and on each ends the second order sections (Section 1 and Sections 17) appears slightly darker as well as the narrow second order sections (S3, S6, S9, S12, S15). Figure III.30 right shows the same pattern in the dark with 632nm laser light inject from the right side. The light intensity decrease from right to left, with high light corresponding to second order grating sections. The second order sections both the large (S1, S17) and narrow sections (S3, S6, S9, S12, S15) clearly diffract light contrary to first order sections (Section 2, 4, 5, 7, 8, 10, 11, 13, 14, 16). The 25  $\mu\text{m}$  width horizontal stripe is visible on the right side where the thickness is 140 nm as a consequence of more guide modes than in the 50 nm thick ITO stripe. This is a preliminary indications that second order grating effectively couple light out of the plan of the grating.

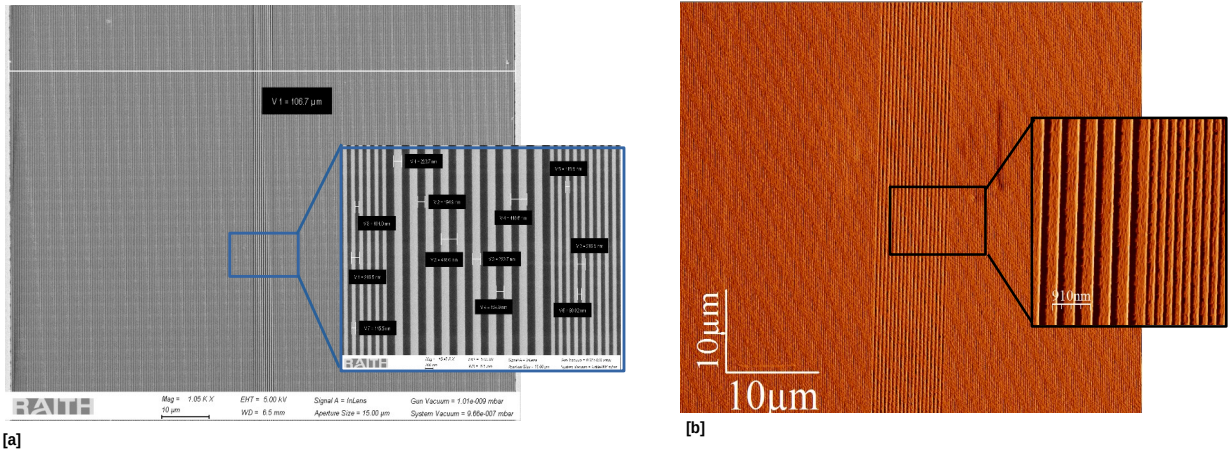


Figure III.28: Micro-cavity structure; [a] SEM and [b] AFM images of a DFB grating

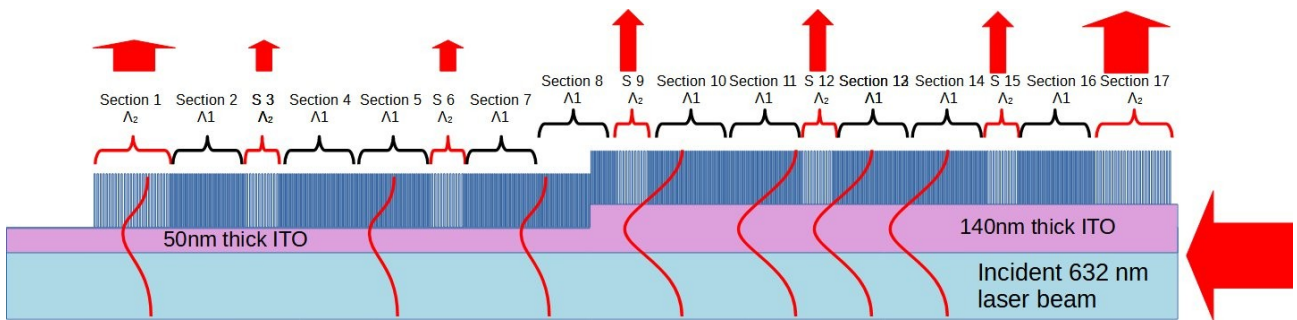


Figure III.29: longitudinal section of the multisection pattern with first order and second order grating. 632 laser light is injected in the glass from the right side

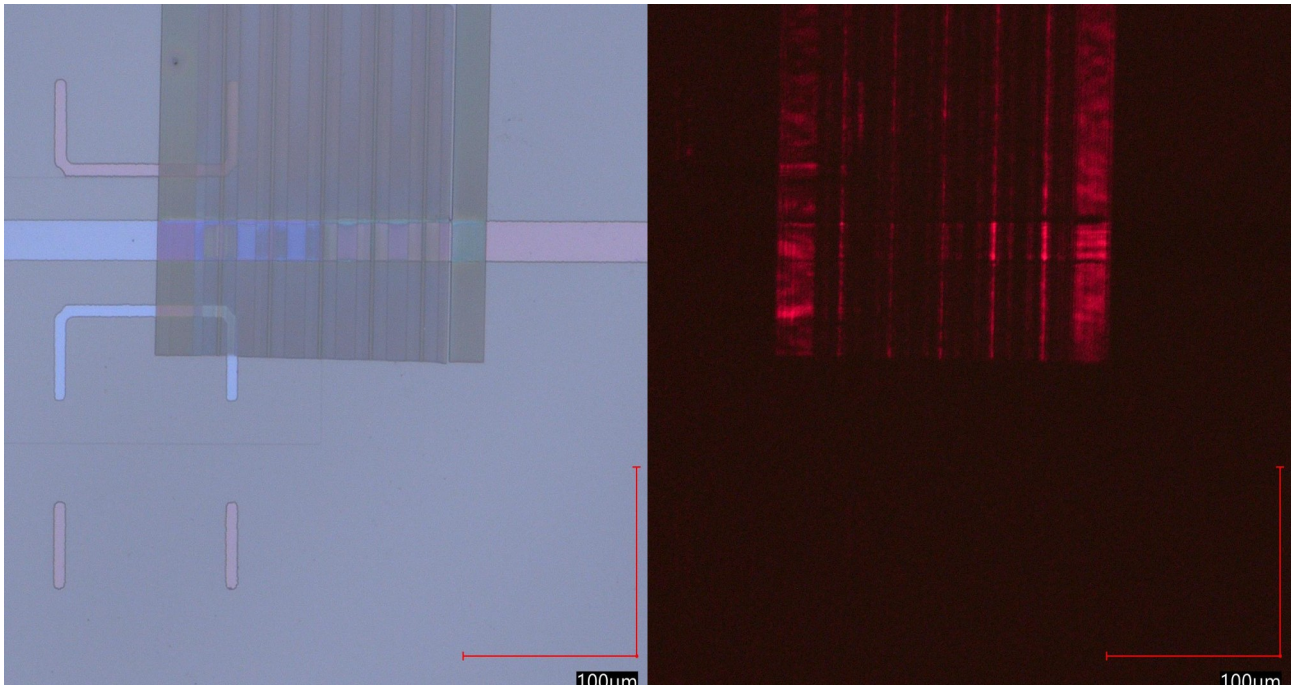


Figure III.30: Digital microscope observation of a multisection first order and second order pattern: left: with ambient lighting and without laser illumination, light purple stripe is ITO arm thinned down to 50nm, rose is unthinned 140nm ITO arm, right: with red 632nm laser injection in the glass substrate, coupled to the ITO and guided in the ITO stripe and diffracted by the second order grating section.

## III.6. Organic hetero-structure deposition

The OLED deposition is performed through sub-process 3 consisting in 6 steps

### III.6.1 Small-molecule organic stack

The organic heterostructures and their energy levels used in this work are presented in Fig.III.31 and III.32. This is a reference structure already been used in several previous works [7]. After cleaning of the samples (Step 3.1 of Fig. III.1) they are placed in a vacuum chamber and aligned with the organic hollow-mask aligned (Mask 3) (Step 3.2) before the organic layers are deposited (Step 3.3) On top of ITO anode, a layer made with 35 nm of m-MTDATA (4,4',4'' Tris[phenyl(m-tolyl)amino]triphenylamine) is used as Hole Injection Layer (HIL). With a HOMO level of 5.1eV it stands slightly below the ITO work function (4.7eV). The second layer consists of 15 nm of NPD (N,N'-Di(1-naphthyl)-N,N'-diphenyl-(1,1'-biphenyl)-4,4'-diamine) and plays the role of Hole Transporting layer (HTL) with a significant mobility holes and with an intermediate HOMO level between that of the HIL and that of the emitting layer. The emitting layer (EL) is 30 nm thick and uses a guest-host system. The host is Alq3 (Tris-(8-hydroxyquinoline)aluminum) and the guest molecule is a red organic dye (DCM, DCM2 or DCJTb see Table III.11 for definition) with a concentration of 2% of that of the host molecule obtained by co-evaporation. To enforce recombination to occur in the EL despite hole mobility larger than that of electrons a Hole Blocking Layer (HBL) is introduced between the EL and the cathode. We use 5 nm of TPBI (2,2',2''-(1,3,5-Benzinetriyl)-tris(1-phenyl-1-H-benzimidazole) or BCP (2,9-Dimethyl-4,7-diphenyl-1,10-phenanthroline, BCP) as a HBL. It exhibits a very large HOMO level preventing holes to travel through the cathode. A 25 nm thick Electron Transporting Layer uses Alq3 with a limited energy difference with the work function of the aluminium cathode. To reduce the energy barrier between the EIL and the cathode so as to reduce the threshold voltage in the I-V characteristic, a thin layer of LiF (Lithium fluoride) is introduced.

### III.6.2 Vacuum evaporation

The organic layers and the aluminum cathode are deposited by a thermal vacuum evaporation. The vacuum evaporation is a type of physical vapor deposition of thin films onto surfaces. The principle consists of heating by means of resistances system, the evaporating materials placed on crucible to produce a flux of vapor which be deposited onto a surface. This act happens in a vacuum chamber where the pressure is order of  $10^{-7}$  torr. When the sublimation temperature is reached and the evaporation rate stabilizes at the desired value, the cover above the crucible is opened and the heated material is deposited. Two different hollow masks are used, an organic mask (Mask 3) dedicated to the organic materials and another hollow mask (Mask 4) through which the aluminum

cathode is evaporated. It requires a critical manual alignment performed outside the vacuum chamber in the glove box (Step 3.4 in Fig. III.1) The alignment is very critical because the aluminum stripe defining the dimension of active region have to be aligned in the middle of the horizontal ITO arm and have to overlap the  $\mu$ -cavity pattern. we. The aluminum thickness is thicker than in conventional OLED to avoid the risk of electrical discontinuity at the edge of the 50 nm (or 140 nm) thick ITO horizontal arm (Step 3.5 in Fig. III.1) \*The deposited layers is controlled in-situ by a quartz piezoelectric micro-balance located near the sample.

### III.6.3 macro-molecule stack

On one occasion we will investigate a polymer OLED fabricated by spin coating and based on macromolecules (fig.III.32). The PEDOT:PSS (Poly(3,4-ethylenedioxythiophene) polystyrene sulfonate) layer is deposited at 3000 rpm for 60 second and then baked for 10 minute at 120°C. The emitting layer F8:F8BT (20:1) (Poly(9,9-di-n-octylfluorenyl-2,7-diyl : Poly(9,9-dioctylfluorene-alt-benzothiadiazole) is spincoated at 2000 rpm for 60 seconds and baked at 80°C for 10min. Like for small molecule, The aluminum cathode is evaporated under vacuum.

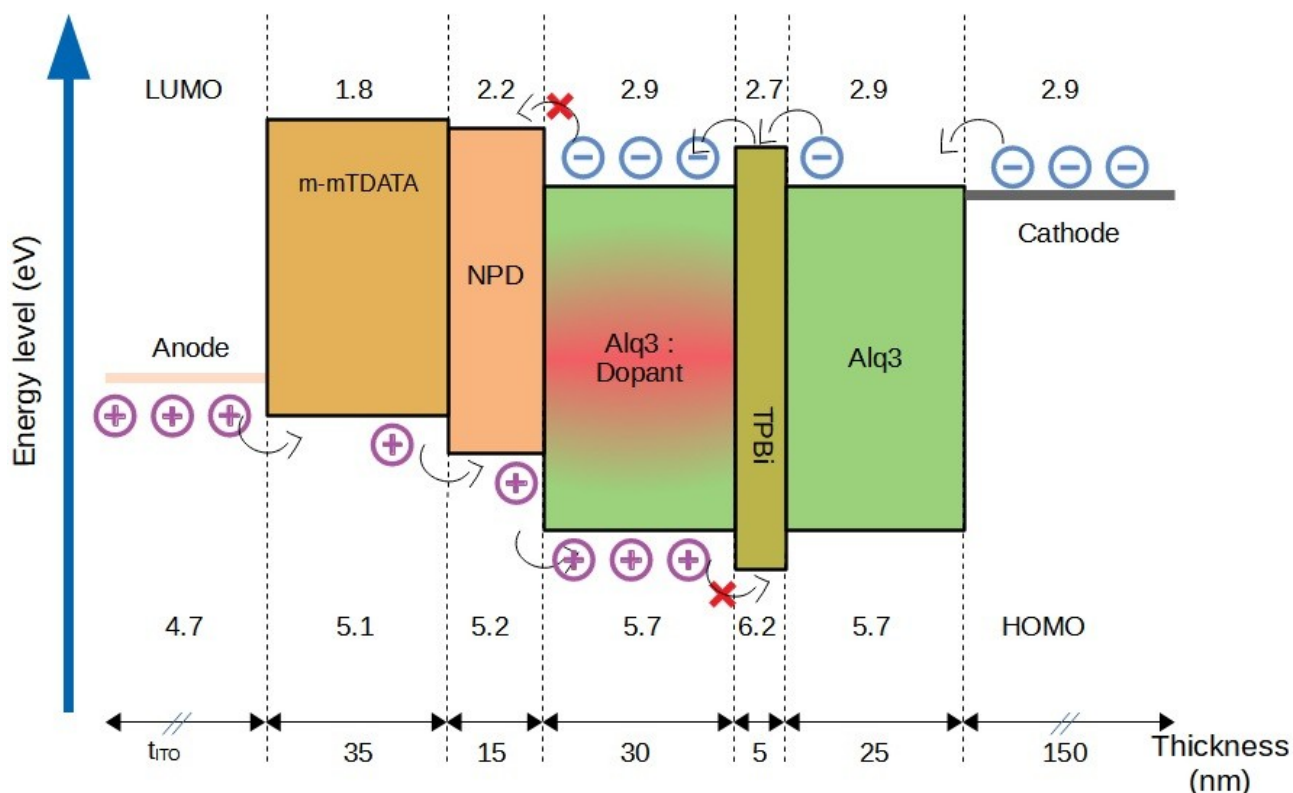


Figure III.31: OLED stack based on small molecule

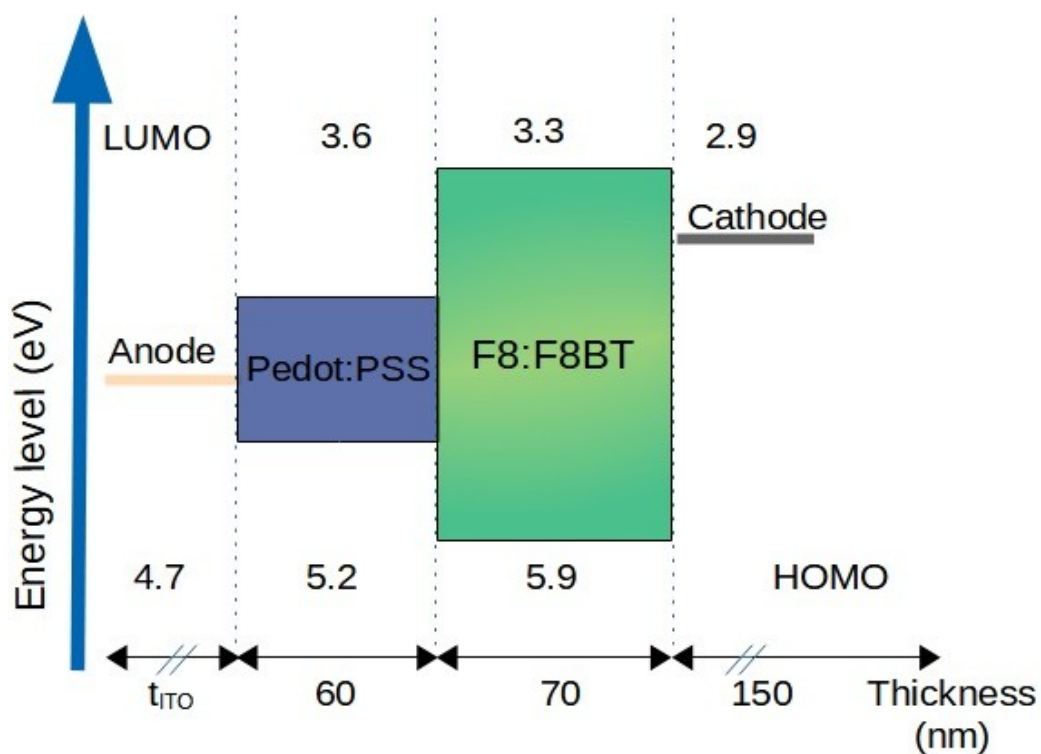


Figure III.32: OLED stack based on polymer molecule

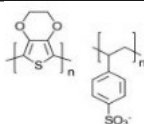
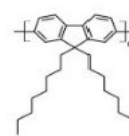
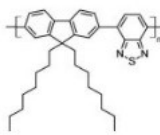
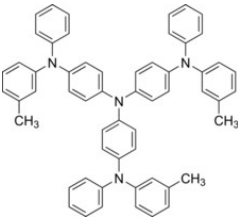
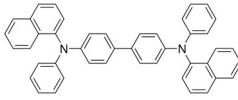
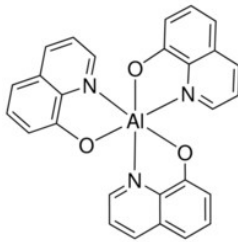
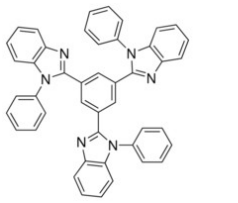
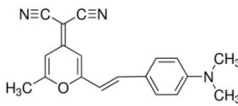
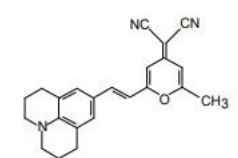
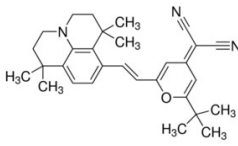
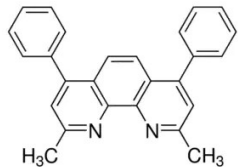
Full name	Synonym	Chemical structure	HOMO LUMO	Application
Poly(3,4-ethylenedioxythiophene) polystyrene sulfonate	PEDOT:PSS		-5.2 -3.6	HIL
Poly(9,9-di-n-octylfluorenyl-2,7-diyl)	F8			Host
Poly(9,9-dioctylfluorene-alt-benzothiadiazole)	F8BT		-5.9 eV -3.3eV	Guest



Table III.11: Small molecule [7]

Full name	Synonym	Chemical structure	HOMO LUMO	Application
4,4',4'' Tris[phenyl(m-tolyl)amino]triphenylamine	m-MTDATA		-5.1 eV -1.8 eV	HIL
N,N'-Di(1-naphthyl)-N,N'-diphenyl-(1,1'-biphenyl)-4,4'-diamine	NPD NPB		-5.2 eV -2.7 eV	HTL
Tris-(8-hydroxyquinoline)aluminum	Alq3		-5.7 eV -3.3 eV	EL (Host) EIL
2,2',2''-(1,3,5-Benzinetriyl)-tris(1-phenyl-1-H-benzimidazole)	TPBi		-6.2 eV -2.7 eV	ETL HBL
4-(Dicyanomethylene)-2-methyl-6-(4-dimethylaminostyryl)-4H-pyran	DCM			EL (Guest)
[2-methyl-6-[2-(2,3,6,7-tetrahydro-1H,5H-benzo[ij]quinolizin-9-yl) ethenyl]-4Hpyran-4-ylidene] propane-dinitrile	DCM2			EL (Guest)
4-(dicyanomethylene)-2-tert-butyl-6-(1,1,7,7-tetramethyljulolidin-4-yl-vinyl)-4H-pyran	DCJTb			EL (Guest)
2,9-Dimethyl-4,7-diphenyl-1,10-phenanthroline	BCP Bathocurproi ne			

### III.7. Conclusion

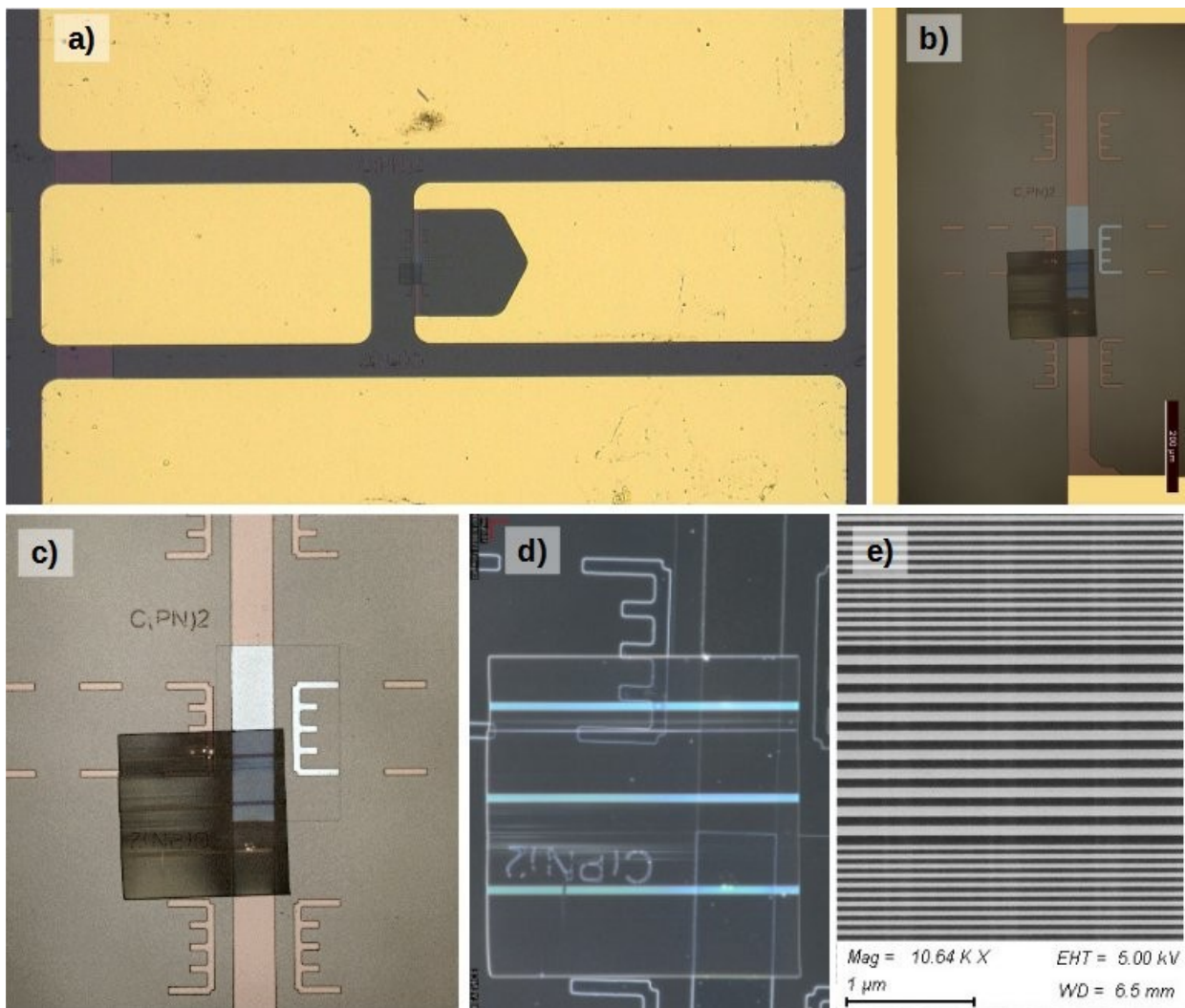
On the basis of an elaborated process consisting of 3 sub-process and 33 steps, we designed masks, and fabricated coplanar waveguided electrodes, on top of which we patterned  $\mu$ -cavities before OLEDs were deposited.

We fabricated coplanar waveguided electrodes by etching and gold-metalizing 140nm (or 340nm) thick ITO layer with 1500 $\mu$ m large central lines separated from ground planes by a gap  $G=316\mu$ m resulting in 50 $\Omega$  characteristic impedance (Fig.III.33.a). With built-in measurement resistances  $R_m \sim 5\Omega$  ( $\sim 2.5\Omega$  for 340nm thick ITO), with serial resistance  $R_s \sim 43\Omega$ ,  $\sim 61\Omega$ , and  $\sim 105\Omega$ , (20 $\Omega$ , 28 $\Omega$ , 34 $\Omega$  for 340nm ITO) and parasitic capacitance of 3pF, 0.7pF, and 0.2pF for respectively 100X100 $\mu$ m<sup>2</sup>, 50X50 $\mu$ m<sup>2</sup>, 25x30 $\mu$ m<sup>2</sup> OLED active areas, according to Eq.2.1.4 in chapter 2, the resulting electrical time constants are estimated about 144ps, 46ps, and 22ps (67ps, 21ps, 7ps for 340nm ITO) much below 1ns. These are a first indications that we have fabricated high-speed OLED electrodes with electrical times constants potentially better than the state of the art [8].

Intermediate ends of the CPW electrodes are terminated with unmetalized 100 $\mu$ m, 50 $\mu$ m, or 25 $\mu$ m large and 800 $\mu$ m long ITO arms in the middle of which  $\mu$ -cavities are implemented as illustrated in Fig. III.33.b. A 250 $\mu$ m long section of the arm located in the middle of the arms thinned down to 50nm in thickness is intended to improve the confinement factor, and to maximize the index contrast. It appears as light-blue rectangle whereas the unthinned ITO arm is brownish-rose. The implemented  $\mu$ -cavities appear as dark square overlapping the thinned and un-thinned sections as shown in Fig. III.33.c. The exact positioning of the  $\mu$ -cavities in the center of the thinned section is challenging to obtained and only some samples get it correctly positioned. The  $\mu$ -cavity pattern fabricated by e-beam lithography in hydrogen silsesquioxane (HSQ) electro-sensitive resist consist of a first-order grating interrupted three times with three second-order gratings. Best visible under dark-field observation, the second-order gratings diffract light in the direction perpendicular to the plan as shown with blue light in Fig. III.33.d. For a cavity resonance of  $\lambda=605$ nm, the 300nm thick HSQ first-order gratings are made with  $\Lambda_1=101$ nm wide quarter-wavelength lines spaced from each other with  $\Lambda_{1s}=99$ nm wide quarter-wavelength spacing while second-order grating are with  $\Lambda_2=202$ nm and  $\Lambda_{2d}=198$ nm. Figure III.33.e shows the quarter-wavelength mirrors interrupted with 21 half-wavelength defects made of second order lines and spacings observed with a scanning electron microscope. For a resonance at 632nm the first-order gratings are made with  $\Lambda_1=107$ nm wide quarter-wavelength lines spaced from each other with  $\Lambda_{1s}=104$ nm wide quarter-wavelength spacing. The resolution of EBL in the nanometer scale, and most of all the indirect access on the

effective index via the calculation induce a relatively large uncertainty on the resonance which is key for optimizing the laser threshold.

OLED deposition on top of the electrodes with the  $\mu$ -cavities is accomplished with fluorescent organic materials and red emitters (DCM, DCM2, or DCJTB) in a guest-host configuration with Alq3 as a host. The organic heterostructure is deposited through a hollow mask (Mask 3) before the metalization mask (Mask 4) is aligned manually in glove box with an accuracy better than  $50\mu\text{m}$  using special alignment tools and markers developed specifically. Under this condition  $100\mu\text{m}$ ,  $50\mu\text{m}$ , and  $30\mu\text{m}$  wide aluminum cathodes are deposited in the middle of the  $250\mu\text{m}$  long thinned ITO section and overlaps the  $200\mu\text{m}\times 200\mu\text{m}$   $\mu$ -cavity pattern with an accuracy better than  $25\mu\text{m}$ . According to the preliminary observation and measurements, the fabricated devices seem to match the objectives and we can proceed to the advanced characterizations in particular with time-resolved electrical, optical, and spectral measurements.





## References

- [1] CHIME Alex Chamberlain, “Etude théorique et expérimentale de micro-OLEDs rapides sur électrodes coplanaires en régime d'impulsions à haute densité de courant”, Thesis from Université Paris 13, Decembre 2017
- [2] R. Fang, W. J. Jiang, X. Guo, J. R. Han, and G. D. Shen, “A study on the Cl<sub>2</sub>/C<sub>2</sub>H<sub>4</sub>/Ar plasma etching of ITO using inductively coupled plasma,” in 2009 Asia Communications and Photonics conference and Exhibition (ACP), Nov. 2009, vol. 2009-Supplement, pp. 1–7.
- [3] Kenji Odagawa, Noriyuki Yanagawa, and Mitsuru Sadamoto, “High Performance Etching of ITO Films by Inductively Coupled Plasma using HI.,” Jan. 16, 2013.  
[http://www2.iee.or.jp/ver2/honbu/14-magazine/log/2003/2003\\_02a\\_11.pdf](http://www2.iee.or.jp/ver2/honbu/14-magazine/log/2003/2003_02a_11.pdf)
- [4] Y. Chen, “Nanofabrication by electron beam lithography and its applications: A review,” *Microelectronic Engineering*, vol. 135, pp. 57–72, Mar. 2015, doi: [10.1016/j.mee.2015.02.042](https://doi.org/10.1016/j.mee.2015.02.042).
- [5] H. Namatsu, T. Yamaguchi, M. Nagase, K. Yamazaki, and K. Kurihara, “Nano-patterning of a hydrogen silsesquioxane resist with reduced linewidth fluctuations,” *Microelectronic Engineering*, vol. 41–42, pp. 331–334, Mar. 1998, doi: [10.1016/S0167-9317\(98\)00076-8](https://doi.org/10.1016/S0167-9317(98)00076-8).
- [6] Jeanne Solard, « Conception et réalisation de cavités à cristaux photoniques à base d'ITO pour des applications dans le domaine de la photonique organique » Thesis from Université Paris-Nord - Paris XIII, 2021. [tel-03561712](https://tel.archives-ouvertes.fr/tel-03561712)
- [7] Lei ZENG, “Étude théorique et expérimentale de  $\mu$ -OLED en régime impulsionnel à très haute densité de courant”, Thesis from the Université Paris 13, 2016
- [8] A. C. Chime, A. P. A. Fischer, S. Bensmida, J. Solard, M. Chakaroun, and H. Nkwawo, “Analysis of Optical and Electrical Responses of  $\mu$ -OLED With Metallized ITO Coplanar Waveguide Electrodes Submitted to Nanosecond Electrical Pulses,” *IEEE Trans. Electron Devices*, vol. 66, no. 5, pp. 2282–2289, May 2019, doi: [10.1109/TED.2019.2905839](https://doi.org/10.1109/TED.2019.2905839).

# **Chapter IV- Experimental results and analysis**

## **IV. Experimental results and analysis**

### **IV.1. Introduction**

This chapter is divided in 3 sections. The first section is dedicated to the description of the characterization benches used to study the different devices and to measure the different electrical, optical and spectral responses. In the second section, the experimental results and their analysis are presented. Finally section 3 is devoted to the conclusion and perspectives.

The first goal of the device characterizations consists in checking and confirming several electrical and optical properties both in the stationary state and in the pulse mode. Continuous and time-resolved measurements require different setup with different equipments.

- Continuous measurements are devoted to basic qualification. The goal is to verify the correct functioning of the device and to validate fabrication steps. For example, measuring the current and the light intensity as a function of the applied voltage eliminates any short-circuit or open circuit hypothesis. On the other hand, the spectral measurement is essential not only at the qualification step but also for the calibration of the optical bench and to measure the residual absorption. As a qualification step, the measurement resistance will be measured using a multi-meter.
- Time-resolved measurements includes the electrical, optical and spectral responses of the device as a function of the electrical excitation. In the nanosecond range, this require setup with equipment in the GHz regime.

A computer with Matlab, and LabView are used to automate operations. Note that all measurements are performed in ambient air.

### **IV.2. Characterization setup**

Two types of characterization setup are used for the DC regime and for the pulse regime. The figures IV.1 and IV.2 present the block diagrams of the different characterization setups. Their principles of implementation are described in the following paragraphs.

#### **IV.2.1. DC characterization setup**

The principle is to increase step by step a constant voltage applied to the OLED device and to measure the current passing through it as well as the resulting light intensity and spectrum. As shown in fig.IV.1, it is performed for relatively low excitation voltage (0-15V range), using a dedicated setup with a Keithley 2635A source-meter used both to apply a voltage to the OLED and to acquire the corresponding current value and a Newport 2935C optical power meter coupled to a Newport 918D-calibrated photodiode UV-OD3R is used to measure the light intensity for each step of the applied voltage. A computer is used to control the sourcemeter and the photometer and acquire the measured data in a LabVIEW environnement. To measure the spectrum in DC regime, a constant voltage is applied to the OLED and the light output is send to an optical spectrometer (model 2000 from Ocean Optics) connected to a computer for acquisition.

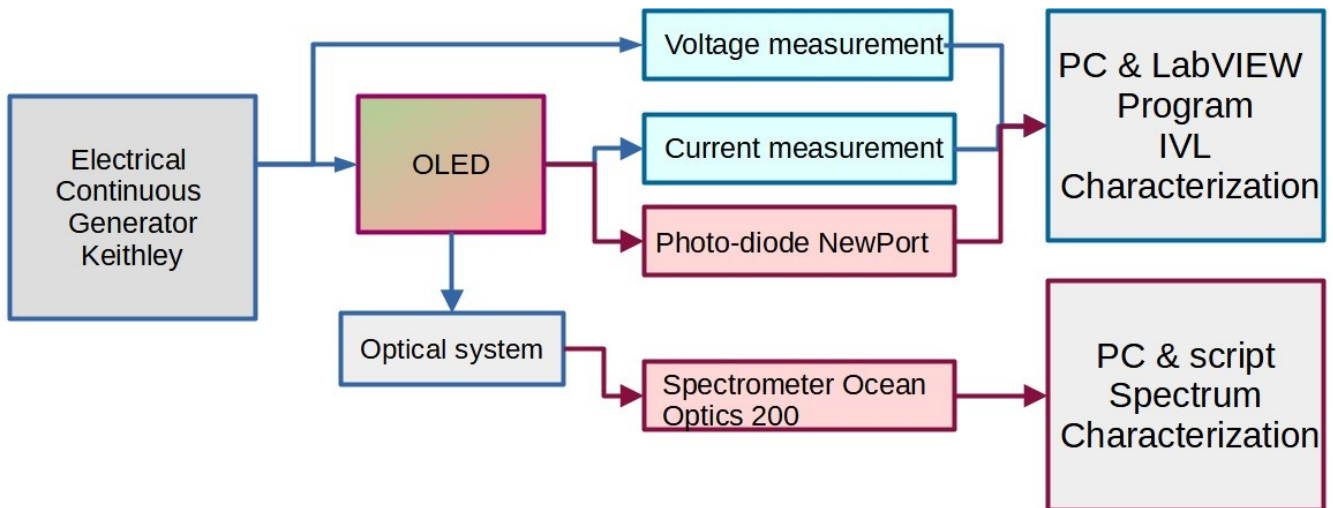


Figure IV.1: Block diagram of the DC characterization setup

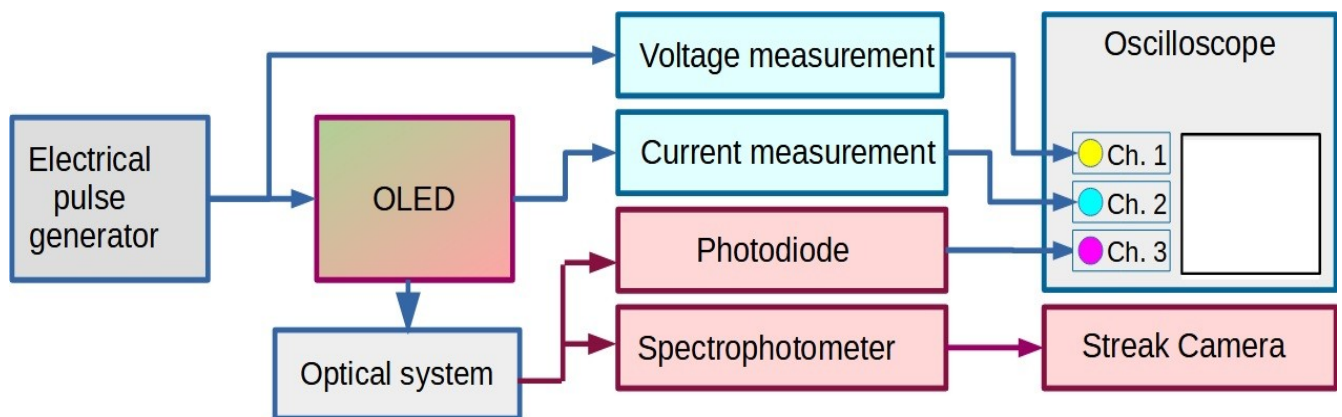


Figure IV.2: Block diagram of the time-resolved characterization setup

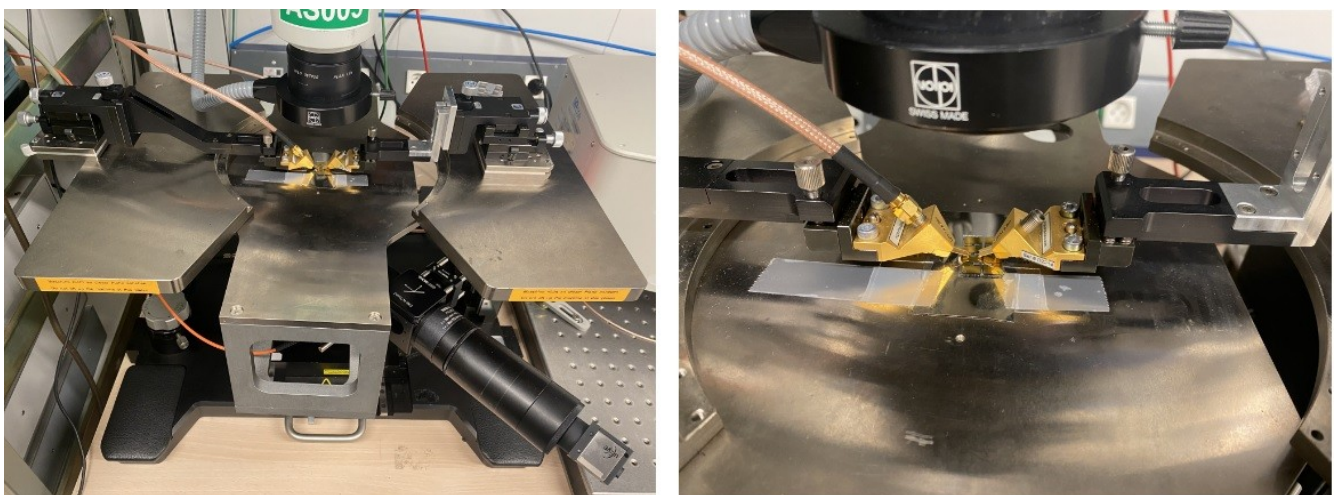


Figure IV.3: Manual optoelectronic probe station (Cascade PM5)

## IV.2.2. Time-resolved characterization setup

The characterization setup allowing simultaneous measurements of the electrical, optical and spectral responses under a high pulsed excitation, consists of three parts; a probe station, an electrical excitation part and optical measurement part.

### IV.2.2.1 Probe station

The OLED devices are positioned on a manual optoelectronic probe station (Cascade PM5) shown in fig.IV.3. The probe station allows sub-millimeter accurate positioning of the probes on the electrode sample with x-y-z translation stage. Two specific RF probes in a Ground-Signal-Ground (GSG) configuration with a 2000 $\mu\text{m}$  pitch are used both to deliver electrical excitation pulses and to measure the HS- $\mu\text{OLED}$  current. They are connected to a pulse driver and to a scope with semi rigid- RF cables with SMA connectors.

### IV.2.2.2 Pulsed electrical excitation

The pulsed electrical excitation is performed with high-voltage pulse drivers from AVTECH. Model 1 delivers pulses with duration tunable from 200ps to 2.5ns pulse with amplitude in the range [0 40V]. Model 2 delivers pulses in the range 2.5ns to 100ns with amplitude in the range 0-120V. With high-voltage impulse with a duration in the range of few 100ps to few ns and low repetition rate or even single shot, current density up to some tens of kilo-amperes per square centimeter can be targeted. Under a high pulsed excitation, it's necessary to characterize the electrical, optical and spectral responses simultaneously.

### IV.2.2.3 Optical setup

The challenge in the OLED light measurement is fivefold. Firstly, the OLED active area being micrometric the emitted light intensity is weak. Secondly, the OLED optical power being emitted in the half space the collection of a maximum of the OLED light emission is difficult. Thirdly the targeted pulse duration being in the nanosecond range, time resolved measurement is compulsory. Fourthly, the optical measurement is to be performed simultaneously with the electrical, and spectral measurements. Fifthly the optical setup is to be mounted in a very compact way because of limited space between the plateau of the probe station and its substrate holder. Eventually a camera is mounted on the setup to observe the effective active area of the OLED and its alignment.

The optical setup that fulfill these conditions is shown in fig.IV.4. The OLED source on a 700 $\mu\text{m}$  thick glass substrate is placed at a distance of 1mm ( $WD_{O_1}$ ) from the collection objective.

The light emitted by the source is collected by an infinity corrected objective from Nikon. It is a plan apochromatic 20x objective with numerical aperture  $NA_{O_1}=0.75$ , an effective focal length  $f_{O_1}=10\text{mm}$  and a working distance  $WD_{O_1}=1\text{mm}$ . The output beam of this objective is parallel and reflected by a mirror at 45° to a beam-splitter 50/50. The light is then splitted into two path; first path is for time-resolved optical signal measurement, and the second path is either for the time-resolved spectral measurement or for device active area measurement with a CCD camera, depending on the presence of a “magnetic” mirror. In the first case the light is focused on a 600 $\mu\text{m}$  diameter optical fiber (NA=0.25) through a second infinity corrected objective from Olympus. It is a plan achromatic x10 objective with a numerical aperture,  $NA_{O_2}=0.25$ , an effective focal length  $f_{O_2}=18\text{mm}$  and a working distance  $WD_{O_2}=10.6\text{mm}$ .

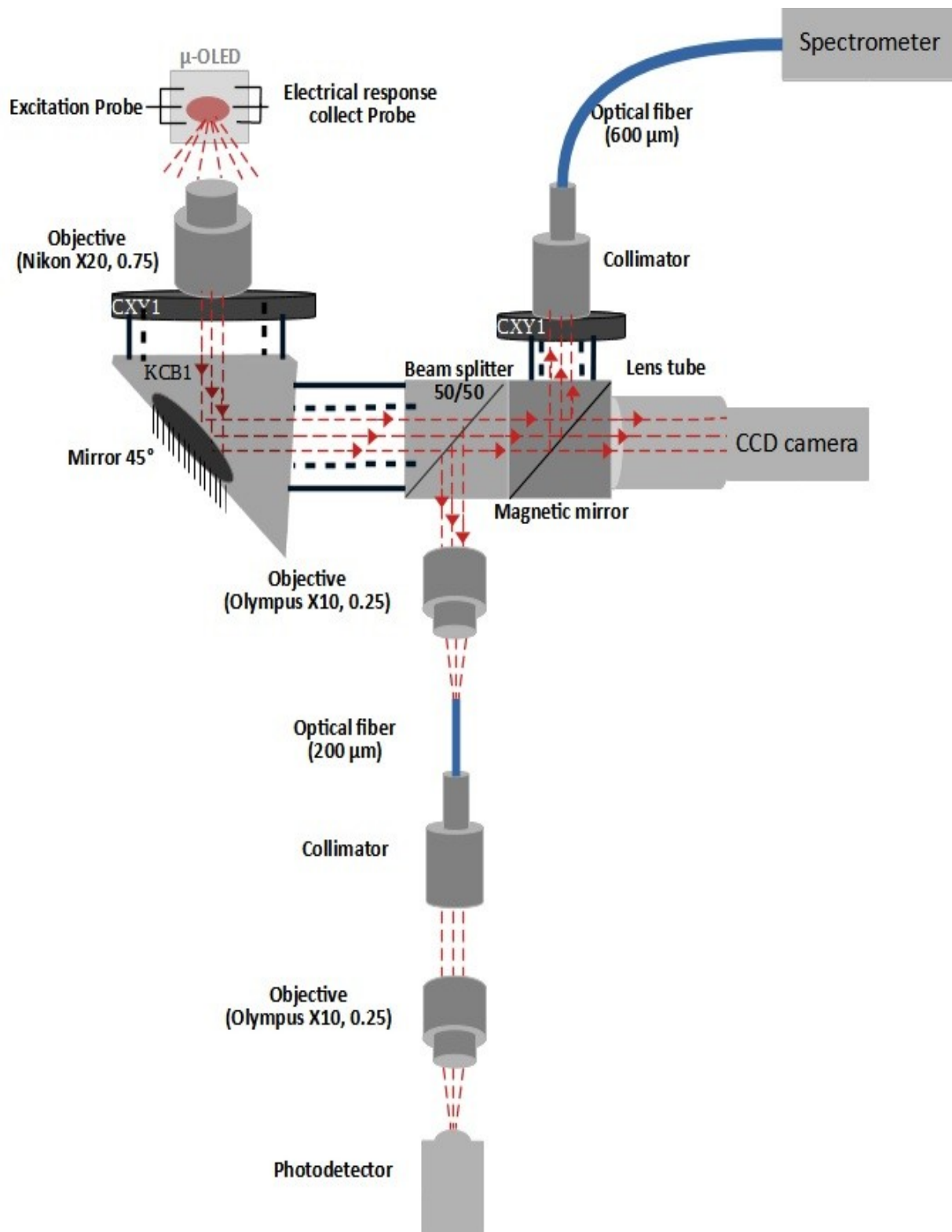


Figure IV.4: time-resolved optical characterization setup

The beam is then collected by a collimator. The output beam is focused on a large bandwidth photo-detector via a third Olympus x10 objective. The magnification factor of this path  $G_1=1.55$ . The second path is used when the magnetic mirror is present; then a collimator focus the light into a fiber which will be analyzed using a spectrometer. The image shows a magnification factor  $G_2=f_c/f_{o1}=3.541$  of the active area. When the “magnetic mirror” is removed, the light beam is sent to a CCD camera through a tube lens ( $f_t=200\text{ mm}$ ). Using the image saved with the CCD camera, the effective active area of the OLED is accurately estimated. The light collect system is mounted between the two plateaus of the probe station as presented in fig.IV.5.a). An avalanche photodiode with 400 MHz bandwidth (Thorlabs APD 430A2) used to measure the light intensity of the OLED under a pulse excitation (fig.IV.5.b). The photodiode circuit allows the conversion of the photon to an output voltage proportional to the illumination. This output voltage is sent to the digital oscilloscope (Tektronix TDS 6604). A computer is used to control the setup and acquire the measured data in a Matlab environment. To measure the time-resolved spectra of the device under an electrical pulse excitation, a spectrophotometer (Horiba Scientific IHR550) coupled to a streak camera (Optronis) is used as shown in fig.IV.5.c. This system is connected to a computer for measurements acquisition. The whole setup enables simultaneous measurements of the electrical injection current density, the emitted light intensity and its time-resolved spectrum of the device.

### IV.3. Measurements of OLED without cavity

This sections consists of the characterization of the OLED without optical cavity fabricated according to the process reported in chapter III. The organic hetero-structure consists of 35 nm of m-MTDATA (HIL), 15 nm of NPD (HTL), 30 nm of Alq3 doped with 2% of DCM as light emitting layer, 5 nm of TPBi (2,20,2"-(1,3,5-Benzinetriyl)-tris(1-phenyl-1-H benzimidazole) as HBL, 25 nm of Alq3 as electron transporting layer, and a final cathode layer of LiF (1 nm)/Al (120 nm). The serial resistances is measured by VNA  $R_{s2}=23\Omega$  and its measurement resistance is measured by a multimeter  $R_{meas}=2.9\Omega$ . IVL characteristics and optical spectrum under DC electrical excitation will be firstly presented then we will proceed with the time-resolved characterization.

#### IV.3.1. DC measurement (JVL) and spectral

This qualification characterization verify the OLED device characteristic to evaluate the quality of the fabrication. Electrically, the short-circuit and the open circuit can be detected by measuring the current density and the light intensity as a function of the excitation voltage. Figures IV.6.a and fig.IV.6.b present the typical JVL measurements of a micro-OLED. This characteristic confirms the correct operation of the device which behaves like a nominal diode. This OLED emits light once current appears for a voltage threshold around 4V. Optically, the spectral measurement is necessary to measure the residual absorption and to deduce the resonance wavelength using to determinate the dimension of the cavity. The spectrum shown in fig IV.6.c presents an emission in red wavelength centered at 600nm which is the spectrum of DCM.



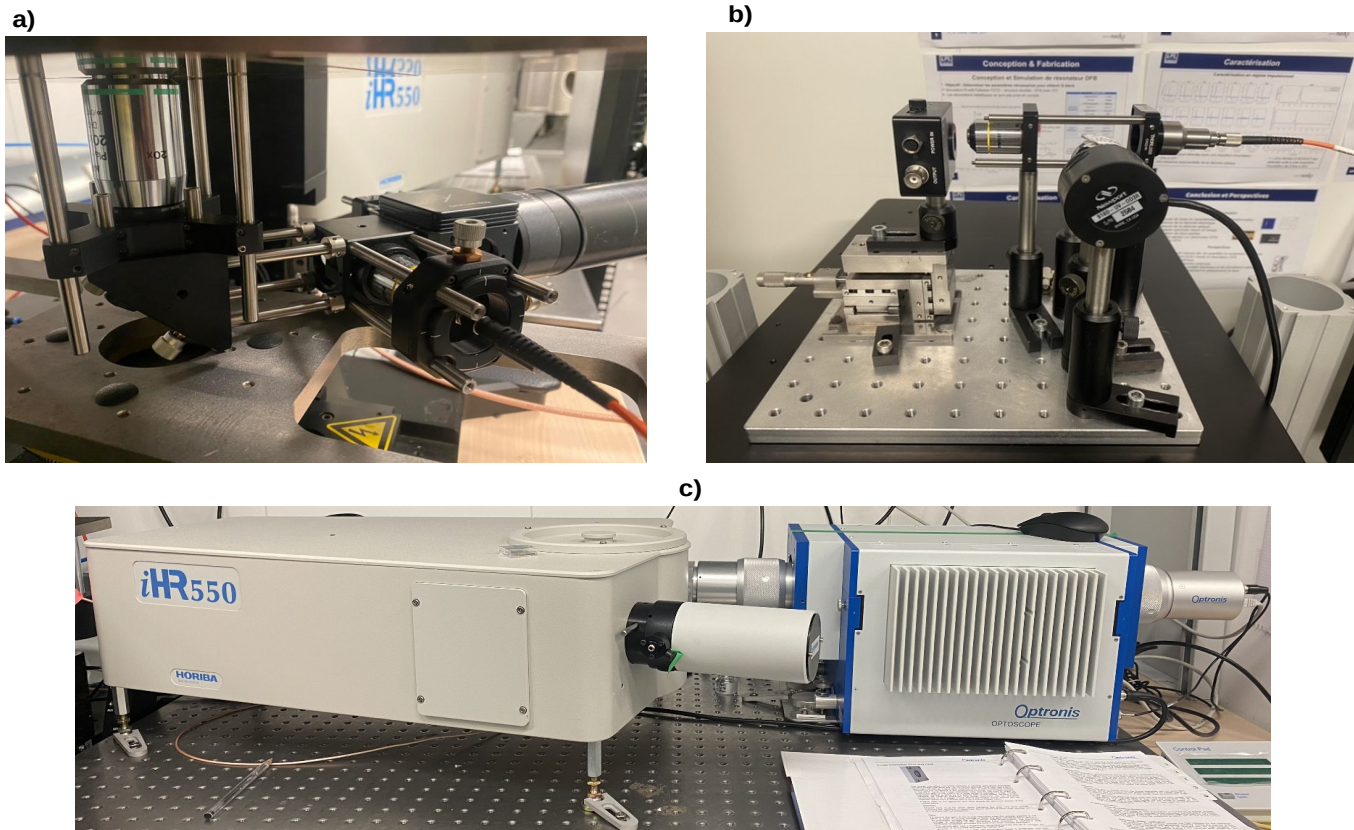


Figure IV.5: Time-resolved characterization setup: a): light collect system, b): light intensity measurement setup, c): spectrum measurement system

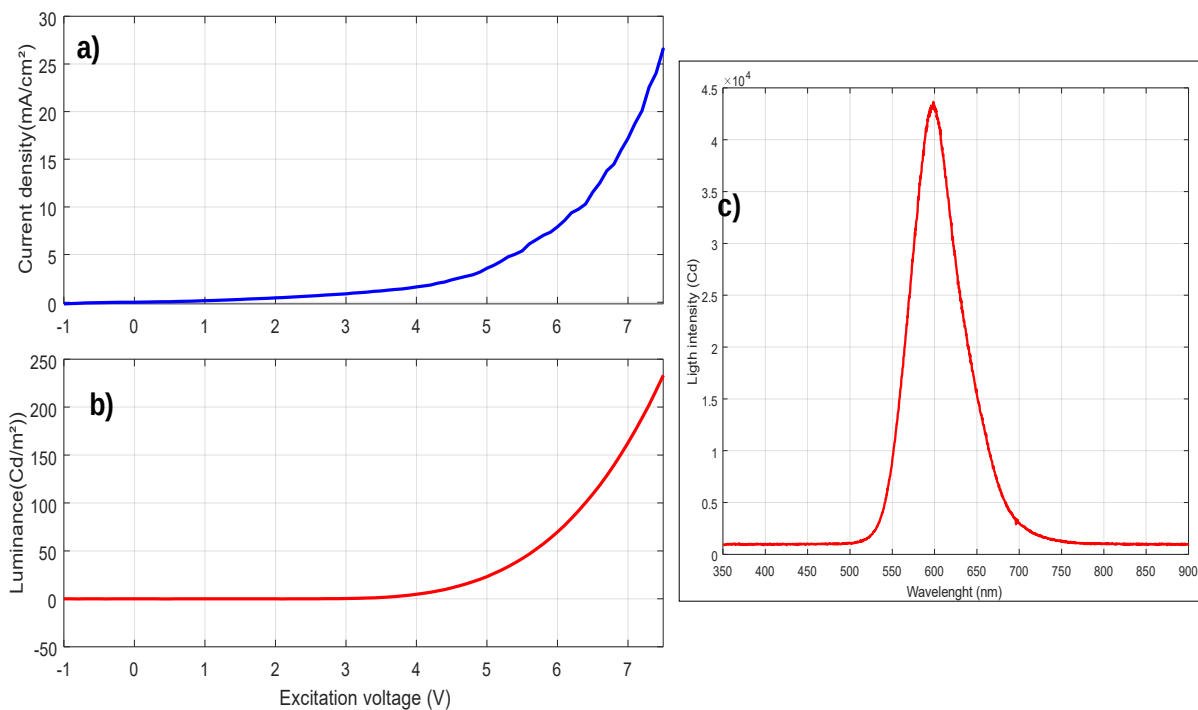


Figure IV.6: Characterization of OLED in continuous regime: a): Current density as a function of applied voltage, b) Light intensity as a function of applied voltage, c): Spectrum of OLED



### IV.3.2. Optical and Electrical pulsed measurements

The objective of this experiment is to identify the higher current density that can be measured to reach the laser threshold. OLEDs based on Alq3 dopant by DCM and fabricated according to the processes in chapter III are characterized under an electrical pulse excitation. Figures IV.7, figIV.8 and fig IV.9 present the measurement for OLEDs with  $100 \times 100 \mu\text{m}^2$ ,  $50 \times 100 \mu\text{m}^2$  and  $25 \times 100 \mu\text{m}^2$  as an active area respectively. These OLEDs are submitted to electrical pulses duration of 5ns (first column), 10.5ns (second column) and 20ns (third column). The nominal amplitude of the excitation varies between 30V to 69V. Each figure presents three arrows; the first one shows the excitation pulses applied to the OLEDs. The middle arrow presents the measurement of the current density as an electrical response and the third arrow displays the light intensity emitted by OLED as an optical response.

For the  $100 \times 100 \mu\text{m}^2$  device (fig IV.7), current densities follow the excitation pulses and it has a maximum values of  $4 \text{ kA/cm}^2$ ,  $4.8 \text{ kA/cm}^2$  and  $4.5 \text{ kA/cm}^2$  for an excitation pulses of 5ns, 10.5ns and 20ns of duration respectively. For the  $50 \times 100 \mu\text{m}^2$  OLED (fig IV.8), current densities of  $7 \text{ kA/cm}^2$ ,  $9 \text{ kA/cm}^2$  and  $9.5 \text{ kA/cm}^2$  are reached when the device is submitted to a 40V pulse voltage and 5ns, 10.5ns and 20ns pulse duration respectively. The optical responses follow the electrical one. For the  $25 \times 100 \mu\text{m}^2$  micro-OLED, the current density in the device under an electrical pulse excitation with 40V as a voltage amplitude and 5ns as a duration reaches the  $12.9 \text{ kA/cm}^2$ . For the same voltage and 10.5ns and 20ns as a pulse duration, the electrical response exceed  $15 \text{ kA/cm}^2$ . Increasing the voltage of the excitation pulse the current density increase to reach  $30 \text{ kA/cm}^2$ .

Note that, as motioned in chapter II section electrical modeling, when the active area decreases, the current densities increase.

The current density ranges giving by these experimental measurements are 4 to  $4.8 \text{ kA/cm}^2$  for the bigger micro-OLED and 12 to  $30 \text{ kA/cm}^2$  for the smallest micro-OLED. Theses values offer a large current density budget to achieve the laser threshold.

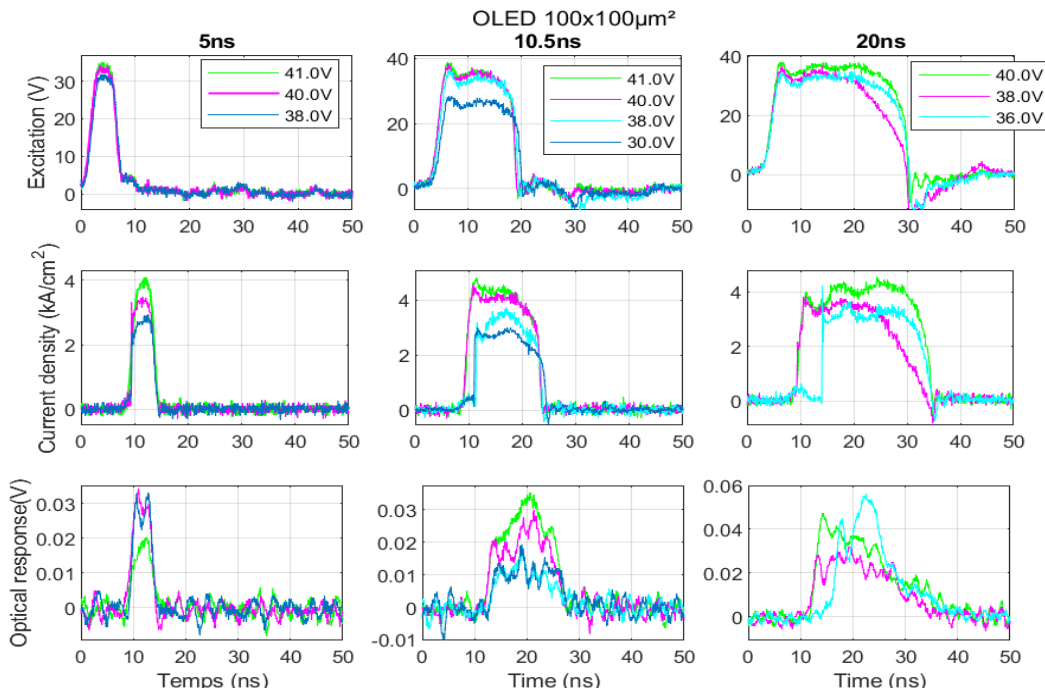


Figure IV.7: Time-resolved characterization of Alq3:DCM based  $100 \times 100 \mu\text{m}^2$  OLED

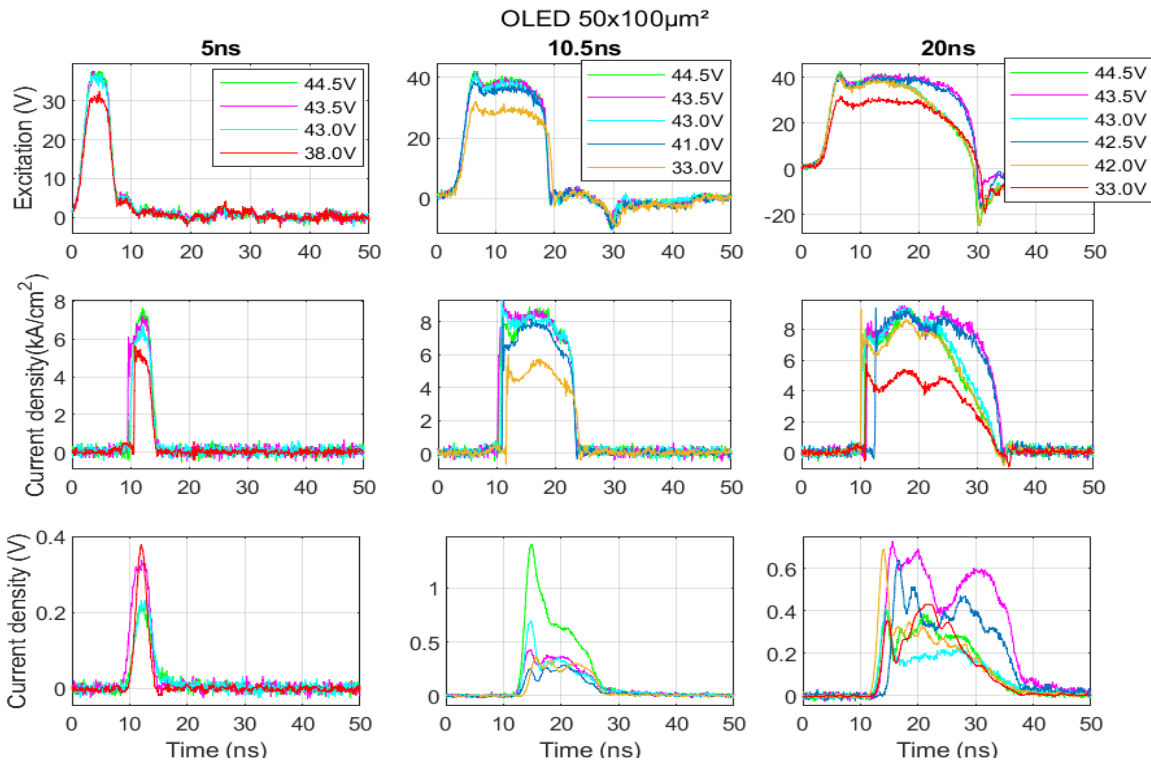


Figure IV.8: Time-resolved characterization of Alq3:DCM based  $50 \times 100 \mu\text{m}^2$  OLED

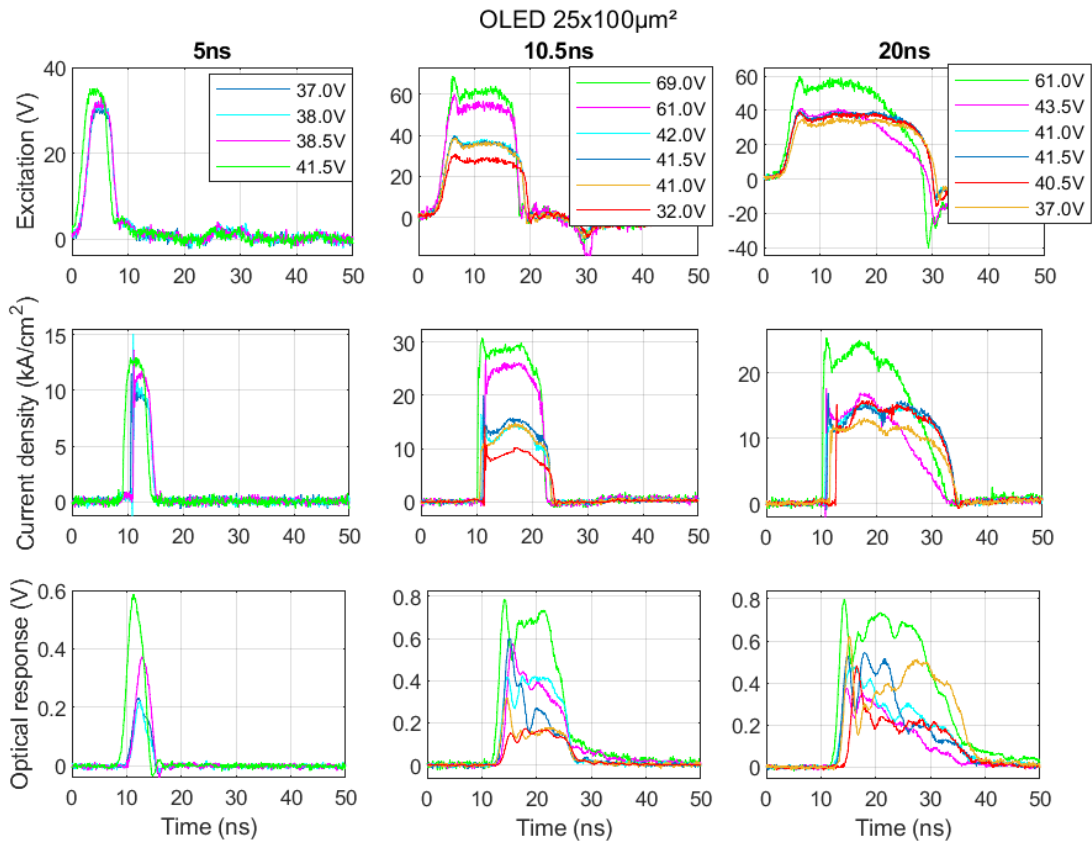


Figure IV.9: Time-resolved characterisation of  $25 \times 100 \mu\text{m}^2$  Alq3:DCM based OLED

### IV.3.2.1 Experimental Validation of the proposed laser model

The reliability and relevancy of the model is checked by confronting the dynamical response of the simulation with experimental results. More precisely, the objective is to compare the calculated dynamics of the photon density with the measured optical response of an OLED under similar pulsed electrical excitation.

The first considered high-speed organic hetero-structure (OLED1) has been deposited on a coplanar waveguide electrode etched on ITO coated glass substrate, similar to what was reported in [3], but with local gold metallization to reduce the serial resistances to  $R_{s1}=43\Omega$  and with a measurement resistance of  $R_{meas1}=13\Omega$  and a parasitic capacitance of  $C=4.2\text{ pF}$ . The resulting electrical time constant at  $V=0$  (Dynamical resistance is infinite) is  $\tau_{RC}=225\text{ ps}$  [1,2,3]. The organic hetero-structure of OLED 1 consists of 30 nm of m-MTDATA (4,40,4"-Tris (N-3-methylphenyl-Nphenyl-amino)triphenylamine) as hole injection layer (HIL), 10 nm thick NPD (N, N0-Di (1-naphthyl-N, N0-diphenyl-(1,10-biphenyl)-4,4'diamine) as hole transporting layer (HTL), 30 nm of Alq3 (tris(8-hydroxyquinoline)aluminum) doped with DCM ((E)-2-(2-(4-(dimethylamino)styryl)-6-methyl-4H-pyran-4-ylidene)malononitrile) as light emitting layer, 5 nm of BCP (2,9-Dimethyl-4,7-diphenyl-1,10-phenanthroline) as hole blocking layer (HBL), 25 nm of Alq3 as electron transporting layer, and a final cathode layer of LiF(1 nm)/Al (120 nm).

In a second sample (OLED 2), the organic hetero-structure consists of 35 nm of m-MTDATA (HIL), 15 nm of NPD (HTL), 30 nm of Alq3 doped with 2% of DCM as light emitting layer, 5 nm of TPBi (2,20,2"-(1,3,5-Benzinetriyl)-tris(1-phenyl-1-H benzimidazole) as HBL, 25 nm of Alq3 as electron transporting layer, and a final cathode layer of LiF (1 nm)/Al (120 nm). The serial resistances is reduced to  $R_{s2}=23\Omega$  and its built-in measurement resistance has been reduced from  $R_{meas1}=13\Omega$  to  $R_{meas2}=4\Omega$ . The active area has been reduced to  $S_2=50\mu\text{m}\times 100\mu\text{m}$  resulting in a reduction of the capacitance to  $1.3\text{ pF}$ . The resulting electrical time constants at  $0\text{ V}$  is  $\tau_{RC2}=35\text{ ps}$ .

#### IV.3.2.1.1 Comparison between calculated response and experimental results

A 20 ns, 45 V (respectively 43 V) pulses excitation voltage is applied to the OLED 1 (respectively OLED 2) and the electrical injection current is measured and recorded together with the emitted light intensity. The measured current is taken as the source term in the polaron rate equation (II.40). The photon density is then calculated from the set of equations (II.40)-(II.48) with the model parameters listed in table 1 except for those in table IV 1 which have been fine tuned for fitting purpose. The resulting calculated population densities are then plotted in fig IV.10 and fig IV.10, together with the measured optical response of the OLED for the sake of comparison.

Figure IV.10.a shows the effective current density (dark blue solid line) peaking at  $0.45\text{ kA/cm}^2$ , calculated according to a previously developed equivalent electrical model [3], and from which the polaron density is calculated according to Eq.(II.40) (Cyan dash curve). From the polaron population dynamics, the respective singlet and triplet host populations are calculated and plotted in fig.IV.11.b respectively with green solid line and dash lines. whereas the dopant singlet (magenta solid line) and triplet density (magenta dashes) are plotted in fig IV.10.c.

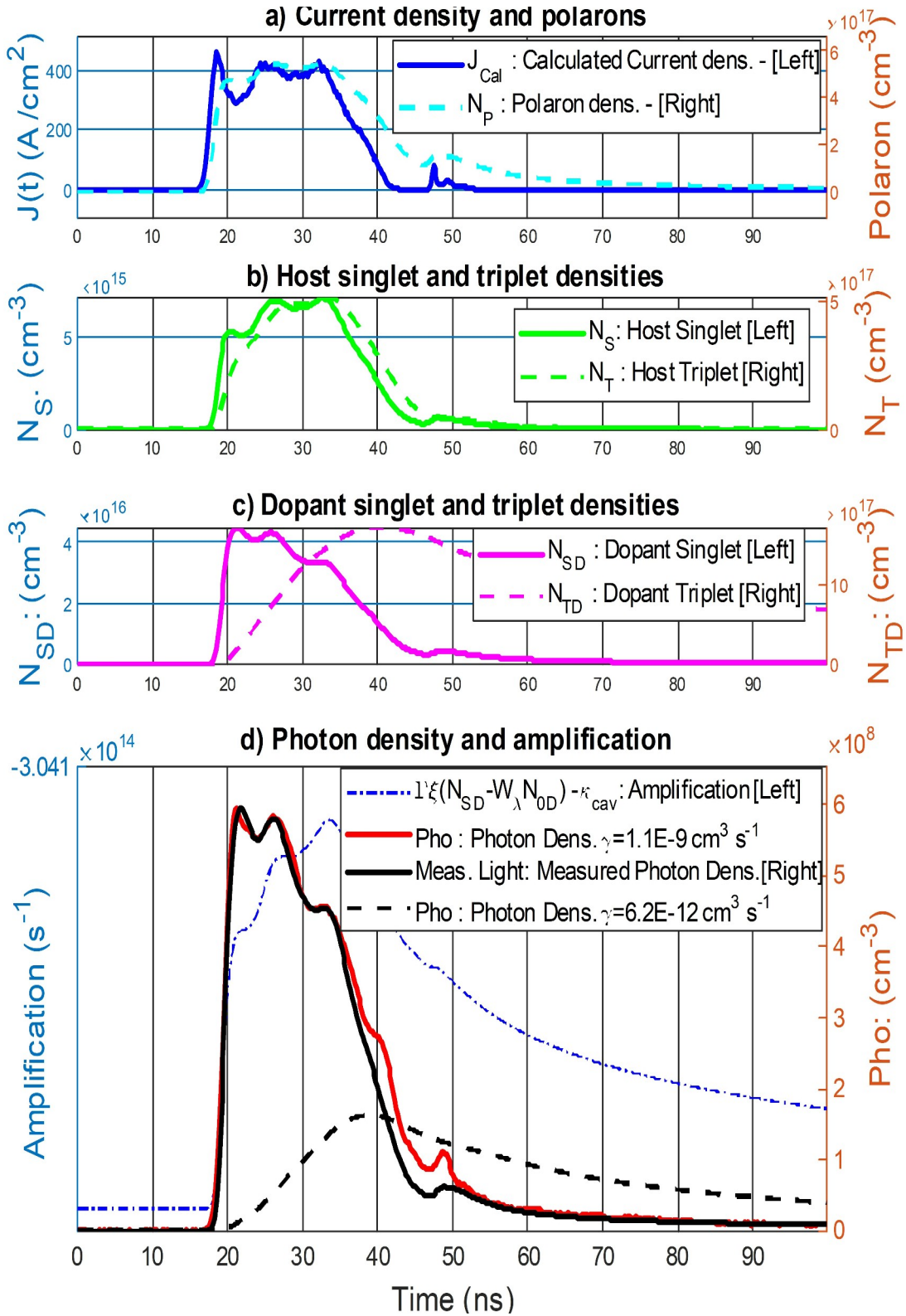


Figure IV.10: Comparison between measurements and simulation of the dynamical optical responses of a CPW OLED under a peak current density of 0.4kA/cm<sup>2</sup>. The parameters are fine tuned to  $g = 1.08 \times 10^{-9}$  cm<sup>3</sup> s<sup>-1</sup>,  $k_{sp} = 5.0 \times 10^{-10}$  cm<sup>3</sup> s<sup>-1</sup>,  $k_{st} = 62 \times 10^{-10}$  cm<sup>3</sup> s<sup>-1</sup>.

Table IV 1: Model parameters used to simulate experiment		
Symbol	OLED 1	OLED 2
$S$	$1.5 \times 10^{-4} \text{ cm}^2$	$0.5 \times 10^{-4} \text{ cm}^2$
$d$	$30 \times 10^{-7} \text{ cm}$	$30 \times 10^{-7} \text{ cm}$
$\gamma$	$5.6 \times 10^{-9} \text{ cm}^3 \text{ s}^{-1}$	$5.6 \times 10^{-9} \text{ cm}^3 \text{ s}^{-1}$
$\kappa_S$	$8.3 \times 10^7 \text{ s}^{-1}$	$8.3 \times 10^7 \text{ s}^{-1}$
$\kappa_T$	$6.5 \times 10^2 \text{ s}^{-1}$	$6.5 \times 10^2 \text{ s}^{-1}$
$\kappa_{SP}$	$1.0 \times 10^{-11} \text{ s}^{-1}$	$1.0 \times 10^{-11} \text{ s}^{-1}$
$\kappa_{ST}$	$2.5 \times 10^{-10} \text{ cm}^{-3} \text{ s}^{-1}$	$2.5 \times 10^{-10} \text{ cm}^{-3} \text{ s}^{-1}$
$\kappa_{FRET}$	$1.15 \times 10^{10} \text{ s}^{-1}$	$1.15 \times 10^{10} \text{ s}^{-1}$
$\kappa_{DEXT}$	$2.0 \times 10^8 \text{ cm}^{-3} \text{ s}^{-1}$	$2.8 \times 10^8 \text{ cm}^{-3} \text{ s}^{-1}$
$\kappa_{ISC}$	$2.2 \times 10^4 \text{ s}^{-1}$	$2.2 \times 10^4 \text{ s}^{-1}$
$\kappa_{TP}$	$2.8 \times 10^{-13} \text{ cm}^{-3} \text{ s}^{-1}$	$2.8 \times 10^{-11} \text{ cm}^{-3} \text{ s}^{-1}$
$\kappa_{TT}$	$2.2 \times 10^{-12} \text{ cm}^{-3} \text{ s}^{-1}$	$5.5 \times 10^{-12} \text{ cm}^{-3} \text{ s}^{-1}$
$\kappa_{SS}$	$3.5 \times 10^{-12} \text{ cm}^{-3} \text{ s}^{-1}$	$3.5 \times 10^{-12} \text{ cm}^{-3} \text{ s}^{-1}$
$\kappa_{SSD}$	$9.6 \times 10^{-13} \text{ cm}^{-3} \text{ s}^{-1}$	$9.6 \times 10^{-13} \text{ cm}^{-3} \text{ s}^{-1}$
$\kappa_{SD}$	$1.0 \times 10^9 \text{ s}^{-1}$	$1.0 \times 10^9 \text{ s}^{-1}$
$\kappa_{ISCD}$	$2.2 \times 10^4 \text{ s}^{-1}$	$2.2 \times 10^4 \text{ s}^{-1}$
$\kappa_{TTD}$	$8.0 \times 10^{-12} \text{ cm}^{-3} \text{ s}^{-1}$	$2.0 \times 10^{-11} \text{ cm}^{-3} \text{ s}^{-1}$
$\kappa_{SPD}$	$3.0 \times 10^{-11} \text{ cm}^{-3} \text{ s}^{-1}$	$3.0 \times 10^{-11} \text{ cm}^{-3} \text{ s}^{-1}$
$\kappa_{STD}$	$3.7 \times 10^{-10} \text{ cm}^{-3} \text{ s}^{-1}$	$3.7 \times 10^{-10} \text{ cm}^{-3} \text{ s}^{-1}$
$\kappa_{TPD}$	$9.0 \times 10^{-11} \text{ cm}^{-3} \text{ s}^{-1}$	$9.0 \times 10^{-11} \text{ cm}^{-3} \text{ s}^{-1}$
$\xi$	$1.4 \times 10^{-5} \text{ s}^{-1}$	$1.4 \times 10^{-5} \text{ s}^{-1}$
$\kappa_{cav}$	$3.0 \times 10^{14} \text{ s}^{-1}$	$3.0 \times 10^{14} \text{ s}^{-1}$
$\beta$	$1.3 \times 10^{-3}$	$2.6 \times 10^{-4}$
$W_\lambda$	$2.6 \times 10^{-2}$	$2.6 \times 10^{-2}$

Figure IV.10.d shows the net-amplification (blue dash-dot line), the measured photon response (red solid line), the photon density calculated with  $\gamma_1=5.6 \times 10^{-10} \text{ cm}^3 \text{ s}^{-1}$  (solid black line) together with the literature value  $\gamma_2=6.2 \times 10^{-12} \text{ cm}^3 \text{ s}^{-1}$  (black dashes). It clearly that the simulation with  $\gamma_1$  shows a very good qualitative agreement between with the measurement especially for the rising flank, the top of the pulse and the far tail. However with  $\gamma_2$  no agreement can be achieved. Clearly, in this high current density and nanosecond regime, the literature value of the Langevin recombination rate ( $\gamma_2=6.2 \times 10^{-12} \text{ cm}^3 \text{ s}^{-1}$ ) is too small to explain both the slope of the rising flank and the tail of the pulse of the photon response as shown in fig. IV.10.d. Note that, among the parameters fine-tuned to improve the fit, the Langevin recombination rate  $\gamma_1=5.6 \times 10^{-10} \text{ cm}^3 \text{ s}^{-1}$  is 2 orders of magnitude larger. We attribute this to the exponential dependence of the mobility on the square root of the electric field expressed in Eq(II.49). The fact that the model is able to reproduce qualitatively the optical response of an OLED on the basis of the same excitation current density signal is a strong indication of the validity of the model. The calculated dynamics of the photon density is then compared with the measured optical response under higher pulsed current density of OLED 2. The polarons, singlet, triplets and photon populations are calculated with the fine tuned parameters presented in table 2 (third column) and are plotted in fig IV.11. Figure IV.11.a exhibits a current density reaching  $8.8 \text{ kA/cm}^2$ , resulting in a polaron density maximum of  $5.5 \times 10^{18}$ . The maxima of host and dopant singlet densities in fig. IV.11.b and IV.11.c are respectively  $3.5 \times 10^{17} \text{ cm}^{-3}$  and  $1.7 \times 10^{18} \text{ cm}^{-3}$ .

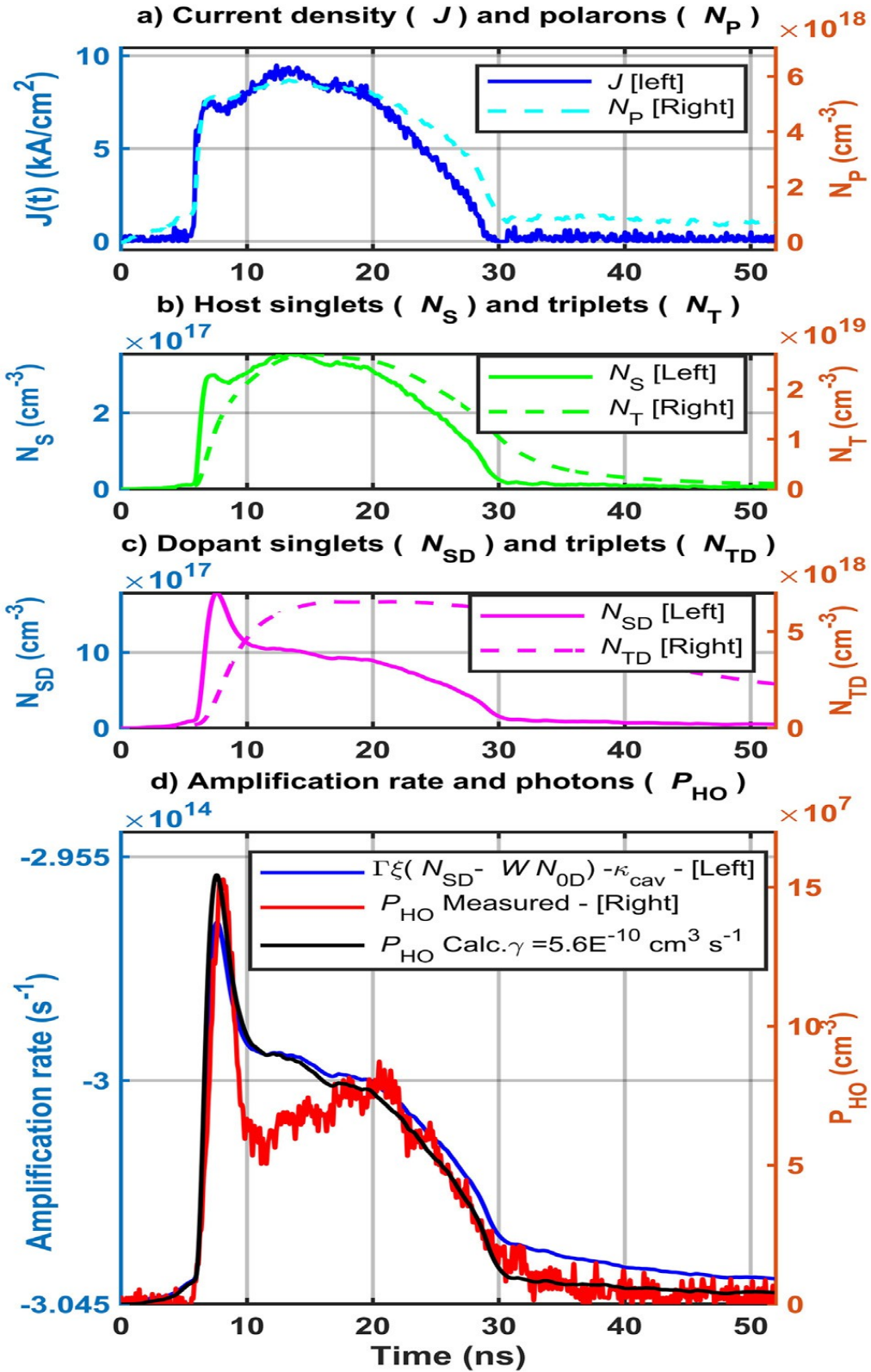


Figure IV.11: Comparison between measured and calculated optical response of a CPW OLED under a current density of 10 kA/cm<sup>2</sup>. The parameters are fine tuned to  $g = 1.3 \times 10^{-9} \text{ cm}^3 \text{ s}^{-1}$ ,  $k_{sp} = 1.3 \times 10^{-10} \text{ s}^{-1}$ ,  $k_{st} = 5.0 \times 10^{-11} \text{ cm}^{-3} \text{ s}^{-1}$ ,  $k_{DEXT} = 4.7 \times 10^7 \text{ cm}^{-3} \text{ s}^{-1}$ ,  $k_{TT} = 1.2 \times 10^{-10}$ ,  $k_{SD} = 0.2 \times 10^9$ ,  $k_{TTD} = 750.0 \times 10^{-12} \text{ cm}^{-3} \text{ s}^{-1}$ ,  $k_{SPD} = 1.0 \times 10^{-11} \text{ cm}^{-3} \text{ s}^{-1}$ ,  $k_{STD} = 8.0 \times 10^{-9} \text{ cm}^{-3} \text{ s}^{-1}$ ,  $k_{TPD} = 900.0 \times 10^{-13} \text{ cm}^{-3} \text{ s}^{-1}$

Figure IV.11.d presents the calculated and measured photon density which exhibit larger divergence compared to the first experiments, specifically during some 10ns directly following the peak.

We believe this less satisfactory fit in the ultra-high current density case, is due to higher current density and leading to larger non-homogenous spatial distribution of the polarons within the organic layers. Taking into account both the time and spatial dependences is beyond the scope of this paper.

Nevertheless, With these experimental validations a more reliable laser threshold prediction can be made.

### **IV.3.3. Ultra-short response under electrical excitation**

#### **IV.3.3.1 Objectives of the experiments**

In 1970, Peterson, Tuccio and Snavely identified that the laser conditions have to be reached very quickly (0.1 to 1  $\mu$ s) before triplet accumulation limits the operation of dye lasers[4]. Indeed, for the dye lasers, the lasing process is based upon transition of singlet and is accompanied by losses associated with the accumulation of triplet at the inter-system crossing rate  $\kappa_{ISC} \simeq 2.2 \times 10^4 \text{ s}^{-1}$  to  $1.0 \times 10^7 \text{ s}^{-1}$  (see table 10 chapter II). What is true for dye lasers under optical pumping, becomes even more imperative for solid state organic lasers under electrical excitation because triplet population is fed directly by current and thus is increased much faster. A consequence shown by simulations in chapter II is that stimulated emission occurs under pulse electrical excitation and last only 7ns after the turn on before accumulation of triplet increases losses, reduces net gain and switch off the stimulated emission. The difference in speed dynamics induced either by electrical excitation or optical pumping is related to the Langevin recombination rate ( $6.2 \times 10^{-12} \text{ cm}^3 \text{ s}^{-1}$ ) and to  $\kappa_{ISC}$  the inter-system crossing rate respectively. For this reason, to reach the laser conditions it's necessary to operate with devices offering rise time much shorter than the time window.

Hence, we need to verify the dynamical properties of the fabricated samples. More precisely, we would like to check that the electrical time constant is 100ps or less. This will be accessed through the measurement of the OLED current rise time and fall time. We will check that the optical response follows the electrical dynamics by measuring the rising flank and the falling edge of the optical signal.

#### **IV.3.3.2 Results**

We analyze different types of devices, firstly Alq3 only OLED and thirdly F8BT polymer OLED as presented in chapter III section III.6.

Figure IV.12 presents the electrical and optical responses of three sizes of OLED with Alq3 based light emitting layer excited with 25V impulses. The pulse duration instructions are 400ps (blue), 800ps (red) and 1ns (green). The first, second and third column presents the measurement of 100x100 $\mu\text{m}^2$ , 50x50 $\mu\text{m}^2$  and 25x25 $\mu\text{m}^2$  OLED respectively. The first row presents the excitation signal, the second row shows the electrical response of OLED and the third row presents the OLED optical response.

Each figure includes an inset showing more clearly the pulse width and amplitude.

For the 100x100 $\mu\text{m}^2$  OLED, the excitation signals exhibit full width at half maximum (FWHM) pulse widths of 997ps, 783ps and 406ps with amplitudes of 24,7V, 24,3V and 22,3V respectively.



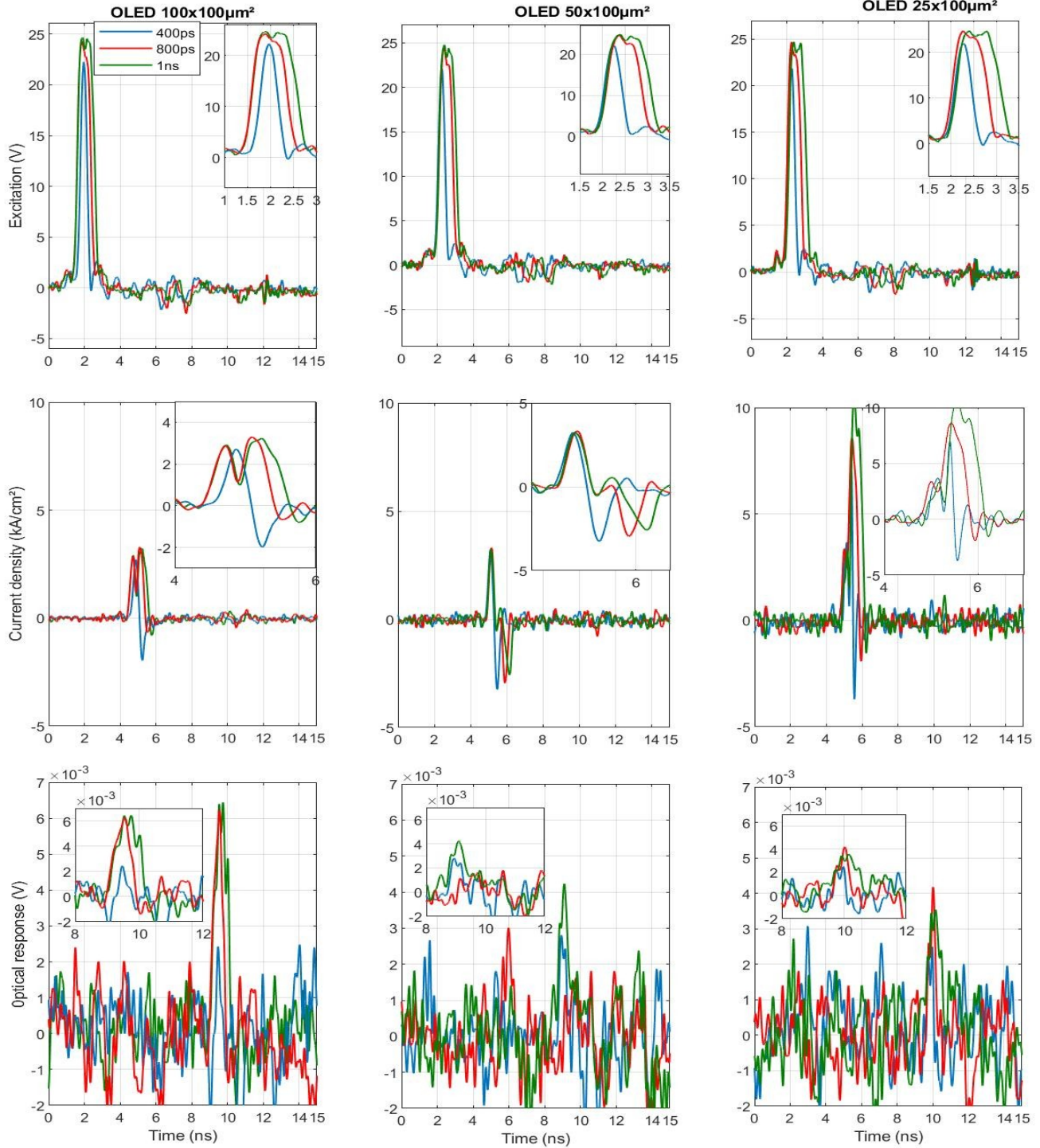


Figure IV.12: Electrical response and optical response of Alq<sub>3</sub> based OLED; 100x100 $\mu\text{m}^2$  OLED (column 1), 50x100 $\mu\text{m}^2$  OLED (column 2) and 25x100 $\mu\text{m}^2$  (column 3), excitation signal (arrow 1), current density response (arrow 2), optical response (arrow 3), nominal pulse width: 1ns (green line), 800ps (red line), 400ps (blue line)



The electrical responses show pulse widths of 946ps, 754ps and 294ps and current densities of 3,2kA/cm<sup>2</sup>, 3,3kA/cm<sup>2</sup> and 2,7kA/cm<sup>2</sup> respectively. The 10-90% rise times are relatively constant 232ps, 225ps and 232ps while the fall times are 299ps, 225ps and 145ps.

The optical responses exhibit pulse widths of 887ps, 610ps and 206ps and amplitudes of 6,4x10<sup>-3</sup>V, 6,2x10<sup>-3</sup>V and 2,7x10<sup>-3</sup>V respectively. The rising flank (and falling edge) are 423ps (120ps), 448ps (270ps) and 119ps (261ps). The signal to noise ratio is about 3 for the 1ns and 800ps cases but it is only 1 for the 400ps case. These measurements are presented in table IV 2.

Note that the optical pulse widths are shorter than the current pulse widths itself shorter than the measured pulse widths of the excitation signal. These reductions of the pulse widths exist for all three values 1ns, 800ps and 400ps but become more pronounced when the pulse duration is decreased. For example in the 400ps case, the optical pulse width (206ps) is ~51% of excitation width (406ps). This ratio is 78% in the 800ps case and 93% in the 1ns case. Such reductions should be taken carefully because non-linearities are necessary to explain them.

Note that the increase of the current densities from 3.2kA/cm<sup>2</sup> to 10.4kA/cm<sup>2</sup> when the active area is reduced from 100x100μm<sup>2</sup> to 25x100μm<sup>2</sup> for 1ns nominal width confirms the prediction of the electrical model illustrated in chapter II fig. II.4. The same is true for other pulse width.

The same trends hold for the smaller OLEDs except that the optical signals become noisy because smaller OLEDs induce smaller luminous flux. Note, that in the 800ps case, the current densities for the 25x100μm<sup>2</sup> OLED reach about ~8.6kA/cm<sup>2</sup> which is 2.6 times that of the 100x100μm<sup>2</sup> OLED (3.3kA/cm<sup>2</sup>) while having 4 times smaller active area. Although the current density is increased by 2.6 the four-fold decrease of the active area results in a reduction of the light output by 0.65 which is exactly the ratio of the measured optical pulse amplitudes.

Note that the time constants (rise time and fall time) presented in table IV 2 are clearly in the sub-ns time scale which confirm the electrical model predicting electrical time constant of 92ps according to the fabrication.

Figure IV.13 presents the electrical and optical responses of three sizes of polymer OLED with F8:F8BT based light emitting layer excited with 25V impulses. The pulse duration instructions are 300ps (magenta), 400ps (blue), 800ps (red) and 1ns (green). The first, second and third column presents the measurement of 100x100μm<sup>2</sup>, 50x50μm<sup>2</sup> and 25x25μm<sup>2</sup> OLED respectively. The first row presents the excitation signal, the second row shows the electrical response of OLED and the third row presents the OLED optical response. Each figure includes an inset showing more clearly the pulse width and amplitude.

For the 100x100μm<sup>2</sup> polymer OLED (POLED), the excitation signals exhibit full width at half maximum (FWHM) pulse widths of 990ps, 787ps and 400ps with amplitudes of 24,2V, 23,6V and 21,3V respectively. The electrical responses show pulse widths of 950ps, 757ps and 388ps and current densities of 2.5kA/cm<sup>2</sup>, 2.2kA/cm<sup>2</sup> and 2kA/cm<sup>2</sup> respectively. The 10-90% rise times are relatively constant 230ps, 245ps and 247ps while the fall times are 332ps, 172ps and 200ps.

Table IV 2: Time analysis of the excitation signal, electrical and optical responses of Alq3 based OLED for different size and different pulse duration: pulse width, rise time and fall time

OLED size	Nominal width		Excitation signal	Electrical response (current density)	Optical response
100x100 $\mu\text{m}^2$	1ns	Pulse width	997ps	946ps (3.2kA/cm <sup>2</sup> )	887ps
		Rise time	-	232ps	423ps
		Fall time	-	299ps	120ps
	800ps	Pulse width	783ps	754ps (3.3kA/cm <sup>2</sup> )	610ps
		Rise time	-	225ps	448ps
		Fall time	-	189ps	270ps
	400ps	Pulse width	406ps	294ps (2.7kA/cm <sup>2</sup> )	206ps
		Rise time	-	232ps	119ps
		Fall time	-	145ps	261ps
50x100 $\mu\text{m}^2$	1ns	Pulse width	983ps	290ps (3.2kA/cm <sup>2</sup> )	558ps
		Rise time	-	152ps	150ps
		Fall time	-	157ps	295ps
	800ps	Pulse width	776ps	285ps (3.3kA/cm <sup>2</sup> )	Not measurable
		Rise time	-	188ps	Not measurable
		Fall time	-	137ps	Not measurable
	400ps	Pulse width	440ps	257ps (3.2kA/cm <sup>2</sup> )	421ps
		Rise time	-	190ps	139ps
		Fall time	-	136ps	225ps
25x100 $\mu\text{m}^2$	1ns	Pulse width	969ps	763ps(10.4kA/cm <sup>2</sup> )	874ps
		Rise time	-	169ps	Not measurable
		Fall time	-	247ps	440ps
	800ps	Pulse width	781ps	492ps (8.6kA/cm <sup>2</sup> )	433ps
		Rise time	-	216ps	333ps
		Fall time	-	295ps	320ps
	400ps	Pulse width	409ps	124ps(7.0kA/cm <sup>2</sup> )	355ps
		Rise time	-	96ps	77ps
		Fall time	-	60ps	128ps

The optical responses exhibit pulse widths of 1.54ns, 1.5ns and 1.35ns and amplitudes of  $26 \times 10^{-3} \text{V}$ ,  $17 \times 10^{-3} \text{V}$  and  $7 \times 10^{-3} \text{V}$  respectively. The rising flank (and falling edge) are 1.03ns (730ps), 1.07ns (752ps) and 818ps (653ps). These measurements are presented in table IV 3.

For the case of POLEDs  $100 \times 100 \mu\text{m}^2$  and  $50 \times 100 \mu\text{m}^2$ , the electrical pulse widths are shorter than the measured pulse widths of the excitation signal. The increase of the current densities from  $2.5 \text{kA/cm}^2$  to  $6.5 \text{kA/cm}^2$  when the active area is reduced from  $100 \times 100 \mu\text{m}^2$  to  $50 \times 100 \mu\text{m}^2$  for 1ns nominal width confirms the prediction of the electrical model illustrated in chapter II fig. II.4. The same is true for other pulse width.

Note that the optical pulse widths are larger than the current pulse widths. These increasing of the pulse widths exist for all three values 1ns, 800ps and 400ps. For example in the 400ps case, the electrical response width (388ps) is  $\sim 29\%$  of the optical pulse width (1.35ns). This ratio is 50% in the 800ps case and 61% in the 1ns case. This phenomenon can be explain by the singlet life time limit.

In the case of  $25 \times 100 \mu\text{m}^2$  POLED, the excitation pulse widths much shorter than the nominal pulse width wich increase a decrease of current density compared to  $50 \times 100 \mu\text{m}^2$  POLED. Note that same trends (electrical and optical) hold for this POLED.

### IV.3.3.3 Analysis

At first sight, nano-second and sub-nanosecond pulse widths with rise time and fall time down to 100ps have been achieved. This results meet the requirements defined in the design step in chapter II.

However these sub-ns results rise numerous questions;

- How come the current pulse width is shorter than the excitation pulse width?
- How come the optical pulse widths are shorter than the current pulse widths for the Alq3 based OLED?
- How come optical pulses of 800ps and bellow are possible knowing the fluorescence lifetime of Alq3 is 12ns?
- Why the optical pulse widths of the polymer OLED behave differently than the Alq3 OLED remaining almost constant while the excitation pulse widths decrease by 2.5?

To investigate these questions, two different levels must be considered; the electrical level and the optical level.

#### IV.3.3.3.1 Electrical level

At the electrical level, the current density is driven by the Langevin recombination rate  $\gamma_{Langevin}$  [5].

$$\gamma = \frac{e(\mu_e + \mu_h)}{\epsilon_0 \epsilon_r} \quad \text{Eq. (IV.1)}$$

According to the Poole-Frenkel model, the mobilities show exponential dependencies on the square root of the electric field  $F = \frac{V_D(t)}{d}$  [6,7]. Thus the Langevin recombination rate evolves exponentially with the excitation voltage  $V_D(t)$  applied to the OLED:

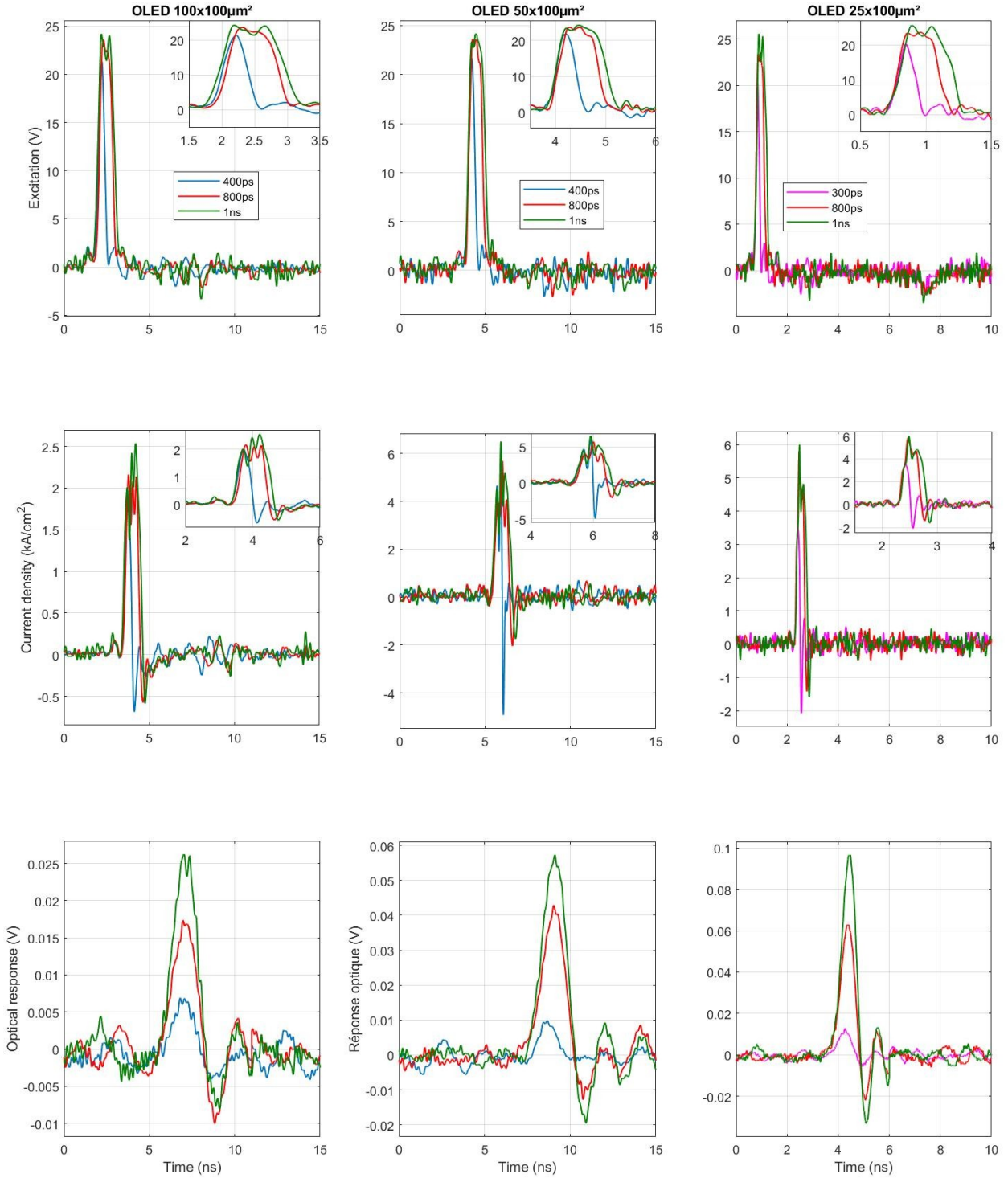


Figure IV.13: Electrical response and optical response of polymer OLED; 100x100 μm<sup>2</sup> OLED (column 1), 50x100 μm<sup>2</sup> OLED (column 2) and 25x100 μm<sup>2</sup> (column 3), excitation signal (arrow 1), current density response (arrow 2), optical response (arrow 3), nominal pulse width: 1 ns (green line), 800 ps (red line), 400 ps (blue line) and 300 ps (magenta line)

$$\gamma(t) = \gamma_0 \exp\left(\sqrt{\frac{V_D(t)}{V_0}}\right) \quad \text{Eq. (IV.2)}$$

with  $V_0$  an adjustable parameters to be determined, and the Langevin recombination rate without field dependence is estimated to  $\gamma_0 = 6.2 \times 10^{-12} \text{ cm}^3 \text{ s}^{-1}$  in the literature [8].

At the pulse onset when the voltage increases the recombination rate increases exponentially and in turn the current increases exponentially reshaping the pulse by stretching it in amplitude.

In a more mathematical approach, one should consider the polaron equation (II.4) presented in chapter II, that govern the dynamical behavior of the (polaronic) current:

$$\frac{dN_P}{dt} = \frac{J(t)}{ed} - \gamma N_P^2$$

Here, the time constant (the inverse of  $\gamma_{Langevin}$ ) associated with the generation of singlets increases and decreases exponentially with the applied voltage on the one hand boosting the spontaneous emission with a sharp rising flank at the pulse onset and on the other hand shortening the rise time at the pulse fallout.

#### IV.3.3.3.2 Optical level

Indeed, under electrical excitation the effective singlet lifetime of the organic emitter differs from that under optical pumping justifying to differentiate the fluorescence lifetime  $\tau_{fluo}$  measured under optical pumping from the electroluminescence lifetime  $\tau_{elec}$  measured under electrical excitation with:

$$\tau_{fluo} = \frac{1}{\kappa_s + (\kappa_{ISC} + \frac{7}{4}\kappa_{SS}N_S + \kappa_{ST}N_T)} \quad \text{Eq. (IV.3)} \quad \text{and}$$

$$\tau_{elec} = \frac{1}{\kappa_s + (\kappa_{ISC} + \frac{7}{4}\kappa_{SS}N_S + \kappa_{ST}N_T + \kappa_{SP}N_P)} \quad \text{Eq. (IV.4)}$$

where  $\kappa_s$  the singlet-exciton decay rate (inverse singlet lifetime ( $1/\kappa_s = 12 \text{ ns}$  for Alq3) account for radiative recombination,  $\kappa_{ISC}$  is the Inter System Crossing lifetime ( $1/\kappa_{ISC} \approx 1 \mu\text{s}$ ),  $N_S$ ,  $N_P$ ,  $N_T$  are respectively the singlet, the polaron and the triplet densities, and  $\kappa_{SS}$ ,  $\kappa_{SP}$ ,  $\kappa_{ST}$  are respectively the singlet-singlet annihilation rate, the singlet-polaron annihilation rate, and the singlet-triplet annihilation rate. The terms in between brackets corresponds to the non-radiative decays. The point is that under electrical excitation the non-radiative terms becomes more important for two reasons:

- Firstly, the polarons modify the decay time when the  $\kappa_{SP}N_{SP}$  term becomes non-negligible over the term  $\kappa_s + (\kappa_{ISC} + 7/4\kappa_{SS}N_S + \kappa_{ST}N_T)$

Table IV 3: Time analysis of the excitation signal, electrical and optical responses of F8:F8BT polymer OLED for different size and different pulse duration: pulse width, rise time and fall time

OLED size	Nominal width		Excitation signal	Electrical response (current density)	Optical response
100x100 $\mu\text{m}^2$	1ns	Amplitude	24.2V	2.5kA/cm <sup>2</sup>	(0.026V)
		Pulse width	990ps	950ps	1.54ns
		Rise time	330ps	230ps	1.03ns
		Fall time	410ps	332ps	730ps
	800ps	Amplitude	23.6V	2.2kA/cm <sup>2</sup>	(0.017V)
		Pulse width	787ps	757ps	1.50ns
		Rise time	296ps	245ps	1.07ns
		Fall time	347ps	172ps	752ps
	400ps	Amplitude	21.3V	2kA/cm <sup>2</sup>	(0.007V)
		Pulse width	400ps	388ps	1.35ns
		Rise time	282ps	247ps	818ps
		Fall time	240ps	200ps	653ps
50x100 $\mu\text{m}^2$	1ns	Amplitude	24.16V	6.5kA/cm <sup>2</sup>	(0.057V)
		Pulse width	1.01ns	785ps	1.54ns
		Rise time	280ps	270ps	1.05ns
		Fall time	400ps	320ps	800ps
	800ps	Amplitude	23.62V	5.65kA/cm <sup>2</sup>	(0.043V)
		Pulse width	815ps	720ps	1.64ns
		Rise time	285ps	230ps	1.35ns
		Fall time	275ps	130ps	560ps
	400ps	Amplitude	21.72V	6.06kA/cm <sup>2</sup>	(0.01V)
		Pulse width	410ps	370ps	1.13ns
		Rise time	295ps	260ps	545ps
		Fall time	240ps	45ps	890ps
25x100 $\mu\text{m}^2$	1ns	Amplitude	25.56V	5.99kA/cm <sup>2</sup>	(0.096V)
		Pulse width	400ps	362ps	607ps
		Rise time	147ps	132ps	500ps
		Fall time	172ps	122ps	288ps
	800ps	Amplitude	23.56V	5.8kA/cm <sup>2</sup>	(0.063V)
		Pulse width	314ps	303ps	612ps
		Rise time	126ps	136ps	477ps
		Fall time	133ps	67ps	290ps
	300ps	Amplitude	20.22V	3.57kA/cm <sup>2</sup>	(0.013V)
		Pulse width	142ps	132ps	536ps
		Rise time	105ps	90ps	526ps
		Fall time	96ps	59ps	362ps

- Secondly, under electrical excitation the triplet population  $N_T$  is directly fed by the Langevin recombination mechanism at  $3/4 \gamma N_p^2$  and thus increases at a much larger rate than with the inter system crossing  $\kappa_{ISC}$  alone. The  $\kappa_{ST} N_T$  term is much larger under electrical excitation than under optical pumping

In the Alq3-based OLED case, assuming  $\kappa_{ISC} + 7/4 \kappa_{SS} N_S \ll \kappa_S$  and with  $N_p \approx 8 \times 10^{18} \text{ cm}^{-3}$ ,  $N_T \approx 2 \times 10^{18} \text{ cm}^{-3}$  the fall time is estimated to [9]:  $t_{fall} \sim \frac{1}{\kappa_S + \kappa_{Sp} N_{Sp} + \kappa_{ST} N_T} \approx 500 \text{ ps}$ . This is much shorter than the singlet decay rate  $1/\kappa_S = 12 \text{ ns}$ . The rise time of an Alq3-based green OLED is estimated at  $t_{rise} \sim \left( \frac{3eAd}{\gamma \kappa_S I_D} \right)^{1/3} \approx 0.87 \text{ ns}$  [9].

In the case of polymer OLED, the system F8:F8BT is not clearly known as a host:guest system or only a host material. This makes the theoretical interpretation of time constants complicated. In addition, the fluorescence life time of this system is not available in the literature. In perspective, investigation of this aspect will be conducted by the experimental measurement of the fluorescence life time of F8:F8BT using the Time Correlated Single Photon quantify (TCSP) method.

## IV.4. Devices with DFB cavities

This section is devoted to the characterization and the analysis of OLED including DFB pattern as fabricated in chapter III. As a preliminary step, It must be checked if these structures offer the expected properties of a laser cavity. It will be investigated in section IV.4.1 with patterns filed with organic laser gain medium under optical pumping. Once the laser micro-cavity effect is established we will investigate OLED with this DFB micro-cavities under electrical excitation in section IV.4.2.

### IV.4.1. Laser properties of DFB patterns under optical pumping

To check that the DFB patterns offer the expected properties of a laser cavity, the samples prepared according to chapter 3 presented in section IV.4.1.1 are submitted to optical pumping using a dedicated experimental setup presented in section IV.4.1.2 and the experimental results are presented in section IV.4.1.3. Among the properties expected from patterns to constitute laser micro-cavities, the most important are; Firstly, the matching of the microcavity resonance with the maximum of the organic material photoluminescence, secondly, high quality factor ideally above  $Q \sim 1000$  as indicated by the simulation (chapter II, section 3.4) to achieve threshold current densities in the  $\text{kA/cm}^2$  range.

#### IV.4.1.1 Samples

On a glass sample coated with 140nm of ITO, 30 patterns have been e-beam lithographed in a 300nm thick HSQ electron-sensitive resist following the process described in chapter III section 3.5. The 30 motifs are divided into 5 rows and 6 columns corresponding to 5 different geometries and 6 different doses as shown in fig.IV.14.(a). Each pattern repeated every  $500 \mu\text{m}$  horizontally and  $400 \mu\text{m}$  vertically consists of three sections; first and third sections are made of parallel lines with width  $l_{1H}$  varying between 91nm and 103nm and spaced by  $l_{1l}$  varying between 107 and 121nm. The second section is made of 10 parallel lines with a nominal width of  $l_{2H} = 2 l_{1H}$  and 11 spacings with a nominal width of  $l_{2l} = 2 l_{1l}$ . The length of section 2 varies between 3.5 and  $5.6 \mu\text{m}$ .

Five couples (  $l_{1H}$  ,  $l_{1L}$  ) defining five different geometries are used as shown in table IV 4. The nominal resonance wavelength of quarter-wavelength grating reads:

$$\lambda_{Bragg} = 2(n_H l_{1H} + n_L l_{1L}) \text{ Eq. (IV.5)}$$

with a large uncertainty on the effective index  $n_H$  and  $n_L$  . Because of this uncertainty, the bulk refractive indices are used in a first approach. The nominal resonance wavelengths are presented in the first column of table IV 4.

<b>Table IV 4: Nominal dimensions of micro-cavity lines and spacing</b>					
Nominal Bragg wavelength $\lambda_{Bragg}$ (nm)	$l_{1H}$ (nm)	$l_{1L}$ (nm)	$l_{2H}$ (nm)	$l_{2L}$ (nm)	Length of section 2 ( $\mu\text{m}$ )
<b>622</b>	91	107	183	214	4.085
<b>642</b>	94	111	189	221	4.150
<b>662</b>	97	114	195	228	4.300
<b>682</b>	100	118	201	235	4.421
<b>702</b>	103	121	206	242	4.523

From  $l_H$  and  $l_L$  the dimension of the spacing and the line widths, the nominal Bragg wavelength is calculated according to eq.2 using  $n_H=1.7$  and  $n_L=1.45$  the bulk refractive index resulting in

$$622\text{nm} \leq \lambda_{Bragg} \leq 682\text{nm}$$

Six different doses are introduced to investigate the potential impact on the geometry and thus on the effective resonance wavelength. This is an indirect way of varying  $l_H$  with respect to  $l_L$  because when the dose is increased the width of the HSQ lines increase at the cost of the decrease of the spacing. This is due to the electron diffusion.

The laser gain medium evaporated on the patterns consists of 200nm of Alq3 doped with 2% of DCM2. For this concentration, the maximum of spontaneous emission is obtained at 607nm. Note the pedestal at 515nm a residual emission of Alq3.

#### **IV.4.1.2 Experimental setup**

We pump the emitting layer deposited on the DFB grating with a tripled Nd-Yag laser (Team Photonic) ( $\lambda=355\text{nm}$ ) with pulse duration of 12ns via x40 microscope objective resulting in a spot size estimated to  $\sim 100\mu\text{m}$  in diameter. The spot of detection is  $10\mu\text{m}$  in diameter spatially separated from the pumping spot and are tangent. The collected light is send to a spectrometer (Ocean Optics 2000+ with 0.2nm of resolution and analyzed in the wavelength range [344.79nm 1036.61nm]). Another spectrometer (Ocean Insight Flame) offers a resolution of 0.05nm with a wavelength range from 578.91nm to 688.66nm. The energy of the pump is varied with a half-wavelength plate followed by a linear polarizer and a spectrum is acquired by integrating over 10s. The maximum of the spectrum is used to quantify the output light.

#### **IV.4.1.3 Experimental results**

Figure IV.14 shows the output light intensities for different energy densities of the pump in log-log scale. The curve exhibits a S shape typical of laser behaviors. In A (blue circle) and B (red circle), the spectra shown in blue and red in the inset (b) exhibit a FWHM linewidth (  $\delta\lambda$  ) of 61nm and 57nm respectively. In C (green circle), with a pump energy of  $125\mu\text{J}/\text{cm}^2$ , the spectrum shows a peak enhancement with a line-widht reduction to 47nm. Above this pump energy value the light output increases more rapidly indicating that the threshold value was exceeded.



In D (cyan circle) for  $167\mu\text{J}/\text{cm}^2$ , E (magenta dot) for  $269\mu\text{J}/\text{cm}^2$  and F (orange dot) for  $477\mu\text{J}/\text{cm}^2$ , the spectra measured with the  $0.2\text{nm}$  resolution spectrometer shown in the inset (c) narrow further down to  $1.1\text{nm}$ ,  $1.3\text{nm}$  and  $1.7\text{nm}$  respectively. With the  $0.05\text{nm}$  resolution spectrometer, not only the FWHM are measured respectively down to  $0.38\text{nm}$ ,  $0.46\text{nm}$  and  $0.73\text{nm}$ , but also several peaks appear indicating multimode emission as displayed in Fig.IV.14 inset (d). The small increase of the line-width above threshold is thus explained by the multi-mode emission as in Fabry-Perot lasers contrary to DFB lasers.

The origin of this multiple modes can be searched either in the different TE and TM modes allowed by the  $140\text{ nm}$  thick ITO planar wave-guide, or in the multiple reflections from the adjacent cavities. The free spectral range (FSR) of  $\Delta\lambda \simeq 0.25 \pm 0.05\text{ nm}$  gives a first indication about this origin. The cavity length corresponding to this FSR is  $e = \lambda_0^2 / (2n_a \Delta\lambda) \simeq 500\mu\text{m}$  with  $\lambda_0 = 627\text{ nm}$  is the central wavelength,  $n_a = 1.6$  the average refractive index of the cavity medium. This indicates that the FSR probably corresponds to the spacing between two adjacent cavities as in the inset (a).

In the case of  $140\text{nm}$  thick ITO,  $200\text{nm}$  thick organic layers and  $300\text{nm}$  of HSQ, the system presents only two modes ( $TE_0$  and  $TM_0$ ) as shown in the chapter II section 4.3.3.2 whereas five peaks are visible in the inset (d) of fig. IV.14. This indicates that the multi-mode emission does not find its origin in the waveguide modes.

The FWHM of the different peaks are estimated to  $0.12\text{nm}$  and  $0.13\text{nm}$  for the cyan spectra ( $167\mu\text{J}/\text{cm}^2$ ),  $0.17\text{nm}$  and  $0.14\text{nm}$  for magenta spectra ( $269\mu\text{J}/\text{cm}^2$ ) and  $0.17\text{nm}$  for yellow spectra ( $477\mu\text{J}/\text{cm}^2$ ). Under lasing operation, the ratio  $(\lambda/\delta\lambda)$  is different from the cold cavity quality factor but still give an estimation in the range  $3687$  to  $5226$  as presented in table IV 5.

It is expected that the nominal resonance wavelength is detuned from the observed resonance wavelength because of three type of uncertainties;

- the effective indices that depend on the effective thickness of the different layers
- the width of the grating lines that depends on the geometry design and on the dose
- the precise emission spectra of the organic material that shifts with the effective concentration of the dopant

To investigate the effects of the different parameters, we fabricated the matrix shown in the inset of fig.IV.15 with different geometries and different doses to quantify how the emission wavelengths change in the different cases. Figure IV.15 presents in different colors the different spectra for the different cavities identified with a frame of the same color under an optical pump excitation of  $211\mu\text{J}/\text{cm}^2$ . Only four cavity geometries allow laser emission as shown by magenta (case 1), green (case 2), blue (case 3) and red (case 4) spectra. They correspond to pattern with nominal Bragg wavelength of  $662\text{nm}$  ( $l_L = 114\text{ nm}, l_H = 97\text{ nm}$ ) and  $682\text{nm}$  ( $l_L = 118\text{ nm}, l_H = 100\text{ nm}$ ) and doses of  $600\mu\text{C}/\text{cm}^2$ ,  $700\mu\text{C}/\text{cm}^2$  and  $800\mu\text{C}/\text{cm}^2$ . The observed laser wavelengths are  $624.1\text{nm}$ ,  $625.5\text{nm}$  and  $643.5\text{nm}$  corresponding to relative detunings of  $5.7\%$ ,  $5.4\%$  and  $5.6\%$  (table IV 6). To identify the origin of these detunings we will firstly study the impact of the dose on the geometry variations and secondly from there quantify the effective indices.

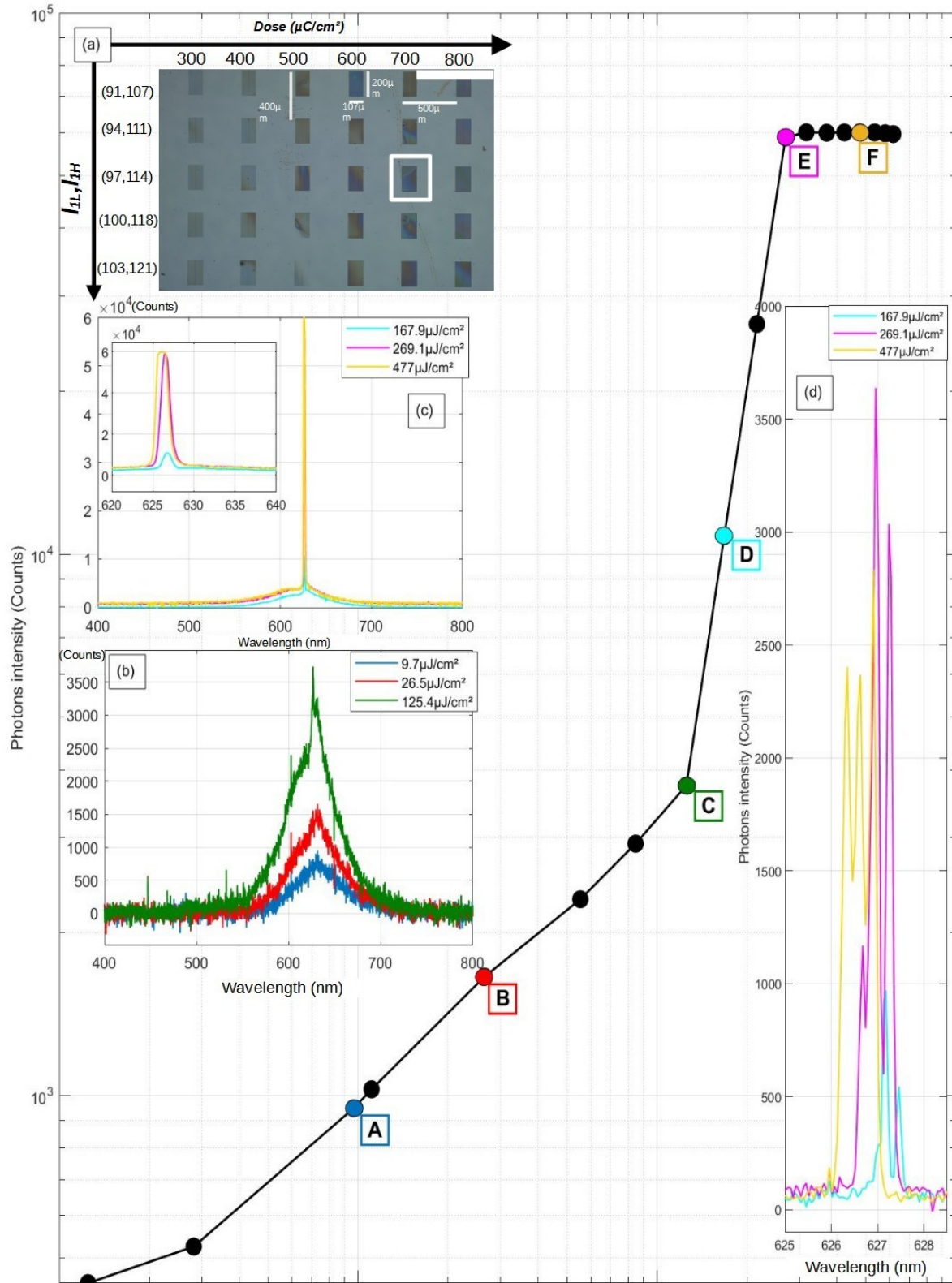


Figure IV.14: S curve behavior of micro-cavity: (a) the sample, (b) spectrum in A (blue line), in B (red line) and in C (green line), (c) spectrum in D,E and F points (cyan, magenta and orange lines respectively), (d) zoom of the inset (c)

As mentioned in chapter 3, varying the electron dose results in a variation of the dimensions of the grating, especially the width of the SiO<sub>2</sub> lines and spacings change because of electron retrodiffusion. Also, the widths vary from line to line. Column 3 to 7 of Table IV 6 present the minimum ( $l_{Lmin}, l_{Hmin}$ ) and the maximum ( $l_{Lmax}, l_{Hmax}$ ) widths of SiO<sub>2</sub> lines and spacings.

Pump energy ( $\mu\text{J}/\text{cm}^2$ )	Resonance wavelength $\lambda_R$ (nm)	FWHM $\delta\lambda$ (nm)	$Q_{warm} = \lambda_R/\delta\lambda$
167 $\mu\text{J}/\text{cm}^2$ (Cyan)	627.2	0.12	5226
	627.5	0.13	4826
269 $\mu\text{J}/\text{cm}^2$ (Magenta)	627.0	0.17	3688
	627.2	0.14	4480
477 $\mu\text{J}/\text{cm}^2$ (Yellow)	626.9	0.17	3687

The typical standard deviations measured from the SEM pictures (section 6 chapter 3) are  $\sigma l_L = 11 \text{ nm}$  and  $\sigma l_H = 15 \text{ nm}$ . From these variations, we can infer the refractive indices.

From equation IV.5,  $n_H$  the high refractive index expressed as a function of  $n_L$  the low refractive index reads;  $n_H = \frac{\lambda_{Bragg}}{2l_H} - \frac{n_L l_L}{l_H}$  Eq. (IV.6)

Because of the variations of the widths of SiO<sub>2</sub> lines and spacings, we introduce for each case the following lines;

$$n_{H1} = \frac{\lambda_{Bragg}}{2l_{Hmin}} - \frac{n_L l_{Lmax}}{l_{Hmin}} \quad \text{Eq. (IV.7)} \quad \text{and} \quad n_{H2} = \frac{\lambda_{Bragg}}{2l_{Hmax}} - \frac{n_L l_{Lmin}}{l_{Hmax}} \quad \text{Eq. (IV.8)}$$

Nominal wavelength $\lambda_{Bragg}$ (nm)	Dose ( $\mu\text{C}/\text{cm}^2$ )	Width of SiO <sub>2</sub> line $l_L$ (nm)		Width of spacing $l_H$ (nm)		Observed peak wavelength $\lambda_R$ (nm)
		$l_{Lmin}$	$l_{Lmax}$	$l_{Hmin}$	$l_{Hmax}$	
Without cavity						607
622		103		90	97	615
642		105	109	92		613.6
662	600 (case1)	115		93	101	624.1 (lasing)
	700 (case2)	119		91	102	626.5 (lasing)
682	700 (case3)	116	129	95	102	643.5 (lasing)
	800 (case4)	138	160	60	90	643.5 (lasing)

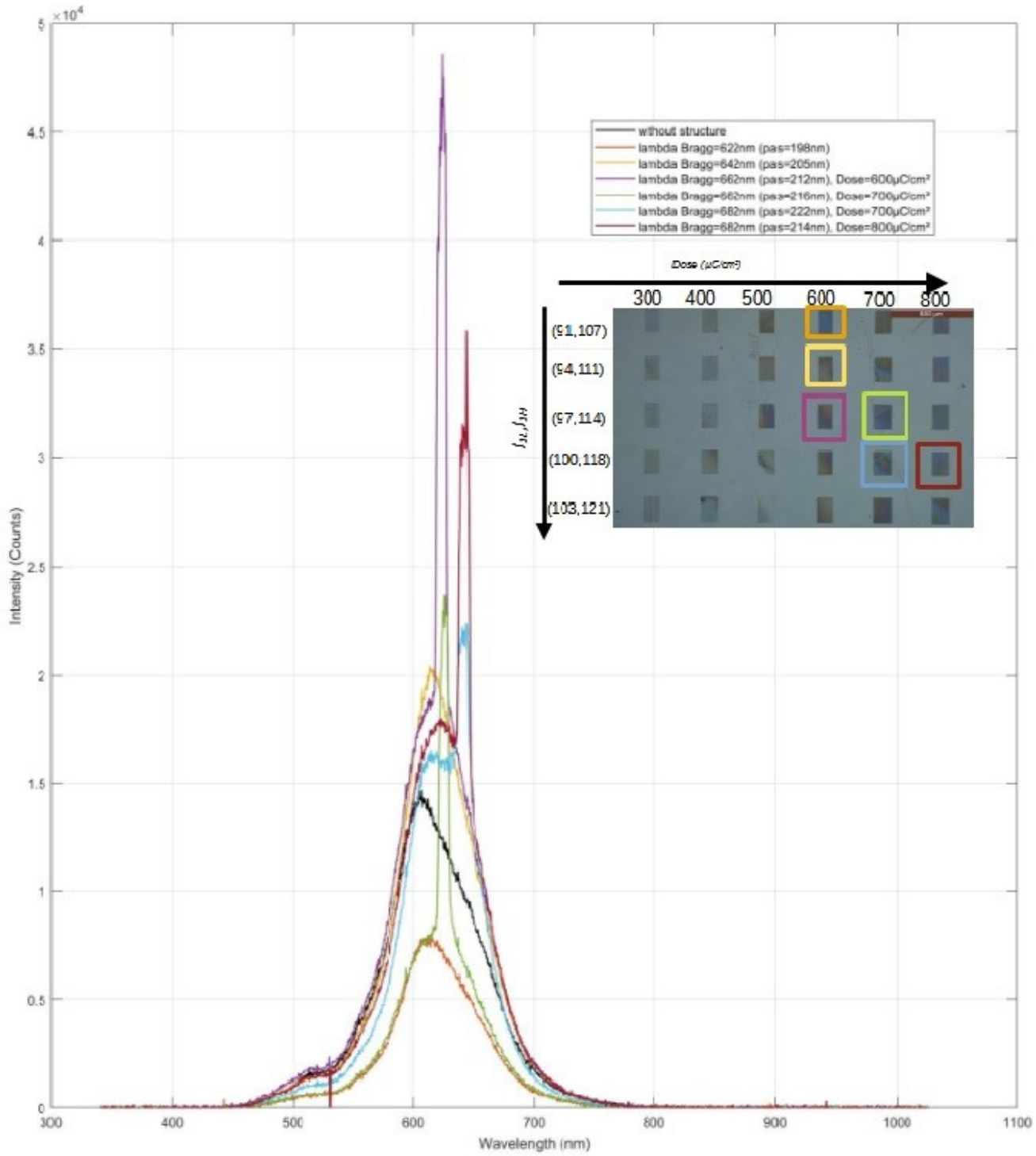


Figure IV.15: Spectrum of different structures

These lines bound solution areas call sectors and mapped in light colors in fig.IV.16. For example, the case 1 ( $\lambda_R=624.1\text{ nm}$ ) offers solutions in between the solid ( $l_{min}=115\text{ nm}, l_{Lmax}=101\text{ nm}$ ) and stripped ( $l_{imax}=115\text{ nm}, l_{Lmin}=93\text{ nm}$ ) magenta lines defining the sector in light magenta as shown in upper fig.IV.16. Similarly, green sector is mapped for the case 2. Solutions of the system are to be sought in the intersection of both sectors.

To restrict the number of solutions, one should remember that solutions are couples  $(n_H, n_L)$  with  $n_H > n_L$  and thus above the line  $y=x$  (black stripped line). Moreover the “a priori” solutions are to be searched in the interval defined by the refractive index of un-densified  $\text{SiO}_2$  ( $n=1.4$  instead of 1.45) and that of ITO ( $n=1.8$ ). These ensemble of solutions is displayed as a grey triangle. The final ensemble of solutions is the area defined by the part of the plan located in between [(1.4,1.603) (1.4,1.489) (1.442,1.441) (1.484,1.484)] and highlighted in yellow.

The same reasoning applies to the cases 3 and 4 lasing at  $\lambda_R=643.5\text{ nm}$  and providing an ensemble of solutions mapped in cyan in lower fig.IV.16. This cyan sector is bounded by the  $(n_H, n_L)$  couples (1.401,1.554), (1.439,1.513), (1.459,1.459), (1.428,1.428), (1.4,1.466).

The intersection of the yellow and the cyan sectors is the green area bounded by [(1.401,1.554) (1.439,1.513)) (1.459,1.459) (1.442,1.442) (1.4 1.49)]. These values of refractive indices are much lower than those calculated for 140nm of ITO and 200nm of organic layer (chapter 2 section 4.4.2) resulting in  $(n_H=1.696, n_L=1.639)$ . Fortunately, the index contrast calculated with these latter values ( $\Delta_{neff}=0.057$ ) is available. Indeed, in the green sector since the index contrast is as large as  $\Delta_n=0.074$  for (1.439,1.513).

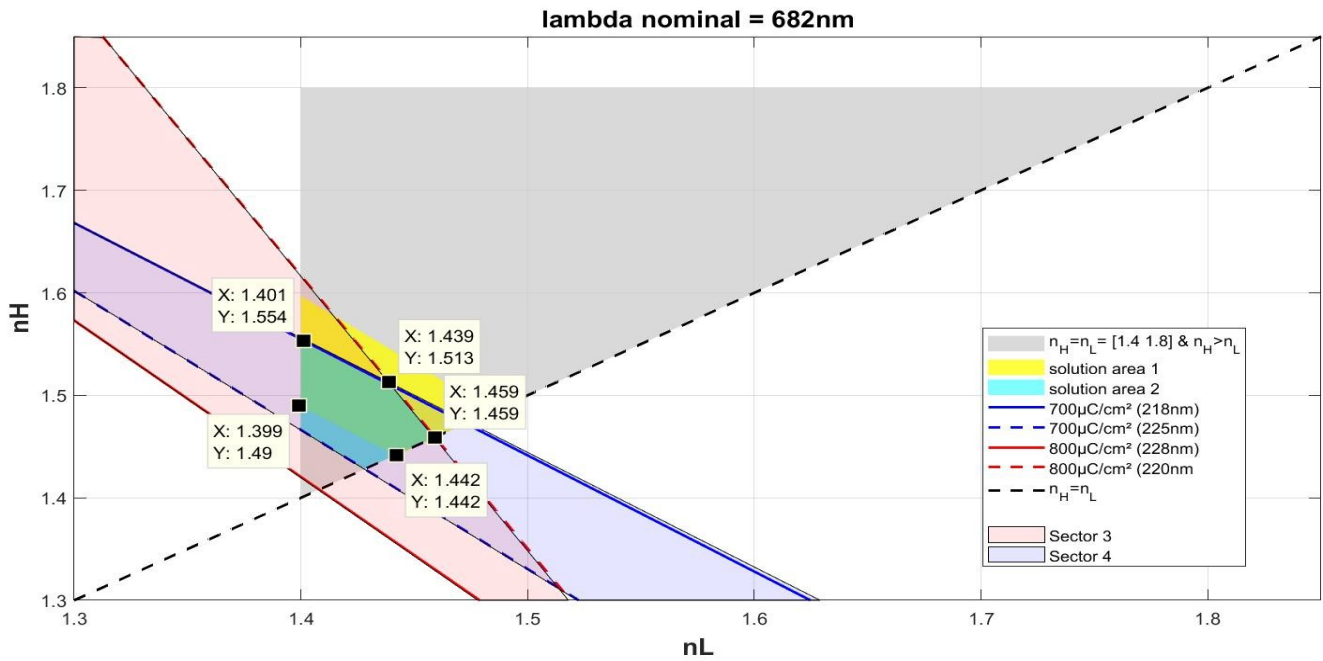
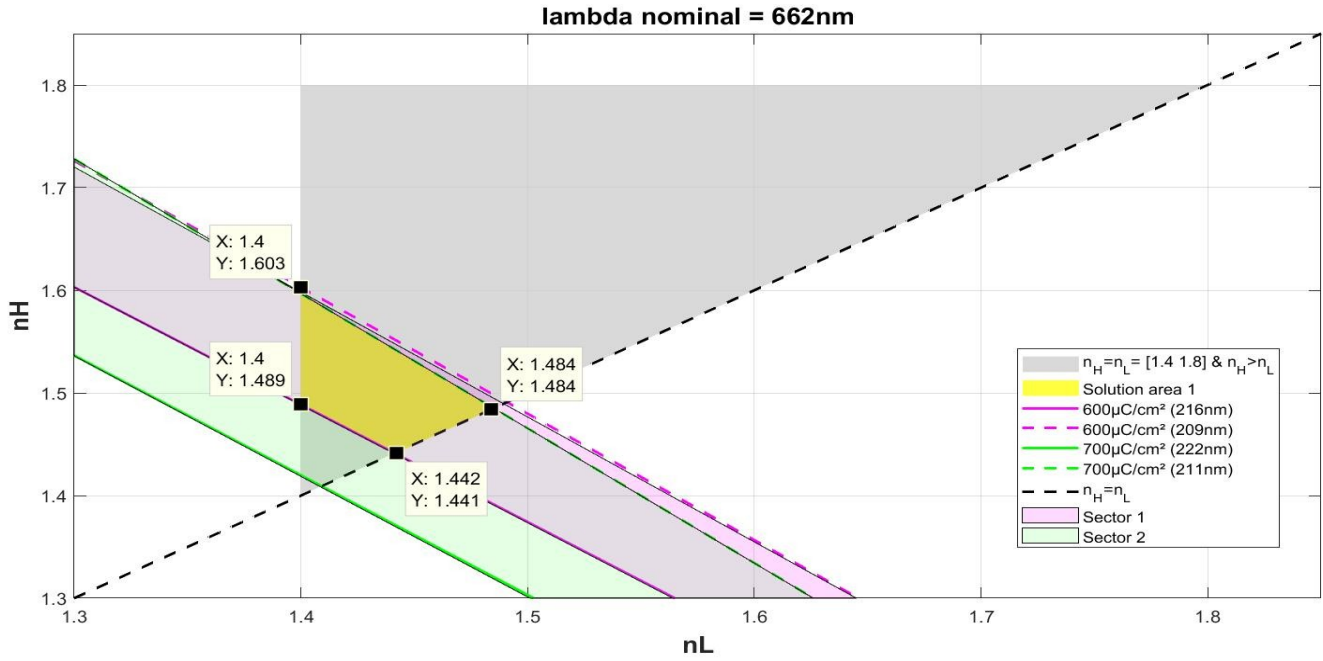


*Figure IV.16: Refractive index estimation*

## IV.4.2. OLED with DFB micro-cavity under high current density

### IV.4.2.1 Sample description

The following experiments are performed with sample #17 containing devices without cavities (column a) used as reference and devices with cavities fabricated according to chapter III section 5 (column b). The device without cavity exhibits measurements resistance  $R_m=6.36\Omega$  and while the devices with cavity exhibits  $R_m=6.55\Omega$ . The organic heterostructure (35 nm of m-MTDATA (HIL), 15 nm of NPD (HTL), 30 nm of Alq3 doped with 2% of DCM as light emitting layer, 5 nm of TPBi (2,20,2''-(1,3,5-Benzinetriyl)-tris(1-phenyl-1-H benzimidazole) as HBL, 25 nm of Alq3 as electron transporting layer, and a final cathode layer of LiF (1 nm)/Al (120 nm)) has been evaporated on the entire sample having an ITO thickness of 140nm. With 2% DCM the peak of electroluminescence is  $\lambda_{EL}=605\text{nm}$ . The cavity grating is based on SiO2 line width of 114nm and inter line spacing of 97nm that exhibited a resonance at 627nm in the optical pumping experiment reported in section IV.4. The reported measurements are performed using the  $100\mu\text{m} \times 100\mu\text{m}$  active area devices; S17\_100a for OLED without cavity and S17\_100b with cavity.

### IV.4.2.2 Measurements

Fig IV.18 presents the measurements acquired using the setup described in section IV.2.2 and compares an OLED without cavity (red line) and OLED with cavity (blue line) measured successively. Using the Avetech AVI-V-HV2A-B pulse driver, electrical excitations are applied with nominal amplitude of 100V and pulse duration of 10ns.

The top figure presents very similar electrical excitation applied to the OLED without cavity (red line) and OLED with cavity (bleu line). For both excitation pulses, we measure the same peak voltages of 93.6V and FWHM pulse durations of 9.3ns.

The middle figure presents the current responses reaching  $I_1=1.3\text{A}$  for OLED without cavity and  $I_2=1.2\text{A}$  for OLED with cavity. In the first case the pulse duration is 8.5ns while the OLED with cavity undergoes a sharp step current at 12.8ns with a rise time of 300ps reducing the pulse duration to 6.2ns. Considering active areas of  $A=10^{-4}\text{cm}^2$ , the OLED without cavity exhibits a current density of  $J_1=13\text{kA/cm}^2$  while the OLED with cavity exhibits a slightly lower current density of  $J_2=12\text{kA/cm}^2$  0.92 times lower.

The bottom figure shows the optical responses measured with the same setup under the same conditions. The OLED without cavity (red line) exhibits a pulse response with a FWHM duration of 8.3ns reaching a plateau value of  $p_1=0.087\text{a.u}$  while the OLED with cavity (blue line) reaches a peak value of  $p_2=0.252\text{a.u}$  2.9 times higher.

#### **How come the OLED with cavity emits 2.9 times more light with 0.92 less current?**

When considering the 112nm width insulating lines of the grating separated by the 95nm width OLED, the effective active area is to be corrected by a factor 0.46, and the current density of OLED with cavity becomes  $26\text{kA cm}^{-2}$  twofold  $J_1$ . Even in this case, the OLED with cavity emits 2.9 times more light with 2 times more current. Which phenomenon explains the nonlinear increase of light emission in the case of OLED with cavity compared to the OLED without cavity? Transparency, amplified



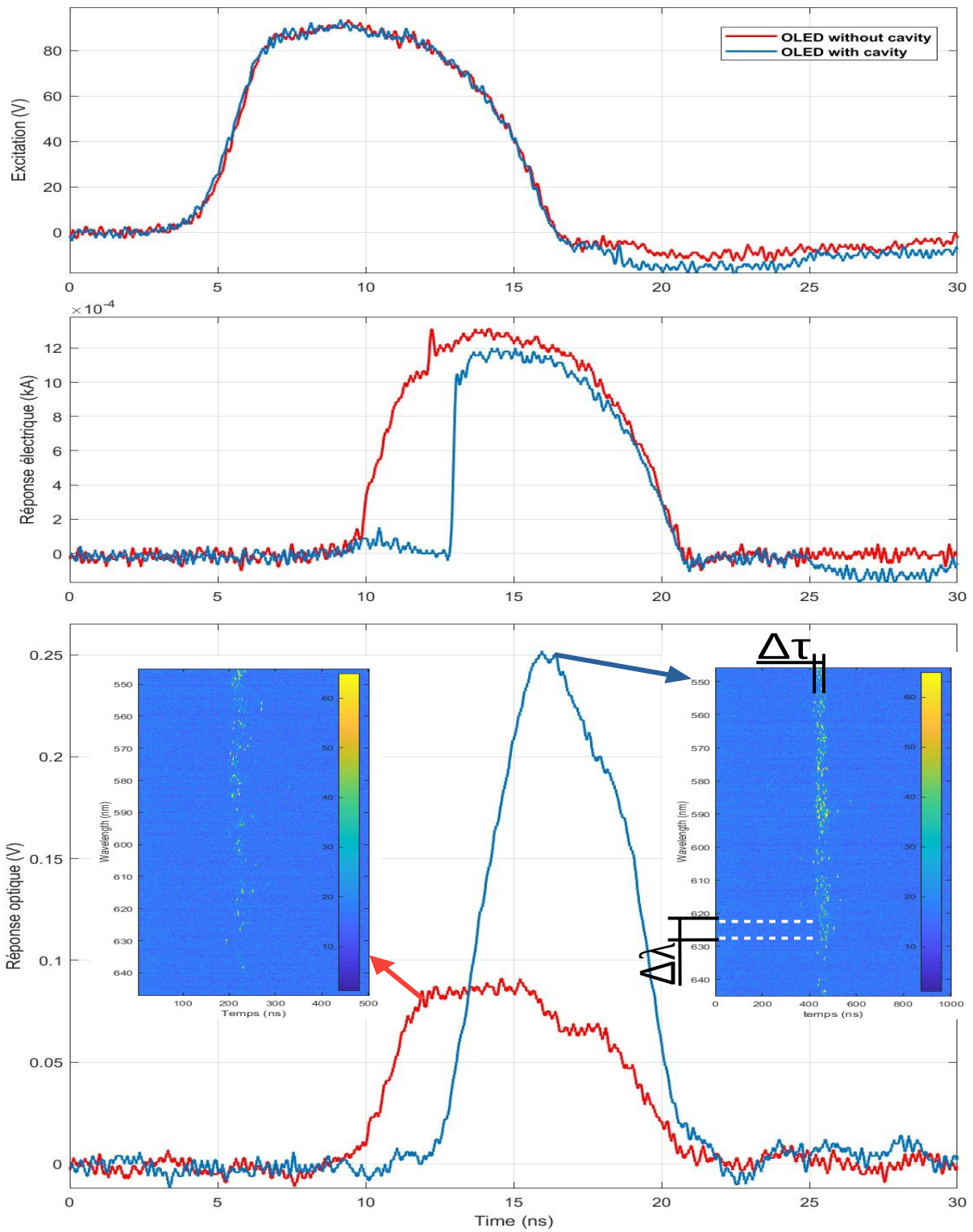


Figure IV.17: Comparison of electrical excitation (top), electrical response (middle) and optical response (bottom) of OLED without cavity (red line) and with cavity (blue line). Insets show the time-resolved optical spectra of OLED without cavity (left) and with cavity (right). OLED with cavity emits 2.9 times more light than the OLED without cavity with 0.92 less current.



spontaneous emission, stimulated emission are three scientific paths to be considered to explain the light increase by 2.9.

Note that the pulse duration difference (6.2ns versus 8.5ns) inducing less charges contributing to the light emission dynamics. With the same pulse durations for OLEDs with and without cavity, more than 2.9 times as much light is expected, thus a stronger non linear effect is to be predicted.

Left and right insets in the lower figure IV.18 present the time-resolved optical spectra of OLEDs without and with cavity respectively with time in horizontal axis and wavelength in the vertical axis. Streak measurements confirm the higher light intensity of OLED with cavity, while the spectra spread over the same wavelength range. This result is not in favor of stimulated emission.

#### IV.4.2.3 Analysis

To analyze our measurement and explain the light increase, we rely in a first step (section IV.4.2.3.1) on the simulations based on the model presented in chapter II. If the simulations do not explain the measurements, the model will have to be improved (section IV.4.2.3.2).

##### IV.4.2.3.1 Simulations with the current model

The scientific approach is in two steps; In the first step, OLED parameters are tuned to fit the measured optical response of the OLED without cavity, using its measured current as an input. Once the best fit parameters are identified, they are considered to also apply to the OLED with cavity, except for the quality factor which is estimated at 6 for the OLED without cavity, and which must re-evaluated for the OLED with cavity. In the second step, the simulations are run with the same parameters and the enhanced quality factor, using the measured current of the OLED with cavity as an input. It is expected to reproduce both experiments with a difference between both calculated optical responses showing the 2.9 factor.

Figure IV.19 presents simulations of polaron, singlet, triplet and photon density dynamics calculated with the current density measured for the OLEDs with (solid and dash lines) and without (dot and dash-dot lines) cavity. The OLEDs parameters were determined in two steps, first an extrapolation of the relevant parameters as a function of the current from the two column of tables IV 1, and then refined by try and error. The final parameters used for these simulations are  $\kappa_{TT}=7.5\times 10^{-12}$ ,  $\kappa_{TDD}=27\times 10^{-12}$ ,  $\kappa_{TP}=8\times 10^{-11}$  and  $\beta=19\times 10^{-7}$ . The quality factor can be estimated from the optically pumped experiment (section IV.4), but knowing there is a difference between the cold quality factor and the one measured from the laser linewidth, we choose to underestimate  $Q_f=500$ .

Figure IV.19.a shows the different pulses in current with the sharp rising flank in the case of the OLED with cavity and the dynamics of the polaron populations both reaching  $N_p=6.6\times 10^{18} cm^{-3}$ . Figure IV.19.b displays the host singlet and triplet densities reaching  $N_T=13\times 10^{18} cm^{-3}$  with and  $N_T=14\times 10^{18} cm^{-3}$  without cavity. In fig.IV.19.c, the magenta dotted curve reaches the dopant singlet density of  $N_{SD}=2.8\times 10^{18} cm^{-3}$  for the case without cavity while the dopant singlet density clamps at  $N_{SD}=2.0\times 10^{18} cm^{-3}$  which is a first signature of lasing phenomenon. The maximum dopant triplet densities reach  $N_{TD}=2.9\times 10^{18} cm^{-3}$  in both cases. Figure IV.19.d and insets present the net amplification (left axis) and the photon densities as optical responses (right axis).

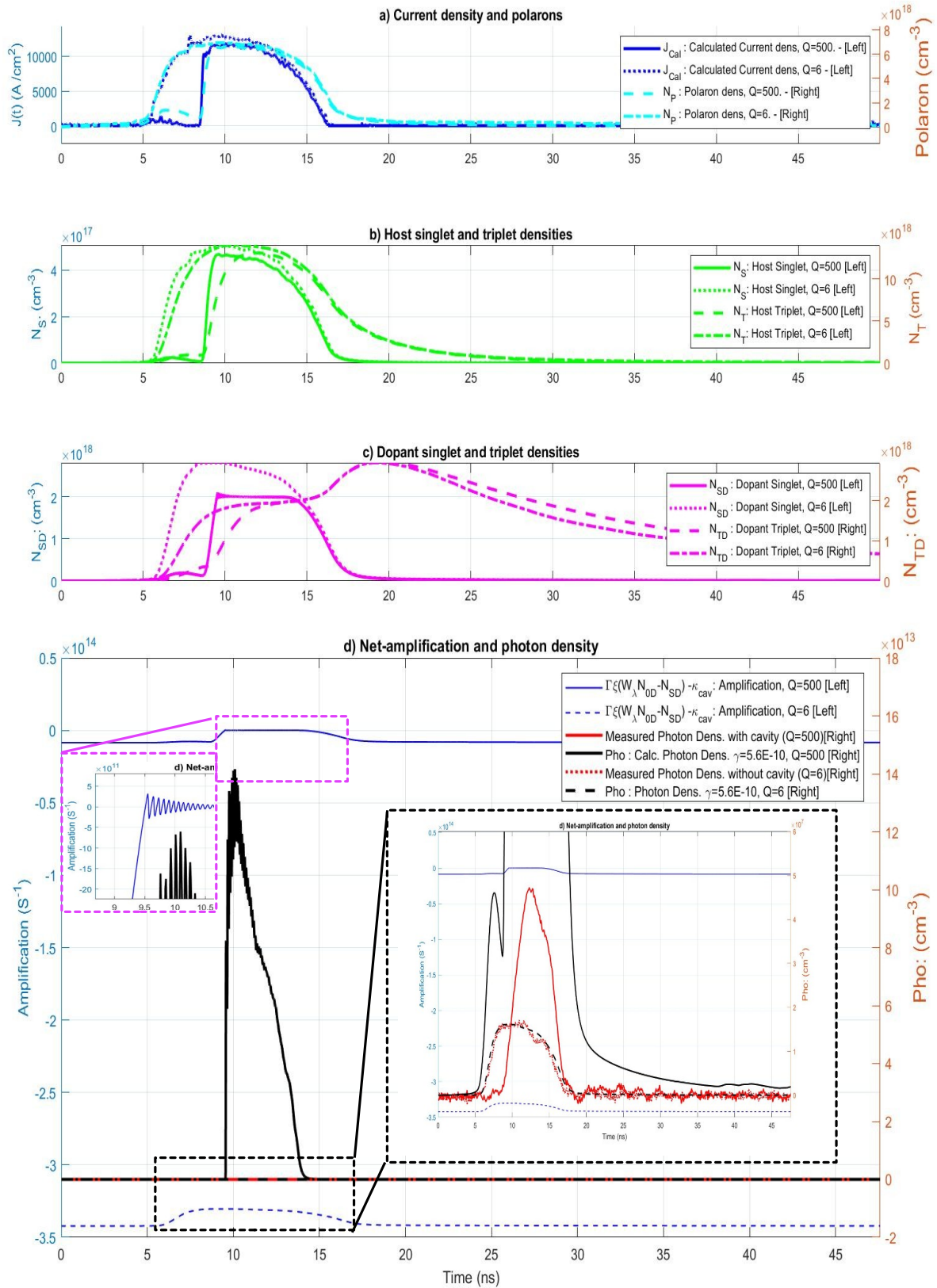


Figure IV.18: Fit of the optical responses for OLEDs with and without cavity based on the model presented in section II.

There is a huge difference between the net amplification and the optical responses of the OLEDs with and without cavity that requires different scales for the different OLEDs justifying the black and magenta insets.

For the OLED without cavity (black right inset), the simulated optical response (black dash curve) calculated with the above mentioned parameters and  $Q_f=6$  fits properly the measurement (red dotted curve) reaching a photon density  $N_{pho}=1.6 \times 10^7 \text{ cm}^{-3}$ . The net amplification  $G_0 = \Gamma \xi (N_{SD} - W N_{0D}) - K_{cav}$  varies between  $-3.4 \times 10^{14} \text{ s}^{-1}$  and  $-3.3 \times 10^{14} \text{ s}^{-1}$ . The good agreement between the measurement and the simulations gives confidence for a faithful prediction for the OLED with cavity.

In contrast, the simulated optical response (black solid line) calculated with the same parameters except  $Q_f=500$ , rises up to a photon density of  $N_{pho-calc}=14 \times 10^{13} \text{ cm}^{-3}$  6 orders of magnitude greater than the case with  $Q_f=6$ . Note that the ratio would be even greater if the quality factor would not have been underestimated. Simulation also shows relaxation oscillations and net-amplification clamped to zero (upper left magenta inset) which are signatures of laser. Clearly, from the simulations it is expected that the OLED with cavity exhibits lasing whereas the measurement (red solid line) shows a very different situation; the photon density reaches only  $N_{pho}=4.5 \times 10^7 \text{ cm}^{-3}$  at maximum, the measured profile of the optical response is very different from the simulated one and no sign of relaxation oscillations appears.

Still, these simulations do not explain the 2.9 factor and probably this case corresponds to an intermediate situation with some light amplification but without reaching the lasing stage. The current model fail to reproduce this intermediate situation and consequently is to be improved.

#### IV.4.2.3.2 Improved model

To explain the 2.9 factor, we develop a scientific approach in 3 steps; firstly, identify the intermediate situation, secondly, upgrade the OLD model and thirdly run simulations and identify the best fit parameters with the measurement.

##### ***Identifying the intermediate situation: the transparency Threshold***

This intermediate situation to be identified, with some light amplification but without reaching the laser stage can be explored using the effective net amplification  $G_{eff}$  assuming additional losses  $A$  :

$$G_{eff} = \Gamma \xi (N_{SD} - W N_{0D} - A) - K_{cav} \quad \text{Eq. (IV.9)}$$

For the sake of clarity in the explanation we introduce:

$$G_{mat} = \Gamma \xi (N_{SD} - W N_{0D} - A) \quad \text{Eq. (IV.10)}$$

It is related to the material proprieties only with  $W N_{0D} + A$  being optical losses in the material. When  $N_{SD}$  increases up to compensate the material losses, a situation is reached where  $G_{mat}=0$ . This situation corresponds to the transparency state. Hence, the threshold of transparency is reached when  $G_{eff} = -K_{cav}$ .

In contrast, the laser threshold is achieved when  $G_{eff} \geq 0$  and in this case  $G_{mat} = K_{cav}$ .

Thus, the intermediate situation with some light amplification but without reaching the lasing stage can be translated mathematically into:

$$-K_{cav} \leq G_{eff} < 0 \quad \text{Eq. (IV.11)}$$

### Upgrade the OLD model: Taking into account polaronic and triplet losses

The nature of the additional losses in the organic materials has been recently investigated by the Adachi's group [10]. They claim that a small excited-state absorption cross-section is important for low thresholds and high stability, because it decreases exciton losses in population inversion. Among the excited states optical absorption, the polaronic and the triplet absorptions are to be considered. We propose to define  $A$  as a combination of polaronic and triplet optical absorptions:

$$A = W_P N_P + W_T N_T + W_{TD} N_{TD} \quad \text{Eq. (IV.12)}$$

$W_P$ ,  $W_T$  and  $W_{TD}$  are unknown quantities to be quantified in our case by fitting simulations and measurements.

Introducing the new expression of the losses  $A$  in the effective net amplification  $G_{eff}$  it reads

$$G_{eff} = \xi \Gamma (N_{SD} - W N_{0D} - W_P N_P - W_T N_T - W_{TD} N_{TD}) - K_{cav} \quad \text{Eq. (IV.13)}$$

The Organic laser diode model can thus be upgraded with the following photonic equation

$$\frac{dP_{HO}}{dt} = \beta_{sp} \kappa_{SD} N_{SD} + \left[ \xi \Gamma (N_{SD} - W N_{0D} - W_P N_P - W_T N_T - W_{TD} N_{TD}) - K_{cav} \right] P_{HO} \quad \text{Eq. (IV.14)}$$

This photonic equation replace the equation II.45 while other equations of the OLD dynamical model remain unchanged.

### Simulation with the upgraded model

This upgraded model is implemented in the Matlab function "HostDopantSystemV3A.m" (see Appendix 1) and solved as stiff differential equations using the variable order method ODE15s.

To run the simulation values should be attributed to  $W_T$ ,  $W_P$  and  $W_{TD}$ . To our best knowledge, no value exists in the literature for Alq3:DCM and therefore we rely on the transparency and the laser conditions  $-K_{cav} \leq G_{eff} < 0$  to estimate the parameters. The losses  $A$  are framed by two expressions:

$$N_{SD} - W N_{0D} - \frac{K_{CAV}}{\xi M_E} \leq A < N_{SD} - W N_{0D}$$

If the losses  $A$  are replaced by a single contribution term  $W_x N_x$ , with  $x \in \{P, T, TD\}$ , the parameter reads:

$$\frac{1}{N_x} \left( N_{SD} - W N_{0D} - \frac{k_{cav}}{\xi M_E} \right) \leq W_x \leq \frac{1}{N_x} (N_{SD} - W N_{0D})$$

The  $W_x$  parameters estimated on the basis of the population density computed in the case without cavity are presented in table.IV 7.

<i>Table IV 7: Estimation of the <math>w_x</math> parameters for the excitedstate optical absorption</i> $N_{0D} = 4.2 \times 10^{19} \text{ cm}^{-3}$ $N_{SD} = 2.8 \times 10^{18} \text{ cm}^{-3}$ $N_P = 6.6 \times 10^{18} \text{ cm}^{-3}$ , $N_T = 14 \times 10^{18} \text{ cm}^{-3}$ and $N_{TD} = 2.9 \times 10^{18} \text{ cm}^{-3}$		
	$Q_f = 500$ $k_{cav} = 4 \times 10^{12}$	$Q_f = 1000$ $k_{cav} = 2 \times 10^{12}$
$W_P$	$0.10 \leq W_P \leq 0.26$	$0.18 \leq W_P \leq 0.26$
$W_T$	$0.05 \leq W_T \leq 0.12$	$0.08 \leq W_T \leq 0.12$
$W_{TD}$	$0.24 \leq W_{TD} \leq 0.59$	$0.41 \leq W_{TD} \leq 0.59$

Note that it is very unlikely that an optical absorption from the dopant triplet level exists occurs because from the dopant T1 level bellow the dopant singlet state it is expected that absorption wavelength is shifted away to longer wavelength than the emission spectrum.

Note also that the values for  $W_T$ ,  $W_P$  and  $W_{TD}$  are calculated with population densities that are sensitive to the parameters used for the simulation. Therefore, these values are to be considered only as a starting point for the simulation, and to be refined by try-and error method.

The best fit presented in fig IV.1 is obtained with the parameters presented in table IV 8.

<i>Table IV 8: Upgraded OLD model parameters used to simulate experiment OLED with cavity</i>	
Parameter symbols	Parameter values for OLED with cavity
$\kappa_{TT}$	$7.5 \times 10^{-12} \text{ cm}^3 \text{ s}^{-1}$
$\kappa_{TTD}$	$27 \times 10^{-12} \text{ cm}^3 \text{ s}^{-1}$
$\kappa_{TP}$	$34 \times 10^{-11} \text{ cm}^3 \text{ s}^{-1}$
$W$	$2.6 \times 10^{-2}$
$W_T$	$16.8 \times 10^{-2}$
$W_P$	$31.2 \times 10^{-2}$
$\beta$	$0.43 \times 10^{-7}$
$Q_f$	500

With the same signal in current as before used as an input for the simulation presented in fig IV.1.a, the polaron dynamics (cyan dash line) remain unchanged compare to previous simulations and reach again  $N_P=6.6 \times 10^{18} \text{ cm}^{-3}$ . In fig IV.1.b, with the host singlet (green solid line) reaching  $N_S=5.2 \times 10^{17} \text{ cm}^{-3}$  and the host triplets (green dash line) reaching  $N_T=3.8 \times 10^{18} \text{ cm}^{-3}$ , the density populations are different from those in the tableIV 7. This is the reason why  $W_T$  and  $W_P$  are different from the values of tableIV 7. Figure IV.1.c shows the dopant singlet (magenta solid line) reaching  $N_{SD}=3.8 \times 10^{18} \text{ cm}^{-3}$  and the dopant triplets (magenta dash line) reaching  $N_{TD}=5.6 \times 10^{17} \text{ cm}^{-3}$  again the triplet population is different from previous simulation. Figure IV.1.d displays  $G_{eff}$  the effective net amplification (blue dash line) as defined in Eq(IV.9) a blue horizontal solid line indicating the transparency threshold for  $Q_f=500$ , the measured photon density (red solid line) and the calculated photon density (black solid line). The calculated photon density profile fits the measurement reproducing the pulse duration and shape of the measurement. The calculated photon density reaches  $N_{pho-calc}=4.7 \times 10^7 \text{ cm}^{-3}$  as in the measurement, 2.9 times the amplitude measured with the OLED without cavity. By a try-and-error method we have identified parameters that allow to reproduce the measurement fairly accurately by simulation. With the same parameters, the simulation shows that during the pulse, the effective net amplification exceeds the transparency threshold while remaining strictly negative:  $-\kappa_{cav}(Q_f=500) < G_{eff} < 0$ . Both conditions on the fair fit and on the transparency being fulfilled, we believe that it is very likely that we have reached the transparency threshold with our OLED with DFB cavity. The ratio of the spontaneous emission factors of the OLED with optical cavity by the one without cavity  $\beta_{with}/\beta_{without}=2\%$  is an indication that the grating has modified the conditions on light extraction from the device.

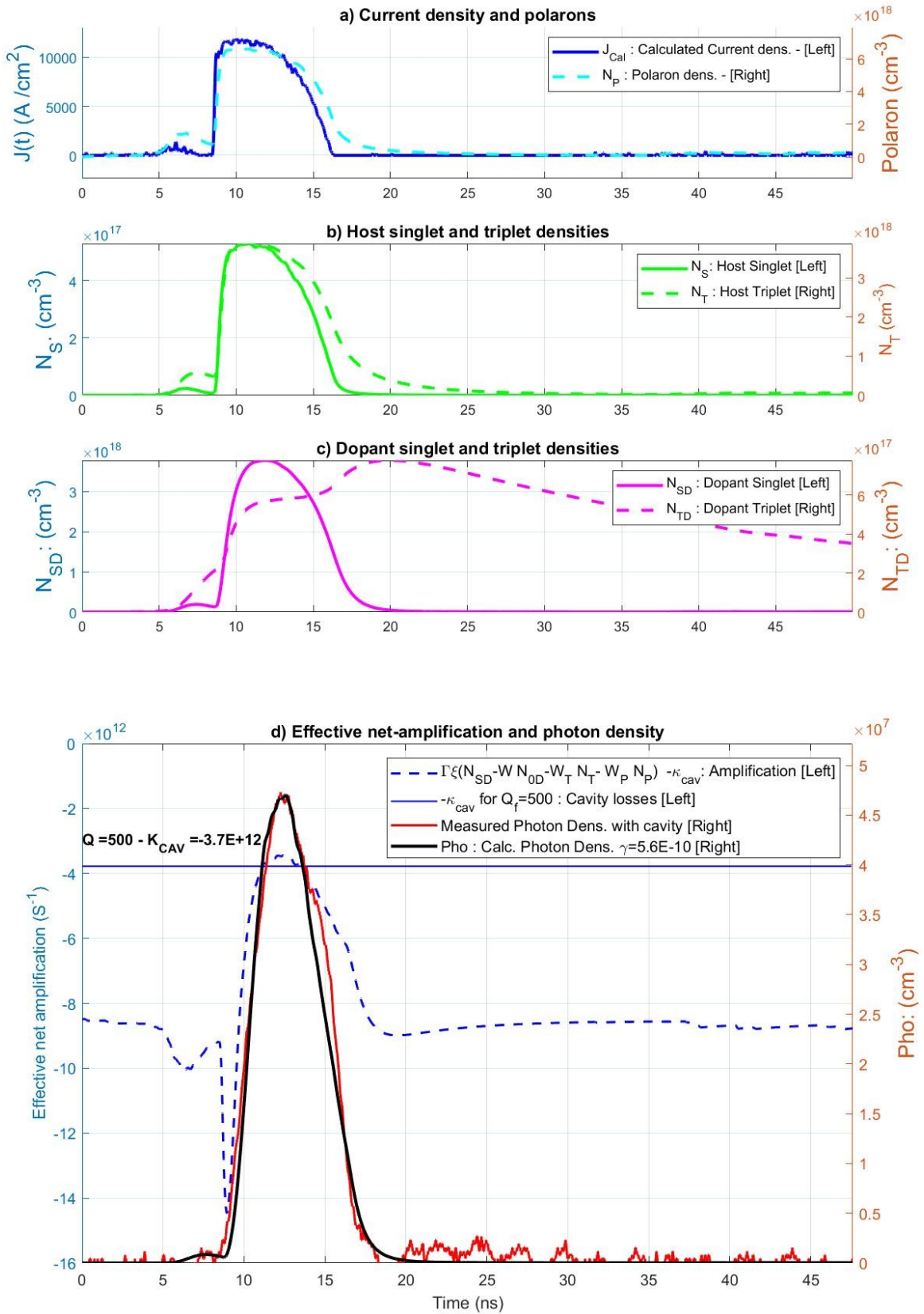


Figure IV.19: Fit of the optical responses for OLEDs with and without cavity based on the upgraded model

The fact that the ratio is less than one shows that the increase in light intensity by a factor of 2.9 obtained by the simulation in accordance with the measurement is not the result of the artificial increase in the spontaneous emission factor. In fact, the 2.9 times more intense light intensity obtained corresponds to an increase in the second right-hand term of the photonic equation, that is, the term of laser amplification. The fact that the factor is only 2% compared to the six orders of magnitude observed during the simulation of the laser effect Figure 1.3 indicates that it is not an artificial attenuation either. The grating disturb the way of light extracted from OLED, and we assume this is the reason why the  $\beta$  factor has to be changed.

#### **IV.4.2.4 Conclusion**

This chapter was dedicated to the electrical and optical experimental characterizations of OLEDs with micro-cavities fabricated according to the process presented in chapter III. The scientific approach consisted of six stages; first, the development and improvement of a specific characterization setup, allowing in a second stage the electrical and optical characterization of OLED without cavity. It leads in a third stage to the comparison of the measurement and the simulation based on the laser dynamics theory of OLED proposed in chapter II. In a fourth stage, the study of the dynamics was expanded to the limits of the OLED responses to ultrashort electrical pulses in the nanosecond and sub-nanosecond time scale. In the fifth stage, the micro-cavity was characterize under an optical pumping to check for the possibility of lasing before integration in OLEDs for electrical and optical characterization as a sixth stage.

In a first stage, a specific characterization setup was required to perform time-resolved data acquisitions of electrical, optical signals as well as optical spectra in the nano-second and sub-nanosecond time scales. We improved a time-resolved measurement setup based on a pre-existing microwave probe station [11] coupled to a specifically-developed light collection system allowing simultaneous measurements of 1.5GHz bandwidth optical signals and optical spectra using a spectrophotometer and a 20ps resolute streak-camera which is an unprecedented setup at this time scale for OLEDs. Another improvement of this setup was the automation using Matlab to perform single shot acquisitions.

This setup was then used in a second stage, to investigate first the maximum current density across OLEDs of different sizes leading to break-down. Current density in excess of 25kA/cm<sup>2</sup> as plateau value and 30kA/cm<sup>2</sup> as peak value was demonstrated in a quasi reproducible manner with 25x100 $\mu$ m<sup>2</sup> OLEDs under pulsed electrical excitation of 10.5ns in duration and 40-60V in amplitude. These current-densities better than the state-of-the-art, corresponding to almost 5 times the best current-densities obtained by Chime, offer an unrivaled electrical excitation budget giving confidence for the next stages that the laser threshold can be met.

In a third stage, measurements acquired under 20ns pulsed electrical excitation were then compared to simulations based on the model proposed in chapter II. Signals in current with maximum current densities of 400A/cm<sup>2</sup> and 8.8kA/cm<sup>2</sup> acquired during the measurements were used as inputs to calculate the dynamics of polaron, singlets and triplets densities of both host and dopant. Finally, we identified material parameters finely tuned to match the computed photon density dynamics with the measured optical responses. This demonstrates fair validity of the proposed model and open the possibility to predict spontaneous and stimulated emission in organic optoelectronic devices.

In a fourth stage, the time-resolved measurement setup has then been used to investigate experimentally the limits of optical responses of OLED submitted to ultra-short electrical pulses in the pico-second time scale. It has been reported that OLED with Alq3 as light emitter shows optical responses as short as 200ps in duration at the noise limit, while F8:F8BT polymer OLED exhibits 1.35ns in duration when submitted to 400ps electrical pulses. These results in the picosecond range constitute a world premiere that rise numerous questions among which how come the optical response is 15-fold short in duration than the Alq3 fluorescence lifetime of 12ns. This is because organic semiconductors exhibit specific non-linear properties; firstly the Langevin recombination rate follows the Poole-Frenkel law for mobility and therefore increases exponentially with the excitation voltage applied to the OLED [12]. Hence, the time constant varies non-linearly with the applied voltage. It has two effects; boosting the spontaneous emission with an abrupt rising flank at the pulse onset and shortening the fall time at the end of the pulse. A second non-linear effect results from polarons that exist only under electrical excitation and that participate to the dynamics modifying the decay time. Therefore, the resulting effective decay time called electroluminescence lifetime differs significantly from the fluorescence lifetime [9]. Theoretical results are in agreement with some experimental results. While some other experimental results require more theoretical explanations, this primary results open the possibility for a new generation of ultra-fast optoelectronic components based on organic semiconductors[9].

As a preliminary step before integration in OLEDs and investigation of a full device, we intended in a fifth stage, to check DFB microcavities for possibilities of lasing. Multiple section of first and second order DFB gratings with different periods and different e-beam doses covered with Alq3:DCM 2% were optically pumped and their light emissions measured for different pump intensities. Lasing was observed for a limited number of DFB patterns and doses notably those made with 112nm and 96nm resulting in an emission at 627nm with a laser threshold of 9.7 $\mu$ J/cm<sup>2</sup>. This result gives confidence that organic laser diode can be achieved with the integration of this cavity in organic hetero-structure.

In a final step, we investigated a 100x100 $\mu$ m<sup>2</sup> Alq3:DCM(2%) based OLED implemented with a multiple sections of first and second order DFB microcavity as characterized previously and submitted it to a 13kA/cm<sup>2</sup>, 20ns electrical pulses. Its optical response was compared with that of a reference OLED without cavity submitted to the same excitation. We observe a large emission spectra and an enhancement of the light intensity by a factor 2.9 compared to the reference OLED, while the laser dynamics model predicts lasing and an enhancement of the light intensity by six orders of magnitude. Our suggestion to explain this phenomenon is that the transparency state has been reached, while the laser threshold is still to be reached. To confirm this explanation, an upgraded model has been proposed that takes into account extra losses issued from the excited-state optical absorptions such as triplet and polaronic absorptions. Based on the upgraded model, the simulations are able first to reproduce fairly the profile of the measured optical response and second to indicate the effective net amplification above the transparency threshold and below the laser threshold. Reaching the transparency threshold with Alq3:DCM is a world premiere knowing that an indication of lasing was only reported by the Adachi's group with another organic material [13].

We believe that the laser threshold can be reached with two improvements; firstly, the resonance wavelength is to be finely tuned with the maximum emission wavelength of OLED and secondly, the gain of the material is to be optimized with a better control of the dopant concentration.



## References

- [1] A.C. Chime, A.P.A. Fischer, S. Bensmida, J. Solard, M. Chakaroun, H. Nkwawo, “Analysis of optical and electrical responses of m-OLED with metallized ITO coplanar waveguide electrodes submitted to nanosecond electrical pulses”, IEEE Trans. Electron. Dev. 66 (5) (May 2019) 2282e2289, DOI:[10.1109/TED.2019.2905839](https://doi.org/10.1109/TED.2019.2905839).
- [2] Lei Zeng, et al., Electrical and optical impulse response of high-speed micro- OLEDs under UltraShort pulse excitation, IEEE Trans. Electron. Dev. 64 (7) (Jul. 2017) 2942e2948, DOI: [10.1109/TED.2017.2706723](https://doi.org/10.1109/TED.2017.2706723).
- [3] A. C. Chime, S. Bensmida, M. Chakaroun, M. W. Lee, H. Nkwawo, and A. P. A. Fischer, “Electrical modelling and design of ultra-fast micro-OLED with coplanar wave-guided electrodes in ON-OFF regime,” Organic Electronics, vol. 56, pp. 284–290, May 2018, DOI: [10.1016/j.orgel.2017.12.026](https://doi.org/10.1016/j.orgel.2017.12.026).
- [4] O. G. Peterson, S. A. Tuccio, and B. B. Snavely, “cw OPERATION OF AN ORGANIC DYE SOLUTION LASER”, Appl. Phys. Lett. 17, 245 (1970) , DOI: [10.1063/1.1653384](https://doi.org/10.1063/1.1653384)
- [5] D. Kasemann, R. Brückner, H. Fröb, and K. Leo, “Organic light-emitting diodes under high currents explored by transient electroluminescence on the nanosecond scale”, Phys. Rev. B 84, 115208 – Published 20 September 2011
- [6] F. Torricelli and L. Colalongo, "Unified Mobility Model for Disordered Organic Semiconductors," in IEEE Electron Device Letters, vol. 30, no. 10, pp. 1048-1050, Oct. 2009, DOI: [10.1109/LED.2009.2027998](https://doi.org/10.1109/LED.2009.2027998).
- [7] P N Murgatroyd, “Theory of space-charge-limited current enhanced by Frenkel effect”, J. Phys. D: Appl. Phys. 3 151, 1970
- [8] C. Gartner, C. Karnutsch, C. Pflumm, and U. Lemmer, “Numerical Device Simulation of Double-Heterostructure Organic Laser Diodes Including Current-Induced Absorption Processes,” IEEE Journal of Quantum Electronics, vol. 43, no. 11, pp. 1006–1017, Nov. 2007, DOI: [10.1109/JQE.2007.905021](https://doi.org/10.1109/JQE.2007.905021).
- [9] D. Lenstra, A. Fischer, A. Ouirimi, A. C. Chime, N. Loganathan, and M. Chakaroun, “Ultra-short optical pulse generation and laser perspective in an Alq3 based micro OLED,” in Organic Electronics and Photonics: Fundamentals and Devices III, May 2022, vol. 12149, p. 1214902. DOI: [10.1117/12.2621432](https://doi.org/10.1117/12.2621432).
- [10] Y. Oyama et al., “Design Strategy for Robust Organic Semiconductor Laser Dyes,” ACS Materials Lett., vol. 2, no. 2, pp. 161–167, Feb. 2020, DOI: [10.1021/acsmaterialslett.9b00536](https://doi.org/10.1021/acsmaterialslett.9b00536).
- [11] CHIME Alex Chamberlain, “Etude theorique et experimentale de micro-OLEDs rapides sur electrodes coplanaires en regime d'impulsions a haute densite de courant”, Thesis from Universite Paris 13, Decembre 2017
- [12] C. Gartner, C. Karnutsch, C. Pflumm, and U. Lemmer, “Numerical Device Simulation of Double-Heterostructure Organic Laser Diodes Including Current-Induced Absorption Processes,” IEEE Journal of Quantum Electronics, vol. 43, no. 11, pp. 1006–1017, Nov. 2007, DOI:[10.1109/JQE.2007.905021](https://doi.org/10.1109/JQE.2007.905021).
- [13] A. S. D. Sandanayaka et al., “Indication of current-injection lasing from an organic semiconductor,” Appl. Phys. Express, vol. 12, no. 6, p. 061010, May 2019, DOI: [10.7567/1882-0786/ab1b90](https://doi.org/10.7567/1882-0786/ab1b90)

## **General conclusion**



# General conclusion

## Summary

By reaching the market stage with efficient OLEDs used in majority of smartphone displays, the funding of academic research on the OLED topic have faded. This is why prominent researchers like Stephen Forrest questioned the future of organic optoelectronics with “What’s beyond OLED displays?” [1]. At the beginning of this thesis in October 2018, the only organic light sources still to be demonstrated was the organic laser diode. Indeed, until 2019, solid-state organic lasers have been demonstrated under optical pumping exclusively. Only in May 2019, 8 months after the beginning of this thesis, an indication of current-injection lasing from an organic semiconductor was reported by the Adachi’s group [2]. Another aspect of the context of this thesis was that OLEDs were considered (apart few exceptions[3, 4, 5]) as slow devices with turn-on time constants in the order of a few milliseconds. However, previous results by Chime demonstrated on the contrary that OLED dynamics is in the nanosecond range as fast as inorganic LEDs[6]. This was confirmed, in the middle of this work, by Samuel’s group in Saint Andrews reporting high-speed OLEDs with 200MHz bandwidth used to transmit data and allowing high-speed organic optoelectronic. It opens a bright future for OLEDs in the field of light communication [7].

This thesis took place in the previous double contexts and as such addressed a topical research topic; its objectives was to design and fabricate a distributed feedback micro-cavity and integrated it with a high-speed coplanar waveguide organic light emitting diode, before characterizing it in a time-resolved manner in nanosecond time scale to progress towards the organic laser diode. Our scientific approach took into account challenges at the electrical, material and optical levels.

At the electrical level, we targeted current density above  $10\text{kA}/\text{cm}^2$  in low charge mobilities  $\pi$ -conjugated organic semiconductors in order to achieve the laser threshold. This targeted twice the state of the art current density.

At the material level, we aimed for a red gain medium offering a high effective net amplification taking into account both the laser gain coefficient and the residual absorption.

At the optical level, the challenge was to integrate a high quality factor micro cavity in the OLED in spite of the low index contrast. The integrated micro cavity was expected not to disturb the OLED electrical behavior

This thesis was first intended to be an experimental work, mainly in a clean room environment, but to cope with the electrical, material and optical challenges, several other skills had to be implemented; modeling (electrical and laser dynamics), simulation programming in Matlab (electrical, laser dynamics, transmittance using the transfer matrix formalism), instrumentation (LabView, Matlab), mounting a measurement setup,...

In the first chapter, we first reviewed the properties of organic semiconductors and OLEDs before conducting a bibliographic study on high-speed OLED and optically pumped organic and dye lasers. We inventoried the different types of organic laser cavities as well as the red emitting gain media reported in the literature. From the bibliographic studies and previous researches conducted in our group, we have chosen to use Guest-host systems with DCM, DCM2 or DCJTb as dopants. These

Guest-host system was to be used as emitting layers in OLEDs deposited on CPW electrodes that allow current densities of the order of  $\text{kA}/\text{cm}^2$  under pulsed excitation. The reduction of OLED size down to the micrometric range unlock access to OLED dynamics at the fluorescence lifetime scale in the nanosecond time range. We choose the distributed feedback micro cavity because it is integrable and allows Q-factor up to 6400<sup>[8]</sup>.

In Chapter II, we modeled, simulated and designed our device at the electrical, material and optical levels.

At the electrical level, we upgraded the dynamical electric model based on coupled differential equations to remove the dependence on the dynamical resistance. This model takes into account leakage resistance and scope impedance. It predicts that electrical time constant equal or shorter than 100 ps are possible and that current density up to  $50 \text{ kA}/\text{cm}^2$  can be reached. We deduced Three electrical design rules; one based on the time constant expression, one on the maximum current density and another one on expressions for CPW electrodes. They induce conditions on the OLED capacitance ( $C < 5 \text{ pF}$ ) which is achievable via the reduction of the active area  $A$ , and on the measurement and serial resistances as well as on the electrode geometry.

At the material level, our conclusions are inherited from the new organic laser diode dynamical model based on 6 coupled differential equations that include electrical excitation, polarons, singlet and triplet populations of host and dopant and a photonic equation. Based on this model, we have launched simulations that use a set of more than 20 parameters reflecting both the material properties including Langevin recombination, singlet lifetime, triplet lifetime, STA, SPA, TTA, ISC, ... and cavity properties including photon cavity lifetime, confinement factors... We have proposed the concept of residual absorption to taking into account the frequency-selective limited reabsorption of photons by the Stoke-shifted ground state population. Using this model and parameters extracted from the literature for DCM as a guest in  $\text{Alq}_3$  as a host, we predicted that stimulated emission occurs under pulse electrical excitation during a time window of 7ns after turn on provided the quality factor is  $Q \geq 1800$ . The laser threshold is predicted to be  $3.5 \text{ kA}/\text{cm}^2$ . From the laser dynamic model, we established two supplementary material design rules based on the net amplification calculated from residual absorption and laser gain coefficient. We decided to choose DCM with a concentration of 2% in  $\text{Alq}_3$  knowing that DCJTb at 4% is an interesting alternative.

At the optical level, our conclusions on the laser cavity are based on an optical waveguide analysis and on the transfer matrix method. Based on the optical waveguide analysis we identified an optical design rule stating that with an ITO layer as thin as  $t_{L1} = 50 \text{ nm}$  and an Organic layer as thick as  $t_{L2} = 200 \text{ nm}$  the confinement factor can be maximized to  $\Gamma = 0.565$ .

Using the transfer matrix method, we identified three conditions on the quarter-wavelength DFB laser micro cavity leading to three supplementary optical design rules; firstly, to enlarge the bandwidth of the DFB reflectance (forbidden bandgap) so as to cover the largest part of the electroluminescence spectrum of the gain medium, to maximize the index contrast, we choose to decrease the ITO thickness to 55nm and increase the organic and  $\text{SiO}_2$  thickness to 125nm and 300nm respectively. For emission at 605nm and with effective indices, the recommended quarter-wavelength spacings and lines are  $\Lambda_1 = 95 \text{ nm}$  and  $\Lambda_2 = 99 \text{ nm}$  respectively. Secondly, to maximize the quality factors ideally as high as several thousands, the number of pairs of quarter-wavelength spacing and lines is to be  $N \geq 66$

and we choose  $N=80$ . Thirdly, to both induce a resonance wavelength in the forbidden bandgap and to couple light in the direction perpendicular to the plan of the cavity for measurement, multiple half-wavelength line defects ( $M < 10$ ) are introduced between the quarter-wavelength mirrors.

In chapter III, we elaborated a process of fabrication consisting of 33 steps gathered in 3 sub-process for the fabrication of the coplanar waveguided electrodes, on top of which we patterned  $\mu$ -cavities before OLEDs were deposited.

We fabricated coplanar waveguided electrodes by etching and gold-metaling 140nm thick ITO layer with 1500 $\mu$ m large central lines separated from ground planes by a gap  $G=316\mu$ m resulting in 50 $\Omega$  characteristic impedance. We fabricated three sizes of OLED (100X100 $\mu$ m<sup>2</sup>, 50X50 $\mu$ m<sup>2</sup>, 25x30 $\mu$ m<sup>2</sup>) with built-in measurement resistances  $R_m \sim 5\Omega$ , with serial resistance  $R_s \sim 43\Omega$ ,  $\sim 61\Omega$ , and  $\sim 105\Omega$  and parasitic capacitance of 3pF, 0.7pF, and 0.2pF. The resulting electrical time constants are estimated about 144ps, 46ps, and 22ps much below 1ns. These were first indications that we fabricated high-speed OLED electrodes with electrical times constants potentially better than the state of the art [9]. On the intermediate ends of the CPW electrodes terminated with unmetallized 100 $\mu$ m, 50 $\mu$ m, or 25 $\mu$ m large and 800 $\mu$ m long ITO arms eventually thinned down to 50nm, we implemented DFB patterns fabricated by e-beam lithography in 300nm thick hydrogen silsesquioxane (HSQ) electro-sensitive resist. The micro cavity pattern consisted of a first-order grating interrupted with second-order gratings. For a cavity resonance of  $\lambda=605$ nm, the 300nm thick HSQ first-order gratings was made with  $\Lambda_1=101$ nm wide quarter-wavelength lines spaced from each other with  $\Lambda_{1s}=99$ nm wide quarter-wavelength spacing while second-order grating are with  $\Lambda_2=202$ nm and  $\Lambda_{2d}=198$ nm. The resolution of SEM in the nanometer scale, and most of all the indirect access on the effective index induced large uncertainty on the resonance which remains challenging to target a specified Bragg resonance wavelength. OLED deposition on top of the electrodes with the  $\mu$ -cavities was accomplished with fluorescent organic materials and DCM as red emitter in a guest-host configuration with Alq3. The organic heterostructure was deposited through a hollow mask before the metalization mask is aligned manually in glove box with an accuracy better than 50 $\mu$ m using special alignment tools and markers developed specifically in framework of this thesis.

In chapter IV, we conducted time-resolved measurements of electrical, optical and spectral responses of the previously fabricated devices following a scientific approach in six stages;

In a first stage, we improved a pre-existing microwave probe station by adding a light collection system to develop a specific measurement setup performing single shot time-resolved data acquisitions of electrical, optical signals. This setup allowing simultaneous measurements of 1.5GHz bandwidth optical signals and optical spectra using a spectrophotometer and a 20ps resolute streak-camera is an unprecedented setup at this time scale for OLEDs characterization.

In a second stage, using the setup we measured break-down OLED current densities up to 25kA/cm<sup>2</sup> as plateau value and 30kA/cm<sup>2</sup> as peak value close to the theoretical predictions. These current-densities, five times better than the state-of-the-art for an OLED[10] and two times better than for a single organic layer [11], constitute a world premiere and offer an unrivaled electrical excitation budget to reach the laser threshold.

In a third stage, we validated the organic laser diode dynamical model by identifying material parameters finely tuned to fit the calculated photon densities with the measured optical responses

acquired under 20ns pulsed electrical excitation with first a current densities of 400A/cm<sup>2</sup> and then 8.8kA/cm<sup>2</sup>. This validation enabled the possibility to predict spontaneous and stimulated emission in organic optoelectronic devices.

In a fourth stage, the limits in pulse durations of OLED optical responses was investigated experimentally. We observed pulse durations as short as 200ps in small molecule Alq3 based OLED and 1.35ns with polymer F8:F8BT based OLED. While some of these findings are theoretically supported by non-linear properties, more experimental results and theoretical explanations are necessary. These results in the picosecond range constitute a world premiere opening the possibility for a new generation of ultra-fast optoelectronic components based on organic semiconductors.

In a fifth stage, we checked the properties of DFB micro-cavities and possibilities of lasing. Under optical pumping, lasing was observed for a limited number of DFB patterns covered with Alq3 doped by 2% of DCM resulting in an emission at 627nm with a laser threshold of 9.7μJ/cm<sup>2</sup>. This result gave confidence that stimulated emission under electrical excitation can be achieved by integrating such a DFB micro-cavity in an OLED.

In a final step, we investigated Alq3:DCM(2%) based OLEDs implemented with DFB microcavity and compared it with a reference OLED without cavity submitted to the same electrical excitation. We observed a large emission spectra and an enhancement of the light intensity by a factor 2.9 compared to the reference OLED. If the simulation based on the laser dynamics model reproduced the optical response of the reference OLED, it was not able to explain the 2.9 factor and instead predicted laser emission. To explore the light intensity enhancement, the model was to be upgraded with excited state optical absorptions. Using this upgrading model, we reproduced the 2.9 times light intensity enhancement with the measured current density of 13kA/cm<sup>2</sup> as an input. It follows from these results that the OLED with a DFB micro-cavity very likely reached a state between the transparency threshold and the laser threshold. Reaching the transparency threshold with Alq3:DCM under electrical excitation is a world premiere knowing that an indication of lasing was reported only by the Adachi's group with another organic material [12].

We believe that the laser threshold can be fully reached with several improvements presented in the next section.

## Perspectives

In order to provide a comprehensive list of improvements, we propose the following analysis grid taking into account the three electrical, material and optical levels and the three skills (Model & simulation, fabrication and instrumentation & characterization).

At the electrical level, a better understanding of the OLED behaviors in ultra-short pulsed regime could benefit from a model taking into account the dynamics of spatial distribution of polarons inside the organic layers and at their interfaces. This could be useful to explain current blocking and sharp rising flanks.

In terms of micro-fabrication, the possibility of making smaller electrodes (<25μm) without increasing the serial resistances is hampered by the need for a micrometric hollow mask alignment system. The CEA process using ALD-based tight encapsulation of OLEDs could be very beneficial for developing post processes. The benefits of micrometric electrodes are the reduction of the optical transverse modes

in the device. Regarding the nano-fabrication, the problem of thin residual insulating resist in between the lines of the grating that blocks the current is a more important and priority issue to solve. A solution to consider, is an improvement of the process with RIE cleansing.

To investigate further picosecond OLEDs and conduct more experiments with different materials and with a larger range of excitation voltage in order to explore the Pool-Frenkel law from the dynamical point of view, the amplification of the pulses delivered by the picosecond pulse driver is necessary. This experimental study will benefit from an implementation in the simulation of the dependence on the electric field to the Langevin factor which should confirm the key role of the excitation voltage in a different manner for the different materials.

At the material level, the priority is to reproduce these experiments with other gain materials and more specifically with DCJTb that offers the second largest laser gain coefficient and hopefully different excited state optical absorptions. Ideally the polaronic and triplet absorption cross sections should be measured but as it required a pump-probe setup it is probably a several years long experiment not to be considered in priority.

At the optical level, the priority is to fine tune the Bragg resonance of the DFB micro-cavity to the electroluminescence peak of the gain medium to maximize the amplification. The difficulty lies in the high resolution (<2nm) required during the e-beam lithography step whereas the e-beam spot is 7nm in diameter. The best measurement technique is probably to measure the emission wavelength under optical pumping rather than AFM and SEM measurements.

From the model and simulation point of view, it could be interesting to consider the couple wave theory as an alternative to the transfer matrix formalism to quantify the coupling coefficient of the second order grating.

From the measurement point of view, more efforts must be made in the time-resolved spectral measurement setup. Indeed, so far, the optical signal received by the streak camera is too weak to conduct a systematical temporal and spectral analysis and the signal-to-noise-ratio of the streak camera is to be improved.

The main perspectives to be considered deal with fabrication issues such as electrical continuity of grating, alternative gain materials to be experimented and as a top priority the fine tuning of Bragg resonance to the electro-luminescence peak. Such a research program requires 18 months with a fully operational clean room.

	Electrical	Material	Optical
Model & simulation	- Dynamical spatial distribution of charge		- Coupled wave theory
Fabrication	- <b>Electrical continuity of grating</b> - Electrode width reduction	- <b>Alternative gain materials</b>	- <b>Fine tuning of Bragg resonance to the electro-luminescence peak</b>
Instrumentation & characterization	- Amplified picosecond electrical pulses	- Polaronic and triplet absorption measurement	- Improved signal-to-noise-ratio of streak camera



## References

- [1] S.R. Forrest, «Waiting for Act 2: what lies beyond organic light emitting diode (OLED) displays for organic electronic?», *Nanophotonics*, V. 10, no.1, pp. 31-40, Aug. 2020, doi: [10.1515/nanoph-2020-0322](https://doi.org/10.1515/nanoph-2020-0322)
- [2] A. S. D. Sandanayaka et al., “Indication of current-injection lasing from an organic semiconductor,” *Appl. Phys. Express*, vol. 12, no. 6, p. 061010, May 2019, doi: [10.7567/1882-0786/ab1b90](https://doi.org/10.7567/1882-0786/ab1b90).
- [3] J. Wang, R. G. Sun, G. Yu, and A. J. Heeger, “Fast pulsed electroluminescence from polymer light-emitting diodes,” *Journal of Applied Physics*, vol. 91, no. 4, pp. 2417–2422, Feb. 2002, doi: [10.1063/1.1434545](https://doi.org/10.1063/1.1434545).
- [4] D. Kasemann, R. Brückner, H. Fröb, and K. Leo, Organic light-emitting diodes under high currents explored by transient electroluminescence on the nanosecond scale, *Phys. Rev B* 84, 115208 (2011), DOI: [10.1103/PhysRevB.84.115208](https://doi.org/10.1103/PhysRevB.84.115208)
- [5] H. Nakanotani, T. Oyamada, Y. Kawamura, H. Sasabe, and C. Adachi, “Injection and Transport of High Current Density over 1000A/cm<sup>2</sup> in Organic Light Emitting Diodes under Pulse Excitation,” *Japanese Journal of Applied Physics*, vol. 44, no. 6A, pp. 3659–3662, 2005, doi: [10.1143/JJAP.44.3659](https://doi.org/10.1143/JJAP.44.3659).
- [6] A. C. Chime, S. Bensmida, M. Chakaroun, M. W. Lee, H. Nkwawo, and A. P. A. Fischer, “Electrical modelling and design of ultra-fast micro-OLED with coplanar wave-guided electrodes in ON-OFF regime,” *Organic Electronics*, vol. 56, pp. 284–290, May 2018, doi: [10.1016/j.orgel.2017.12.026](https://doi.org/10.1016/j.orgel.2017.12.026).
- [7] K. Yoshida et al., “245 MHz bandwidth organic light-emitting diodes used in a gigabit optical wireless data link,” *Nat Commun*, vol. 11, no. 1, p. 1171, Dec. 2020, doi: [10.1038/s41467-020-14880-2](https://doi.org/10.1038/s41467-020-14880-2).
- [8] V. G. Kozlov, V. Bulović, P. E. Burrows, and S. R. Forrest, “Laser action in organic semiconductor waveguide and double-heterostructure devices,” *Nature*, vol. 389, no. 6649, pp. 362–364, Sep. 1997, doi: [10.1038/38693](https://doi.org/10.1038/38693).
- [9] A. C. Chime, A. P. A. Fischer, S. Bensmida, J. Solard, M. Chakaroun, and H. Nkwawo, “Analysis of Optical and Electrical Responses of  $\mu$ -OLED With Metallized ITO Coplanar Waveguide Electrodes Submitted to Nanosecond Electrical Pulses,” *IEEE Trans. Electron Devices*, vol. 66, no. 5, pp. 2282–2289, May 2019, doi: [10.1109/TED.2019.2905839](https://doi.org/10.1109/TED.2019.2905839).
- [10] CHIME Alex Chamberlain, “Etude theorique et experimentale de micro-OLEDs rapides sur electrodes coplanaires en regime d'impulsions a haute densite de courant”, Thesis from Universite Paris 13, Decembre 2017
- [11] Hidetoshi Yamamoto, Hiroki Kasajima, Wataru Yokoyama, Hiroyuki Sasabe, and Chihaya Adachi, “Extremely-high-density carrier injection and transport over 12000A/cm<sup>2</sup> into organic thin films”, *Appl. Phys. Lett.* 86, 083502 (2005); <https://doi.org/10.1063/1.1866230>
- [12] A. S. D. Sandanayaka et al., “Indication of current-injection lasing from an organic semiconductor,” *Appl. Phys. Express*, vol. 12, no. 6, p. 061010, May 2019, DOI: [10.7567/1882-0786/ab1b90](https://doi.org/10.7567/1882-0786/ab1b90)